BOEING

NAS-15196
DRL T-1346
DRD MA - 664T
LINE ITEM 3

CR-151555

D180-20689-2

Part 1 Volume II

System Requirements and Energy Conversion Options

(NASA-CR-151555) SOLAR POWER SATELLITE. SYSTEM DEFINITION STUDY. PART 1, VOLUME 2: SYSTEM REQUIREMENTS AND ENERGY CONVERSION OPTIONS (Boeing Aerospace Co., Seattle, Wash.) 344 p HC A05/MF A01 CSCL 22B G3/15

N78-13100

Unclas
53638

DEC 1977
RECEIVED
NASA STI FACILITY

Solar Power Satellite

SYSTEM DEFINITION STUDY

D180-20689-2

Contract NAS9-15196
DRL Number T-1346
DRD Number MA-664T
Line Item 3

Solar Power Satellite

SYSTEM DEFINITION STUDY

Part 1 Volume II

System Requirements and Energy Conversion Options

July 29, 1977

Submitted to
The National Aeronautics and Space Administration
Lyndon B. Johnson Space Center
In Partial Fulfillment of the Requirements
of Contract NAS 9-15196

Approved By: G.R. Woodcock

G.R. Woodcock
Study Manager

Boeing Aerospace Company
Missiles And Space Group
Space Division
P.O. Box 3999
Seattle, Washington

FOREWORD

The SPS systems definition study was initiated in December 1976. Part I was completed on May 1, 1977. Part I included a principal analysis effort to evaluate SPS energy conversion options and space construction locations. A transportation add-on task provided for further analysis of transportation options, operations, and costs.

The study was managed by the Lyndon B. Johnson Space Center (JSC) of the National Aeronautics and Space Administration (NASA). The Contracting Officer's Representative (COR) was Clarke Covington of JSC. JSC study management team members included:

Lou Livingston	System Engineering and Analysis
Lyle Jenkins	Space Construction
Jim Jones	Design
Sam Nassiff	Construction Base
Buddy Heineman	Mass Properties
Dickey Arndt	Microwave System Analysis
R. H. Dietz	Microwave Transmitter and Rectenna
Lou Leopold	Microwave Generators
Jack Seyl	Phase Control
Bill Dusenbury	Energy Conversion
Jim Cioni	Photovoltaic Systems
Bill Simon	Thermal Cycle Systems
Dick Kennedy	Power Distribution
Bob Ried	Structure and Thermal Analysis
Fred Stebbins	Structural Analysis
Bob Bond	Man-Machine Interface
Bob Gundersen	Man-Machine Interface
Hu Davis	Transportation Systems
Harold Benson	Cost Analysis
Stu Nachtwey	Microwave Biological Effects
Andrei Konradi	Space Radiation Environment
Alva Hardy	Radiation Shielding
Don Kessler	Collision Probability

The Boeing study manager was Gordon Woodcock. Boeing technical leaders were:

Vince Caluori	Photovoltaic SPS's
Dan Gregory	Thermal Engine SPS's
Eldon Davis	Construction and Orbit-to-Orbit Transportation
Hal DiRamio	Earth-to-Orbit Transportation
Dr. Joe Gauger	Cost
Bob Conrad	Mass Properties
Rod Darrow	Operations
Bill Emsley	Flight Control
Jack Gewin	Power Distribution
Don Grim	Electric Propulsion
Henry Hillbrath	Propulsion
Dr. Ted Kramer	Thermal Analysis and Optics
Keith Miller	Human Factors and Construction Operations
Jack Olson	Configuration Design
Dr. Henry Oman	Photovoltaics
John Perry	Structures

The Part I Report includes a total of five volumes:

Vol. I	D180-20689-1	Executive Summary
Vol. II	D180-20689-2	System Requirements and Energy Conversion Options
Vol. III	D180-20689-3	Construction, Transportation, and Cost Analyses
Vol. IV	D180-20689-4	SPS Transportation System Requirements
Vol. V	D180-20689-5	SPS Transportation: Representative System Descriptions

Requests for information should be directed to Gordon R. Woodcock of the Boeing Aerospace Company in Seattle or Clarke Covington of the Future Programs Division of the Johnson Space Center in Houston.

Table of Contents

Table of Contents

2.0 POINT-OF-DEPARTURE CONFIGURATIONS

The point-of-departure data came from four primary sources

(1) A silicon photovoltaic SPS from JSC report 11568 (the "green book").

(2) A Brayton thermal engine configuration from the Space-Based Power study, (Contract NAS8-31628). Boeing final report D180-20309-2.

(3) Earth-to-Orbit transportation systems from the Heavy Lift Launch Vehicle study, contract NAS8-32169, Boeing final report D180-20505-2.

(4) Orbit-to-orbit transportation systems from the Future Space Transportation Systems Analysis Study, contract NAS9-14323, Boeing final report D180-20242 (4 volumes).

The SPS systems were re-sized in order that they be normalized to JSC microwave power transmission system efficiencies. Mass properties data for the initial configurations were not normalized, e.g., the JSC configuration included 50% mass growth whereas the Brayton system included none. Mass properties data were normalized during the course of the study.

2.1 SILICON PHOTOVOLTAIC SPS

The silicon photovoltaic configuraton adapted from the JSC study is shown in Figure 2.1. This configuration employs a geometric concentration ratio of 2 (total projected area of solar collection is twice that of the photovoltaic blankets), using v-ridge aluminized Kapton plastic film reflectors, and is sized to provide a total of 10,000 megawatts of electric power at the output of the two receiving antennas on Earth. This configuration employed estimating factors for solar blanket performance and mass properties from the JSC reference data. A mass properties summary for this configuration is provided in Table 2-1.

2.2 SOLAR BRAYTON CYCLE

The Brayton cycle turbomachine provides a rotating shaft output which drives the generators. Sunlight is highly concentrated by a dish-shaped reflective concentrator to provide temperatures high enough to drive the thermal engine. Thermal energy is added to the helium working fluid in heat exchanger tubing located within the cavity absorber. The hot gas is expanded through the turbine, providing power to turn both the compressor and generator. The recuperator exchanges energy across the loop to increase the system efficiency. Waste heat is rejected through a gas-to-liquid heat exchanger to a liquid metal cooling loop; the liquid metal pumps use power drawn from the generators.

SPS-21

- **Silicon at CR = 2**
- **Nominal truss configuration with η = .060**
- **Orientation P.O.P.**

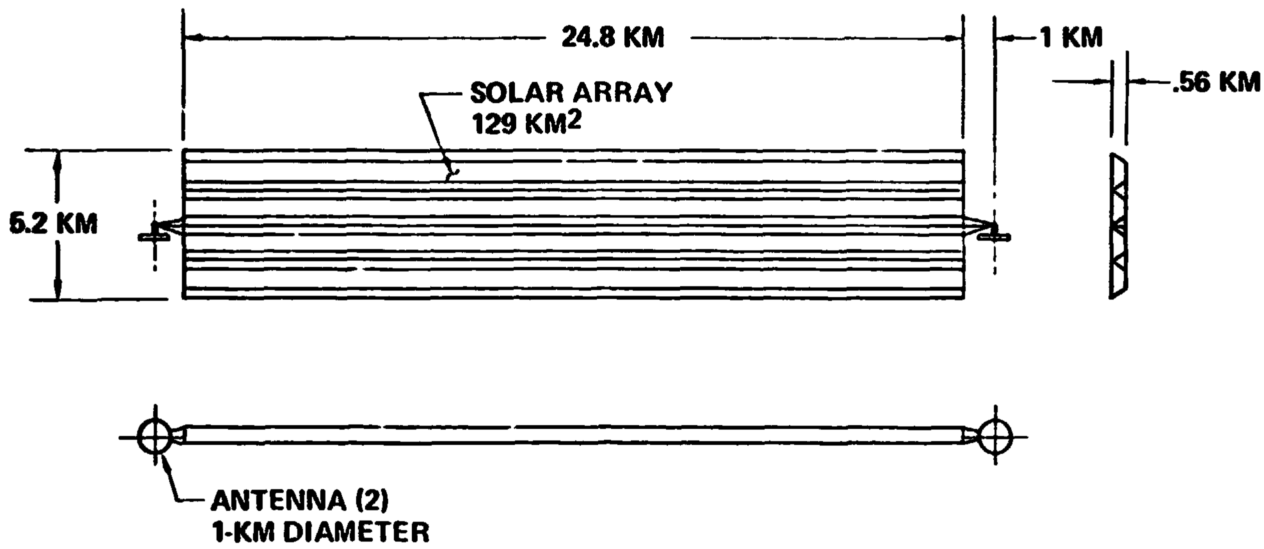

Figure 2-1. Photovoltaic Reference Configuration

Table 2-1. Photovoltaic Reference Configuration

SPS-26

Component	Weight in metric tons (kg/1,000)	Remarks
1.0 Solar energy collection system	(36,616)	128.73 km^2 with η = .060
1.1 Primary structure	2,493	~ to array area
1.2 Secondary structure	189	~ to array area
1.3 Mechanical systems	40	No change
1.4 Maintenance station	85	No change (1,000 m^3 enclosed volume)
1.5 Control	340	200 MT dry weight + 1-yr prop
1.6 Instrumentation/ communications	4	No change
1.7 Solar-cell blankets	25,746	.4 kg/m^2
1.8 Solar concentrators	5,149	.04 kg/m^2
1.9 Power distribution	2,570	~ to 3/2 power of area
2.0 MPTS	15,371	
Subtotal	51,987	
Growth	25,994	50%
Total	77,981	

ORIGINAL PAGE IS
OF POOR QUALITY

The 10,000 volt ac output of the generators is stepped-up to 382,000 volts in transformers; this high voltage facilitates on-board distribution. Step-down occurs in the rotary transformers. Figure 2-2 diagrams the cycle. Figure 2-3 shows the size-normalized SPS configuration and Table 2-2 provides the point-of-departure mass statement.

The radiator system for the baseline Brayton SPS is composed of water heat pipe panels fed by a NaK manifold system. Since the satellite is divided into four modules, the radiator area is divided into four sections. Each section cools 16 Brayton turbomachine sets. The radiator system for a single engine is made up of 184 panels each 10M x 20M. These panels each have four connections which require welds; the manifold sections also require welds. The basic flow diagram of a radiator section is shown in Figure 2-4.

The panel size of 10M x 20M is set by the assumed capability of the heavy lift launch vehicle. Each panel has four 20 cm diameter "throughpipe" stubs extending outward 30 cm. These require welding; they can also be used to hold the panel. 10M lengths of single tapered header are launched prewelded to one quarter of the panels; one quarter of the panels have no headers preattached.

The header/panel assembly takes place on a framework having no gaps larger than 100M. The headers are attached to this frame with swinging links to allow expansion/contraction in the system.

All radiator tubes are stainless steel. The heat pipe panels come preloaded with water. The manifolds and headers must be filled with NaK after all welds are completed.

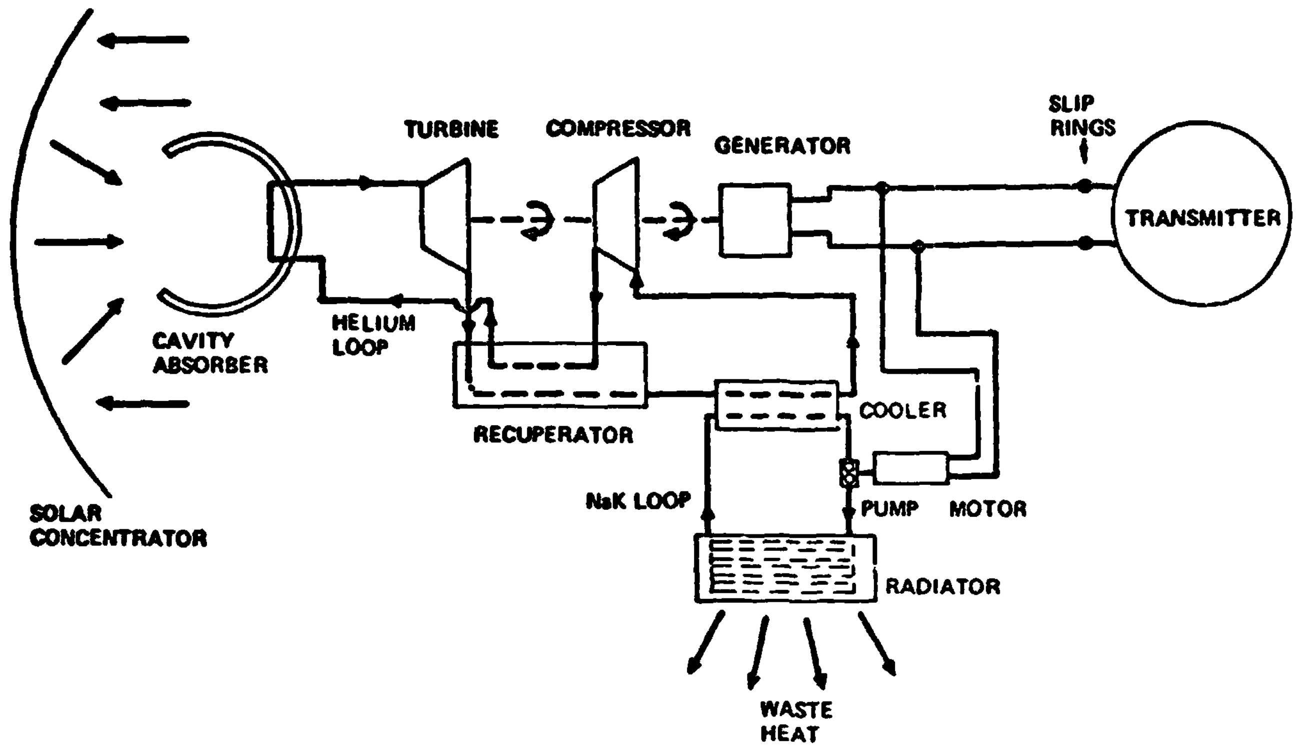

Figure 2-2. Solar Brayton Cycle

SPS-14

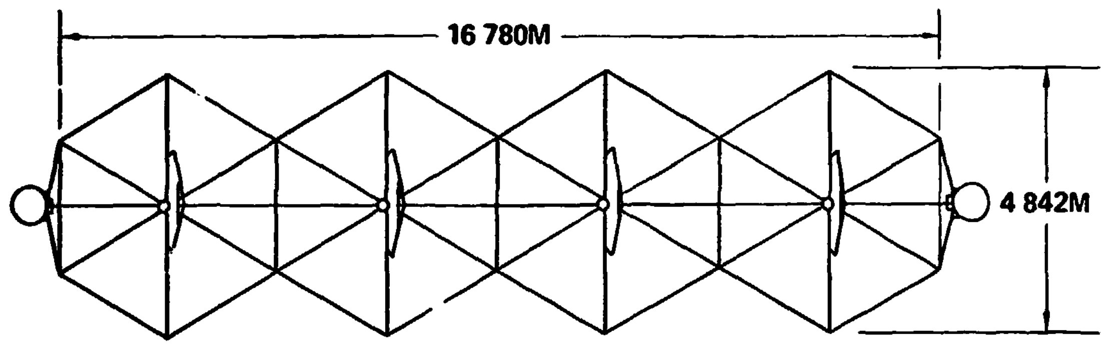

CONCENTRATION RATIO	2,260
OVERALL EFFICIENCY	12.2%
TOTAL AREA	60.93 KM^2
TURBINE INLET TEMPERATURE	1.652°K

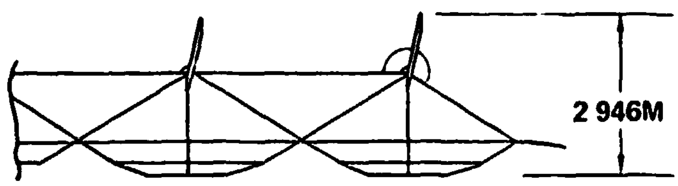

Figure 2-3. Thermal Engine Reference Configuration

ORIGINAL PAGE IS
OF POOR QUALITY

SPS-16

Table 2-2. Brayton SPS Mass Statement

	Weight in metric tons (kg/1,000)
Solar concentrators	
Facets	4,310
Structure	10,460
	14,770
Conductive spine	1,180
Cavity absorber:	
Tubing	3,850
Insulation/skin/frame	1,270
Turbomachines	2,120
Recuperators/coolers	6,250
Generators, with cooling	4,420
Step-up transformer with cooling	2,070
Rotary transformer with cooling	2,630
Rectifier/filter, with cooling	6,110
Radiators with pumps	42,550
Attitude control, stationkeeping	1,550
MPTS	15,371
Total *	102,591

*(no growth)

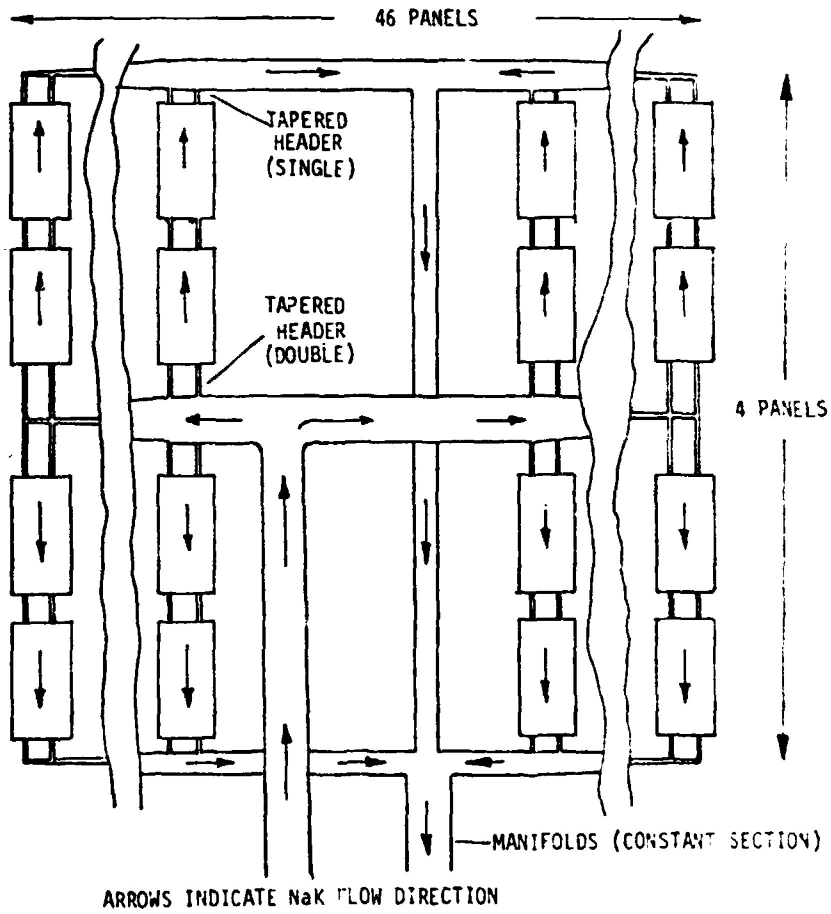

Figure 2-4. Radiator Schematic

Table of Contents

PRECEDING PAGE BLANK NOT FILMED

PRECEDING PAGE BLANK NOT FILMED

2.3 TRANSPORTATION

Point-of-departure transportation systems included Earth-to-orbit and orbit-to-orbit systems.

2.3.1 Earth-to-Orbit Systems

2.3.1.1 Heavy Lift Launch Vehicle

A class 4 ballistic recoverable two stage configuration was selected as the point-of-departure vehicle.

The vehicle consists of two fully recoverable ballistic stages and a non-recoverable payload shroud. The configuration of the vehicle is shown in Figure 2-5 and includes two optional shroud sizes. The longer shroud would handle low density 20 kg/m^3 (about 1 lb/ft^3) payloads, the shorter 100 kg/m^3. For reference, the low density shroud is about the overall length of the first two stages of Saturn V and 1.66 times the diameter. The payload is cantilevered from the forward face of the second stage and the shroud protects the payload during boost. The vehicle's payload capability to 270 nm orbit is 272 000 kg (599,000 lb).

First Stage Design—The LOX/RP-1 first stage of the vehicle is a sea landing ballistic entry stage. The stage is conical in shape to facilitate installation of the engines and their closure doors, to provide a low entry velocity and good stability in the sea. Nine gas generator cycle LOX/RP-1 engines of a new design with a thrust of 20.7×10^6 N each, power the first stage. The LOX and RP-1 tanks provide both propellant containment and ullage space. Pressurization gas is heated GOX for the LOX tank and heated helium for the RP-1 tank. Helium is stored in aluminum tanks within the LOX tank. Three SSME's (ϵ=20) are installed to provide terminal deceleration prior to a sea landing.

Second Stage Design—The second stage configuration is dictated by aerodynamic balance requirements at entry. Seven SSME's provide the main propulsion resulting in a T/W of approximately 0.9 at ignition. Two RL-10 engines provide on-orbit maneuvering and de-orbit thrust. The stage is deorbited by the RL-10 engines and enters ballistically. Drogue deployed parachutes provide initial deceleration and ballutes are used to pitch the stage over for landing "engines first" on deployed legs. Two SSME's provide final braking just before touchdown on land.

2.3.1.2 Crew Transportation Vehicle

The crew transportation vehicle, a liquid booster growth version of the shuttle, was adopted from the FSTSA study. The Space Shuttle Growth concept represents a direct evolution of the current system into an improved version which increases the payload capability to approximately 47 600 kg (105,000 lb) and lowers the operational cost. A representative candidate, shown in Figure 2-6, replaces the SRB's with a liquid propellant recoverable booster and was selected for use in this study. This configuration is a tandem arrangement, series burn vehicle with a ballistically recoverable first stage. The External Tank propellant load of 705 000 kg (1,550,000 lb) has been retained for the series burn ascent mode.

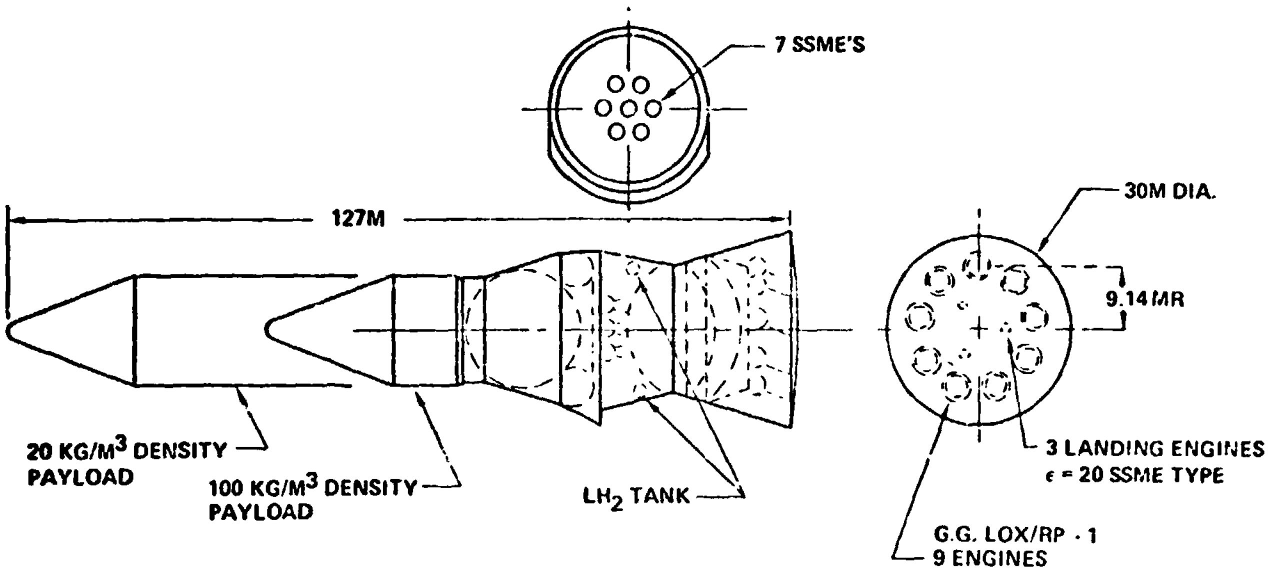

	10^6 KG	10^6 LB
GLOW	6.485	14.300
BLOW	4.405	9.714
ULOW	1.808	3.987
PAYLOAD	0.272	0.599

Figure 2-5. HLLV–Two Stage Configuration

FST-350

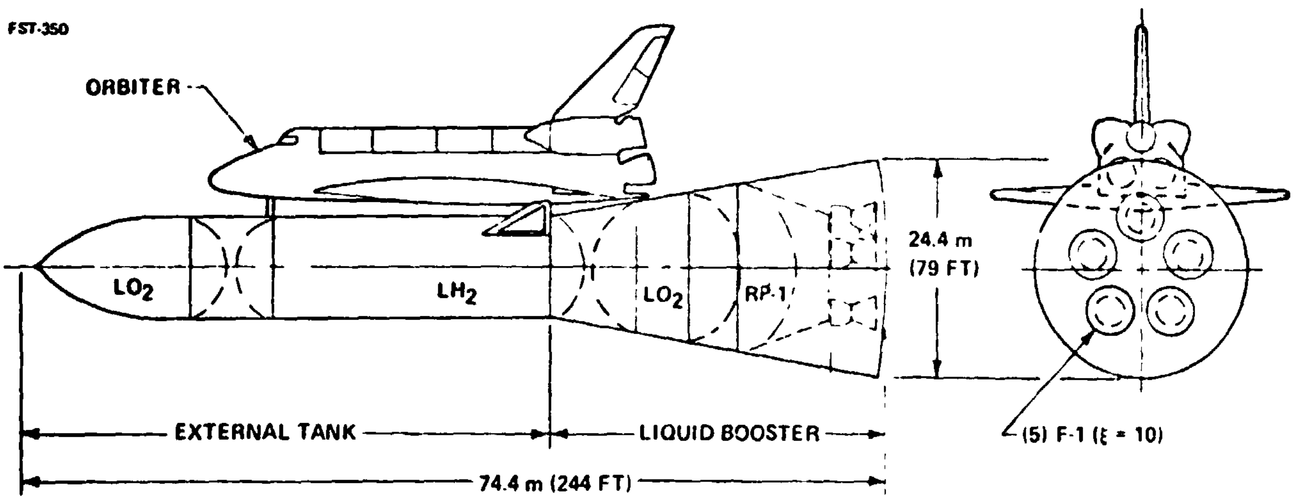

	10^6 KG	10^6 LB
GLOW	2.680	5.896
BLOW	1.805	3.972
W_{P_1}	1.591	3.50
OLOW	0.875	1.924
W_{P_2}	0.705	1.550
PAYLOAD	0.050	0.110

Figure 2-6. Shuttle Growth Configuration

ORIGINAL PAGE IS
OF POOR QUALITY

The LO_2/RP-1 ballistic recoverable booster incorporates a conical shape for aft end forward entry and is powered by five F-1 engines. The sequence of events following F-1 engine shutdown includes the following: the booster separates, doors close over the engine openings in the aft heat shield, the stage is oriented for entry by the reaction control system, and finally 3 modified SSME's used for landing engines are ignited for a powered down-range sea landing. The landing engines provide deceleration to near zero velocity. Nominally, this zero velocity occurs about 3 meters (10 ft) from the sea surface, where the engines are throttled back to a thrust to weight of 0.8 allowing the stage to settle on the surface at a nominal impact velocity of 3m/sec (10 fps). The booster shape provides inherent upright floating stability in the water due to its broad base and aft center of gravity location.

2.3.2 Orbit-to-Orbit Transportation

Orbit-to-orbit transportation is required for crews and for SPS hardware. Crew transportation is assumed to always use a high acceleration mode. High and low acceleration modes were considered for SPS hardware, as illustrated in Figure 2-7. Orbit transfer mission modes are defined by the vehicle acceleration level available and by where the SPS construction is to take place. Electric propulsion systems involve very low acceleration requiring several months to complete the trip from low Earth orbit to geosynchronous orbit. The self-powered option assumed low Earth orbit construction and the separate powered options geosynchronous construction.

The GEO assembly option for SPS requires a large common-stage LO/LH_2 orbit transfer vehicle. Characteristics of the point-of-departure system are shown in Figure 2-8. This vehicle was sized for SPS hardware transportation but can be adapted for crew transportation; for the latter purpose, scaling down in size was to be evaluated. Low thrust separate (independent) power options for SPS hardware transportation were considered in the FSTSA study but were not included in this SPS study as they have no apparent advantage over the LO_2/LH_2 high thrust system. A representative, self-power orbit transfer system installation concept from the FSTSA study is shown in Figure 2-9, assuming division of the photovoltaic satellite into 4 modules for orbit transfer. Some characteristics of the installation at each corner (8 total installations per SPS):

Electric power consumption 172 000 KW_e
Electric Thrust 8750 N (1970 lb_f)
Propulsion hardware mass 835 000 kg (1,840,000 lb)
220 electric thrusters of 1 megawatt peak capacity
38 propellant tanks
22 000 m^2 (240,000 ft^2) of radiator area
Orbit transfer system cost $150 million (per corner)

This illustration shows magnetoplasmadynamic (MPD) propulsion hardware. In the SPS study, emphasis was shifted from MPD to ion thrusters because interface characteristics could be better defined.

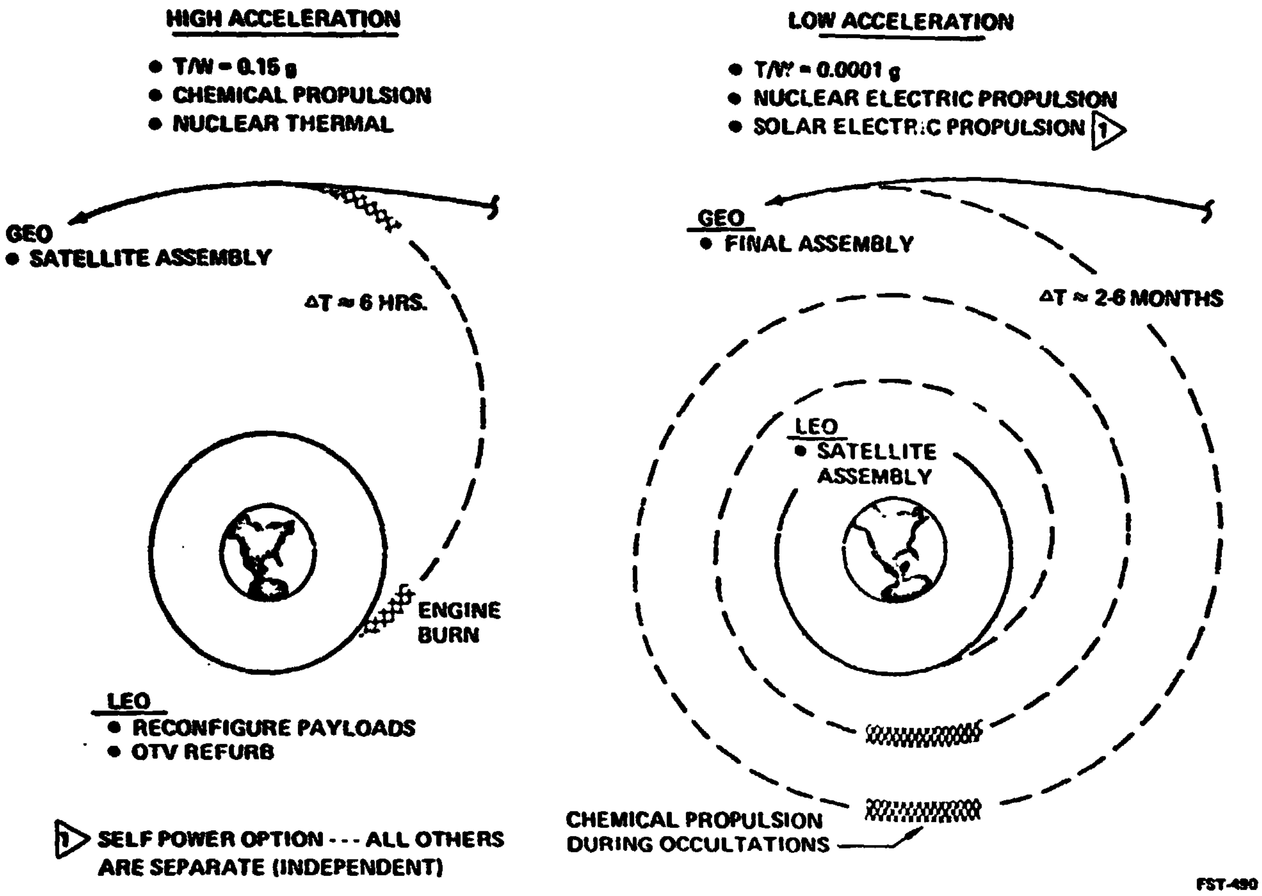

Figure 2-7. Orbit Transfer Mission Modes

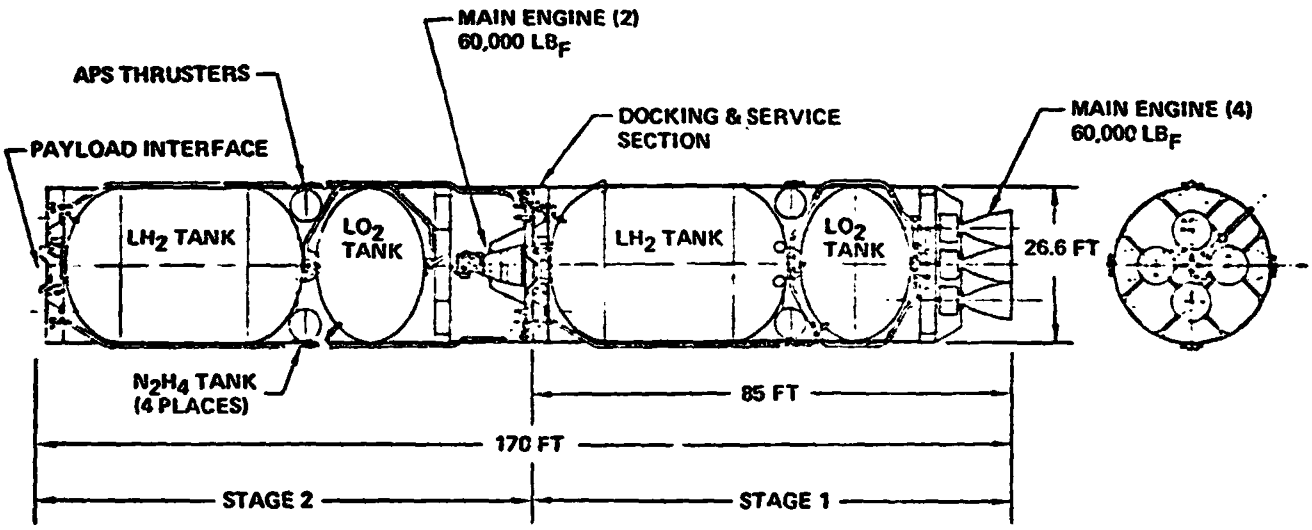

- PAYLOAD CAPABILITY = 500,000 LB
- OTV STARTBURN MASS = 1,100,000 LB
- STAGE CHARACTERISTICS (EACH)
  - PROPELLANT = 490,000 LB
  - INERTS = 45,000 LB

Figure 2-8. SPS GEO Assembly OTV Common Stage LO_2/LH_2

ORIGINAL PAGE IS
OF POOR QUALITY

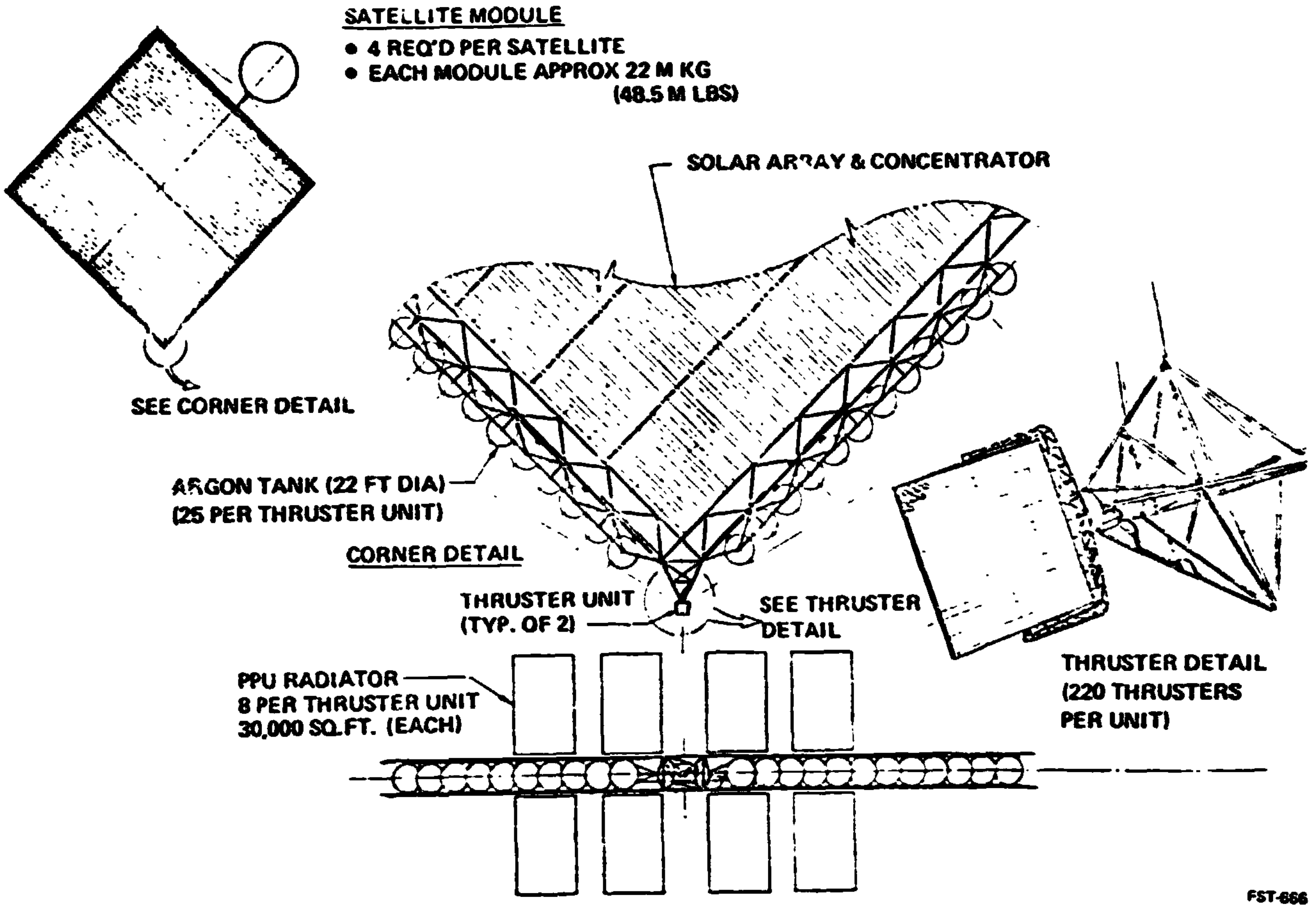

Figure 2-9. Electric OTS Installation Nominal MPD Propulsion System

Table of Contents

PRECEDING PAGE BLANK NOT FILMED

3.0 ANALYSES CONDUCTED

The point-of-departure configurations were analyzed in considerable depth. in addition. the additional energy conversion options shown in Figure 3.0-1 were analyzed. The description of analyses conducted are ordered as follows:

3.1 SPS Requirements 3.2 Photovoltaic Energy Conversion and SPS Configurations 3.3 Thermal Engine Energy Conversion and SPS Configurations	Vol. II
3.4 Construction Analyses 3.5 Transportation Analyses 3.6 Collision Analyses 3.7 Cost Analyses	Vol. III

Each section excepting the transportation analysis section is organized to provide a record of the work accomplished and a description of results. In accordance with the Part I Statement of Work as revised by the add-on task, the transportation effort is to be separately documented. Volume III therefore presents only transportation results.

3.1 SPS REQUIREMENTS

One of the sub-objectives of the SPS System Definition Study is to identify and define requirements on the SPS as a system.

The SPS is intended to serve as a long-range nondepletable energy system. As such it should meet a set of nine general requirements applicable to any such system:

(1) The source of the energy should be nondepletable over time scales of at least hundreds of years. (A solar energy system clearly meets this requirement.)

(2) The system should not be capacity-limited. i.e.. it should be possible to install as much capacity as is desired. (If hydroelectric power could meet this requirement. there would be no energy crisis.)

(3) The system should be usable for baseload. i.e.. continuous service.

(4) The system should produce much more energy over its lifetime than is invested to create and operate the system.

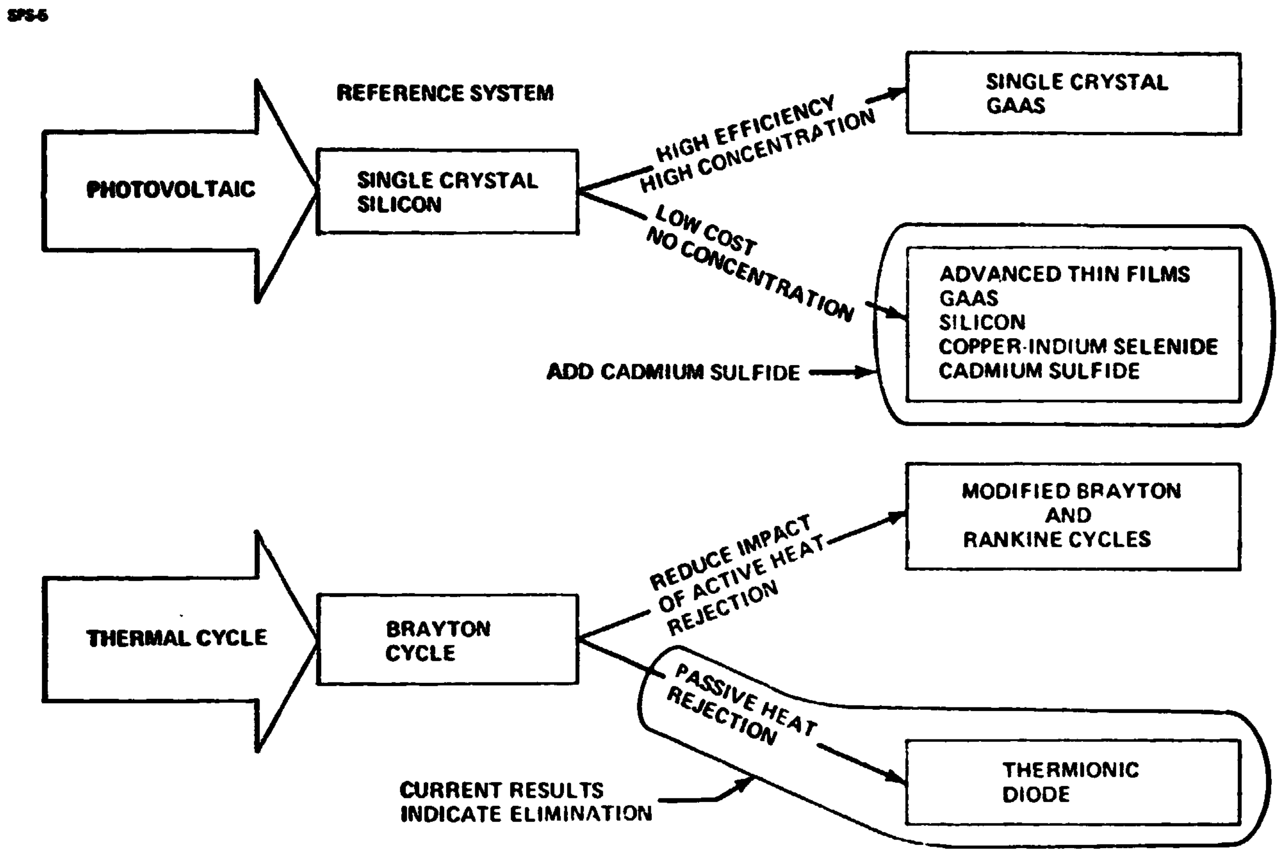

Figure 3.0-1. Energy Conversion Candidates

(5) The system should have acceptable economics. In the simplest terms, it should produce electric power th. consumers and industry can afford to buy.

(6) The system should be environmentally acceptable in all respects, including air pollution water pollution, thermal pollution, hazards, land use, and any other unique factors associated with the particular nature of the system. The SPS, for example, must meet environmental standards (presently not well-defined) as regards communications experience and public exposure to its microwave beam.

(7) The system should not require excessive consumption of critical resources even to install the greatest plausible total capacity. (One SPS option studied about two years ago, for example, requred excessive use of tungsten and was subsequently dropped from further consideration.)

(8) The system should have the potential for compatibility with power grids as regards reliability, availability, power characteristics, plant size, and ability to serve all regions of the world.

(9) The system should admit to an orderly, manageable development program without excessive risk, cost, or calendar time required to reach initial commercial status.

From these can be derived system and design requirements applicable to the SPS. The following partially complete set of requirements will be updated and expanded during Part II of the SPS systems study to provide a more complete high-level specification for SPS systems.

3.1.1 The Solar Power Satellite Concept

Figure 3.1-1 illustrates the basic principle of the Solar Power Satellite (SPS). A power generating system converts sunlight into electric power which is converted into a narrow (total divergence angle of approximately 1/100 degree) microwave beam by the microwave transmitter. These systems are located in equatorial geosynchronous orbit and thus remain in line-of-sight with their associated microwave power receiving stations on the ground. At these stations the microwave power is converted into electricity suitable for integration into the local power network.

Power conversion systems can be either photovoltaic or thermal cycle types, but in either case the electricity generated is to be used to power a microwave power transmission system to deliver the energy to Earth.

The microwave power receiving stations for the SPS consist of a large number ($\sim 10^9$) of dipole antennas with associated rectifiers, integrated in an oval array. Rectification of the received energy to direct current is accomplished by circuit elements which are integral to the dipole antennas. Figure 3.1-2 is an artist's concept aerial view of such an array.

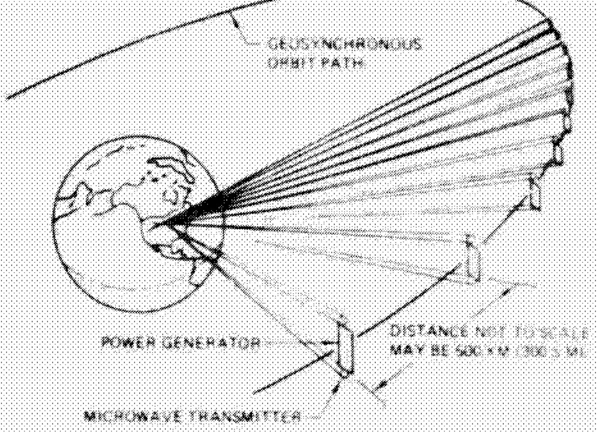

Figure 3.1-1. Satellite Power Stations

Figure 3.1-2. Receiving Antenna

ORIGINAL PAGE IS
OF POOR QUALITY

Since the antenna intercepts and converts nearly all of the microwave energy but is nearly transparent to sunlight, it is possible that agriculture could be accomplished beneath it. Surrounding the antenna is a buffer zone to prevent public exposure to stray microwave radiation more energetic than the continuous exposure standard (assumed to be more than 10 times more stringent than the current standard). These antennas could be placed relatively near demand points (note the city in the background of Figure 3.1-2).

3.1.2 System Requirements Basis

Utilization of space-based power generation could conceivably occur as a legislated action, prompted by the resultant increase of national energy independency, reduced pollution, infinite source, etc. However, about three-fourths of our electric power currently is produced by private utilities, suggesting that economics may be a major factor influencing space-based power incorporation. Thus, market elasticity must be considered, i.e., sales will be influenced by the price of the product.

Many factors have contributed to the increases in installed capacity (kW) and consumption (kWh).

(1) Population growth–from 1956 to 1973 the rate was 1.3% per year. The rate is predicted to decline to 0.8% in the 1973 to 1990 period. Resultant populations, millions (1):

1964	192
1974	212
1984	232
1995	252

(2) Rising standard of living–disposable income per person has been increasing; the trend is expected to continue (1):

Year	1976 $/year per person disposable income
1964	3740
1974	5287
1984	6784
1995	8542

(3) Relative reduction in electricity cost–as pointed out by Hannon (2), the cost of electricity energy has reduced relative to labor costs (electricity does not strike for higher wages). It thus seems appropriate that about 40% of our national electricity use is for process heat and industrial power while only 9% goes for lighting (3). In the following plot (Figure 3.1-3) from (2)

the ratio of manufacturing workers hourly wage to industrial kWh cost of electricity is represented as 1.0 in 1951 on the ratio index scale.

This item and the previous one are ultimately related, i.e., the rising standard of living is in part explainable in terms of the wage/electricity ratio. Thus minimizing energy costs is important to maintaining a high standard of living.

Figure 3.1-4 shows trends in national installed generating capacity. Note the difference between the 1973 and 1974/76 forecasts. (There was no significant change between 1974 and 1976.) It is significant that the 1973 article in (5) was titled "Utilities Plan Expansion to Meet Records Demands" and that the 1974 title in (1) was "Slower Growth in Sales and Peaks Sparks Sharp Cut in Expansion Plans and Cost."

An explanation for the change in forecast is given in (1): at the end of 1973 an increase of 33,100 MW in the summer peak requirement was forecast. An increase of 43,607 MW in capacity was planned for 1974 to meet this peak, retire some obsolescent units and raise the national reserve margin to 21%. However, energy conservation (partly from recession-caused production decreases) cut the load growth, to only 15,530 MW, resulting in a generating margin of 26.2%. Mild winters in the 1974-76 period also contributed to the large reserve margins. (The severe 1977 winter appears to be reversing the trend; statistics are not presently available.) Consequently some of this margin can be applied to subsequent growth needs, depressing the growth curve. Figure 3.1-5 shows variation of this margin with time. 18% is generally considered by utilities to be desirable; the margin was 16.6% in 1969 when reductions and curtailments occurred.

Some authors have forecast and/or recommended very low or even zero energy growth rate. Hannon (2) recommends a more labor intensive economy, i.e., one in which, in essence, human muscles perform rather than electric motors, thereby making more (lower paying) jobs. One factor is the growing labor pool resulting from population growth. If the birth rate instantly dropped to zero, the labor pool would still increase in size for two decades.

A more rational view is that energy growth is essential to economic health. Federal Energy Administrator Zarb has recommended a 3.5% to 4.5% installed capacity growth rate for 1975 to 1985 (6). This range was plotted in Figure 3.1-4.

It is possible for national energy consumption to remain constant while the amount of electricity generated increases. In 1968, 21.2% of the energy expended went to produce electricity. The last column shows a potential of 70.7% utilization without significant changes in energy use technology; for example, electricity could be used for all process heat.

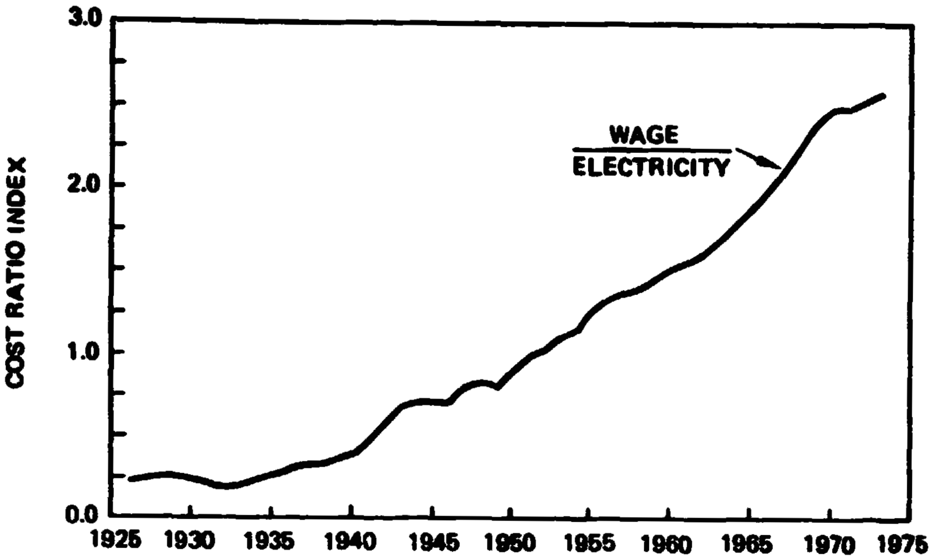

Figure 3.1-3. Labor Electricity Cost Ratio

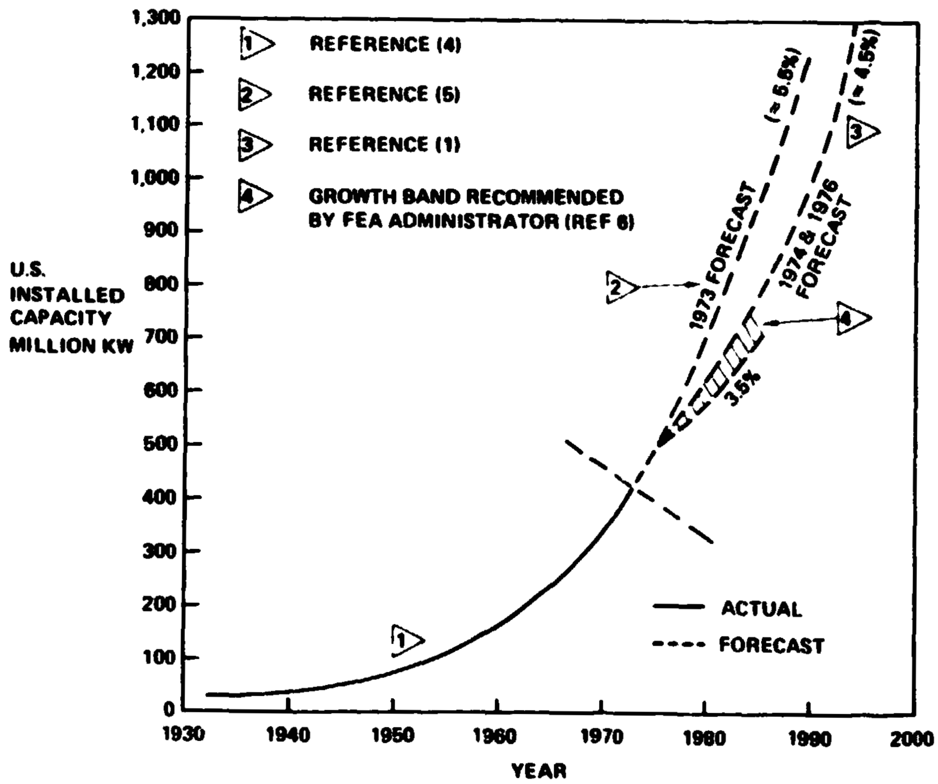

Figure 3.1-4. Growth in U.S. Installed Capacity

ORIGINAL PAGE IS
OF POOR QUALITY

Current Predictions

Figure 3.1-6 shows historical (4) and forecasted (1 and 5) annual additions to U.S. installed capacity. Note that these are net additions after retirement of obsolete capacity. Actual sales are 1% to 2% greater. Again note the dramatic changes resulting from the capacity margin produced by reduced electricity consumption. The projected 1973 addition rate for the year 1990 was 64 GW (64000 MW); the 1974 projection is for 53 GW per ye r for 1990. The 1976 forecast shows a significantly reduced growth rate beyond 1990, and a greatly reduced nuclear growth rate.

In 1973, nuclear generated electricity provided 4.8% of our capacity. This was 16 years from the initial power reactor and nine years after the first "commercially competitive" reactor of 1964. In the 16 years from 1964 until 1980 nuclear energy is forecast to grow to capture 13.6% of the electric power market. In another 15 years it will represent 30% of our capacity (but provide over 50% of the kWh) (1). It thus appe reasonable to assume early market capture rates of 15% for SPS's (assuming equivalent economics). In England, nuclear capacity was added at approximately five times the percentage rate of the United States. Should superior economics be achieved, i.e., very low costs for space based power, the capture rate could be even higher.

Other factors could also accelerate space power incorporation, such as nuclear power moratoriums or legislation which levies the full "social" costs of fossil fuel usage on the electric power customer. The current social cost for the use of coal, for example, may be 13 to 15 mills/kWh (7).

REFERENCES

(1) Electrical World, September 15, 1974.

(2) Hannon, B., "Energy Conservation and the Consumer," Science, 11 July 1975 (Vol. 189, No. 4197).

(3) Hauser, L. G., "Future Trends in Energy Supply," 1974 Textile Industry Conference.

(4) Moody's Public Utility Manual, 1974.

(5) Electrical World, September 15, 1973.

(6) "World News Beat," Electrical World, July 1, 1975.

(7) Morgan, M. G., Barkovich, B. R. and Meier, A. K., "The Social Costs of Producing Electrical Power from Coal: A First Order Calculation," IEEE Proceedings, Vol. 61, No. 10, October 1973.

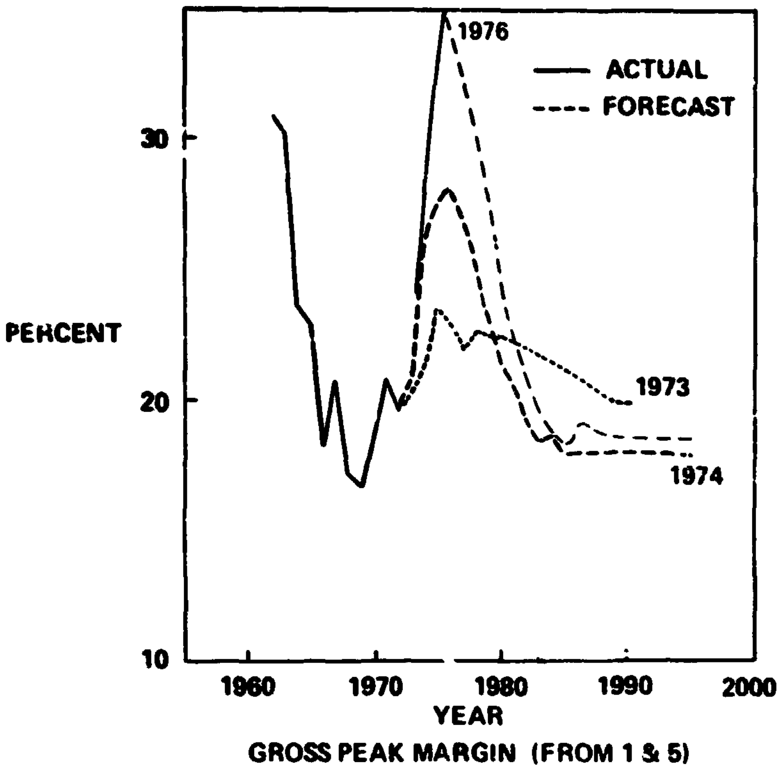

Figure 3.1-5. U.S. Capacity Margin

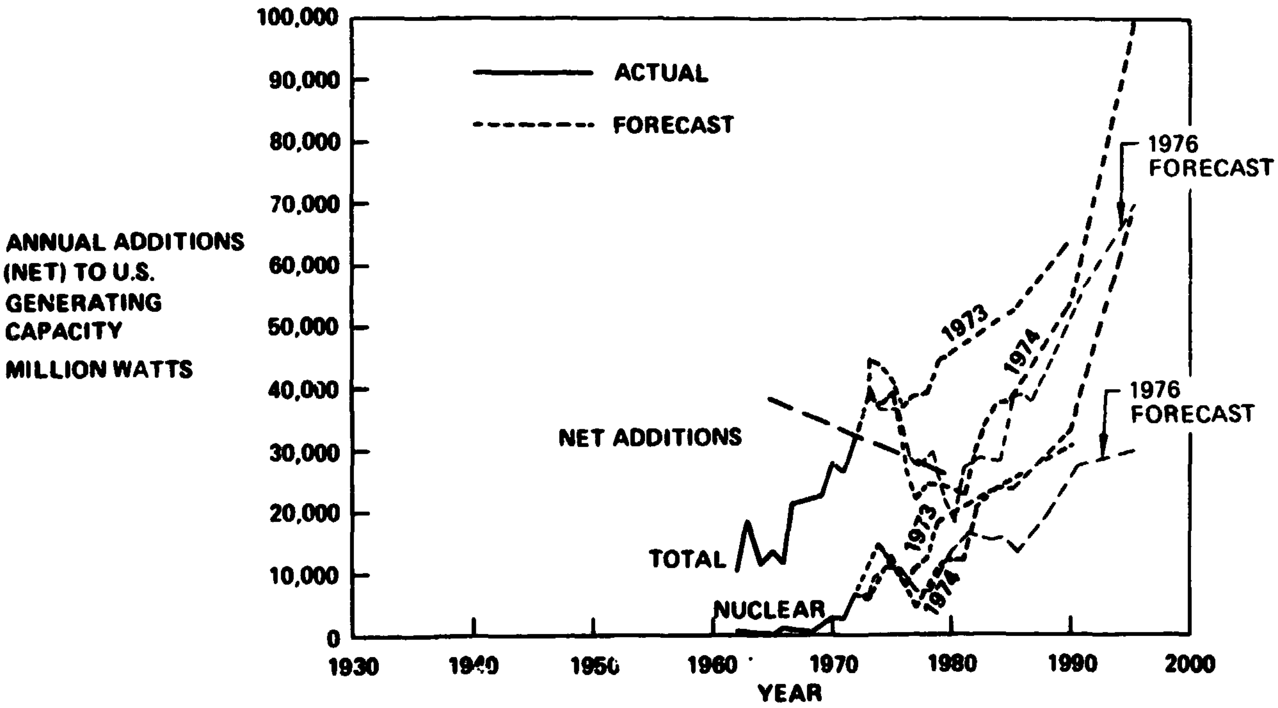

Figure 3.1-6. Annual Additions to Installed Capacity

ORIGINAL PAGE IS OF POOR QUALITY

3.1.3 SPS System Requirements

This is a preliminary draft of SPS system requirements. Requirements are organized according to the SPS system work breakdown structure. This WBS is also to be used for system descriptions and cost data collection. (The WBS is being updated in Part II of the study.)

WBS 1.01 SPS System

1.01-1 The SPS system shall provide electric power for commercial utilization within the United States. Power output of the associated individual ground installations shall be at 5 GW (5×10^9 Watts) each, with output form as required by local power network.

1.01-2 The power source for these ground stations shall be located in geostationary orbit, with power transfer by a microwave link.

1.01-3 The system concepts for these programs, including facilities, launch equipment, etc., shall provide for annual system additions in accordance with JSC scenario "B" (Figure 3.1-7). The addition rate shown in the figure shall be interpreted as a net capacity addition rate. Power output degradation effects shall be compensated such that the figure represents actual total realizable output versus time with seasonal variations averaged over a year.

1.01-4 Nominal life of the satellite and ground receiving stations shall be 30 years assuming appropriate maintenance. This lifetime shall be used for investment amortization in cost and economics studies. The system shall be designed to allow indefinite extension of operating life with appropriate refurbishment.

1.01-5 The system design philosophy shall be to minimize consumer costs for electric power derived from this source, assuming JSC Scenario B as a reference capacity addition program and assuming that all developmental and operating costs, including transportation and other support costs, are recovered from operating revenues. (This requirement is not intended as a recommended pricing policy.)

1.01-6 The nominal system total capacity design limit shall be set at 1000 GW for North America (about ten times the total installed electrical generating capacity for the U.S. in 1976). SPS satellites must therefore be capable of operating at inter-satellite separation distances as small as 50 km. This requirement applies to stationkeeping capability, inter-satellite uplink RF interference, and propulsion jet interference between satellites.

1.01-7 Microwave Safety the design standards following shall not be construed as reflecting any currently applicable standards or as a recommendation or forecast as to any possible future standards. They represent stringent design requirements containing considerable margins to allow for unforeseen effects.

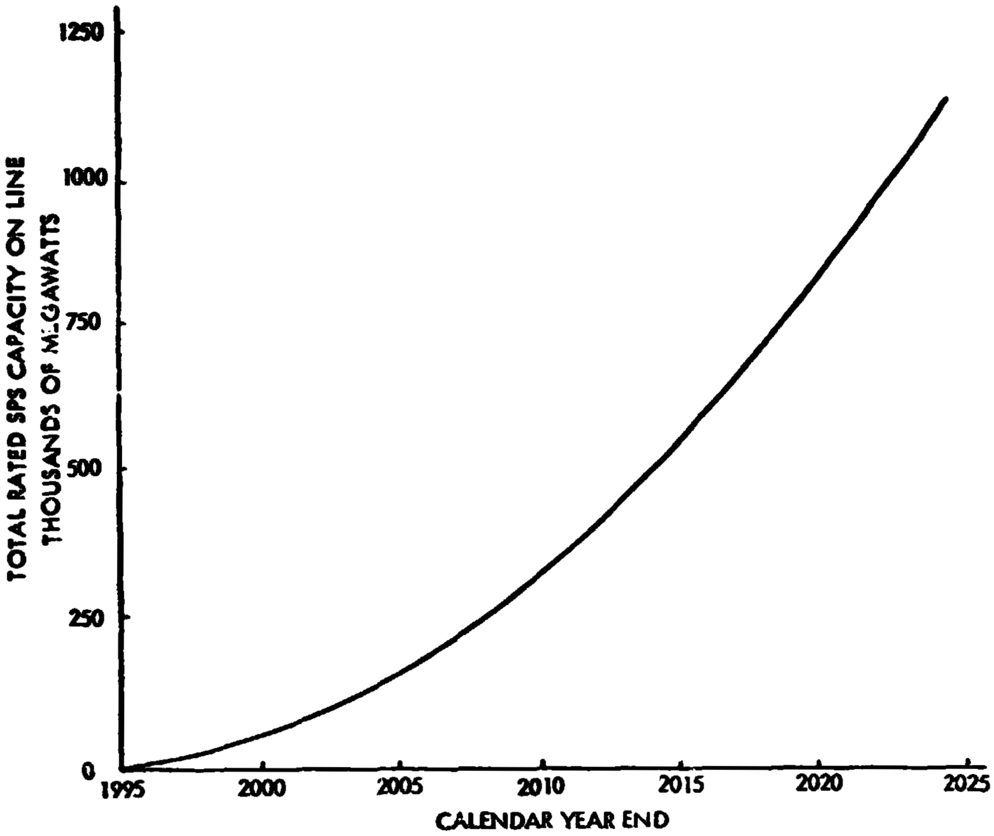

Figure 3.1-7. SPS Capacity Addition JSC Scenario

ORIGINAL PAGE IS
OF POOR QUALITY

1.01-7.1 Microwave flux density in the ionosphere shall not exceed 25 mw/cm^2. (This requirement may be modified upward or downward at such a time as experience warrants.)

1.01-7.2 Microwave flux density outside the restricted-access receiving site area shall nowhere exceed 0.1 mw/cm^2 with a nominal design goal of 0.01 mw/cm^2. The system shall be designed to minimize or eliminate restricted access land area not actually used for the power receiving antenna.

1.01-7.3 The *average* microwave flux density (outside the restricted receiving site areas) over the U.S. or any other large populated area resulting from operation of the system at rated capacity (5000 GW) shall not exceed 0.01 mw/cm^2.

1.01-7.4 Microwave flux exposure limits for system workers shall be set at 1 mw/cm^2 for continuous (i.e., 8 hour workday) exposure and at 10 mw/cm^2 for exposure periods not to exceed 1 hour per 24-hour day. Personnel working in areas of flux higher than these limits shall be suitably protected, e.g., by a Faraday shield.

1.01-8 System sizing shall be referenced to beginning-of-life conditions with any seasonal variations averaged over a year. The systems shall provide suitable means to maintain nominal output rating up to the beginning-of-life rating.

1.01-9 Energy Conversion option comparisons shall use the following microwave power transmission link performance as a reference (Table 3.1-2). (These figures shall not in any way be construed as firm requirements or design guidelines on the microwave system.)

WBS 1.01.01 Solar Power Satellite (SPS)

1.01.01-1 Orbit

1.01.01-1.1 The nominal operational orbit for SPS's shall be circular at 0° inclination and 35786 km altitude (radius=42164 km). This is the geostationary orbit condition; each satellite will nominally remain stationary over its assigned longitude point on the Earth's equator.

1.01.01-1.2 The orbit shall remain trimmed such that longitude drift due to perturbing effects does not reduce inter-satellite distance below 50 km for a nominal spacing of 75 km. Nominal orbit error allocations are: out of plane 2.2° equivalent to 15.5 km longitude error; eccentricity 0.0004, equivalent to 16.87 km longitude error; long-period drift 10 km. These allocations RSS to 25 km total random error. To the extent that the satellites can fly formation, e.g., in a cooperatively perturbed mode, the longitude of individual satellites can exceed 25 km from the nominal assigned location.

Table 3.1-2. Reference MPTS/MCRS Nominal Efficiencies

Antenna power distribution	.98
DC-RF conversion	.87
Phase control	**
Waveguides (I^2R)	.98
Mechanical alignment	.98
Atmosphere	.98
Energy collection	.88
RF-DC conversion	.90
Power interface	.99
Overall	.629

*From JSC 11568, fig. IV-A-1-1, "SPS Efficiencies"

**Included in energy collection

ORIGINAL PAGE IS
OF POOR QUALITY

1.01.01-1.3 SPS assigned longitudes shall be clustered together with a minimum nominal spacing of 75km (0.102°) in order to preserve open spaces in geosynchronous orbit for other types of satellite services.

1.01.01-2 SPS's shall be designed to have sufficient attitude control torque capability and structural integrity to recover from a loss-of-attitude-control event, i.e., to reorient from a gravity gradient stable attitude to nominal flight attitude.

1.01.01-3 SPS's shall be designed to a capacity factor of 90%, including planned and unplanned outages and degradation due to failed elements. The 90% shall be applied to nominal output if all SPS elements are functioning. Output degradation, e.g. solar cell degradation, due to natural environment effects or aging is not charged against capacity factor.

1.01.01-4 No single failure or causative result thereof shall cause output from either SPS antenna to fall below 50% of nominal. This requirement does not apply to shadowing by the earth or by other SPS's.

1.01.01-5 Partial shadowing by an adjacent SPS shall not cause disruption of operation of or damage to, an SPS. Loss of output appropriate to the extent of shadowing is, of course, acceptable.

1.01.01-6 Each SPS shall have sufficient onboard storage capability for all necessary consumables to sustain a minimum of one year of normal operations without resupply. This requirement includes support of any crew that would be resident onboard an SPS either intermittently or continuously. (*Resident onboard* implies living aboard the SPS. Crews living aboard support vehicles or systems are not included).

1.01.01-7 The SPS shall be designed for construction in space from prefabricated elements and other materials delivered to the space construction site(s) from earth by a space transportation system. Design features and construction methods shall support the minimum cost requirement (1.01-5).

1.01.01-8 The SPS shall be capable of highly controlled startup such that lockon and flux pattern control of the microwave power transmission system can be verified at low power levels before ramping up to full power. The entire startup and rampup process shall be controllable to maintain complete control of the power beam and avoid damage due to transients or out-of-tolerance operations of any SPS elements. Partial or complete shutdown shall be similarly controllable. This requirement shall also apply to any possible transient illumination patterns resulting from partial or complete shadowing of the SPS.

1.01.01-9 The SPS shall be designed to the following ionizing radiation environments:

High Energy Particles

For the high energy trapped electrons and portons, the electron flux maps AE-4[1] and AE-6[2] and the proton flux maps AP-5[3], AP-6[4], and AP-7[5] shall be used. The anticipated AP-8 proton flux map shall be used when it becomes available. These flux maps, described in a series of publications by J. Vette and co-workers at the National Space Science Data Center, are the standard high energy trapped particle data source.

The solar proton environment expected at GEO has been predicted by a number of workers, but the model of J. King[6], and the survey and predictions of W. R. Webber[7], [8] have gained wide usage in the technical community. These data sources shall be used to define both an expected and a worst case solar proton environment.

Low Energy Particles

Electrons of energy less than 250 keV, and protons below 0.5 MeV are not treated in the trapped particle flux maps and must be defined from the research literature. The S/C charging article by DeForrest[9] is typical of the data available in this area that shall be used.

Ionosphere Environment Definition

The NASA Space Vehicle Design Handbook ionosphere environment shall be used.

References for Requirement 1.01.01-9

1. G. Singley & J. Vette. A Model Environment for Outer Zone Electrons. NSSDC-72-13. 1972.
2. M. Teague. K. Chan. J. Vette. "AE6: A Model Environment of Trapped Electrons for Solar Maximum". NSSDC 76-04. May. 1976.
3. J. King. "Models of the Trapped Radiation Environment. Vol. IV. Low Energy Protons". NASA SP-3024, 1970.
4. J. Larine and J. Vette, Models of the Trapped Radiation Environment. Vol. V. Inner Belt Protons. NASA SP-3024, 1970.
5. J. Larine and J. Vette. Models of the Trapped Radiation Environment, Vol. VI. High Energy Protons. NASA SP-3024. 1970.
6. J. King. "Solar Proton Fluences as Observed During 1966-1972 and as Predicted for 1977-1983 Space Missions". NASA Goddard X-601-73-324. 1973.
7. W. R. Webber. "An Evaluation of the Radiation Hazard Due to Solar Particle Events". Boeing Document D2-90469. 1963.
8. W. R. Webber. "An Evaluation of Solar Cosmic Ray Events During Solar Minimum". Boeing Document D2-84274-1. 1966.
9. S. DeForrest. "Spacecraft Charging at Synchronous Orbit". J. Geophys. Res. 77. 651, 1972.

ORIGINAL PAGE IS
OF POOR QUALITY

WBS 1.01.01.01 Energy Collection & Concentration Subsystem
(Note: Some SPS concepts may not include this subsystem)

1.01.01.01-1 The energy collection subsystem shall be designed to avoid variation in concentrated sunlight intensity that would damage or seriously interfere with operation of, the energy conversion subsystem.

1.01.01.01-2 The energy collection subsystem shall actively or passively compensate for variations in sun elevation due to satellite attitude, e.g., flying perpendicular to the orbit plane (POP). The energy collection subsystem shall also compensate for expected structural deformations in the SPS due to space environment and other operational factors.

1.01.01.01-3 The energy collection subsystem shall be designed to provide the concentration of ambient sunlight required by the energy conversion subsystem, after accounting for losses associated with reflectivity, scattering, and geometric errors. The *concentration ratio* shall be defined as the ratio of (average concentrated solar flux per unit area of absorber surface)/(ambient solar flux). The *geometric concentration factor* shall be defined as the ratio of total projected area of sunlight intercepting surface to total absorber suface area. The ratio of concentration ratio to geometric concentration factor is the energy collection efficiency.

1.01.01.01-4 The energy collection subsystem shall be designed to preclude arcing and/or other potentially damaging effects associated with electrostatic charge buildup due to the geosynchronous orbit natural or induced environments.

1.01.01.01-5 The energy collection subsystem, if it uses actively-controlled elements, e.g., for high concentration ratios, shall

a. employ distributed independent control and actuation systems such that no single failure will significantly degrade total output;

b. not be based on maintenance of geometric precision of the main SPS structure to achieve the required optical performance;

c. employ control passband frequencies selected to not interfere with overall attitude control of the SPS.

WBS 1.01.01.02A Energy Conversion Subsystem (Photovoltaic)

1.01.01.02A-1 The photovoltaic system shall be modularized into space installable blankets of TBD KWe nominal generating capacity each at beginning of life under monimal operating conditior including applicable sunlight concentration. The nominal voltage output of each module shall be 44,000 volts. (Value subject to change).

1.01.01.02A-2 The photovoltaic system shall employ radiation shielding and/or annealing of the photovoltaic converters as appropriate to requirement 1.01-5 (minimum power cost).

1.01.01.02A-3 Individual converters (cells) shall be wired into the blanket array such that either open or short-circuit failures of individual converters do not cause 1) loss of array output disproportionate to the loss of the individual converter's contribution, or 2) arcing.

1.01.01.02A-4 The photovoltaic system shall be designed such that a blanket module and/or its switchgear can be isolated from the operating onboard electric power distribution system, and its generated electrical potential reduced to safe levels, so that it may be serviced without shutdown of the entire energy conversion subsystem.

WBS 1.01.01.02B Energy Conversion Subsystem (Thermal Engine)

1.01.01.02B-1 The thermal engine systems shall be modularized into space installable elements, with a nominal generating capacity per machine set of TBD kw_e. The nominal DC voltage output of each machine set shall be controllable within the range 40,000 to 45,000 volts at rated power output. (Voltage values subject to change.)

1.01.01.02B-2 Individual generators shall be provided with controls and connected to the onboard power distribution system such that planned or unplanned shutdown of an individual generator does not impair operation of the SPS except for loss of the output contributed by that generator.

1.01.01.02B-3 Individual engine generators shall be designed to allow service, including entry to fluid systems, without shutdown of functioning engine-generators, except in the case where access to the interior of the cavity absorber may be required.

1.01.01.02B-4 Fluid systems shall include scavenging and/or inventory control such that intentional or unintentional breaches of fluid system integrity will not cause excessive loss of fluid. Such fluids losses as do occur shall be controlled to the degree necessary to prevent interference with or degradation of SPS operation, e.g., by vacuum plating, or electrical arcing.

1.01.01.02B-5 The cavity absorber assembly shall include light shields as necessary to divert stray concentrated light (i.e., cavity aperture spillover) so that it does not induce a deleterous thermal environment in the turbogenerator area and does not interfere with equipment service operations. The light shields shall not present false targets to the solar concentrator control systems.

1.01.01.02B-6 The thermal engine energy conversion system shall be capable of surviving without damage a maximum-duration geosynchronous occulation (72 minutes) when entering the shadow cold, i.e., after an extended shutdown period, and then reaching full power within one hour.

1.01.01.02B-7 Normal restart after occulation, i.e., upon entering the shadow hot, shall reach full power within five minutes after leaving the shadow.

1.01.01.02B-8 The net angular momentum due to rotating machinery and circulating fluid for any SPS module shall be no more than 10% of that angular momentum value represented by rotating the *entire* module one revolution per day about a principal axis parallel to the turbogenerator shafts. (This requirement is intended to minimize effects of machinery momenta on the flight control system.)

WBS 1.01.01.03 Power Distribution System

1.01.01.03-1 The power distribution system shall conduct DC electrical power from the energy conversion system interfaces to the transmitter rotary joint interfaces. (It is assumed that there are two 5-GW antennas and associated rotary joints per SPS.) The distribution system shall supply the following nominal voltages and currents to the rotary joint interface.

Bus A 40,800 volts at 138,600 amps (5.65 GW)

Bus B 38,700 volts at 59,400 amps (2.30 GW)

A common return for these two supplies shall be provided.

This requirement is based on estimated Klystron characteristics described in the following, and is subject to revision.

1.01.01.03-1 Supporting Rationale Reference Klystron Parameters

The following are the proposed parameters for the reference DC to RF converter:

Tube Type: Klystron - Depressed Collector
RF Power Output: 70.9 KW
Efficiency: 0.87
Number of Depressed Collectors: 3
Modulating Anode Voltage: 21.052.5V±0.5%
Body Anode Voltage: 42.105V±0.5%
Body Anode Current: 0.11 Amperes
Beam Current: 2.20 Amperes

TUBE ELEMENT REQUIREMENTS

ELEMENT	VOLTAGE (VOLTS DC)	CURRENT (AMPERES)	POWER (WATTS)	% POWER
COLL. A	40,000±5%	1.320	52,800	64.8
COLL. B	37,895±5%	.616	23,343	28.7
COLL. C	4,211±5%	.154	648	.8
REG.ANODES	42,105±0.5%	.110	4,632	5.7
HEATER			30	
TOTALS	N/A	2.200	81,453	100.0

The tube output was increased to 70.9 KW in order to bring the collector voltages up to near 40 KV. The proposed method for obtaining the required converter voltages is as follows:

VOLTAGE	SOURCE
Collector A	From power generation source @ 40 KV ± 5%
Collector B	From power generation source @ 37.9 KV ± 5%
Modulating Anode Body Anode Heater Collector C	From power processors on antenna. Power source for processor is 40 KV from collector A supply.

A simplified description is shown in Figure 3.1-8.

1.01.01.03-2 The power distribution system shall employ dedicated aluminum conductors (not part of main structure) which are passively cooled by radiation to free space.

1.01.01.03-3 The power distribution system shall be sized to minimize the combined mass of itself and the remainder of the SPS, considering power distribution system mass, dissipative losses, and variations of resistivity with operating temperature.

1.01.01.03-4 The power distribution system shall have switching and control equipment as necessary to isolate the rotary joint and power transmission system from energy conversion system startup and shutdown transients. This requirement may be in part met be delayed activation of power distribution provided that the delay is not greater than 10 minutes.

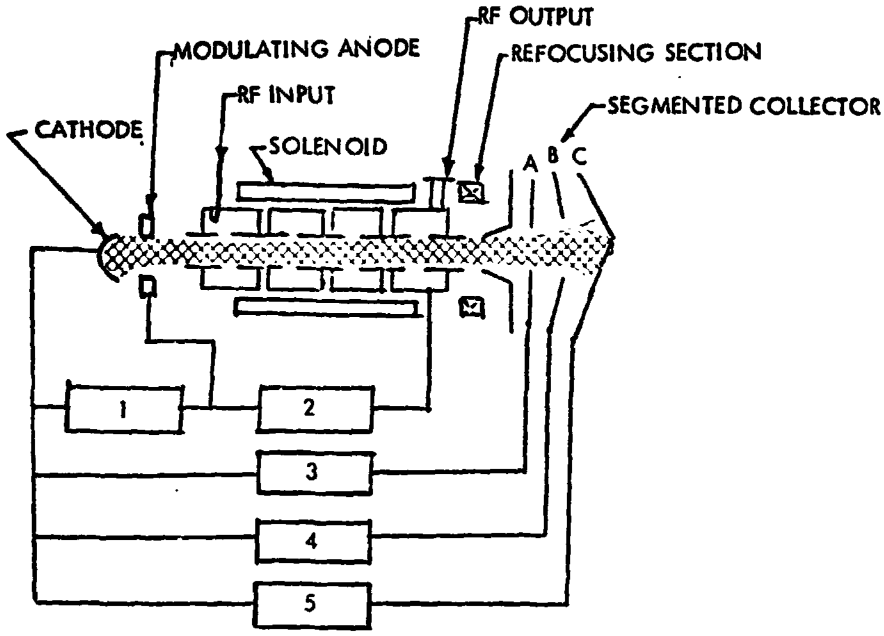

DEPRESSED COLLECTOR OPERATION (EST.)

CATHODE BODY $V_o = 42.1$ KV

PERVEANCE $K = .25 \times 10^{-6}$

TOTAL CURRENT = 2.20 AMPS $= I_o$

RF POWER OUTPUT - $.765\ V_oI_o = 70.9$ KW

THREE SEGMENTED DESIGN

1. MOD. ANODE SUPPLY	$.5V_o$, $.05I_o$	$= .025\ V_oI_o$
2. BODY SUPPLY -	$.5V_o$, $.05I_o$	$= .025\ V_oI_o$
3. COLLECTOR A =	$.95V_o$, $.60I_o$	$= .570\ V_oI_o$
4. COLLECTOR B	$.90V_o$, $.28I_o$	$= .252\ V_oI_o$
5. COLLECTOR C	$.10V_o$, $.07I_o$	$= .007\ V_oI_o$

TOTAL BEAM POWER $.879V_oI_o$

NET EFFICIENCY = .765/.879 = 87%

Figure 3.1-8. SPS Klystron Design Estimate

ORIGINAL PAGE IS
OF POOR QUALITY

3.2 PHOTOVOLTAIC SPS CONFIGURATION ANALYSIS

This section deals with the analyses that supported definition of the photovoltaic SPS options. A brief summary of photovoltaic results is as follows:

The factor that perhaps made us feel most comfortable, in terms of evaluating the whole SPS concept, is that silicon cost did not appear too high. There has been a tendency to think "if we must go with the silicon satellite, it's going to cost too much and maybe it won't make it." But our cost analyses indicate that silicon cost will not be too high, and that is probably most important. Silicon also is less sensitive to cell performance than supposed. We found, especially for silicon, that the simpler satellite at a concentration ration of 1 is preferable.

Annealing is a critically important technology. Preliminary test results showed high promise for the eventual success of annealing. With annealable satellites, self-power orbit transfer after LEO construction appearing promising.

It is becoming clear that new sources would be required to supply gallium for SPS's even at the quantities required for the thinnest of our fims. New sources of supply may be available. Questions of production rate (can enough of it be supplied per year) are very bothersome. Even if a new supply were available at a reasonable recovery rate, thin film technology is critical for gallium. Higher concentration ratios migh alleviate this problem somewhat.

3.2.1 Silicon Photovoltaics

3.2.1.1 Array Analyses

The reference solar array was the basis for comparison of alternate concepts. It was derived from the JSC concentrating configuration using silicon solar cells, modified by the incorporation of 50 μm (2 mil) fused silica covers to provide more-optimum protection from solar-flare protons during a 30-year life. Features of the reference array concept are as follows:

ORIGINAL PAGE IS
OF POOR QUALITY

FEATURE	SELECTION	RATIONALE
Concentration ratio	2, less reflection and misorientation losses	Designated as reference case
Substrate	Type HF Kapton, with integral printed circuit interconnections	Best available strength for weight. Compatible with printed-circuit cell-to-cell connections made by welding
Concentrators	Aluminized Kapton at 60° with respect to plane of solar cells, oversized to fully illuminate cells when misoriented in worst-case manner.	Lightest weight of feasible alternates

The solar cell design for the reference array is shown in Figure 3.2-1, with features and their selection rationale outlined in Table 3.2-1. The manner in which cells are interconnected to form strings on a 650 by 496 meter module is shown in Figure 3.2-2. Each of these modules would contain 110 of these 44-kV strings.

Having both p and n contacts available on the back side of the solar cell is important for automated assembly of the blanket. One way of achieving this feature is to run the n-layer doping around the edges of the cell to contacts on the back. Recent work sponsored by NASA's Lewis Research Center indicates that better cell performance will be obtained if only the metallization, appropriately insulated from the silicon, is run around the edge of the cell.

The initial output of a solar cell in an array depends on the temperature and light intensity. We used a -0.43 percent per °C temperature coefficient of maximum power, a value measured by Comsat with their violet cells. We also used their temperature coefficient of -0.37 percent per degree C for voltage.

A 257.07 mW/cm^2 solar intensity was used in calculating the performance of cells as summarized in Table 3.2-2. It was based on the concentrators having a 0.9 reflectance, which heated the cells to 115°C. We subsequently found that the reflectors would have a reflectance of 0.85, reducing initial cell temperature to 106°C. This revised intensity and temperature were not incorporated into the trade study inasmuch as it would not have changed the conclusion.

The blanket assembly factors represent optimistic values of packing factor and cell uniformity. The low cover absorption can be achieved with tantalum pentoxide anti-reflective coated cells.

The performance calculations shown in Table 3.2-3 were grouped to illustrate the true reflector contribution to blanket output. For the area concentratio atio = 2 option, these data show that the effective concentration ratio is considerably lower.

SPS-234

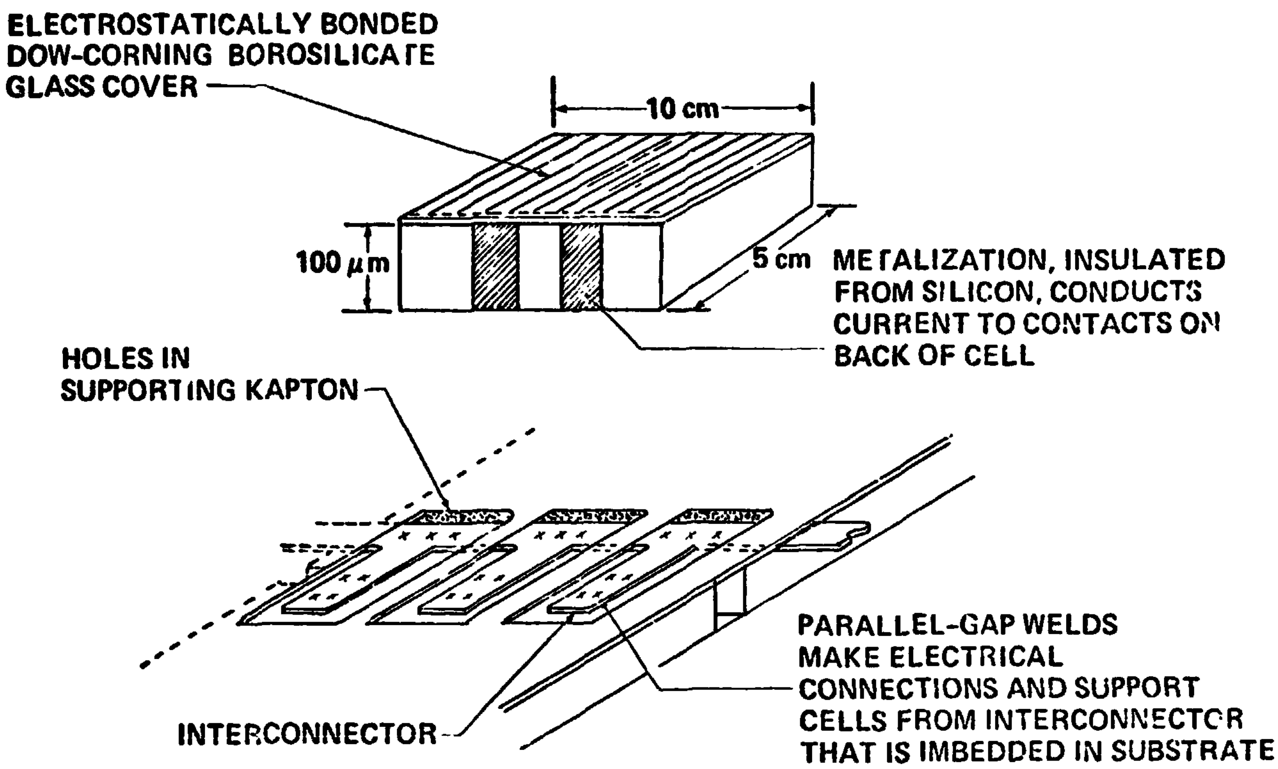

Figure 3.2-1. Solar Cell Design for Solar Power Satellite

Table 3.2-1. Reference Array Concept–Solar Cells

FEATURE	SELECTION	RATIONALE
TYPE	SILICON	DESIGNATED AS BASELINE
SEMI CONDUCTORS	N-ON-P	MORE RADIATION-RESISTANT THAN P-ON-N. MOST OF THE SILICON SOLAR CELL DEVELOPMENT WORK IS BEING DONE ON N-ON-P CELLS.
RESISTIVITY	2 OHM-CM	BOEING TESTS HAVE SHOWN THAT 2 OHM-CM VIOLET CELLS HAD THE HIGHEST OUTPUT AFTER IRRADIATION WITH 7×10^{10} ONE-MeV PROTONS.
CELL SIZE	5 CM WIDE	A POSSIBLE WIDTH FROM EDGE-DEFINED, FILM-FED GROWTH PROCESS (EFG).
	10 CM LONG	REASONABLE TO HANDLE, AND OBTAINABLE FROM HEAT-TRANSFER CRYSTAL-GROWTH PROCESS. PROTOTYPES OBTAINABLE FROM 5-CM DIAMETER BOOL. LARGER CELLS WOULD HAVE LOWER EFFICIENCY BECAUSE OF SHADOWING BY CURRENT-COLLECTING GRID.
CONNECTIONS	ON BACK OF CELL	COMPATIBLE WITH AUTOMATED ASSEMBLY OF ARRAY BLANKET.
EFFICIENCY	18 PERCENT WITH AIR-MASS-ZERO SUNLIGHT, 25°C	APPEARS ACHIEVABLE IN PRODUCTION BY 1985.
COVER	2-MIL FUSED SILICA, ELECTROSTATIC-BONDED	BEST COMPROMISE, WITH THICKER COVERS INCREASING ARRAY WEIGHT BECAUSE OF QUANTITY OF QUARTZ, AND THINNER COVERS INCREASING WEIGHT BECAUSE OF GREATER AREA TO COMPENSATE FOR GREATER LOSS OF POWER FROM RADIATION DEGRADATION DURING 30-YEAR LIFE.
OPERATING TEMPERATURE	115°C	BASED ON THERMAL ANALYSIS.

ORIGINAL PAGE IS
OF POOR QUALITY

SPS-235

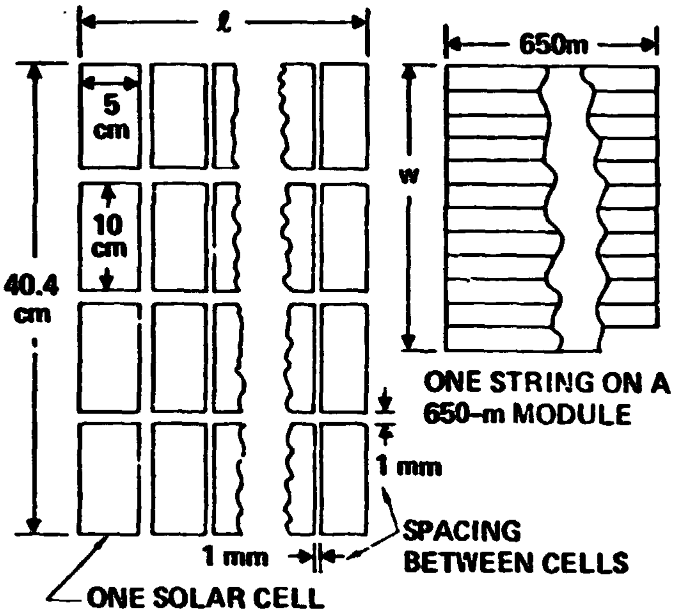

Cover thickness (μm, mils)	Voltage at load (kV)	Cells per string*	ℓ for one string (km)	w (m)
50 (2)	44.0	521,760	6.65	4.16

Figure 3.2-2. Solar Cell String for Supplying Load Voltage

SPS-231

Table 3.2-2. Solar Array Output Calculations

Cell performance factors:	$T = 115^oC$ $P_T = P_{25^oC}\ (1 - 0.0043\ \Delta T)$ $V_T = V_{25^oC}\ (1 - 0.0037\ \Delta T)$ $S = 135.3 + 0.9 \times 135.3 = 257.07\ \text{mW/cm}^2$
Blanket assembly factors:	Lost area = 0.96 Cover absorption ≐ 0.98 Cell mismatch ≐ 0.99 I^2R loss in section = 0.975 Total = 0.9081
Initial blanket output:	$P_o = 257.07 \times 0.18\ (1 - 0.0043\ [115^oC - 25^oC])\ (0.9081)$ $= 25.76\ \text{mW/cm}^2 = 257.6\ \text{W/m}^2$

SPS-209

Table 3.2-3. Reference Configuration Energy Conversion B.O.L.

Array specific output at 1 sun/direct illumination (55°C)		188.8W/m^2
Array temperature degradation at CR = 2 (106°C)	- 38.5 W/m^2*	
Array specific output (106°C) from reflected sun	-128.5 W/m^2*	
Reflector flatness factor 5%	- 13.9 W/m^2	
Net output increment due to reflectors		76.1 W/m^2
Integrated specific output		264.9 W/m^2
Effective CR = $\frac{\text{integrated output}}{\text{1 sun direct output}}$ = 1.40		
Efficiency		= 9.55%

* Items subject to degradation

The reference solar array has a geometric concentration ratio of 2.0, with the direct sunlight seen by each cell being supplemented by sunlight reflected from each side of the blanket, as shown in Figure 3.2-3. With perfect reflectors each cell would be illuminated with sunlight having twice normal intensity.

The actual sunlight at the solar cells is less than twice the direct sunlight. It is reduced by absorption in the reflectors, non-flatness of the reflecting surface. Also, the reflectors must be oversized to fully illuminate all cells under worst-case misorientation.

The solar array blanket is shown in Figure 3.2-4. This is representative design whose characteristics were incorporated in the photovoltaic SPS definition.

3.2.1.2 Reference Configuration

The reference silicon configuration is shown in Figure 3.2-5 as adjusted for the revised sizing criteria. The trough width has been reduced to 619m as required for uniform illumination and the additional beam frames required to react the reflector tensioning loads are shown. Mass properties for the reference configuration are shown in Table 3.2-4, tracing evolution from the point-of-departure mass statement. This mass statement includes a 50% growth allowance as used by JSC in JSC-11568 to facilitate comparisons. Other mass data presented in this report do not include growth allowances. allowances.

The reference configuration does not meet the requirement of maintaining rated output over 30 years life. Both the solar blankets and the reflectors degrade. End-of-life performance is summarized in Table 3.2-5. Detailed analyses of solar cell and reflector degradation were conducted, as reported in sections 3.2.5 and 3.2.6 respectively. Results are summarized in Figure 3.2-6. The basic energy conversion performance chain has been revised to reflect the 30 year degradation values for both cells and reflector. The effective concentration ratio is again considerably reduced from the area concentration ratio of two.

3.2.1.3 Power Maintenance Analysis

Power maintenance methods include initial oversizing, annealing, and array addition. Initial oversizing is the least attractive option (see section 3.2.1.5). Annealing is the most attractive, if it can be made to work as well as current preliminary test results indicate. Array addition maintains solar array output by adding increments to restore capacity lost by radiation degradation. The refurbishment schedule shown assumes that the solar power satellite always delivers 10 GW from its Earth receiving station, and that at the end of each 5 years an appropriate solar array increment is added.

SPS-236

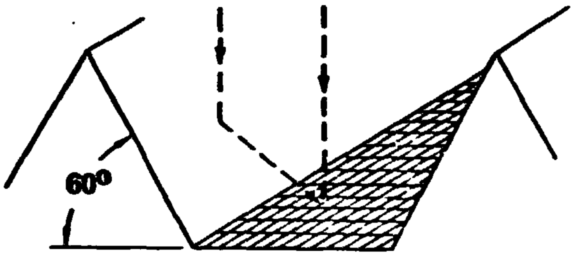

Feature	Selection	Rationale
Concentration ratio	2, less reflection and misorientation losses	Designated baseline
Substrate	Type HF Kapton, with integral printed-circuit interconnections	Best available strength for weight. Compatible with printed-circuit cell-to-cell connections made by welding.
Concentrators	Aluminized Kapton, oversized to fully illuminate cells when misoriented in worst-case manner	Lightest weight of feasible alternates

Figure 3.2-3. Reference Solar Array Concept

SPS-380

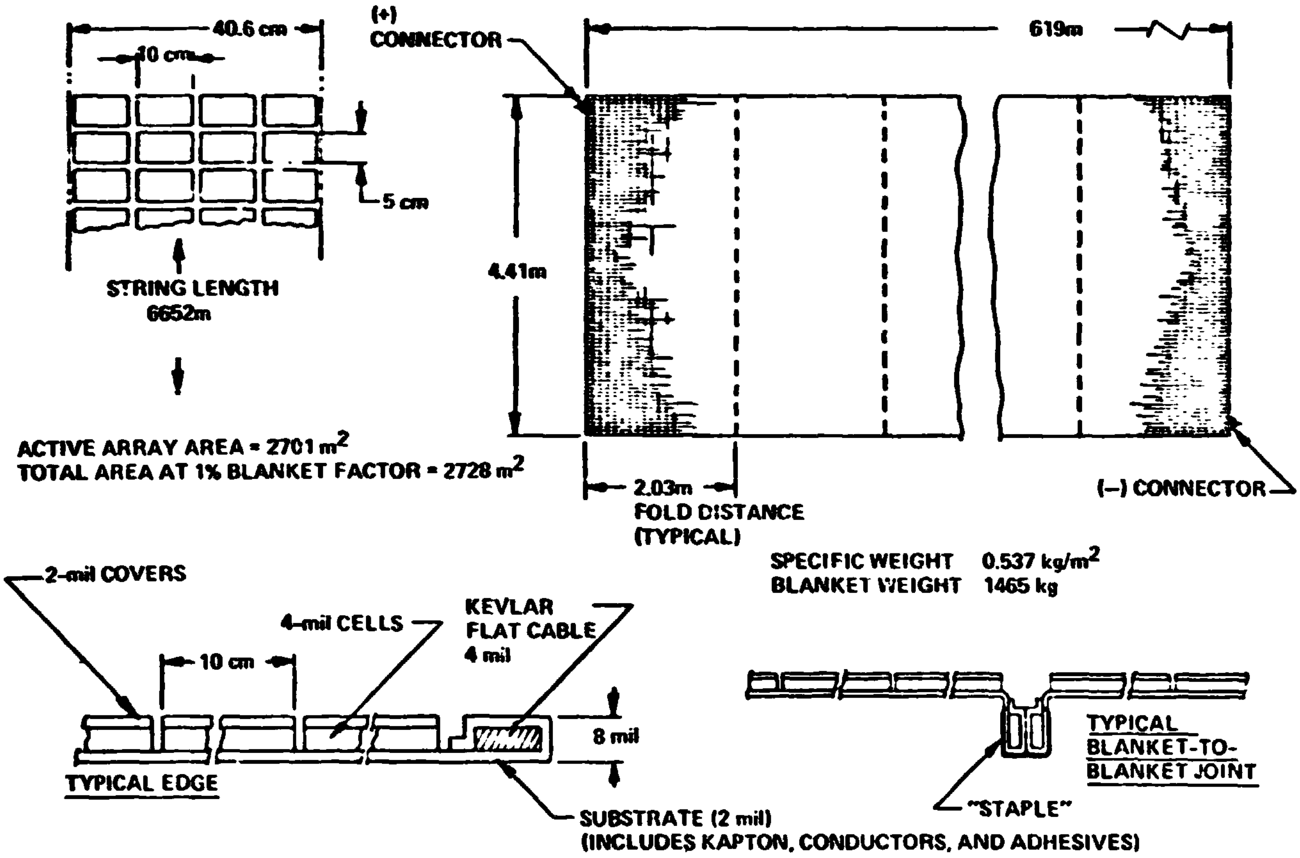

Figure 3.2-4. Reference Silicon Blanket Design (Design Voltage 44 000 V.E.O.L.)

ORIGINAL PAGE IS
OF POOR QUALITY

Pages 40 - 42 are blank

SPS-646

Table 3.2-4. Photovoltaic Reference Configuration Nominal Mass Summary Weight in Metric Tons

COMPONENT	ORIENTATION	MIDTERM	CURRENT	REMARKS
1.0 SOLAR ENERGY COLLECTION SYSTEM	(36,616)	(59,313)	(49,512)	INITIAL AREA = 129 km^2, MIDTERM & CURRENT=146 km^2
1.1 PRIMARY STRUCTURE	2,493	14,970	8,000	OPTIMIZED CIRCULAR CHORDS + REDUCED MEMBRANE STRESS LEVEL
1.2 SECONDARY STRUCTURE	189	209	209	~TO ARRAY AREA
1.3 MECHANICAL SYSTEMS	40	40	40	NO CHANGE
1.4 MAINTENANCE STATION	85	---	—	DELETED TO BE CONSISTENT WITH THERMAL ENGINE
1.5 CONTROL	340	340	340	NO CHANGE (200 M.T. DRY WET + 1 YR PROPELLANT)
1.6 INSTRUMENTATION/ COMMUNICATIONS	4	4	4	NO CHANGE
1.7 SOLAR-CELL BLANKETS	25,746	37,592	34,111	SPECIFIC WEIGHT DOWN TO .49 kg/m^2 (FROM .54 kg/m^2)
1.8 SOLAR CONCENTRATORS	5,149	2,978	3,276	INCLUDES TENSIONING/INSTALLATION FACTOR
1.9 POWER DISTRIBUTION	2,570	3,180	3,532	INCLUDES SWITCH GEAR & INSTALLATION FACTOR
2.0 MPTS	15,371	15,371	15,371	NO CHANGE
SUBTOTAL	51,987	74,684	64,883	13% REDUCTION FROM MIDTERM – 25% HIGHER THAN INITIAL
GROWTH	25,994	37,342	32,442	(50%)
TOTAL	77,981	112,026	97,325	

ORIGINAL PAGE IS OF POOR QUALITY

PRECEDING PAGES BLANK NOT FILMED

Table 3.2-5. Reference Configuration Energy Conversion E.O.L. (30 years)

SPS-268

Array specific output at 1 sun direct illumination (2-mil coverglass, 55°C)*		119.1 W/m^2
Array temperature degradation (89°C) at CR = 2	-15.7 W/m^2*	
Array specific output (89°C) from reflected sun	+61.8 W/m^2*	
Reflector flatness factor 5%	- 9.1 W/m^2	
Net output increment due to reflectors		37.0 W/m^2
Integrated specific output		156.1 W/m^2

$$\text{Effective CR} = \frac{\text{integrated output}}{\text{1 sun direct output}} = 1.31$$

Efficiency = 5.6%

* Items subject to degradation

SPS-419

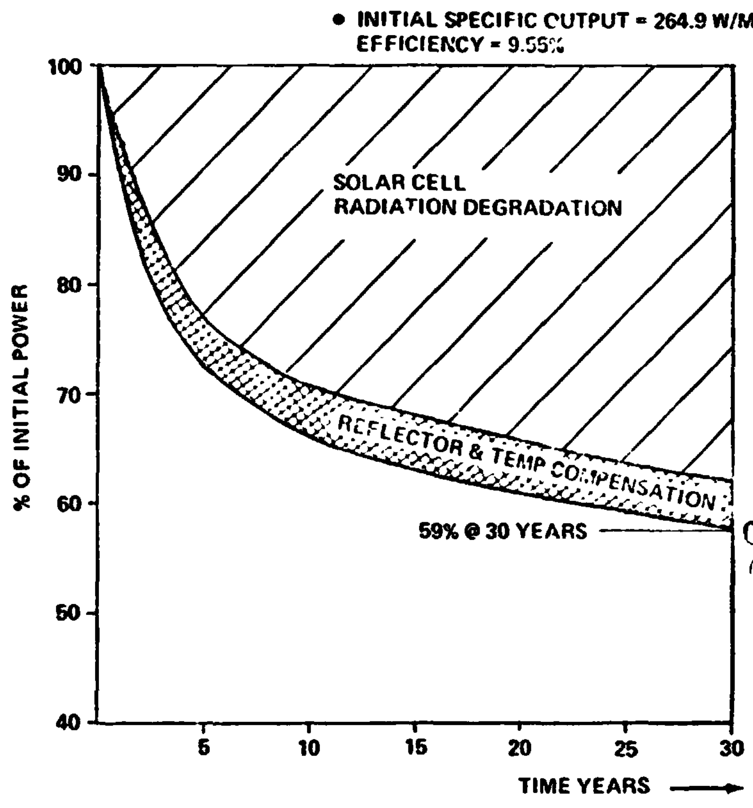

ORIGINAL PAGE IS
OF POOR QUALITY

Figure 3.2-6. Array @ "CR = 2" Integrated Degradation

The comparison of savings to be encountered for different maintenance schedules for a hypothetical 1985-18 percent silicon solar cell was needed.

Knowing the volt-ampere characteristics of the solar arrays, degradation was taken into account and curves for short-circuit current, open-circuit voltage, maximum power voltage, and maximum power vs. years of operation were generated, as shown in Figure 3.2-7.

From this data three approaches were considered for installing the strings of solar cells in the array. Scheme 1 uses the total array installed initially, scheme 2 has its initial array sized to accept a five year add-on schedule, and scheme 3 has its initial array sized to accept a one year add-on schedule. All three schemes were analyzed using a lower limit of 17.6 GW and letting the initial array reach its maximum power voltage at 30 years. The three schemes are shown in Figure 3.2-8.

It is evident that a savings of over three percent can be realized by using the five year maintenance schedule over installing the total array initially. A savings of only 0.80 percent can be realized for using the one year over the five year maintenance schedule.

Thermal annealing is probably the best method of restoring a degraded solar-cell array. Investigators at Simulation Physics, our subcontractor, have found from the literature that thermal annealing will restore proton damage. As a part of this study a test was conducted by Simulation Physics in which both electron beam and laser heating were used to anneal proton-irradiated cells that had been severely damaged by the equivalent of 10^{16} one-MeV electrons. About 50 percent of the lost capacity was restored. Results are reported in more detail in section 3.2.5.

The concentration ratio 2 configuration revised to meet the requirements of a 5 year power output maintenance is considerably larger as shown in Figure 3.2-9. A trough was added on each side and the overall array was increased in length by more than 3 KM.

3.2.1.4 Nonuniform Illumination Analysis

At a given illumination intensity and temperature the current and voltage of a solar cell will always correspond to some point on the cell's volt-ampere curve. The cell is oblivious of external circuit elements and parameters.

Shown in Figure 3.2-10 are two volt-ampere curves, one for a fully illuminated cell and the other for a cell which is not receiving illumination from one of the reflectors. The poorly illuminated cell runs cooler, hence can produce higher voltage, but its maximum current is less. Both cells, being in series, must carry the same current. The dimly lit cell cannot carry much more than its short-circuit current, because if forced to do so, it would act as a reverse-biased diode and absorb voltage.

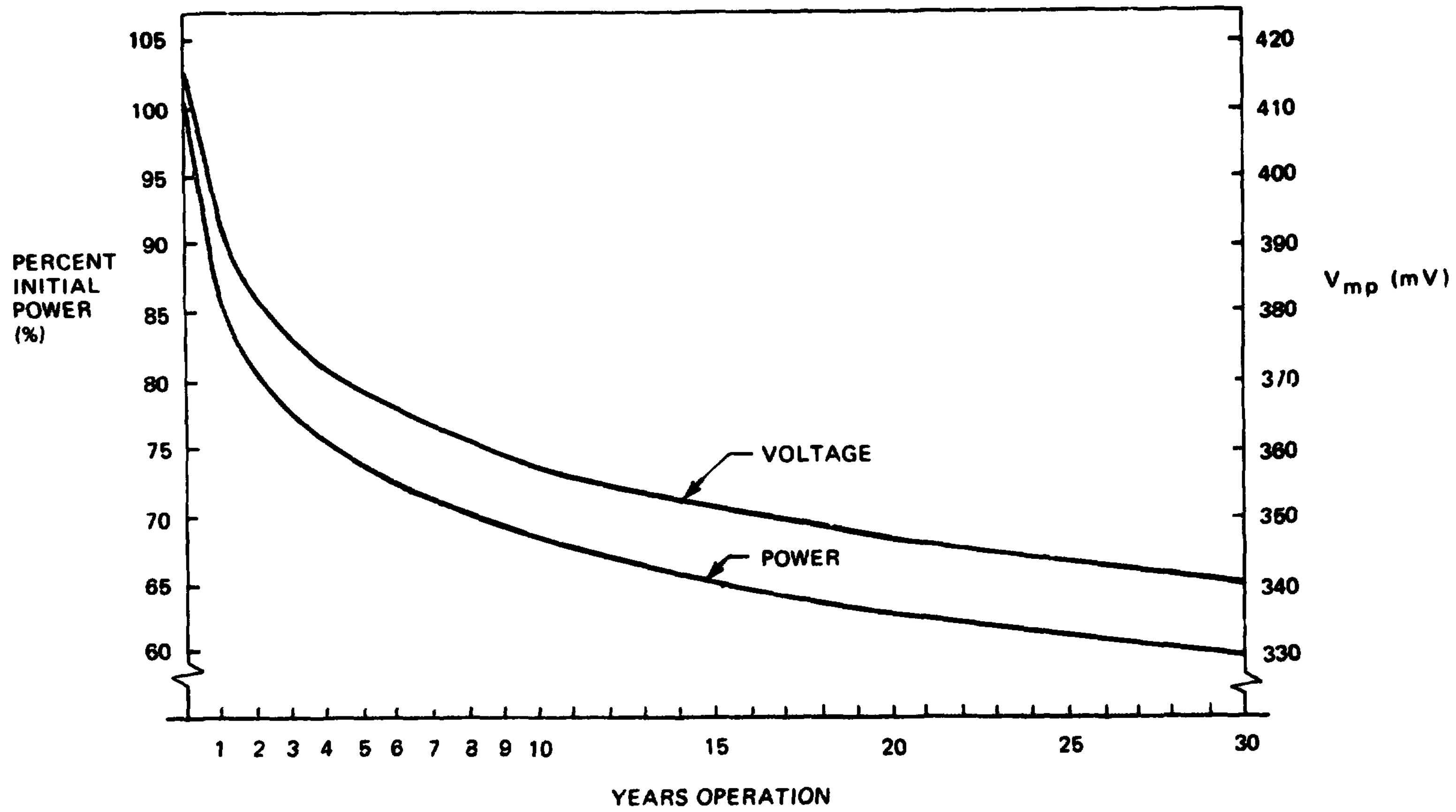

Figure 3.2-7. Degradation Effect on Power and Maximum Power Voltage

ORIGINAL PAGE IS
OF POOR QUALITY

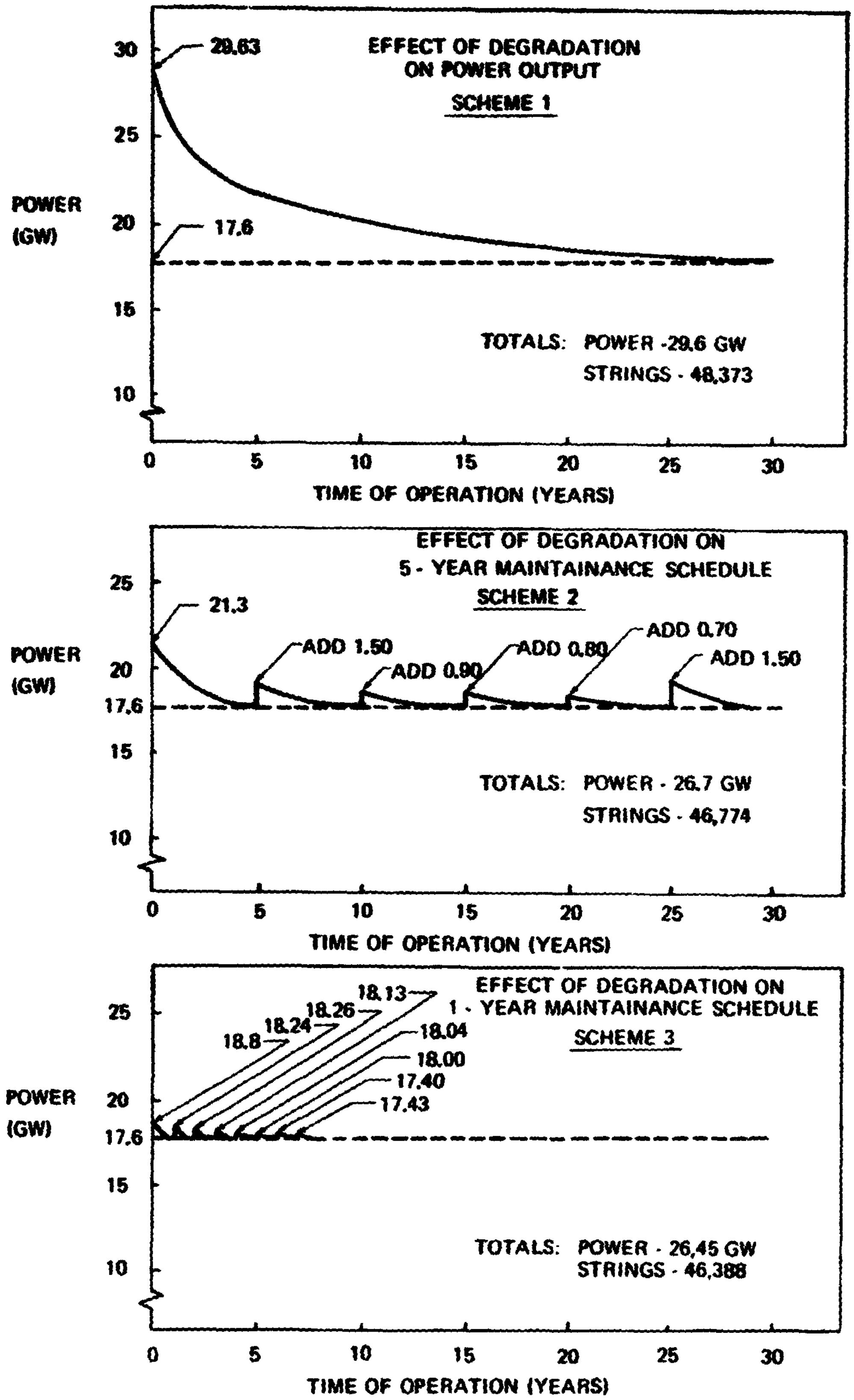

Figure 3.2-8. Alternatives for Power Maintenance

ORIGINAL PAGE IS
OF POOR QUALITY

SPS-384

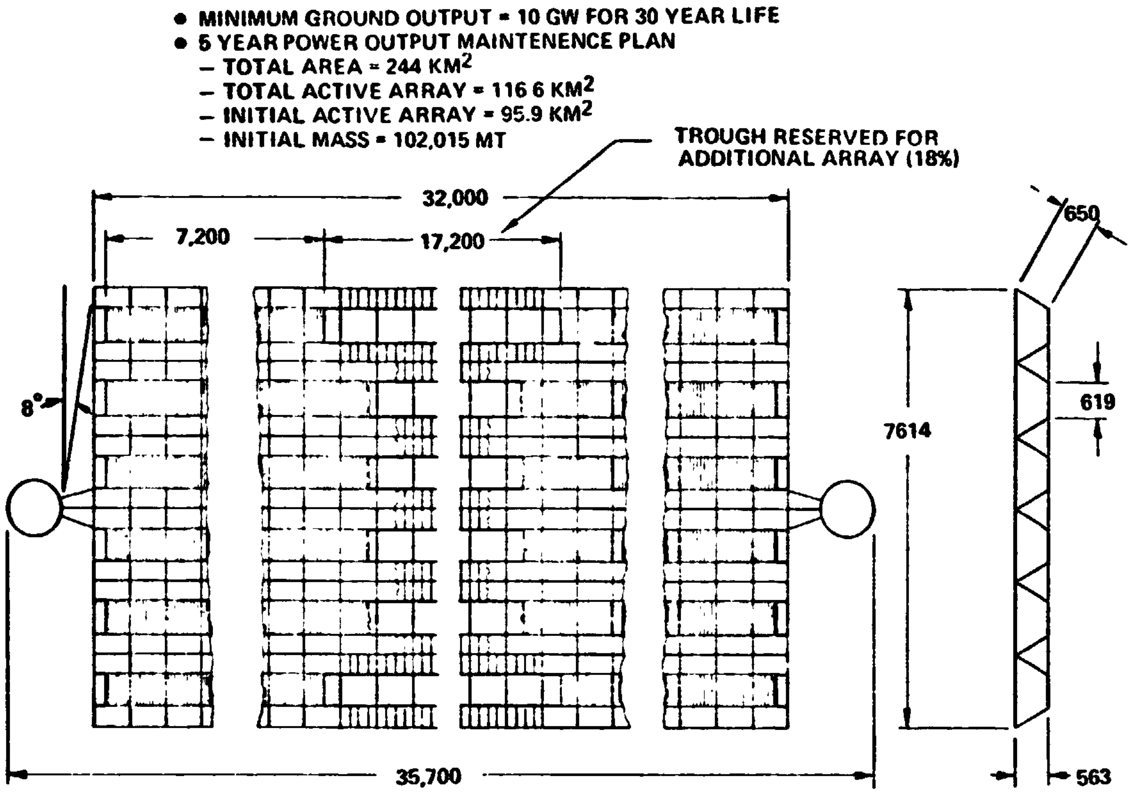

Figure 3.2-9. Array Addition Silicon Configuration

SPS-237

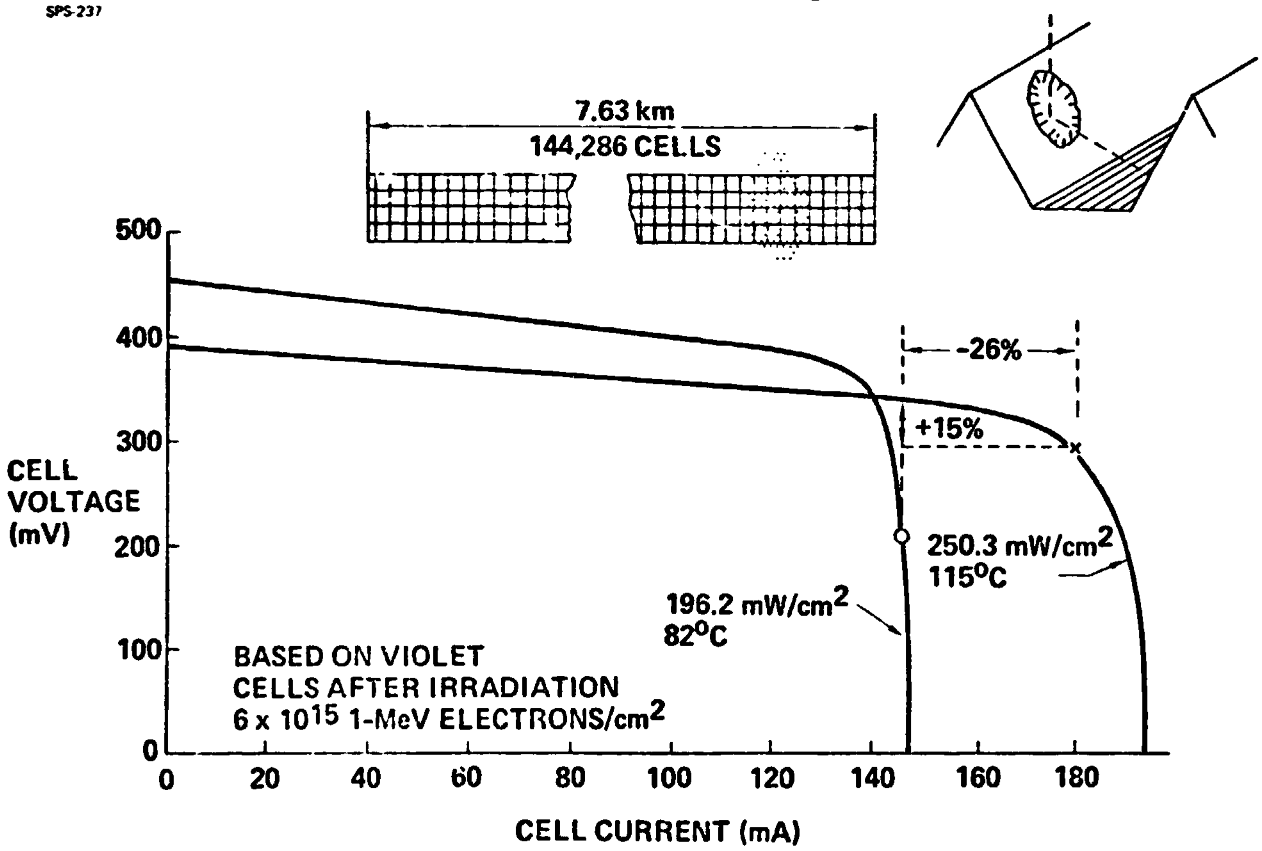

Figure 3.2-10. Dimmed Cells Limit String Current

A solar cell can withstand some reverse bias without overheating. Consider the dimly illuminated cell. At its maximum power point it receives 196.2 mW/cm^2 of sunlight, and radiates 182 watts of this as heat. At zero voltage it would radiate as heat all of its input, and at 380 mV reverse bias it would radiate 210 mW/cm^2. All of these values of radiated heat are less than what the cell normally radiates when illuminated with 250.3 mW/cm^2 of sunlight.

If only 15 percent of the string is dimmed, then the fully illuminated cells can produce 15 percent extra voltage by dropping back to 74 percent of their maximum-power current, reducing string output at 44 KV by 26 percent. Thus it can be seen that partial shadowing causes a disproportionate reduction of string output.

Further examples of the effect of reflected-sunlight loss are shown on a plot of string output as a function of average illumination of the cells in a series string (Figure 3.2-11). By average illumination is meant the sum of sunlight times area falling on fully illuminated cells, plus that on partly illuminated cells, divided by string area.

The solid line represents the maximum output that the string can have, assuming that illumination intensity does not change cell efficiency. Note the suppressed zeros on the axes.

Again it is evident that reflector defects significantly reduce string output.

The reference CR=2 structural configuration requires beams crossing the reflector ridges in the manner shown in Figure 3.2-12. A solar cell under the beam would see at times 0.5-meter sections of the beam cross the Sun's disk. If the 0.5m beam is 520m above the solar cell, it could absorb 14 percent of the sunlight that would otherwise arrive at the cell.

The best arrangement for the solar cell strings would be one in which the beam shadow passes over a few strings in the trough, rather than crossing all the strings in the trough.

3.2.1.5 Configuration Comparisons

A series of configuration comparisons was developed to show the influences of the major tradeoffs. A gross cost estimating model, derived from the more detailed cost estimates described in section 3 7, was used for cost comparisons.

All satellites were defined to provide a minimum of 10 gigawatts throughout their 30-year life. The one reference system shown in Figure 3.2-13 is a beginning-of-life sized system comparable to the JSC point-of-departure configuration. It is compared to a 30-year, initially oversized system. Initial oversizing is a severe penalty; and there are better solutions.

SPS-238

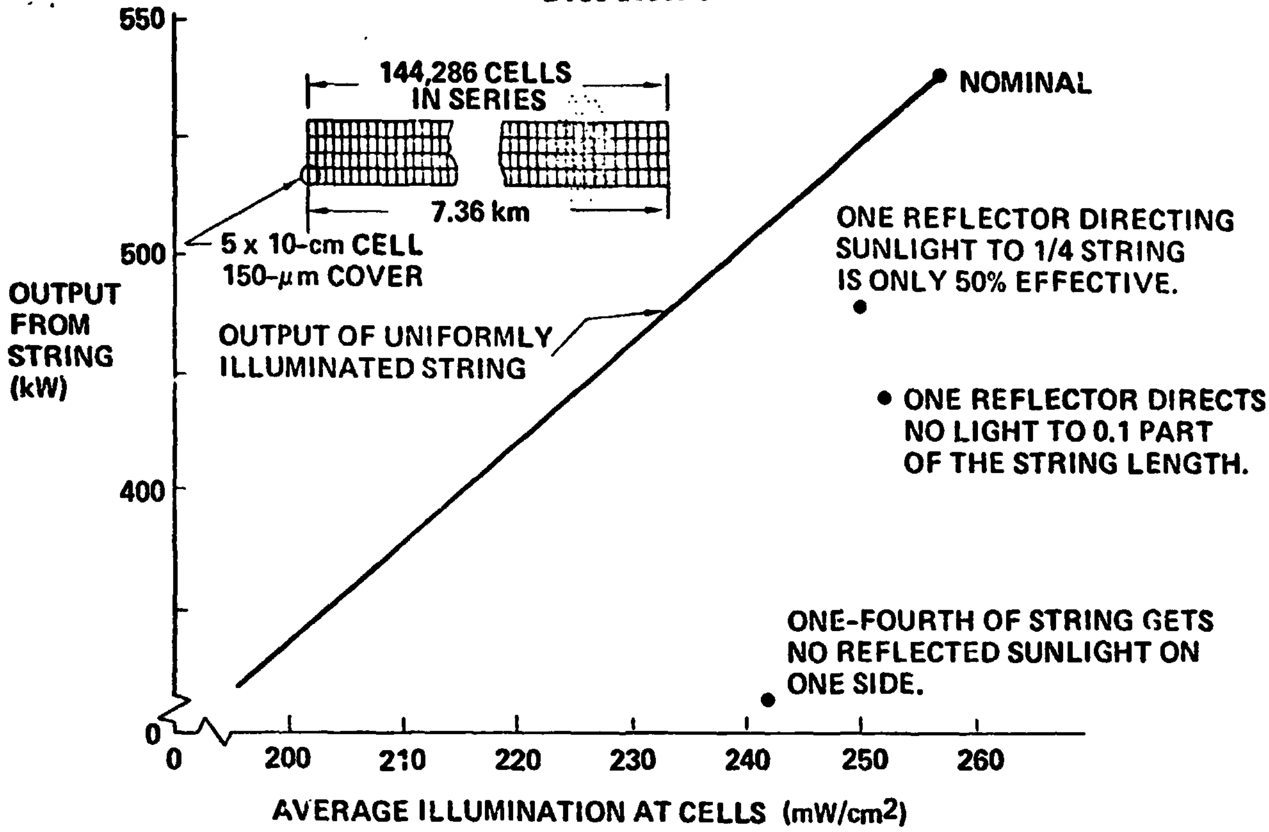

Figure 3.2.11. Effect of Nonuniform Illumination on Output of Solar Array String

SPS-239

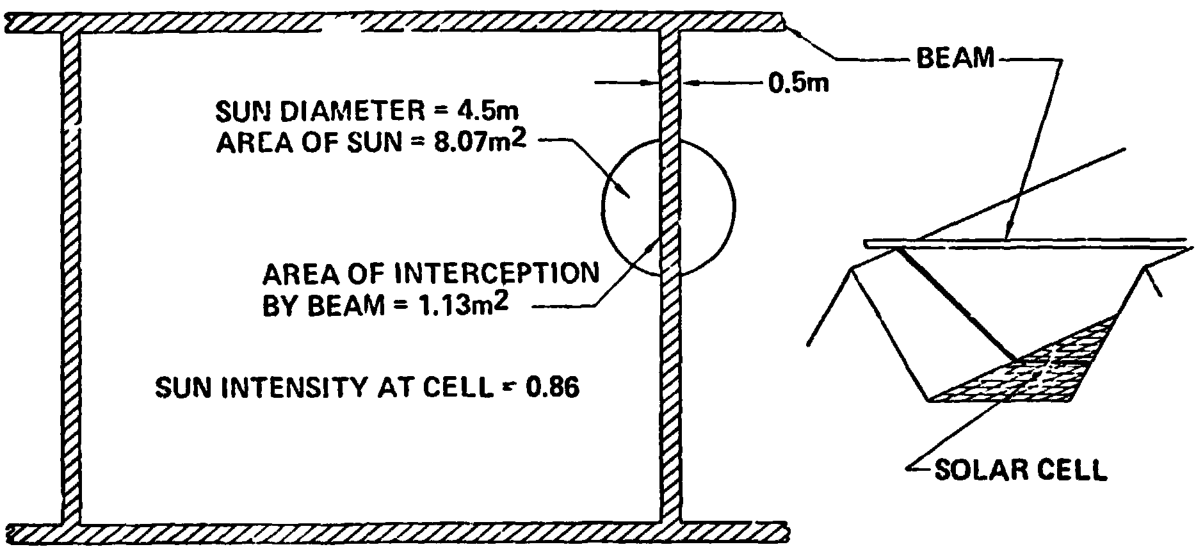

Figure 3.2-12. Solar Cell View of Sun behind Beam

ORIGINAL PAGE IS OF POOR QUALITY

The set of comparative configurations shown in Figure 3.2-14 assumes geosynchronous construction and concentration ratio 2. The oversized configuration has an estimated cost of some 15 billion dollars. An improved way to take care of the end of life/beginning of life problem is to add array at intervals. We found that a 5-year interval achieved most of the gain. Shorter than 5-year intervals provided little further improvement. Annealing provides the least-cost approach.

The satellite configurations illustrated in Figure 3.2-15 compare concentration ratio 1 (no concentration) and concentration ratio 2 with array addition for power maintenance. Although the CR2 system is very slightly lower in mass, its larger size and greater complexity result in somewhat higher cost.

As illustrated in Figure 3.2-16, the CR2 versus CR1 trade strongly favors CR1 with annealing. This is because the reflectors of the CR2 configuration also degrade, but cannot be restored by annealing. Therefore, the satellite must be oversized as required to compensate for reflector degradation.

Annealing shows a major advantage over array addition for the LEO assembly option. This is because the solar blankets used to power the transfer are severely degraded (about 50%, depending on coverglass thickness and transfer time) and the satellite must be correspondingly oversized. In the transportation study, an analysis of the use of thicker coverglasses on that portion of the array used for transfer power showed that the added mass of coverglass almost exactly countered the reduced degradation; no cost advantage was found. The power maintenance options for LEO assembly are compared in Figure 3.2-17.

The additional radiation exposure resulting from the LEO/GEO transfer also increases the advantage of CR1 over CR2, again because reflector degradation cannot be restored The comparison is shown in Figure 3.2-18.

The LEO versus GEO trade is summarized in Figure 3.2-19 for the case without an annealable array. The best maintenance scheme is then adding array at five year intervals; and here we have an indication of a switchover. (Detailed transportation cost analyses, however, indicate a slight advantage for LEO.) The reduced cost of transportation is countered by the higher acquisitions cost for the larger and more massive LEO assembly self-power option. LEO assembly with the annealing-capability CR1 configuration shows a significant cost advantage because transfer degradation penalties are minimized.

Silicon performance sensitivities, starting from a reference figure of 18% and dropping 2 points per step, are shown in Figure 3.2-20. Even at 14% efficiency there is not a dramatic change in either mass or cost. This indicates that achieving low cell costs is much more important than maximizing efficiency.

SPS 735

Radiation Degradation Requires Sizing Penalty for 30-Year, 10 GW Minimum Output

REFERENCE
SILICON
CR=2

10 GW BOL

TOTAL AREA: 146 Km^2

ACTIVE ARRAY AREA: 70 KM^2

TOTAL MASS: 64,883 MT

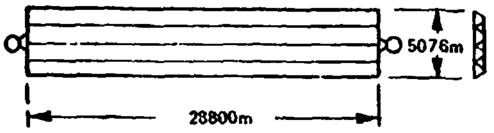

SILICON
CR=2

10 GW FOR 30 YRS.
VIA INITIAL OVERSIZE

TOTAL AREA: 253.1 Km^2

ACTIVE ARRAY AREA: 120.5 Km^2

TOTAL MASS: 105,794 MT

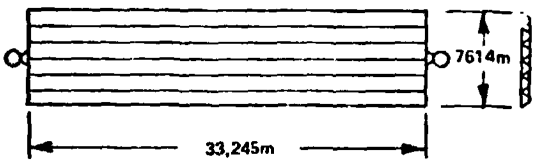

Figure 3.2-13. Silicon Satellite Sizing for 30-Year Minimum Output

SPS 736

Periodic Array Additions Reduce Initial Cost Outlay by 13%
(4% Total Without Interest)
Annealed Satellite 21% Less $$ Than Oversized Satellite

SILICON

30 YR. OVERSIZE

CR=2	
10 GW MIN. FOR 30 YRS.	
TOTAL AREA:	253.1 Km^2
ACTIVE ARRAY AREA:	120.5 Km^2
MASS:	105,794 MT
PRODUCTION COST $ \$\sim10^6$	6844.0
TOTAL COST $ \$\sim10^6$	15446.0

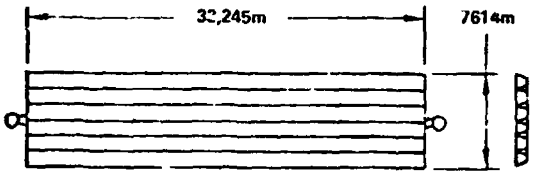

ARRAY ADDITION

CR=2		
10 GW MIN FOR 30 YRS.		
TOTAL AREA:	238.3 Km^2	
ACTIVE ARRAY AREA:	90.3 Km^2	(113.3 EOL)
MASS:	86295 MT	(100,480 EOL)
PRODUCTION COST $ \$\sim10^6$	6171.6	(6642.6 EOL)
TOTAL COST $ \$\sim10^6$	13184.6	(14811.4 EOL)

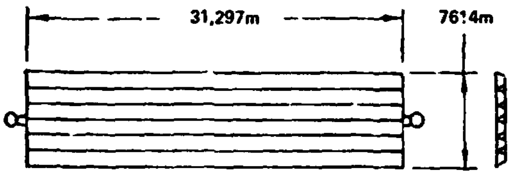

ANNEALING

CR=2	
10 GW MIN. FOR 30 YRS	
TOTAL AREA:	182.2 Km^2
ACTIVE ARRAY AREA:	86.4 Km^2
MASS:	76,075 MT
PRODUCTION COST $ \$\sim10^6$	5956.5
TOTAL COST $ \$\sim10^6$	12145.2

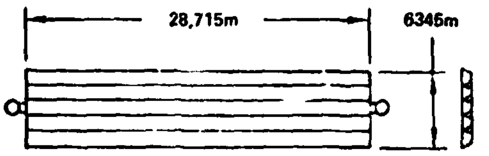

Figure 3.2-14. Silicon Satellite Different Approaches to 30-Year Minimum Output

ORIGINAL PAGE IS
OF POOR QUALITY

SPS 737

For GEO Assembled Silicon Satellites Without Annealing.
CR 2 Impact on Costs Other Than Array Result in 4%
Advantage to CR 1 Even Though CR 1 is Initially 5% Heavier

CR=2

TOTAL AREA:		283.3 Km^2	
ACTIVE ARRAY AREA:		79.8 Km^2	(113.3 EOL)
MASS:		80589 MT	(100,420 EOL)
PRODUCTION COST:	$\$ \sim 10^6$	6171.6	(6642.6 EOL)
TOTAL COST:	$\$ \sim 10^6$	13184.6	(14811.4 EOL)

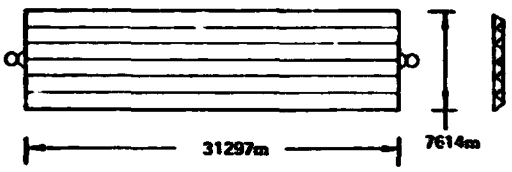

CR=1

TOTAL AREA:		141.8 Km^2	
ACTIVE ARRAY AREA:		113.0 Km^2	(141.8 EOL)
MASS:		84,575 MT	(100,387 EOL)
PRODUCTION COST:	$\$ \sim 10^6$	5784.6	(6244.9 EOL)
TOTAL COST:	$\$ \sim 10^6$	12655.5	(14404.5 EOL)

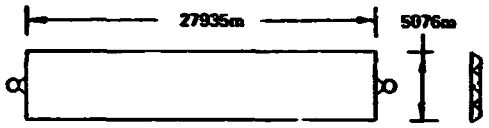

Figure 3.2-15. Silicon Satellite, CR 1 vs CR 2, No Annealing

SPS 738

The CR2 vs CR1 Comparison Emphasized when
Array Degradation Reduced Via Annealing
(4% CR1 Advantage Grows to 6%)

SILICON—10 GW MIN. FOR 30 YRS. VIA ANNEALING—GEO ASSEMBLY

CR=2

TOTAL AREA:	182.2 Km^2
ACTIVE ARRAY AREA:	86.4 Km^2
MASS:	76,075 MT
PRODUCTION COST $\$ \sim 10^6$	5956.5
TOTAL COST $\$ \sim 10^6$	12,145.2

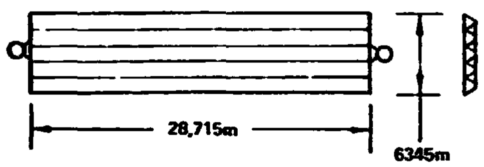

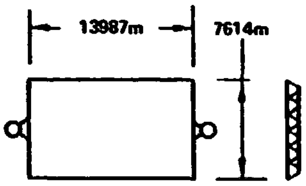

CR=1

TOTAL AREA:	106.5 Km^2
ACTIVE ARRAY AREA:	106.5 Km^2
MASS:	71,728 MT
PRODUCTION COST $\$ \sim 10^6$	5682.5
TOTAL COST $\$ \sim 10^6$	11408.1

Figure 3.2-16. Silicon Satellite CR2 vs CR1 With Annealing GEO Assembly

ORIGINAL PAGE IS
OF POOR QUALITY

SPS 740

For LEO Assembly and Self Power, Annealing Shows 21% Cost Advantage

SILICON 10 GW MIN. FOR 30 YEARS—CR=2
LEO ASSEMBLY MAINTAINED VIA ARRAY ADDITION

TOTAL AREA:	309.5 Km^2	
ACTIVE ARRAY AREA:	122.8 Km^2	(147.5 EOL)
MASS:	110,426 MT	(130,267 EOL)
PRODUCTION COST \$ ~ 10^6	7047.1	(7664.1 EOL)
TOTAL COST \$ ~ 10^6	14399.2	(16308.3 EOL)

MAINTAINED VIA ANNEALING

TOTAL AREA:	182.2 Km^2
ACTIVE ARRAY AREA:	86.4 Km^2
MASS:	78515 MT
PRODUCTION COST \$ ~ 10^6	6032.1
TOTAL COST \$ ~ 10^6	11327.5

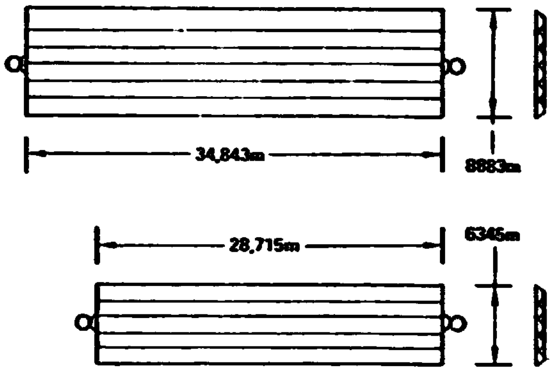

Figure 3.2-17. Silicon Satellite Power Maintenance for LEO Assembly

SPS 741

CR 1 Advantage Increases Again Due to Higher Leo Scar on CR 2

SILICON—10 GW MIN. FOR 30 YRS. VIA ANNEALING—LEO ASSEMBLY

CR = 2

TOTAL AREA	182.2 KM^2
ACTIVE ARRAY AREA:	86.4 Km^2
MASS:	78821 MT
PRODUCTION COST: \$ ~ 10^6	6032.1
TOTAL COST: \$ ~ 10^6	11327.5

CR = 1

TOTAL AREA:	106.5 Km^2
ACTIVE ARRAY AREA:	106.5 Km^2
MASS:	73,177 MT
PRODUCTION COST: \$ ~ 10^6	5620.2
TOTAL COST: \$ ~ 10^6	10535.8

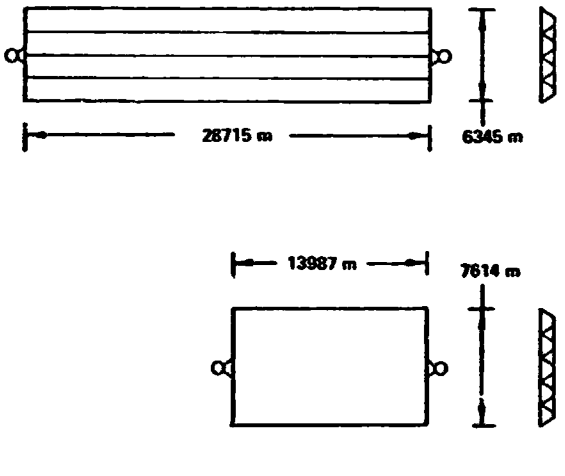

Figure 3.2-18. Silicon Satellite CR 2 vs CR 1 With Annealing, LEO Assembly

SPS 739

GEO Assembly More Attractive for Array Addition Maintenance Scheme Due to Severe Cell Degradation in Orbit Transfer (8% Initial $, 9% Total $)

SILICON – 10 GW MIN FOR 30 YRS. VIA ARRAY ADDITION

LEO ASSEMBLY

CR=2		
TOTAL AREA:	309.5 Km^2	
ACTIVE ARRAY AREA:	122.8 Km^2	(147.5 EOL)
MASS:	110,426 MT	(130,267 EOL)
PRODUCTION COST: $\$\sim10^6$	7047.1	(7664.1 EOL)
TOTAL COST: $\$\sim10^6$	14399.2	(16308.3 EOL)

GEO ASSEMBLY

CR=2		
TOTAL AREA:	283.3 Km^2	
ACTIVE ARRAY AREA:	79.8 Km^2	(113.3 EOL)
MASS:	80,529 MT	(100,480 EOL)
PRODUCTION COST: $\$\sim10^6$	6171.6	(6642.6 EOL)
TOTAL COST: $\$\sim10^6$	13184.6	(14811.4 EOL)

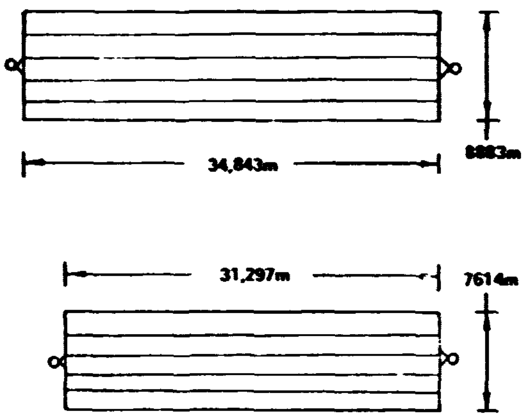

Figure 3.2-19. Silicon Satellite Periodic Array Addition LEO vs GEO Assembly

SPS 743

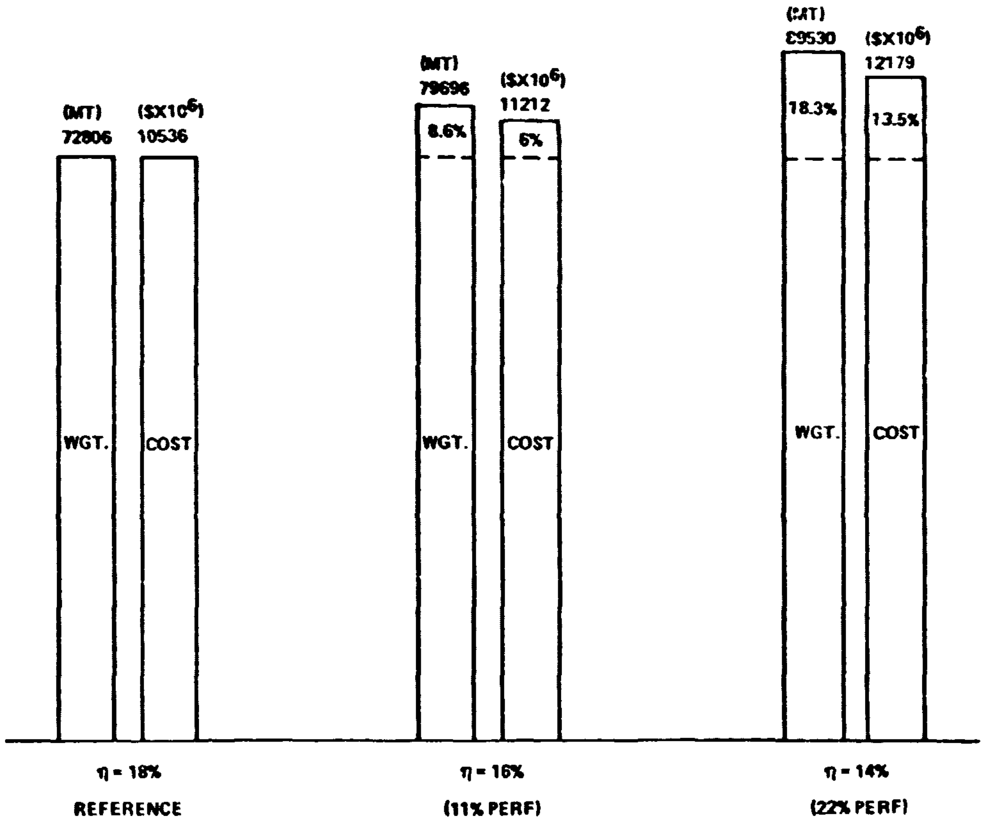

Figure 3.2-20. Silicon Satellite @ CR=1 Sensitivity to Cell Performance

ORIGINAL PAGE IS
OF POOR QUALITY

3.2.2 Gallium Arsenide Photovoltaic

3.2.2.1 Solar Cell and Array Analysis

The gallium arsenide solar cell and array analyses were performed by Hughes Research Laboratories (3011 Malibu Canyon Road, Malibu, Calif. 90265) under subcontract. Their report is included here without revision.

GaAs SOLAR CELL STUDY FOR SOLAR POWER SATELLITE

S. Kamath, R.C. Knechtli, and R. Loo

April 1977

Final Report
Contract N-933265-9167

Prepared for
BOEING AEROSPACE CORPORATION
Seattle, Washington 98124

SECTION 1

SOLAR CELL PERFORMANCE PREDICTIONS

A. EFFICIENCY AT ROOM TEMPERATURE

Our purpose is to predict the performance to be anticipated from optimized GaAs solar cells in the 1990 time period, for solar power satellite (SPS) applications. To this effect, a single-crystal structure of the type illustrated on Figure 1 is considered first. This structure is basically the same as that used in experimental cells presently under development at Hughes Research Laboratories and at other laboratories. The efficiency of a cell of this type has been calculated for a number of combinations of design parameters. Representative results of our calculations for operation at room temperature and in the absence of radiation damage are reproduced on Figure 2. These calculations correspond to the following values of the critical design parameters, which we consider realistic for future optimized solar cells:

- Doping level of GaAs: $N_D = 2 \cdot 10^{17}\ cm^{-3}$, $N_A = 2 \cdot 10^{18}\ cm^{-3}$
- Minority carrier Diffusion length in GaAs: $L_p = 3\ \mu m$, $L_n = 6\ \mu m$
- (AlGa)As window thickness: $D = 0.2\ \mu m$
- Normalized series resistance: $R_s = 0.1\ \Omega cm^2$
- Shadowing ratio: 5%

Values of the parameters shown above have already been measured in selected samples of GaAs material or on experimental solar cells, even though the combination of all the above parameters in one

ORIGINAL PAGE IS
OF POOR QUALITY

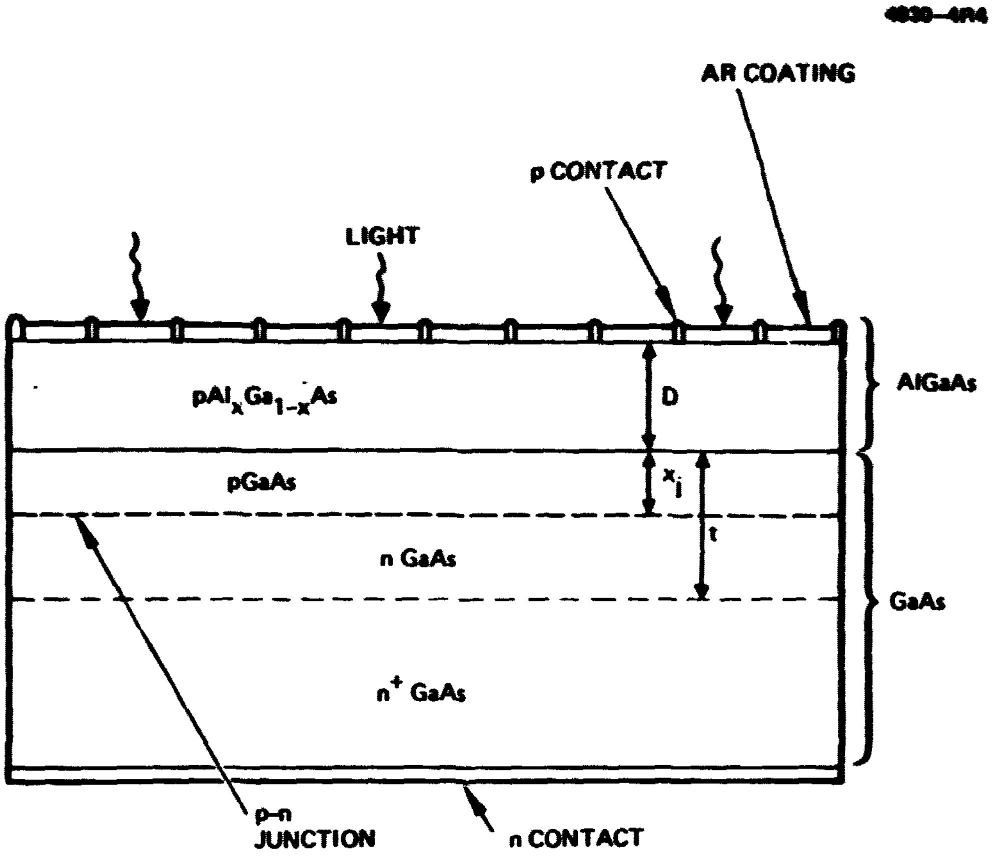

Fig. 1. GaAs solar cell structure.

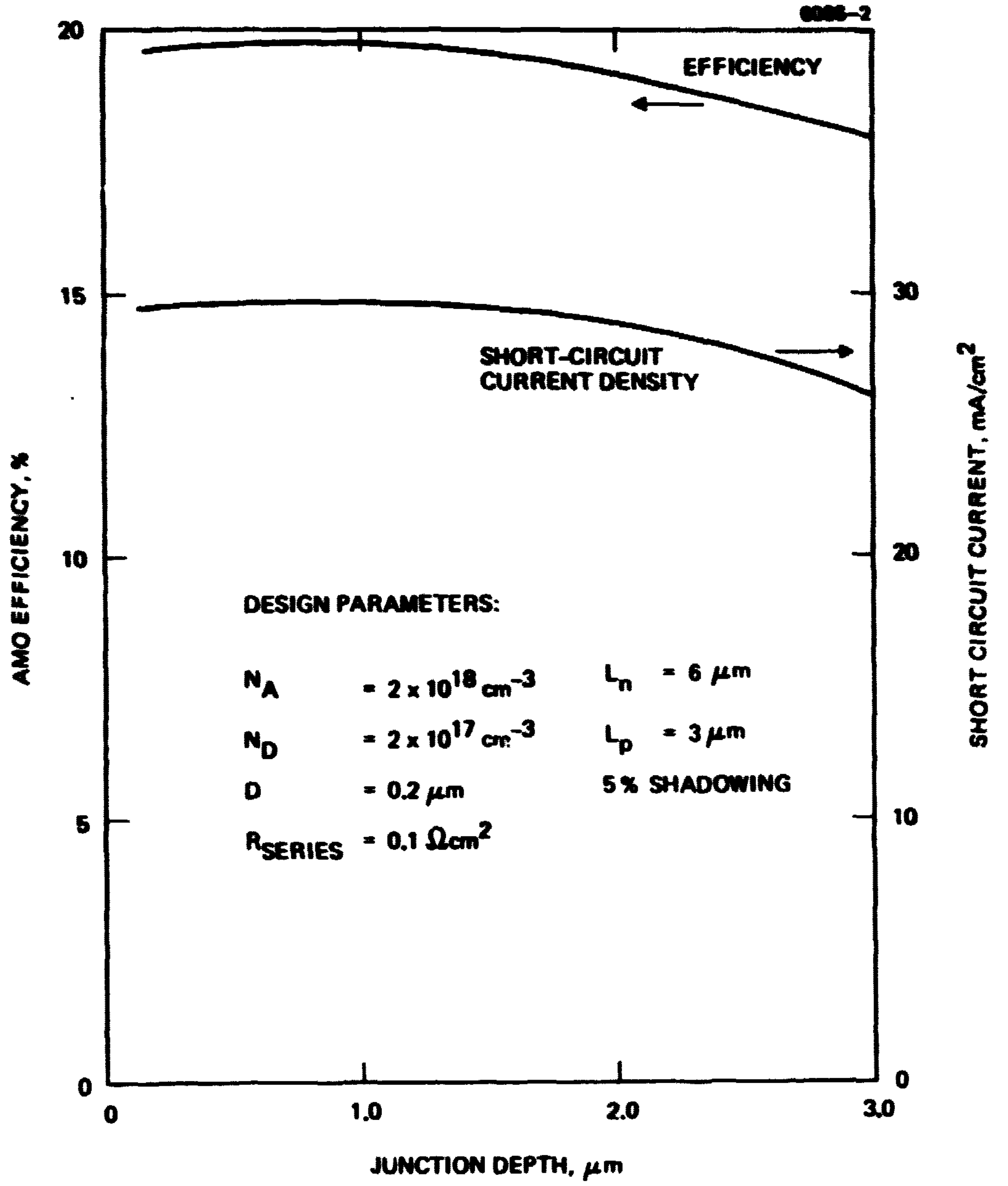

Fig. 2. AMO efficiency and short-circuit current density of (AlGa)As GaAs solar cell.

ORIGINAL PAGE IS
OF POOR QUALITY

optimized solar cell has not yet been accomplished. The rate of progress toward achieving such optimization has, however, been rapid enough to give us confidence that the type of performance predicted by Figure 2 will be available by 1990, for practical GaAs solar cells. This rate of progress can be illustrated by the data of Figure 3 which shows how the maximum efficiency of 2-cm x 2-cm GaAs solar cells made at the Hughes Research Laboratories has been increasing with time. It should be noted in the same context that IBM has already succeeded in making a limited number of smaller-area cells (~0.1 cm^2) with an AMO efficiency as high as 18.5%.

On the basis of these results and of the above considerations, the beginning-of-life efficiency of a GaAs solar cell under AMO illumination and in the absence of solar concentration is predicted to be, for the 1990 time period:

$$\boxed{\eta\ (\mathrm{AMO}) = 20\%}$$

B. EFFECT OF TEMPERATURE ON EFFICIENCY

Conventional solar cells are optimized for room temperature operation. When a cell operates at elevated temperatures there is a significant decrease in the cell's open-circuit voltage and a slight increase in the short-circuit current.

The open-circuit voltage is expressed as

$$V_{oc} = \frac{nKT}{q}\left(\ln\frac{J_{sc}}{J_o} + 1\right) \tag{1}$$

J_o is the diode saturation current given by

$$J_o = qn_i^2(T)\left(\sqrt{\frac{D_p}{\tau_p}}\frac{1}{N_d} + \sqrt{\frac{D_N}{\tau_N}}\frac{1}{N_A}\right) \tag{2}$$

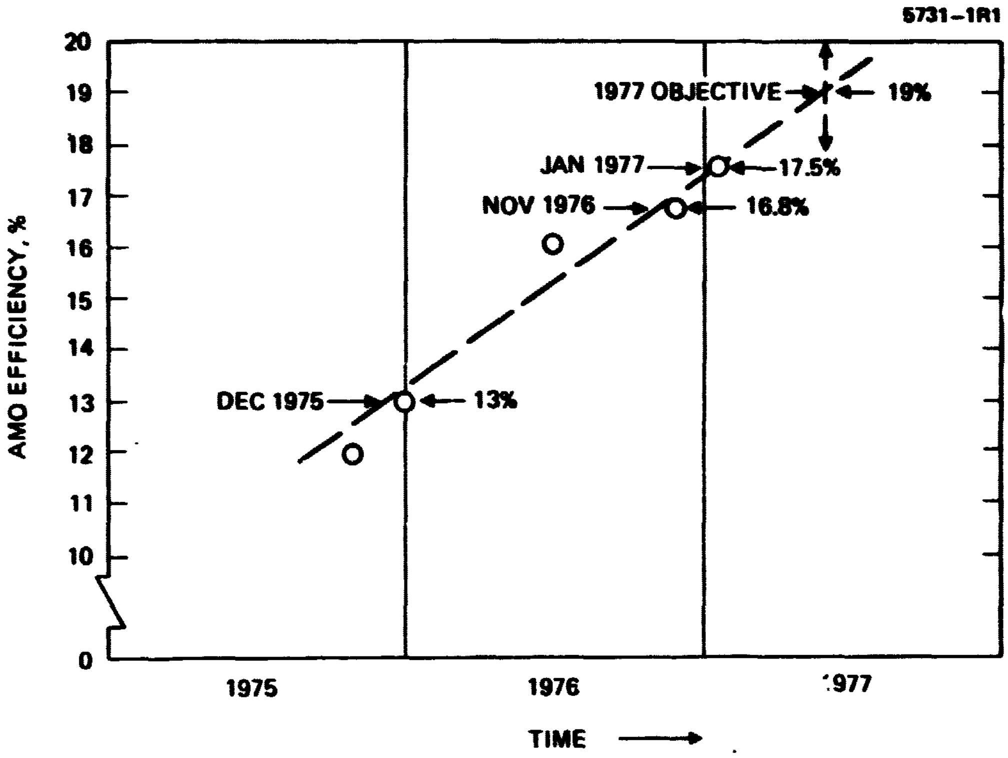

Fig. 3. Hughes Research Laboratories GaAlAs/GaAs solar cell efficiency.

ORIGINAL PAGE IS
OF POOR QUALITY

where

$$n_i^2(T) = N_c N_v e^{-\frac{E_g}{KT}} \tag{3}$$

The variation of V_{oc} with temperature has been calculated from these equations and is shown on Figure 4. A representative set of measured values is also shown on Figure 4, and is found to be in reasonable agreement with theory.

The variation of the short-circuit current I_{sc} with temperature is determined by the temperature variation of the optical absorptions coefficient and of the minority carrier diffusion length, thus affecting the quantum efficiency. The relative importance of these effects on non-optimized GaAs cells is illustrated by a representative set of measurements reproduced in Figure 5. In an optimized cell, however, the quantum efficiency is expected to be close enough to unity so that this effect becomes less important. For a conservative estimate of the variation of the total AMO efficiency of an optimized GaAs solar cell as a function of temperature, we therefore do not include the effect of increasing I_{sc} with temperature. The predicted variation of efficiency with temperature is illustrated on Figure 6 for two cases: the conservative case just outlined above, and the case where I_{sc} increases with temperature at the rate determined experimentally on Figure 5, between 300 and 400 K.

C. THIN FILM VERSUS SINGLE CRYSTAL CELLS

The predictions of performance given above were made for single-crystal solar cells. Thin-film cells will approach the same performance under the following conditions:

- GaAs film thickness t is large when compared to optical absorption depth $1/\alpha$: $t > (1/\alpha)$ where α = optical absorption coefficient of GaAs for photons of an energy larger than the bandgap of GaAs.

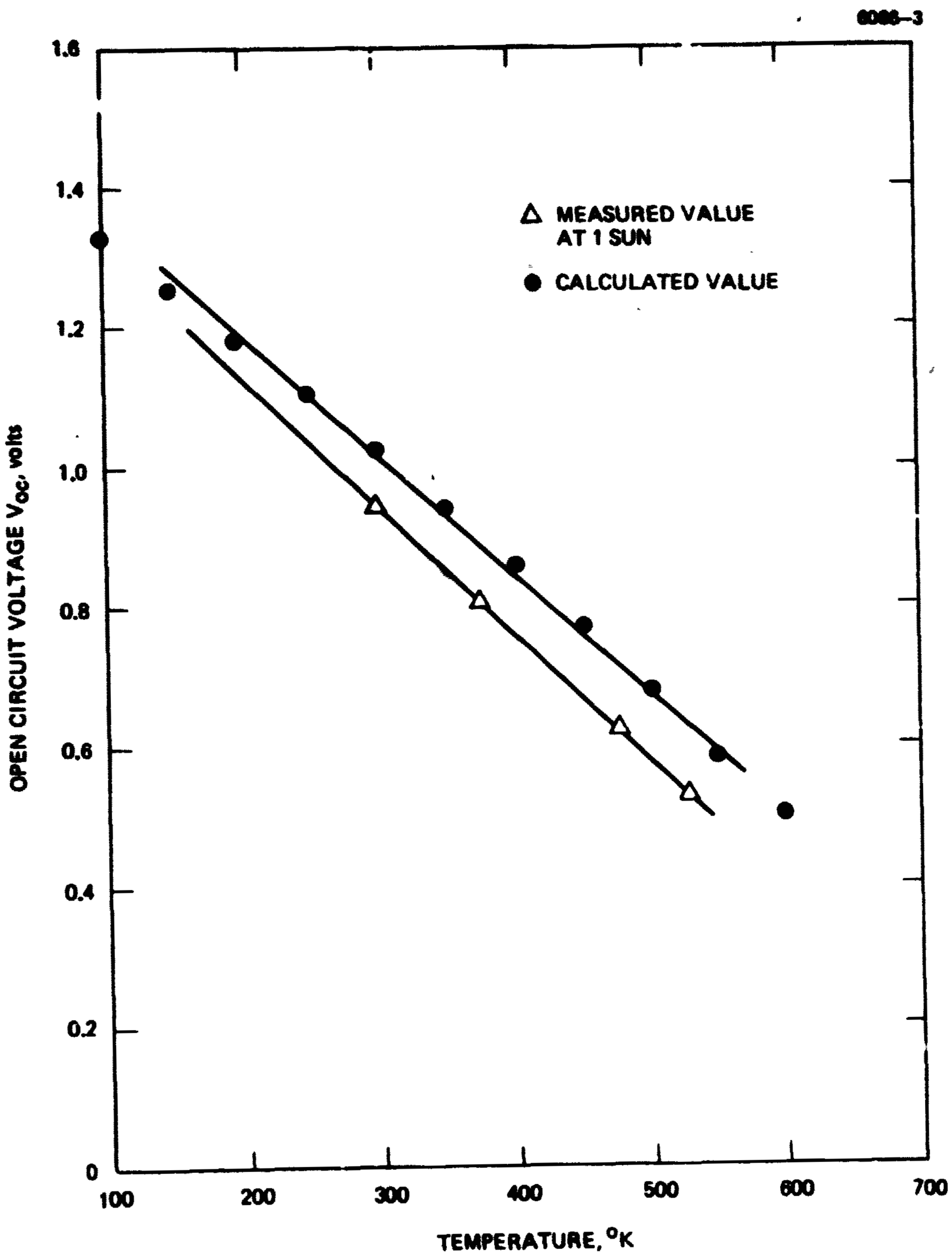

Fig. 4. Open-circuit voltage versus temperature.

ORIGINAL PAGE IS
OF POOR QUALITY

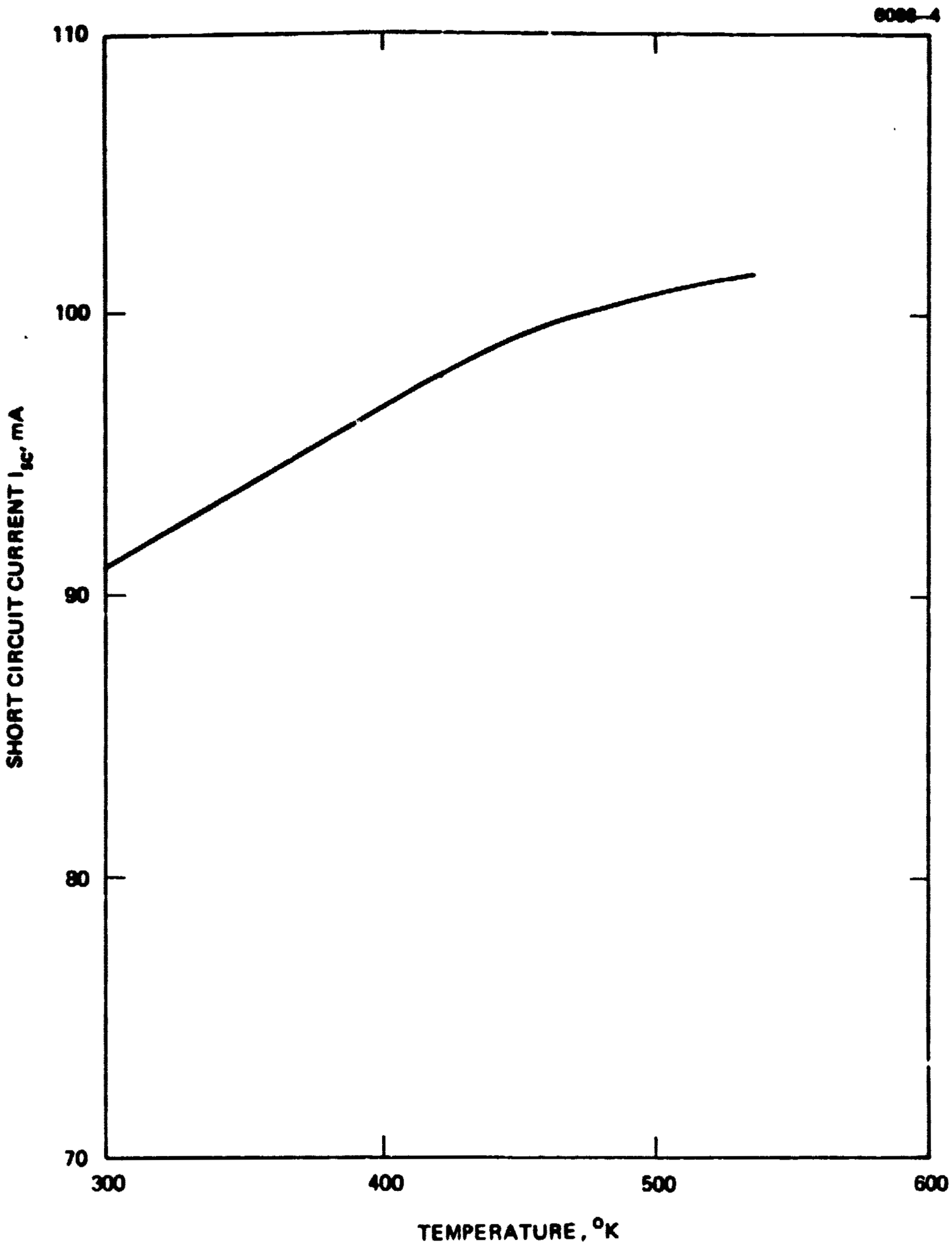

Fig. 5. Short-circuit current versus temperature in experimental (AlGa)As-GaAs solar cell.

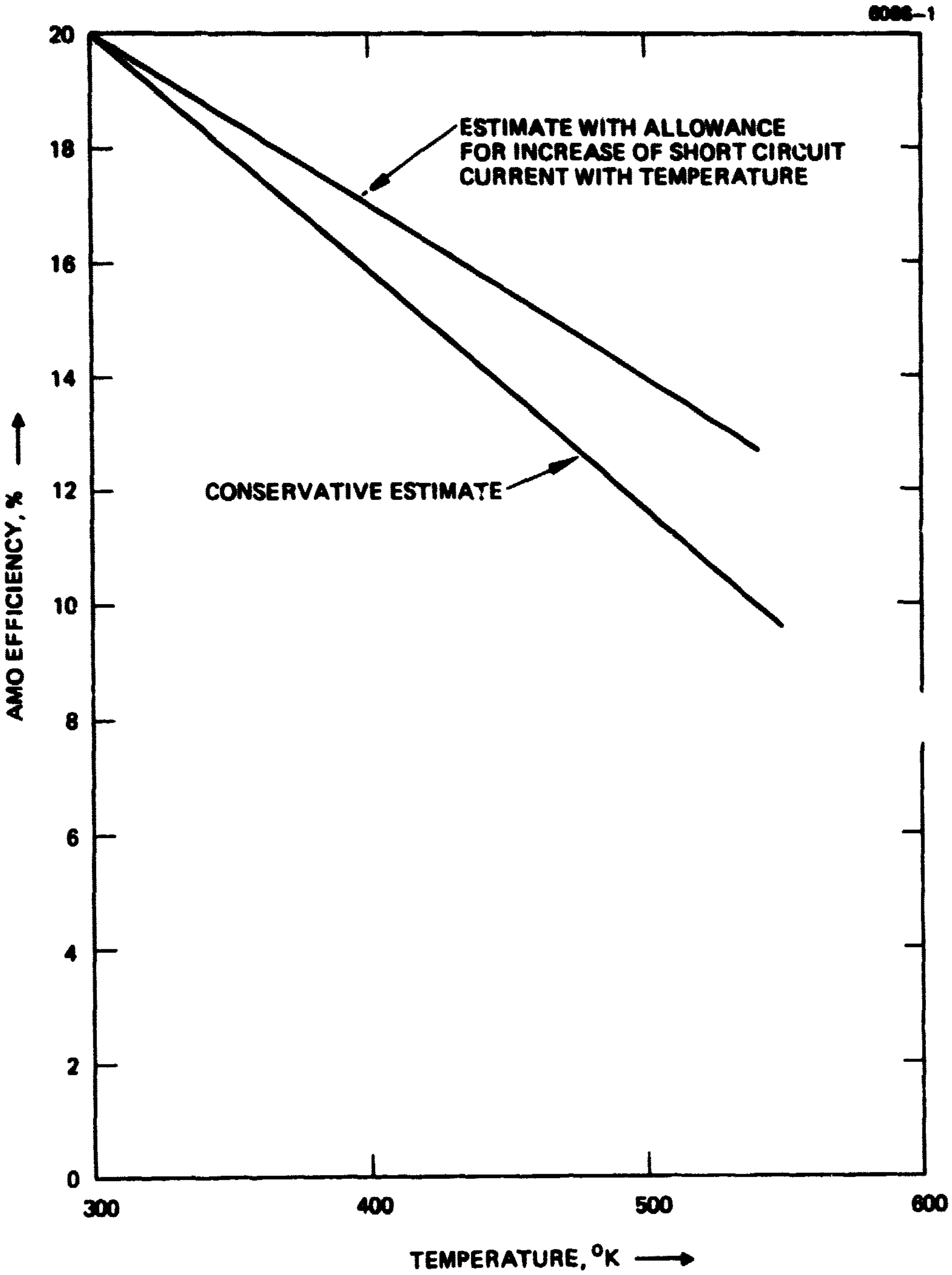

Fig. 6. AMO efficiency versus temperature.

ORIGINAL PAGE IS
OF POOR QUALITY

- Size of individual crystals is large when compared to $1/\alpha$, if GaAs film is polycrystalline.
- Negligible leakage current occurs along crystal boundaries, if GaAs film is polycrystalline.

The first condition is required for efficient absorption of the light in the GaAs thin film. Insofar as $\alpha \gg 10^3$ for GaAs, this first condition will conservatively be satisfied for any film thickness $t > 10$ μm.

The second condition is required to avoid excessive surface recombination losses at the crystal boundaries, assuming that these boundaries exhibit a high surface recombination velocity. This second condition is also likely to be satisfied if $t > 10$ μm if the crystal dimensions are on the order of the film thickness t.

The third condition must be satisfied to avoid loss of open-circuit voltage. The ability to avoid leakage current along crystal boundaries depends on surface doping and on surface states; it is intimately related to the thin-film growth technique to be used.

A number of thin-film growth techniques applicable to GaAs are presently under investigation. They include: (1) the vapor-phase chloride system,[1] (2) the peeled film technology,[2] (3) metalorganic chemical vapor deposition,[3,4] and (4) the planar reactive deposition technique.[5] The vapor-phase chloride system so fas has been used mostly for the growth of AlAs or GaAs, but it is also being considered for the growth of GaAs on low-cost substrates. The planar reactive

1. W.D. Johnston, Jr., and W.M. Callahan, Appl. Phys. Lett. 28, 150 (1976).

2. M. Konagai and K. Takahashi, Proc. of the International Symposium on Solar Energy (Electrochemical Soc., May 5-7, 1976, Washington, D C.), p. 154.

3. P. Dapkus, Proc. of ERDA Semiannual Solar Photovoltaic Program Review Meeting (Aug. 3-6, 1976, Orono, Maine) p. 714.

4. S. Chu, ibid, p. 7?7.

5. K.R. Zanio, ibid, p. 921.

deposition technique has been used so far for the growth of InP, but it can also be modified to grow GaAs thin film. The other two techniques are presently being explored directly for GaAs and (AlGa)As.

Because of the early stage of these investigations, no meaningful experimental data are yet available to show if any penalty will ultimately be associated with the thin-film approach, when compared to the single-crystal approach. The only meaningful prediction at this time for the performance of future thin-film GaAs solar cells remains, therefore, the limiting-case prediction of a performance equal to that of the single-crystal cells considered above.

ORIGINAL PAGE IS
OF POOR QUALITY

SECTION 2

EFFECT OF RADIATION DAMAGE ON SOLAR CELL PERFORMANCE

A. INTRODUCTION

The solar cell performance predictions given in Section 1 correspond to beginning-of-life conditions (no radiation damage). In the SPS application, however, high-energy-particle radiation is present. It is therefore important to evaluate the effect of this radiation on the performance of the GaAs solar cells considered for this application.

Solar cell radiation damage in a synchronous orbit results from damage induced by protons and electrons. In solar cells, damage produced more than a few diffusion lengths from the junction edge has no effect on either the photocurrent or saturation current. The penetration depth for a high-energy proton is deeper than for a low-energy proton. Thus for a high-energy proton, the distribution of damage centers in the solar cell can be considered in first approximation to be uniform, with most damage centers located far away from the junction. On the other hand, damage centers produced by low-energy protons are not uniform and can do considerable damage to the junction space-charge region. This increases the diode saturation current and decreases the fill factor. This kind of damage can cause serious reduction in the solar cell open-circuit voltage V_{oc}, in addition to reducing the diffusion length, the quantum efficiency, and the short-circuit current. Minimal shielding, however, will make these low-energy proton effects negligible. Electron damage in general is not as severe as proton damage because the electron mass is considerably smaller than that of the proton.

Damage-equivalent, normally-incident (DENI) radiation has been established as a laboratory tool to simulate omnidirectional radiation in space. It is used in this section for the evaluation of the effect of radiation damage on the GaAs solar cells. DENI allows the calculation of an equivalent laboratory monoenergetic, normal-incidence radiation fluence Φ_e equivalent to all components of the actual space radiation. This equivalent fluence Φ_e is defined by the following relationships:

$$\Phi_e = \sum_{E=o}^{\infty} [\Phi(>E) - \Phi(>E + \Delta E)] \times D(E, t) \qquad (4)$$

where

Φ_e = the damage equivalent 1 MeV electron fluence (or 10 MeV proton fluence) incident on a solar cell without coverglass.

$\Phi(>E) - \Phi(>E+\Delta E)$ = the isotropic particle fluence having energies in a small energy increment ΔE greater than energy E, in the space orbit of interest.

$D(E, t)$ = the relative damage coefficient for isotropic fluence of space particles of energy E on solar cells shielded by a cover glass of thickness t.

For Si solar cells, it has been found that a 10-MeV proton fluence can be converted to equivalent 1-MeV electron fluence as follows:

$$\phi_e(1 \text{ MeV electrons}) = 3000 \cdot \phi_e(10 \text{ MeV protons}) \qquad (5)$$

This relationship is an approximation for silicon only. For GaAs, the conversion factor has not yet been determined. For the present estimate, however, it will be assumed to be of the same order of magnitude for GaAs as for Si. This leads to the observation that in synchronous orbit, most of the damage can be expected to be due to the proton flux rather than to the electrons (see paragraph 2. D). Our present estimates of GaAs solar cell radiation damage and life for SPS applications will therefore be based on proton radiation damage in this first-order approximation.

ORIGINAL PAGE IS
OF POOR QUALITY

B. RELATIVE DAMAGE COEFFICIENT

The relative damage coefficient D(E, t) is determined by the relative density of damage centers produced in the semiconductor. This density is expected to be determined by the total range of the incident particles that penetrate the semiconductor. This range is related to the incident particle energy, the angle of incidence, and the coverglass thickness. The range of proton tracks in GaAs is almost identical to the range in Si (see Ref. 6). For the present estimates, we take therefore the relative damage coefficient D(E, t) for GaAs to be the same as for Si, as far as proton radiation damage is concerned. For the present first-order calculations, the values of D(E, t) used for the GaAs solar cells as a function of coverglass thickness are therefore the same as those which have been established for Si and which are given in Ref. 7. (As will be shown further on, this does not mean that the damage constants are the same for GaAs and for Si.)

C. RADIATION ENVIRONMENT IN SYNCHRONOUS ORBIT

To determine the solar cell performance degradation caused by radiation, the radiation environment to which these cells are exposed must be defined. To this effect, the radiation environment of an SPS in the synchronous orbit is assumed to be the same as that applicable to Intelsat.[8] The corresponding electron environment in synchronous equatorial orbit is represented by the following expressions for the time average integral fluence spectrum[8]:

$$E \leq 0.3 \text{ MeV: } \log_{10} \Phi_e(>E) = 03.0\,E + 7.7 \tag{6.a}$$

$$0.3 \leq E < 3.5 \text{ MeV: } \log_{10} \Phi_e(>E) = -1.25\,E + 7.2 \tag{6.b}$$

---

6. R. Hart, "Proton-Induced Atomic Displacements in Si and GaAs," Internal Departmental Correspondence, HRL, Aug. 2, 1976.

7. J.R. Carter and H.Y. Tada, "Solar Cell Radiation Handbook," Report No. 21945-6001-RU-00, TRW Systems, prepared by Jet Propulsion Lab Contract No. 953362 and NAS 7-100, June 1973, pg. 4-6, 4-13.

8. Solar Cell Array Design Handbook, Vol. 1, JPL, October 1976, pg. 2.5-4, 2.5-5.

This fluence represents the number of electrons per cm^2 per sec above energy E in MeV. The integral proton fluence spectrum for the mission is represented by the following expressions

$0.01 \leq E \leq 1.0$ MeV

$$\Phi_p(>E) = 6.5 \times 10^{15} \exp(-9.0\,E) \frac{\text{protons}}{\text{cm}^2 \cdot \text{year}} \qquad (7.a)$$

$1.0 < E$ MeV

$$\Phi_p(>E) = 1.5 \times 10^{12}\, E^{-1.53} \frac{\text{protons}}{\text{cm}^2 \cdot \text{cycle}} \qquad (7.b)$$

D. EFFECT OF RADIATION DAMAGE ON (GaAl)As-GaAs SOLAR CELL CHARACTERISTICS

The damage equivalent fluence for both protons and electrons is calculated using the procedure outlined in paragraph 2.A and the relative damage coefficients given in Ref. 7. The fluence spectrum for both electrons and protons in synchronous orbit and used in this calculation is that defined in paragraph 2.C. Table 1 shows the results of this calculation of the equivalent fluences of 1-MeV electrons and of 10-MeV protons as a function of coverglass thickness.* Table 1 shows that the normalized 1-MeV electron fluence exceeds the normalized 10-MeV proton fluence by less than two orders of

*Table 1 refers to "coverglass thickness," with the implication that the radiation protective material provided on the solar cell surface is glass. The relevant parameter for radiation protection is, however, the density of the material multiplied by its thickness. The primary parameter in Table 1 is therefore the coverglass thickness expressed in g/cm^2. The actual thickness in mils given corresponds to the density of glass. Other materials can be used to provide the same protection, provided the thickness of such material is related to the thickness of the equivalent glass cover by the ratio of the density of this material to the density of glass.

ORIGINAL PAGE IS
OF POOR QUALITY

Table 1. Calculation of Yearly Equivalent Fluence in Synchronous Orbit

Coverglass Thickness		Electron Fluence (Normalized to 1-MeV electron)	Proton Fluence (Normalized to 10 MeV proton)
g/cm^2	mil	$electrons/cm^2$	$protons/cm^2$
0	0	6.7×10^{13}	2.18×10^{14}
0.168×10^{-1}	3	4.64×10^{13}	1.67×10^{12}
0.335×10^{-1}	6	3.72×10^{13}	8.02×10^{11}
0.671×10^{-1}	12	2.65×10^{13}	3.71×10^{11}
0.112	20	1.83×10^{13}	2.08×10^{11}
0.168	30	1.21×10^{13}	1.33×10^{11}
0.335	60	4.04×10^{12}	6.16×10^{10}

magnitude. Alternately, the radiation damage caused by a 10-MeV proton is expected to be at least three orders of magnitude worse than that produced by a 1 MeV electron. (See paragraph 2.A and eq. (5).) This leads to the observation of paragraph 2.A that proton radiation damage will be predominant, and that electron radiation damage can be neglected in our first-order estimates. The equivalent 10-MeV proton fluence shown in Table 1 for various thicknesses of coverglass is also plotted in Figure 7, for 33 years of synchronous orbit.

The damage equivalent fluence can now be used to determine the degradation in the minority carrier diffusion length and the resulting loss in solar cell efficiency. Equation (8) characterizes the

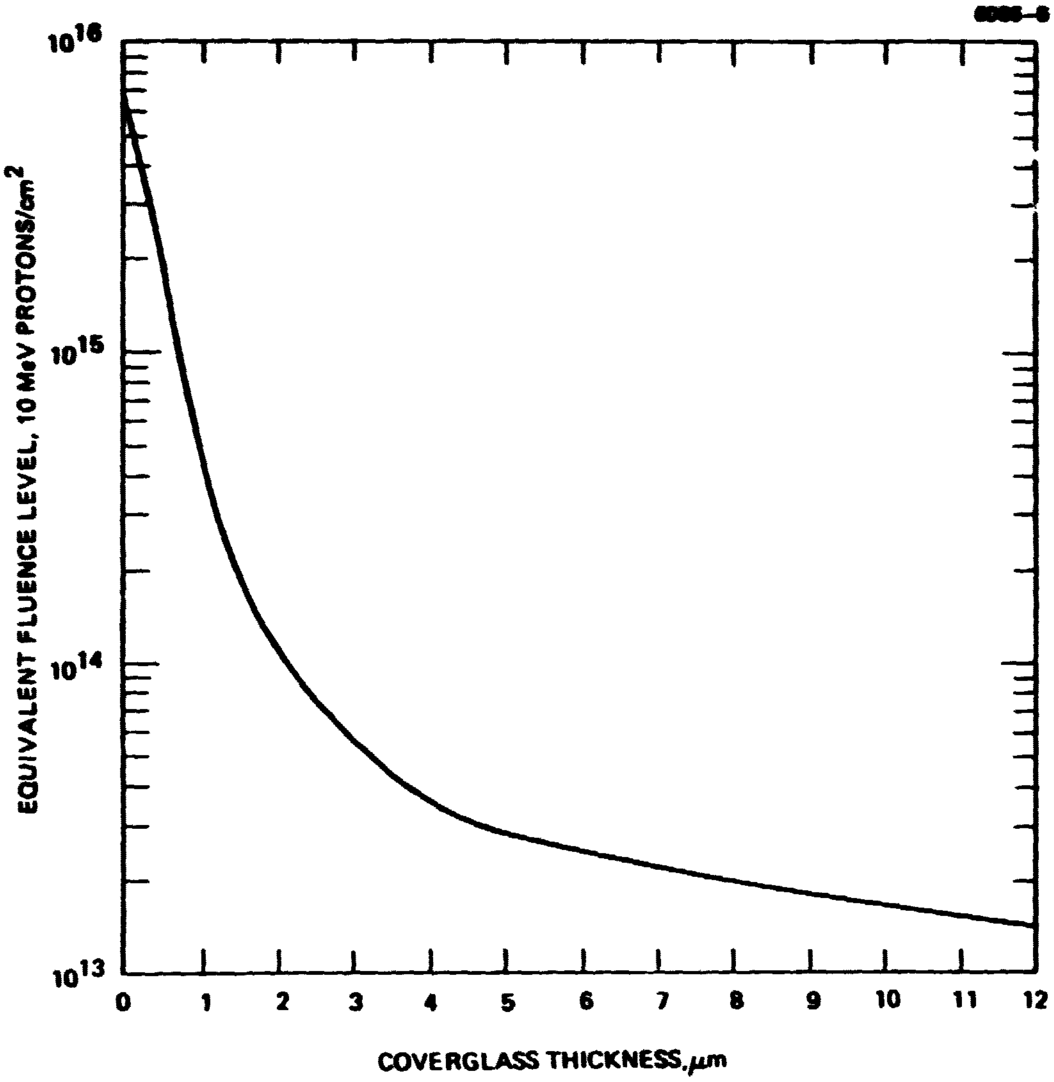

Fig. 7. Calculation of 10-MeV proton equivalent fluence level in synchronous orbit as a function of coverglass thickness, for 33 years.

ORIGINAL PAGE IS OF POOR QUALITY

degradation of solar cells in terms of the changes in the minority carrier diffusion length L:

$$\frac{1}{L^2} = \frac{1}{L_o^2} + K_L \Phi \qquad (8)$$

where L_o is the initial value of the diffusion length and L is the final value. K_L is the damage constant which is directly proportional to the density of recombination centers. Once the damage constant K_L and Φ are known, then the cell's short-circuit current density (I_{sc}), open-circuit voltage (V_{oc}) maximum power (P_m) and output power efficiency (η) can be calculated using the same basic solar cell equations used in Section 1.

The damage constant K_L for silicon has been measured as a function of incident particle energies and is tabulated in Table 2.

Table 2. Diffusion Length Damage Constant for Proton Irradiation

Energy (MeV)	K_L (Si)	K_L (GaAs)
2 MeV	8×10^{-7}	16×10^{-7}
7	4×10^{-7}	8×10^{-7}
10	3.5×10^{-7}	7×10^{-7}
30	3×10^{-7}	6×10^{-7}
70	1.8×10^{-7}	3.6×10^{-7}
100	1.6×10^{-7}	3.2×10^{-7}
155	1.3×10^{-7}	2.6×10^{-7}

Furthermore, we estimate (Ref. 6) that the atom displacement density caused by proton impact in GaAs is approximately twice that of silicon. If one assumes that the recombination center density is proportional to the atom displacement density in both materials, and since K_L is also directly proportional to the recombination center density, then one can expect K_L for GaAs to be two times larger than for silicon, for the first order approximation. This is also shown in Table 2. With the values of K_L given in Table 2 for GaAs and the values of equivalent 10-MeV proton fluence shown in Figure 7, the corresponding values of minority carrier diffusion length, short circuit current density, and solar cell efficiency after 33 years (3 solar cycles) in synchronous orbit can be calculated. The results of such a calculation are summarized on Table 3. The solar cell efficiency anticipated after 33 year life according to Table 3 is plotted on Figure 8 as a function of coverglass thickness. Figure 8 provides our best present estimate for the tradeoff between GaAs solar cell efficiency and coverglass thickness* for SPS applications, accounting for the radiation damage expected from 33 years in synchronous orbit.

Inspection of Figure 8 shows at once that GaAs solar cells are expected to be much more resistant than are Si solar cells to radiation damage in synchronous orbit. This is consistent with the expectation that most of this damage is caused by exposure to high-energy protons, provided a minimal amount of coverglass protection is present for shielding against the lowest-energy protons. The outstanding ability of GaAs solar cells to resist high-energy proton damage as compared to Si solar cells had already been observed in the earliest studies of GaAs solar cells.[9] A qualitative explanation for this capability is the observation that the optical absorption coefficient of GaAs is much larger than that of Si. The thickness of the active part

*See footnote to paragraph 2.D for radiation protective cover materials different from glass.

[9] J. J. Wysocki, "Radiation Studies on GaAs and Si Devices," IEEE Transactions on Nuclear Science, Nov. 1963, p. 60-70.

ORIGINAL PAGE IS
OF POOR QUALITY

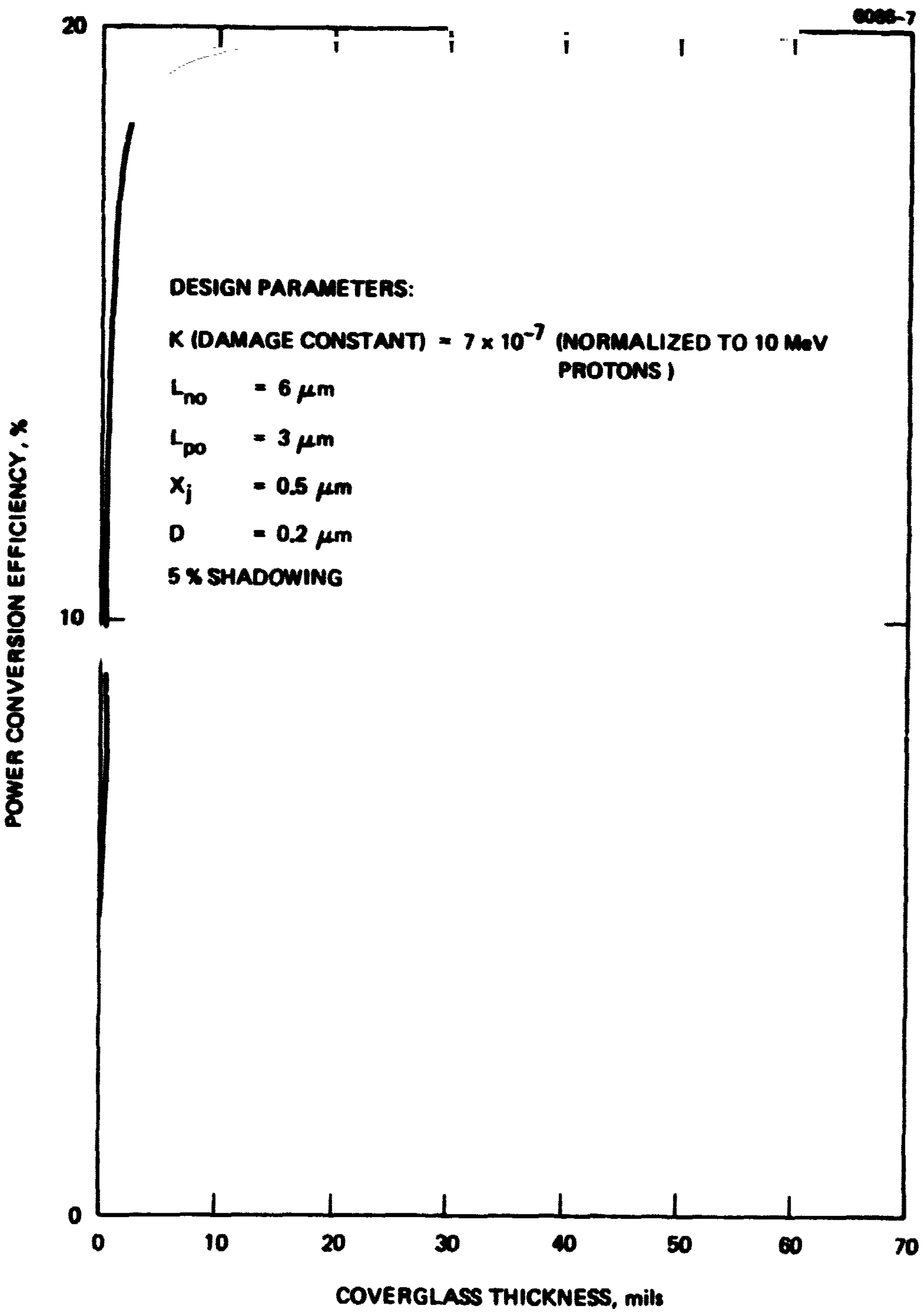

Fig. 8. Power conversion efficiency versus coverglass thickness after 33 years in synchronous orbit.

Table 3. (GaAl)As-GaAs Solar Cell Radiation Characteristics in Synchronous Orbit Normalized to 10 MeV Proton
$K = 7 \times 10^{-7}$

Coverglass Thickness (mil)	Total Equivalent Fluence/cm^2 -33 yr.	Short Circuit Current Density I_{sc} mA/cm^2 5% Shadowing	Maximum Power Output (mW) P_n	Power Conversion Efficiency %
0	7.2×10^{15}	6	6.79	5
1.5	2×10^{14}	25.19	22.7	16.76
3	5.5×10^{13}	28.06	25.35	18.73
6	2.64×10^{13}	28.86	26.1	19.27
12	1.22×10^{13}	29.36	26.56	19.62
20	6.86×10^{12}	29.58	26.76	19.77
30	4.39×10^{12}	29.69	26.86	19.8
60	2.0×10^{12}	29.80	26.9[illegible]	19.92

of the GaAs solar cell is consequently much smaller than that of the Si cell. The minority carrier diffusion length required in the GaAs cell is correspondingly much smaller. This means that a higher proton fluence will be tolerable in a GaAs cell than in a Si cell, before it decreases the minority carrier diffusion length to values sufficiently low to have a noticeable effect on the cell's efficiency.

While the predictions of Figure 8 and the above considerations indicate prospects for a superior radiation resistance of GaAs solar cells, it is essential to emphasize that the predictions of Figure 8 still lack a solid experimental foundation. One assumption that is

ORIGINAL PAGE IS OF POOR QUALITY

open to question is that the recombination center density is assumed to be directly proportional to the atom displacement density, with the same proportionality constant for GaAs and for Si.

E. ANNEALING EFFECTS

The purpose of the coverglass is to prevent radiation particles, especially low-energy protons, from reaching the semiconductor and producing damage centers. Alternatively, once such damage centers are produced, it becomes of interest to examine the possibility of removing them from the active regions of the solar cell. This can be achieved[10] either by thermal annealing or by minority carrier injection or by both. Such annealing could permit reduction of the coverglass thickness to a nominal value (1 mil or less) sufficient for protection against the lowest energy protons only (protons of energy <1 MeV, which are expected to be the most damaging ones).

Table 4 summarizes the results of electron irradiation studies and of the corresponding thermal annealing on GaAs material. This shows that most of the defects can be annealed at temperatures between 200C to 300C. In addition to this, Rockwell International has obtained encouraging results[11] in annealing (AlGa)As-GaAs solar cells at temperatures as low as 125C, after exposure of these cells to 1-MeV electron radiation. Extrapolation of these results to the GaAs solar cells to be used on an SPS is hazardous because these results apply to damage caused by electron irradiation. While it is plausible that similar effects will be available to anneal radiation damage due to

---

[10] D.V. Lang and L.C. Kimerling, "Observation of Recombination-Enhanced Defect Reactions in Semiconductors," Phys. Rev. Letters Vol. 33, No. 8, Aug. 1974.

[11] J.F. Madewell and A.A. Nussberger, "A Solar Power System with GaAs Solar Cells," AIAA Conf. on the Future of Aerospace Power Systems, St. Louis, Mo., March 3, 1977.

Table 4. Electron Irradiation Thermal Annealing Results

Authors	Type of Material	Type and Energy of Irradiation	Levels Found	Carrier Removal Rate cm^{-1}	Annealing
Brehm & Pearson	GaAs Epitaxial (liquid phase)	Co^{60} - 1.25 MeV at room temp.			
	n-type (Sn-doped) 1-4 x 10^{15} cm^{-3}		0.13, 0.16, 0.3 eV Below Ec (Hall Effect)	0.0079 at 297 K 0.0123 at 77 K	500 K
	p-type (Zn-doped) 4 x 10^{15} cm^{-3}		0.059 and 0.10 eV Above Ev (Hall Effect)	0.0011 at 297 K 0.0022 at 77 K	500 K
Kalma & Berger	GaAs Bulk all n-type	electron 1 MeV 30 MeV	Ec - 0.15 eV intrinsic defect	1.6-2.2 4.5-5.9	200-300°C, Ea 1 2 eV
	n-type (Si-doped) 2 x 10^{17} cm^{-3}	1 MeV 30 MeV	Ec - 0.02 eV	1.1 7.5	200-300°C 200-300°C
	p-type (Zn-doped) 6.5 x 10^{17} cm^{-3}	1 MeV 30 MeV 30 MeV	Ev + 0.17 eV Ev + 0.17 eV Ev + 0.06 eV	2.7 6 4.5	150-200°C 150-200°C 150-200°C
Jeong, et. al.	GaAs Bulk	electron 1.5-2.0 MeV at 77 K	Ec - 0.15 eV		250 K and 460 K
Stein	GaAs Epitaxial n-type (S-doped) 2 x 10^{15} cm^{-3}	electron 2 MeV at 80 K neutron at 76 K	Ec - 0.14 eV	2.9 at 80 K 3.0 at 296 K	250 K and 500 K small anneal in range 76-100 K
Mattauch & Healy	GaAs Bulk n-type (Si-doped) 2 x 10^{16} cm^{-3}	electron 7 MeV at 300 K	Ec - 0.31 eV	0.0023 at 77 K	265°C-385°C Ea 1.07 eV

the proton flux which is of primary concern in the SPS application, experimental investigation is still required.

The thermal annealing time required for effective recovery of solar cell performance can be expected to be relatively short, on the order of hours at most. This provides the opportunity of periodically annealing groups of cells by forcing an adequate forward diode current through these cells and obtaining the required temperature by electrical

ORIGINAL PAGE IS OF POOR QUALITY

ORIGINAL PAGE IS OF POOR QUALITY

heating over limited periods of time. Assuming therm..l radiation cooling of the cells, the cell temperature could, . instance, be raised from an operating temperature of 50 C to . annealing temperature in excess of 150 C by providing, via forward current, an electric power input of less than 0.2 W/cm^2.

SECTION 3

EFFICIENCY VS CONCENTRATION RATIO

The short-circuit current density of the (GaAl)As-GaAs solar cell has been derived for a number of conditions.[12] Figure 9 shows this short-circuit current density as a function of (GaAl)As window layer thickness. The short-circuit current density is seen to increase when the (GaAl)As window layer becomes very thin ($D < 0.5$ μm), which favors thin window layers.

The total series resistance of the cell has also been derived.[13] It can be expressed through the following relationship:

$$R_s = \underbrace{\frac{\rho_s}{12D} b^2}_{\substack{\text{window}\\ \text{layer}}} + \underbrace{\frac{b}{w} \frac{\rho_f}{3h} a^2}_{\substack{\text{contact}\\ \text{finger}}} + \underbrace{\frac{b}{w} R_c}_{\substack{\text{contact}\\ \text{proper}}} \tag{9}$$

where

ρ_s = semiconductor resistivity ((GaAl)As window layer)

D = thickness of (GaAl)As window layer

$2a$ = finger length

b = finger spacing

w = finger width

h = finger height (thickness)

---

[12] Interim Technical Report, Contract F33615-76-C-212, Dec. 1976.

[13] Quarterly Progress Report 1, Contract 05-0164, Feb. 1977.

ORIGINAL PAGE IS
OF POOR QUALITY

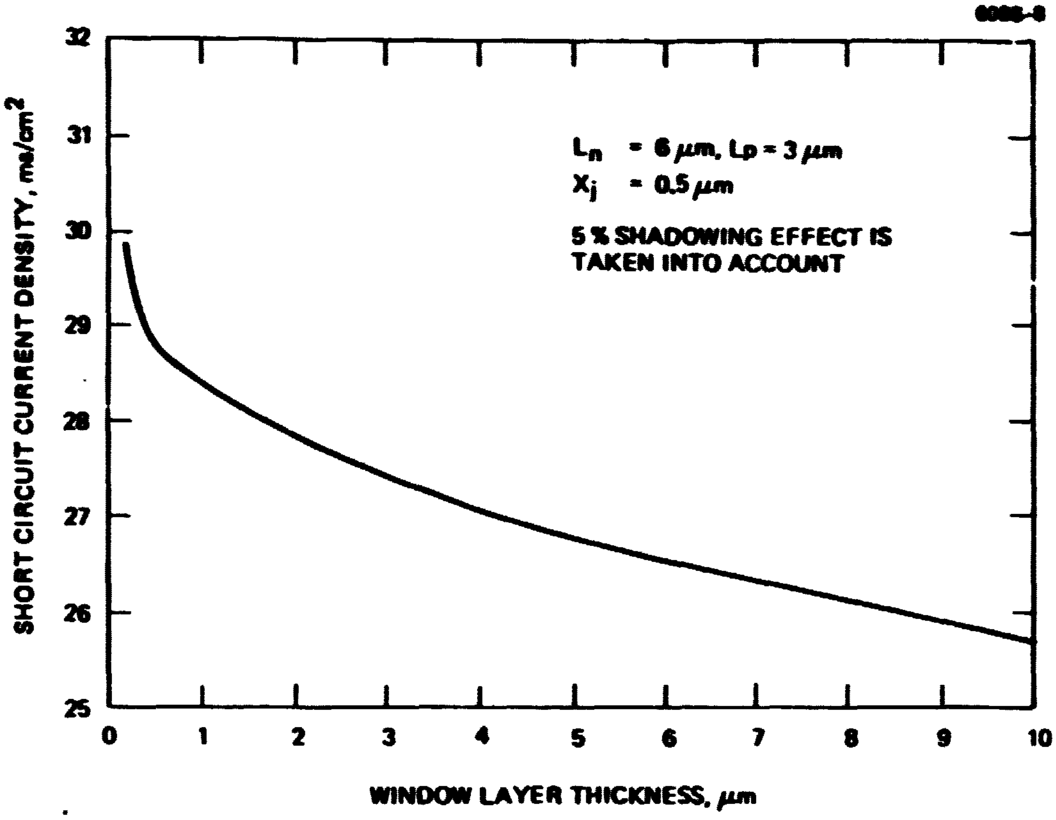

Fig. 9. Short-circuit current density versus window layer thickness.

ρ_f = resistivity of finger metal

R_c = normalized metal-semiconductor contact resistance (Ω cm^2)

The first term of the right-hand side represents the resistance of the (GaAl)As window layer, the second term represents the losses due to the resistance of the contact fingers, and the third term represents semiconductor-metal contact resistance. Figure 10 shows the total series resistance as a function of window layer thickness. Figure 10 shows that for a thin (GaAl)As layer (D < 0.5 μm) the total series resistance increases substantially. This variation of series resistance with window layer thickness is only a second-order effect for 1 sun illumination at AMO. However, this may become a serious effect for a thin-window (AlGa)As layer at higher concentration ratio. Figure 11 shows the power conversion efficiency versus concentration ratio for several thicknesses of (GaAl)As layer. For optimum solar cell design as a function of solar concentration ratio, the envelope of the curves of Figure 11 can be used. This is shown in Figure 12.

ORIGINAL PAGE IS
OF POOR QUALITY

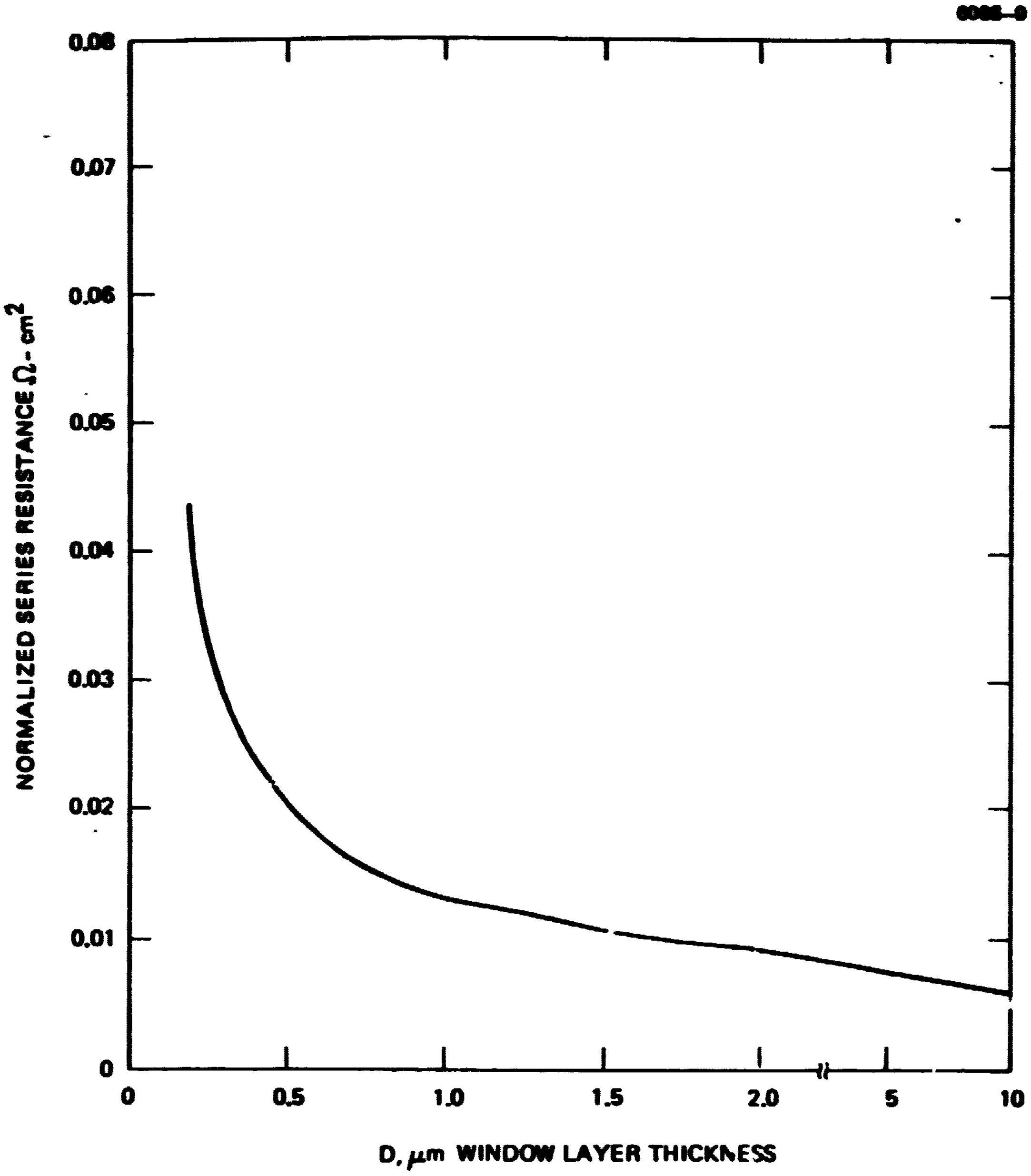

Fig. 10. Series resistance versus window layer thickness.

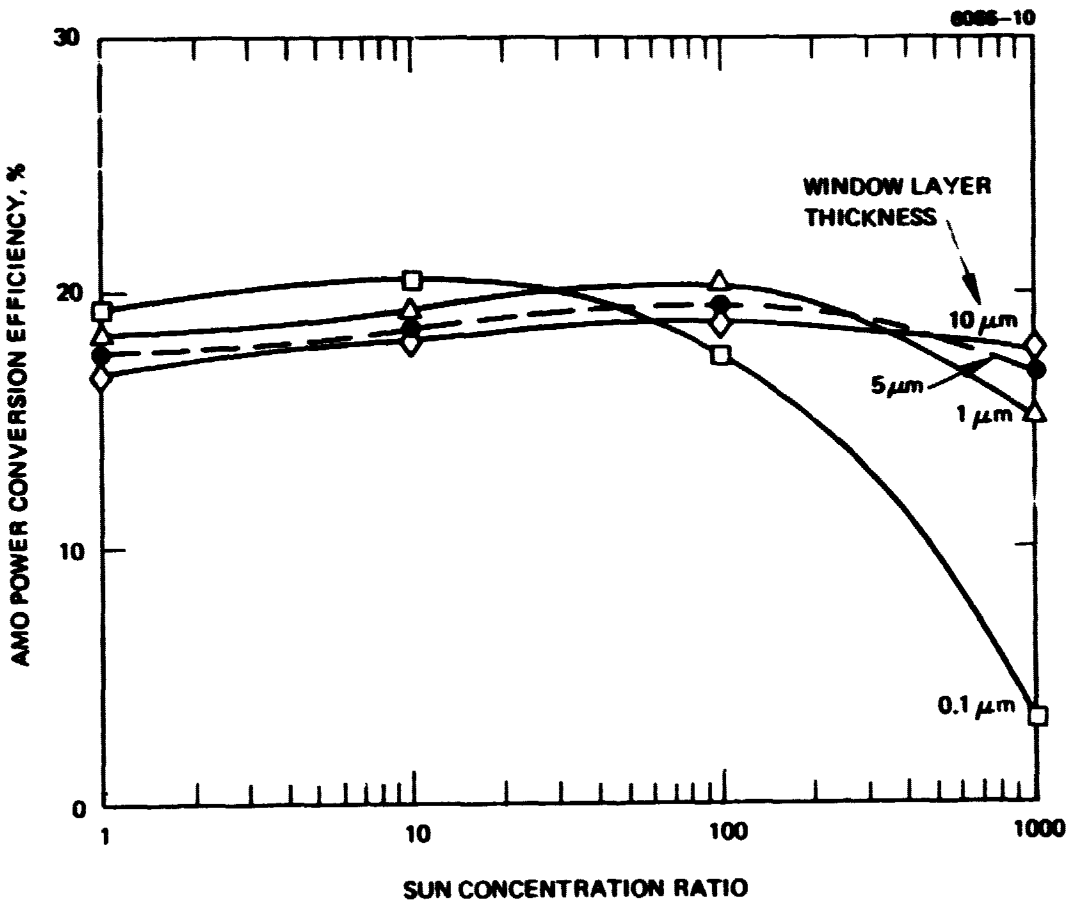

Fig. 11. AMO power conversion versus concentration ratio, fo- various window thicknesses.

ORIGINAL PAGE IS
OF POOR QUALITY

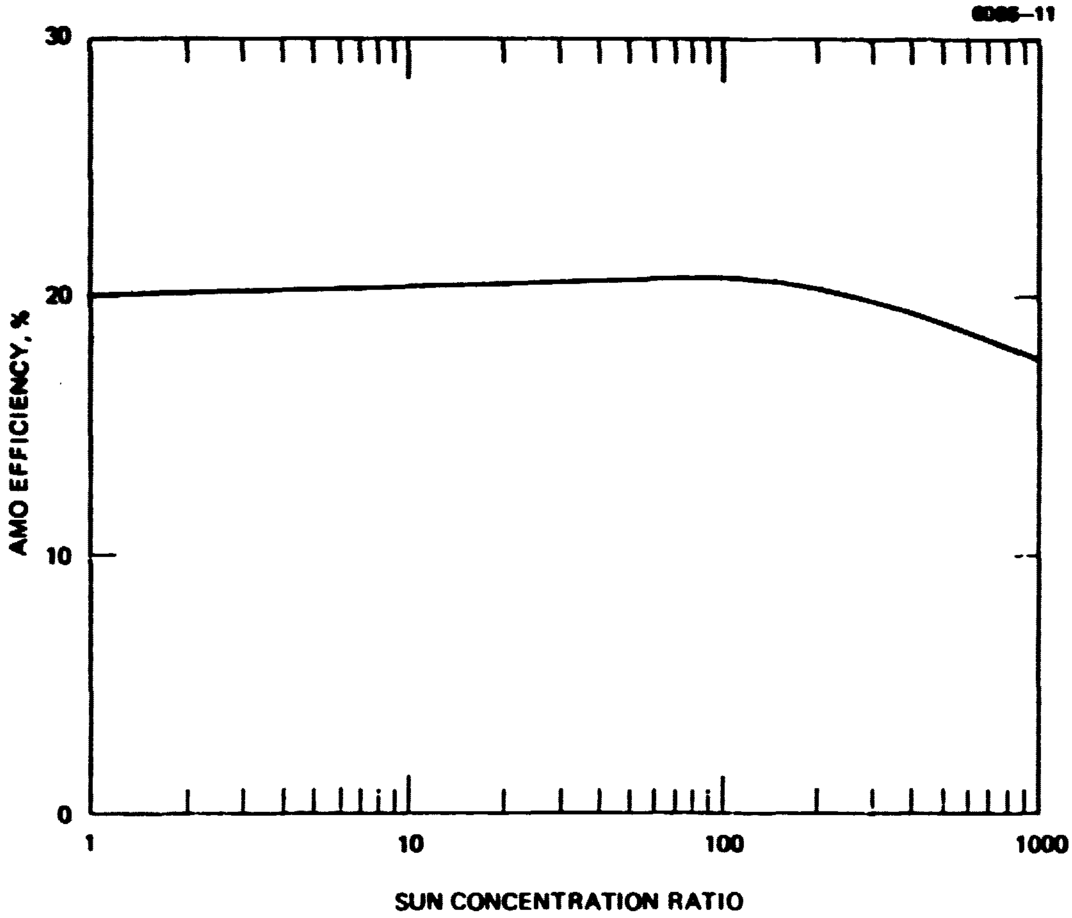

Fig. 12. Power conversion efficiency versus concentration ratio.

SECTION 4

GaAs SOLAR CELL COST AND WEIGHT ESTIMATES

The estimates of cost and weight of the solar cell payload for SPS applications have to be made on the basis of present technology as well as on what is ultimately realizable. Practical solar cells made today are based on single crystals of silicon or GaAs. Single-crystal substrates 8 mil thick have been used successfully for the fabrication of GaAs solar cells, and the fabrication method can be successfully developed for a manufacturing line. The cost and weight of cells manufactured on this basis are calculated to be below the values both for discrete cells with moderate concentration and for flat panels. The use of thin-film cells is much more attractive. Even though the technology for these cells is still in its infancy, the advantages to be gained are significant enough to justify its development.

In all of our calculations that follow, certain simplifying assumptions are made.

(1) An efficiency of 20% AMO is assumed for the GaAs cell, both single-crystal and thin-film. It is our feeling that at the present stage of GaAs cell technology, any modification of this number would be arbitrary.

(2) The radiation damage in GaAs is not well enough understood to justify quantitatively exact predictions of the end-of-life efficiencies for the cells. However, the information available both at Hughes and in the literature leads us to believe that GaAs cells can be expected to perform with little degradation, especially if temperature annealing can be used (see Section 2). Since future technology will lead to optimization of cell characteristics using the guidelines presently available, we feel justified in assuming that an efficiency close to 20% AMO can be expected from GaAs cells for 30 years in synchronous orbit.

ORIGINAL PAGE IS OF POOR QUALITY

(3) The best way to protect the cells from radiation damage is still open to some question. Our calculations in Section 2 indicate that a glass cover of ~5 mil would be desirable. However, the weight considerations for space applications and the complexity of using thick glass covers in foldable 1-mil plastic blankets would lead us to believe that plastic cover glasses of the order of 1 mil thickness would have to be preferred for the present application. In this case, the cell efficiency would degrade as a function of time in orbit; however, by judicious introduction of annealing cycles as discussed in paragraph 2. E, the GaAs cells can be expected to recover most of their efficiency. With this mode of operation, the efficiency of the cells could be maintained close to the 20% assumed in the calculations.

(4) The use of a concentrator and the optimum concentration ratio are dependent on the cost-weight tradeoffs between cell cost and concentrator cost. At concentrations over 10, cooling becomes more and more demanding and has to be factored in. The cost of GaAs cells, however, can be estimated independently from those for the concentrator, and we have done this for several concentrations. The decrease of system efficiency due to the concentrator proper is not considered in the simple calculations made here, because it is dependent on the specific concentrating system.

A. SINGLE-CRYSTAL CELLS

GaAs cells with 20% AMO efficiency at 1 sun can be fabricated with some extrapolation of the present technology available at Hughes Research Laboratories. With appropriate radiation shielding, we can expect a power output of 27 mW/cm^2 from these cells. The cell area needed would then be 40 cm^2/W. If we assume the cells to be 200 μm thick, 40 cm^2 would have a weight of 4. 5 g. In large quantities, GaAs is expected to cost no more than one dollar per gram for single-crystal material. Since the processing losses are about 50%, the cost of the GaAs for the 4. 5 g of cells should be in the range of $10. 00. Spectrolab* has estimated that the cost of cell fabrication using our present technique

*Hughes Aircraft Company subsidiary.

will be about \$2.50 for a 4 cm^2 cell, making it \$25.00 for 40 cm^2. Thus, the total cost of 40 cm^2 of GaAs cells would be ~\$35.00 for single-crystal cells. The cost of cells would then be \$35.00/W at single-crystal sun concentrations, using 4 cm^2 discrete GaAs cells with 20% AMO efficiency, and appropriate shielding against space radiation.

For the SPS application, we have to consider the tradeoff involved in using moderate levels of concentration to reduce cell area. The judgement can be made on the basis of our discussion in Section 3. The tradeoff is between the weight, cost, and complexity of the concentrator structure with increasing concentration ratio versus the simplicity of the total structure at concentrations below ~10 suns. At low concentrations no special cooling of the cells is necessary and the concentrator can bemade of lightweight (1 mil thick) plastic. The area of cell required, and its weight, will go down by a factor almost equal to the concentration ratio. The actual gains will be reduced somewhat due to the sun-pointing inaccuracy of the concentrator, and due to reflection losses. In our calculations we neglect these factors, since a number of improvements on simple concentrator structures to reduce the effects of sun misalignment are in progress. Table 5 summarizes the above cost-weight considerations for various concentration ratios.

B. THIN-FILM CELLS

The alternative to single-crystal cells is the use of thin films to produce the GaAs solar cells. Since the minority carrier diffusion length in GaAs is of the order of 5 μm, a thin film about 20 μm would be adequate to give an acceptable solar cell. This would be a factor of 10 less than the 8-mil single-crystal cells considered in the previous section and hence should reduce the cell weight proportionately. The materials cost should also be proportionately lower, and the utilization of material probably more efficient, since thin-film

Table 5. Cost-Weight Estimates as a Function of Concentration Ratio for Single-Crystal GaAs Solar Cells

Concentration Ratio	Cell Area (cm^2/watt)	Cell Weight (g/watt)	Power/kW/Kg (cell)	Cost (GaAs) ($/watt)	Comments
1	40	4.5	0.2	35	Radiational cooling sufficient
10	4	0.5	2	3.5	
100	0.5	0.05	18	0.40	Some cooling necessary. Concentrator cost?
1000	0.07	0.005	160	0.05	Extensive cooling including liquid circulation. Complex and costly concentrator.

technology is capable of more efficient GaAs deposition than is single-crystal processing. The processing cost for the cell may also be lower ultimately than that for single crystals. However, it should be noted that there are still many difficult questions to be answered concerning thin-film cell operation and its ultimate reliability. All the known results on silicon thin-film technology would lead us to the conclusion that, with sufficient time and effort, one could hope to develop thin-film cells that could match single-crystal cells. On the basis of this projection, we postulate a 25-μm GaAs thin-film cell on a conducting metal film deposited on a one-mil plastic foil.

The weight of 40 cm^2 of "cell" would be only about 0.5 g of GaAs on such a structure. The weight of the plastic and metal would be comparable. The cost of GaAs would be ≈\$0.50. This means that a watt of energy could be produced for a GaAs weight of 0.5 g, and a cost of \$0.50 for materials. No documented forecast for the fabrication cost of thin-film cells can be made before further development of the relevant fabrication technology. It can be assumed as an arbitrary guideline that fabrication costs will ultimately be no higher than materials cost. On this basis, a fabrication cost of \$0.50/watt is obtained, leading to a total cell cost of \$1/watt. A concentration of ~5 can be considered for thin-film GaAs cells. If the plastic concentrator is made as an integral foldable sheet with the GaAs thin-film cell at the focus of the concentrating structure, the GaAs weight and cost can be reduced below that of the continuous thin film. The cost tradeoff will be between the simplicity of the thin-film deposition in a continuous sheet against the deposition of discrete elements on the concentrator structure. The weight advantage will probably rest with the plastic concentrator design if a 1-mil-or-less foil thickness can be used economically for this structure. The thin-film cost consideration can be summarized as follows:

Cost-Weight Estimate for Thin Film (GaAs) Solar Cells

Concentration Ratio	Cell Area (cm^2/watt)	Cell Weight (g/watt)	Power/Weight (kW/kg)(cell)	Cost/watt
1	40	0.5	2	1.00
5	8	0.1	10	0.20

All the arguments given in the concentrator design for the single-crystal cells are equally valid for the thin-film cells. The misalignment with the sun will lower the efficiency somewhat and will decrease the cost benefit to be gained from concentration. It would also appear that the thin film would be more susceptible to problems arising from grain boundaries, especially as the current density increases with higher concentration. These factors must be understood better before quantitative conclusions can be reached.

C. SUMMARY

The options for the SPS systems definitions should include GaAs cells since they have demonstrated higher efficiency and excellent life expectancy and stability from the data presently available. The cost/weight tradeoff with a concentration below 10 and using a simple plastic panel seems to be very attractive from projections that can be made based on data presently available. These will become even more convincing if thin-film GaAs solar cells can be developed and shown acceptable for long-term space applications.

ADDENDUM

At the time of writing this report, we have obtained preliminary experimental evidence on the magnitude of 10-MeV proton radiation damage for state-of-the-art (AlGa)As-GaAs solar cells. This indicates that the values for the 10-MeV proton irradiation damage constant K_L indicated on Table 2 may be too optimistic. An important consequence of this observation is that the possibilities of thermal annealing of radiation damage on these cells may gain critical importance (see Section 2.E). The tradeoff between end-of-life (33 years) power conversion efficiency and coverglass thickness indicated on Fig. 8 is too optimistic. Heavier protective cover thicknesses will most likely be required in the absence of thermal annealing, leading to unacceptable weight penalties. This penalty can be avoided if thermal annealing is found to be sufficiently effective. Alternately, a system using relatively high solar concentration ratios could tolerate relatively thick solar cell coverglass without substantial system weight penalty, if thermal annealing cannot be relied upon.

3.2.2.2 Gallium Required for Solar Power Satellites

Plotted in Figure 3.2-21 is the quantity of gallium required for each 100 km^2 of solar array, as a function of thickness of gallium arsenide. The active layer of gallium arsenide need by only 3 to 5 μm thick. However, a technique is not yet available for making high-efficiency solar cells from gallium arsenide layers so thin.

Possible annual U.S. gallium production quantities, shown as arrows, are from "Availability of Gallium and Arsenic" by Dr. R. N. Anderson, Professor of Materials Science and Metallurgy, Stanford University. He states that today's techniques can recover 10 percent of the gallium in bauxite and flyash from coal combustion. Ways of increasing gallium production are:

- o Recover more gallium from bauxite. The French have a process that recovers 20 percent of the gallium.
- o Extract gallium from sea water.
- o Develop foreign sources.
- o Extract gallium from oil sludge.

3.2.2.3 Gallium Arsenide Configuration Comparisons

For gallium arsenide, we did not look at array addition as a power maintenance option. Oversizing and annealing are compared in Figure 3.2-22. With its less severe degradation characteristics, the overall difference for gallium arsenide would be 1 to 2% in total array mass. The initial difference in area would only be about 6 to 7% (less than for initial oversizing). The advantages of annealing are substantial but certainly not what was seen for silicon. One of the interesting things about gallium arsenide is the low projected dollar value. However, later charts show some sensitivities which should temper that view somewhat.

Shown in Figure 3.2-23 is the concentration ratio 2 versus concentration ratio 1 for geosynchronous construction. With the high cost of the gallium arsenide array CR2 has a slight advantage. Probably the most important factor was the superior performance of the gallium arsenide array at concentration ratio 2. The difference is small and it doesn't account for several other factors which would be an eventual trade. 1) Concentration ratio 1, as the construction analysis showed, appears to be substantially simpler to build. 2) The smaller satellite will have less problems concerned with control and station keeping.

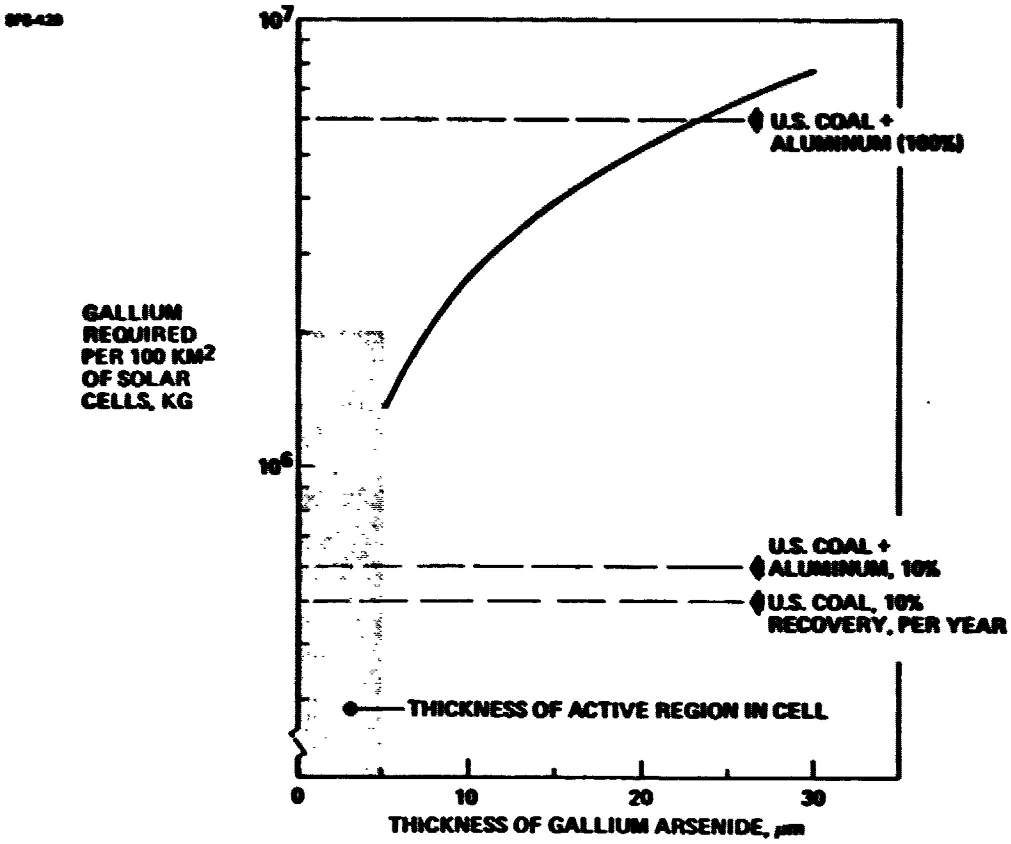

Figure 3.2-21. Gallium Required for Solar Power Satellites

SPS 742

GaAs Annealing Advantage is 14% as Compared to 21% for Silicon Satellites

GaAs—10 GW MIN. FOR 30 YRS.—CR=2 GEO ASSEMBLY

MAINTAINED VIA INITIAL OVERSIZE

TOTAL AREA:	136.2 Km^2
ACTIVE ARRAY AREA:	64.5 Km^2
MASS:	52,130 MT
PRODUCTION COST: $\$ \sim 10^6$	5510.2
TOTAL COST: $\$ \sim 10^6$	9740.7

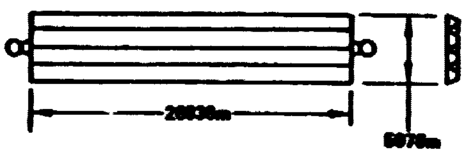

MAINTAINED VIA ANNEALING

TOTAL AREA:	98.7 Km^2
ACTIVE ARRAY AREA:	46.6 Km^2
MASS:	42,736 MT
PRODUCTION COST: $\$ \sim 10^6$	4882.9
TOTAL COST: $\$ \sim 10^6$	8346.9

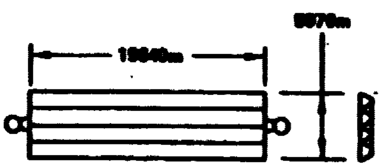

Figure 3.2-22. GaAs Satellite Power Maintenance Comparison

ORIGINAL PAGE IS
OF POOR QUALITY

The same match up of satellites is shown in Figure 3.2-24 but instead of at GEO they are assembled at LEO and self-transported. There is no change in the CR-1 – CR-2 comparison. There appears to be no substantial advantage over the geosynchronous assembly option. The mass totals indicate the reason the transportation costs are a smaller factor in the total. As a result, the LEO/GEO cost difference is relatively insignificant compared to the production of the satellite.

The final look at gallium arsenide shown in Figure 3.2-25 compares low earth orbit construction versus geosynchronous with two different maintenance schemes, annealing and initial oversizing. The oversized satellite is less sensitive to the LEO-GEO transfer radiation environment than is the analogous silicon satellite.

The gallium arsenide system should be a thin film technology. In Figure 3.2-26 we show the sensitivity of cost and mass to the thickness of the film using the cost parameters described earlier. The cost sensitivity is large compared to the mass sensitivity. All of these are very thin films. Even at 2 mils (50 microns) although the cost exceeds the silicon nominal, the mass doesn't. Gallium arsenide thin film technology is critical not only in terms of gallium supplies but in achieving SPS performance competitive with what we can expect from silicon.

We analyzed the performance sensitivities for gallium arsenide as we did for silicon. The performance sensitivity is not as great as for gallium arsenide film thickness. We are starting to observe in Figure 3.2-27 the effects of constant microwave power transmission mass and cost.

3.2.3 Thin Film Systems

We found very little data base available on thin films. We did have Boeing in-house studies and those sponsored by ERDA looking at copper-indium-selenide. We had as a part of our subcontract with GE a space-fabricated silicon thin film study. Both of these are in a stage best described as process exploration. They certainly lack experimental data to verify any performance. There are data available based on the University of Delaware fabrication of cadmium sulfide cells and measurements of their performance. Our best information is that AMO performance is about 6% now. There are old data available which indicated very favorable radiation degradation characteristics for the same film. We defined a "representative satellite" as shown in Figure 3.2-28. It assumes a cadmium sulfide satellite with 1 mil cover glasses assuming performance for the cells of 12 percent. The satellite that results is about the same size as the reference system and substantially lighter at 61,000 metric tons. If higher thin film performance can be achieved, (say 15 to 17%) thin films will become a very advantageous technology. However, the data base was sketchy not only in terms of experimental data on performance but on long-term stability of the films themselves.

SPS 743

> CR 1 and CR 2 are Very Close in GaAs, (1%) with the Higher Cost of the GaAs Array reducing the CR 1 Advantage Seen in Silicon

GaAs–10 GW MIN. FOR 30 YRS. VIA ARRAY ANNEALING–GEO ASSEMBLY

CR-2

TOTAL AREA:		98.7 Km^2
ACTIVE ARRAY AREA:		48.6 Km^2
MASS:		42,736 MT
PRODUCTION COST:	$\$\sim10^6$	4882.9
TOTAL COST:	$\$\sim10^6$	8346.9

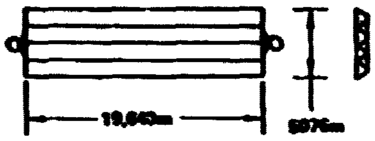

CR-1*

TOTAL AREA:		68.4 Km^2
ACTIVE ARRAY AREA:		68.4 Km^2
MASS:		42,150 MT
PRODUCTION COST:	$\$\sim10^6$	5025.9
TOTAL COST:	$\$\sim10^6$	8442.7

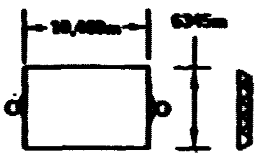

Figure 3.2-23. GaAs Satellite, CR 2 vs CR 1, @ GEO

SPS 745

> LEO Assembly and Selfpower Does Not Change CR 1 and CR 2 Comparison and with Annealing Shows No Substantial Advantage Over GEO Assembly

GaAs–LEO ASSEMBLY–10 GW MIN. FOR 30 YRS. VIA ANNEALING

CR-2

TOTAL AREA:		104.9 Km^2
ACTIVE ARRAY AREA:		55.9 Km^2
MASS:		45820 MT
PRODUCTION COST:	$\$\sim10^6$	5027.4
TOTAL COST:	$\$\sim10^6$	8117.0

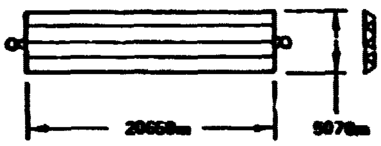

CR-1

TOTAL AREA:		71.7 Km^2
ACTIVE ARRAY AREA:		71.7 Km^2
MASS:		45113 MT
PRODUCTION COST:	$\$\sim10^6$	5197.9
TOTAL COST:	$\$\sim10^6$	8313.0

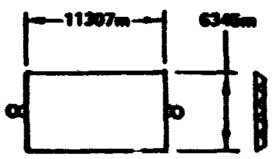

Figure 3.2-24. GaAs Satellite, CR 2 vs CR 1 @ GEO

ORIGINAL PAGE IS
OF POOR QUALITY

SPS 744

GaAs Not as Sensitive to LEO/GEO Trade as Silicon.
Annealing Has Same Relative Advantage

GaAs–CR–2–10 GW MIN. FOR 30 YRS.

GEO ASSEMBLY–MAINTAINED VIA ANNEALING

TOTAL AREA:	98.7 Km^2
ACTIVE ARRAY AREA:	46.6 Km^2
MASS:	42736 MT
PRODUCTION COST: $\$\sim10^6$	4882.9
TOTAL COST: $\$\sim10^6$	8346.9

MAINTAINED VIA INTIAL OVERSIZE

TOTAL AREA:	136.2 Km^2
ACTIVE ARRAY AREA:	64.5 Km^2
MASS:	52,130 MT
PRODUCTION COST: $\$\sim10^6$	5510.2
TOTAL COST: $\$\sim10^6$	9740.7

LEO ASSEMBLY–MAINTAINED VIA ANNEALING

TOTAL AREA:	104.9 Km^2
ACTIVE ARRAY AREA:	55.9 Km^2
MASS:	45820 MT
PRODUCTION COST: $\$\sim10^6$	5027.4
TOTAL COST: $\$\sim10^6$	8117.0

LEO ASSEMBLY–INITIAL OVERSIZE

TOTAL AREA:	143.3 Km^2
ACTIVE ARRAY AREA:	67.9 Km^2
MASS:	56848 MT
PRODUCTION COST: $\$\sim10^6$	5718.3
TOTAL COST: $\$\sim10^6$	9903.9

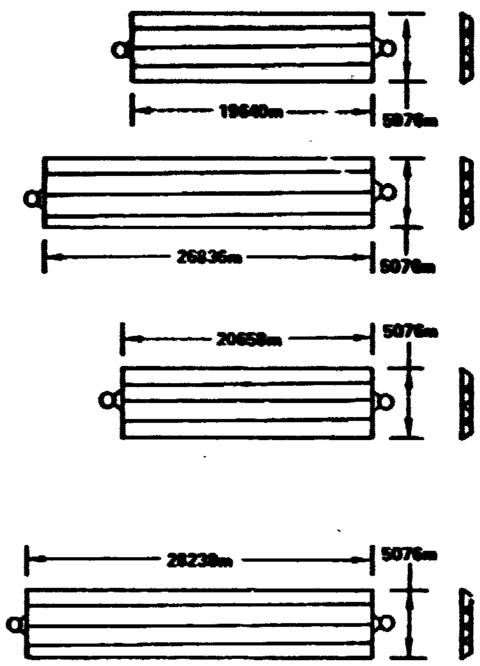

Figure 3.2-25. GaAs Satellite LEO vs GEO

SPS 746

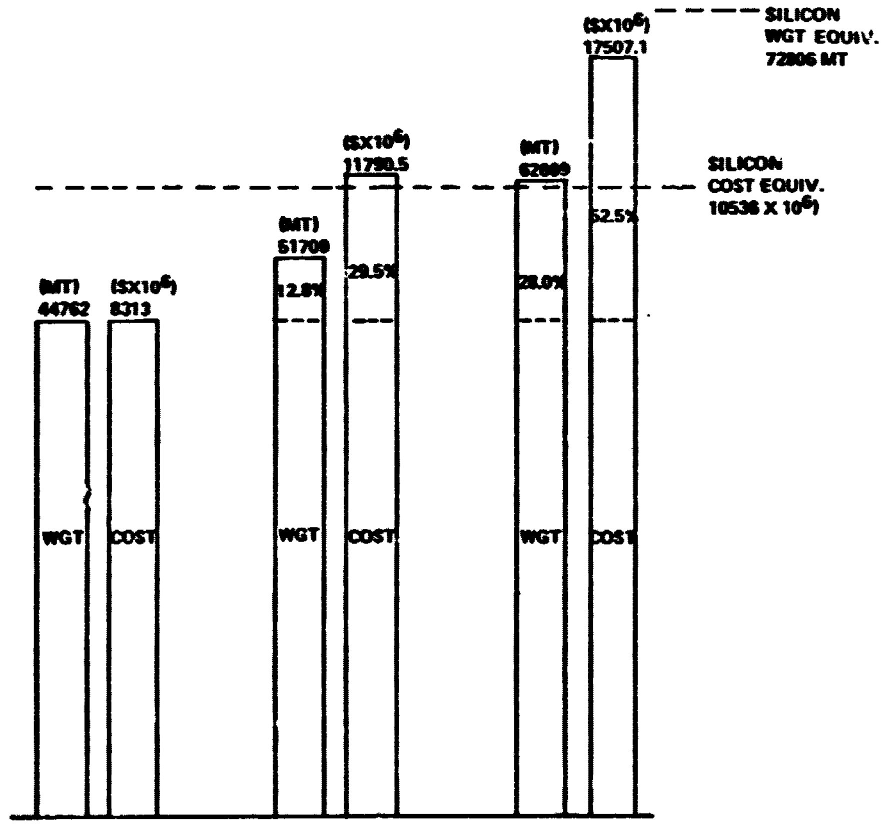

Figure 3.2-26. Sensitivity of Satellite Weight and Cost to GaAs Solar Cell Thickness

SPS 747

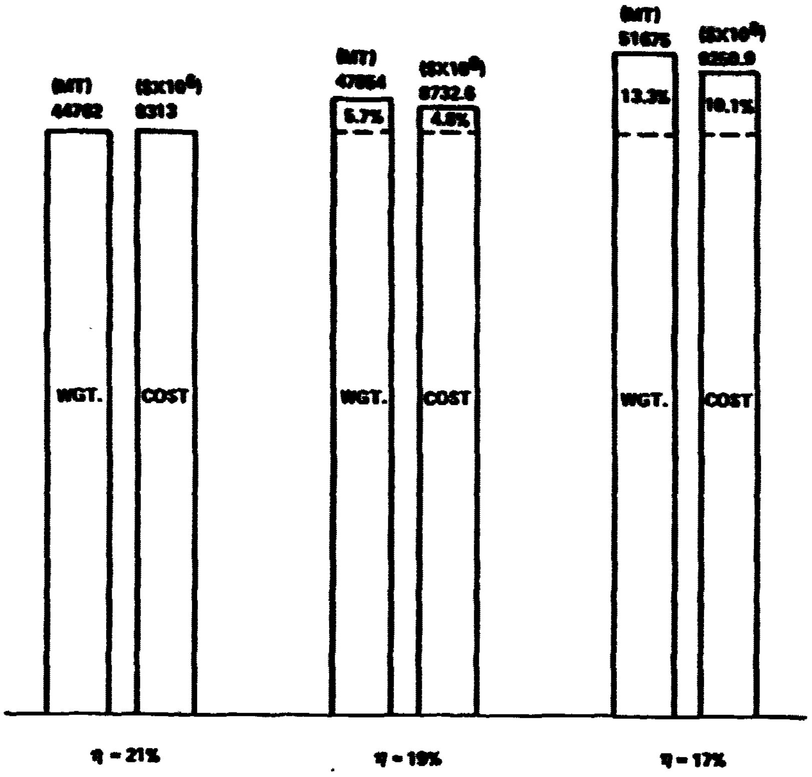

Figure 3.2-27. GaAs Satellite @ CR=1 Sensitivity to Cell Performance

SPS 753

CANDIDATES: CADMIUM SULFIDE, COPPER-INDIUM SELENIDE, SILICON+(GAAS)

ISSUES: PERFORMANCE, RADIATION DEGRADATION, COST

DATA BASE:

SILICON – GE/ERDA
CuInSe – BOEING/ERDA } PROCESS EXPLORATION

CADMIUM SULFIDE – UNIVERSITY OF DELAWARE – 6% AMO EFFICIENCY
NASA LEWIS – 1965 TESTS INDICATE LITTLE RADIATION/DEGRADATION

- REPRESENTATIVE SATELLITE

BLANKET CHARACTERISTICS
PROJECTED CELL EFFICIENCY – 12%
DEGRADATION (30 YEARS) – 5%
BLANKET OUTPUT 10.4%
BLANKET THICKNESS ≈ 100 μm (4 MILS)
BLANKET MASS ≈ 275 g/m²

APPEARS COMPETITIVE EVEN @ LOWER EFFICIENCY BUT REQUIRES SUBSTANTIALLY BETTER DATA BASE

- CR = 1 WITH INITIAL OVERSIZE FOR 30 YRS.

ARRAY REQUIRED = 141.7 Km²

SATELLITE MASS = 61532 M.T.

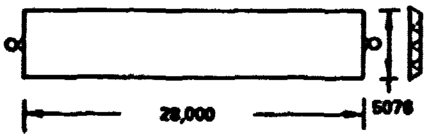

Figure 3.2-28. "Thin Films"

ORIGINAL PAGE IS
OF POOR QUALITY

3.2.3.1 Radiation Damage to Thin-Film Solar Cells

A search for data on radiation degradation of thin-film solar cells was conducted; nothing was found in the recent literature.

A telephone call to Dr. Henry W. Brandhorst at NASA Lewis Research Center confirmed that no radiation damage testing had been done recently on thin-film solar cells. The reason is that development funding provided by ERDA for these cells is directed at terrestrial applications where radiation degradation is not a problem. NASA Lewis Research Laboratory will radiation-test any thin-film solar cells that turn out to be promising for space applications.

Dr. Brandhorst also explained that the lack of radiation degradation of thin-film solar cells results from the fact that long diffusion lengths are not a requirement for thin-film cell operation. The initial minority-carrier lifetime in cadmium sulfide, for example, is only 0.5 ns. As a result, a fluence of 10^{17} one MeV electrons had virtually no effect on the output of the cell. Figure 3.2-29, reproduced from the reference, illustrates the point.

Dr. Brandhorst felt that the most advanced thin-film cell today is the one being developed by the University of Delaware, using cadmium sulfide. They are getting 8 percent efficiency in terrestrial sunlight, which corresponds to about 6 percent in space.

3.2.3.2 Silicon Thin-Film Concept

A space-manufactured silicon thin-film process concept was provided by General Electric under subcontract. The remainder of this section presents their report.

For power satellite applications, the semiconductor thickness and configuration should be designed to optimize the cost and mass needed to generate the required power.

The left hand of Figure 3.2-30 indicates the inherent efficiency obtainable from one ohm-cm Si with back surface field as a function of Si thickness (from "Semiconductors and Semimetals", Vol. II, "Solar Cells" by H. J. Hovel, Academic Press, 1975). The efficiency climbs toward a limiting value of about 17% with most of the increase occuring at thicknesses less than 10 to 20 microns. The right hand part of the figure shows the specific power (watts/gram) considering the increased weight of Si as its thickness is increased and assuming this is added to a constant mass consisting of 10 micron Al substrate, front metallization of conventional structure, anti-reflection coating and a 25μ cover glass on each side of the cell. As can be seen, increasing the Si thickness to 20 microns or more causes a drop from the peak specific power which occurs at about 10 microns. This occurs because the relative increase in efficiency is less than the relative increase of weight in this range.

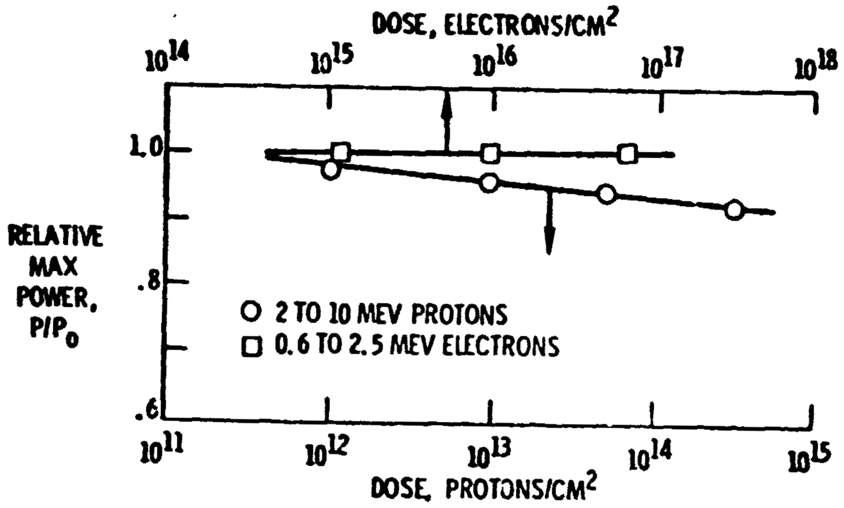

Figure 3.2-29. Radiation Damage to Cadmium Sulfide Film Cells

GENERAL ELECTRIC

space division

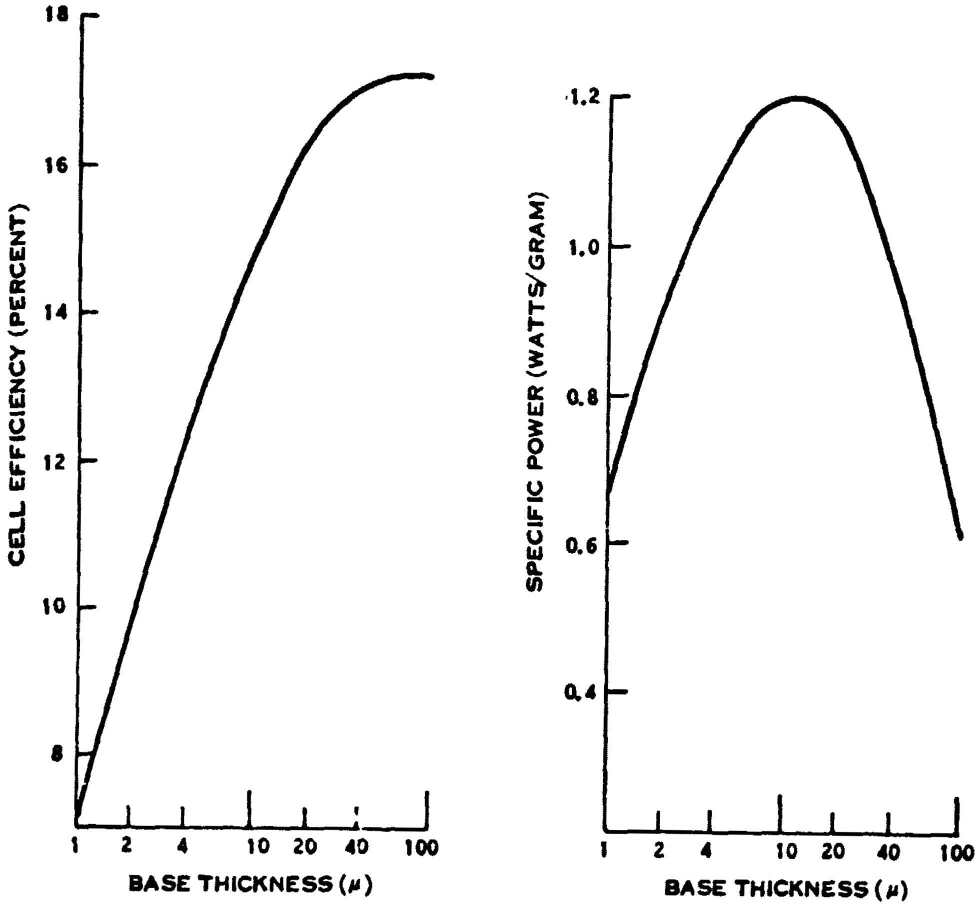

Figure 3.2-30. Inherent Efficiency and Specific Power Thin Film Solar Cell with Back Surface Field 25μ Cover Glass Each Side

ORIGINAL PAGE IS
OF POOR QUALITY

Further work is needed to determine the actual efficiencies obtainable. However, it is likely that an optimum Si thickness of about 10 microns will still apply.

Figure 3.2-31 shows the thin film series collection concept. It has the following features:

o n-p polycrystalline silicon film–Fraction of a micron n-type layer deposited on thin film p-type polycrystaline silicon.

o Grains sufficiently wide to approach single crystal efficiency–calculations by Hovel indicates that the grains' size should be 2-3 times the grain thickness to obtain efficiencies approaching single crystal materials.

o 10 micron alumium backing–it is addaptable to the GE continuous strip production technique. The aluminum provides for the series connection through a shingle overlay.

o Shingle series connections with parallel strip front metallizing–it removes the width restriction on the cells and affords a technique for continuous series connections.

o 25 micron electrostatically bonded glass cover slip–this is specified reference design in this study. It is suggested that this should be glass (instead of Kapton) because it can be electrostatically bonded (therefore no adhesive required).

o Silicon thickness chosen to give maximum specific power (near 10 microns)–gives maximum power per unit weight.

o Back surface field to improve initial efficiency and to reduce radiation degradation–adapts itself easily to vapor deposition technique using multiple sources.

The cost of the thin film cells was estimated based on a continuous strip production facility in low earth orbit (LEO).

Material cost is based upon a structure consisting of a 10μ Al conducting substrate coated with 10μ of Si. The Schottky barrier metallization is a 30 A layer of platinum. 10% of the Pt is covered by 15μ strips of Ag conductor. A 1000 A anti-reflection coating is assumed to cover the front face and a 25μ thick cover glass is assumed on each face. Total weight of the cells is 165 gm/m^2. Since masks, shields, etc. will become coated with the various evaporated materials, an additional 40% is added to the materials cost to cover cost of recovery of this material. Material costs are based on current market costs for the metals and semiconductor. Cost of glass encapsulation is based upon information from "Integral Glass Encapsulation for Solar Arrays," 2nd quarter report (Nov. 1976) ERDA/JPL 954521-76/2.

GENERAL ELECTRIC

space division

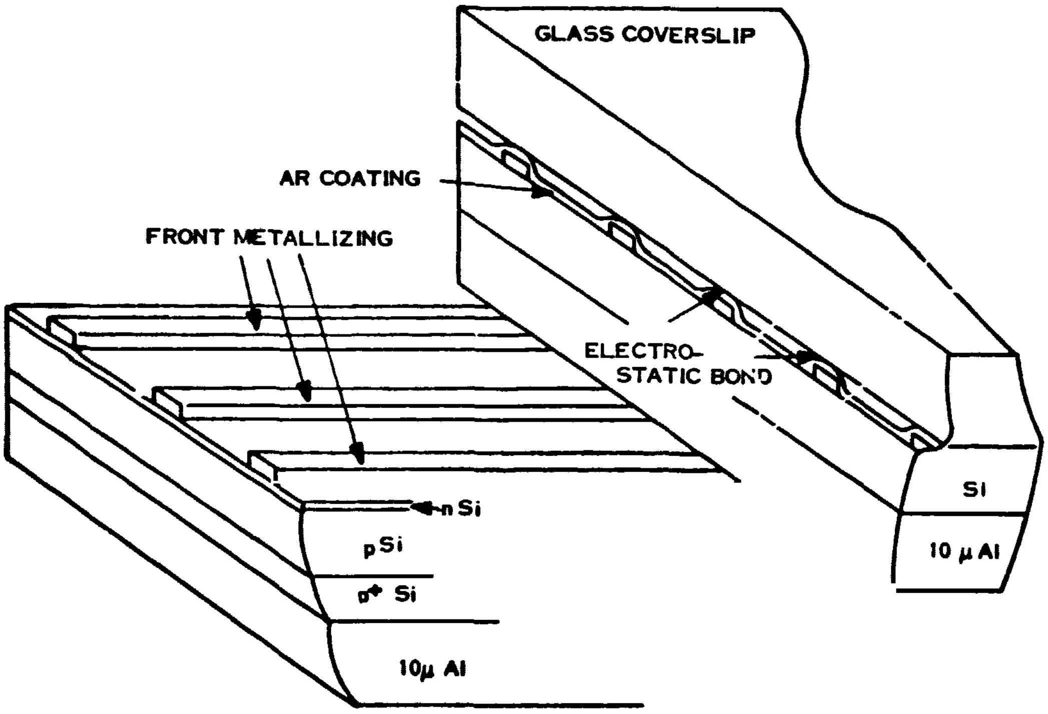

Figure 3.2-31. Thin Film Si on Metal Substrate Series Connection by Shingle Overlap

ORIGINAL PAGE IS
OF POOR QUALITY

We assume a \$40 x 10^6 facility cost based on cost data derived for other types of space manufacturing facilities and satellites.

The transportation cost to LEO is assumed to be \$10/pound. Results are shown in Table 3.2-6.

3.2.4 Power Distribution for Photovoltaic SPS

3.2.4.1 Design Objectives and Assumptions

The design objective for the power distribution system is to minimize the total SPS mass required to generate and convert power, while providing are adequate capability to control and regulate power supplied to the microwave power transmission system. Power distribution design requirements were stated under requirements item 1.01.01.03 in section 3.1. The principal design assumptions were, (1) main power would be distributed at or near 40,000 volts; (2) power processing would be minimized to the extent practicable; (3) conductors will be passively-cooled, 1mm thick, aluminum sheet conductors. This thickness was selected as a minimum-gage value.

3.2.4.2 Power Distribution Reference Design

Klystron power and regulation requirements were estimated, including the multiple-voltage requirements for high efficiency depressed–collector operation. The Klystron used as a reference for this study required the power supplies indicated in the following table:

Power Supply	Voltage (VDC)	Current (Amperes)
Collector A	40,000±5%	1.320
Collector B	37,900±5%	0.616
Collector C	4,210±%	0.154
Regulated Anodes (2 ea. 21, 050 V supplies in series)	42,100±5%	0.110
Heater (30 watts)		

Power for the Collector C, the Regulated Anodes, and the Heater can be obtained from a DC/DC converter with outputs for each. A converter efficiency of 96% is assumed. The source for the converter is the same supply that provides power for Collector A. Figure 3.2-32 shows that the satellite can be designed with all solar cell power generator modules of the same design. The thirty power generation modules farthest from the rotary joint are connected in parallel and routed over dedicated conductors to the rotary joint. The conductor voltage drop is sufficient to drop the supply voltage to the required level at the rotary joint. The seventy power generation modules nearest the rotary joint are connected in parallel and routed over separate conductors to the rotary joint. This

Table 3.2-6. Cost of Producing Thin Film Cells

		$/WATT AT 13 EFF.
• MATERIALS		0.06 – 0.08
10 μ Al SUBSTRATE	$0.0006/W	
10 μ Si	0.0052	
30 Å SCHOTTKY BARRIER	0.0022	
15 μ Ag CONDUCTOR	0.0134	
1000 A ANTI-REFLECTION	0.01	
25 μ EACH SIDE COVER GLASS	0.0114 –0.0228	
RECOVERY FROM MASKS, ETC.	0.017 –0.021	
• FACILITY		0.09 – 0.10
FACILITY TO PRODUCT 0.5 X $10^6 M^2$/YR OF CELLS. COST $40 X 10^6/FACILITY AMORTIZED OVER FIVE YEARS		
• TRANSPORTATION		0.02
167 GM/M^2 AT $10/LB (= $0.022 GM)		
• TOTAL		$0.17 – 0.20 WATT

ORIGINAL PAGE IS
OF POOR QUALITY

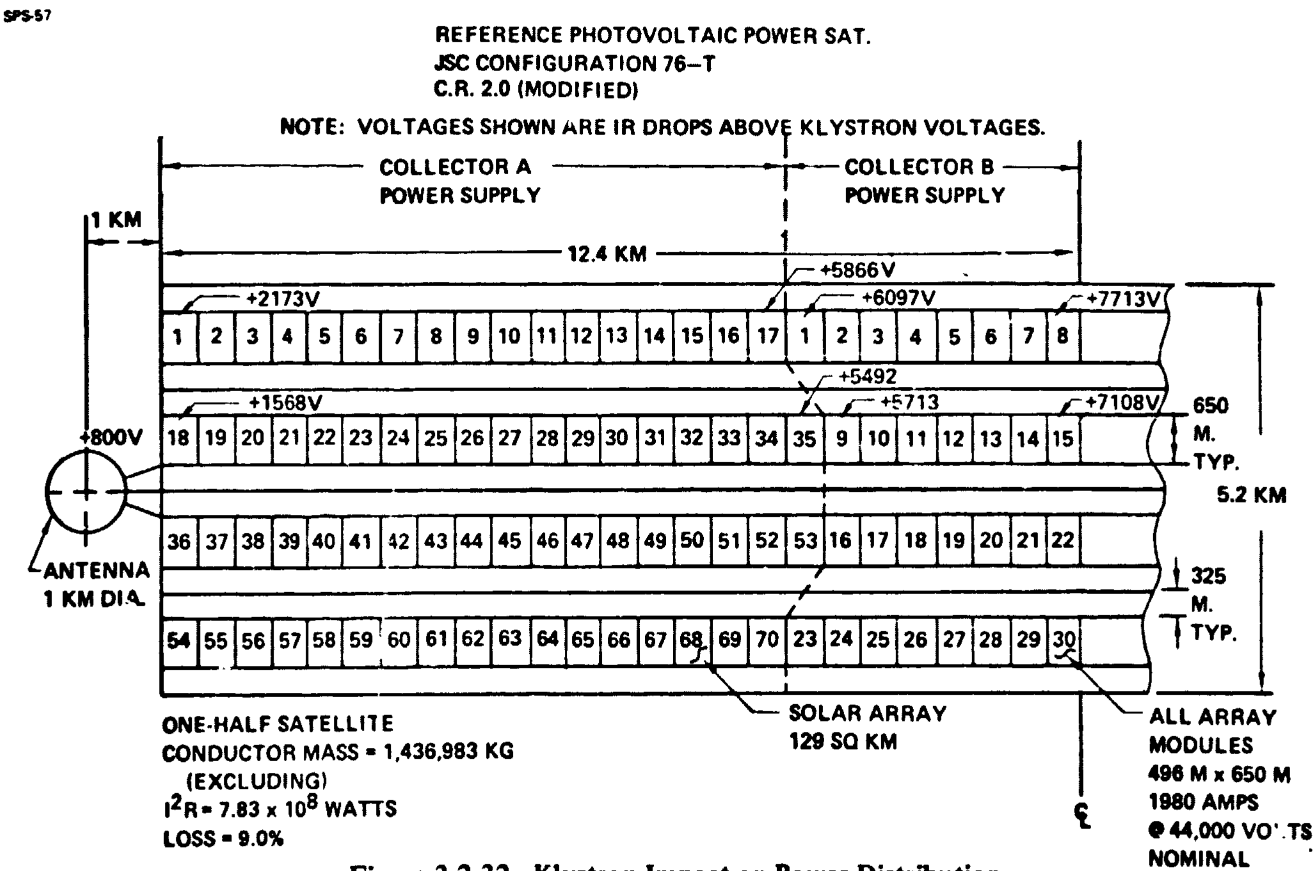

Figure 3.2-32. Klystron Impact on Power Distribution

design concept requires a minimum of three slip rings on the rotary joint; one each for the Collector A and Collector B supplies, and one for the power return. Overall power distribution efficiency is 91%.

A photovoltaic solar power satellite having a given power output must have array area sufficient to generate the regular power, plus an increment of area that generates the power lost in the power transmission network within the array. If the array is made larger to take advantage of cells that use low in cost but low in efficiency, then the loss-generation requires an increment of array that is more remote from the rf amplifiers. The effect becomes more of a problem with lower-efficiency cells and with high aspect ratio configurations.

The effect of transmission losses on array area is shown in Figure 3.2-33 as a function of power distribution distance.

The reference configuration was analyzed to determine the optimum conductor design operating temperature for minimizing the total satellite mass. The optimum conductor design operating temperature is approximately 80°C. As the conductors are made smaller and lighter, their power loss increases, resulting in a requirement for more solar array to generate the power to feed the losses. The optimum occurs where the rate of array mass change begin to exceed the rate of reduction in conductor mass, as shown in Figure 3.2-34.

The concept for conductor and switchgear installation on the reference configuration is shown in Figure 3.2-35. The system electrical schematic is shown in Figure 3.2-36.

3.2.4.3 Alternate Design Approach

Since approximately 140,000 solar cells are required in series to yeild 44,000 volts after 30 years, a configuration which utilized these cells in a straight line was analyzed for power distribution losses and mass.

The configuration selected has the cells connected as shown in the inset of Figure 3.2-37. With this configuration, no shadowing of the cells by superstructure above the cells can be allowed because of the severe decrease in the cell string output caused by shadows. As can be seen, the I^2R losses and the conductor mass required are considerably less for this configuration than for the reference configuration. This approach is particularly attractive for satellites with concentration ratio 1.

3.2.4.4 Startup Control

An analysis was made of the occultation imposed requirements on the power distribution and control system. The requirement to be satisfied is to keep the klystron supply voltages within ±5% of nominal.

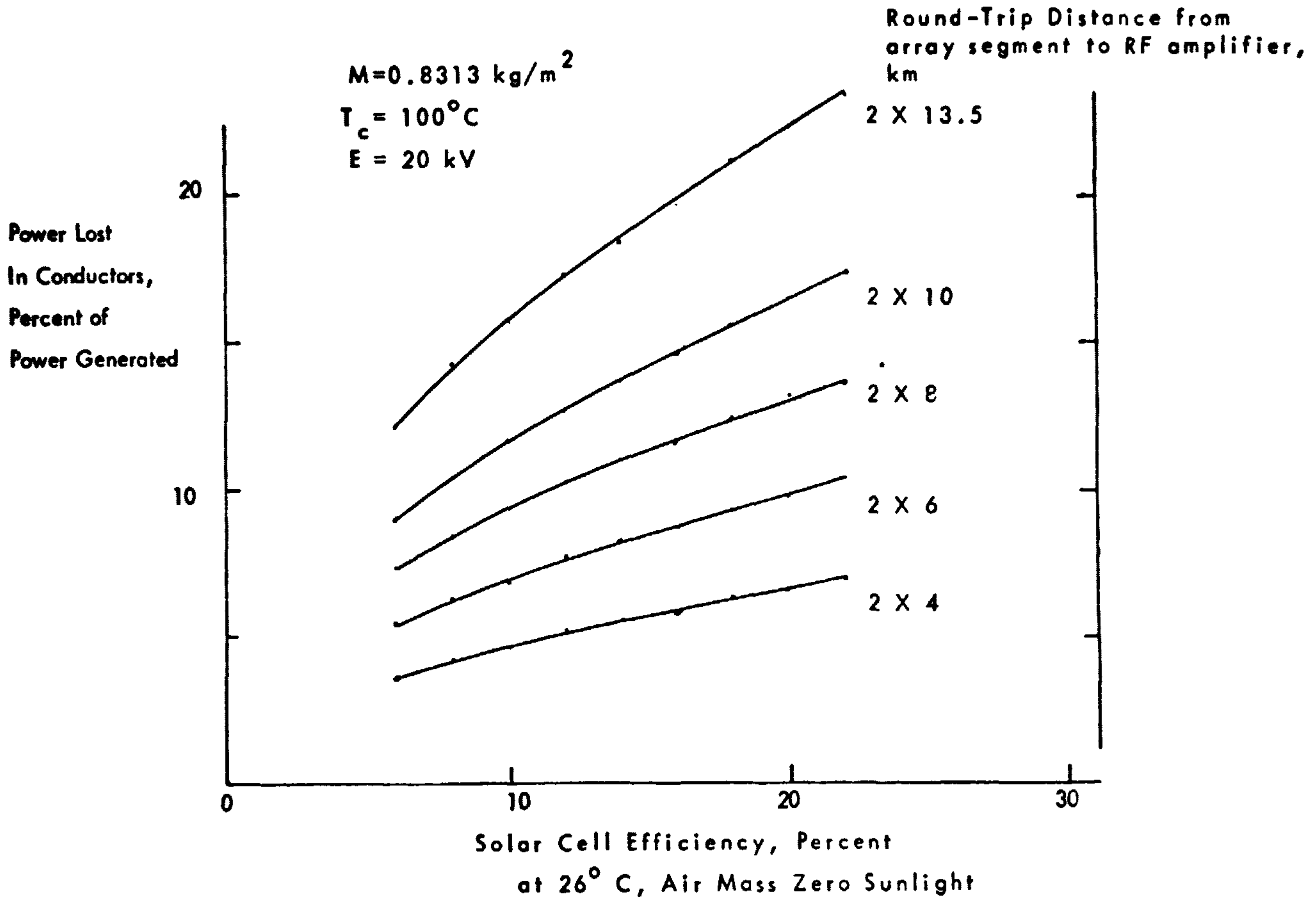

Figure 3.2-33. Power Loss in Optimum-Size Conductor Between Array and Load

ORIGINAL PAGE IS
OF POOR QUALITY

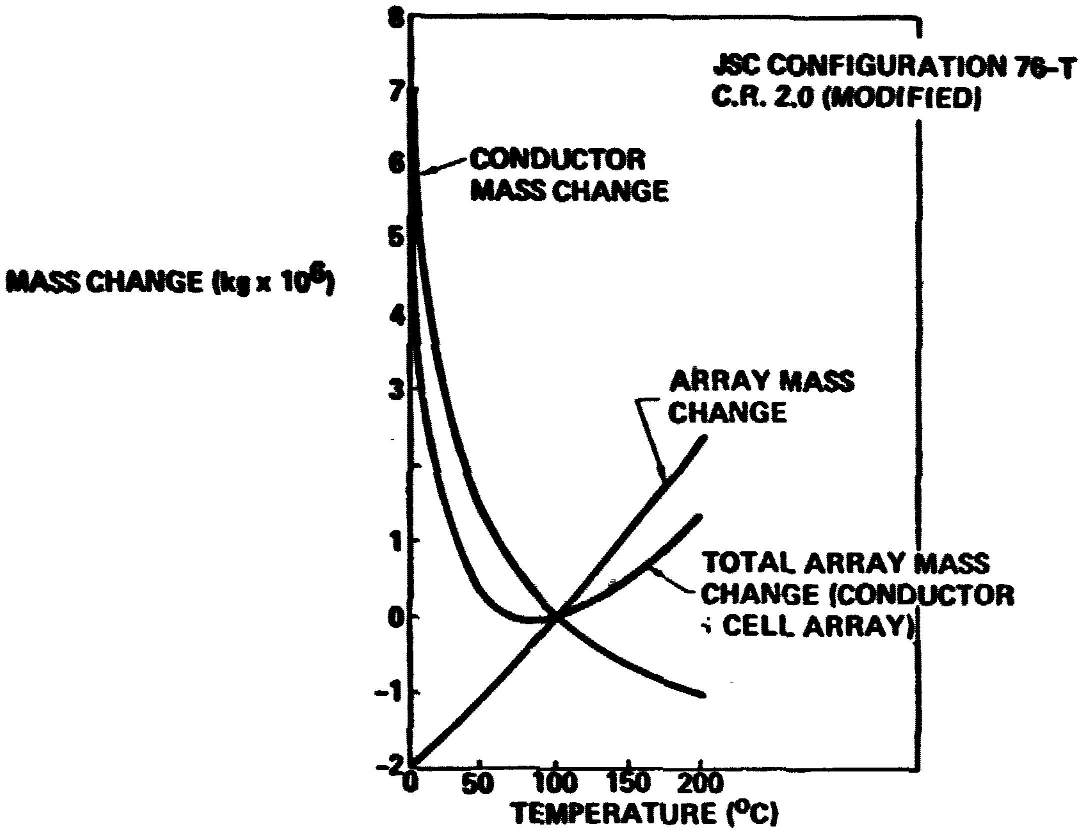

Figure 3.2-34. Optimized Conductor Operating Temperature

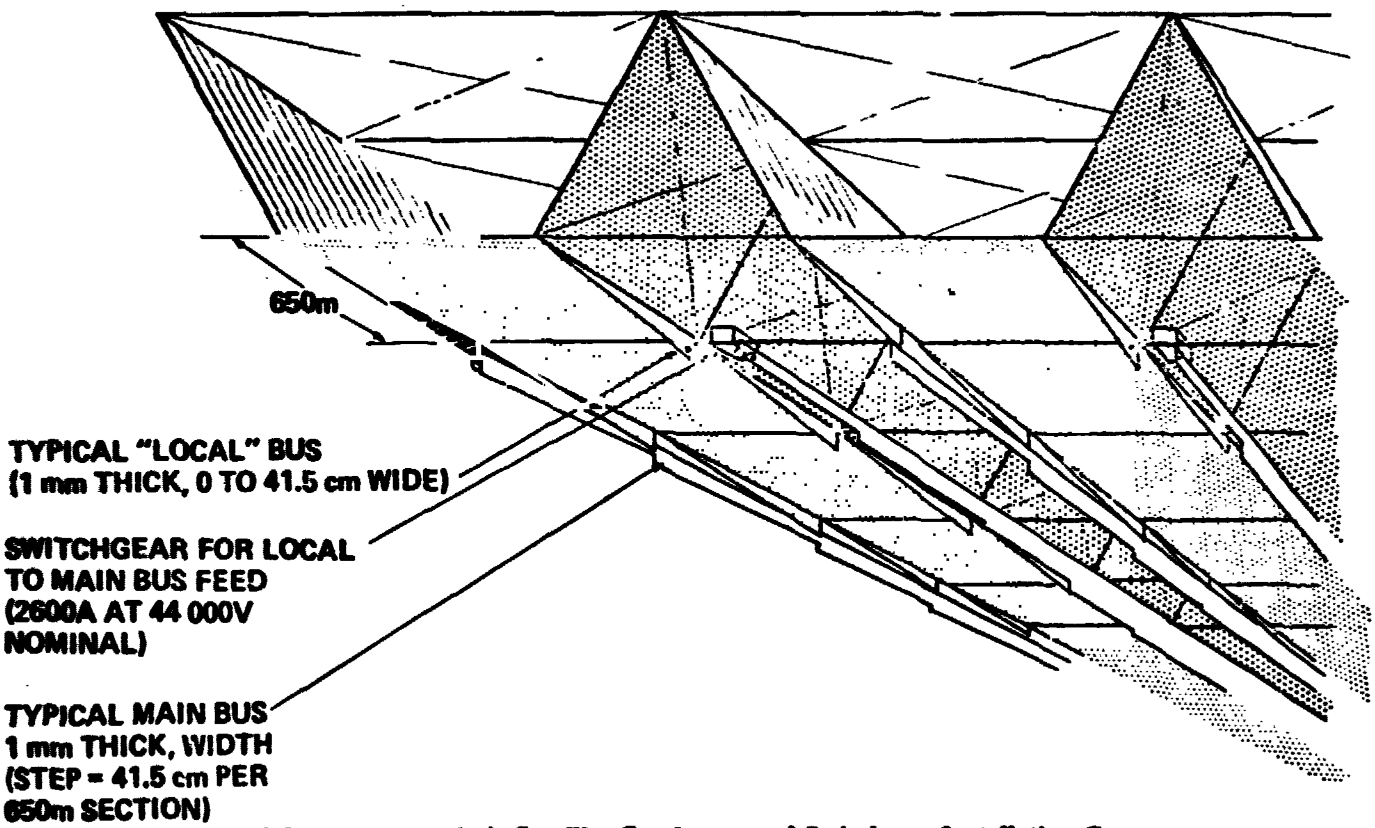

Figure 3.2-35. Photovoltaic Satellite Conductor and Switchgear Installation Concept

FOLDOUT FRAME 1

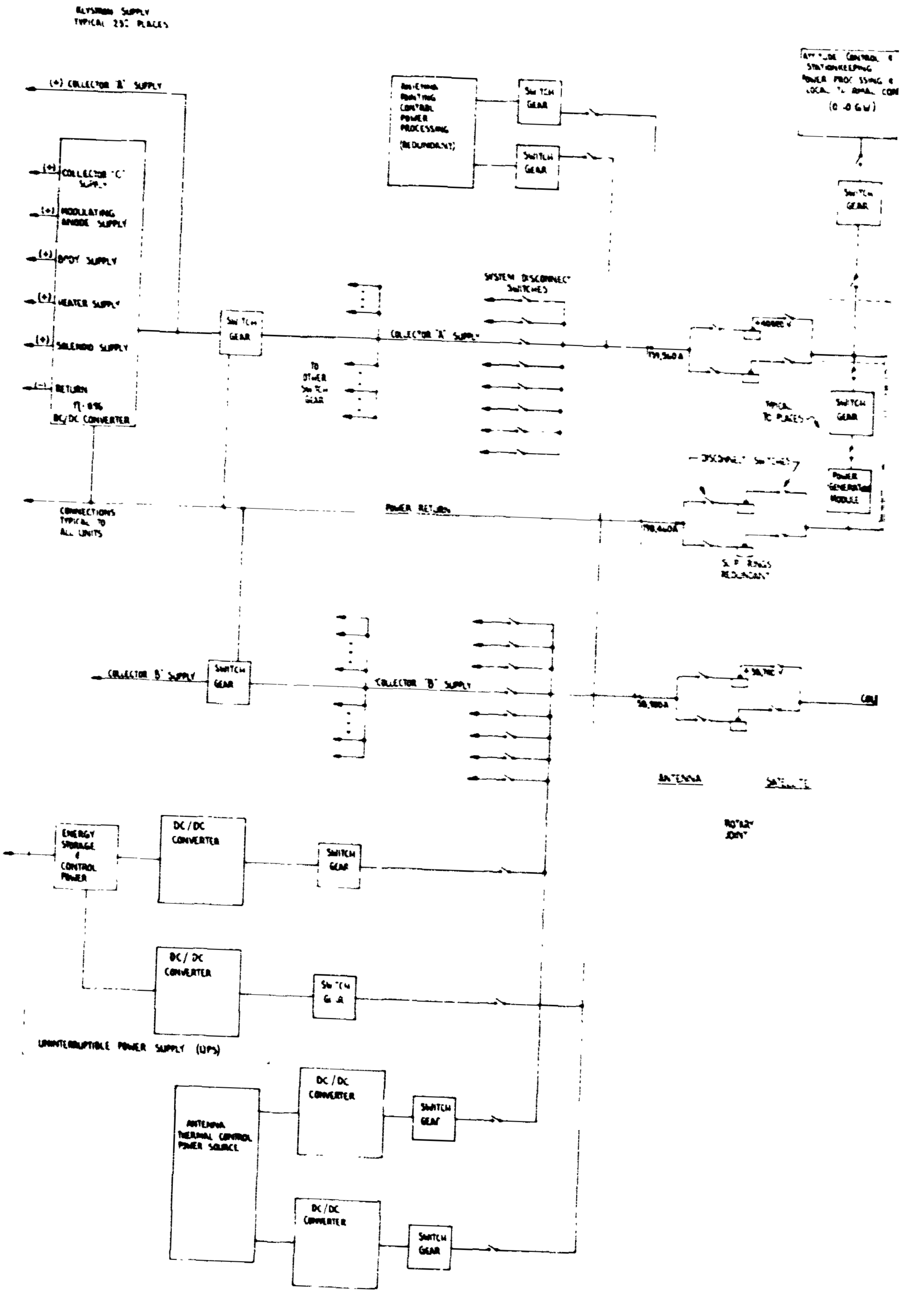

ORIGINAL PAGE IS
OF POOR QUALITY

FOLDOUT FRAME 2

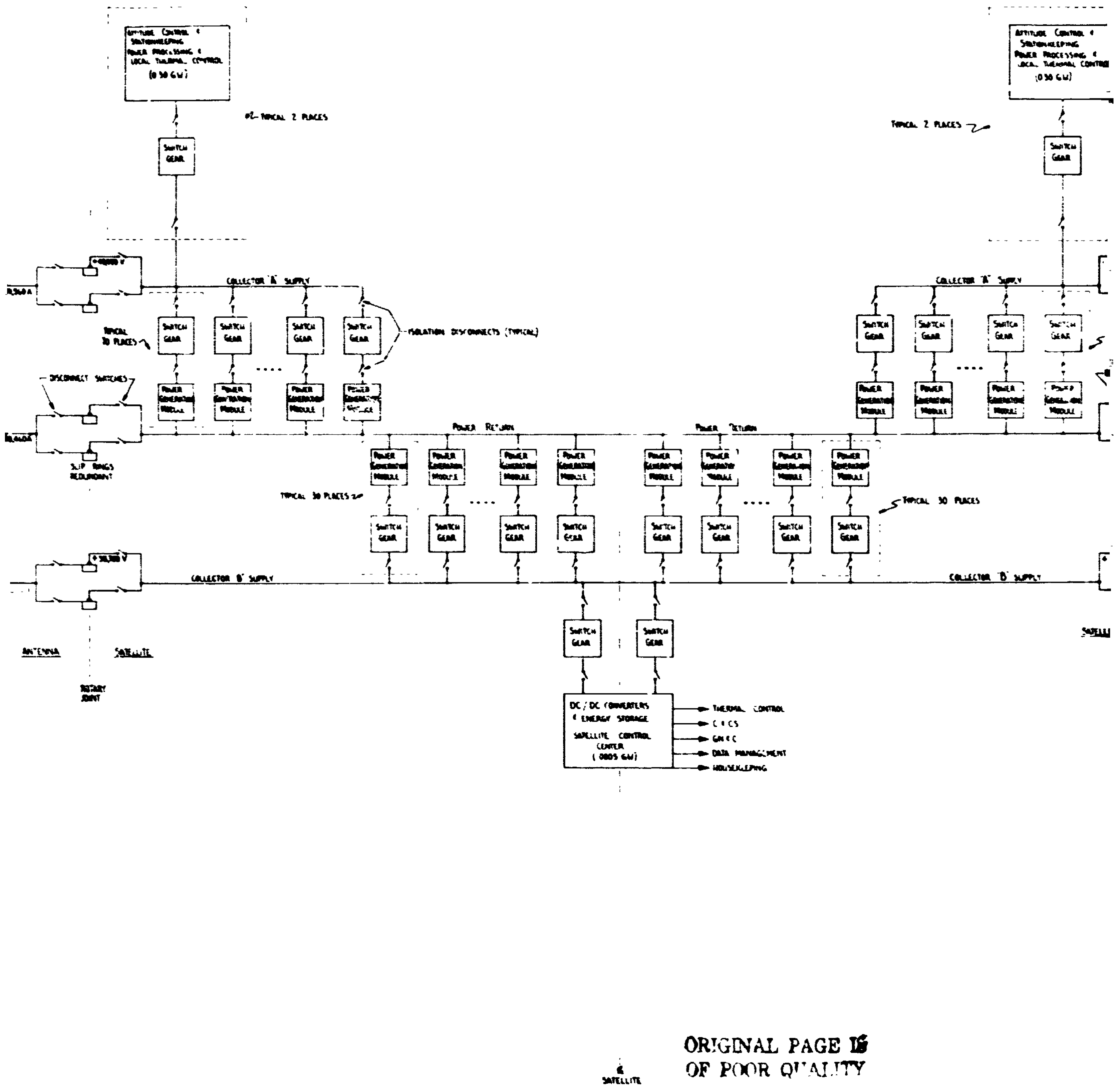

ORIGINAL PAGE IS
OF POOR QUALITY

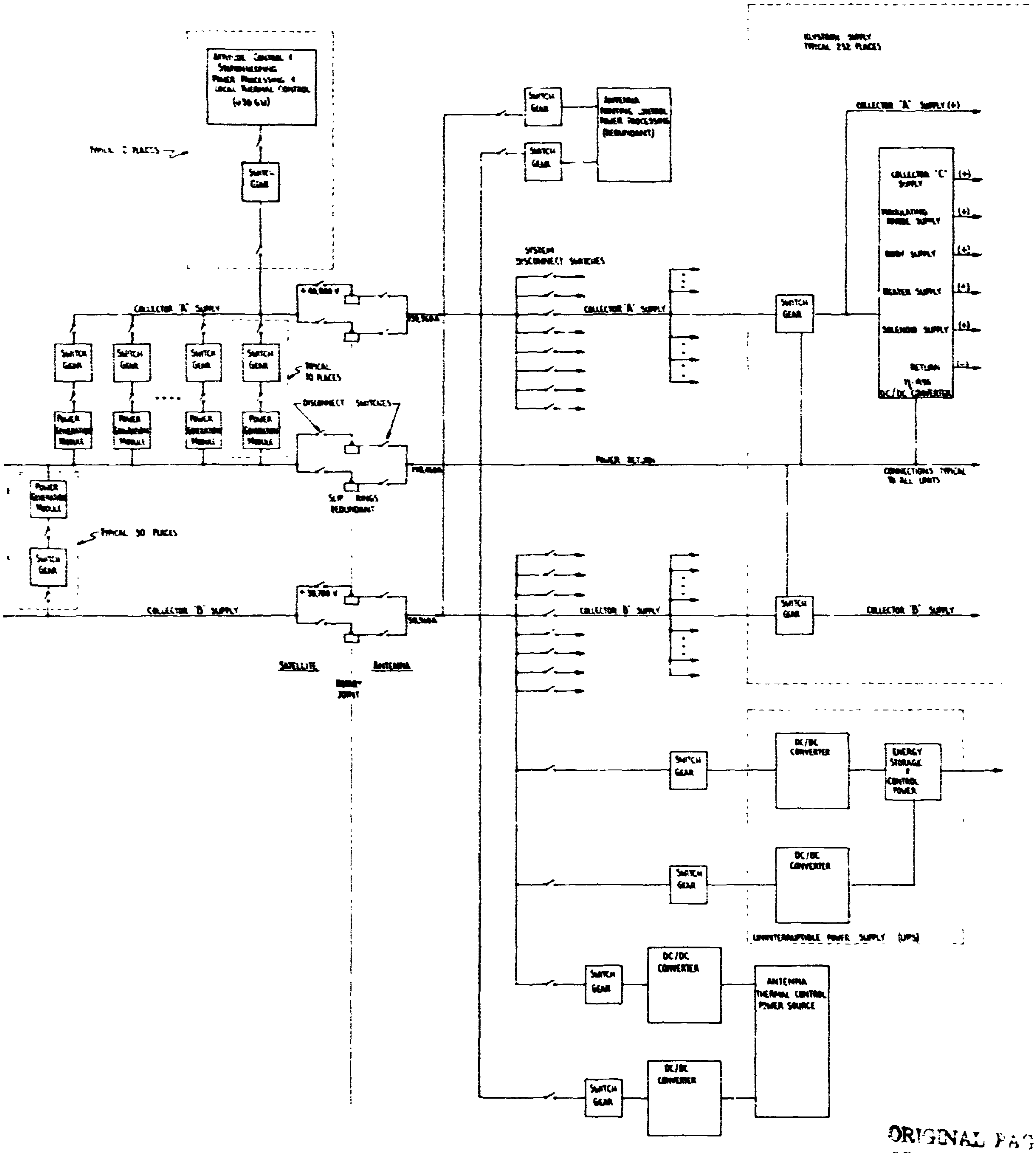

Figure 3.2-36. Electrical Schematic—Photovoltaic

ORIGINAL PAGE IS
OF POOR QUALITY

SPS-222

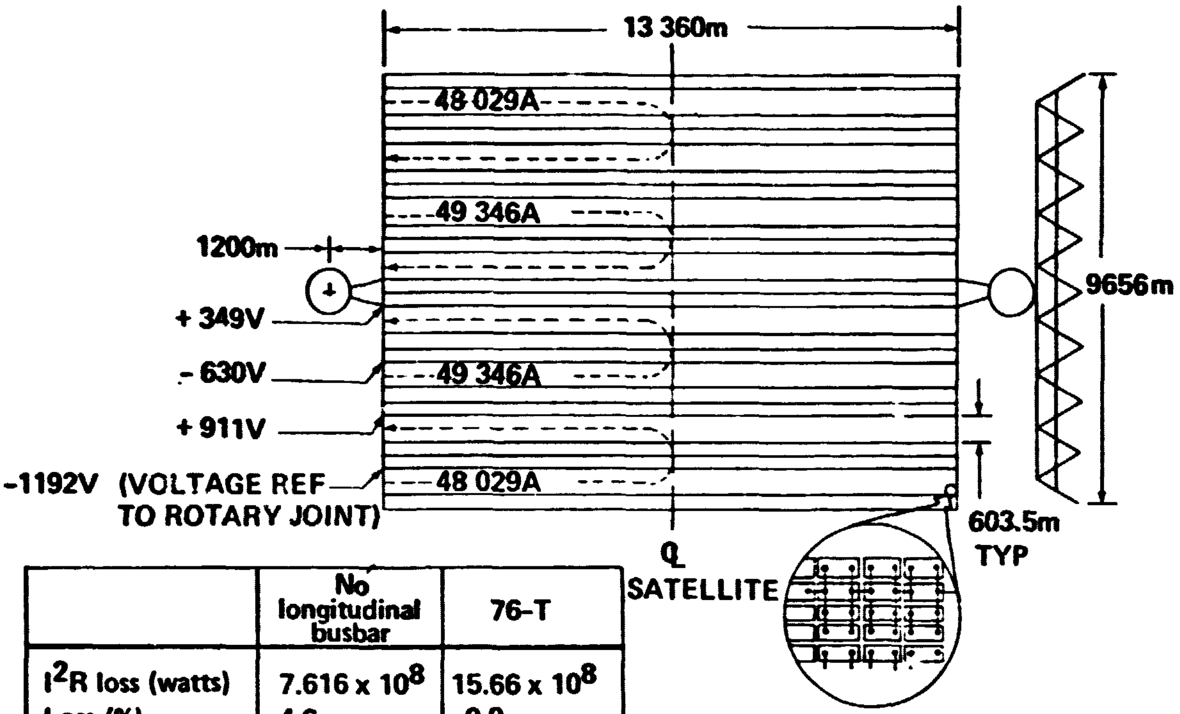

	No longitudinal busbar	76-T
I^2R loss (watts)	7.616×10^8	15.66×10^8
Loss (%)	4.6	9.0
Mass (kg)	1.40×10^6	2.87×10^6

COMPARISON WITH JSC CONFIGURATION 76-T

Figure 3.2-37. "No Longitudinal Busbar" Configuration–Power Distribution

ORIGINAL PAGE IS OF POOR QUALITY

The array specific weight was assumed to be 0.54 Kg/m^2 and the total flux falling on the cell was 2503 w/m^2. Figure 3.2-38 shows the temperature response of the cells when the array is occulted from the sun. A temperature of 121°K is reached at the end of 70 minutes. Upon emergence from the Earth's shadow, cell temperatures rise rapidly as shown in Figure 3.2-39. The rate of temperature rise can be increased significantly by open circuiting the cells. Steady state temperature is reached in 9 minutes open-circuited versus 20 minutes with the cells providing power to external loads.

Figure 3.2-40 shows normalized array output as a function of array temperature. As can be seen, the change in array power and voltage is dramatic. In order to maintain the Klystron supply voltages within the ±5% requirement, the array must be segmented to provide control of the source voltage. Ten switchable levels are required on the array to provide the required voltage regulation (see Table 3.2-7). This regulation requires considerably more complex solar cell blanket and power distribution and control systems than does a nonregulated array.

Based upon the considerably more complex blanket and power distribution and control system and the additional mass required to implement the changes required (approx. 1,000,000 Kg), it was decided to omit the regulation requirement and wait for approximately 6 minutes until the array voltage is within tolerance before beginning klystron operation.

3.2.4.5 Power Distribution and Controls For Self-Powered LEO-GEO Transportation

The reference photovoltaic configuration is 5,076 meters by 28,800 meters excluding the antenna. When divided into 16 segments, each segment is 3,600 meters by 2538 meters as shown in Figure 3.2-41. Thruster panels are required on two diametrically opposed corners.

Earlier estimates of photovoltaic SPS orbit transfer used a value of 7500 sec for argon ion thruster ISP. Current orbit transfer optimizations have reduced this value to 5000 sec. The basic propulsion system consists of a thruster panel on each corner of the 3600 meter by 2538 meter photovoltaic SPS module. Each thrustor panel contains 900 thrusters. Each thruster requires 64,743 watts and each thruster panel requires 58,268,700 watts after power processing. Using a power processing efficiency of 0.95 the input power to the thruster panel was computed to be 61,335,474 watts. Based upon this panel power requirement the deployed array required to deliver the power was computed. Plasma current losses were computed using the data described in the following section (3.2.4.6).

The concept for acquiring power from the solar cell array consists of dividing the bay width up into N segments, each of which provides 1/N of the total bay voltage (i.e. if the bay voltage is 44,000 volts and N=5, each segment provides 8,800 volts). The plasma current was computed and subtracted from the array current to compute the segment output current. Figure 3.2-42 presents the percentage of the solar cells which must be deployed in order to obtain the required thruster power

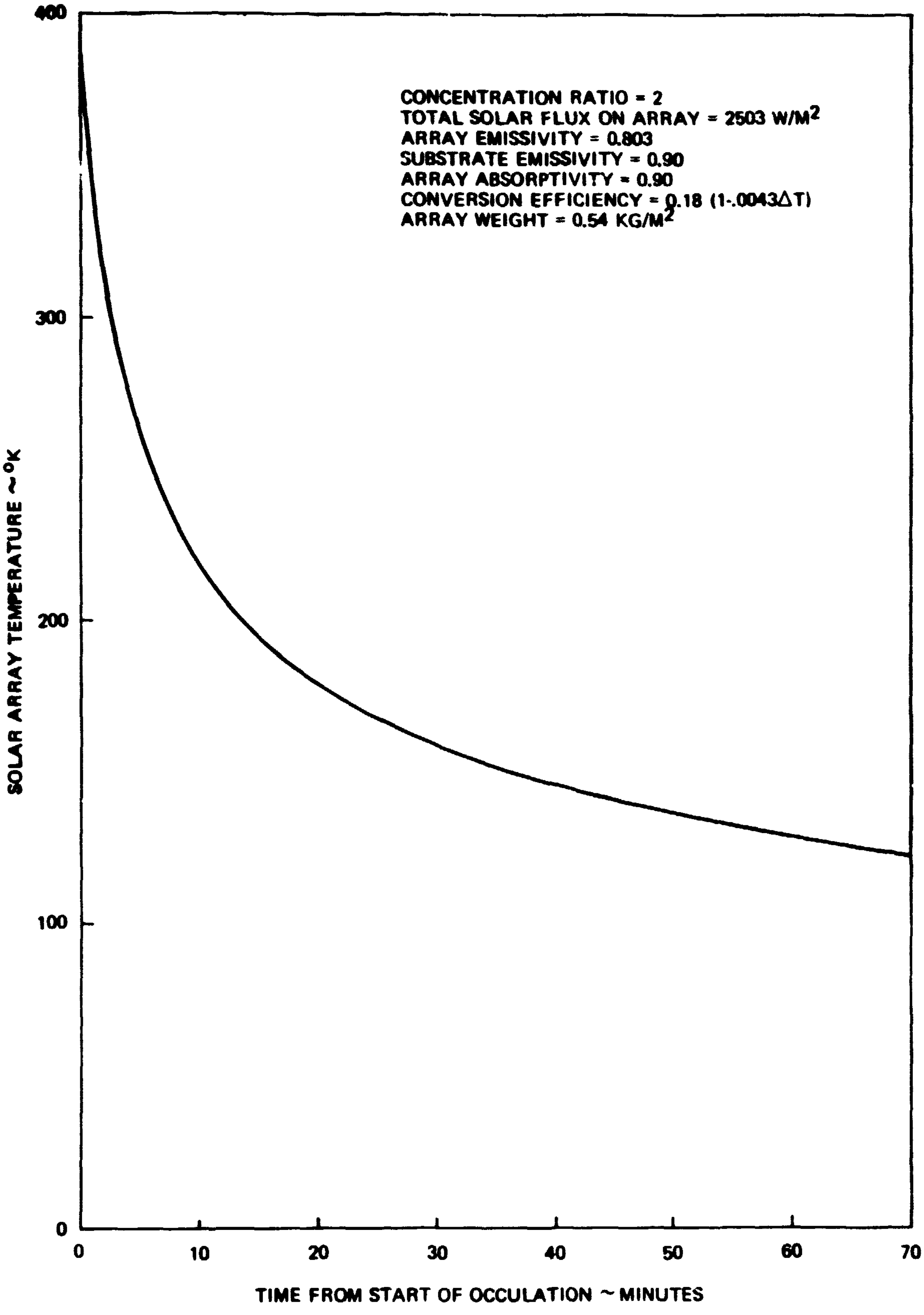

Figure 3.2-38. Array Temperature Response to Solar Occulation

ORIGINAL PAGE IS
OF POOR QUALITY

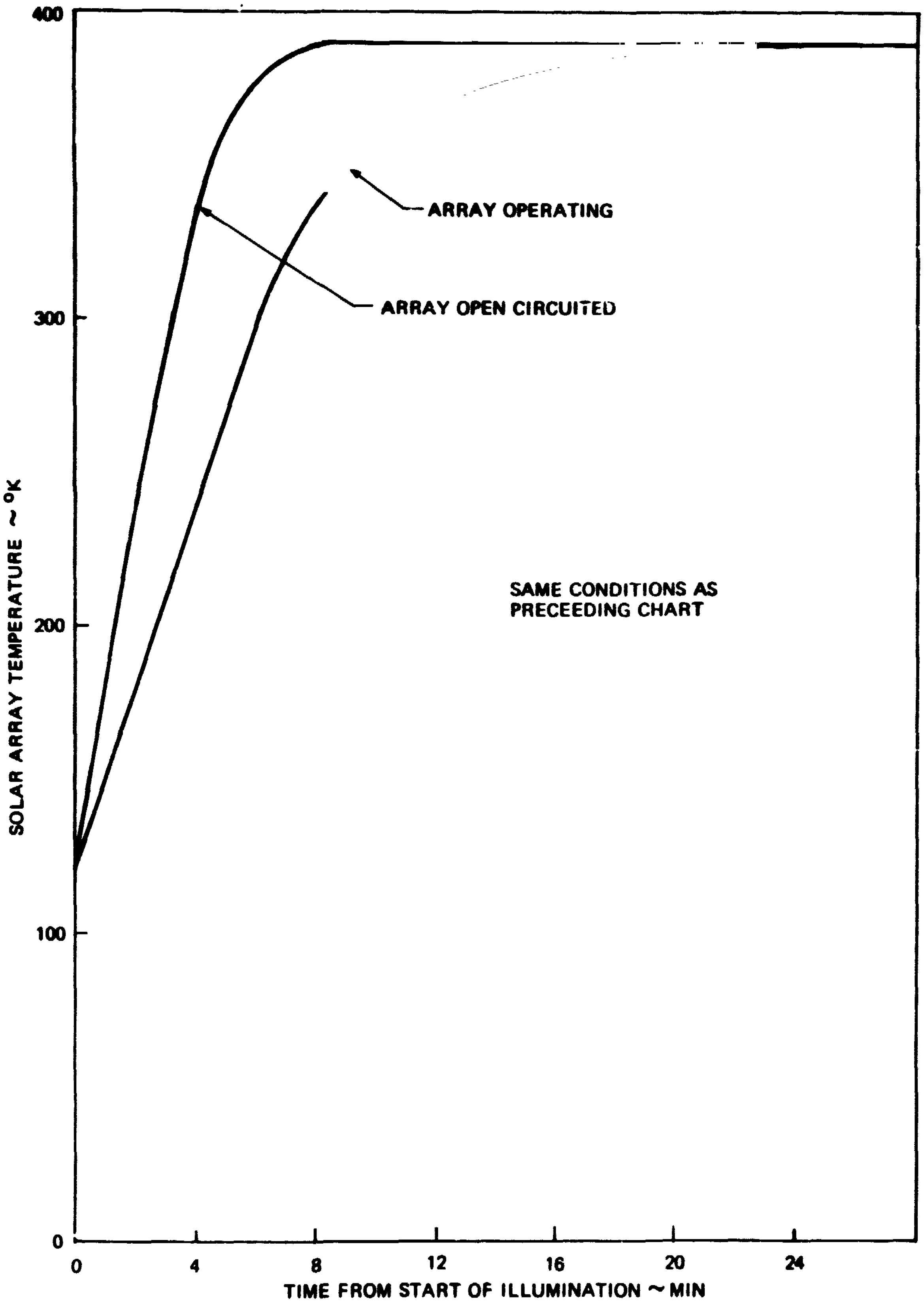

Figure 3.2-39. Array Temperature Response To Emergence Into Sunlight

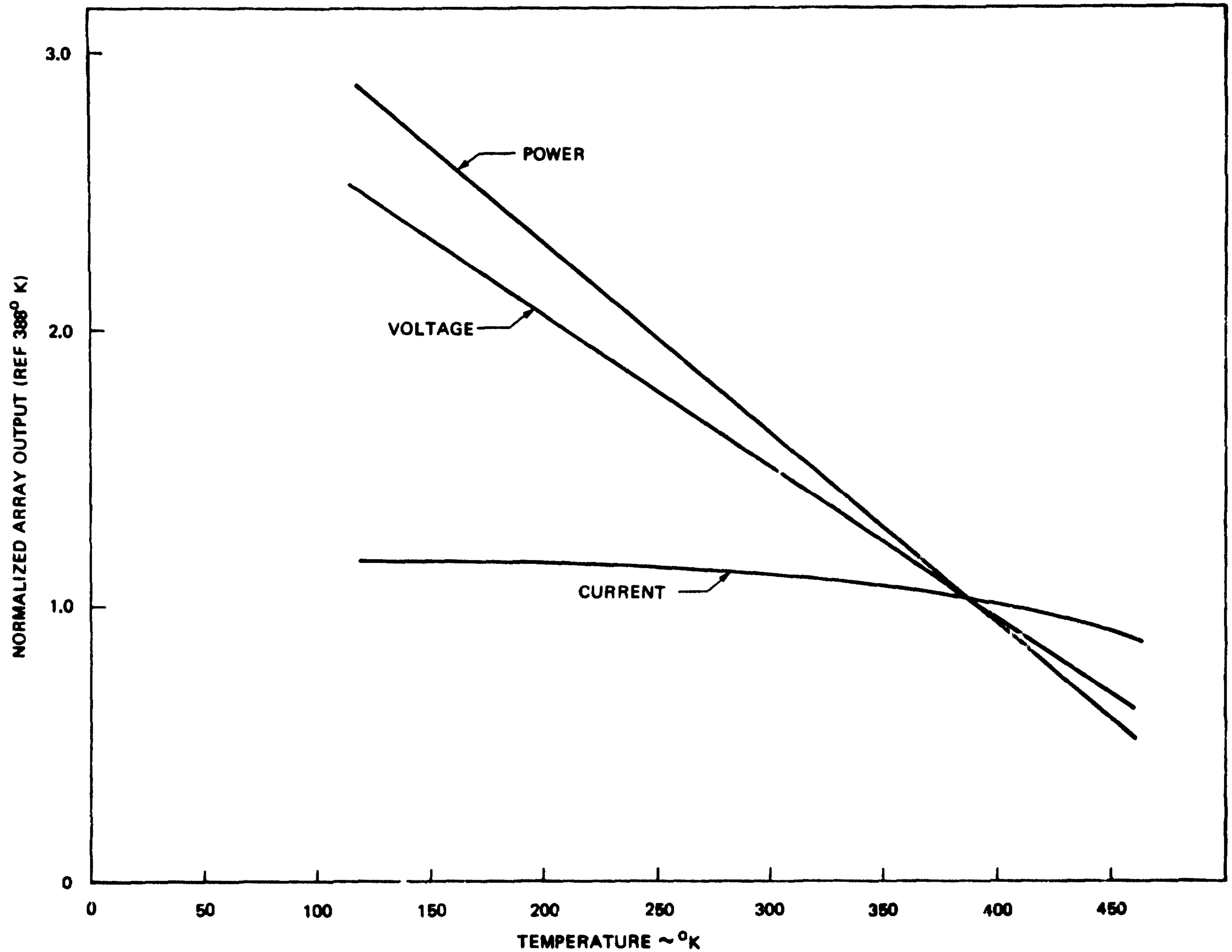

Figure 3.2-40. Solar Array Output vs Temperature

ORIGINAL PAGE IS
OF POOR QUALITY

Table 3.2-7

Switching Steps For Maintaining Array Voltage Output Between 105% And 95% Of Nominal

TEMPERATURE °K	NORMALIZED VOLTAGE	% ARRAY REQ'D FOR 1.05 V_{NOM}
121	2.493	42.17
163	2.256	46.54
202	2.041	51.44
237	1.847	56.85
268	1.670	62.87
297	1.510	69.54
322	1.368	76.75
346	1.237	84.88
367	1.120	93.75
386	1.013	100.00*

*OUTPUT AFTER SWITCHING IS 1.013 V_{NOM}

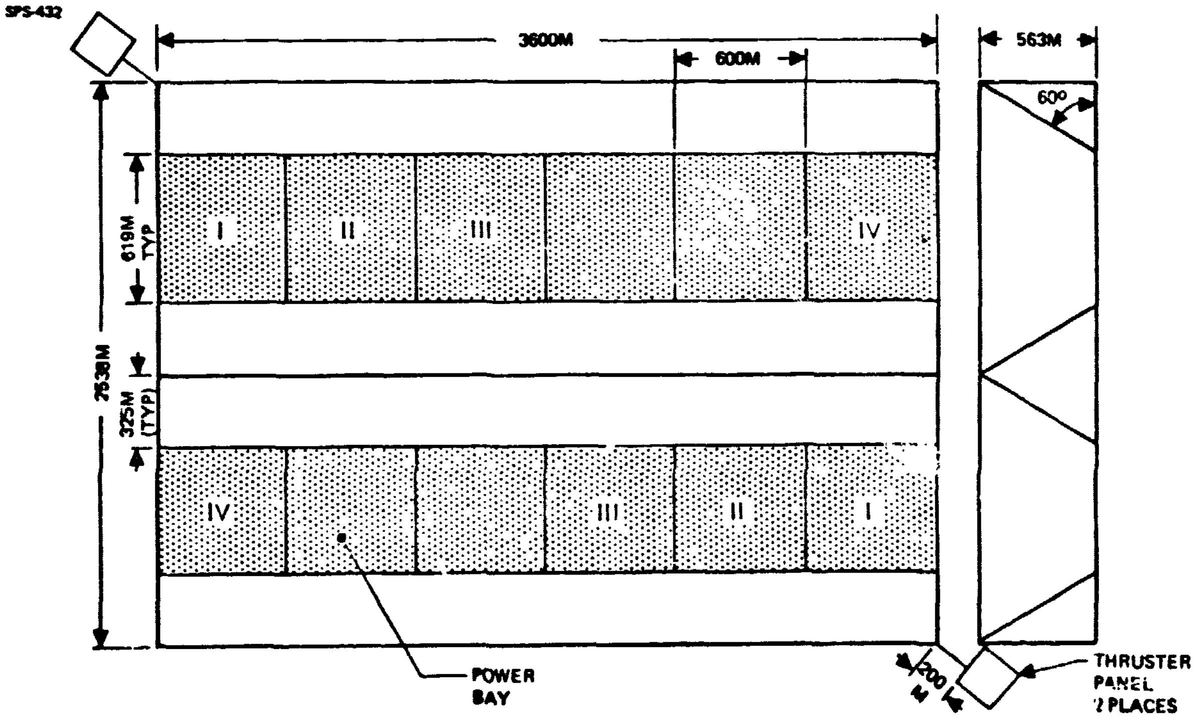

Figure 3.2-41. Photovoltaic SPS LEO-GEO Transfer Module (1-1/6 Total Satellite)

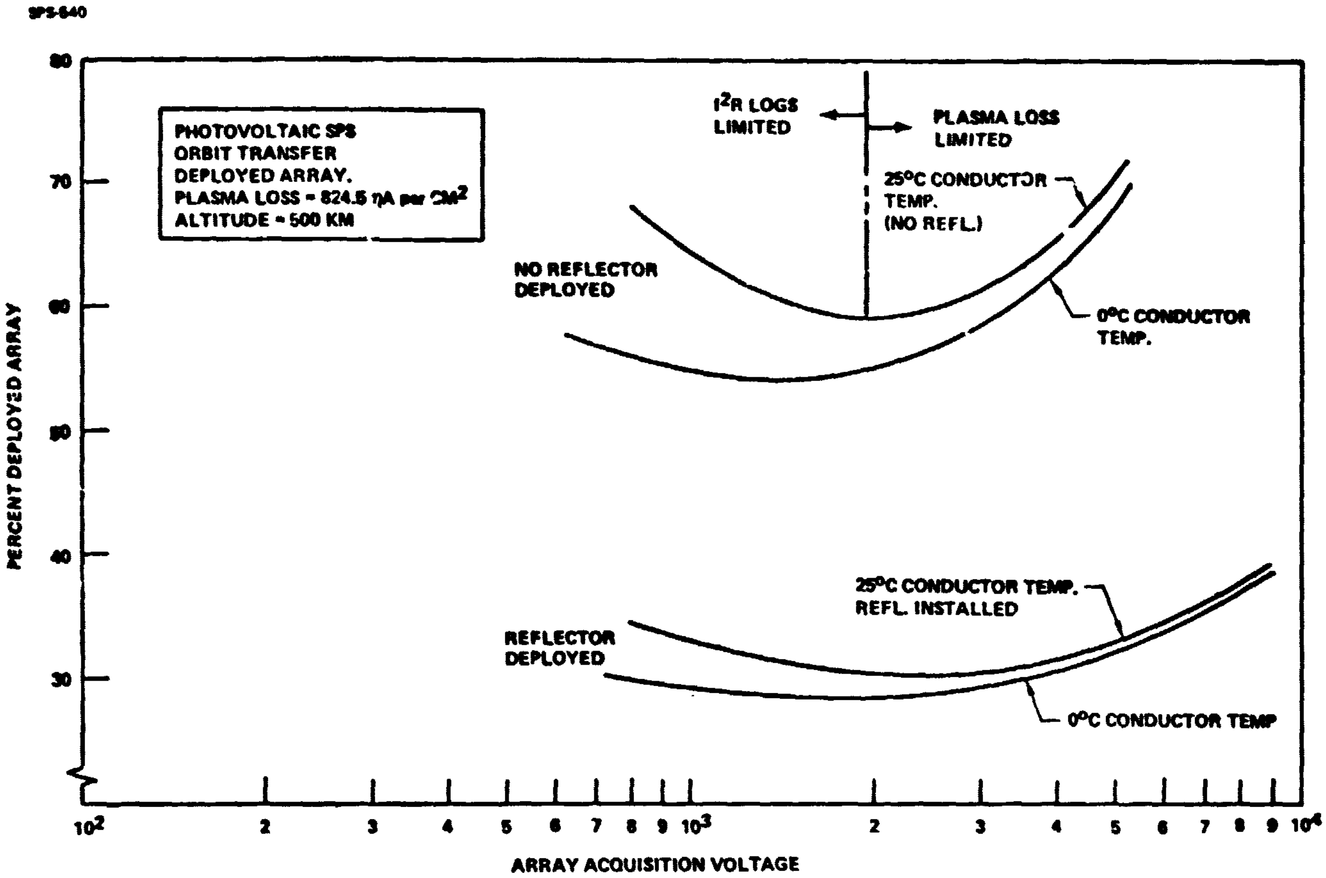

Figure 3.2-42. Deployed Array Required for Orbit Transfer 250 Day Trip Time

ORIGINAL PAGE IS OF POOR QUALITY

for two cases (performing orbit transfer with and without reflectors installed). Much more array is required to be deployed for the case of no reflectors installed for orbit transfer. This large difference is due to the following three principal reasons: 1) the solar cell output is less without reflectors, 2) a larger array area is required to collect the required power causing higher plasma current losses, 3) the larger array area increases the power distribution losses. Figure 3.2-43 shows the percentage plasma current loss for the no reflector and with reflector cases and shows the higher loss for the no reflector case.

The power distribution and thruster panel power processing mass required to provide thruster panel power is shown in Figure 3.2-44. Three discrete points are also shown for the condition of running the thruster screen grid directly from the power bus (i.e. no power processing for the screen grid supply). These points are not optimum from either the power system mass or the percentage of deployed array. As the array acquisition voltage increases the total power distribution and processing mass asymptotically approaches the power processing mass of 245,000 kilograms. Figure 3.2-45 was developed to show the contribution of thruster power, power processing losses, power distribution I^2R losses, and plasma current power losses for the 25^{o}C conductor temperature-reflector installed case. As can be seen in this figure, at higher array voltages the plasma current power loss predominates and at lower voltages the conductor I^2R loss predominates.

3.2.4.6 Power Loss By Leakage Through Plasma

The space between 400 km altitude and the orbits of geosynchronous satellites contains neutral atoms, free electrons, positive ions, and high-energy charged particles. The high-energy particles, although damaging to solar cells and optical surfaces, are not numerous enough to carry a significant current. The free electrons, generated each morning when ultraviolet photons ionize neutral atoms, have energies of around one to two electron volts. This energy is dissipated in reactions with neutral atoms and ions, increasing the temperature of the medium to the region of 500^{o} to 2000^{o} K. The temperature of an electron is related to its energy by Boltzmann's constant, 8.6171 x 10^{-5} eV per ^{o}K.

An electrically neutral gas containing free electrons and ions in equal numbers is called a plasma. A positively charged spherical electrode, say one cm in diameter, will collect electrons when inserted into a plasma. The volume in which electrons are influenced by the electrode, called a sheath, is much larger than the sphere. Some of the electrons will orbit around the electrode and escape back out of the sheath. Current collection is then said to be orbit-limited and is affected in a complex manner by the radius of the electrode, the voltage of the electrode, and the temperature and density of the free electrons.

The high-voltage solar-cell array for a solar power satellite looks more like a sheet electrode than like a spherical probe. For example, let us assume that 10 km^2 of a solar power satellite array is deployed to supply 1500-volt power for electric propulsion thrusters for raising the satellite from

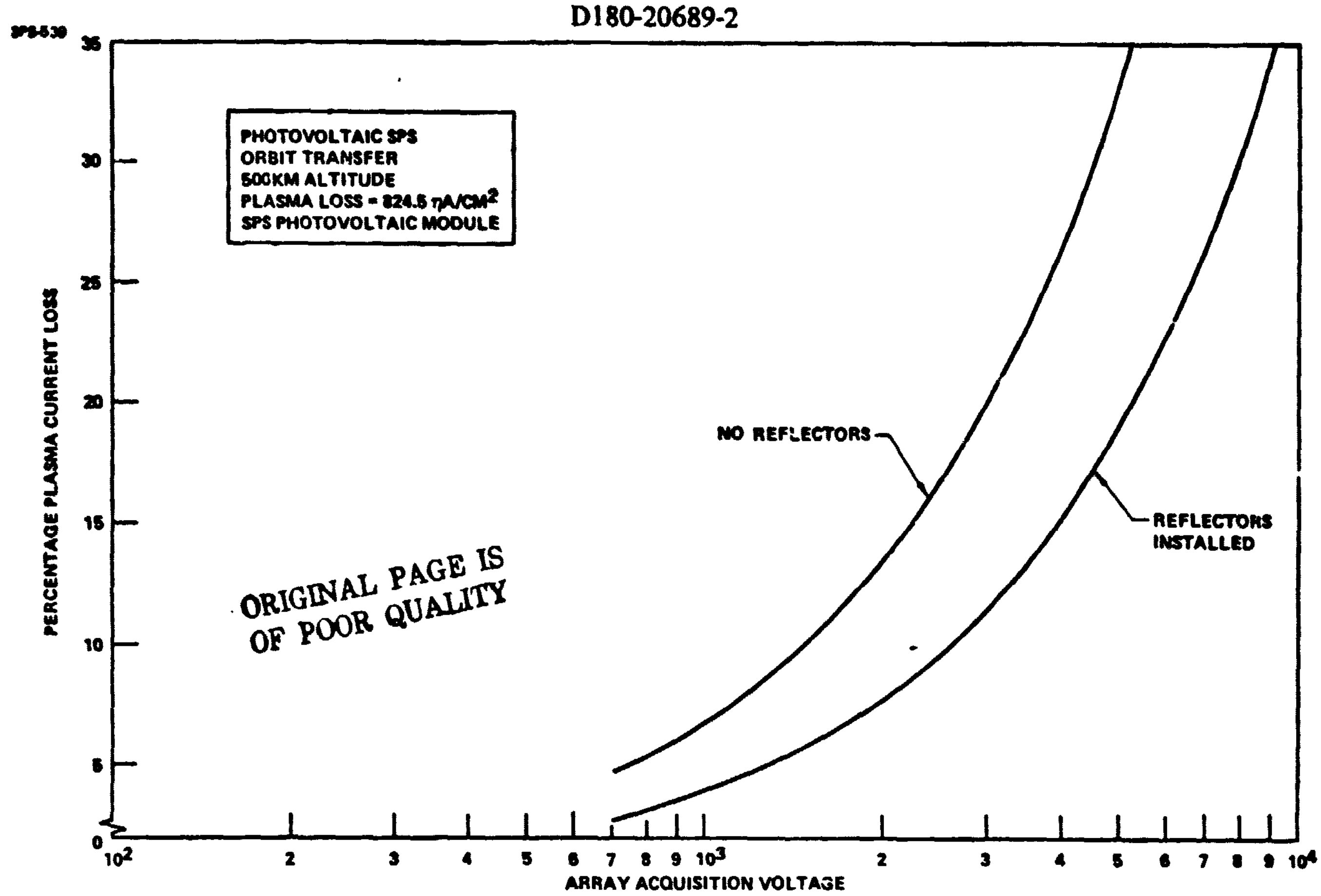

Figure 3.2-43. 500 KM Plasma Current Loss Acquisition Voltage vs Array

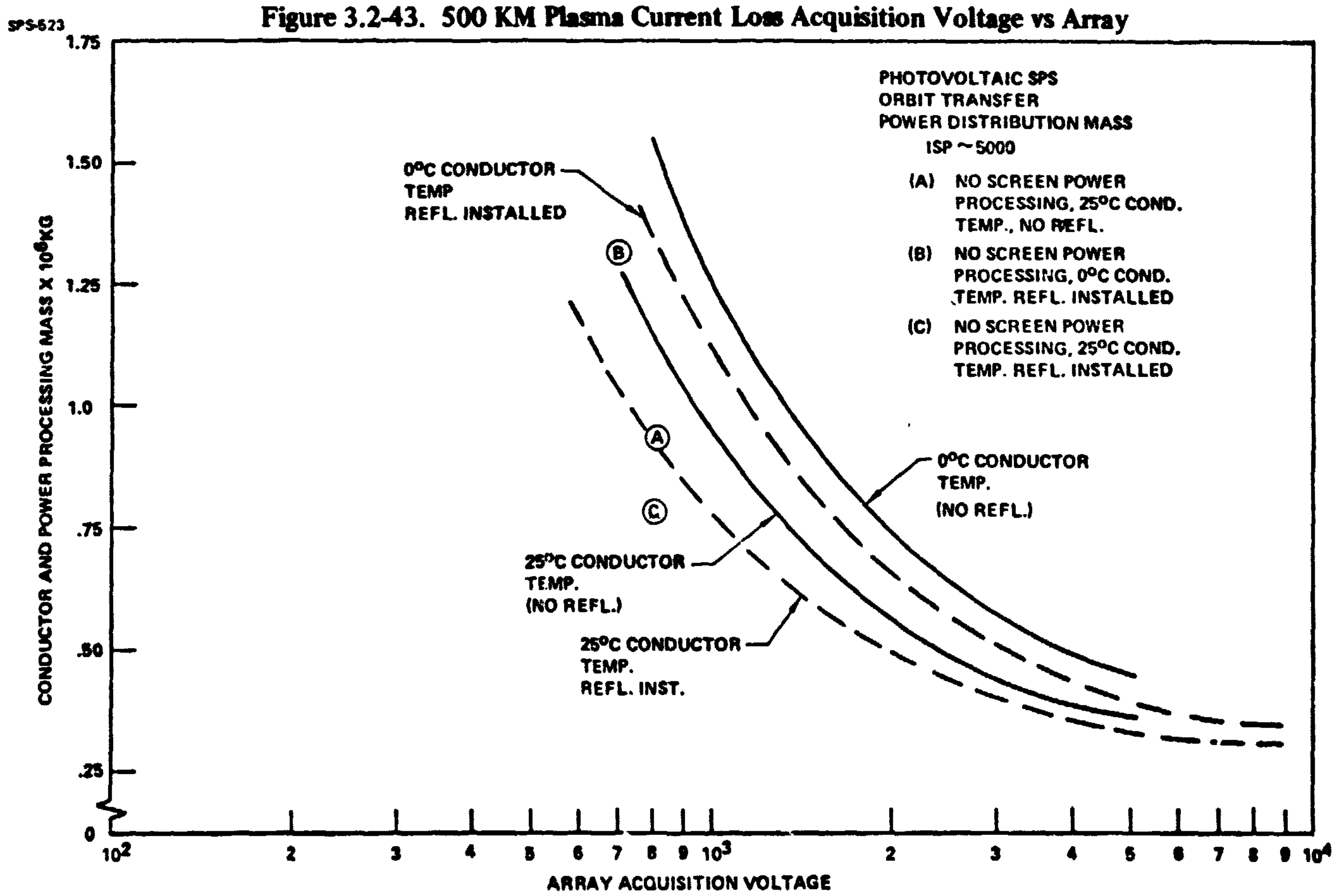

Figure 3.2-44. Conductor and Power Processing Mass vs Array Acquisition Voltage– 250 Day Trip Time

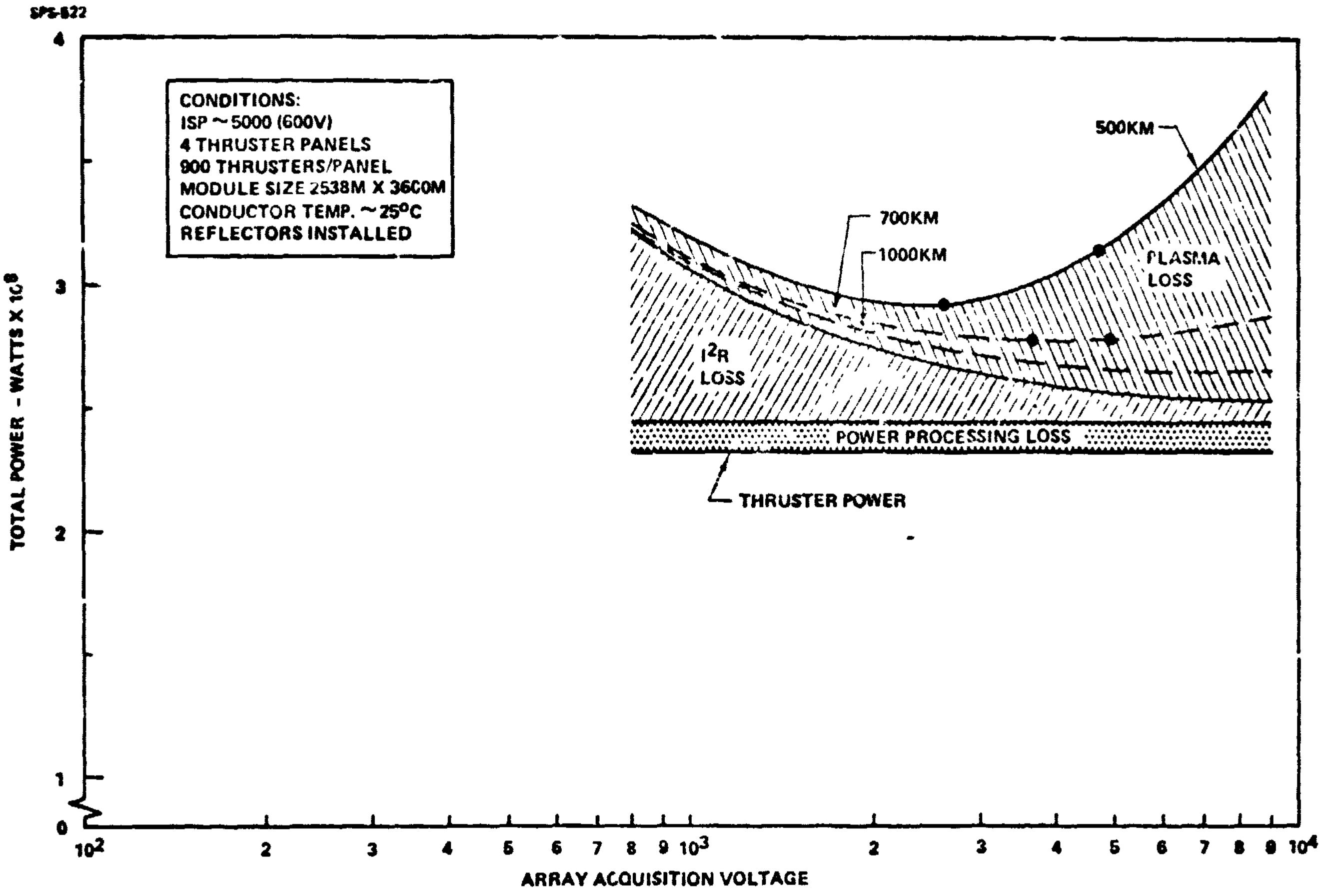

Figure 3.2.-45. Contributions to the Array Power Required For Orbit Transfer–250 Day Trip Time

low-Earth orbit, say 500 km, to geosynchronous orbit. K. L. Kennerud has developed a method of analyzing the leakage current from such arrays (Reference 1) based on fundamental equations developed by I. Langmuir (Reference 2). Kennerud's technique converts the planar array into a sphere having the same area, and then he calculates the radius of the electron sheath surrounding the array. His experiments with small positively charged solar-cell panels correlated well with his predictions. With a negatively charged panel which collected ions, his experimental measurements did not correlate well with theoretical predictions, perhaps because the ion sheath extended to the chamber walls.

Using Langmuir's equations, we determined that at 500 km the electron sheath extends to a few meters above the plane of the solar cells, in the range of electron concentrations, electron temperatures, and array voltages of interest. The calculation of leakage current then simplifies into analyzing the rate at which electrons drift into · electron sheath having essentially the same area as the solar array. This electron current (jr) is simply:

$$j_r = \frac{Ne\ E_e}{3.7 \times 10^{11}} \quad \text{(in A/cm}^2\text{)}$$

where N_e = electron density, in electrons per cm^3

E_e = electron energy in eV

The calculated leakage currents from a 1500-volt array for several altitudes are shown in Table 3.2-8.

A flow of electrons from the plasma to the solar power satellite must be matched an equivalent flow of electrons out of the solar power satellite. Otherwise the satellite will become negatively charged with respect to the plasma, and will cease attracting electrons. This flow of electrons away from the satellite is provided during orbit transfer by electron emitters which are installed for neutralizing the ions emitted by the thrusters. In geosynchronous orbit, where the satellite would be generating power, the electric thrusters would not be in operation. Furthermore, in geosynchronous orbit the electron density is only about 100 per cm^3, so the power lost through plasma leakage, even at 44 kV, would be trivial.

A negatively charged solar array would attract ions rather than electrons. However, ions are less mobile than electrons, and the ion current would be much smaller than the electron current observed with a positively charged solar array. Thus, the positively charged array is the worst case.

Calculations–Irving Langmuir, in Reference (2), provides the following equation for calculating electron urrent from plasma to a positive electrode:

$$I = 4\pi r_o^2 \ j_r \text{ if } r_o < P \qquad (1)$$

ORIGINAL PAGE IS
OF POOR QUALITY

Table 3.2-8. Leakage Current from Positively Charged Solar Array

ARRAY ALTITUDE, KM	ELECTRON DENSITY, N_e ELECTRONS/cm^3	ELECTRON TEMPERATURE °K	LEAKAGE CURRENT nA/cm^2	LEAKAGE CURRENT AMPERES PER 1500 V STRING*	POWER LOSS* PERCENT OF GENERATED
500	6×10^5	3,000	824.5	0.8494	7.72
700	2×10^5	3,000	274.8	0.2831	2.57
1,000	7×10^4	3,000	96.19	0.0990	0.90
2,000	2×10^4	3,200	28.38	0.0292	0.265
5,000	1×10^4	4,400	16.64	0.0171	0.156
10,000	8×10^3	5,400	14.75	0.0152	0.138
20,000	2×10^3	9,000	4.76	0.0049	0.044
30,000	1×10^2	13,600	0.29	0.0003	0

*THE STRING IS 0.404 m BY 255 m, WITH AN AREA OF 133.02 m^2

where

$$r_o = \frac{D}{j_r \alpha^2} = \text{Space-Charge Sheath Radius (cm)} \qquad (2)$$

$$D = 2.336 \times 10^{-6} (\beta V_p)^{3/2}$$

α^2 = a function of r_o/a which is calculated as shown below.

j_r = random current density of plasma electrons (amps/cm^2)

$$= \frac{N_e \quad E_e}{3.7 \times 10^{11}}$$

$$p = a \quad 1 + \frac{\beta V_p}{E_e} = \text{impact parameter (cm)}$$

a = radius of sphere having same area as array
β = fraction of sphere surface area uncovered
V_p = potential applied to array, volts
E_e = average energy of electrons
N_e = electron density (electrons per cm^3)
I = electron current collected by the sphere (amperes)

Langmuir's table relating $\frac{r_o}{a}$ to α is not applicable to the large electrode areas involved in the solar power satellite. The value of α was determined by iteration of the equation,

$$\alpha = \gamma - 0.3\gamma^2 + 0.075\gamma^3 - 0.0143182\gamma^4 + 0.0021609\gamma^5 - 0.00026791\gamma^6 \qquad (3)$$

where

$$\gamma = \log_e \frac{r_o}{a}$$

The analysis technique developed by K. L. Kennerud wraps the solar array area (A_a) around a sphere, which then has radius a. For a 10 km^2 array,

$$a = \frac{A}{4\pi} = \frac{10 \times 10^6 \times 10^4}{4\pi} = 8.92 \times 10^4 \text{ cm}$$

Iterative calculation of α and the radius of the electron sheath results in the following ratio for a 10 km^2 array at 1500V and at 500 km altitude:

$$\frac{r_o}{a} = 1.00292$$

ORIGINAL PAGE IS
OF POOR QUALITY

Thus, the electron sheath is only 260 cm above the array, and for all practical purposes has the same area as the solar array. Therefore, array radius a can be substituted for r_o, and the leakage current simplifies to

$$I = A\, j_r \qquad (4)$$

where

$$j_r = \frac{Ne \quad E_e}{3.7 \times 10^{11}}$$

and $E_e = T_e\, 8.6171 \times 10^{-5}$

with Ne = electron density, electrons/cm^3

T_e = electron temperature, ^oK

The values of leakage current shown in Table 3.2 − 8 were based on the Figure 3.2-46 electron densities and electron temperatures from Reference 3.

Effect of Voltage, Electron Temperature, and Electron Density—It is interesting to note that in large solar arrays the voltage of the array does not significantly affect the leakage current. The array voltage affects only the thickness of the electron sheath which is small compared with its other dimensions. For example, with a 1500-volt, 10 km^2 array the sheath is only 2.6 m thick at 500 km altitude. Increasing the array voltage to 44 KV would increase the sheath thickness by only a few meters.

Sheath thickness is affected by electron density and temperature. For example, in geosynchronous orbit the electron density is only about 100 electrons per cm^3. A 44 K V solar array operating in geosynchronous orbit would have a sheath radius 15 percent larger than the radius of a sphere having the same area as the array. Contributing to this large r_o are the array voltage, the low electron density and hot electron temperature. However, the plasma leakage current in a solar array of a power satellite in geosynchronous orbit is limited, not by the electron supply, but by the inability of the heavy ions to move to the satellite to neutralize the charge deposited by collected electrons. The leakage electron current would no longer be neutralized by the emitters used with the ion propulsion engines, and hence would be trivial.

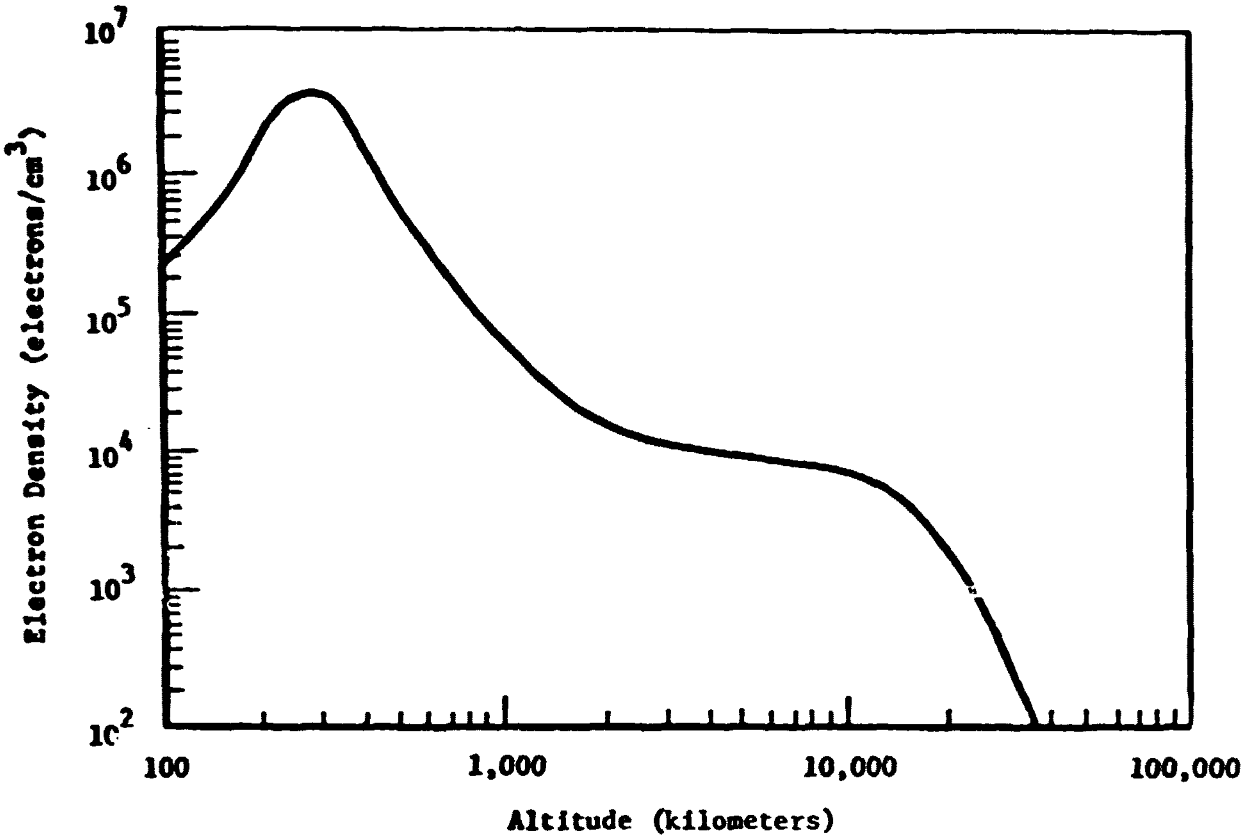

Figure 3.2-46. Electron Density vs Altitude

References

1. Kennerud, K. L., "High Voltage Solar Array Experiments," NASA Lewis document CR-121280, March 1974 (written at Boeing).

2. Langmuir, I. and Blodgett, K. B., "Currents Limited by Space Charge Between Concentric Spheres," Physical Review 23, p. 49 (1924).

3. Doherty, W. R., and Wilkinson, M. C., "High Voltage Solar Array Space Environment Model," Boeing document D2-121333-1 (1970).

ORIGINAL PAGE IS
OF POOR QUALITY

3.2.5 Radiation Degradation Analyses and Annealing

3.2.5.1 Environment Predictions

Predictions of the sunspot number for the coming Cycle 21 are compared in Figure 3.2-47. F. M. Smith bases his prediction on two non-synchronous components related to planet-caused tidal variations on the Sun. W. Gliessberg of the Astronomical Institute in West Germany, bases his predictions on 80-year repeatability of sunspot phenomena. Ted Cohen and Paul Lintz base their prediction on a periodicity of 179 years, obtained from a maximum entropy analysis.

A solar power satellite launched in 1990 will experience Cycles 22, 23 and 24 for which no predictions have yet been made. We therefore used data averaged for us by Prof. W. R. Webber, University of New Hampshire, who is our consultant on solar activity.

The average expected solar proton fluence (> 10 MeV), and a 90% value, are shown in Table 3.2-9). An equivalent 1-MeV electron damage fluence for a 6 mil 10 ohm-cm n/p solar cell with 6 mil cover slip and 3 mils of equivalent back side Kapton, adhesive and mylar shielding is also given. The proton damage coefficient used is shown in Figure 3.2-48 as "1/E." The electron damage coefficient is taken from the TRW Solar Cell Handbook. The incident proton spectral shape is shown in Figure 3.2-49, while the trapped electron spectrum is shown in Figure 3.2-50.

3.2.5.2 Solar Cell Radiation Degradation

A radiation-degraded solar cell in a series string, operating at its maximum-power point to supply a constant-voltage load, will not also operate at its maximum-power point when initially in geosynchronous orbit. The volt-ampere characteristic of the solar cell is needed for calculating the cell performance under the differing illumination, temperature, and degradation conditions in solar power satellite operation.

The characterization of a 1975 OCLI "Violet" cell shown in Figure 3.2-51 was useful in our analysis. We had recorded the voltage-current characteristic of the cell under standard conditions after irradiation by 10^{13}, 10^{14}, 10^{15}, and 10^{16} one-MeV electrons. Estimating the curves for 2×10^{15} and 6 s 10^{15} one-MeV electrons was straightforward.

The estimated maximum power points for higher temperatures and light intensities were based on the current being proportional to light intensity, and a 0.43 percent per degree C coefficient of maximum power.

SPS-127

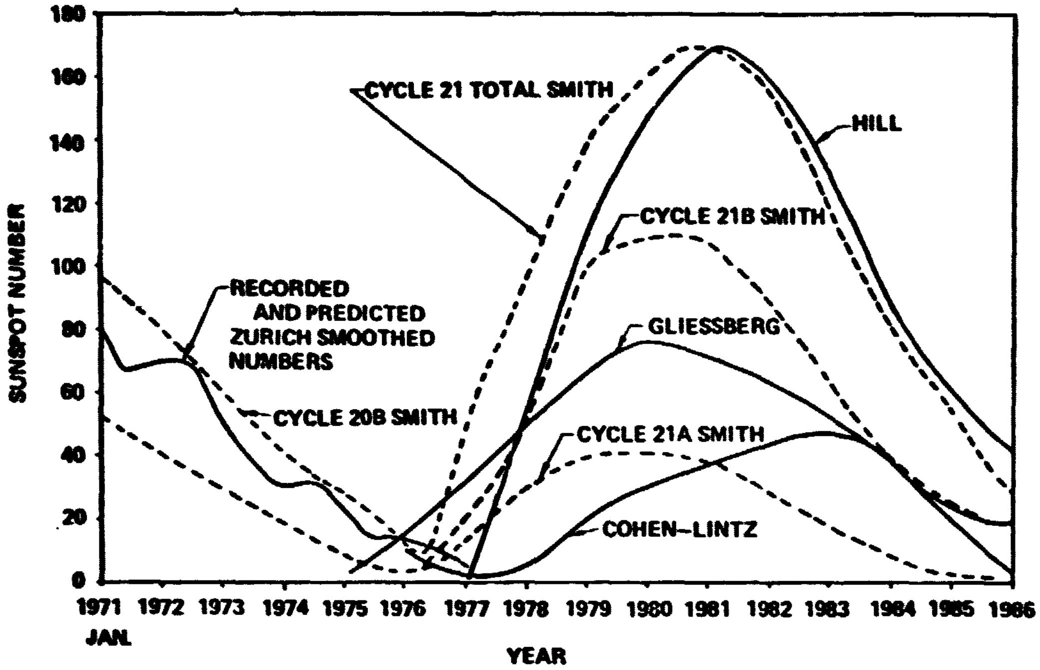

Figure 3.2-47. Predictions For Solar Cycle 21

Table 3.2-9. Solar Proton Fluence

	AVERAGE FLUENCE	90% FLUENCE
SOLAR CYCLE 21		
Q_p (> 10 MeV)/CM^2	3.28×10^{10}	10^{11}
1-MeV DENI ELECTRONS	2.3×10^{14}	6.98×10^{14}
SOLAR CYCLE 21, 22, & 23		
Q_p (> 10 MeV)/CM^2	1.1×10^{11}	2.25×10^{11}
1-MeV DENI ELECTRONS	7.7×10^{14}	1.6×10^{15}
TRAPPED ELECTRON FLUENCE		
YEARLY FLUENCE (>0.25 MeV)	3×10^{14} e/cm^2	
YEARLY 1-MeV DENI FLUENCE (6 MIL COVER SLIPS, 10 OHM-CM, n/p)	2×10^{13} 1-MeV e/cm^2 -YEAR	

ORIGINAL PAGE IS
OF POOR QUALITY

SPS-228

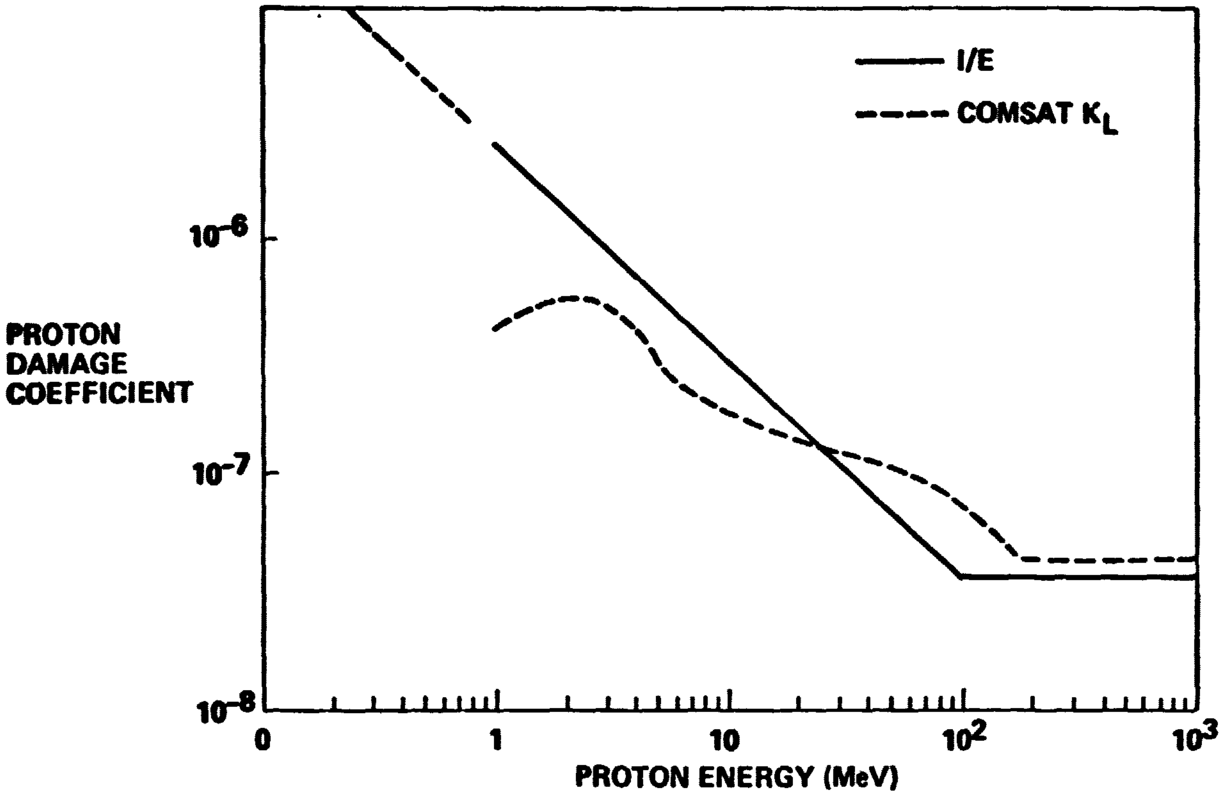

Figure 3.2-48. Damage Coefficient Comparison

SPS-225

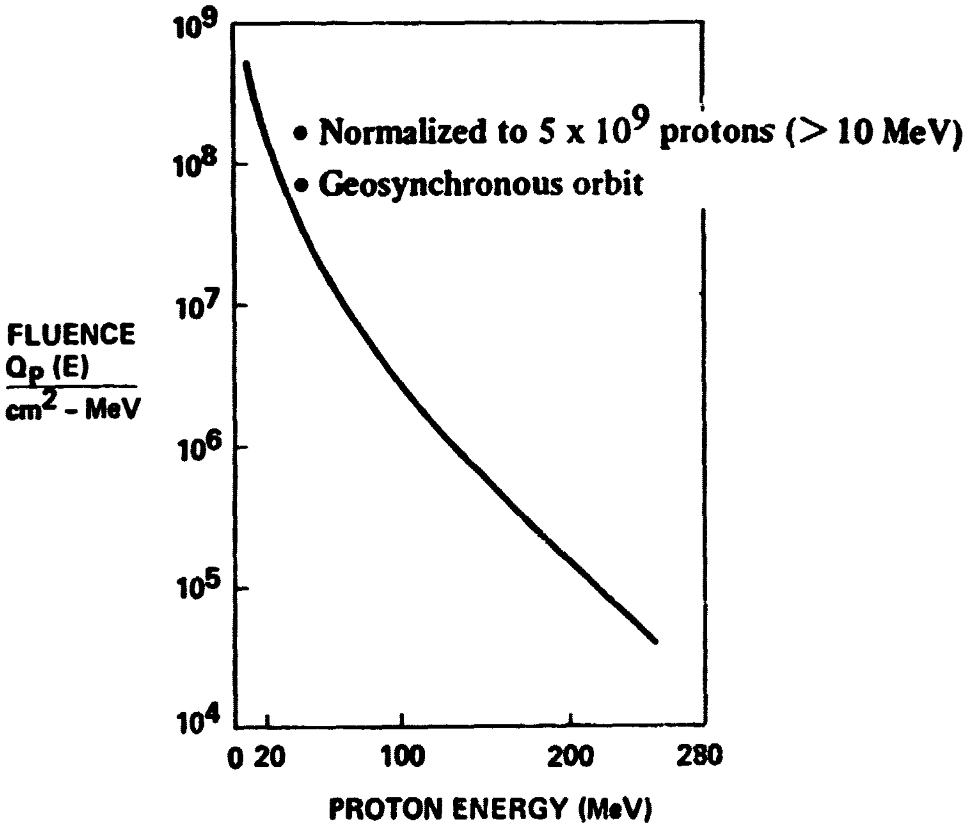

Figure 3.2-49. Spectrum of Protons Incident on Solar Cells on Solar Power Satellite

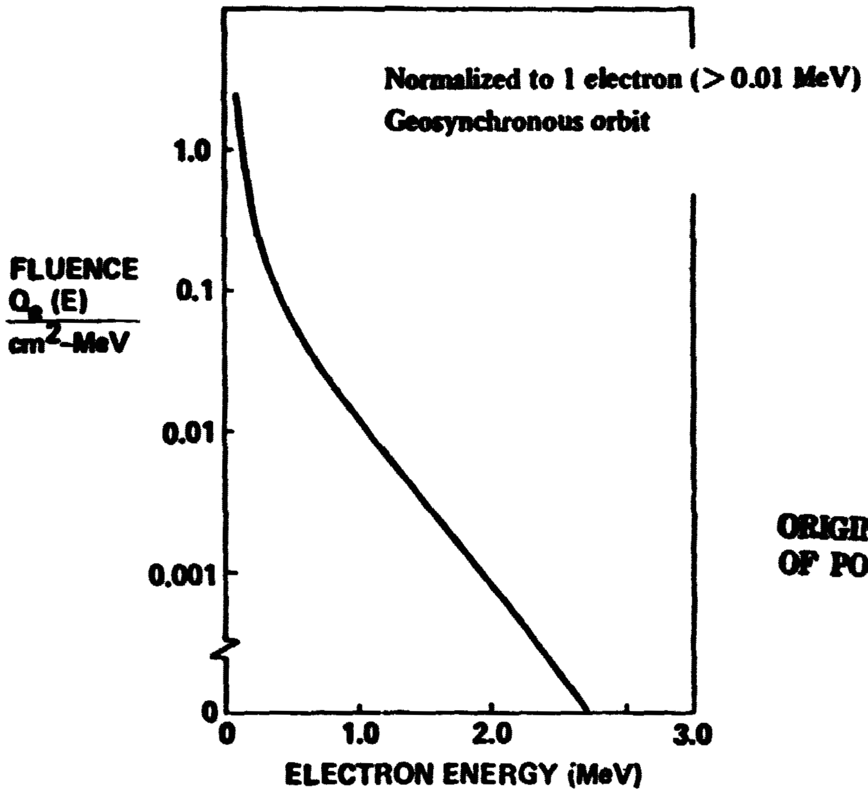

ORIGINAL PAGE IS
OF POOR QUALITY

Figure 3.2-50. Spectrum of Electrons Incident on Solar Cells of Solar Power Satellite

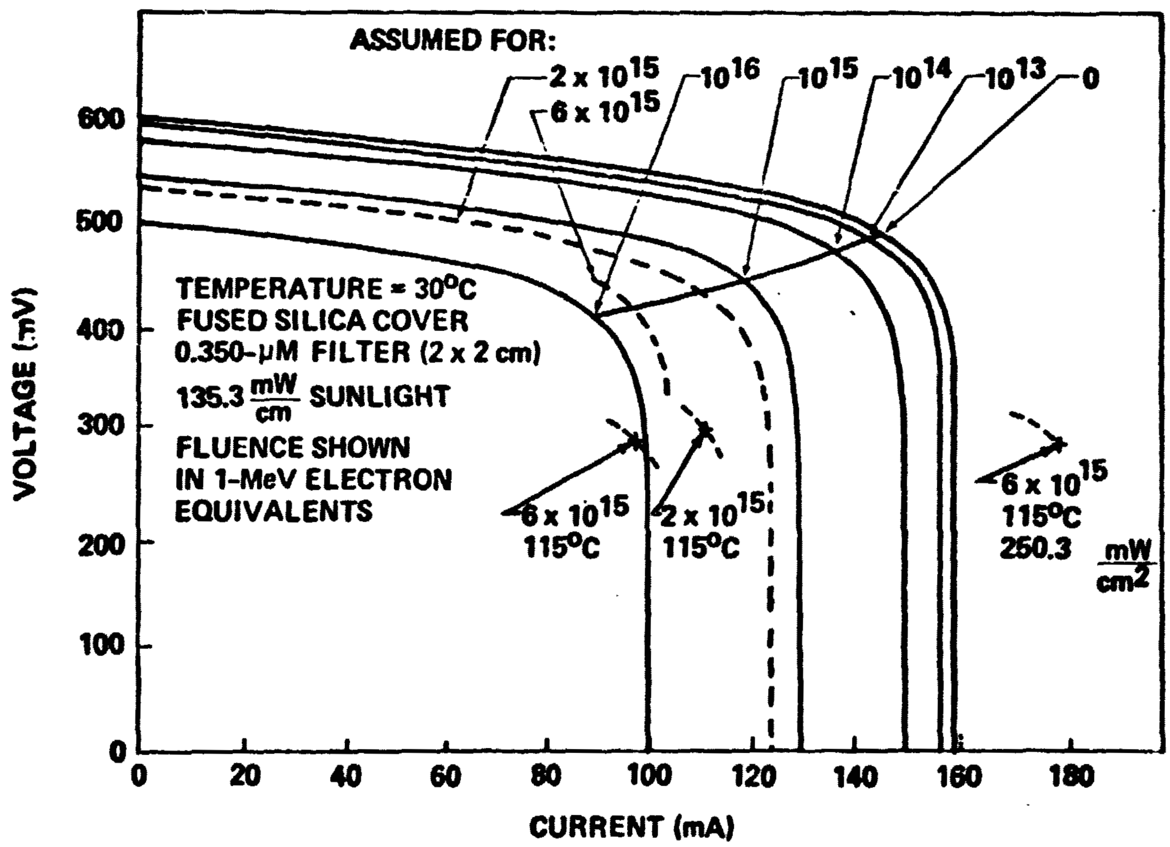

Figure 3.2-51. Output of a Proton-Irradiated 1975 Violet Cell

Thinner solar-cell covers admit more radiation, increasing the radiation damage in the cell. Plotted in Figure 3.2-52 is the relative damage in a solar cell geosynchronous orbit, as a function of cover thickness, normalized to a cover of 6-mils of fused silica.

Note that when covers are thinned below 50 μm, the damage increases rapidly. This curve was used in calculating the performance of solar-cell blankets having various thicknesses of covers.

One mil (25.4μm) of fuxed silica on a 100 km^2 solar array weights about 5x10^6 kg.

The solar power satellite performance estimates are based on, not 1977 solar cells, but rather on 1987 solar cells which are predicted to have an efficiency of 18 percent. Test data from such cells is obviously not available, so array performance predictions had to be based on extrapolations of test data from today's best solar cells.

An example of such extrapolation is shown in Figure 3.2-53 where the maximum power outputs of Comsat's completely nonreflective solar cells, and several others, are plotted as a function of one-MeV fluence. This plot comes from the Fall 1975 Comsat Technical Review. We have added to the plot the fluences that would be experienced by cells during 30 years in geosynchronous orbit when protected by fused silica covers of various thicknesses. Note the extrapolation to 6 x 10^{15} one-MeV electrons, where a nonreflective solar cell with a 2-mil cover has dropped to 63.1 percent of its orihinal maximum power. An 18-percent efficient solar cell was assumed to likewise drop to 63.1 percent of its initial maximum power after 30 years.

The cell voltage establishes how many cells must be in series to develop 44 kV, and hence how long the solar-cell string must be. The voltage of a 1976 back-surface-field cell, as a function of one-MeV electron fluence, appears in the JPL "Solar Array Design Handbook," shown in Figure 3.2-54.

Our prediction of the maximum-power voltage of an 18-percent efficient solar cell is shown as a dotted line. The right-most "X" corresponds to 0.446 volts from a cell protected by a 50μm (2-mil) fused silica cover, after 30 years.

These voltages would be observed at 25°C with the cell illuminated by 135.3 mW/cm^2 sunlight having an air-mass-zero spectrum.

Summarized in Table 3.2-10 are the results of calculations of the performance of a solar-cell string after 30 years in geosynchronous orbit, with varying thicknesses of cell covers. The thinner covers admit more radiation to the cell, reducing power output and voltage. For example, the degraded cell with a 50 μm (2 mil) cover produces only 0.297 volts, requiring 149,390 such cells for 44.44 kV. The extra 0.44 kV is absorbed by IR and diode drops in the string. Each string is composed of groups of 4 cell in parallel.

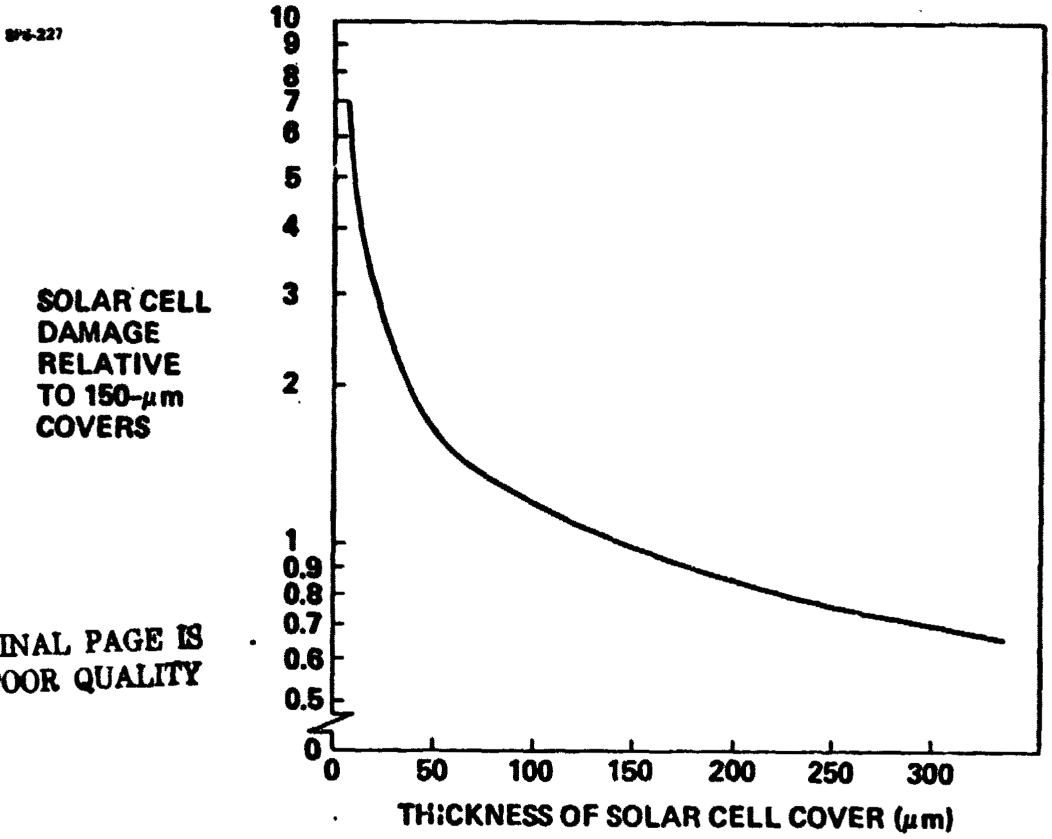

ORIGINAL PAGE IS OF POOR QUALITY

Figure 3.2-52. Reducing Cover Thickness Increases Damage

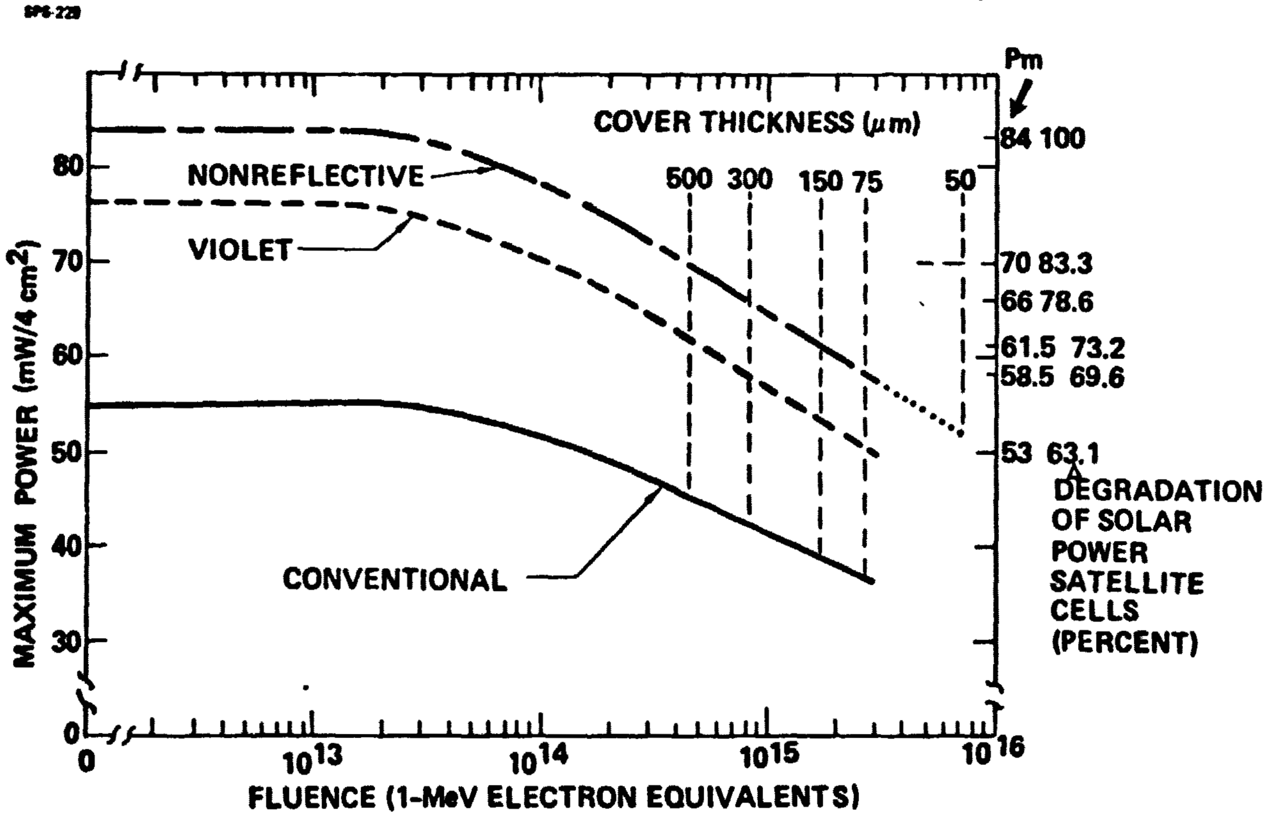

Figure 3.2-53. Thinner Covers Admit More Radiation

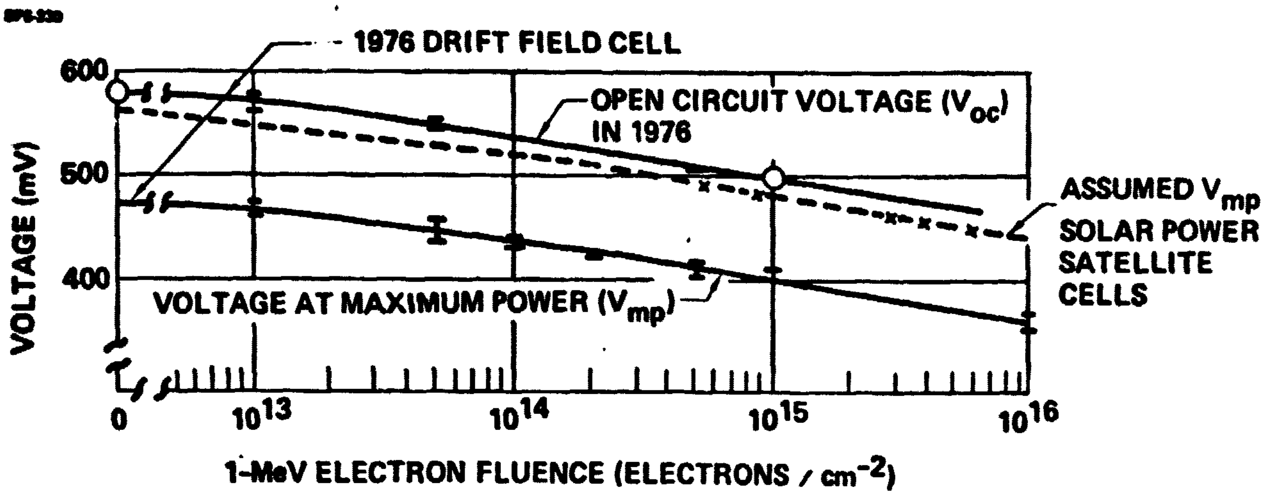

Figure 3.2-54. Radiation Degrades Maximum-Power Voltage

Table 3.2-10. Solar Array Output After 30 Years in Geosynchronous Orbit

SPS-232 Characteristic	Cell cover thickness (mils)				
	2	3	6	12	20
Fluence after 30 years in geosynchronous orbit	6×10^{15}	2.7×10^{15}	1.8×10^{15}	8.5×10^{14}	4.6×10^{14}
Power output after 30 years (mW/cm^2)	15.82	17.46	18.36	18.27	20.89
W/m^2	158.2	174.6	183.6	192.7	208.9
Maximum-power voltage at 115°C (V)	0.297	0.302	0.308	0.318	0.328
Cells in series for 44,440 volts	149,390	147,153	144,286	139,743	135,488
Cells in one string, 4 cells wide	597,560	588,612	577,144	558,992	541,952
String length (5 + 0.1 cm/cell) (km)	7.62	7.5	7.36	7.13	6.91
String width with length constrained to 650 meters (10 + 0.1 cm/cell) (m)	4.73	4.66	4.574	4.43	4.30
Strings per module of 650 by 496m	104.74	106.33	108.45	111.97	115.49
Current per string (A)	10.657	11.561	11.923	12.400	12.740
Current per module (A)	1117.7	1229.35	1293.21	1388.50	1471.46
Power per module (MW)	49.11	54.05	56.90	61.10	64.74

Each string is serpentined into a module 650 meters long. The 7.62 km string of cells with 50 μm (2 mil) covers would occupy a strip 4.73 meters wide in such a module, and 104.74 strings would fill a module having dimensions of 650 by 496 m. The module would generate 49.11 MW after 30 years in orbit.

Note that the module with 50 μm (2 mil) covers generates after 30 years 13.7 percent less power than the module with cells protected by 150 μm (6 mils) of fused silica. However, the thinner covers represent in a 100 km^2 solar power satellite a saving of 20 million kg of mass.

3.2.5.3 Annealing Study

Analyses and tests of silicon solar cell annealing were conducted by Simulation Physica, Incorporated under a subcontract. The remainder of this section presents their report.

ORIGINAL PAGE IS
OF POOR QUALITY

D180-20689-2

PHASE I REPORT

ANNEALING OF RADIATION DAMAGE IN SILICON SOLAR CELLS

A. R. KIRKPATRICK
W. R. NEAL
J. A. MINNUCCI

P.O. N-943415-9174

15 MARCH 1977

SUBMITTED TO:
BOEING AEROSPACE COMPANY

SIMULATION PHYSICS, INC.
SPI

SECTION I

INTRODUCTION

This report covers Phase I of a study of "Thermal Annealing of Radiation Damage in Silicon Solar Cells". Purpose of the study is to establish feasibility for in situ annealing of radiation damage in silicon solar cells on the Solar Power Satellite if the satellite were to be assembled in low earth orbit and transferred to geosynchronous orbit. The study is directed toward consideration of proton damage, but the conclusions made are expected to be qualitatively valid for damage by electron radiation as well.

Content of Phase I of this program has consisted essentially of the following:

(i) A review of existing experience relative to thermal annealing of proton irradiated silicon solar cells.

(ii) Experimental studies to determine feasibility of using directed energy techniques for annealing of proton irradiated cells.

Existing information regarding annealing of radiation damaged solar cells suggests that conventional thermal processes can be effective. However conventional technique, which is essentially a furnace procedure, consists of

ORIGINAL PAGE IS
OF POOR QUALITY

elevating the entire solar cell to an adequate temperature and maintaining that temperature for a sufficient period of time. Because necessary conditions involve periods of minutes at temperatures of the order of 500°C, it is questionable whether such methods would be realistic for a practical array in space.

Investigation of the feasibility of utilizing a concept of directed energy annealing has been undertaken because such an approach could be possible in space, probably even on an array structure which is itself thermally unstable. A directed energy process uses the energy carried in a beam impacting upon the surface of the solar cell undergoing anneal. The energy can be carried in an electron, laser or photon flash beam. It is assumed that the heating produced by the beam is to be transient and spatially localized so as to accomplish necessary annealing of the solar cell without subjecting surrounding components such as the substrate to excessive thermal excursion.

The material presented in this Phase I report can be summarized very briefly as follows:

(i) On the basis of existing information it is definitely possible to anneal proton radiation damage in silicon solar cells using furnace environment conditions.

(ii) Degree of annealing depends primarily upon temperature employed; close to complete performance recovery can be achieved within the thermal limitations of the solar cell itself.

(iii) A substantial degree of proton irradiated solar cell performance recovery has been demonstrated using electron and laser beam directed energy sources.

(iv) Achievable degree of performance recovery using directed energy has not been determined but is probably high.

ORIGINAL PAGE IS
OF POOR QUALITY

SECTION II

REVIEW OF EXISTING INFORMATION CONCERNING ANNEALING OF PROTON DAMAGE IN SILICON SOLAR CELLS

2.1 GENERAL

Since the discovery in 1958 of the presence of large fluxes of charged particle radiations within the earth's geomagnetic field, there has been continuing interest in the effects of radiations upon solar cells for space vehicles. Earlier studies were concerned both with the generation of radiation damage and with possibilities for its repair. As solar array experience increased, the technology tended to standardize around successful history. Radiation damage work shifted to emphasize prevention of severe damage in conjunction with minimization of array initial overdesign necessary to provide for unavoidable effects. In particular, effective coverglass methods allowed nonpreventable proton damage to be reduced to low levels. Further consideration was not given to in situ thermal anneal of proton damage losses.

Proton and electron irradiation of silicon causes lattice atoms to be displaced, leaving interstitials and vacancies. Defect complexes involving the vacancies or interstitials and other elements of the crystal are formed which act to allow carrier recombinations causing loss of minority carrier lifetime and degrading solar cell performance. Although the individual defects created by protons are similar to those with electrons, the heavy mass of the proton results in localized multiple centers as opposed to point defects with electrons. It is generally considered that the cluster defect complexes associated with protons are somewhat more difficult to anneal than are the electron induced defects.

2.2 LITHIUM-DOPED SOLAR CELLS

On the assumption that the major threat to the solar cells of the Solar Power Satellite will be damage by protons able to penetrate a thin protective cover, lithium doped silicon solar cells might be considered. The room temperature annealing behavior produced by lithium in a P/N cell is extremely effective for the multiple defect complexes which are characteristic of damage produced by proton or neutron radiations. The best available information regarding proton damage recovery of lithium doped silicon solar cells is by Anspaugh and Carter(1). They conclude "lithium cells would be a good choice to power a spacecraft in a radiation environment dominated by protons, provided the cells can be annealed periodically at sufficiently high temperature". The high temperature referred to in this instance need be only about 60°C. Figure 1 shows an example of normalized maximum power of N/P and lithium doped P/N cells as functions of 11 MeV proton fluence. Advantages of the lithium doped cell are clear.

ORIGINAL PAGE IS
OF POOR QUALITY

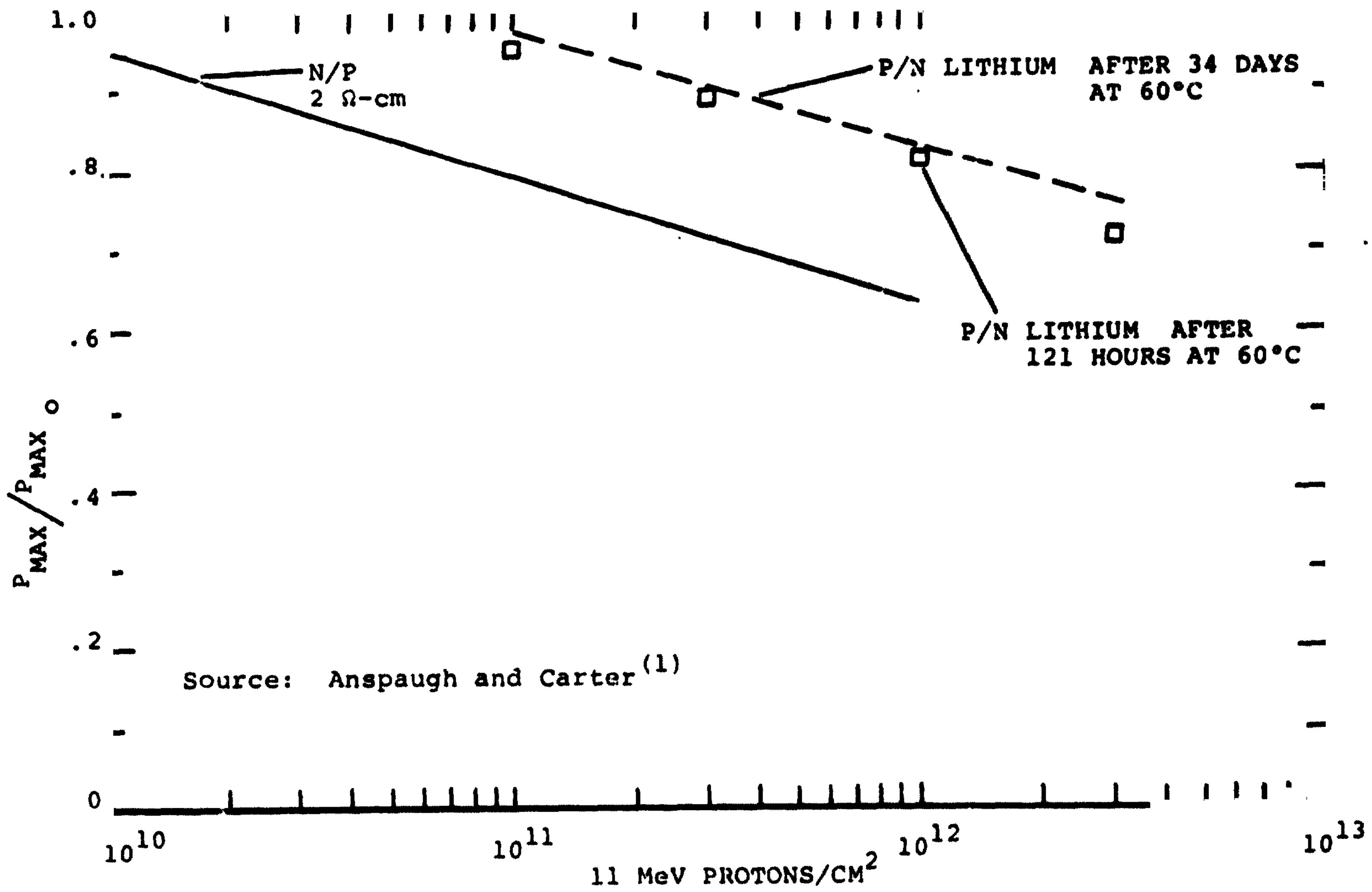

Figure 1. Normalized Maximum Power of N/P and Lithium Doped P/N Cells Versus 11 MeV Proton Fluence

2.3 THERMAL ANNEALING OF PROTON DAMAGE

Most of the work relevant to thermal annealing of proton irradiated solar cells without lithium doping was performed by Beatty and Hill of NASA Langley[2,3] and by Faraday, Statler and Tauke[4,5] of the Naval Research Labortary. Beatty and Hill investigated low to moderate 300°C temperature annealing of damage to silicon by high energy protons while Faraday, Statler and Tauke examined recovery of silicon solar cell damage due to lower energy protons using temperatures up to as high as 600°C.

Beatty and Hill

Beatty and Hill irradiated both n- and p-type 1 ohm-cm silicon with 22, 40 and 158 MeV protons. Since minority carrier lifetime is one of the parameters most sensitive to radiation damage, they chose to monitor the unnormalized percentage of damage remaining, defined as

$$D_\tau \equiv \frac{\tau_o - \tau_A}{\tau_o} \times 100$$

where τ_o and τ_A are the pre-irradiation and post-irradiation annealed minority carrier lifetimes respectively. Limited by an experimental oven facility with maximum temperature of only 300°C, their efforts on silicon fell short of the practical results on solar cells by the NRL group. However, some of their observations are applicable.

ORIGINAL PAGE IS
OF POOR QUALITY

Figure 2 shows percentage of defects remaining in p-type silicon irradiated with 10^{11} 22-MeV protons/cm^2 as a function of annealing time at 100, 200 and 300°C. It is evident that the most recovery occurs at the highest anneal temperature and that, after an initial anneal period at given temperature, relatively little additional recovery will occur as a result of prolonged anneal at the same temperature.

Annealing is fluence dependent. Damage from higher proton fluences does not anneal as readily as damage from lower fluences. Figure 3 illustrates this effect. Annealing at 300°C is seen to be moderately effective on silicon irradiated at 22 MeV to fluence 1×10^{11} protons/cm^2 and almost completely ineffective for fluence of 5×10^{12} protons/cm^2.

The recovery characteristics of n- and p-type silicon are similar but recovered minority-carrier lifetime is apparently slightly better in n-type than in p-type Figure 4 illustrates this observation.

As proton energy increases, the amount of damage remaining after anneal decreases. Figure 5 shows this result for 200°C anneals and 10^{12} protons/cm^2 fluences of 22, 40 and 158 MeV protons on n-type material.

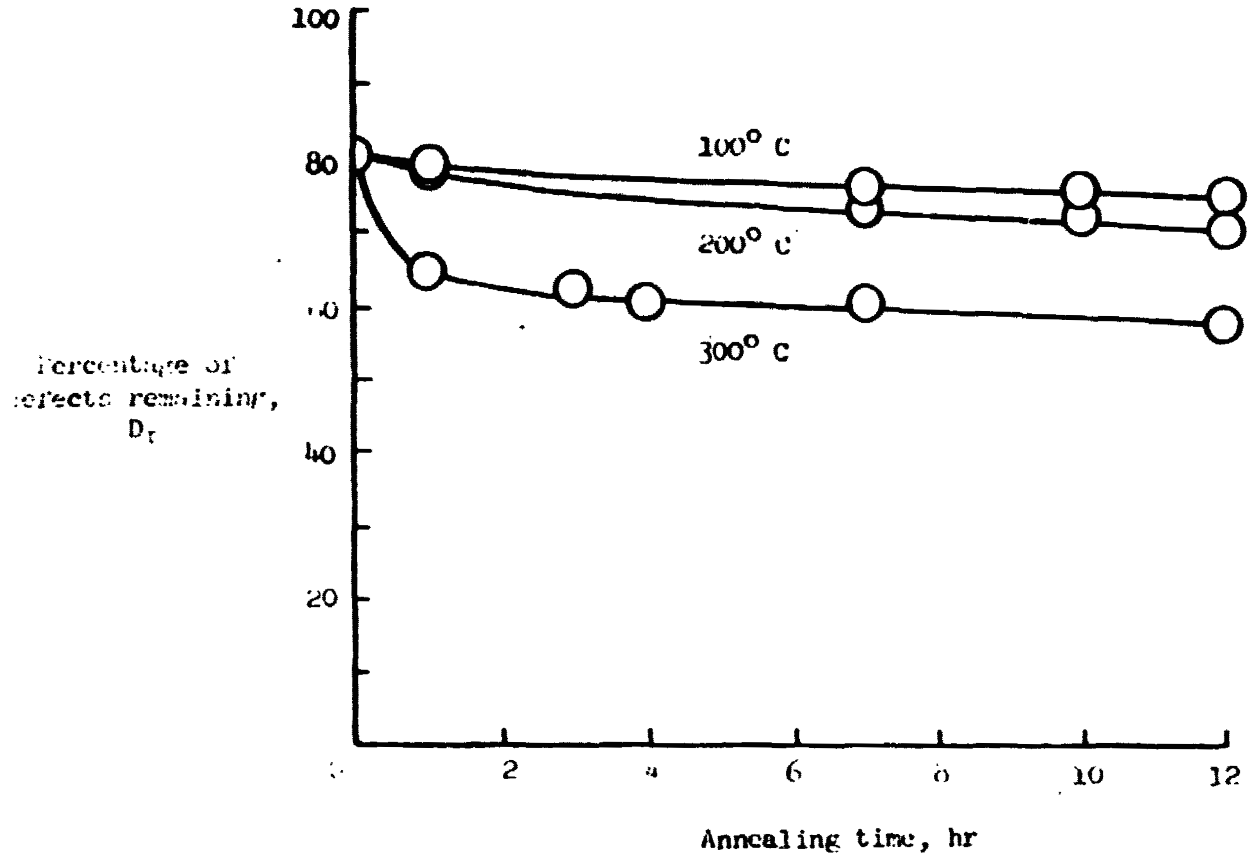

Source: Beatty and Hill(3)

Figure 2. Fraction of Defects Remaining in p-Type Silicon Irradiated with 22 MeV Protons to a Fluence of $\phi = 1 \times 10^{11}$ Protons/cm^2 as a Function of Annealing Time of 100°C, 200°C and 300°C (Unnormalized)

ORIGINAL PAGE IS OF POOR QUALITY

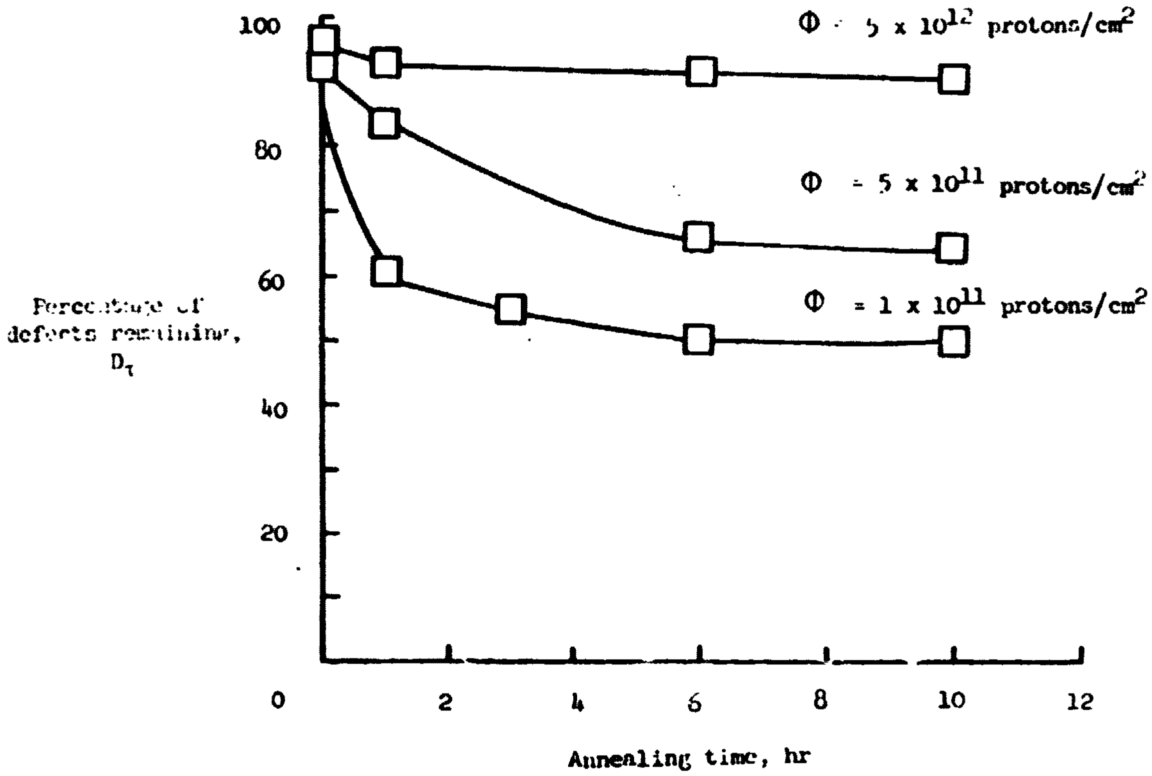

Source: Beatty and Hill(3)

Figure 3. Dependence of Annealing of n-Type Silicon at 300°C on Fluence of 22 MeV Protons (Unnormalized)

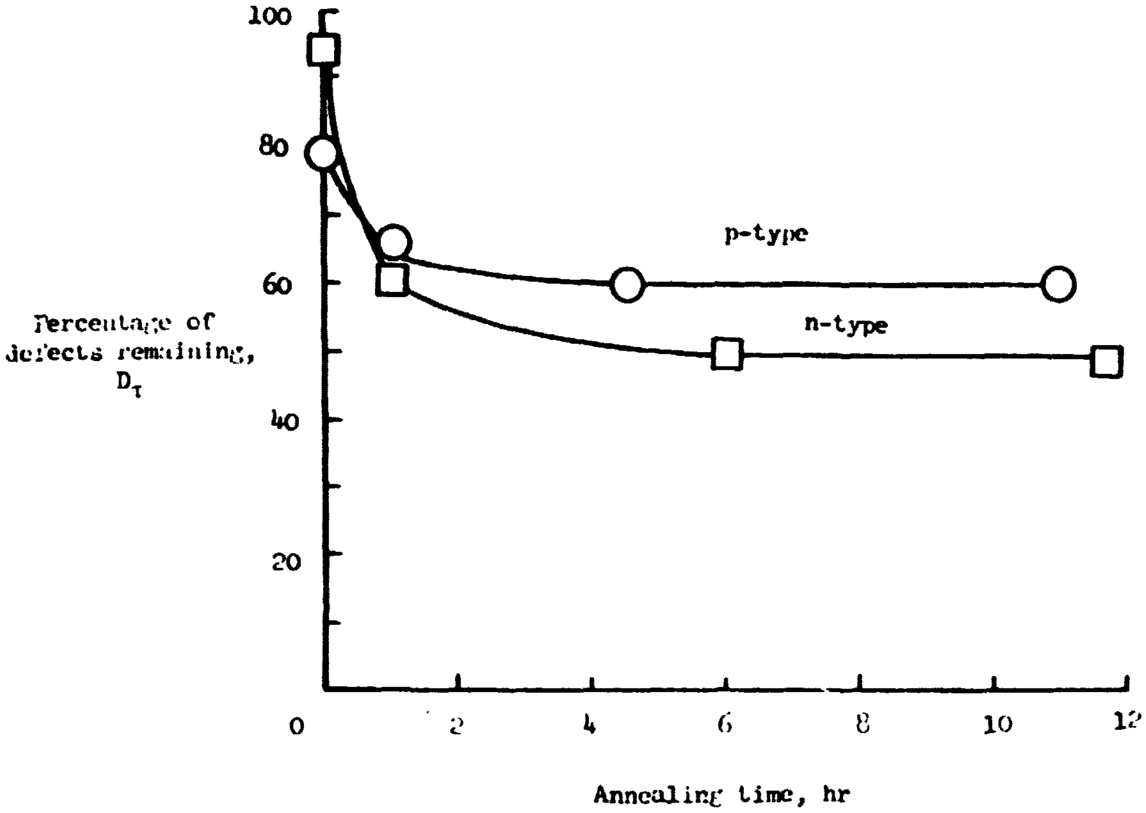

Source: Beatty and Hill(3)

Figure 4. Comparison of Annealing of Typical n- and p-Type Silicon Samples at 300°C After Irradiation with 22 MeV Protons ($\phi = 1 \times 10^{11}$ Protons/cm^2) (Unnormalized)

ORIGINAL PAGE IS
OF POOR QUALITY

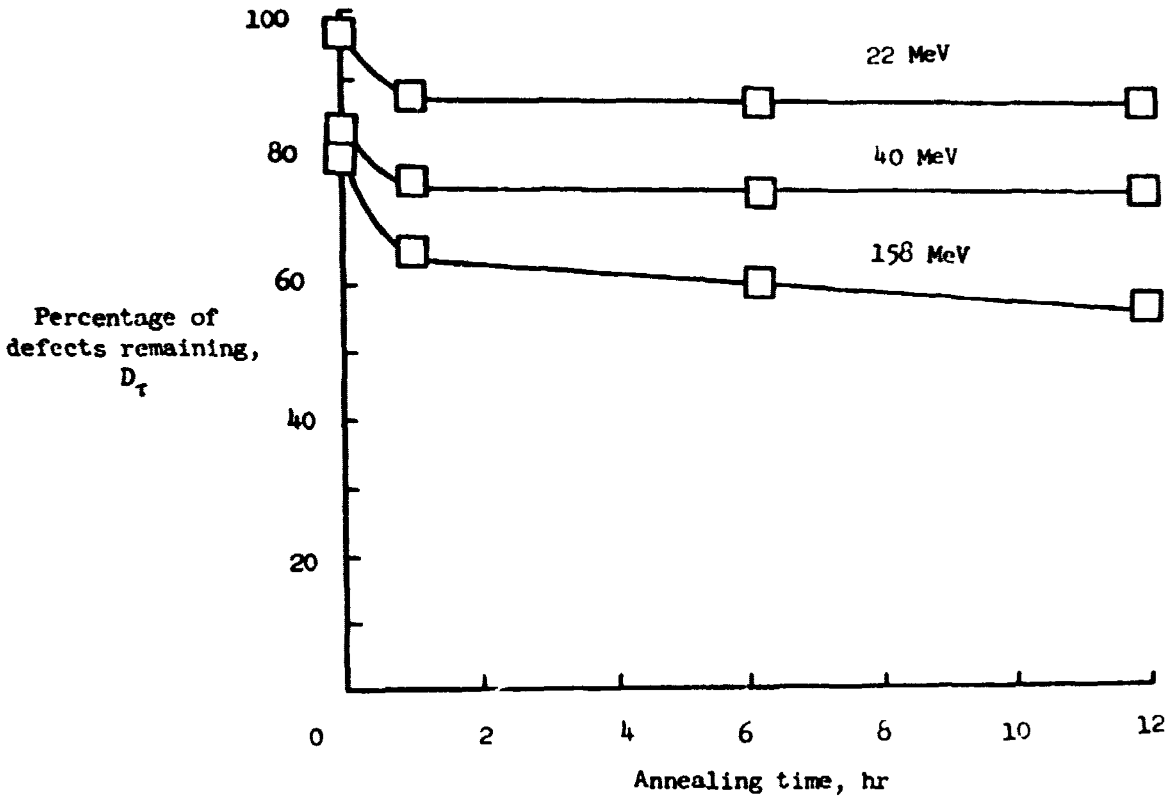

Source: Beatty and Hill (3)

Figure 5. Comparison of 22, 40, and 158 MeV Proton Annealing at 200° for n-Type Silicon Irradiated to a Fluence of $\phi = 1 \times 10^{12}$ Protons/cm^2 (unnormalized)

<u>Faraday, Statler and Tauke</u>

Work at NRL involved 4.6 MeV proton irradiations of 1.5 and 10 ohm-cm N/P Czochralski silicon solar cells. Cell junctions were approximately 0.5 μm deep which is considerably more than is typical of present technology but should have little bearing upon general validity of the results. All anneals were isochronal for 20 minutes in argon. To illustrate the approximate spacial distribution of damage produced by these proton irradiations, Figure 6 shows calculated energy deposition versus depth for 5 MeV protons in silicon.

Figure 7 shows tungsten illumination (2800°K) I-V characteristics of a 10 ohm-cm cell before and after irradiation to 10^{12} protons/cm^2 and after annealing at various temperatures. The 502° characteristic shows close to complete recovery of pre-irradiation performance.

Figure 8 shows recovered maximum power output of 10 ohm-cm cells as a function of annealing temperature for three irradiation fluences. It can be seen that for 10^{10} protons/cm^2 fluence the 500°C anneal does effect complete recovery, but cells exposed to 10^{11} or 10^{12} protons/cm^2 exhibit minor remaining output loss. The shape of the recovery characteristics for these cells suggests that they would have benefited from additional anneal to slightly higher temperature.

ORIGINAL PAGE IS
OF POOR QUALITY

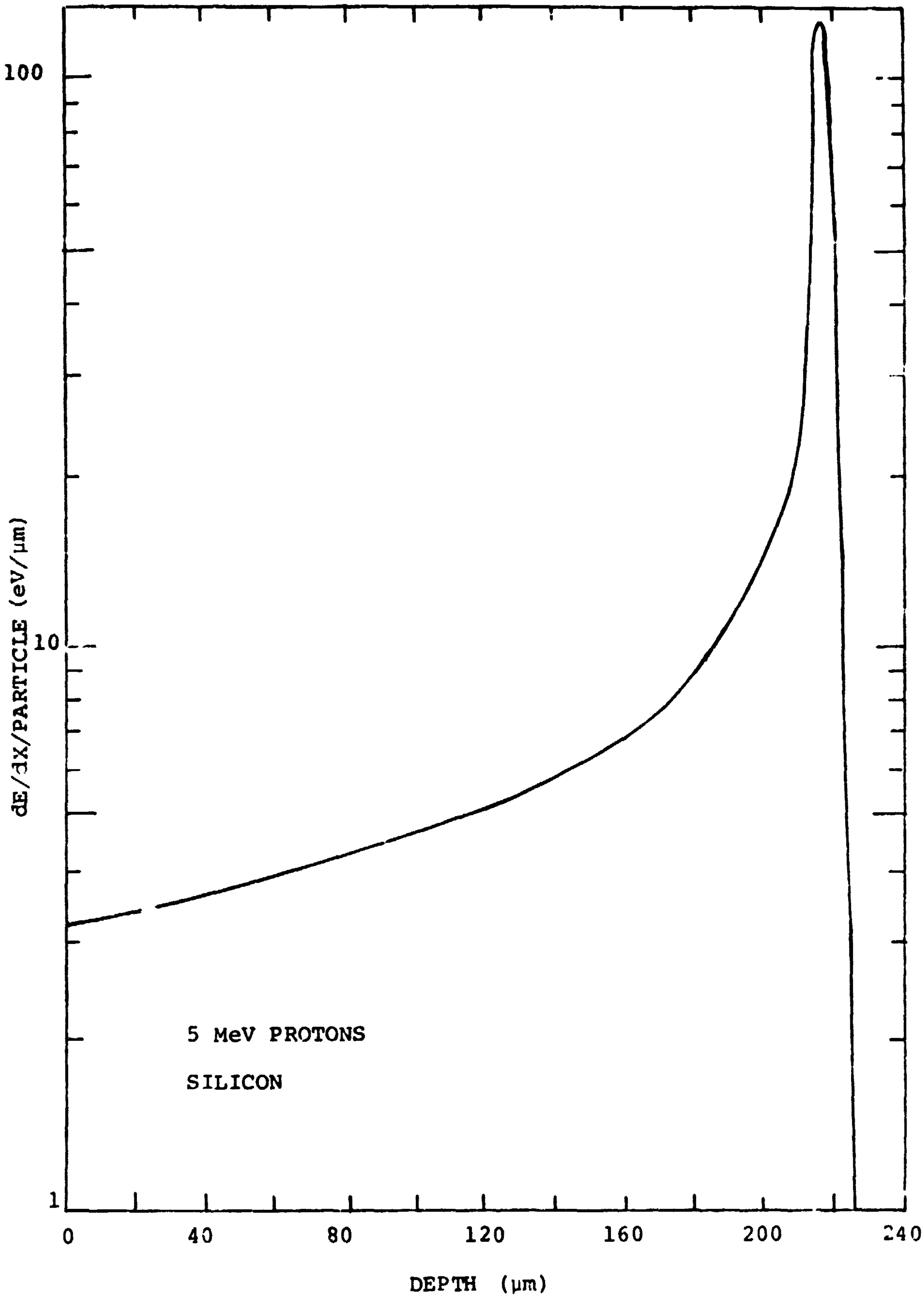

Figure 6. Calculated Depth/Dose Profile for 5 MeV Protons in Silicon

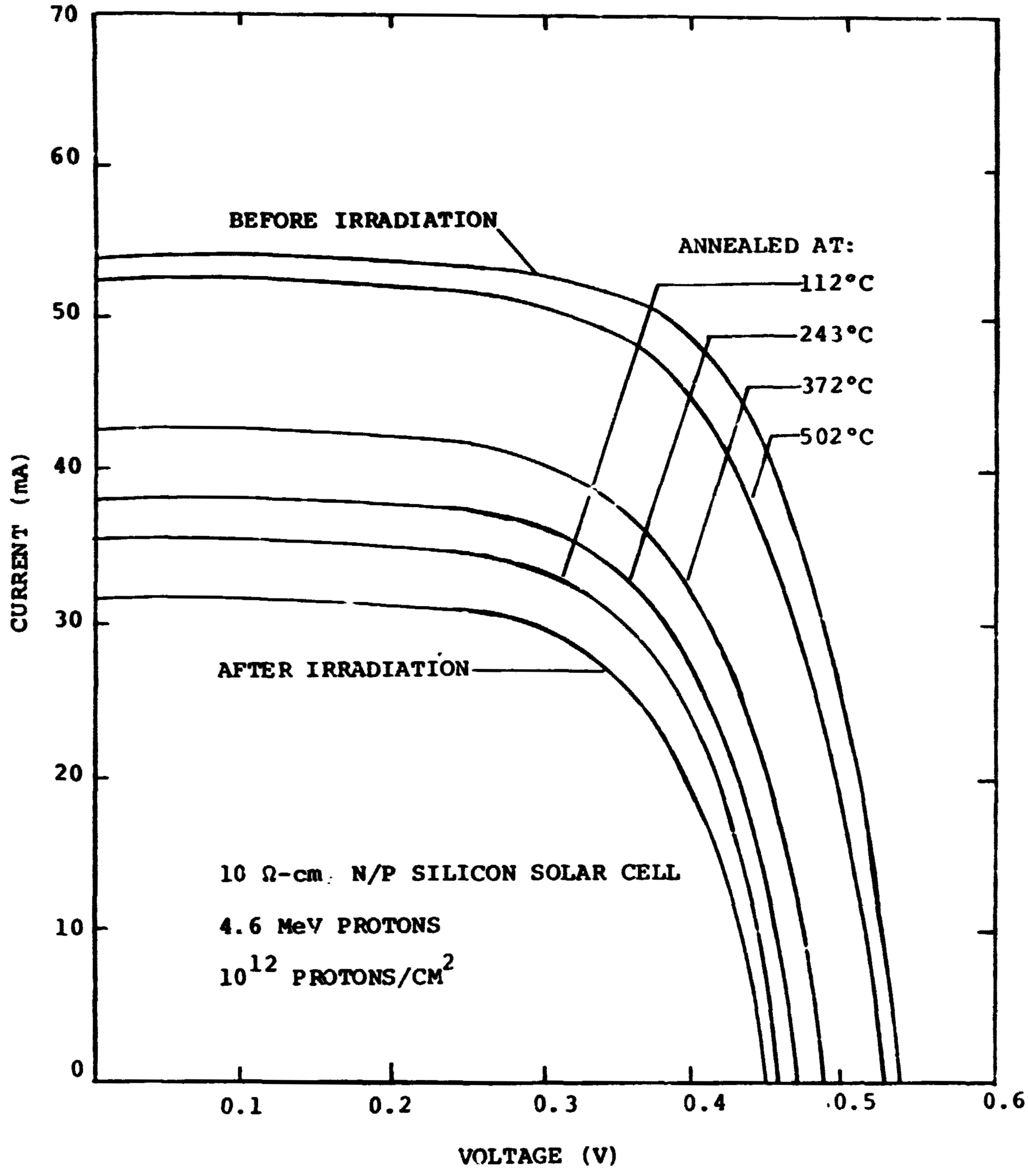

Source: Faraday, Statler and Tauke(5)

Figure 7. I-V Characteristics of Proton Irradiated Cell as Function of Anneal Temperature

ORIGINAL PAGE IS
OF POOR QUALITY

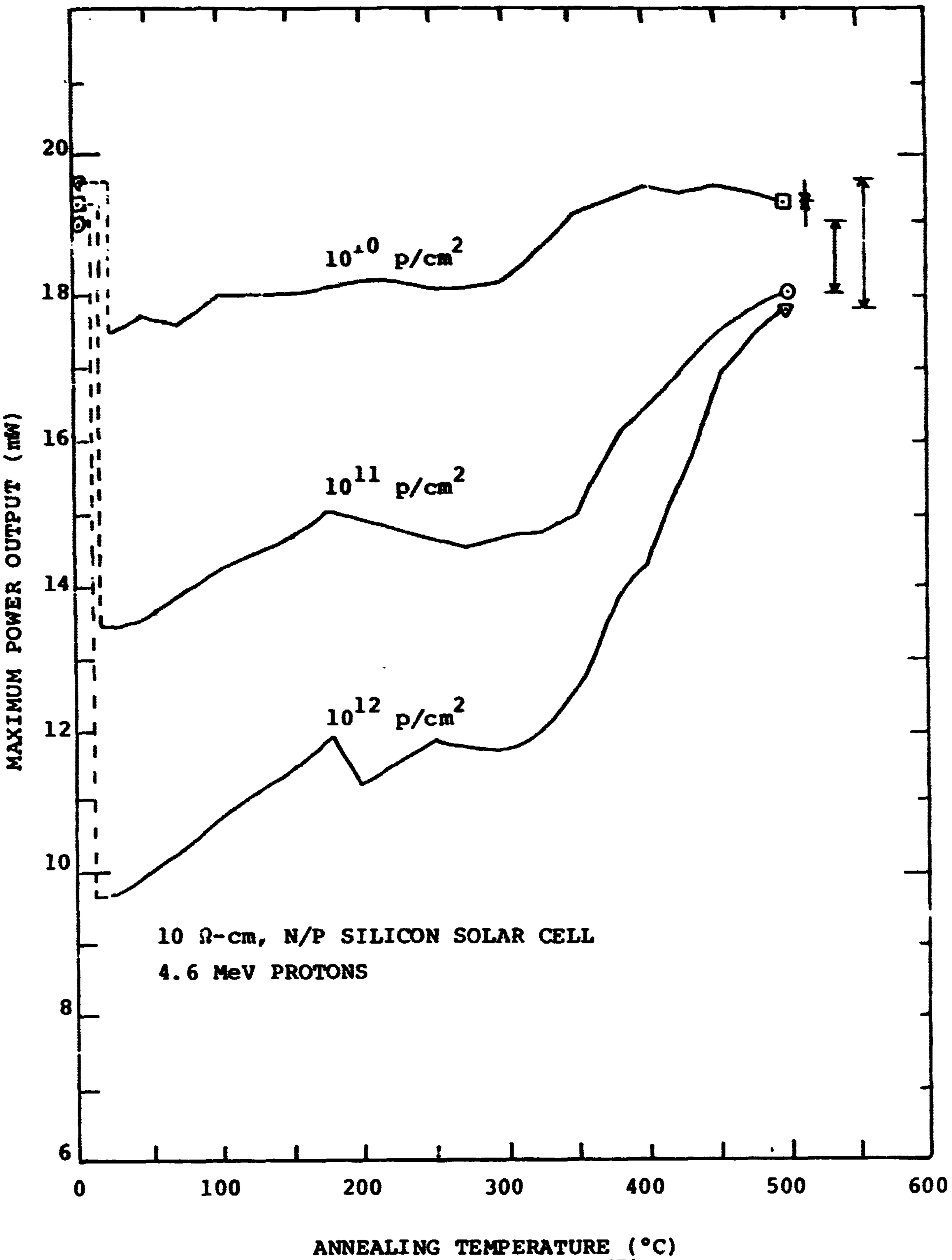

Source: Faraday, Statler and Tauke[5]

Figure 8. Recovered Maximum Power Versus Anneal Temperature as Function of Proton Fluence

An unnormalized percent damage remaining was defined as

$$p\ (I) \equiv \frac{I_o - I_A}{I_o} \times 100$$

where I_o and I_A were short-circuit currents before irradiation and after irradiation and annealing respectively. Figure 9 shows this percent damage remaining as function of annealing temperature for 10 ohm-cm cells exposed to different fluences. Figure 10 compares similar data for 1.5 and 10 ohm-cm cells after 10^{12} proton/cm^2 fluences. It is obvious that a major anneal step occurs at temperature above 300°C and recovery is consistently close to complete after 500°C.

Figure 11 gives the effect of annealing temperature to as high as 600°C on minority carrier diffusion lengths in the proton irradiated cells. NRL considered that this data indicated the hardest damage to anneal is that of high fluences on low resistivity cells. Nevertheless, even under these conditions recovery could be quite effective.

ORIGINAL PAGE IS
OF POOR QUALITY

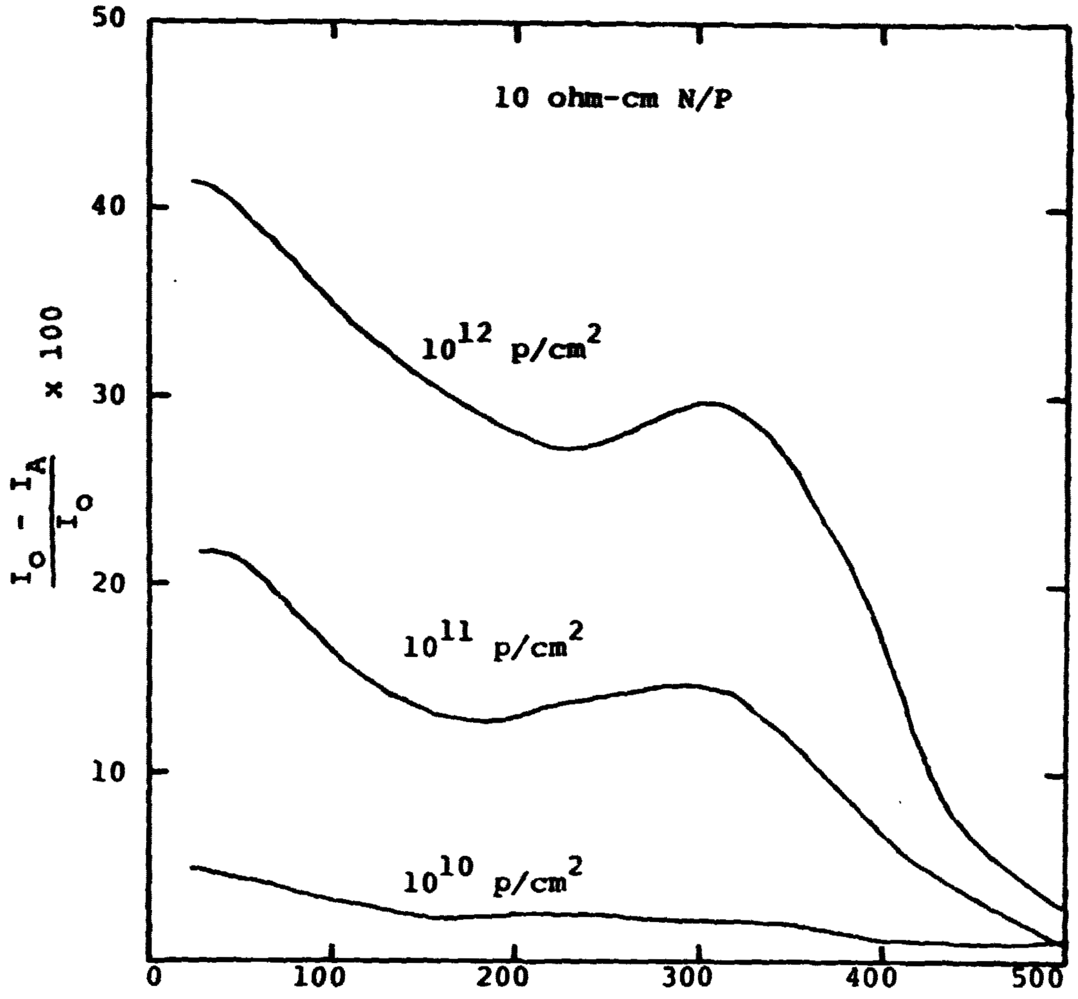

Source: Faraday, Stater and Tauke(5)

Figure 9. Unannealed Fraction of Short Circuit Current Versus Annealing Temperature for 10 Ohm-cm N/P Cells As Functions of 4.6 MeV Proton Fluences

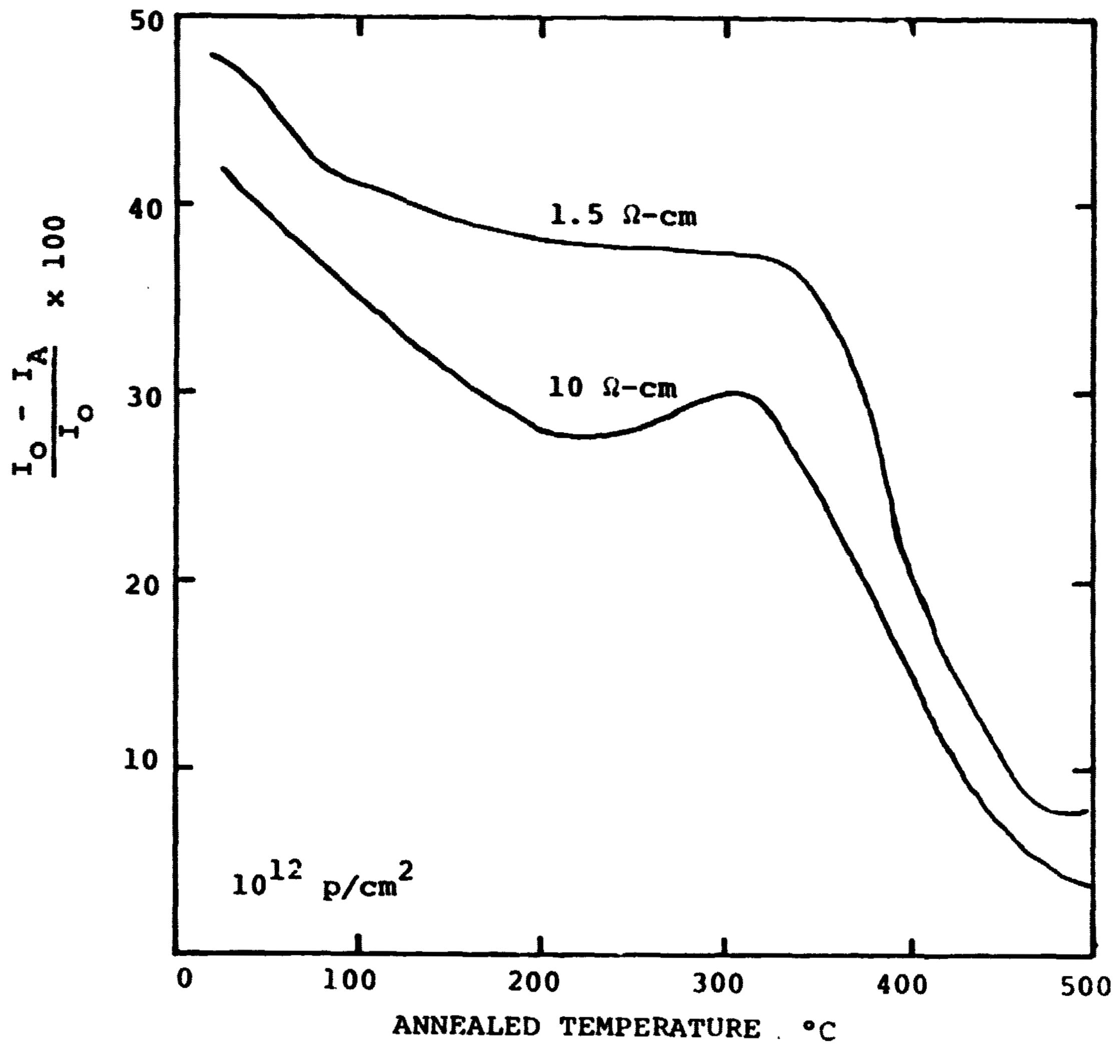

Source: Faraday, Stalter and Tauke[5]

Figure 10. Unannealed Fraction of Short Circuit Current Versus Annealing Temperatures for 1.5 and 10 Ohm-cm N/P Cells Irradiated to 10^{12} p/cm^2

ORIGINAL PAGE IS
OF POOR QUALITY

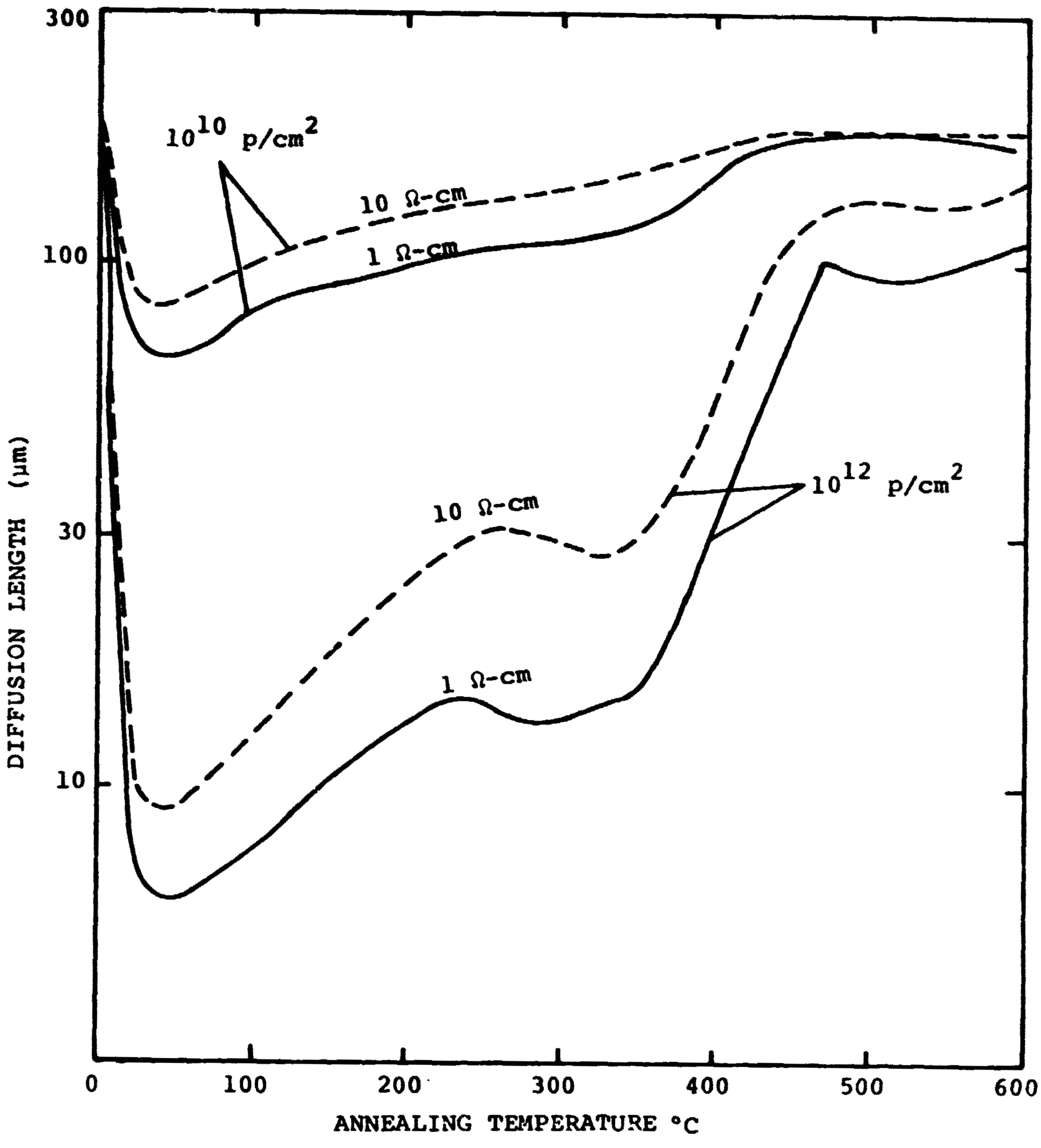

Source: Faraday, Statler and Tauke[5]

Figure 11. Isochronal Annealing of Minority Carrier Diffusion Length in N/P Silicon Solar Cells Following Irradiation by 4.6 MeV Protons

SECTION III

FEASIBILITY STUDIES ON DIRECTED ENERGY ANNEALING OF SILICON SOLAR CELLS

3.1 RATIONALE

The information summarized above shows that it is possible to use thermal annealing to restore performance of a silicon solar cell damaged by proton irradiation. But, is it feasible? It has been shown that temperatures approaching 500°C or even more are required for periods which are probably of the order of minutes. While the solar cell can withstand the environment, the remaining structure of a lightweight array probably cannot. The process involved is essentially an oven anneal and it is difficult to visualize any means to perform the slow exposure without involving the entire array structure.

However the possibility does exist of alternate annealing procedures which would not necessarily subject elements of the array, other than the solar cells, to excessive temperatures. The concept involves the use of directed energy beams to produce temperature transients which could remain primarily localized within the solar cells. As an example of this type of annealing action, Simulation Physics uses a single submicrosecond pulse of relatively low energy electrons to produce the same annealing of ion implant damaged

ORIGINAL PAGE IS
OF POOR QUALITY

layers in silicon as can be achieved in a furnace at 750°C for 30 minutes[6]. The ability to produce satisfactory annealing by a short duration temperature spike results because the temperature achieved is higher than would be used in a furnace but is quenched before any deleterious effects can occur.

3.2 EXPERIMENTAL TESTING

Among the directed energy beam sources which might be considered for annealing of solar cell proton radiation damage are pulsed and scanned lasers, pulsed and scanned electron beams and high intensity photon flashtubes. To experimentally investigate feasibility of directed energy methods, tests were conducted using a scanned DC electron beam and a pulsed Nd:YAG laser.

Solar cells used were assorted high performance types supplied by Boeing. The cells had been irradiated to 5×10^{12} 1 MeV protons/cm^2. Cells did not have protective coverglasses.

DC Electron Beam

Parameters of the scanning DC electron beam selected for solar cell tests were:

Beam diameter:	1.3 cm
Sweep raster:	100 x 1000 Hz
Energy:	60-90 keV
Current:	1 mA
Scan duration:	15 sec

Electron beam energy deposition profiles are shown in Figure 12.

Irradiated solar cells supplied by Boeing were mounted onto aluminum substrates approximately 0.020 inch thick by conductive silver epoxy. The DC electron beam is meant to raise temperature of the entire solar cell. The substrate presented some difficulties with the electron beam heating because heat transfer from the cell to the aluminum heat sink occurred in regions with conductive epoxy but not elsewhere. As a result temperature nonuniformities were produced across the cell area and it was impossible to evaluate local temperatures.

Nd:YAG Laser

Parameters of the neodymium doped yttrium aluminum garnet 1.06 μm pulse mode laser used for testing were:

Beam diameter:	0.3 cm
Pulse width:	10^{-3} sec
pulse energy:	3 joule/pulse

Energy deposition profile for the laser pulse is given in Figure 13. Predicted initial local temperature profile is shown in Figure 14.

ORIGINAL PAGE IS
OF POOR QUALITY

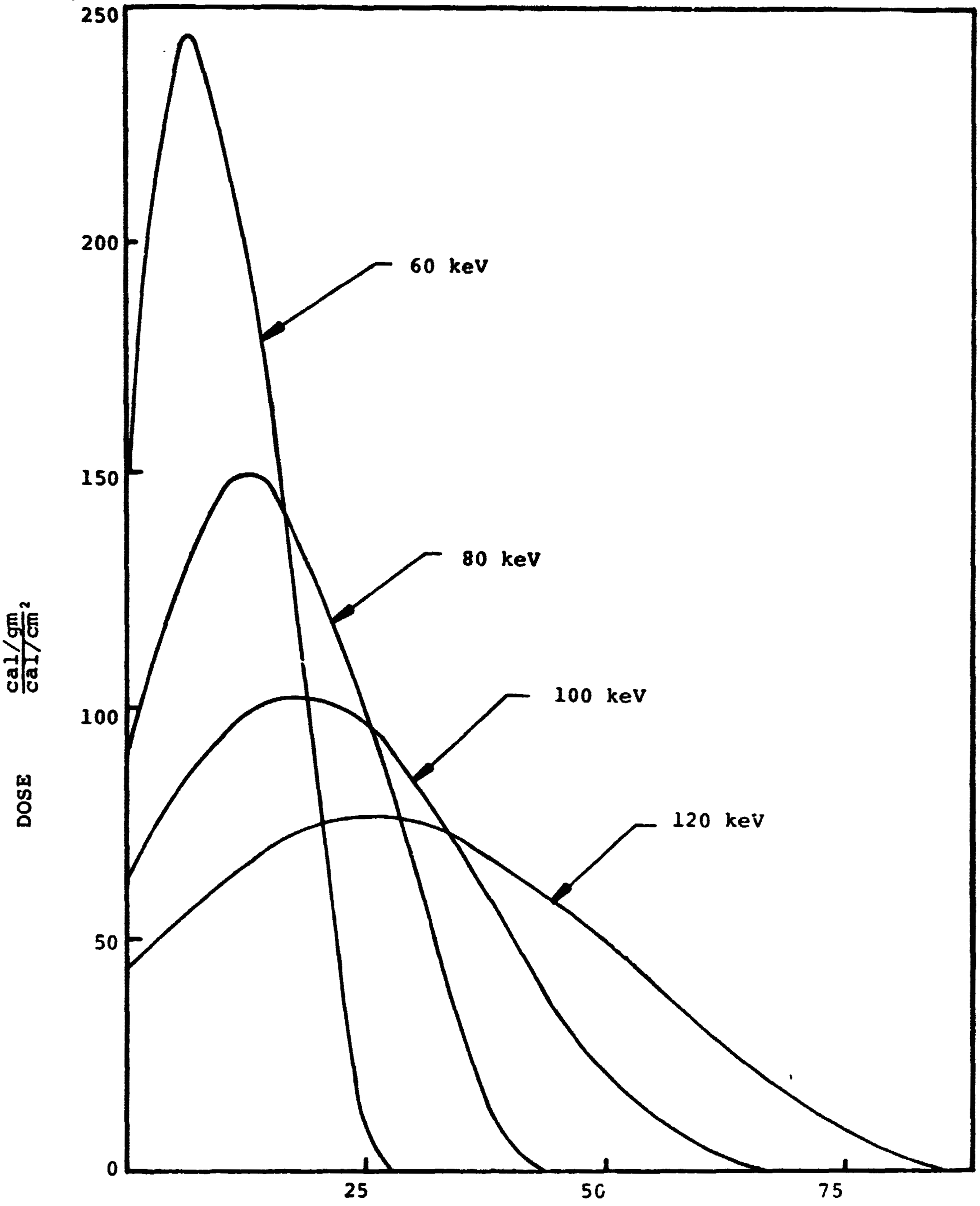

Figure 12 Deposition Profile: Monoenergetic Electron Beams in Silicon

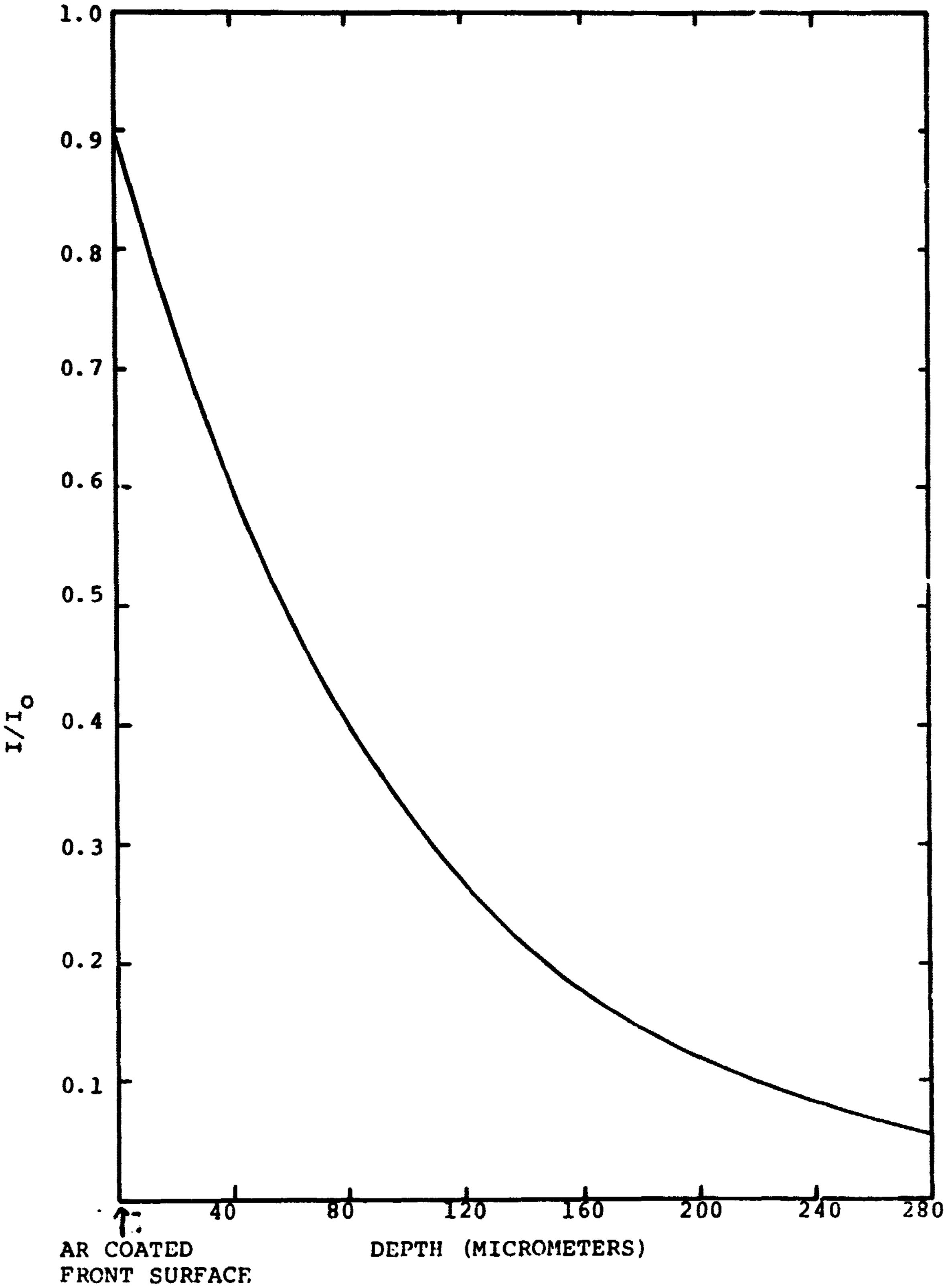

Figure 13. Deposition Profile for 1.06 μm Nd:YAG Laser Into AR Coated Silicon

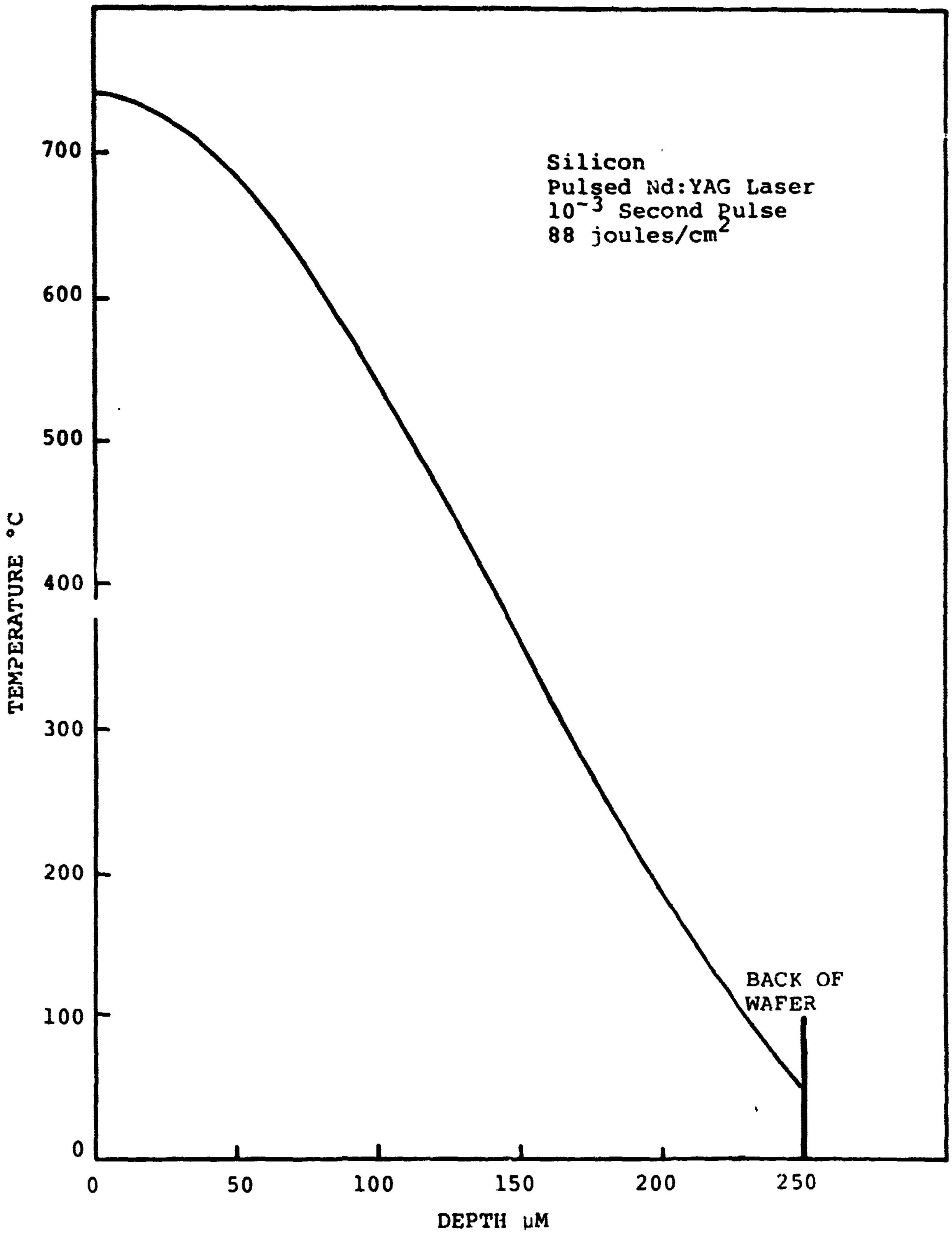

Figure 14. Predicted Temperature Profile in Silicon at Beam Center Following Laser Pulse

Because of the pulsed mode operation and reflection from the back conduct, mounting of the cells by conductive epoxy had relatively little influence on temperature uniformity. Short pulses produce essentially local transient heating with the entire cell eventually to be annealed as the laser pulse is stepped across the surface. Stepping distance for the step and pulse sequence was 0.13 cm on some samples and 0.06 cm on others. Although laser beam diameter was 0.3 cm, nonuniformity of the spot was such that even with the narrow step spacings not all of the cell surface was annealed and the annealed area pattern was visible on surfaces after processing. Power density level of the laser was selected at a level just below that found to produce mechanical damaqe to the silicon.

Boeing provided initial and post proton irradiation Air Mass Zero I-V characteristics on the test cells. Simulation Physics repeated AMO measurements prior to and following anneal. Measurements were made using a Spectrosun X-25 MkII AMO simulator and 25°C test block.

3.3 DIRECTED ENERGY ANNEAL TEST RESULTS

Significant recovery of cell performance was accomplished using both the scanned electron beam and pulsed laser. Table I summarizes test cell data. Figures 15 through 21 present

ORIGINAL PAGE IS
OF POOR QUALITY

Table I

Summary of Electron and Laser Beam Annealing of Proton Irradiated Solar Cells

Anneal	Cell No.	Cell Type	Initial			After 2×10^{15} 1 MeV Protons			After Beam Anneal			% Recovered		
			V_{oc}	I_{sc}	P_{max}	V_{oc}	I_{sc}	P_{max}	V_{oc}	I_{sc}	P_{max}	V_{oc}	I_{sc}	P_{max}
Pulsed Nd:YAG Laser	8E	Violet	599	161.5	75.8	482	87.6	30.5	524	101	39.8	36	18	21
	9C	Hybrid B	581	147.1	66.1	458	78	24.7	508	96	32.8	41	26	20
	12E	Violet	595	159.8	73.0	499	94.2	34.4	550	124	49.8	53	45	40
	55	Violet Control	602	146	68.2	No Irradiation			602	147	68.2	0	0	0
D.C. Electron Beam	8C	Hybrid B	575	146	64.6	491	92.4	33.2	532	117.5	46.9	49	47	44
	9G	Conventional	506	144	51.2	443	94	24.8	505	120	39.4	98	52	54
	67	Violet Control	605	144	66.7	No Irradiation			605	136	62.3	0	-6.0	-7.0

NOTES: All data AMO
Initial & After 2×10^{15} 1 MeV Protons cm^{-2} - Boeing 30°C
After Anneal - SPI 25°C

AMO I-V characteristics of the test cells of Table I and include:

(i) Initial (30°C)

(ii) After 5×10^{12} protons/cm^2 (30°C)

(iii) After pulsed laser or electron beam anneal (25°C)

Figure 18 shows the effect of laser anneal conditions on a control cell without proton irradiation damage. No performance degradation resulted. Figure 21 shows the effect of the electron beam on a nonirradiated control cell. In this case a decrease in short circuit current resulted which is attributed to a change in the AR coating rather than to electron induced damage of the silicon lattice or cell junction. It is expected that AR coating effects could be avoided by variation of the beam parameters.

It is important to again point out that, because the Nd:YAG laser beam spot was nonsymmetrical, the stepping sequence did not cover the total cell area. More cell recovery would have occurred under the same test conditions if the entire cell surface had been processed.

The directed energy anneal feasibility test results are considered to be extremely promising. The short time available and limited scope of this effort prevented any possibility of analytically and/or experimentally optimizing

ORIGINAL PAGE IS
OF POOR QUALITY

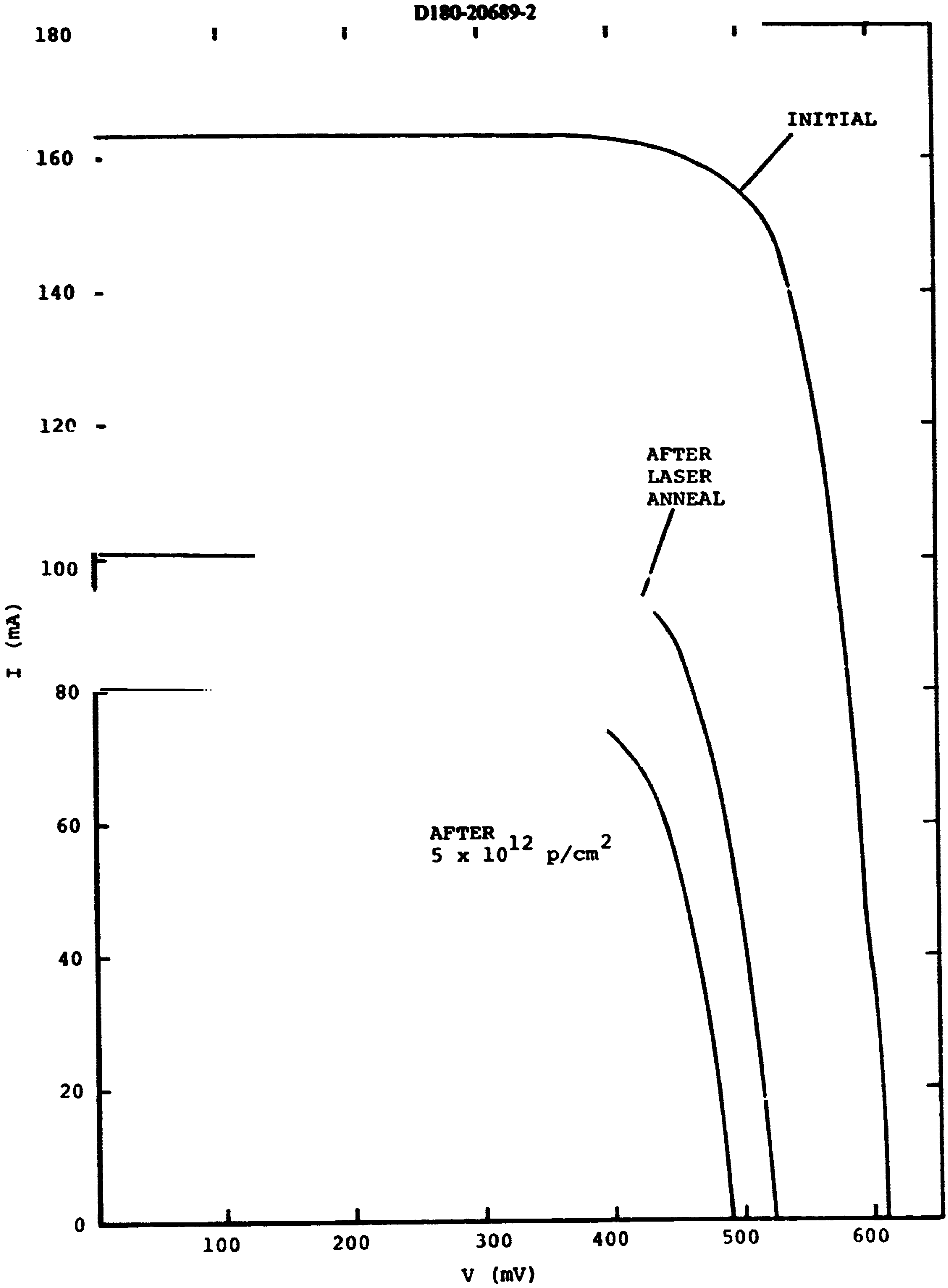

Figure 15. The Effect of Pulsed Laser Anneal on Violet Cell 8E

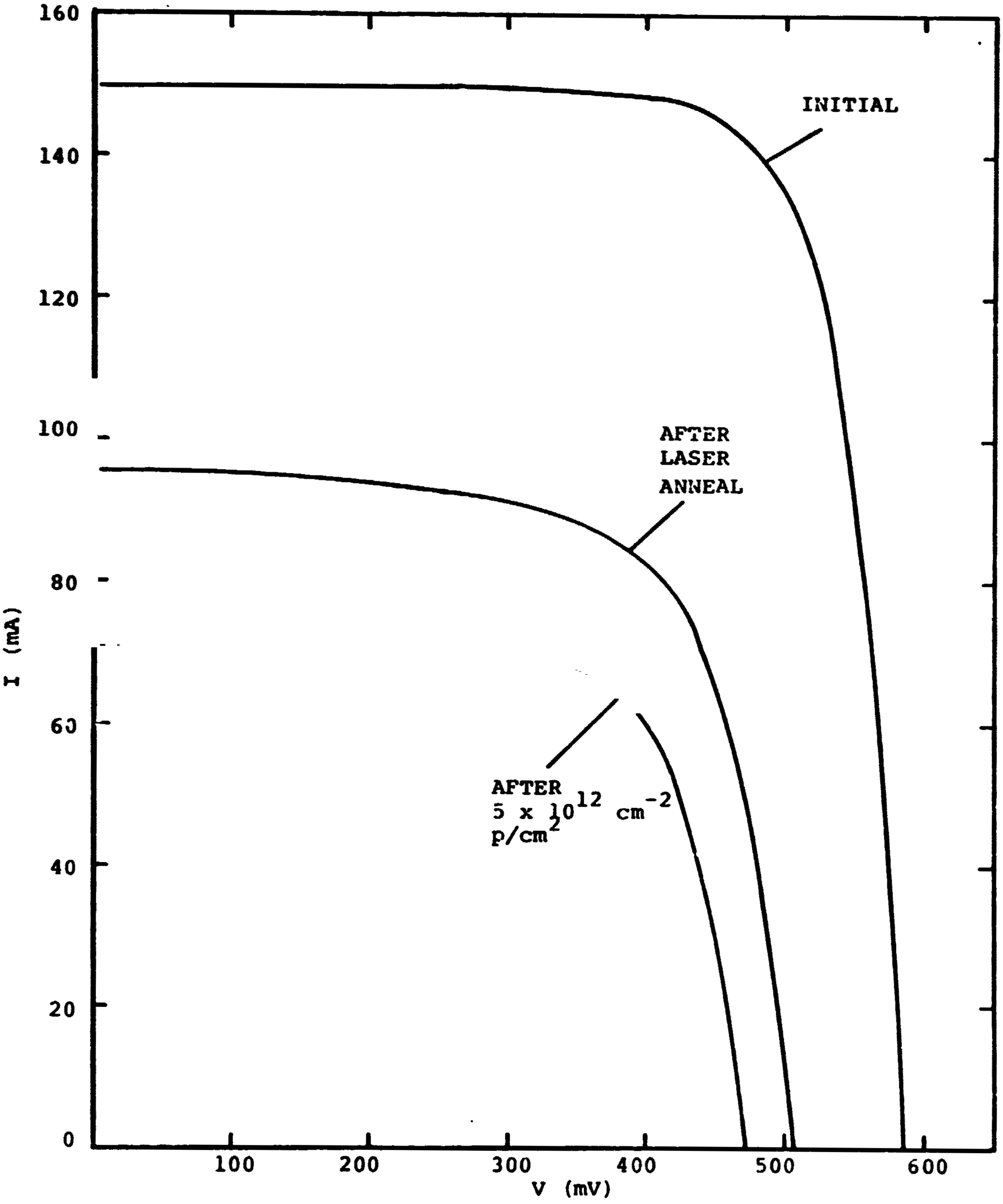

Figure 16. The Effect of Pulsed Laser Anneal on Hybrid N/P Cell 9C

ORIGINAL PAGE IS
OF POOR QUALITY

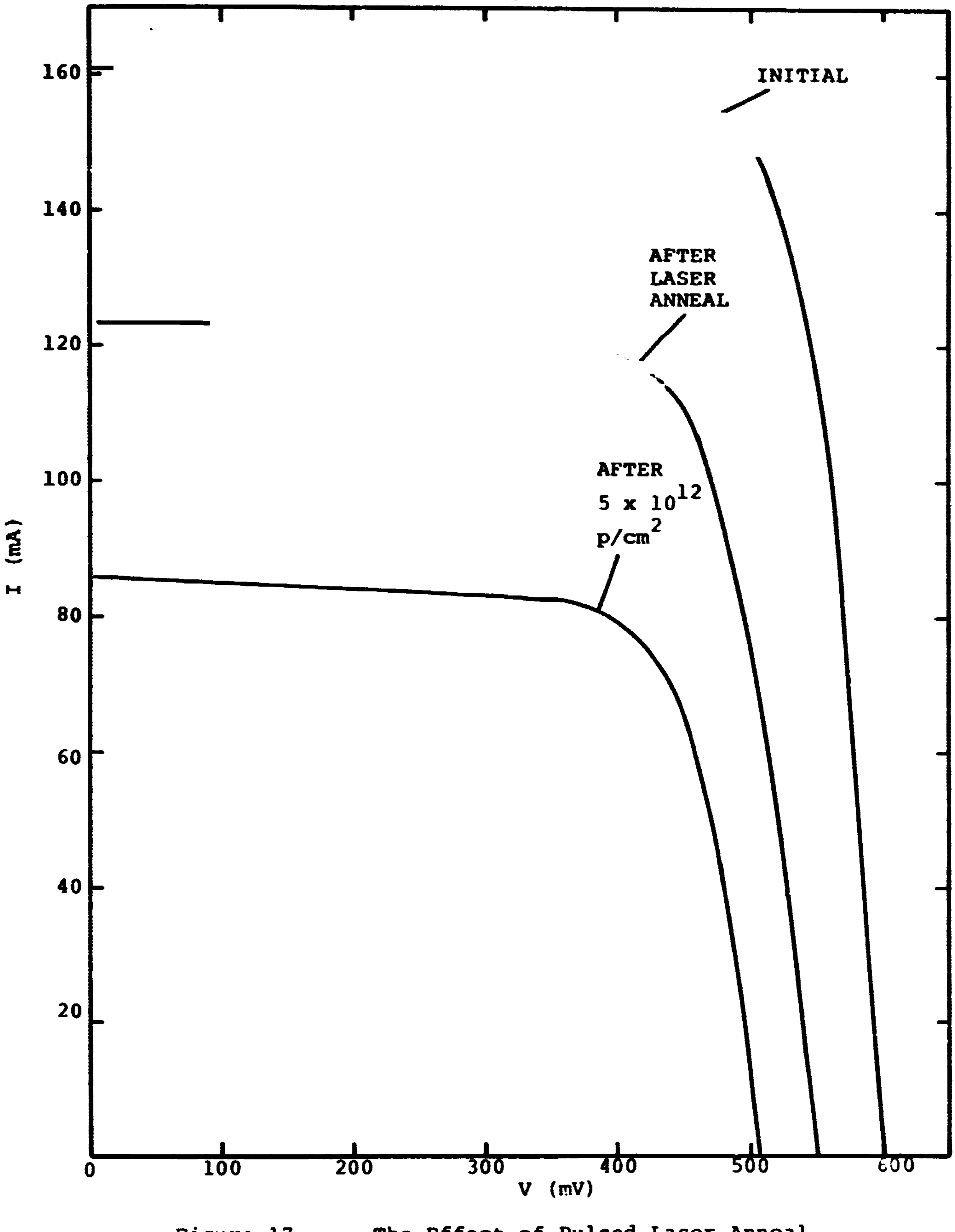

Figure 17. The Effect of Pulsed Laser Anneal on Violet Cell 12E

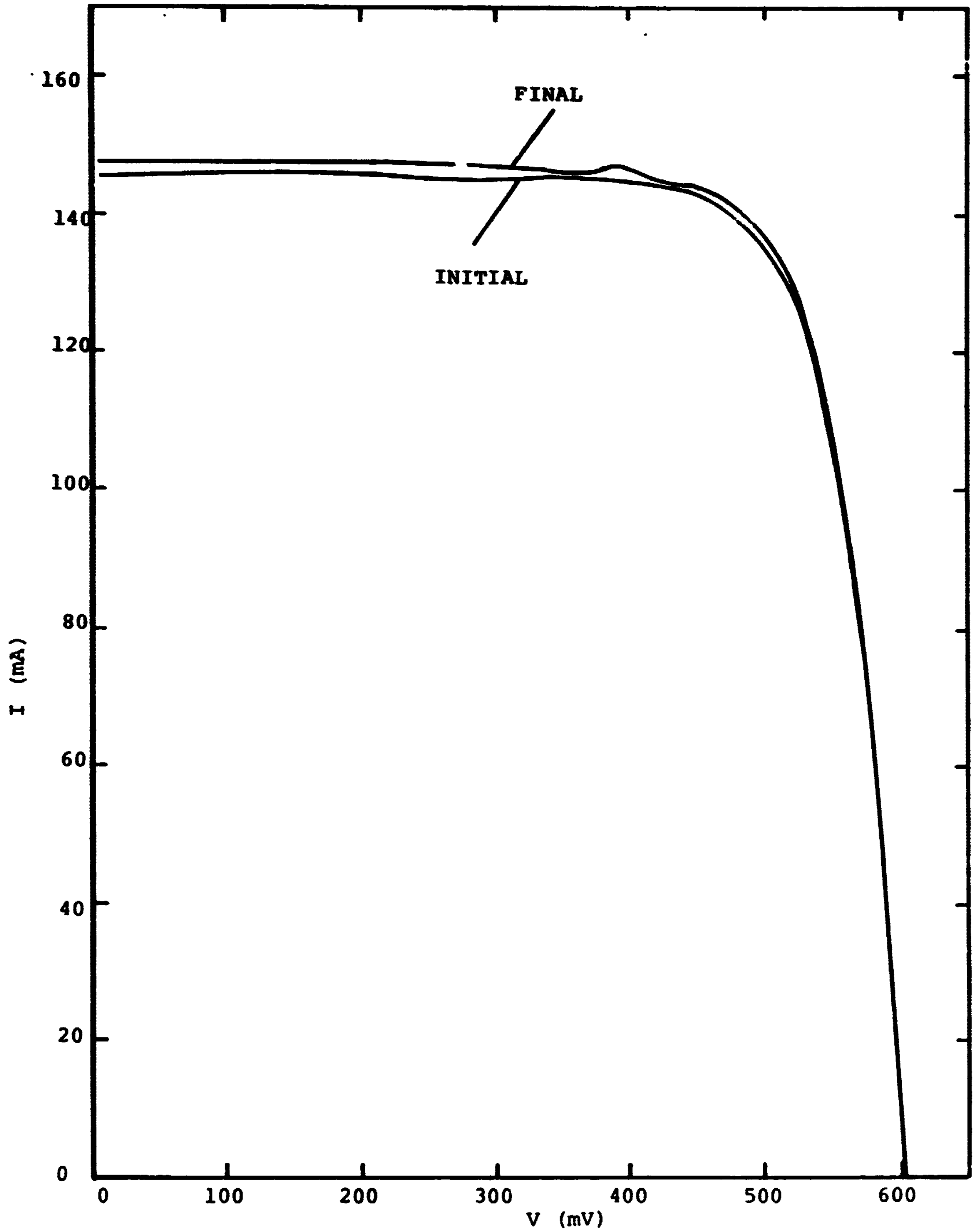

ORIGINAL PAGE IS OF POOR QUALITY

Figure 18. The Effect of Pulsed Nd:YAG Laser on Unirradiated Violet Control Cell

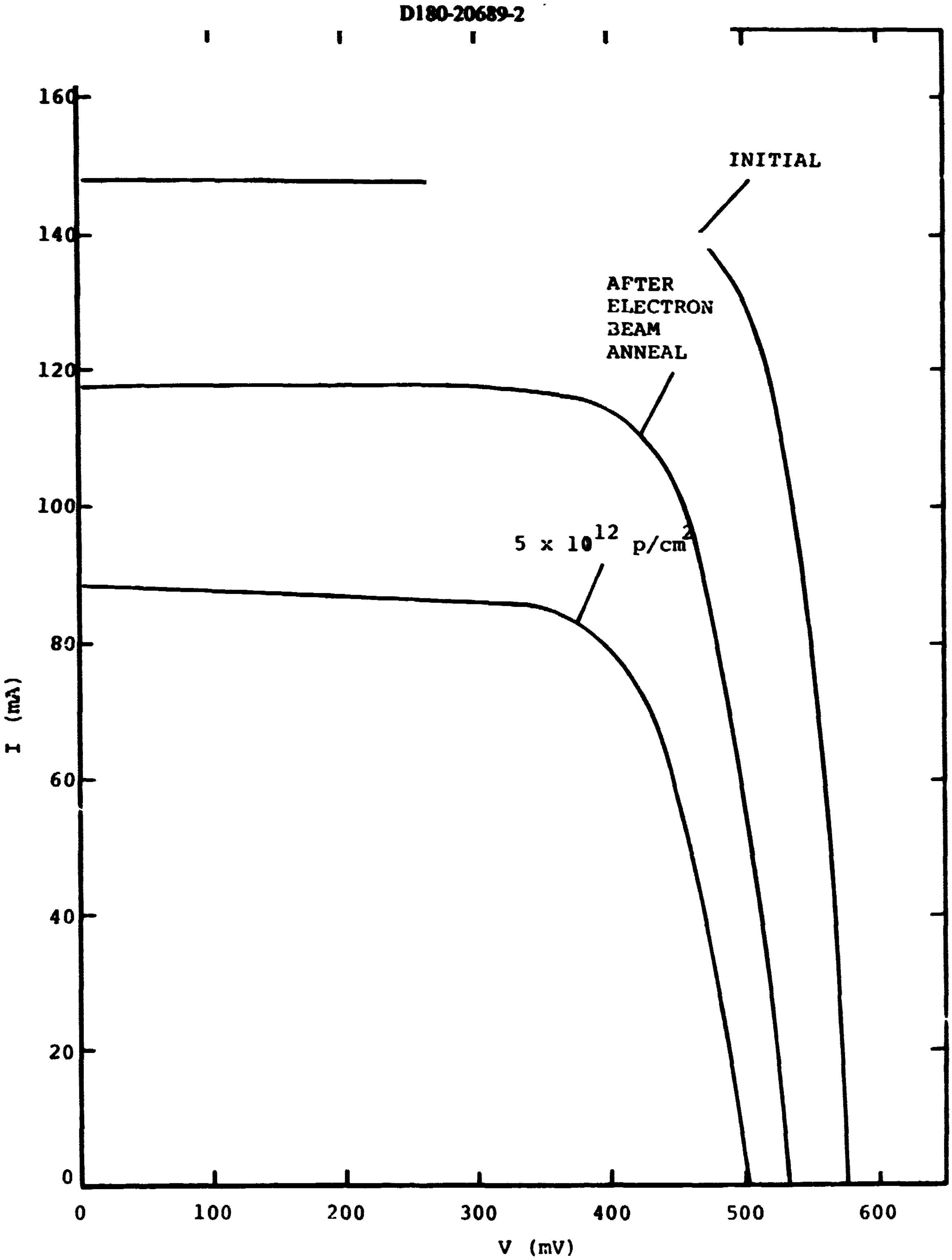

Figure 19. The Effect of DC Electron Beam Anneal on Hybrid N/P Cell 8C

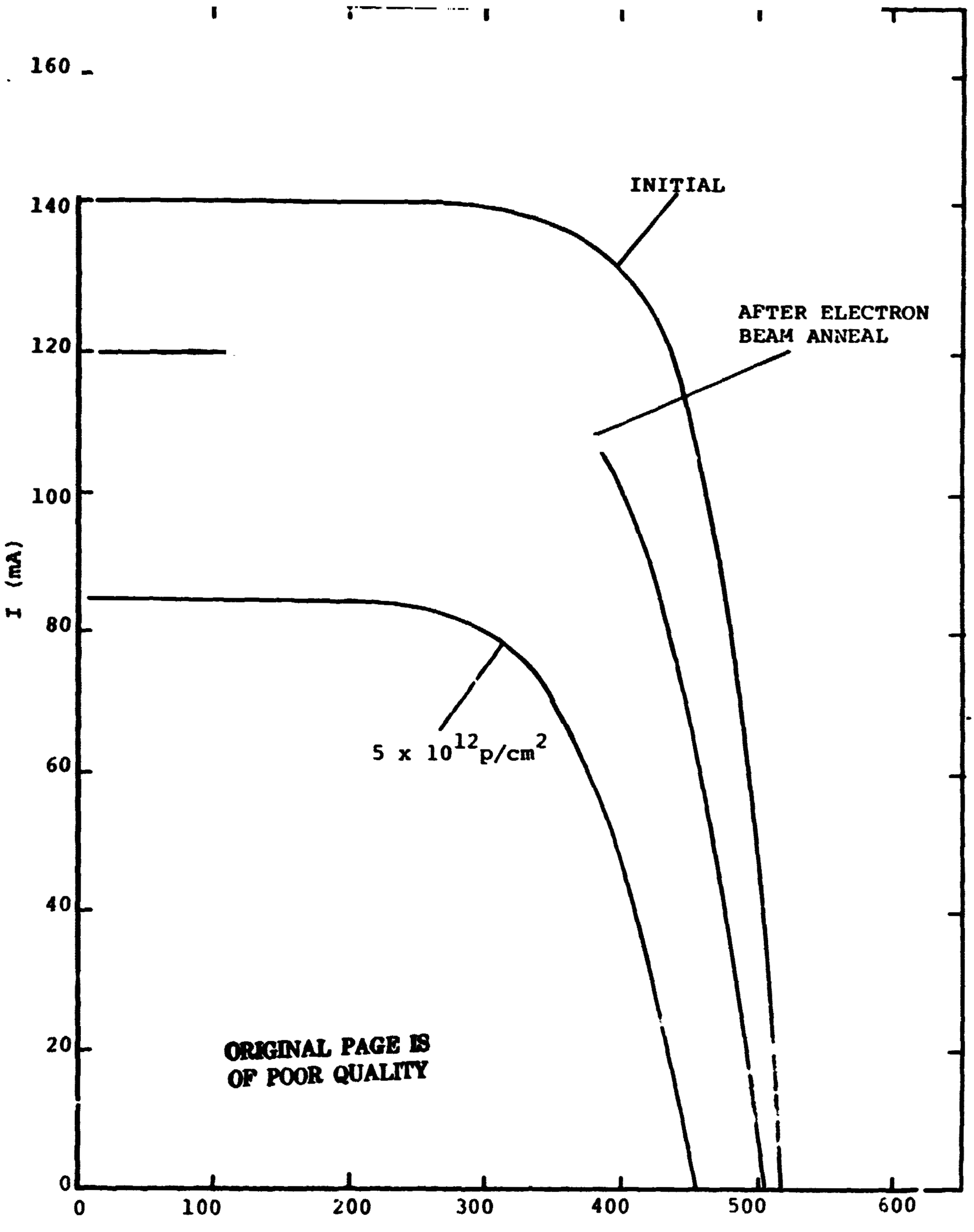

Figure 20. The Effect of DC Electron Beam Anneal on Conventional N/P Cell 9G

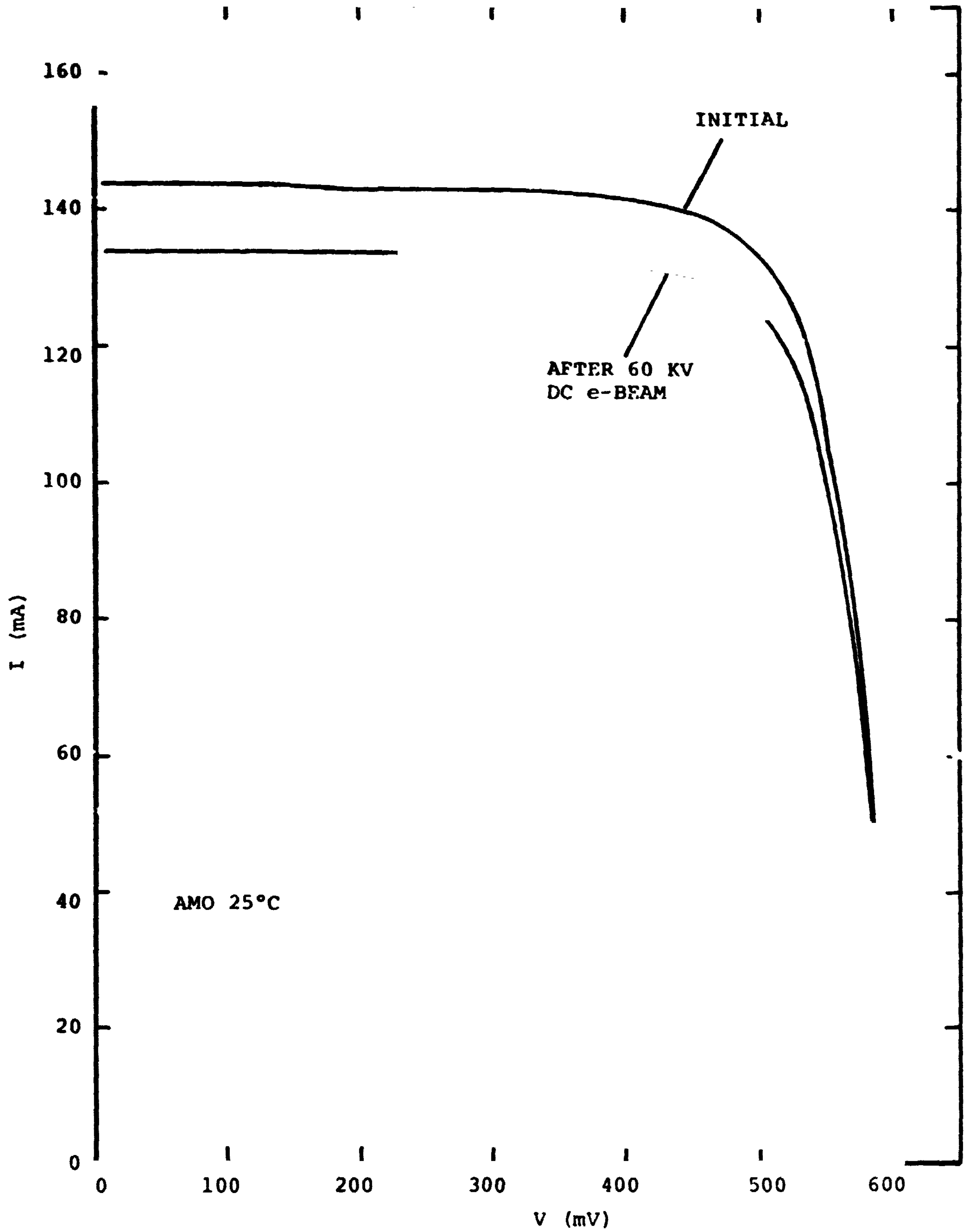

Figure 21. The Effect of DC Electron Beam on Unirradiated Violet Control Cell

process conditions. Test parameters had to be selected almost arbitrarily using immediately available facilities. Even so, substantial annealing was achieved by both directed energy methods.

The results suggest that directed energy techniques and hardware can be developed to produce highly effective short duration annealing of proton irradiated solar cells mounted to an array structure which may be unable to withstand a conventional thermal anneal environment. Such capability could have major impact upon planning of the Solar Power Satellite.

ORIGINAL PAGE IS
OF POOR QUALITY

REFERENCES

(1) Anspaugh, B. E. and Carter, J. R.,"Proton Irradiation of Conventional and Lithium Solar Cells: 11-37 MeV", Record of the Tenth Photovoltaic Specialists Conference, P 366, (November 1973).

(2) Beatty, M. E., and Hill, G. F., "Annealing of High Energy Proton Damage in Silicon", Record of the Sixth Photovoltaic Specialists Conference, Vol. III, IEEE, p. 35, (March 1967).

(3) Beatty, M. E. and Hill, G. F., "Annealing of 22, 40 and 158 MeV Proton Damage in n- and p-Type Silicon", NASA TN D-5119 (April 1969).

(4) Faraday, B. J., Statler, R. L. and Tauke, R. V., "Thermal Annealing of Proton-Irradiated Silicon Solar Cell", Record of the Sixth Photovoltaic Specialists Conference, Vol. III, IEEE, P. 15 (March 1967).

(5) Faraday, B. J. Statler, R. L. and Tauke, R. V., "Thermal Annealing of Proton-Irradiated Silicon Solar Cells", Proc. of IEEE, 56, No. 1, P. 31 (January 1968).

(6) Kirkpatrick, A. R., Minnucci, J. A. and Shaughnessy, T. S., "Silicon Solar Cells by Ion Implantation and Pulse Energy Processing", Record of the Twelfth Photovoltaic Specialists Conference (November 1976).

3.2.6 Reflector Analysis

A detailed analysis of reflector performance was conducted in order to evaluate the performance benefits realizable from the concentration ratio 2 reference SPS configuration. This section presents the results of this analysis. The individual effects presented herein were jointly numerically integrated in order to obtain the reflector performance data described in Section 3.2.1.

Reflectance Versus Specularity: The data shown in Figure 3.2-55 were obtained in tests by The Boeing Engineering and Construction Division in conjunction with an ERDA Contract for ground solar power. It is clear that to obtain high reflectance a measure of non-specularity (beam spread) must be accepted.

Simulated Solar Reflection from Aluminized Film: Figure 3.2-56 illustrates the requirement for biaxially tensioning the reflectors if maximum performance is to be achieved. This relationship appears to be a result of the microfinish of the Kapton substrate.

Reflectance Versus Incidence and Wavelength: Figure 3.2-57 shows that for the sun's circularly polarized light (R_{AW}) the reflectance is reduced with increased incidence until very shallow grazing angles are reached. This change in reflectance is a function of wavelength with the predominant rates of change occurring at approximately 800 millimicrons (mμ).

Reflectance Loss Versus Wavelength at 60° Incidence: Figure 3.2-58 summarizes the losses predicted with previous data for the CR=2 reflector configuration at 60° incidence.

Reflectance Versus Wavelength: The reference in Figure 3.2-59 is for an aluminized optical flat and demonstrates the characteristic loss in reflectance at .8 μm wavelength which is inherent to aluminum. An extrapolation of our aluminized Kapton test data to all wavelengths is also shown in Figure 3.2-59 by the dashed line and the lower line is the net reflectance after considering the losses due to the incidence angle.

Solar Cell Spectral Response: The solar cell spectral response characteristics shown in Figure 3.2-60 were used together with the data from the previous chart to establish an integrated reflectance value for the reflectors at beginning of life of approximately 85%.

Reflector Radiation Degradation: The chief cause of reflector degradation will be the radiation environment. Tests conducted by Boeing During the Project Able investigations provide a sketchy data base upon which the degradation forecast of Figure 3.2-61 is based.

ORIGINAL PAGE IS
OF POOR QUALITY

SPS-277

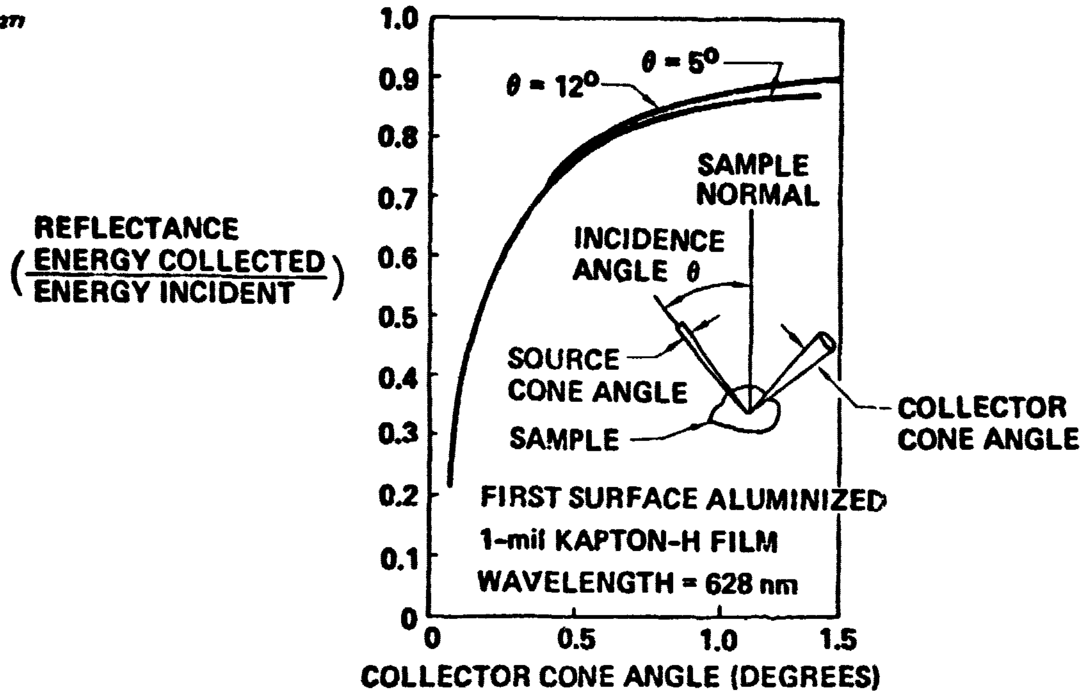

Figure 3.2-55 Reflectance Versus Specularity

SPS-276

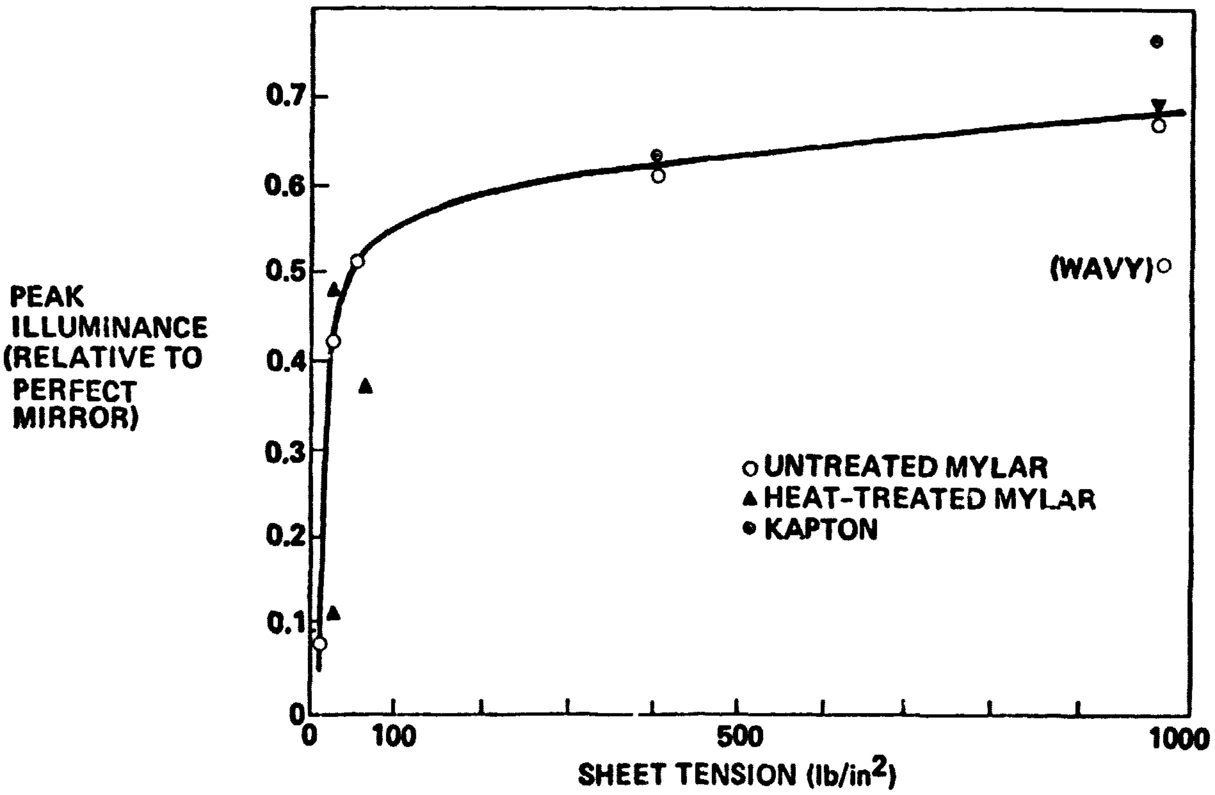

Figure 3.2-56 Simulated Solar Reflection From Aluminized Film

SPS-274

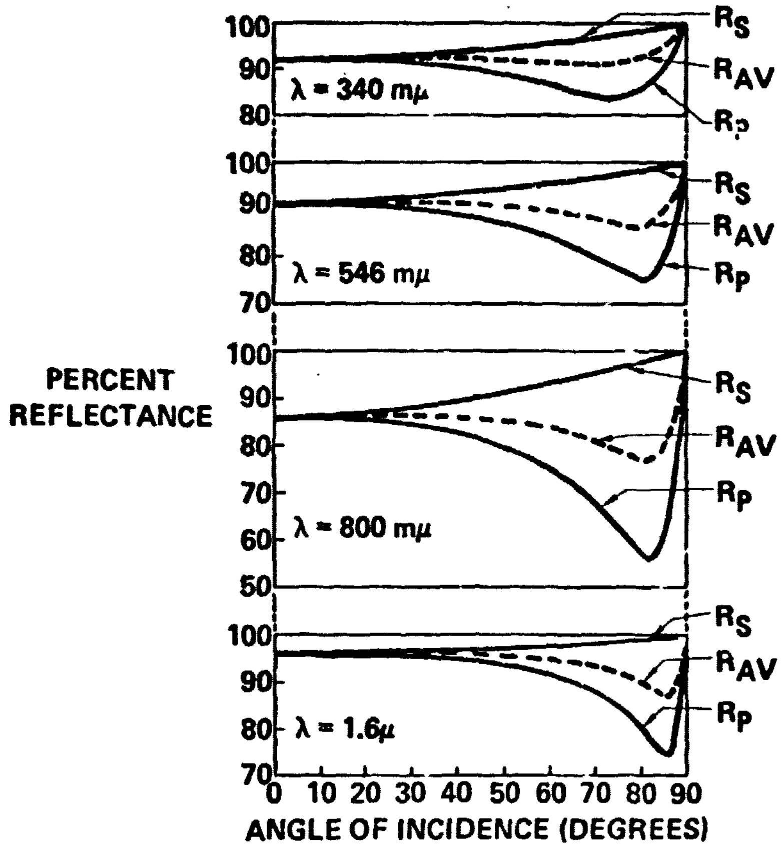

SPS-275

Figure 3.2-57 Reflectance Versus Incidence at Four Wavelengths

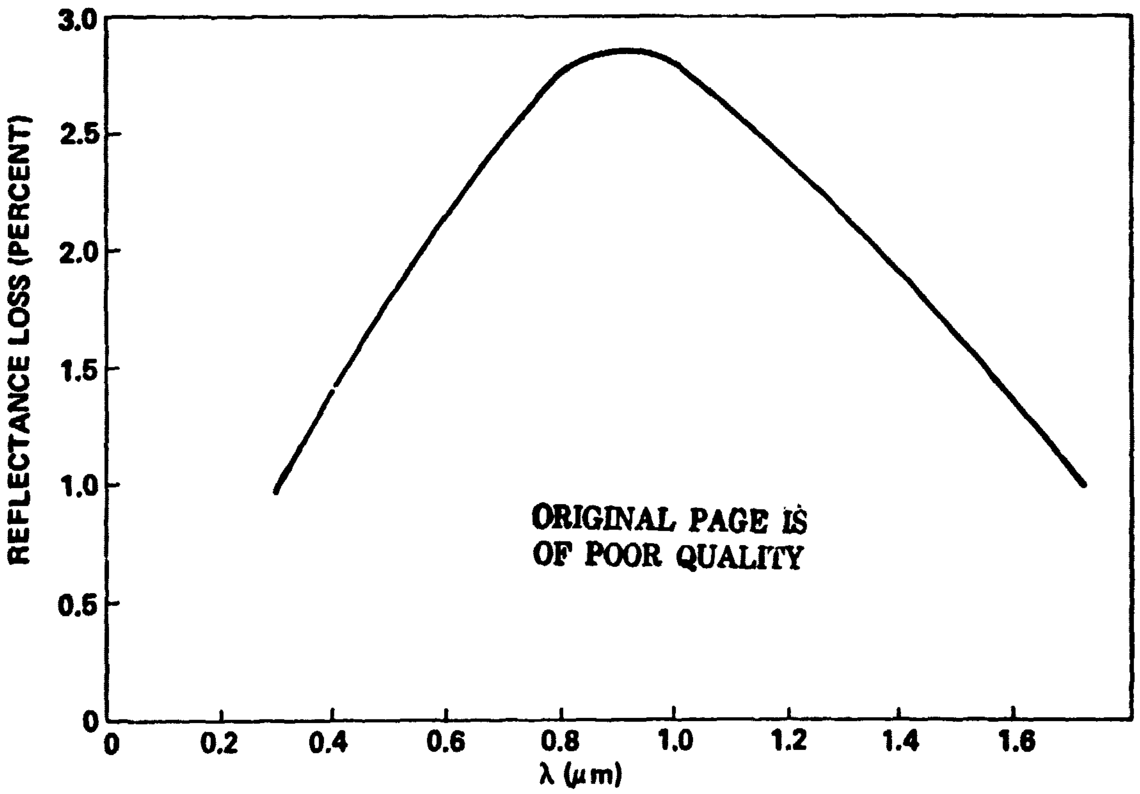

Figure 3.2-58 Reflectance Loss Versus Wavelength at 60° Incidence

SPS-273

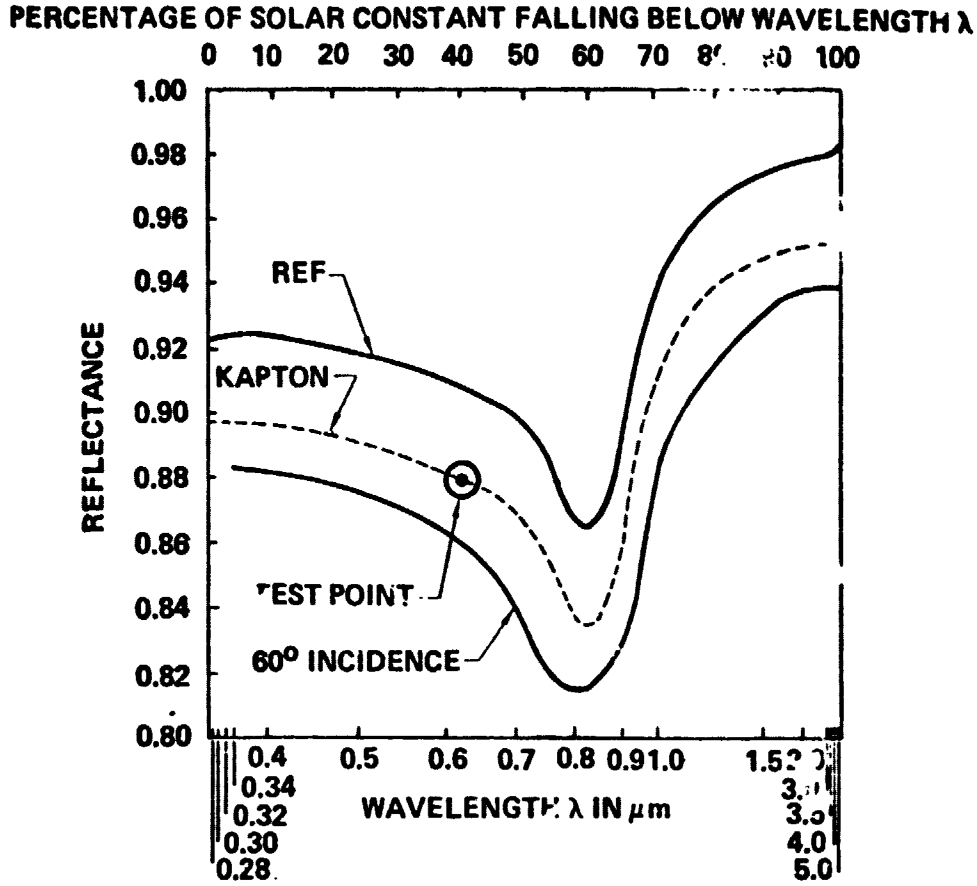

Figure 3.2-59 Reflectance Versus Wavelength

SPS-272

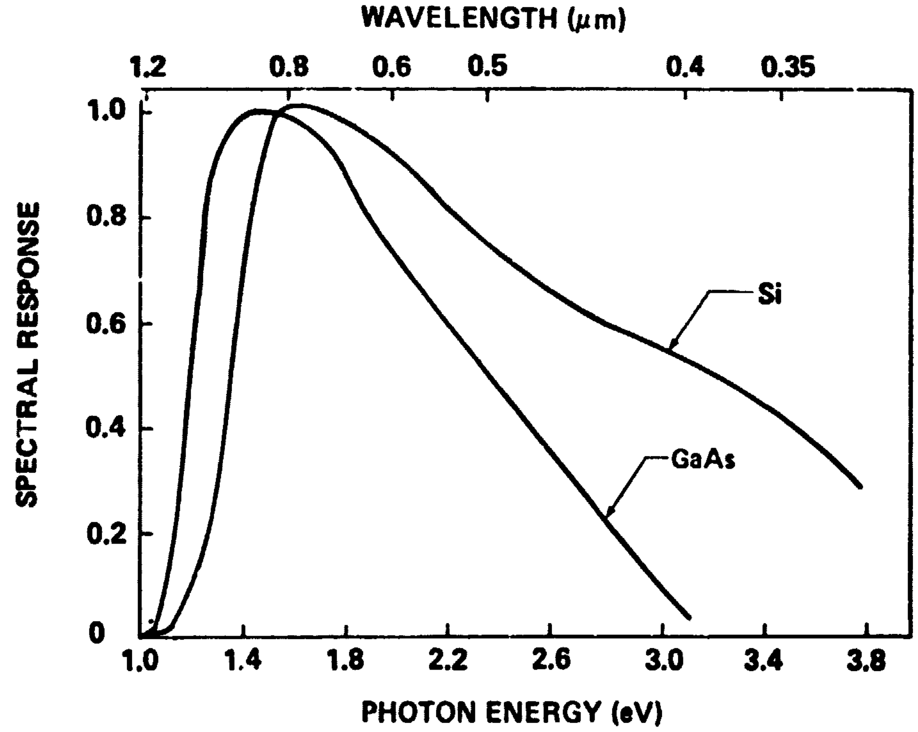

Figure 3.2-60 Solar Cell Spectral Response

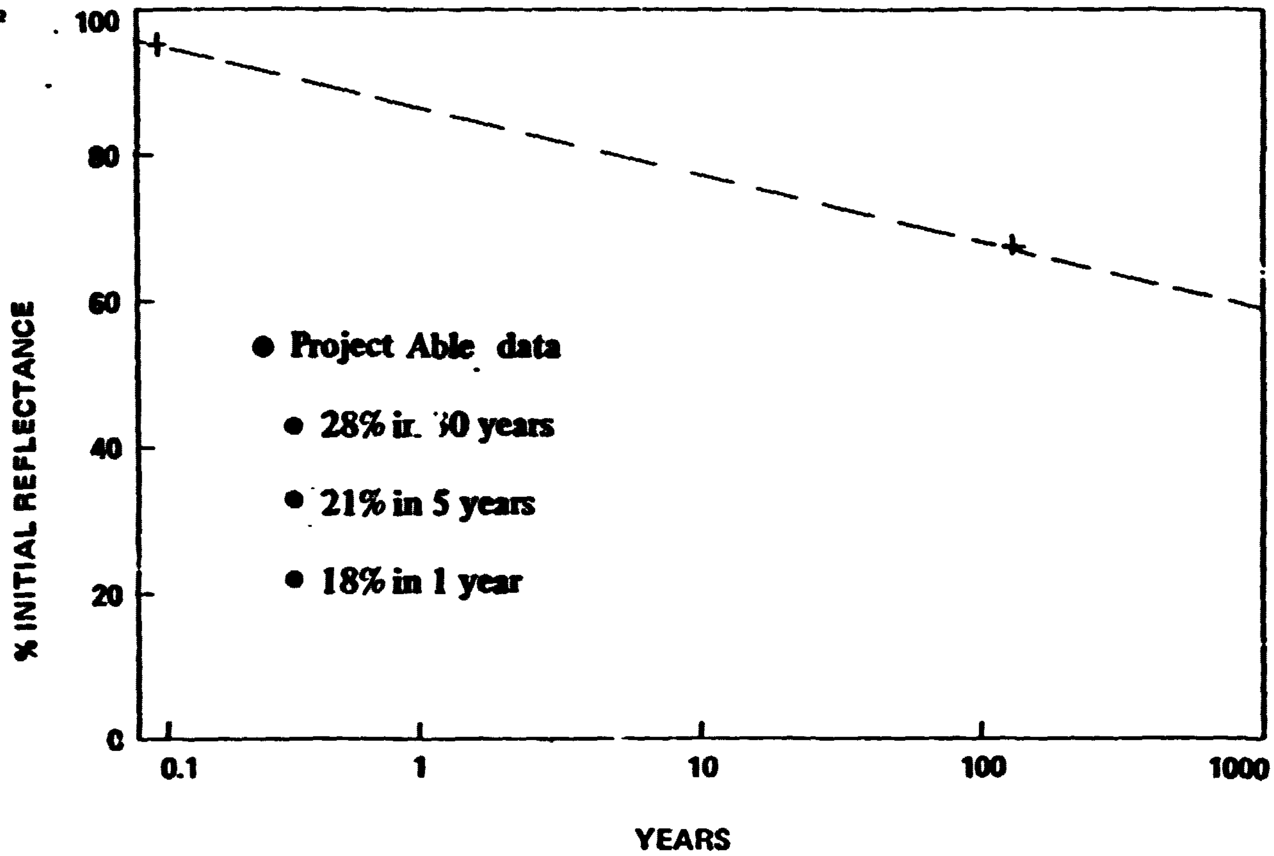

Figure 3.2-61 Reflector Radiation Degradation

ORIGINAL PAGE IS
OF POOR QUALITY

Array Trough Sizing: In addition to basic high reflectance of the reflector material, the chief requirement which the reflectors must meet is to provide uniform illumination of the active solar array. The trough must therefore be reduced in size as a function of the reflected ray beam width in order to avoid nonuniform illumination at the edges, as shown in Figure 3.2-62.

Reflector Temperature Gradient: A further result of the reflected beam width is the illumination overlap at the trough corners. This overlap results in the reflector temperature profile shown in Figure 3.2-63 which represents a design requirement on reflector flatness.

Reflector Membrane Analysis: In order to assess the biaxial stress required to maintain reflector flatness a membrane stress analysis was performed. Results of several identified design cases are summarized in Figure 3.2-64. The effect of the one meter deflection caused by solar pressure is shown on the following chart.

Effect of Thin Film Concentrator Deformation on Local Solar Flux: Data shown in Figure 3.2-65 were calculated using the Boeing "Thermal Radiative Interchange Factor" program and demonstrate the focusing of the reflected light from the solar pressure deformed reflector. If the reflector were ideal then the local concentration ration would be uniform at 1.8. The nonuniformity shown would have a significant performance impact.

Creep in Kapton Reflector: Kapton creep characteristics were found in National Bureau of Standards data which was used in calculating the creep characteristics shown in Figure 3.2-66. These data represent a considerably smaller design problem than earlier estimates that projected creep to continue at the initial rate.

3.2.7 Structures Analyses

The structural analyses for Part I gave primary emphasis to development of credible structural mass properties to support the evaluation of alternate energy conversion and construction location options. Most of the effort was aimed at the reference concentration ratio 2 truss and at a concentration ratio 1 planar truss. These and other options are illustrated in Figure 3.2-67.

The structural mass determined at the midterm of Part I reflected a substantial increase over the JSC reference configuration, from 2500 metric tons to almost 15,000 tons. This was due to a change from a three-tier structure (SPS built from 20-meter beams built from 1-meter beams built from structural elements) to a two-tier structure (SPS built from 20-meters beams built from structural elements). The noncircular beam caps that were shown in Figure 3.2-67 were used. The principal design load came from providing the biaxial stress of 6.9 MPa 1000 psi in the Kapton reflectors.

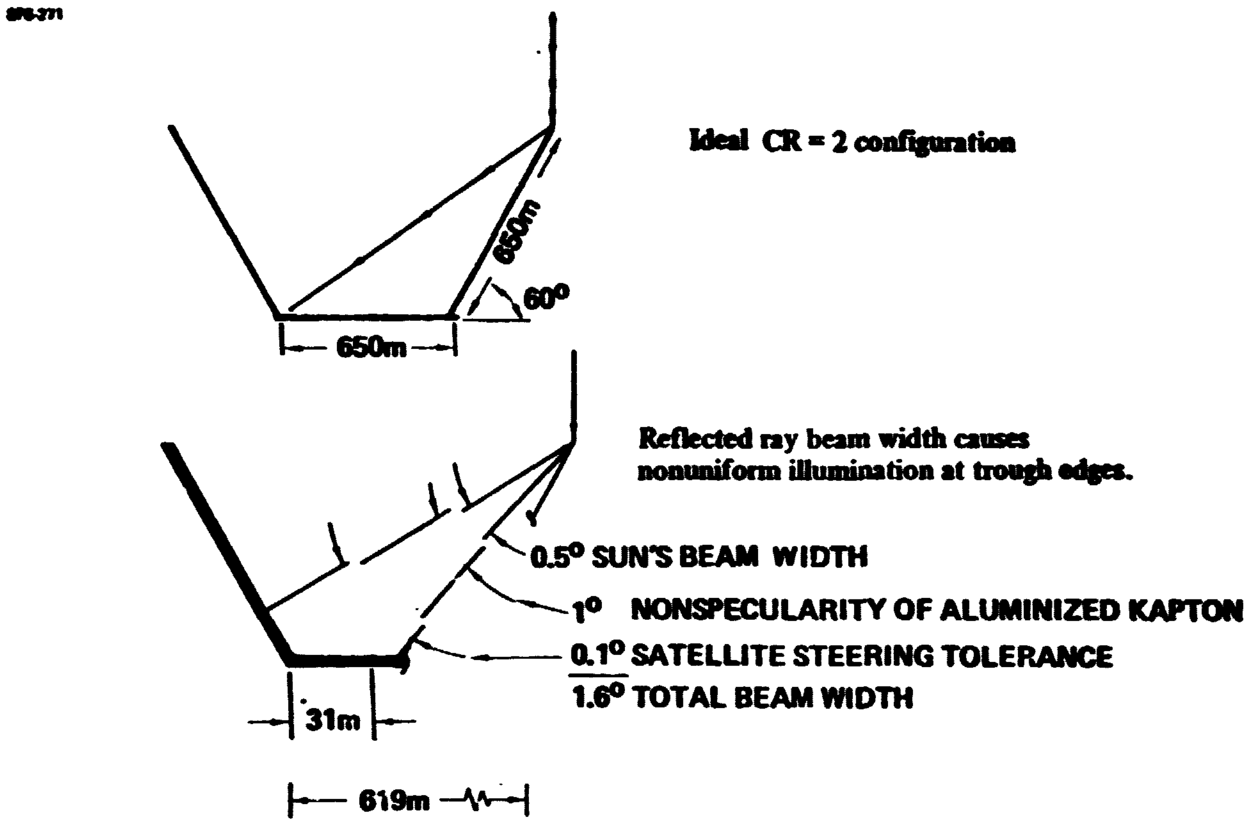

Figure 3.2-62 Array Trough Sizing

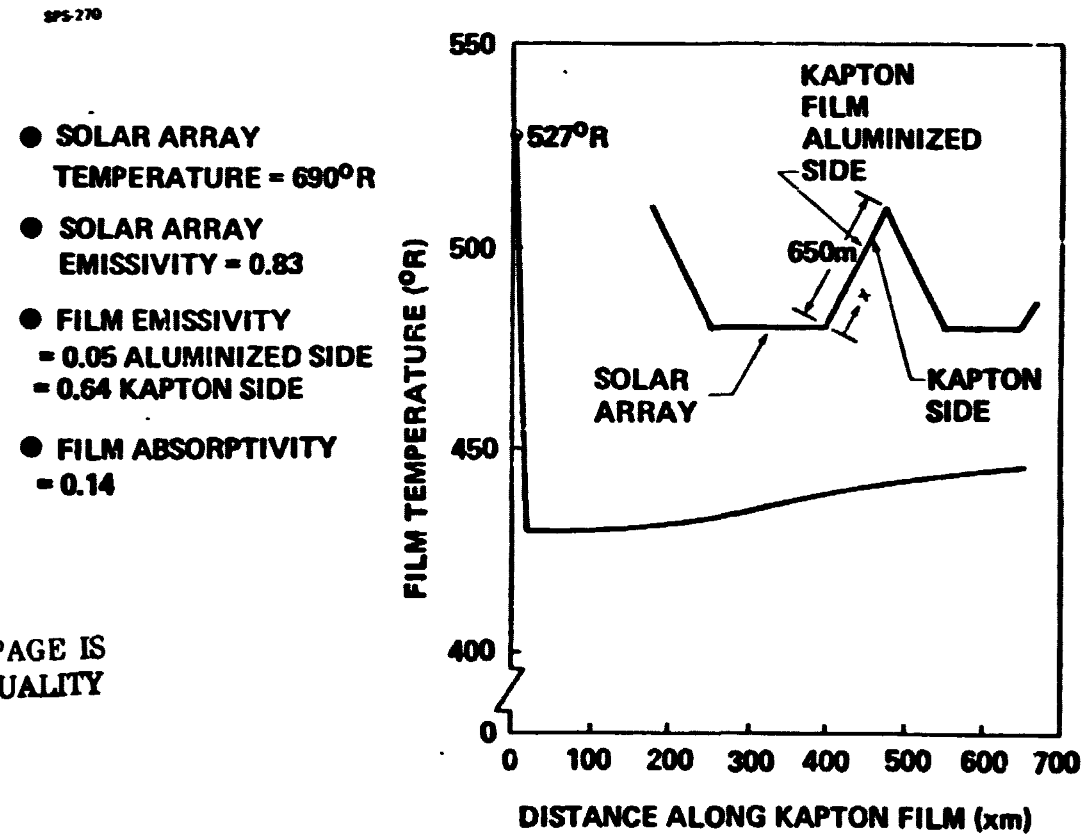

Figure 3.2-63 Reflector Temperature Gradient

ORIGINAL PAGE IS
OF POOR QUALITY

ORIGINAL PAGE IS
OF POOR QUALITY

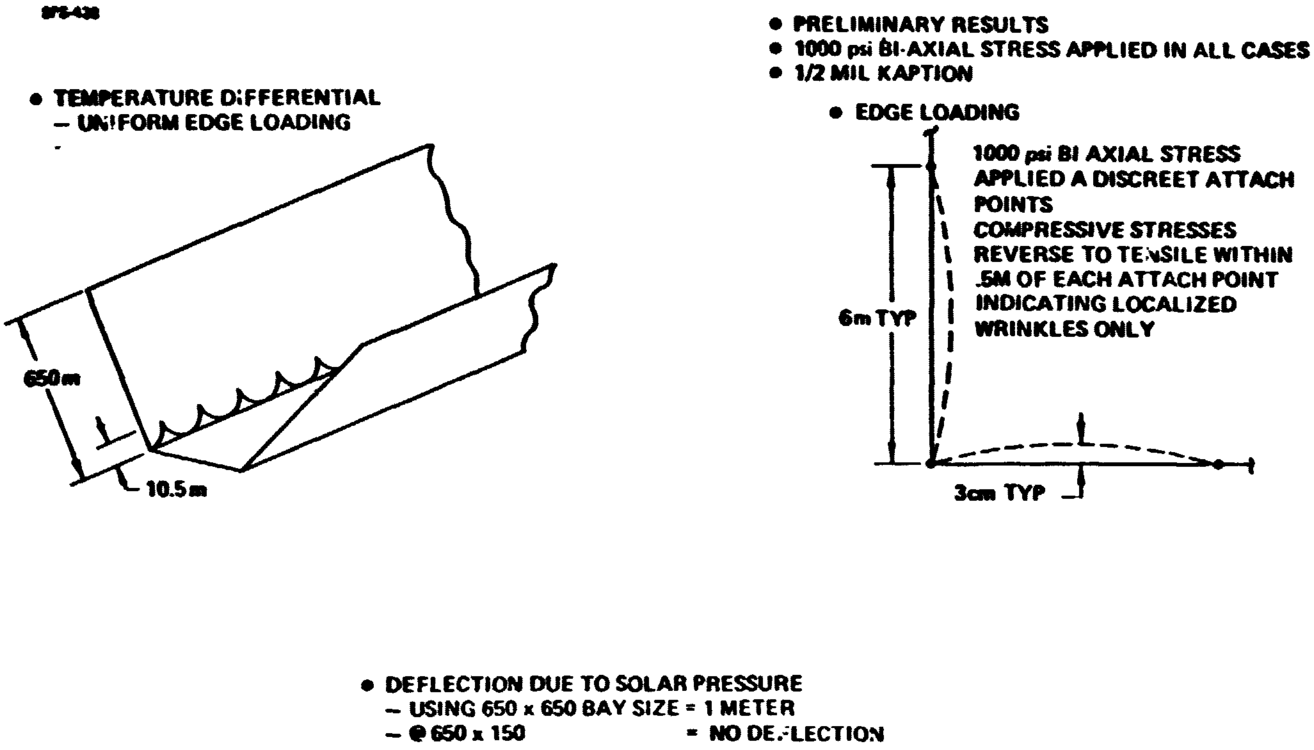

Figure 3.2-64 Reflector Membrane Analysis

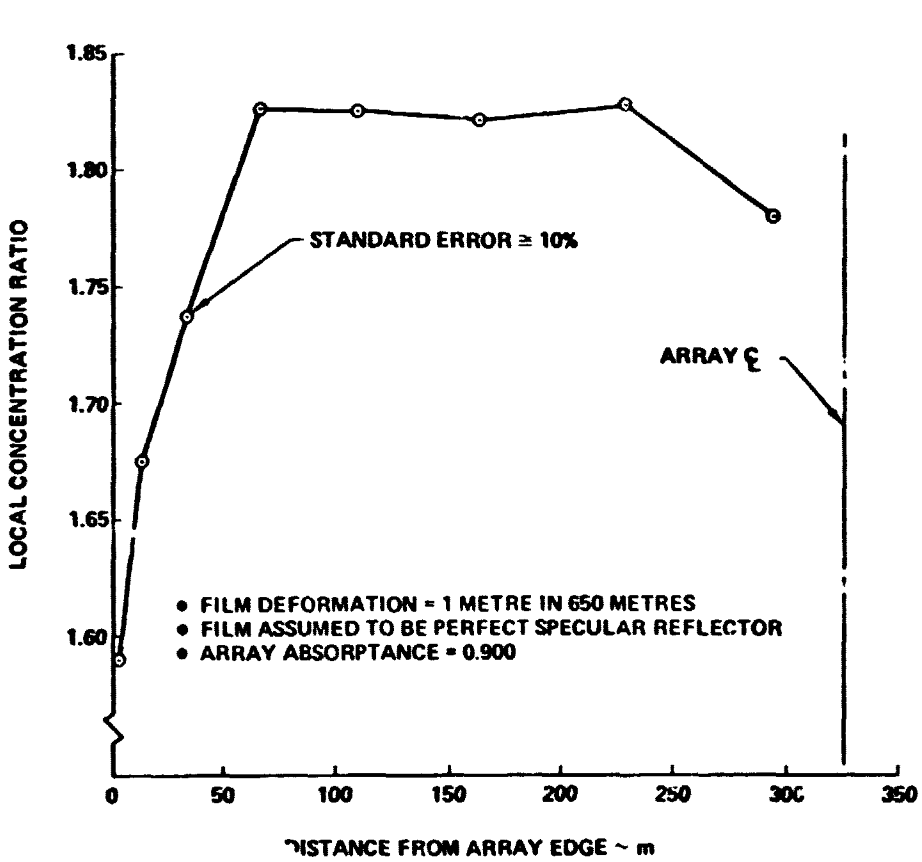

Figure 3.2-65 Effect Of Thin Film Concentrator Deformation On Local Solar Flux

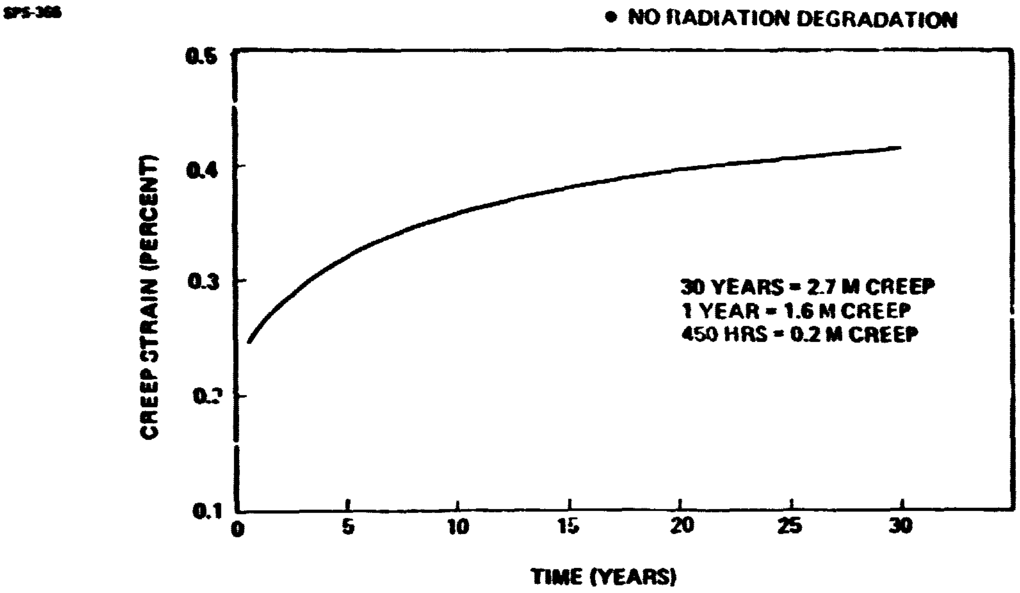

STRESS = 6.895×10^6 N/m^2 (1000 psi)
TEMPERATURE = 294°K (70° F)
*BASED ON INTERIM REPORT 275.05-70-1, "THERMAL-PHYSICAL PROPERTIES OF DACRON THREAD, MYLAR, AND KAPTON" PREPARED BY NBS, BOLDER, COLO. 80302 JULY 1970

Figure 3.2-66 Calculated Creep In Kapton Reflector*

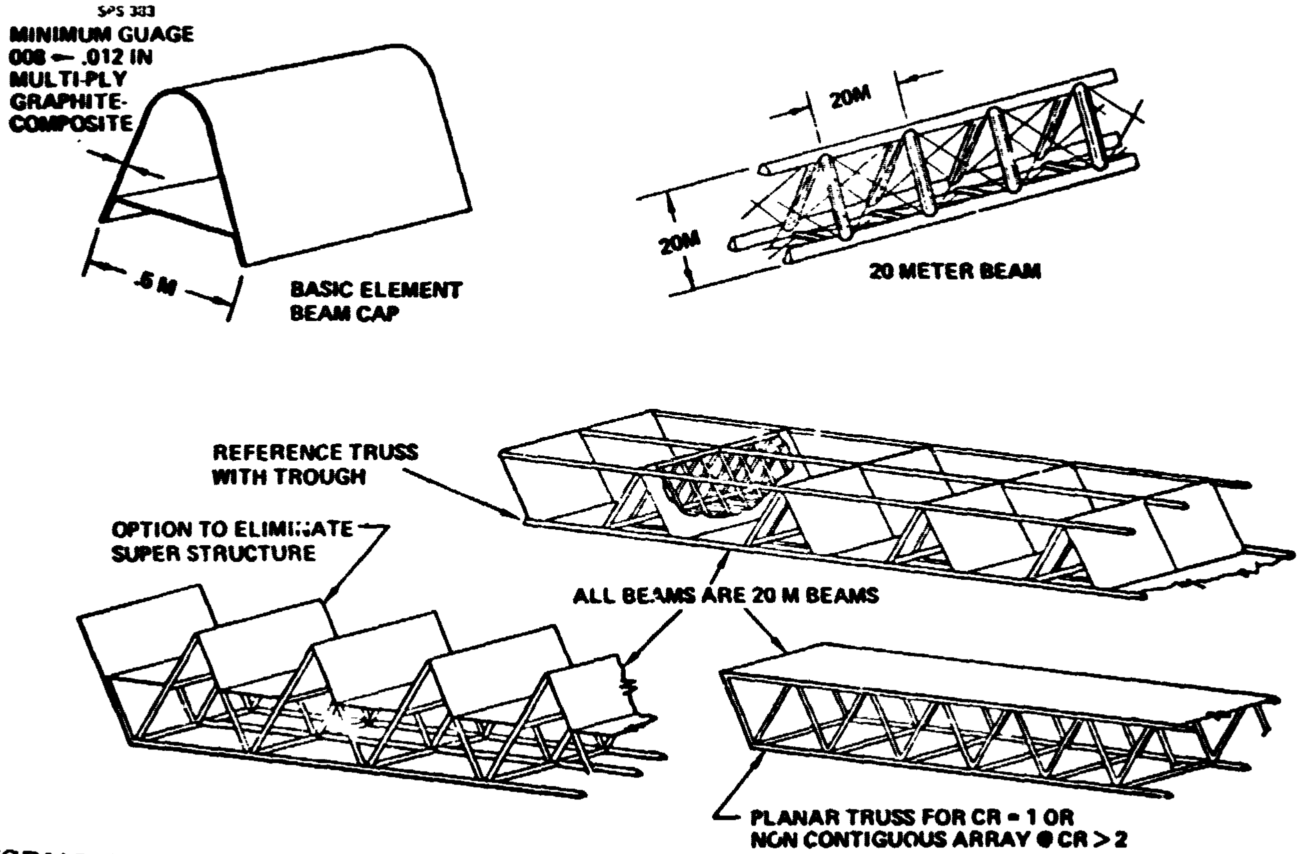

ORIGINAL PAGE IS
OF POOR QUALITY

Figure 3.2-67 Photovoltaic Structural Concepts

Subsequent to the midterm a more detailed analysis of the structure was conducted to reduce the mass. Three levels of biaxial stress were considered: 6.9 MPa (1000 psi), 3.9 Mpa (570 psi), and 1.7 MPa (250 psi). Material density data were reviewed, resulting in a revision downward by 12%. The structure concept and load condition analyzed are shown in Figure 3.2-68.

Assuming all diagonals are tension straps which are wrapped around the basic truss configuration of choads and battens, it follows that there is a precompression load in the battens and a pretension load in the diagonals. If the pretension load in the straps is equal to 50% of the tension load, then it can be shown that after the concentrator film is stretched, the total tension load in one diagonal will increase, while the total tension load in the other diagonal will drop to zero. Likewise, the compression load in the batten will increase.

The analysis proceeded in three steps:

1. Determine allowable long column stress and local buckling stress and the restulting beam cap tube radius, thickness, and mass as a function of column load The results are presented in Figure 3.2-69. There is substantial uncertainty in the local buckling stress as the source data were for aluminum rather than graphite composite and exhibit considerable scatter at high values of R/t. Figure 3.2-70 shows the variation in tube characteristics with column load.

2. Develop structural mass properties assuming no constraints on tube radius or thickness.

3. Develop structural mass properties for representative size constraints (0.254 m radius and 200 μm thickness as minimum gage).

Table 3.2-11 is typical of the calculations used to determine member mass. Figure 3.2-71 shows results. The optimized tubes have a marked advantage over standard-diameter tubes and were selected. All the selected optimized tubes exceed the 200 μm minimum gage thickness. The reflector was tensioned to 3.9 MPa (570 psi) and the structural bays had two intermediate members.

3.2.8 Mass Properites

The mass properties analyses conducted in Part I were directed to developing comparison data and therefore excluded common elements such as controls and the microwave power transmission system.

The silicon mass data shown in Table 3.2-12 are reduced from our previous baseline primarily by a reduction in tolerances on the silicon cells themselves. (Previous values reflected a specification or do-not-exceed mass rather than an average or expected mass.) Both silicon and GaAs have a 15% factor applied. The 75 μm (3-mil) covers and masses shown for silicon were used in all nonannealed cases while 50 μm (2-mil) was retained for annealed arrays.

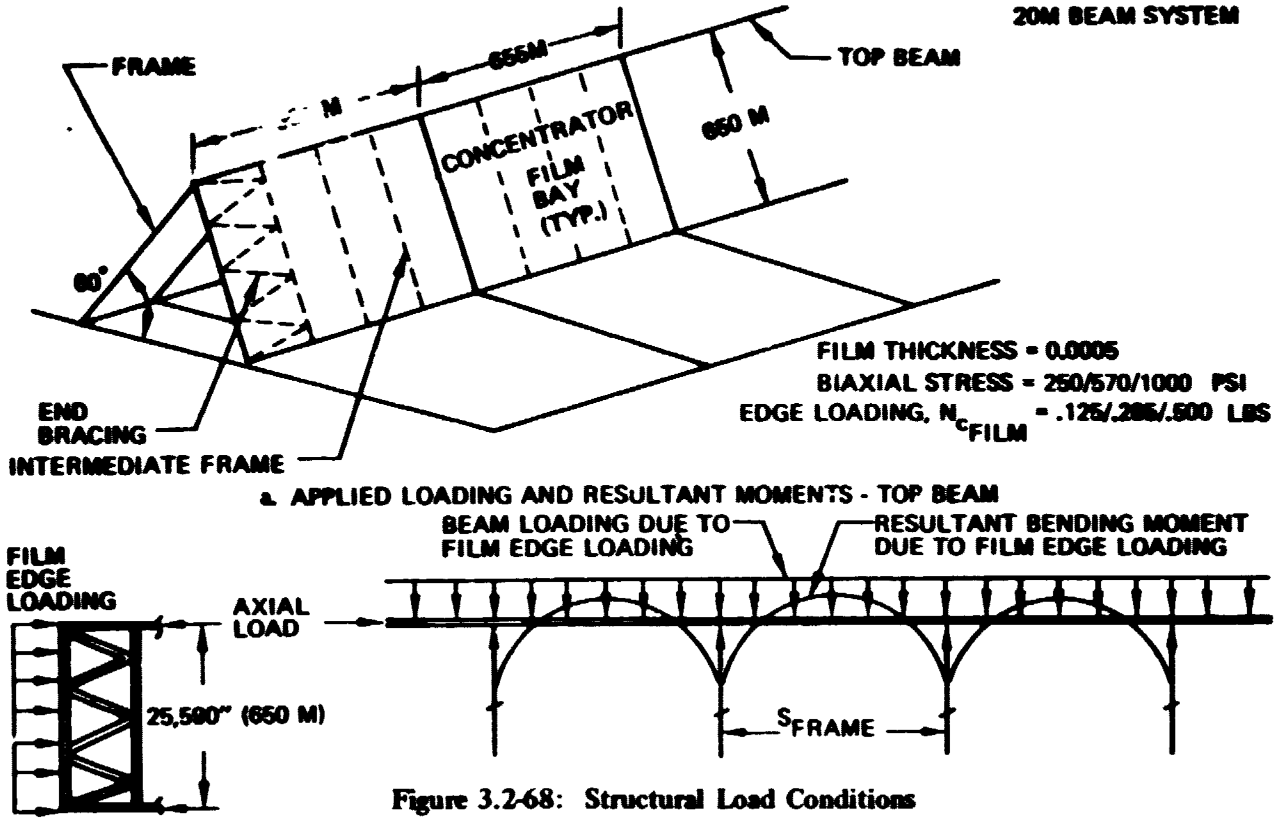

Figure 3.2-68: Structural Load Conditions

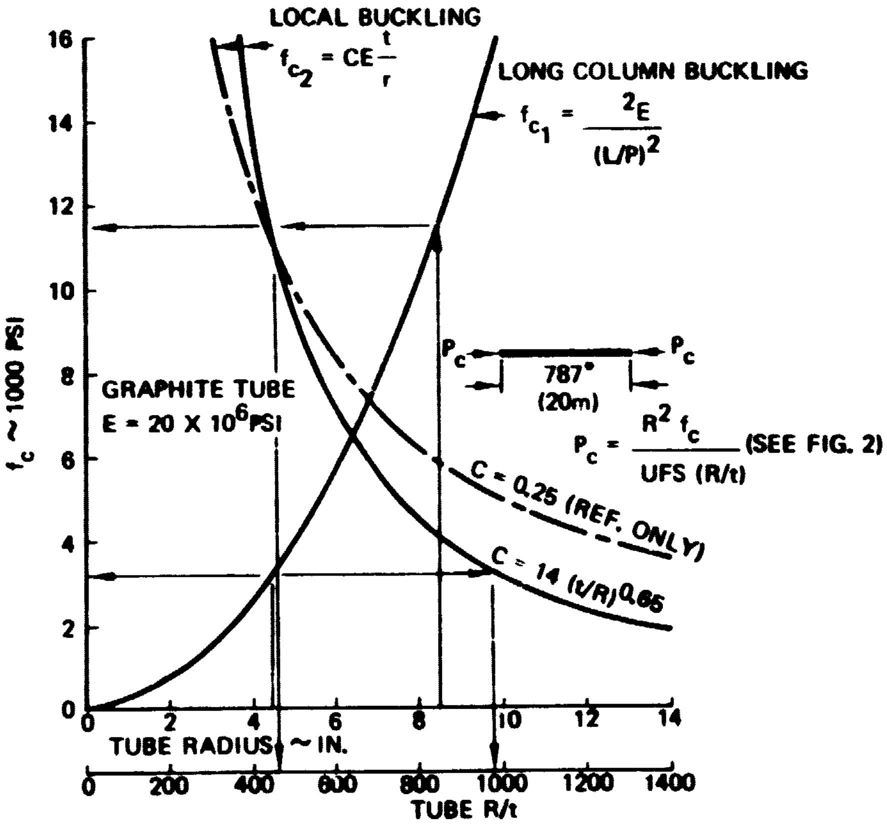

Figure 3.2-69: Compression Allowables for 20 Meter Columns.
(No Contraints on Tube Radius or Thickness)

ORIGINAL PAGE IS
OF POOR QUALITY

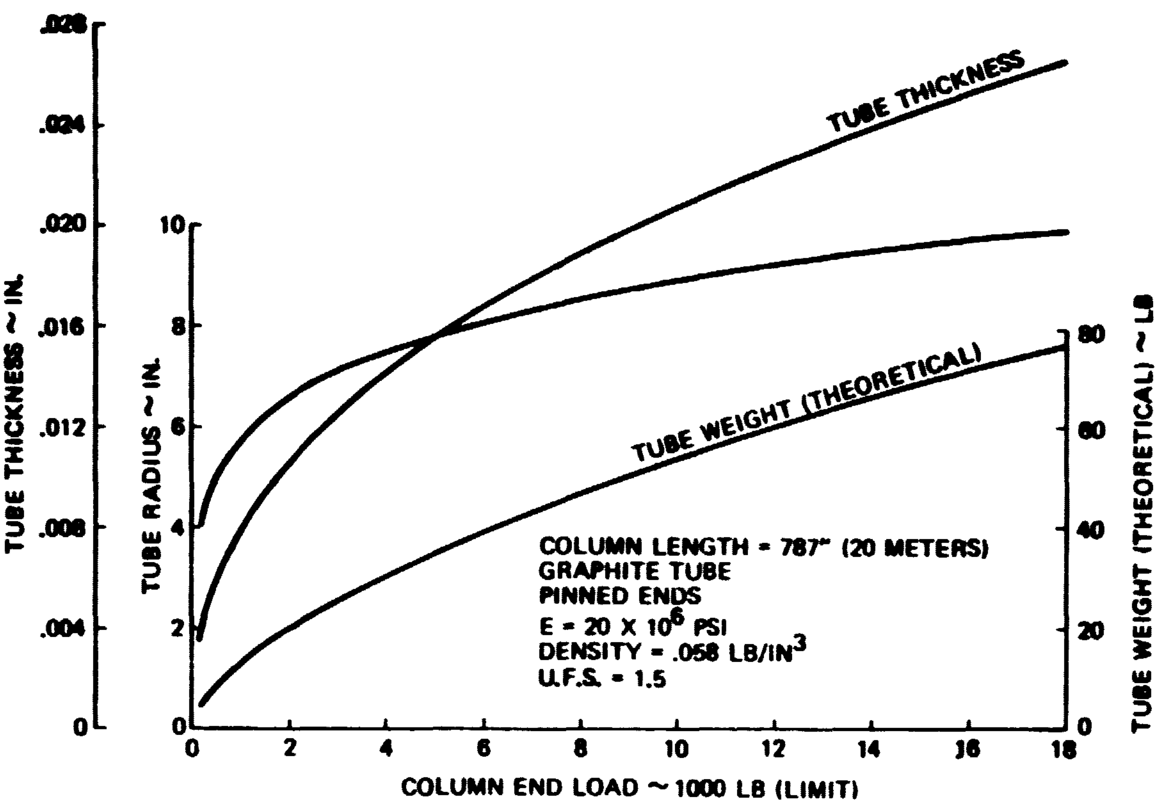

Figure 3.2-70: Tube Radius, Thickness, and Weight Variation with Column Load. (No Constraints on Tube Radius or Thickness)

Table 3.2-11: Chord Sizing (No Constraints on Tube Radius or Thickness)

NUMBER OF INTERMEDIATE FRAMES	S_{FRAME}	N_c FILM	P_c (EQTN 5)	R (FIG 2)	t (FIG. 2)	R/t	L/P $\left(\frac{787}{.707\ R}\right)$	A $(2\pi Rt)$	WT_{THED} (.058 x A x 787) (FIG. 2)
—	IN.	LB/IN	LB	IN	IN	—	—	IN^2	LB
0	25,787	0.125	9794	8.90	.0207	430	125	1.157	52.8
1	12,894	✓	3248	7.20	.0130	564	155	0.588	26.8
2	8596	✓	2036	6.60	.0106	623	169	0.439	20.0
0	25,787	0.285	22,330	10.35	.0296	350	108	1.924	87.8
1	12,894	✓	7405	8.45	.0183	462	132	0.971	44.3
2	8596	✓	4642	7.70	.0150	513	145	0.725	33.1
3	6447	✓	3675	7.35	.0136	540	151	0.628	28.7
4	5157	✓	3227	7.20	.0129	568	155	0.583	26.6
1	12,894	0.500	12,992	9.40	.0233	403	118	1.375	63.0
2	8596	✓	81444	6.65	.0191	452	453	1.038	47.5
3	6447	✓	6446	8.25	.0173	477	135	0.896	41.0
4	5157	✓	5660	8.05	.0164	491	138	0.829	37.8

TUBE DETAILS (R through A)

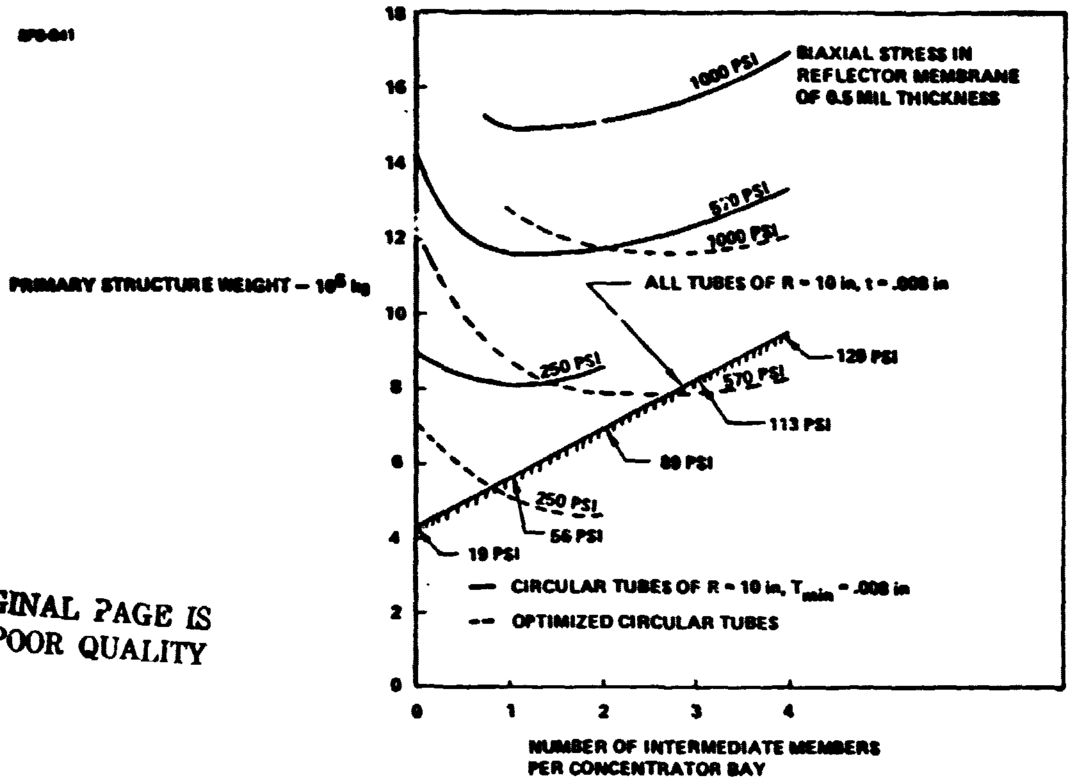

ORIGINAL PAGE IS
OF POOR QUALITY

Figure 3.2-71 Structural Weight Impact of Reflector Stress Level

Table 3.2-12 Photovoltaic Blanket Weight Buildups

SPS-646

Silicon Solar Cell Blanket Weight

ITEM	DENSITY (S.G.)	DENSITY (g/m^2/MIL)	THICKNESS (MILS)	AREA FACTOR	WEIGHT (g/m^2)
COVERS—FUSED SILICA	2.20	55.88	2.00/3.00	0.966	107.96/161.94
CELLS – SILICON	2.36	59.94	4.00	0.966	231.61
INTERCONNECTS – COPPER	8.94	227.08	0.50	0.200	22.71
SUPPORTING FILM – KAPTON*	1.42	36.07	1.00	0.900	32.46
ADHESIVE, CELLS TO FILM	1.40	35.56	0.50	0.900	16.00
ADHESIVE, KAPTON TO KAPTON	1.40	35.56	0.50	0.800	14.22

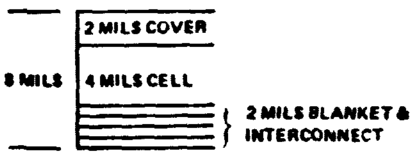

THEORETICAL WEIGHT	424.96/478.94
TOLERANCES & INSTALLATION (15%)	63.74/71.86
ESTIMATED ACTUAL WEIGHT	488.7/550.8
(% SILICON WEIGHT)	(47%/42%)

GaAs Solar Cell Blanket Weight

ITEM	DENSITY (S.G.)	DENSITY (g/m^2/MIL)	THICKNESS (MILS)	AREA FACTOR	WEIGHT (g/m^2)
COVERS – FUSED SILICA	2.20	55.88	2.00	0.966	107.96
CELLS – GaAs	5.32	135.13	0.40	0.966	52.21
SUBSTRATES – TITANIUM	4.50	114.30	0.50	0.966	55.21
INTERCONNECTS – COPPER	8.94	227.08	0.50	0.200	22.71
SUPPORTING FILM – KAPTON*	1.42	36.07	1.00	0.900	32.46
ADHESIVE, SUBSTRATES TO FILM	1.40	35.56	0.50	0.900	16.00
ADHESIVE, KAPTON TO KAPTON	1.40	35.56	0.50	0.800	14.22

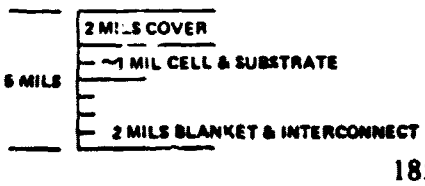

THEORETICAL WEIGHT	300.77
TOLERANCES & INSTALLATION (15%)	45.13
ESTIMATED ACTUAL WEIGHT	345.9
(% GALLIUM WEIGHT)	(7.4%)

*2 LAYERS

The mass summary shown in Table 3.2-13 recovers a substantial amount of the 44% midterm increase. The four major mass contributors in the energy collection system were all addressed to an additional level of definition resulting in decreases to structure and array and increase to the reflectors and power distribution.

This mass statement includes the 50% growth allowance used in the JSC reference configuration definition, for comparison purposes. Mass data shown elsewhere in this document do not include a growth allowance. Included in the Part II effort will be a mass uncertainty analysis and a recommended revision to the mass growth allowance.

3.2.9 Payload Packaging

The goal in packaging SPS components is to have each Earth launch be mass rather than volume limited and therefore result in the least possible number of launches. Various options in terms of the payload mix on each launch and the payload design approach are possible.

In the case of the payload shroud, recoverable designs are desirable since an expendable shroud sized for mass limited payload flights may be quite long (40 meter for low density payloads) and cost approximately $3 million. The maximum length of shroud assumed for a recoverable design when used with a two stage ballistic/ballistic launch vehicle is 23 meters with a diameter (usable) of 17.2 meters. The launch vehicle payload capability was 400,000 Kg; a payload density of 70 Kg/m^3 would fill the specified payload shroud.

Photovoltaic satellite components were found to have densities far greater than the shroud payload density of 70 Kg/m^3 and therefore result in mass limited flights. The assumed component density and number of launches for the major components making up a 69 million Kg satellite (excluding MPTS) are shown in Table 3.2-14.

Payload shroud volume utilization by representative photovoltaic components is illustrated in Figure 3.2-72 for the case of the 23m recoverable shroud. Again, this shroud length was initially assumed because of the 20m segmented beam design and the desire to have reflector widths as large as possible to minimize the number of the on-orbit attachments. As indicated by this simple illustration, a low utilization factor exists and future work could consider shorter shroudlengths.

Table 3.2-13 Photovoltaic Reference Configuration Nominal Mass Summary Weight in Metric Tons

COMPONENT	ORIENTATION	MIDTERM	CURRENT	REMARKS
1.0 SOLAR ENERGY COLLECTION SYSTEM	(36,616)	(59,313)	(49,512)	INITIAL AREA = 129 km^2, MIDTERM & CURRENT=146 km^2
1.1 PRIMARY STRUCTURE	2,483	14,970	8,000	OPTIMIZED CIRCULAR CHORDS + REDUCED MEMBRANE STRESS LEVEL
1.2 SECONDARY STRUCTURE	189	209	209	~TO ARRAY AREA
1.3 MECHANICAL SYSTEMS	40	40	40	NO CHANGE
1.4 MAINTENANCE STATION	85	—	—	DELETED TO BE CONSISTENT WITH THERMAL ENGINE
1.5 CONTROL	340	340	340	NO CHANGE (200 M.T. DRY WET + 1 YR PROPELLANT)
1.6 INSTRUMENTATION/ COMMUNICATIONS	4	4	4	NO CHANGE
1.7 SOLAR-CELL BLANKETS	25,746	37,592	34,111	SPECIFIC WEIGHT DOWN TO .49 kg/m^2 (FROM .54 kg/m^2)
1.8 SOLAR CONCENTRATORS	5,149	2,978	3,276	INCLUDES TENSIONING/INSTALLATION FACTOR
1.9 POWER DISTRIBUTION	2,570	3,180	3,532	INCLUDES SWITCH GEAR & INSTALLATION FACTOR
2.0 MPTS	15,371	15,371	15,371	NO CHANGE
SUBTOTAL	51,987	74,684	64,883	13% REDUCTION FROM MIDTERM – 26% HIGHER THAN INITIAL
GROWTH	25,994	37,342	32,442	(50%)
TOTAL	77,981	112,026	97,325	

ORIGINAL PAGE IS OF POOR QUALITY

Table 3.2-14 Photovoltaic Packaging

Component	Packaging Density (Kg/M^3)	Est. No. of Flights
Structural Beams	1310	54
Solar Array	1480	108
Reflector	2180	25
Conductor	1500	11

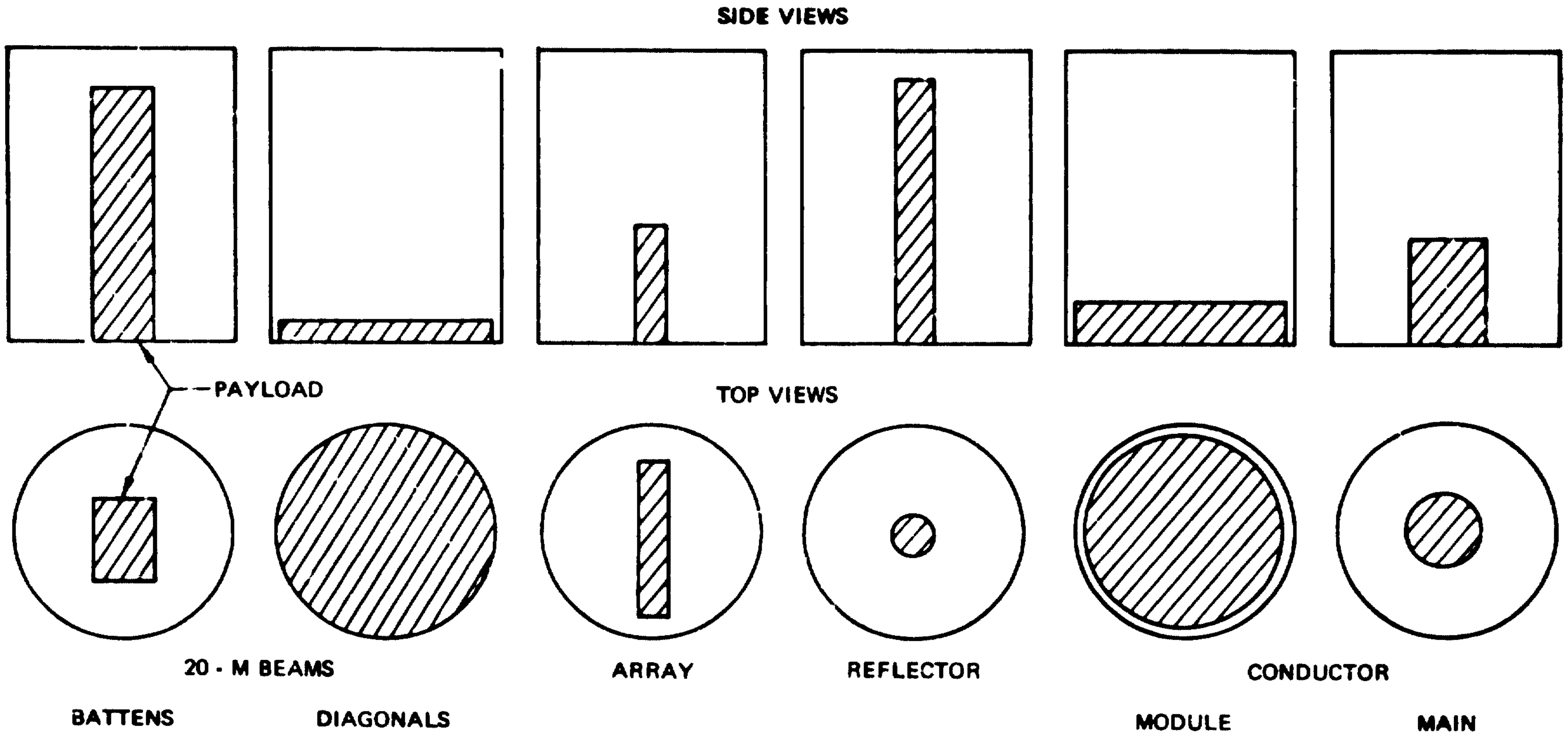

Figure 3.2-72: Typical Photovoltaic Payload Envelopes

3.2.10 Reliability and Maintainability

A reliability and maintenance assessment was conducted for the two reference satellite systems (silicon photovoltaic and Brayton thermal engine). The assessment is limited to the power generation and distribution systems since they cause the major differences in maintenance concept. Reliability data was obtained from Boeing's Experience Analysis Center and preliminary work started to determine expected failure rates. Failure data indicates that a considerable, continuous, maintenance effort will be required to maintain either satellite in operation with the goals of a .95 power output while available. Preliminary results are as follows:

The large number of solar cells on an SPS (14.5×10^9 is typical) leads to a potential reliability problem even though the estimated MTBF per cell is also large, i.e., 10^8 hours. Over the 30-year life of the SPS, approximately 0.6% of the cells would be expected to fail. This is not of itself a very significant value; the problem arises because of the lengthy series-parallel strings, four parallel x 130,000 series. If any two cells out of any four-parallel set fail, the remaining two cannot carry the string current. As the string current drops, its voltage will rise and the delta voltage appears across the failed point. The probability of a two-cell-in-parallel failure somewhere in the string is quite large. This problem can be corrected or minimized by paralleling larger numbers of cells, e.g., 10 instead of 4, and by diode shunting. These measures were adopted for the Part II photovoltaic SPS designs.

The analysis tasks conducted were:

1. Identify subsystem configurations of baseline satellites, down to the line replaceable unit (LRU), including a parts count of lower level
2. From historical data and considerations of application, determine failure modes, maintenance requirements, and mean time between failure (MTBF) or mean time between maintenance (MTBM) data for each part.
3. Compute failure rates and maintenance rates (repair rates) for each part or subassembly. Determine power lost due to failure or maintenance.

These were completed for the satellite configurations identified at the Part I Midterm Briefing. Corrections to system designs were incorporated as a result of this analysis to reduce the impact of maintenance problems identified.

ORIGINAL PAGE IS
OF POOR QUALITY

Table 3.2-15 shows the results of these tasks. The last column identifies the average power lost due to the failure and maintenance. The MTTR column data is primarily based on data obtained from a survey documented in "IEEE Transactions on Industry Applications." The survey report was started in Vol. IA-10,H02, March/April, 1974, in an article entitled "Report on Reliability Survey of Industrial Plants." The MTBF data was obtained from our Experience Analysis Center, MIL-HMBK-217B, the above IEEE Report, and other industry articles used to confirm the validity of data. The maintenance concepts, logistic concepts, and maintenance equipment can be used as a basis for operational maintenance and logistics requirements definition.

The utility industry expended approximately 6% of revenues for maintenance in 1974 and 6.8% in 1973. Of this maintenance expense approximately half was charged to the generation plants. The remainder of the maintenance expenses are charged to power transmission and distribution system.

Surveys of nuclear plant availability have shown that availability increases from approximately 60% to 85% within a six year period after the plant is first brought on line. This is due to an effort towards the improvement of availability and the overcoming of infant mortality failures.

A review of the IEEE reliability survey, mentioned above, was conducted by one of the IEEE subcommittee members. His review indicated that the following 4 items contributed to a very large percentage of plant failures (> 50%).

1. Manufacture-defective components

2. Application engineering, improper application

3. Inadequate installation and testing prior to startup (proof test)

4. Inadequate maintenance.

Table 3.2-16 presents a summary of the historical data reviewed in order to make these predictions.

3.2.11 CPC Concentrator Performance

Three-dimensional compound parabolic concentrators (CPC's) belong to a class of reflective optical concentrators introduced by Winston and co-workers at Argonne National Laboratory in 1974. The surface geometry of these concentrators is achieved by translating and rotating the axis of a parabola relative to a designated optical axis and then rotating the skewed parabola around the optical axis to form a surface of revoltion as shown in Figure 3.2-73. The angle between the optical axis and parabola axis is called the acceptance half-angle θc.

C3

Table 3.2-15:

EQUIPMENT NOMENCLATURE	QUANTITY PER SPS (NHA)	FAILURE OR SCHEDULED MAINT.	MAINT CONCEPT	MAINT EQUIP	LOGISTICS CONCEPT	GND PWR LOSS (KW)	MTBF OR MTBM	REPAIR RATE	MTTR	PWR LOSS DUE TO MAINT
2.0 POWER GENERATION										
2.1 SOLAR CONCENTRATORS										
2.1.1 REFLECTORS (20 METER STRIP)	11,520									
2.1.1.1 SUBSTRATE		CREEP	AUTOMATIC DEVICES FOR TENSIONING	NONE	NONE	—	—	—	—	—
		METEROID DAMAGE	REPLACE DAMAGED SECTION	FREE FLYER	SPARE REFLECTOR STRIPS AT DEPOT	—	—	—	—	—
2.1.1.2 REFLECTIVE COATING		DEGRADATION	ADD ARRAY AS REFLECTOR DEGRADES	FREE FLYER/BEAM WALKER	INSTALL ADDITIONAL ARRAY OVER THE LIFE OF THE SATELLITE	—	—	—	—	—
2.1.2 INSTALLATION DEVICES										
2.1.2.1 REFLECTOR JOINTS	11,512	JOINT OPENS	REPAIR JOINT (SPLICE)	FREE FLYER	REFLECTOR JOINT REPAIR KITS	138	3.4×10^6	3.4×10^3	12	6.6
2.1.2.2 TERMINATION DEVICES	38,400	FAILURE - BREAKS	REPAIR (SPLICE) OR REPLACE	BEAM WALKER OR FREE FLYER	REPAIR KITS AT DEPOT	138	4.5×10^6	8.5×10^3	12	14.1
2.1.2.3 TENSIONING DEVICES		FAILS TO TENSION REFLECTOR	REPLACE DEFECTIVE TENSIONER	BEAM WALKER OR FREE FLYER	SPARE TENSIONING DEVICES (REPAIR AT DEPOT)	276	9.1×10^6	4.2×10^3	12	13.9
2.2 SOLAR CELL BLANKETS										
2.2.1 SOLAR CELL ARRAY STRIP	27,692	NO OUTPUT	REPLACE STRIP	FREE FLYER	SPARE STRIPS AT DEPOT (REPAIR AT DEPOT)	361	8×10^4	35	24	3.03×10^3
2.2.1.1 SOLAR CELLS	(521,760)	FAILED CELL	NO ACTION UNTIL TOTAL STRIP FAILS (4 CELLS IN PARALLEL)	REPLACE STRIP WHEN TOTALLY FAILED WITH FREE FLYER	SPARE SOLAR ARRAY STRIPS	NEG.	1×10^8	5.2×10^{-3}	—	—
2.2.1.2 COVER GLASS		BROKEN OR DAMAGED	NONE UNTIL STRIP OUTPUT FAILS THEN ISOLATE AND REPLACE	FREE FLYER	SPARE SOLAR ARRAY STRIPS	NEG.	—	—	24	—
2.2.1.3 SUBSTRATE		BROKEN OR DAMAGED	REPLACE WHEN STRIP OUTPUT FAILS	FREE FLYER	SPARE SOLAR ARRAY STRIPS	NEG.	—	—	24	—
2.2.1.4 INTERCONNECT	(1,043,520)	OPEN	NONE UNTIL STRIP OUTPUT FAILS THEN REPLACE	FREE FLYER	SPARE SOLAR ARRAY STRIP	NEG.	1.75×10^8	8.3×10^{-4}	24	—
2.2.2 INSTALLATION DEVICES										
2.2.2.1 BLANKET JOINTS	27,688	JOINT OPENS	REPAIR	FREE FLYER	BLANKET JOINT REPAIR KITS	NEG.	3.4×10^6	8.1×10^{-3}	12	—
2.2.2.2 TERMINATION DEVICES	55,384	BREAKS	REPAIR OR REPLACE	FREE FLYER OR BEAM WALKER	REPAIR KIT OR REPAIR AT DEPOT	NEG.	4.5×10^6	1.2×10^2	12	—
2.2.2.3 TENSIONING DEVICES	55,384	FAILS TO TENSION BLANKET	REPLACE	BEAM WALKER OR FREE FLYER	SPARE TENSIONING DEVICES (REPAIR AT DEPOT)	NEG.	9.1×10^6	6.1×10^{-3}	12	—

ORIGINAL PAGE IS OF POOR QUALITY

Table 3.2-15 (Continued):

EQUIPMENT NOMENCLATURE	QUANTITY PER SPS (NHA)	FAILURE OR SCHEDULED MAINT.	MAINT. CONCEPT	MAINT. EQUIP.	LOGISTICS CONCEPT	GND PWR LOSS (KW)	MTBF OR MTBM	REPAIR RATE	MTTR	PWR LOSS DUE TO MAINT (KWH)
4.0 POWER DISTRIBUTION										
4.1 CONDUCTOR SYSTEM										
4.1.1 CONDUCTOR										
4.1.1.1 MODULE ACQUISITION BUS	384	BREAK IN CONDUCTOR	SPLICE BROKEN SECTION AFTER ISOLATION	BEAM WALKER OR FREE FLYER	SPARE CONDUCTOR & SPLICE MATERIALS	26×10^3	1.0×10^9	3.84×10^{7}	15	.15
4.1.1.2 MAIN BUS	16	BREAK IN CONDUCTOR	SPLICE BROKEN SECTION AFTER ISOLATION	BEAM WALKER OR FREE FLYER	SPARE CONDUCTOR & SPLICE MATERIALS	2.5×10^6	1.0×10^9	1.6×10^{-7}	15	.6
4.1.2 TERMINATIONS	1560	BREAK IN TERMINATION	ISOLATE & REPLACE	BEAM WALKER OR FREE FLYER	SPARE INTERCONNECTS	26×10^3	2.0×10^9	7.7×10^{-7}	5.5	.11
4.1.3 INSTALLATION DEVICES (INSULATORS SUPPORTS ETC)	48,500	BROKEN INSULATOR	REPLACE (CANNOT DETECT FROM PERF DATA)	BEAM WALKER OR FREE FLYER	SPARE INSULATORS & SUPPORT MATERIAL	NEG.	1.0×10^9	4.85×10^{-5}	6.0	
		SHORTED OR LEAKY INSULATOR	ISOLATE & REPLACE	BEAM WALKER OR FREE FLYER	SPARE INSULATORS	NEG.				
4.2 SWITCHGEAR	196									
4.2.1 DISCONNECTS	196	INTERMITTENT OR OPEN CONTACT	ISOLATE & ADJUST OR REPLACE	BEAM WALKER OR FREE FLYER	SPARE DISCONNECTS (REPAIR AT DEPOT)	26×10^3	2.13×10^5	9.3×10^{5}	13	31.4
		FAILURE IN MECHANISM	ISOLATE & ADJUST OR REPLACE	BEAM WALKER OR FREE FLYER	SPARE DISCONNECTS (REPAIR AT DEPOT)					
4.2.2 ZERO CURRENT SIMULATION DEVICES	196									
4.2.2.1 INDUCTORS	196	OPEN OR SHORTED WINDINGS	ISOLATE & REPLACE	BEAM WALKER OR FREE FLYER	SPARE INDUCTORS (REPAIR AT DEPOT OR SCRAP)	26×10^3	1.67×10^8	1.2×10^{-4}	13	4
4.2.2.2 CAPACITORS	196	OPEN OR SHORTED	ISLOATE & REPLACE	BEAM WALKER OR FREE FLYER	SPARE CAPACITORS (SCRAP)	26×10^3	5.6×10^6	3.5×10^{-4}	13	1.18
4.2.2.3 SPARK GAP	196	SHORTED OR FAILURE TO IGNITE	ISOLATE & REPLACE	BEAM WALKER OR FREE FLYER	SPARE SPARK GAPS (REPAIR OR SCRAP AT DEPOT)	26×10^3				
		SCHEDULED REPLACEMENT BASED ON NO. OF CYCLES	ISOLATE & REPLACE	BEAM WALKER OR FREE FLYER	SPARE SPARK GAPS (REPAIR AT DEPOT)					
4.2.3 DC INTERRUPTERS	196	FAILURE TO OPERATE	ISOLATE & REPLACE	BEAM WALKER OR FREE FLYER	SPARE DC INTERRUPTER (REPAIR AT DEPOT)	26×10^3	2.3×10^6	8.5×10^{-5}	12.0	26.5
		SCHEDULED INSPECTION	ISOLATE, INSPECT, REPLACE IF REQ'D	BEAM WALKER OR FREE FLYER	SPARE DC INTERRUPTER (REPAIR AT DEPOT)					

ORIGINAL PAGE IS OF POOR QUALITY

Table 3.2-15 (Continued):

EQUIPMENT NOMENCLATURE	QUANTITY PER SPS (NHA)	FAILURE OR SCHEDULED MAINT.	MAINT CONCEPT	MAINT. EQUIP.	LOGISTICS CONCEPT	GND PWR LOSS (KW)	MTBF OR MTBM	REPAIR RATE	MTTR	PWR LOSS DUE TO MAINT (KWH)
4.0 DISTRIBUTION (CONTINUED)										
4.3 POWER CONVERTER (DC/DC, DC/AC)	6	FAILS TO REGULATE OR PROVIDE OUTPUT	ISOLATE & REPLACE CONVERTER	BEAM WALKER OR FREE FLYER	SPARE CONVERTER (REPAIR AT DEPOT)	—	(1.62×10^6)	3.7×10^{-6}	24	—
4.3.1 TRANSFORMERS		OPEN OR SHORTED WINDINGS	ISOLATE & REPLACE CONVERTER	BEAM WALKER OR FREE FLYER	SPARE CONVERTER (REPAIR AT DEPOT)		1.33×10^8			
4.3.2 SEMICONDUCTORS										
4.3.2.1 THYRISTORS		FAILED THYRISTOR	ISOLATE & REPLACE CONVERTER	BEAM WALKER OR FREE FLYER	SPARE CONVERTER (REPAIR AT DEPOT)		2.33×10^7			
4.3.2.2 DIODES		FAILED	ISOLATE & REPLACE CONVERTER	BEAM WALKER OR FREE FLYER	SPARE CONVERTER (REPAIR AT DEPOT)		2.33×10^7			
4.3.2.3 TRANSISTORS		FAILED	ISOLATE & REPLACE CONVERTER	BEAM WALKER OR FREE FLYER	SPARE CONVERTER (REPAIR AT DEPOT)					
4.3.2.4 INTEGRATED CIRCUITS		FAILED	ISOLATE & REPLACE CONVERTER	BEAM WALKER OR FREE FLYER	SPARE CONVERTER (REPAIR AT DEPOT)		2.86×10^5			
4.3.3 INDUCTORS		FAILED OPEN OR SHORTED	ISOLATE & REPLACE CONVERTER	BEAM WALKER OR FREE FLYER	SPARE CONVERTER (REPAIR AT DEPOT)		1.67×10^8			
4.3.4 CAPACITORS		FAILED	ISOLATE & REPLACE CONVERTER	BEAM WALKER OR FREE FLYER	SPARE CONVERTER (REPAIR AT DEPOT)		5.56×10^6			
4.3.5 RESISTORS		FAILED	ISOLATE & REPLACE CONVERTER	BEAM WALKER OR FREE FLYER	SPARE CONVERTER (REPAIR AT DEPOT)		3.33×10^7			
4.3.6 CONNECTIONS		FAILED	ISOLATE & REPLACE CONVERTER	BEAM WALKER OR FREE FLYER	SPARE CONVERTER (REPAIR AT DEPOT)		1.0×10^4 (SOLDERED)			

ORIGINAL PAGE IS OF POOR QUALITY

Table 3.2-16 Photovoltaic Solar Power Satellite

	MTBF (HRS)	FAIL/10^6 OPER HRS	ENVIRO	ADJ FAC	ADJ VAL FAIL/10^6 HR	MTTR	SOURCE
REFLECTORS							
SUBSTRATE, KAPTON							
COATING, ALUM							
INSTALLATION DEVICES							
JOINTS, ZIPPERS	-	2.04	GND	7	.29		FRD VOL I, PG 107
TERM, CLAMPING DEVICE	-	1.51	GND	7	.22		FRD VOL I, PG 143
TENSIONING, SPRING	-	.110	CMP LAB	NONE	.110		D180-18389-1, PG 201
SOLAR CELL ARRAY	R=.99952		SPC				D2-114080-1, PG 16
SOLAR CELL	-	.01	SPC	NONE	.01		SPECTROLAB DOC 021219*
SUBSTRATE, KAPTON	-						
INTERCONNECT, PRINTED CIRCUIT	-	.0008	CMP LAB	NONE	.0008		D2AGM 12101-1, PG 44
CONDUCTOR SYSTEM							
CONDUCTOR (SHEET ALUM)	-						
TERMINATIONS - WELDS	-	.0005	CMP LAB	NONE	.0005		D2AGM 12101-1
INSULATORS (CERAMIC)							

*1-16-73 (BOEING S-3 SOLAR ARRAY PROG) PG 3

Table 3.2-16 Continued

	MTBF (HRS)	FAIL/10^6 OPER HRS	ENVIRO	ADJ FAC	ADJ VALUE FAIL/10^6HR	MTTR	SOURCE
SWITCH GEAR							
SOLENOID, KNIFE SWITCH	-	1.87	GND	4	.47		FRD VOL I FG 394
CAPACITORS (40000v-2000A)	-	.20	CMP LAB	NONE	.20		D180-18309-1, PG 28
CIRCUIT BREAKER	3,279	305	GND	2	152.5		LMEC 69-7, VOL I TABLE 1-40 PG 1-97
POWER CONVERTOR							
TRANSFORMER	3,636	275	GND	6	45.83		LMEC 69-7 VOL I TABLE 1-40 PG 1-97
SEMI CONDUCTORS							
DIODES	-	.043	SPC	NONE	.043		FRD VOL I, PG 341
THYRISTORS	-	.043	SPC	NONE	.043		FRD VOL I, PG 341
INDUCTORS	-	.006	SPC	NONE	.006		FRD VOL I, PG 77
CAPACITORS	-	.180	SPC	NONE	.180		FRD VOL I, PG 42
RESISTORS	-	.030	SPC	NONE	.030		FRD VOL I, PG 280
CONNECTIONS							
WELDED	-	.0005	CMP LAB	NONE	.0005		D2AGM 12101-1, PG 38
SOLDERED	-	.00001	SPC	NONE	.00001		SPECTROLAB DOC 021219 PG 3, 1-16-73

ORIGINAL PAGE IS
OF POOR QUALITY

Table 3.2-16 Continued

	MTBF (HRS)	FAIL/10^6 OPER HRS	ENVIRO	ADJ FAC	ADJ VAL FAIL/10^6 HR	MTTR	SOURCE
ENERGY STORAGE							
NI CAD BATTERIES	104,167	9.60	ACFT-FLT	20	.48		EAC COORD SH SEP 25, '73
SILVER ZINC BATTERIES	171,527	5.83	SAT	NONE	5.83		02 AGM 12101-1, PG 18
THERMAL CONTROL							
HEAT PIPE	30,000	33.33	GND	2	16.67		N544-77-3
COMMERCIAL REFRIGERATION							
UNIT (10-20T)							
RADIATOR	7,407	135	SHP	20	6.75		FRD VOL I, PG 250
PUMP COOLANT	1,538	650	ACFT-FLT	30	21.67		RADC-TR-75-22, PG 2-181
PUMP MOTOR	8,000	125	GND	6	20.83		LMEC 69-7 VOL I TABLE 1-34 PG 1-82
CONTROLS	166,667	6.0	GND	4	1.5		FRD VOL I, PG 177
MICROWAVE GENERATORS	N/A						
PREAMPLIFIERS	N/A						
POWER AMPLIFIERS	N/A						
PHASE CONTROL SYS	N/A						
CENTRAL	N/A						
SUB ARRAY	N/A						

Table 3.2-16 Continued

	MTBF (HRS)	$FAIL/10^6$ OPER HRS	ENVIRO	ADJ FAC	ADJ VALUE $FAIL/10^6 HR$	MTTR	SOURCE
WAVEGUIDES	N/A						
SLOTTED WAVEGUIDES	N/A						
END WALLS	N/A						
FREED WAVEGUIDES	N/A						
POWER DIVIDED	N/A						
LARGE COMPUTER COMPLEXES							
E-3A IBM DATA PROC FUNC GRP	1,500	666.67	ACFT-FLT	12	55.56		MEMO 2-6682-0020-007
IBM COMP COMPLEX (360-75)	R=.944		GND				191 PD-12
B1 COMPUTING EQUIP (CONTROL UNIT COMPLEX)	500	2,000	ACFT-FLT	12	166.67		D229-10096-1

ORIGINAL PAGE IS OF POOR QUALITY

ORIGINAL PAGE IS OF POOR QUALITY

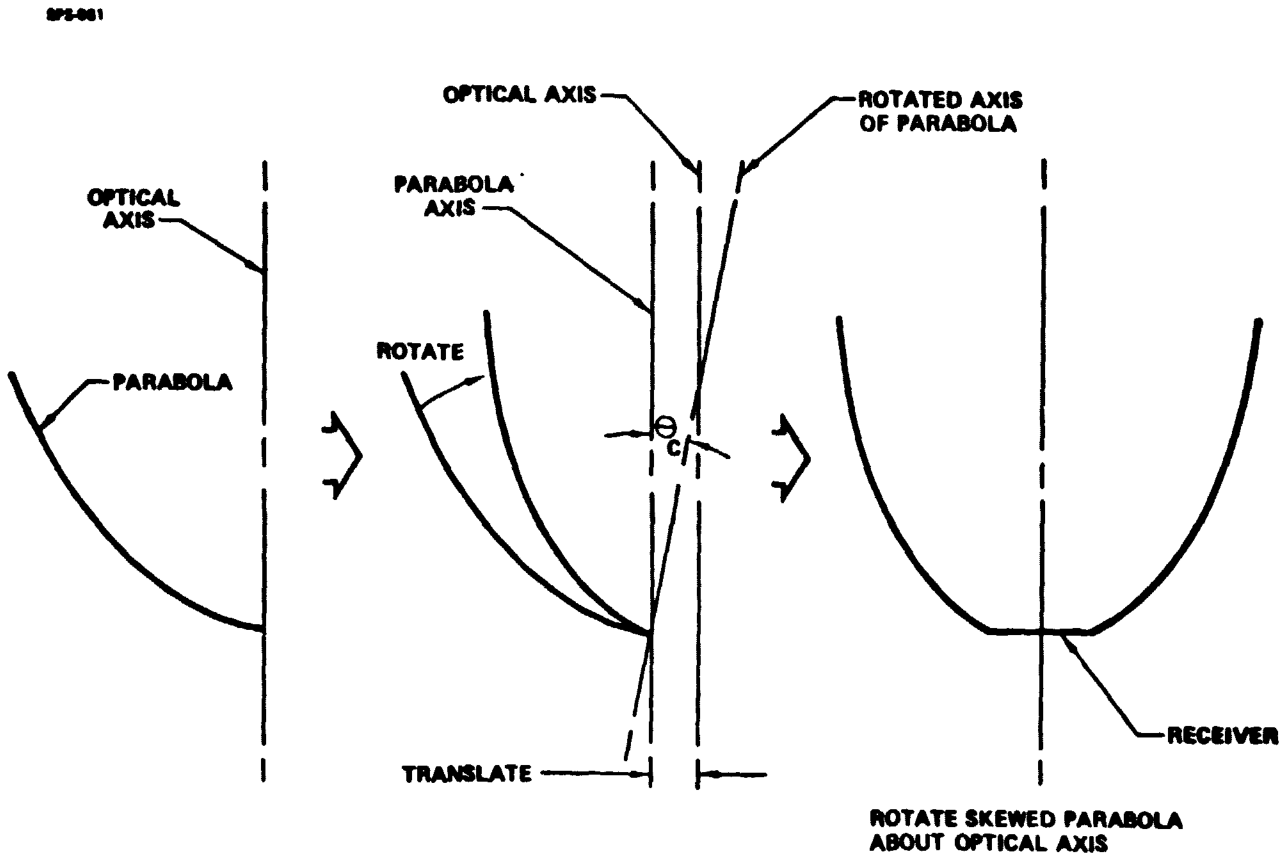

Figure 3.2-73 CPC Surface Generation

CPC's represent an alternative means for concentrating solar energy on photovoltaic arrays. Boeing developed a concentrated SPS photovoltaic array concept using CPC's under contract NAS 8-31628. In the current study, an evaluation of the performance of CPC's was performed. In particular, the following questions were answered to help determine the advantages or disadvantages of CPC's compared to more conventional "V" ridge concentration concepts.

1. What is the off-axis performance of three-dimensional CPC's?

2. How does the choice of acceptance half-angle, θc, affect CPC performance?

3. What is the distribution of solar flux over the concentrator receiver area?

4. How is the geometry of the CPC affected by acceptance half-angle?

A Monte-Carlo ray-trace computer program was modified to accept the CPC geometry. The nominal angle between the CPC optical axis and rays entering the aperture was specified along with the dispersion angle between rays (0.5 degrees for solar flux at Earth orbit).

Other input variables were CPC acceptance half angle θc, concentration ratio and receiver diameter. The program computed the distribution of flux on the receiver aiea, and average number of reflections experienced by all rays reaching the receiver.

Computed off-axis performance of a three dimensional CPC with a concentration ratio of 6 is shown in Figure 3.2-74. The total energy loss is broken down into cell reflection loss, mirror reflection loss and rejection loss. The cell reflection loss accounts for the fact that 10% of the energy reaching the cell was reflected. Mirror reflection loss arise from the absorption or solar energy by the CPC reflective surface. In this particular case, it was assumed that 15% of the solar energy incident on CPC surfaces was absorbed and 85% reflected specularly. Rejection loss accounted for energy which was reflected back out of the CPC aperture after several reflections from the CPC surface. This rejection loss would occur if the CPC surface were a perfect reflector and the receiver a perfect absorber. At high off-axis angles, the amount of energy reflected back out the aperture became significantly large. A rule of thumb for estimating the off axis performance of CPC's is that rejection loss is only a few percent until the angle between the optical axis and incident rays approaches the acceptance halt angle.

A comparison of off-axis performance of CPC's with 24^o and 11.5^o acceptance half-angles is presented in Figure 3.2-75. Concentration ratio is 6 for both options. Where the angle between the CPC optical axis and incident rays was small, total performance of the 11.5^o acceptance half-angle CPC was greater than that of the 24^o half-angle CPC. The performance of the 11.5^o acceptance half-angle CPC dropped off steadily at off-axis angles in excess of 8^o while the 24^o acceptance half-angle CPC performance remained essentially constant out to an off-axis angle of 16^o to 20^o and then decreased rapidly.

Figure 3.2-76 shows a typical predicted flux distribution on the receiver surface of a concentration ratio 6 CPC for a zero degree off-axis angle. Local concentration ratio, from the receiver centerline out to 30% of radius, was constant at 0.9. This area received only those rays which entered the aperture and intercepted the receiver with no intermediate reflections from the CPC walls. Energy reflected from CPC walls fell in two distinct rings, one centered about a radius ratio of 0.6, and one at the outer radius of the receiver.

The relationship between CPC depth and acceptance half-angle is shown in Figure 3.2-77 for a concentration ratio 6 device. Transaction of the CPC produces a shorter and therefore lighter device, however, off axis performance is degraded as was shown in Figure 3.2-75.

ORIGINAL PAGE IS
OF POOR QUALITY

SPS-962

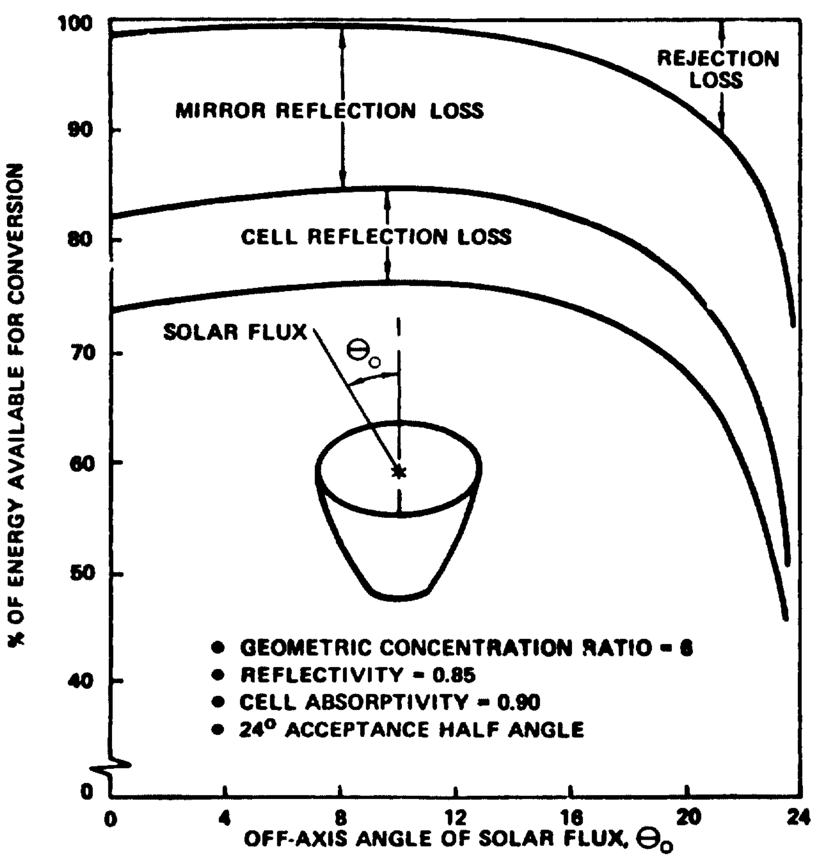

Figure 3.2-74 CPC Off-Axis Performance Breakdown

SPS-963

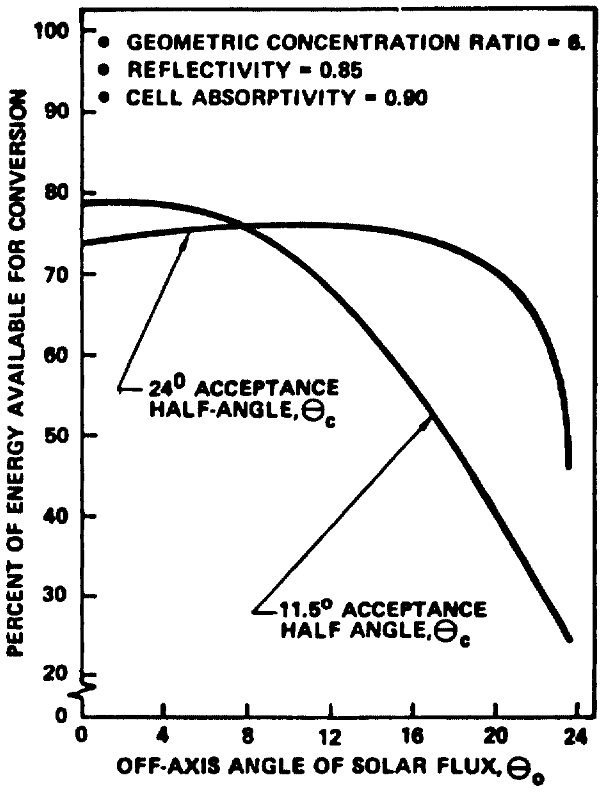

Figure 3.2-75 Effect of Acceptance Half-Angle On Off-Axis Performance

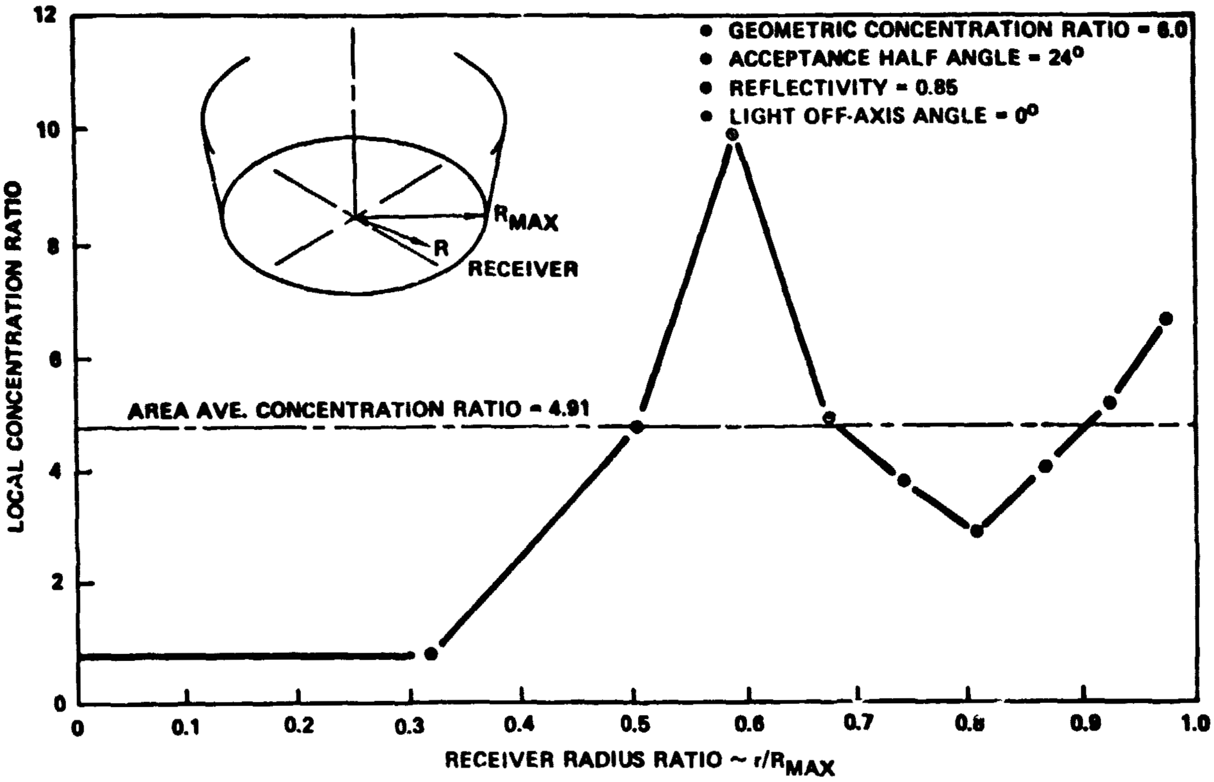

Figure 3.2-76 Flux Distribution On CPC Receiver

SPS-985

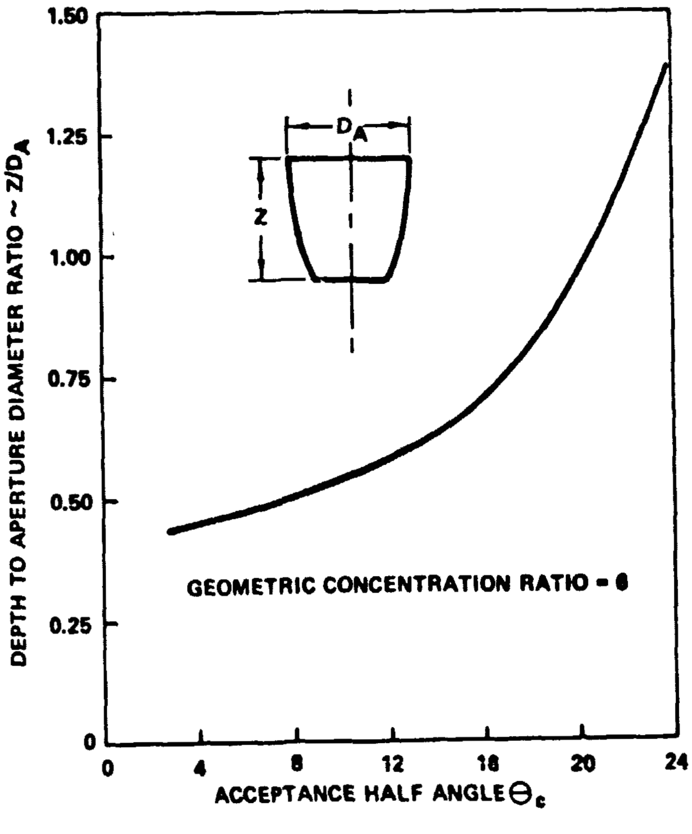

Figure 3.2-77
Relationship Between CPC Dimensions And Acceptance Half-Angle

ORIGINAL PAGE IS
OF POOR QUALITY

Table of Contents

202
1
[redacted]

3.3 Thermal Engine SPS Configuration Analyses

This section of the Part I report covers the thermal engine options. There are three varieties: (1) thermionics, which is a type of non-mechanical engine that works on thermodynamic principles, (2) gas cycle, and (3) Rankine vapor cycle.

In Part I, several key problems and issues were addressed: on a system involving plumbing, pumps, valves, and rotating machines, reliability and maintenance is an important question as is the definition of cycle state points. Power generation module size was also addressed. Going from 4 to 16 modules, for example, actually turned out to make the system lighter. We have consistently endeavored to reduce the mass of the system. We have carefully looked at what materials we use, as regards costs, and to the general availability of reserves, etc In the thermal engine system, up to this point, we have used reflectors made up of a large number of individual facets, which must be pointed. We analyzed the impact of flying a thermal engine satellite module by self-power from low orbit to geosynchronous orbit, and what must be done to the module in order to accomplish that. And we considered what must be done with thermal engine component designs to package them into the launch vehicles. We had to make some design adjustments in this area.

Principal thermal engine results were as follows: Three options were recommended for rejection. (1) the thermionics SPS system continued to show total masses approaching twice those of Brayton, potassium Rankine, or silicon photovoltaic. (2) Organic Rankine is temperature limited by pyrolysis of the material such that good cycle efficiency cannot be obtained at heat rejection temperatures of practical interest. (3) Steam Rankine is not temperature limited by water decomposition but the thermodynamic properties of water are such that condensation must take place at lower temperatures than desired. A steam cycle operated at the minimum mass statepoints would be almost a steam Brayton cycle, with no advantages over helium Brayton.

The Brayton and potassium vapor Rankine cycles are quite attractive from the mass and cost standpoint. Costs for these options are quite comparable and were based on industrial turbogenerator experience.

Conceptual design solutions were developed for all of the major system elements. The general appearance of the thermal engine SPS's was significantly modified to enhance constructability. This included reducing the module size from about 4000 megawatts to about 1000 megawatts (onboard) output and changing to a simpler concentrator geometry.

Sensitivity analyses were conducted on Brayton and Rankine turbine inlet temperatures. The sensitivity was small enough to merit consideration of lower temperatures for developmental systems; this could reduce development cost.

The three types of thermal engines have common subsystem elements as indicated by Table 3.3-1. For example, a reflector (the optical concentrator) is used by all candidates. The cavity absorber is also common, as is the use of graphite-epoxy structure throughout, and the use of heat pipe radiators. The thermionic system does not use pumped fluids in the radiator; localized heat pipes are used instead. Turbo generators are not required in the thermionic system; however, it is necessary to use motor generators to step up the low voltage DC output of the thermionic diodes to high voltage DC. Therefore, the thermionic system has rotating components also.

Subsystems analyses are described primarily in terms of the Brayton reference systems; these results were also applied to the other options.

3.3.1 Solar Brayton Cycle SPS

The simplified schematic shown in Figure 3.3-1 illustrates the fundamental elements of the Brayton SPS.

The solar concentrator reflects and focuses highly concentrated sunlight into the cavity absorber aperture. The cavity absorber is an insulated shell lined with heat exchanger tubing. Helium gas flowing through this tubing becomes heated (simultaneously preventing cavity over heating).

Hot helium expands through the turbine, doing the work of turning the compressor and the generator. The compressor forces the helium flow around the cycle loop. Minimum gas temperature occurs at the exit of the cooler, which is a gas-to-liquid heat exchanger interfacing the helium loop to the radiator system. The recuperator is a gas-to-gas heat exchanger which increases the system efficiency by exchanging energy between the "hot" and "cold" sides of the cycle. The recuperator causes the average turbine temperature to be higher and the average compressor temperature lower for given maximum and minimum cycle temperatures.

Waste heat is rejected by a liquid metal radiator system. The working fluid is a solium-potassium eutectic (NaK). NaK pumping is by a motor/pump system drawing power from the generator.

ORIGINAL PAGE IS
OF POOR QUALITY

Table 3.3-1 Thermal Engine Candidates Have Common Elements

	THERMIONIC	BRAYTON	RANKINE
FACETED CONCENTRATOR	✓	✓	✓
CAVITY ABSORBER	✓	✓	✓
GRAPHITE EPOXY STRUCTURE	✓	✓	✓
PUMPED RADIATOR MANIFOLDS	—	✓	✓
HEAT PIPE RADIATOR	✓	✓	✓
TURBOGENERATORS	—	✓	✓

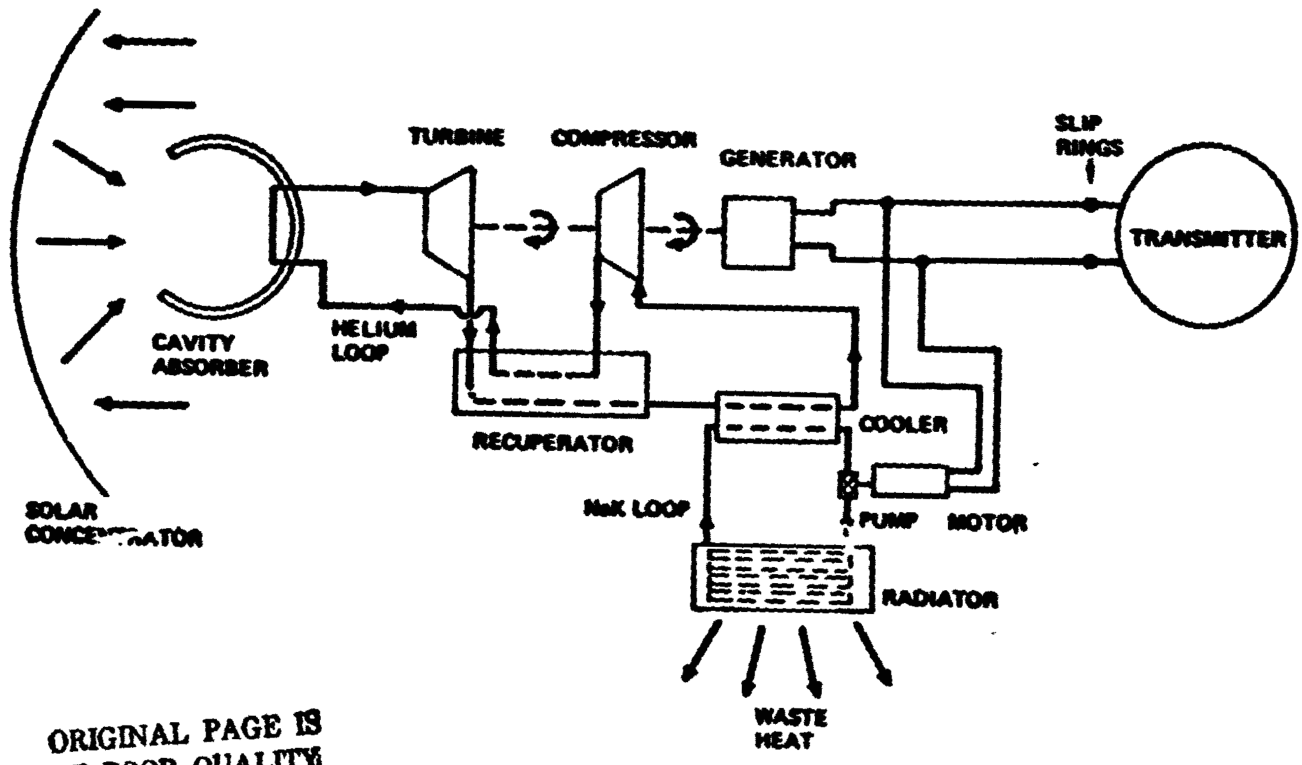

ORIGINAL PAGE IS
OF POOR QUALITY

Figure 3.3-1 Solar Brayton Cycle

3.3.1.1 Configuration Evolution

Seven changes from previous study results were introduced as follows:

1. The JSC MPTS was used, with two 5-GW transmitters supplied at 40 000V.
2. Direct current power distribution (resulted from this change).
3. Graphite epoxy structure was employed.
4. Beam builders were assumed for structure fabrication.
5. The SPS was sized for average effective insolation.
6. Reflector degradation data were incorporated.
7. Hardware was sized for shroud of two-stage ballistic/ballistic HLLV (roughly 17m dia by 25m long).

The ground output remains at 10 GW, but is now divided between two transmitters. These are Klystron type, at 40,000 volts dc. As a result, the SPS is less massive with a d.c. power distribution system.

The structure system baselined is graphite epoxy. Triangular beams are formed in orbit, from canisters of flat parts, using "beam machines." The system is sized to provide an annual average output of 10 GW despite variations in solar illumination (including occultation). System sizing also includes allowance for radiation induced degradation of the plastic film reflectors (using test data from project "ABLE") All hardware must also be transportable within a 17 meter shroud diameter.

The initial configuration resulting from these changes is shown in Figure 3.3-2.

The reference SPS was flown perpendicular to the orbit plane – rather than directly facing the sun. It maintained a horizontal attitude with respect to the Earth's equator below. This attitude avoids the persistent gravity gradient torques that would result from directly facing the sun, and reduces control problems and propellant expenditure. As a result, the sunlight incident on the satellite varies seasonally with direction, as shown in Figure 3.3-3. There is, associated with this apparent motion, a concentrator performance loss of several percent.

By rolling the satellite 180° about the axis to the sun at each equinox, the apparent motion of the sun could be halved as illustrated in Figure 3.3-4.

FOLDOUT FRAME 1

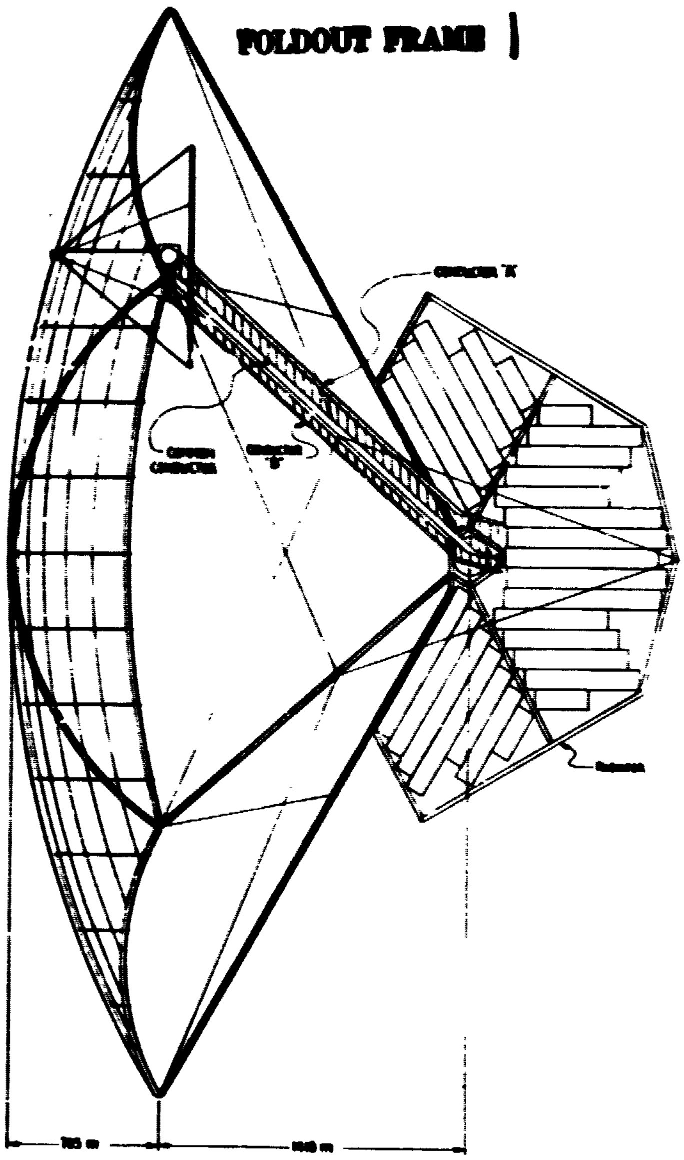

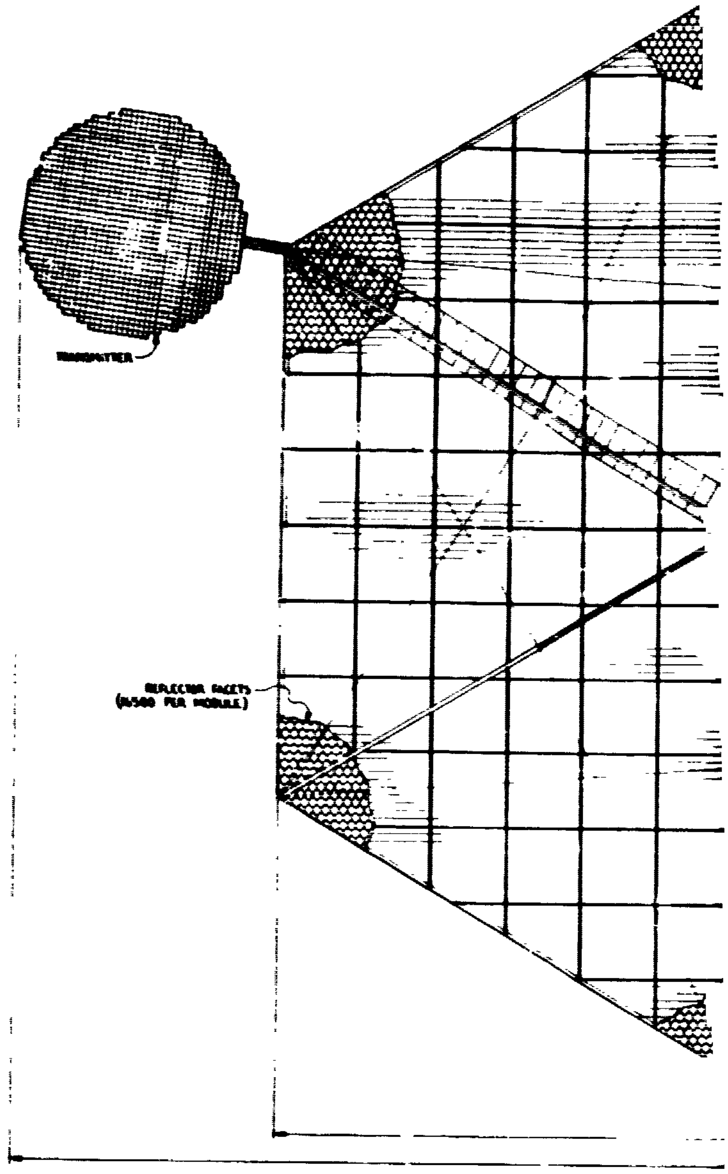

ORIGINAL PAGE IS
OF POOR QUALITY

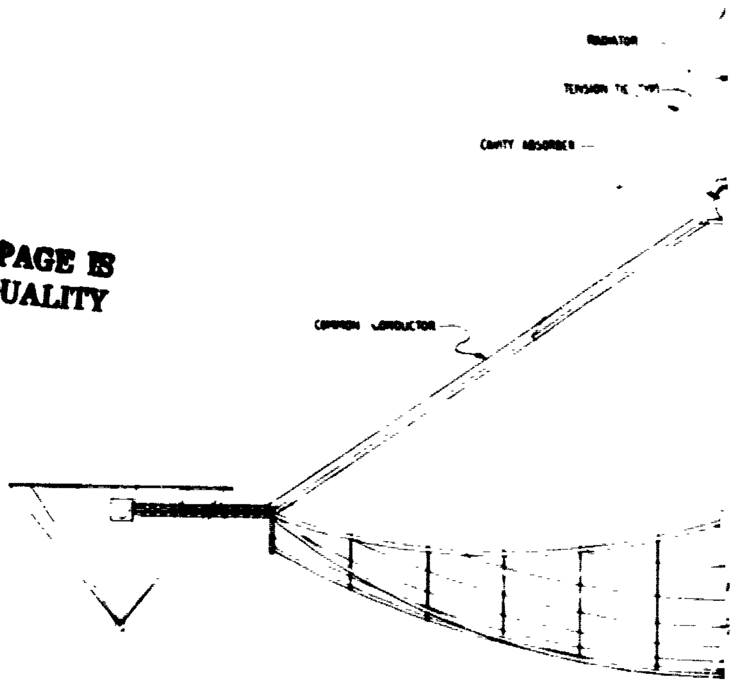

FOLDOUT FRAME 2

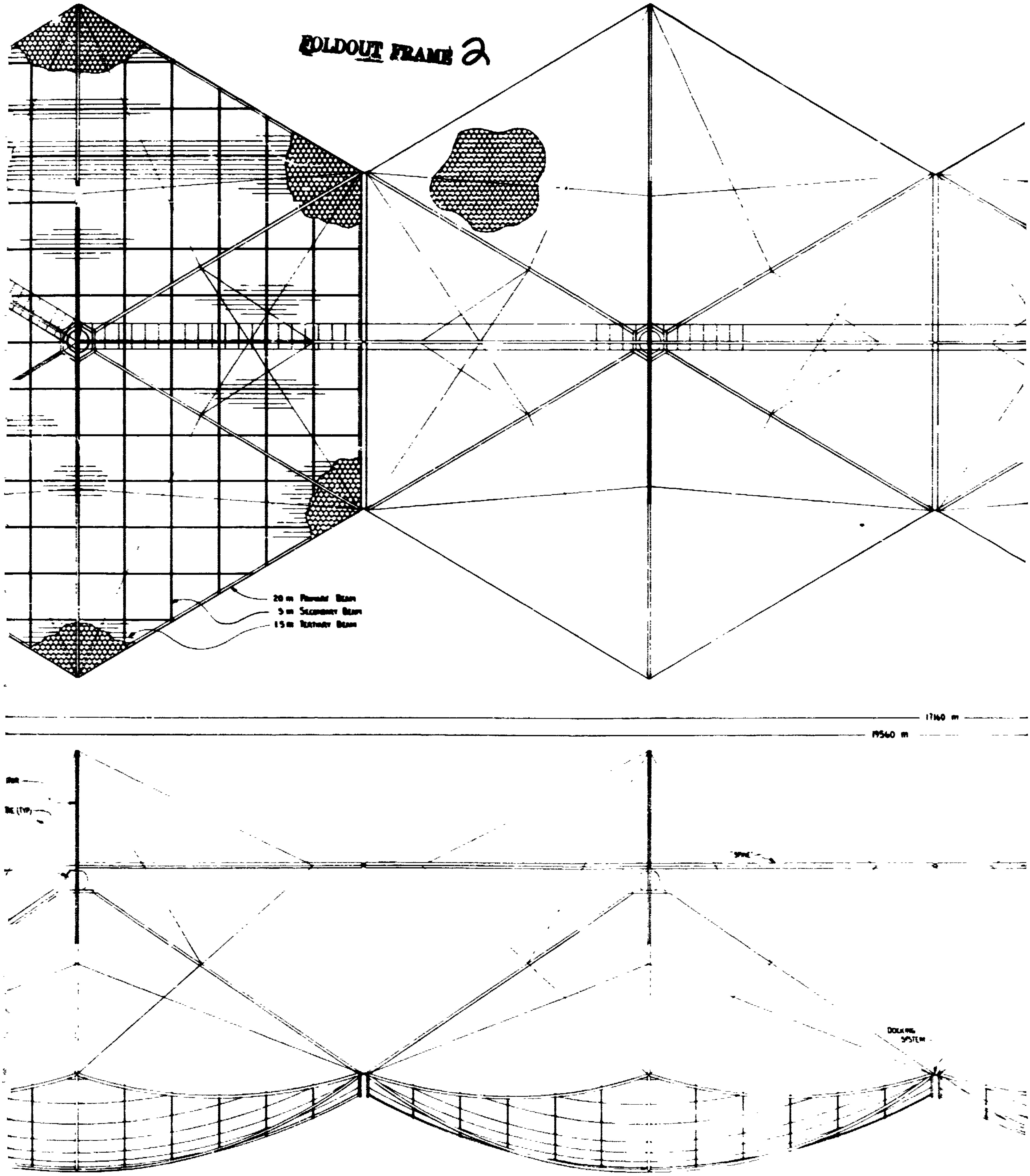

FOLDOUT FRAME 3

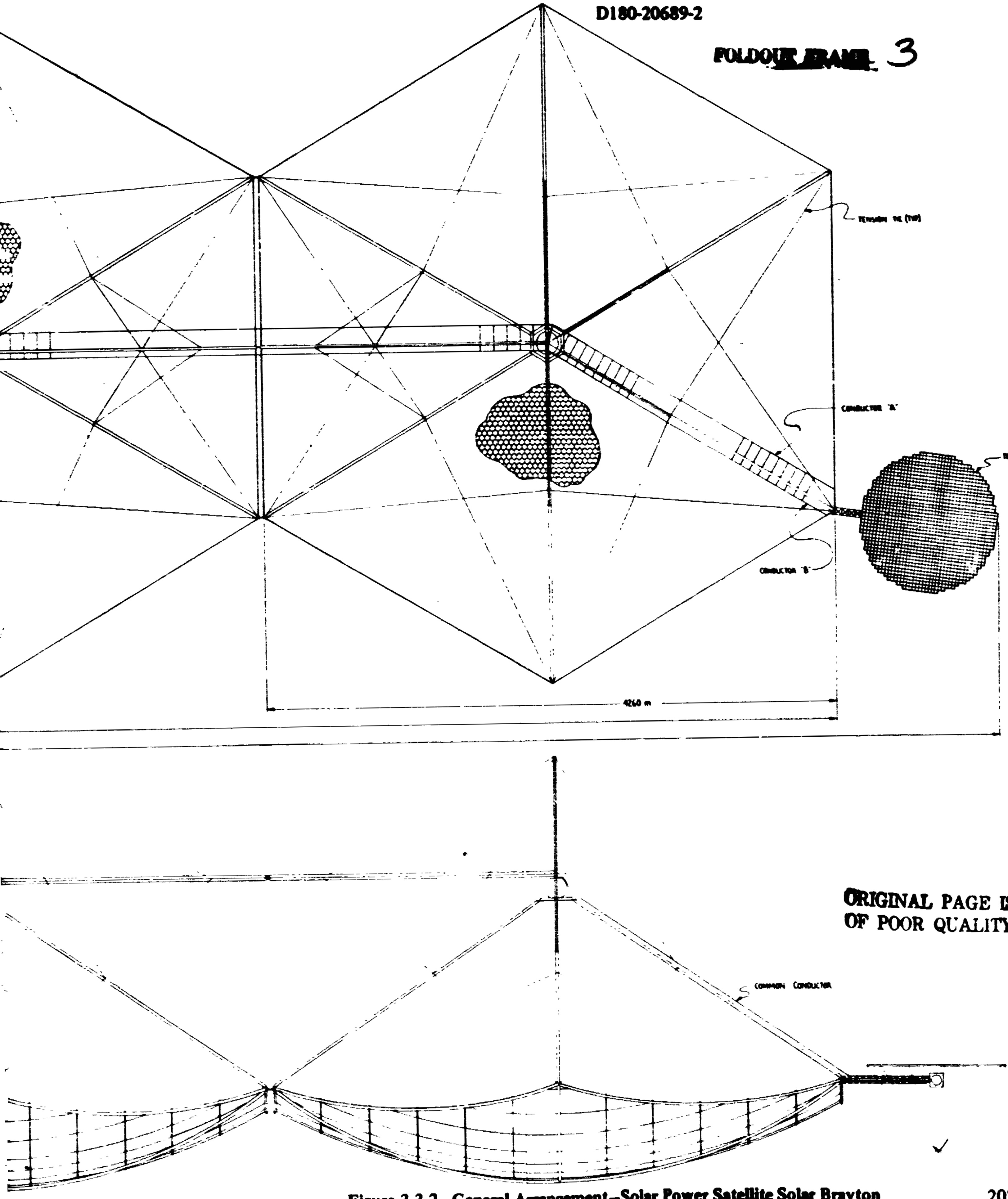

ORIGINAL PAGE IS
OF POOR QUALITY

Figure 3.3-2 General Arrangement—Solar Power Satellite Solar Brayton

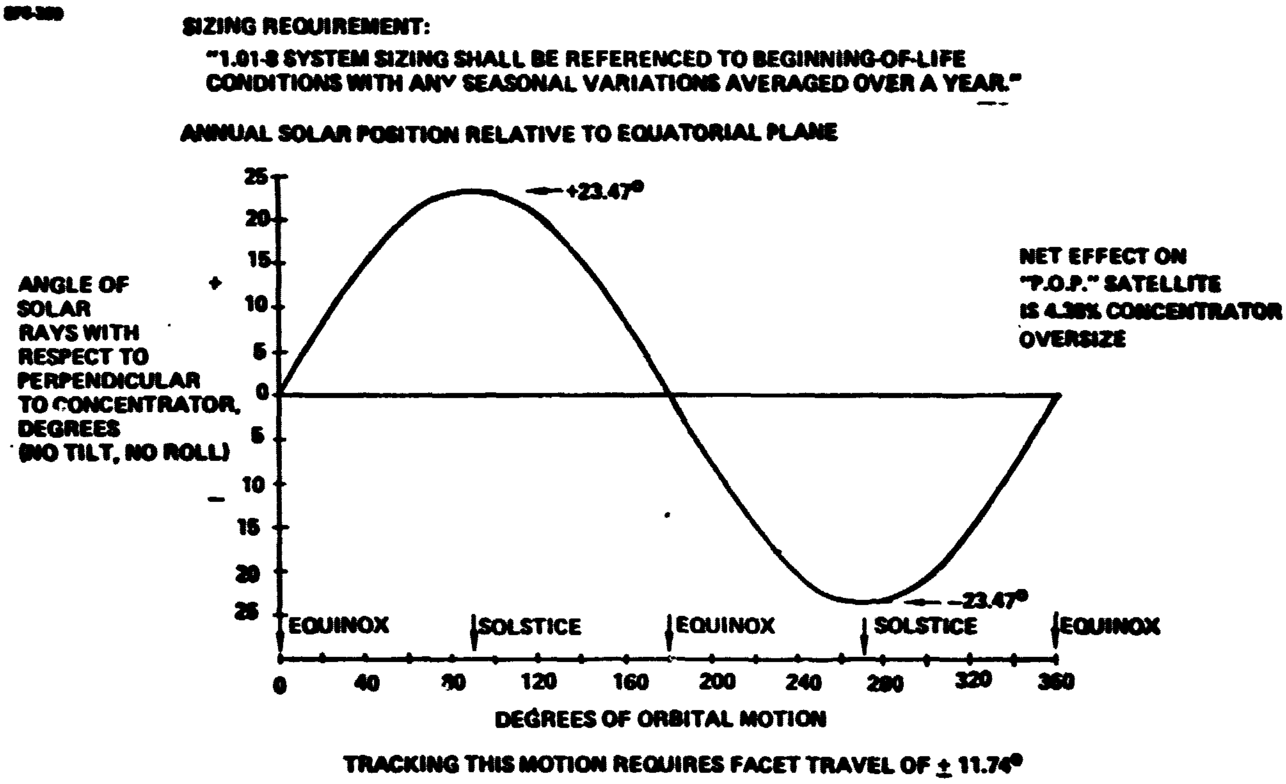

Figure 3.3-3 SPS Orientation

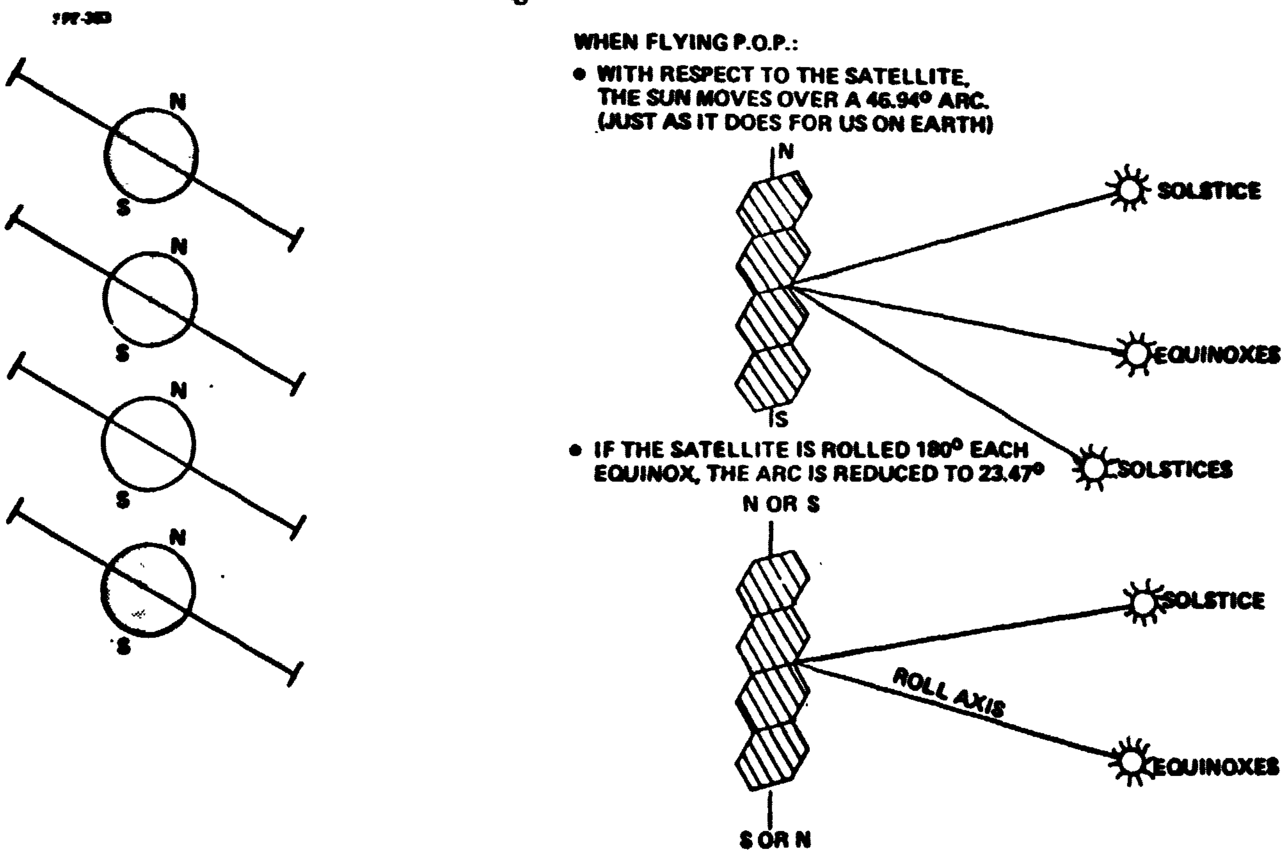

Figure 3.3-4 Solar Orientation Effects

ORIGINAL PAGE IS
OF POOR QUALITY

The apparent solar motion with respect to the tilted solar concentrator dishes is only + and -11.74° shown in Figure 3.3-5.

If the roll motion is accomplished by thrusters near the antennas, only 50,000 kg of propellant would be required at each equinox for a specific impulse of 10,000 seconds. If the tips are to see no more than 0.001 G (0.00982 m/sec^2) four hours would be required for the roll maneuver.

An alternative approach yielding higher efficiency would be articulation of the four dishes, which would then be constantly adjusted to face the sun (roll would not be required).

The tilt and roll maneuver increases annual system efficiency about 7%. Articulation would yield a total improvement of about 10%.

The general arrangement of the resulting SPS configuration is shown in Figure 3.3-6. Modules are attached mechanically at three points: two apexes of the concentrator "dish" and the end of the "spine."

The four modules are each mounted with an 11.74° tilt with respect to the long axis. Note that antenna mounting is at the apex of the hexagonal concentrators rather than at the center of an edge. This allows power distribution down a cavity absorber support arm. Thus the north-south axis of the SPSis not parallel to the spine.

The construction concept selected for the photovoltaic SPS designs in effect "extrudes" the satellite. The initial concept for construction of the four module thermal engine satellite involved a small facility surrounding the cavity absorber and "free-form" construction of the solar concentrators. Construction equipment moved about using the SPS structure as support. A "facilitized" construction concept for the thermal engine "dish" concentrators was developed. While the concept appears feasible it does not appraoch the simple "extrusion" concept.

Therefore, the thermal engine SPS configuration was revised to permit "extrusion." One module of such a satellite is shown in Fig. 3.3-7. As with the previous hexagonal dish configuration, a "halo" radiator surrounds the cavity absorber, which is mounted above the solar concentrator by two support arms. The solar reflector facets are arranged in the form of a trough; the trough is a straight line along the north-south axis of the satellite and is parabolic in cross section. The north-south dimension of the module is 0.707 of the width of the trough; looking down on the module the facet area would be seen to be circular except for the straight portions at the north and south ends.

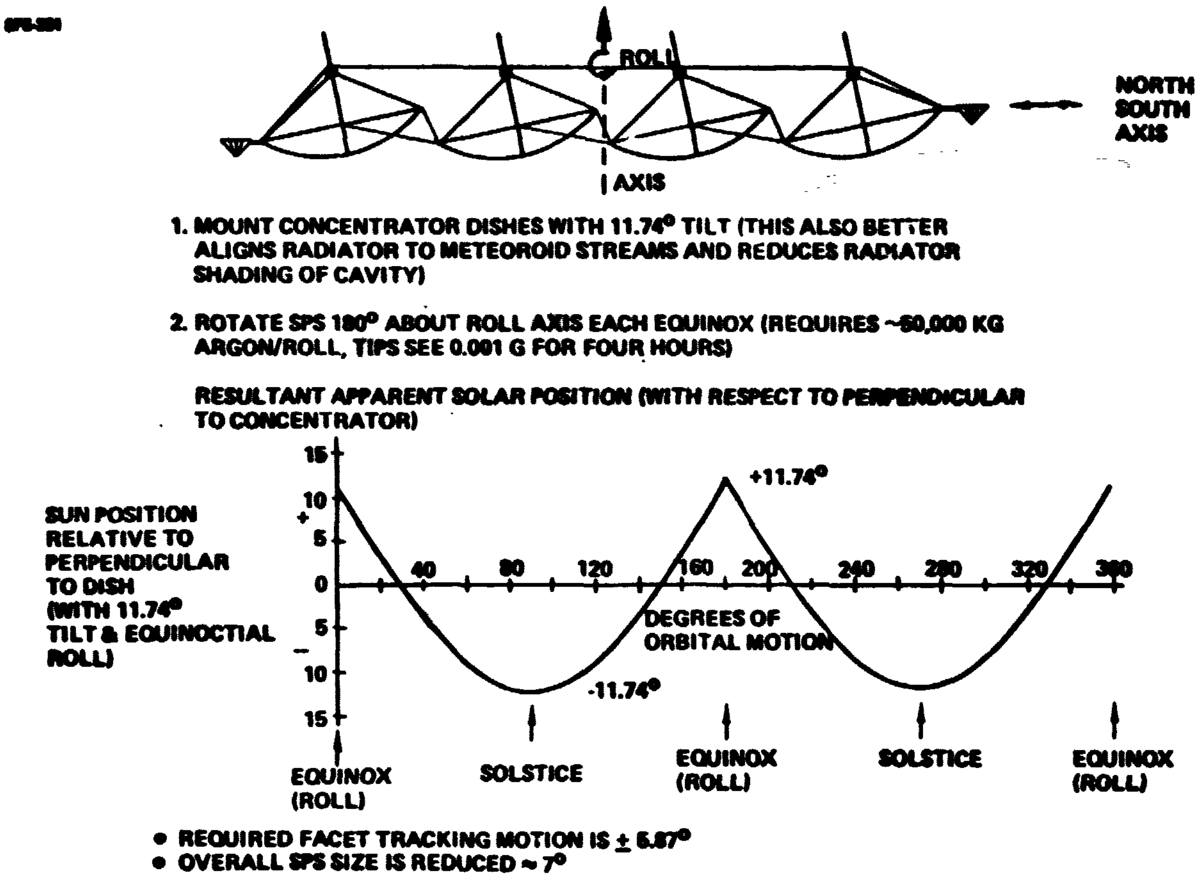

Figure 3.3-5 An Approach To Achieving Higher Annual Efficiency: "Tilt And Roll"

ORIGINAL PAGE IS
OF POOR QUALITY

FOLDOUT FRAME 1

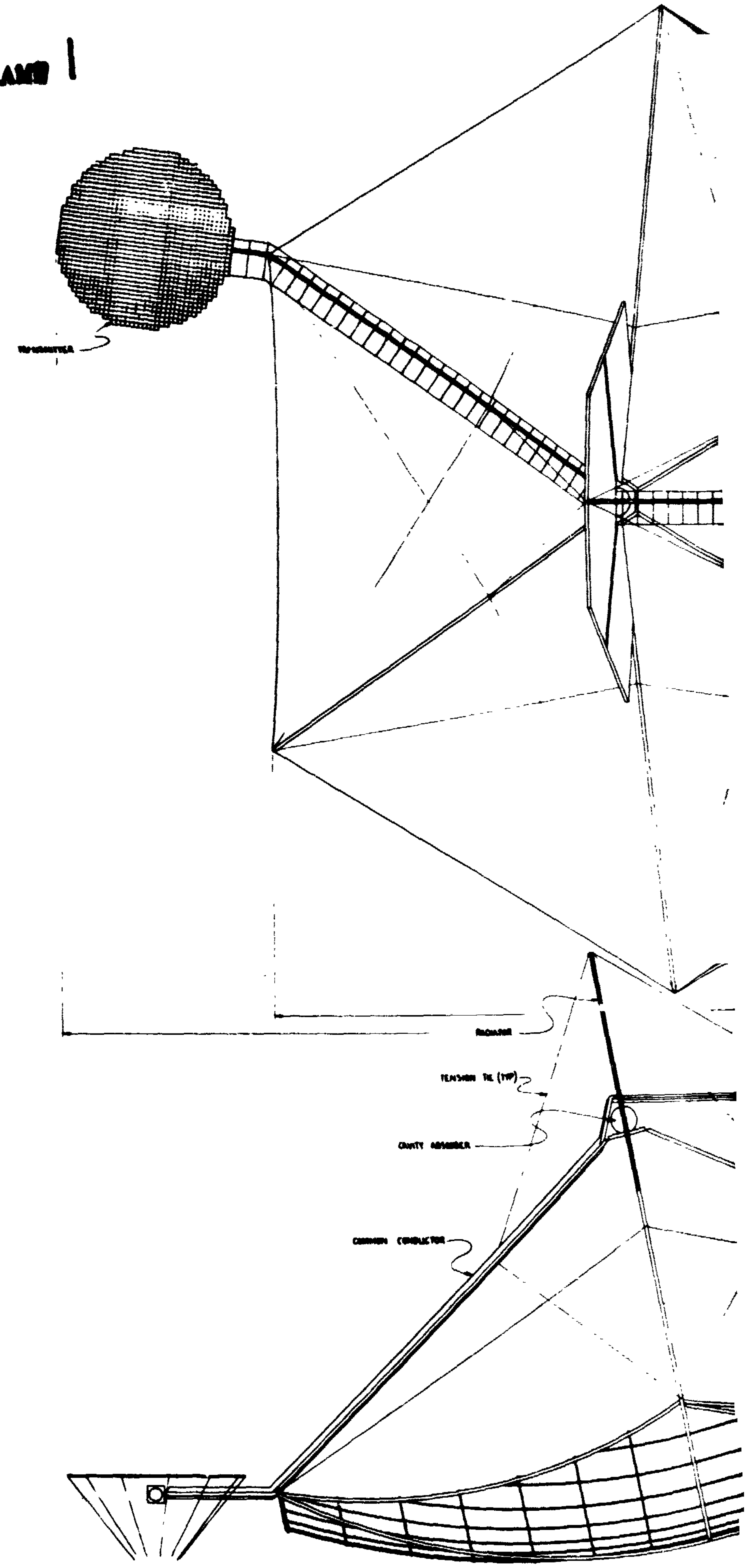

FOLDOUT FRAME 2

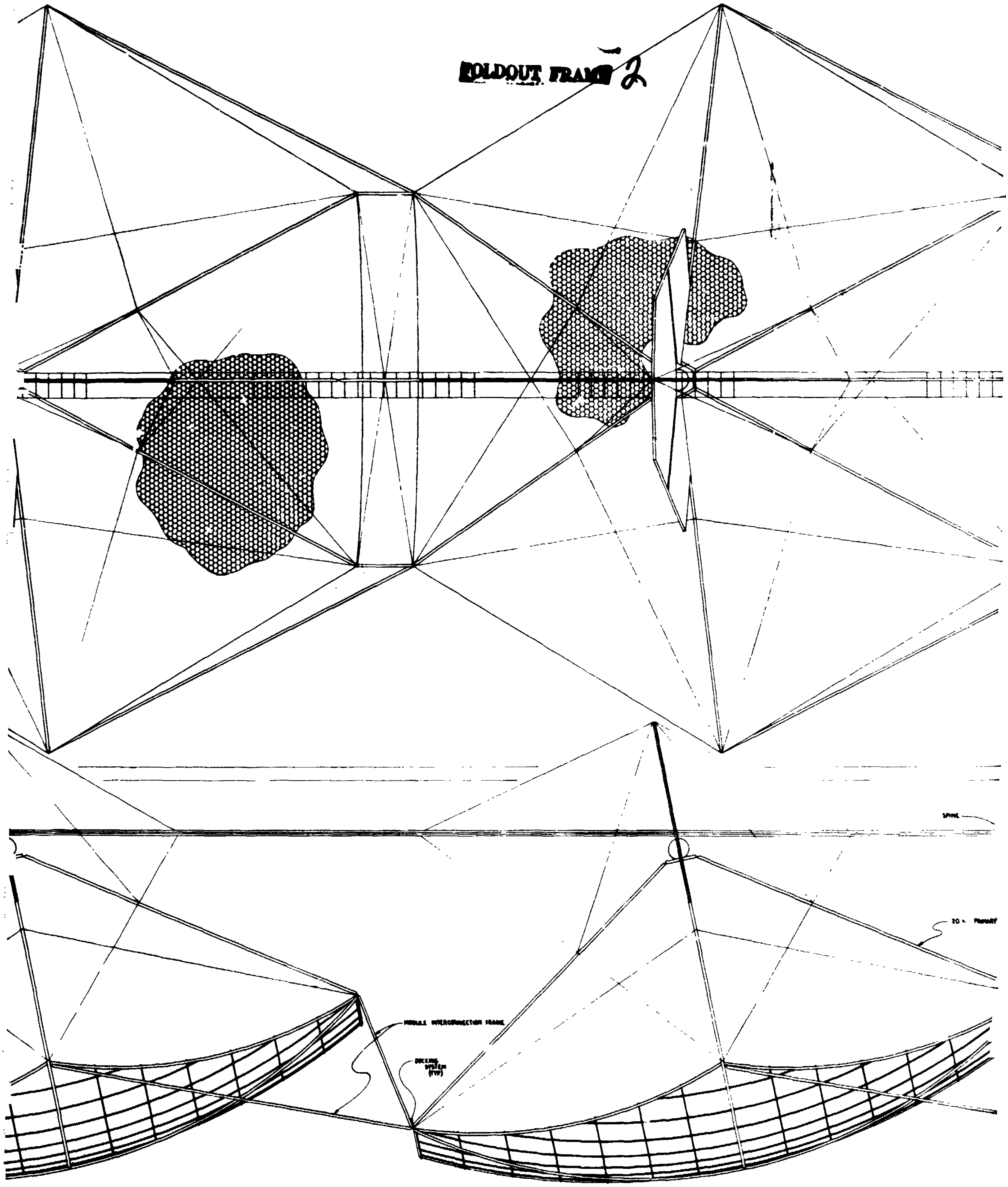

FOLDOUT FRAME 3

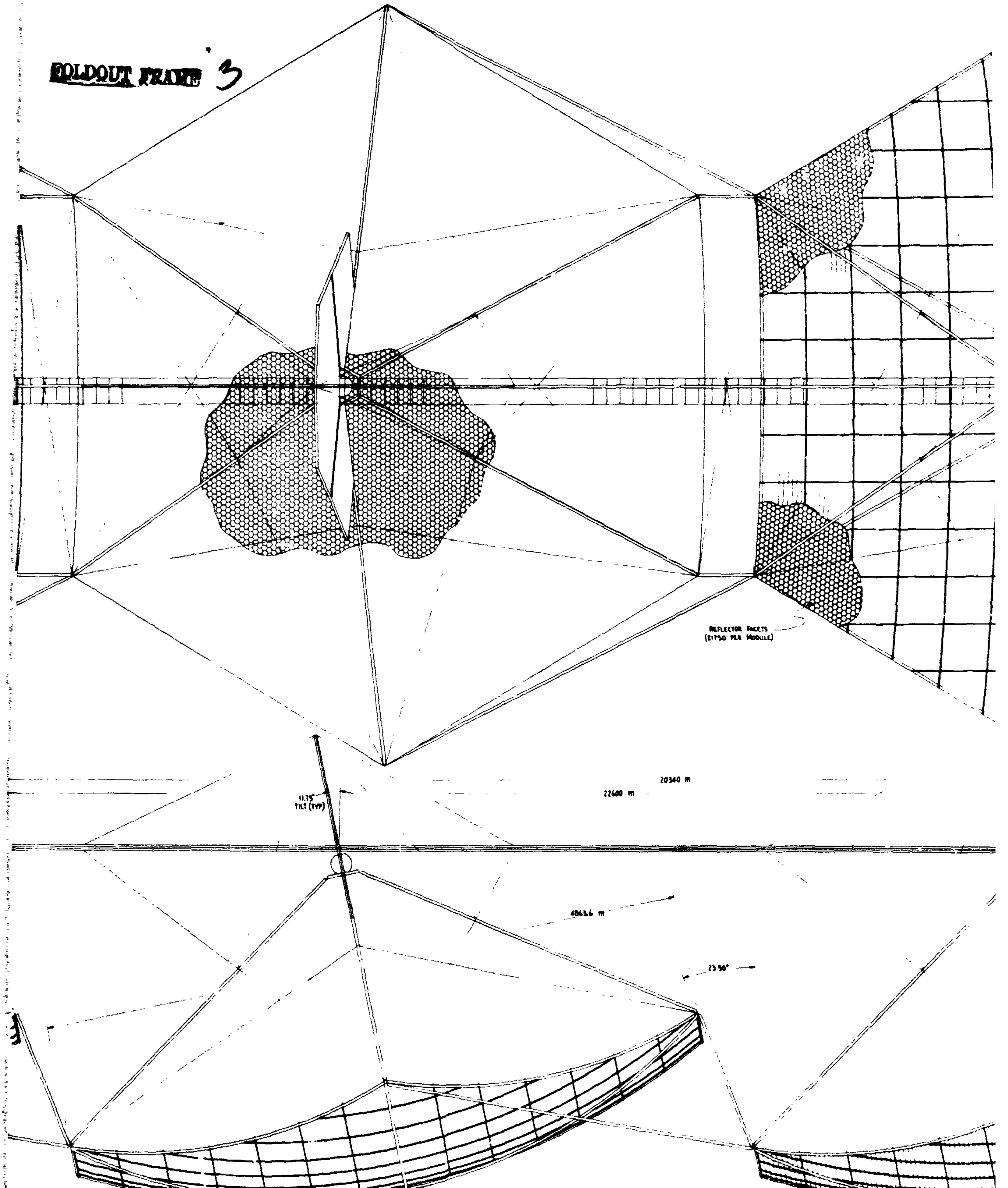

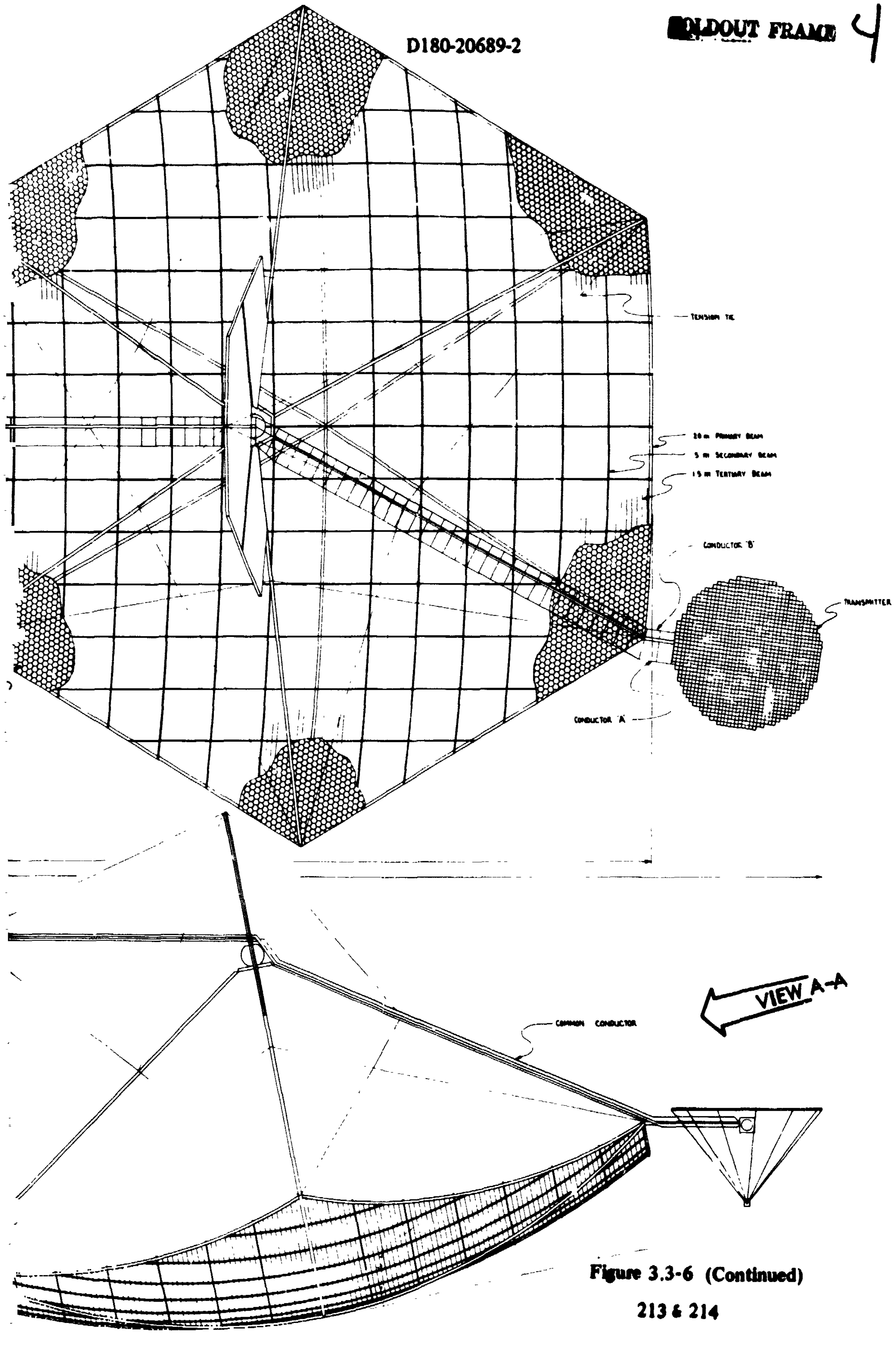

Figure 3.3-6 (Continued)

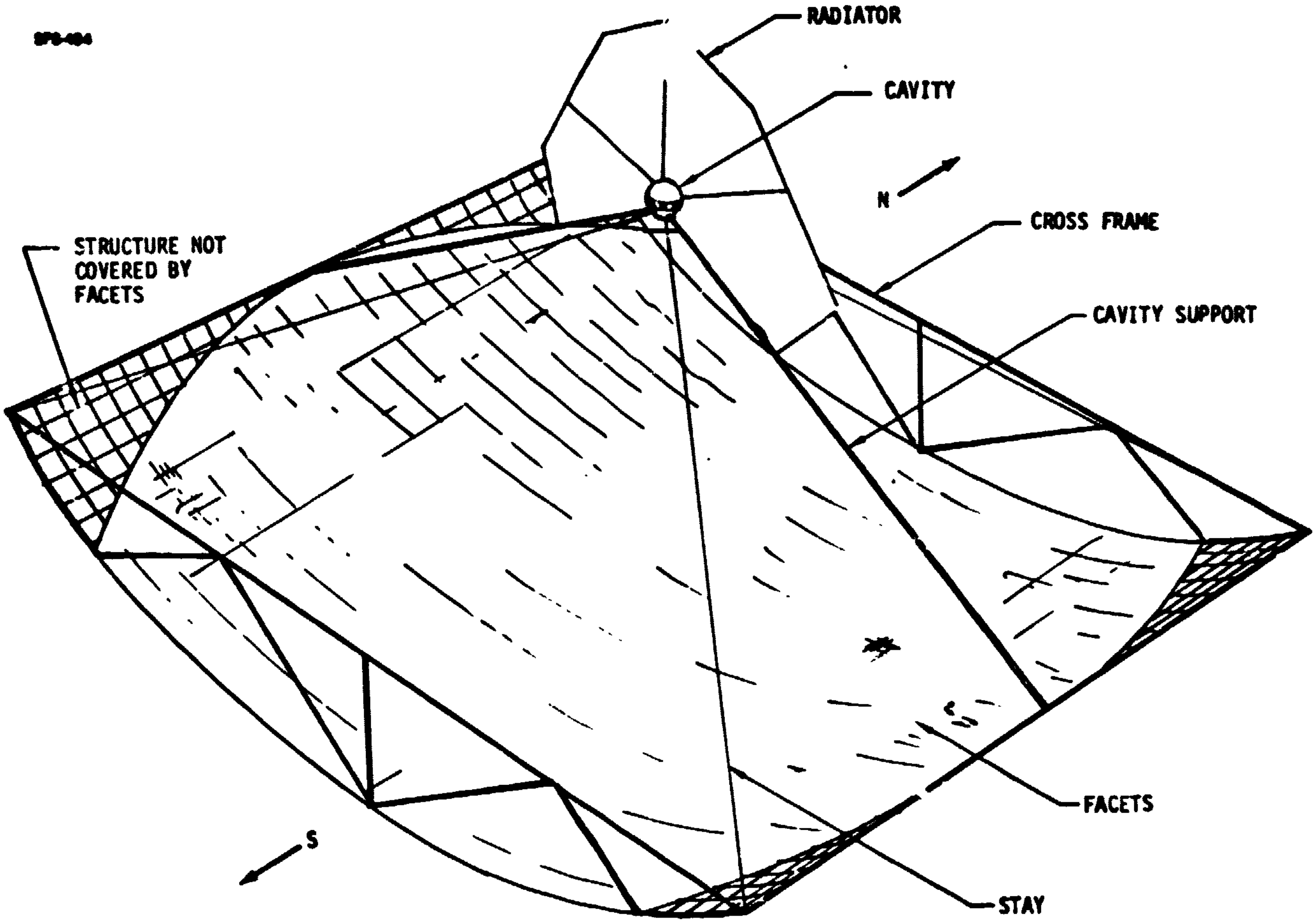

Figure 3.3-7 Trough Type Module

ORIGINAL PAGE IS
OF POOR QUALITY

While better suited for construction, this concept will not have the optical efficiency of the dish configuration. The efficiency relative to the 1.0 of a perfect circular paraboloid is expected to 0.92; the previous hexagonal dish efficiency was 0.96. In the hexagonal dish the facets were arranged with a space just large enough to preclude mechanical interference. In the trough arrangement the facets under the cavity can also be close together. At the north and south edges the facets must be tilted and spaced apart to prevent shadowing. The antishadowing gaps between facets are now estimated at 16% of the reflector area. Thus the concentrator structure is increased 16% in area over hexagonal dish, but the facet area is increased only 4.3%.

At the time this change was made, the module size was also reduced, therefore, requiring a total of 16 modules to obtain the required total output. Such a system using the "trough" concept described above is shown in Fig's 3.3-8 and 3.3-9. Six modules are arranged along the north-south axis, with the transmitters mounted at each end. Three power distribution "spines" interconnect the modules and antennas.

This configuration provides two benefits in addition to constructability:

- The module size is appropriate to a large-scale pilot plant;
- An entire module can be shut down for servicing of machinery without excessive impact on plant output.

3.3.1.2 Brayton Cycle Analysis

Brayton cycle analysis employed a hierarchy of manually-interfaced computer models initially developed during an earlier study. The overall modeling approach is diagrammed in Figure 3.3-10. Concentrator-absorber and radiator models and analyses are described under sections 3.3-4 and 3.3-6, respectively. Cycle analyses were conducted over a range of temperatures. Results are shown in Figures 3.3-11 and 3.3-12. Table 3.3-2 summarizes state points for the Brayton system at two representative temperatures.

To facilitate the evaluation of intercooling and reheat as potential performance improvement features for the closed Brayton cycle a simple efficiency prediction technique has been developed which closely approximates the more detailed computer analyses. In this technique the cycle efficiency is calculated by:

$$\text{cycle} = \eta_{misc}\eta_c\eta_T E_R \quad \frac{\left(T_4 + \frac{T_3 - T_4}{2}\right) - \left(T_o + \frac{T_1 - T_o}{2}\right)}{\left(T_4 + \frac{T_3 - T_4}{2}\right)}$$

where:

misc	=	Efficiency factors of bearing loss & turbine disk cooling = 0.98
c	=	Compressor efficiency = 0.875
T	=	Turbine efficiency = 0.920
E_R	=	Recuperator effectiveness = $\frac{T_2 - T_1}{T_4 - T_1}$
T_o	=	Cooler gas outlet temperature
T_1	=	Compressor outlet temperature
T_2	=	Cavity heat absorber inlet temperature
T_3	=	Cavity absorber outlet temperature
T_4	=	Turbine outlet temperature

ORIGINAL PAGE IS
OF POOR QUALITY

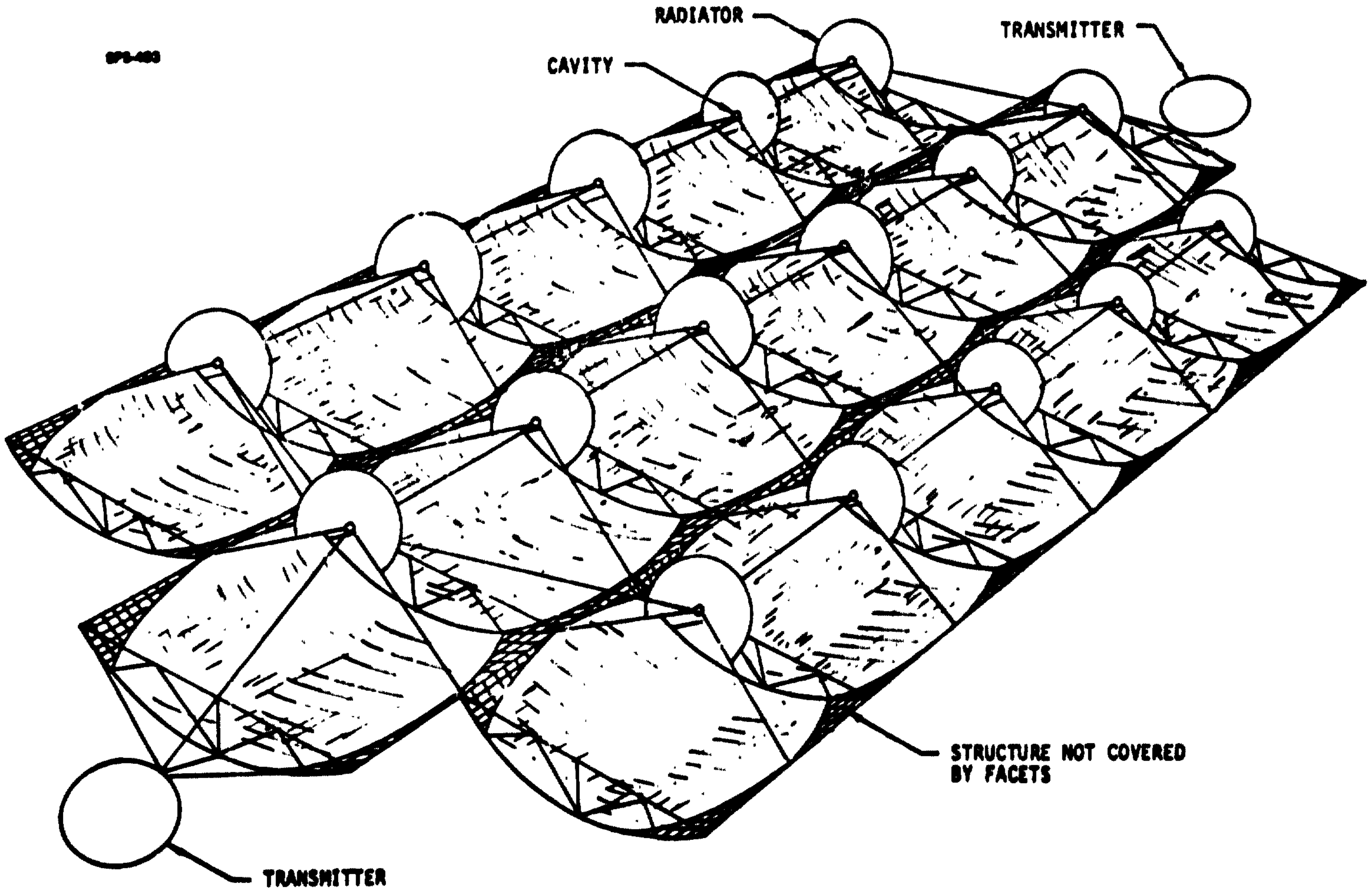

Figure 3.3-8 16 Module SPS Configuration

FOLDOUT FRAME

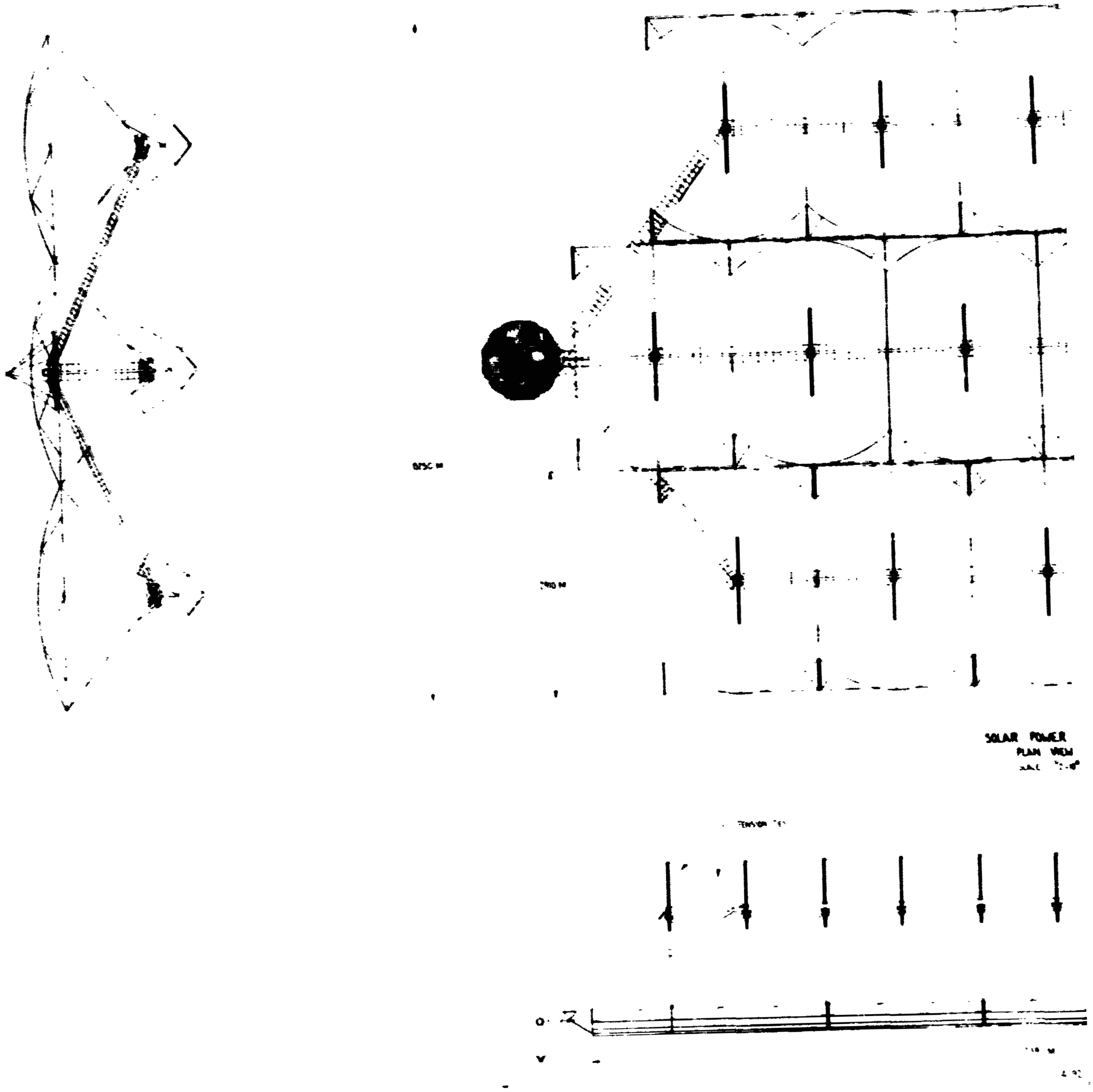

ORIGINAL PAGE IS
OF POOR QUALITY

FOLDOUT FRAME 2

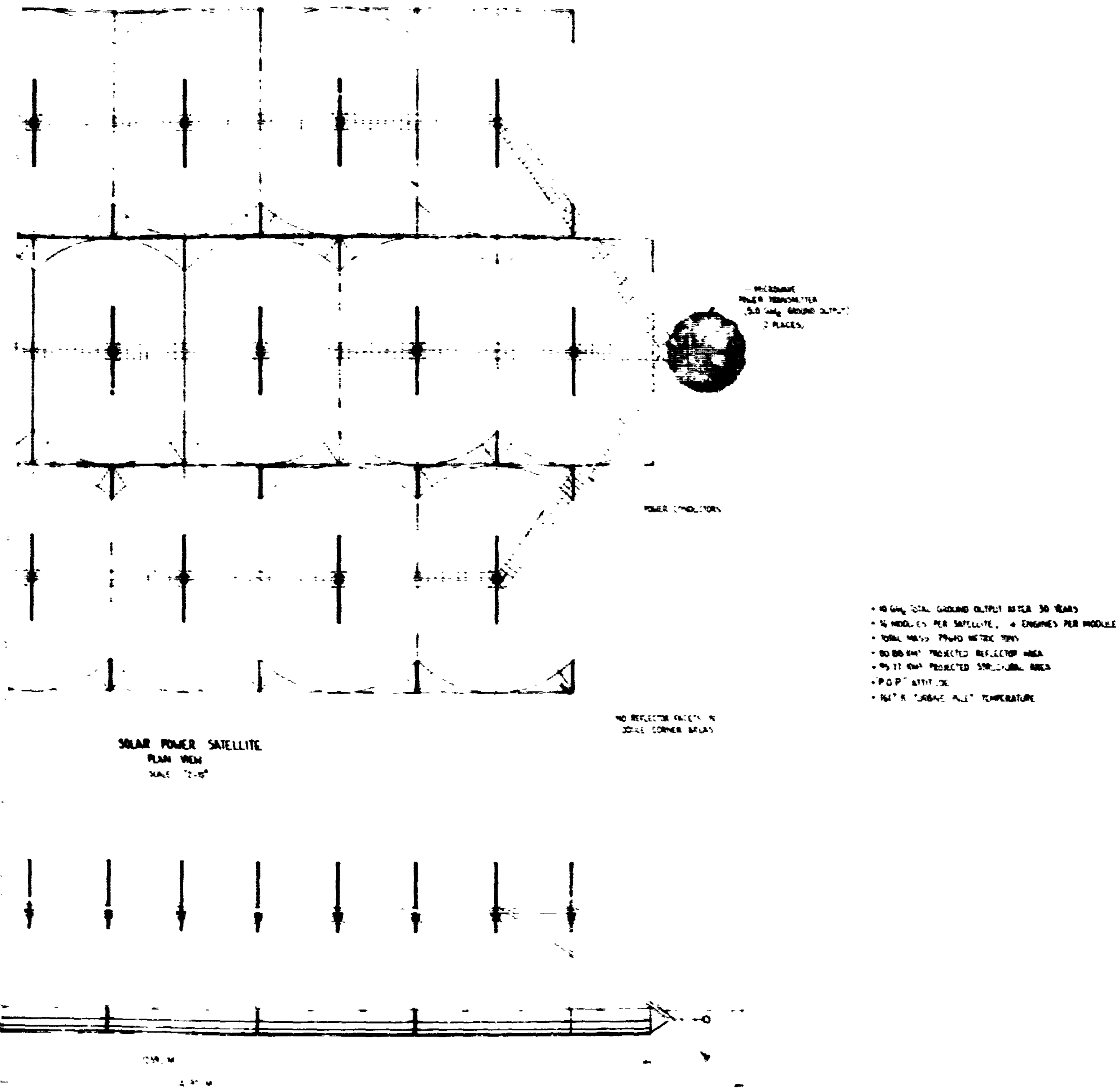

Figure 3.3-9 Solar Power Satellite–Brayton Turbomachine

ORIGINAL PAGE IS
OF POOR QUALITY

FOLDOUT FRAME 1

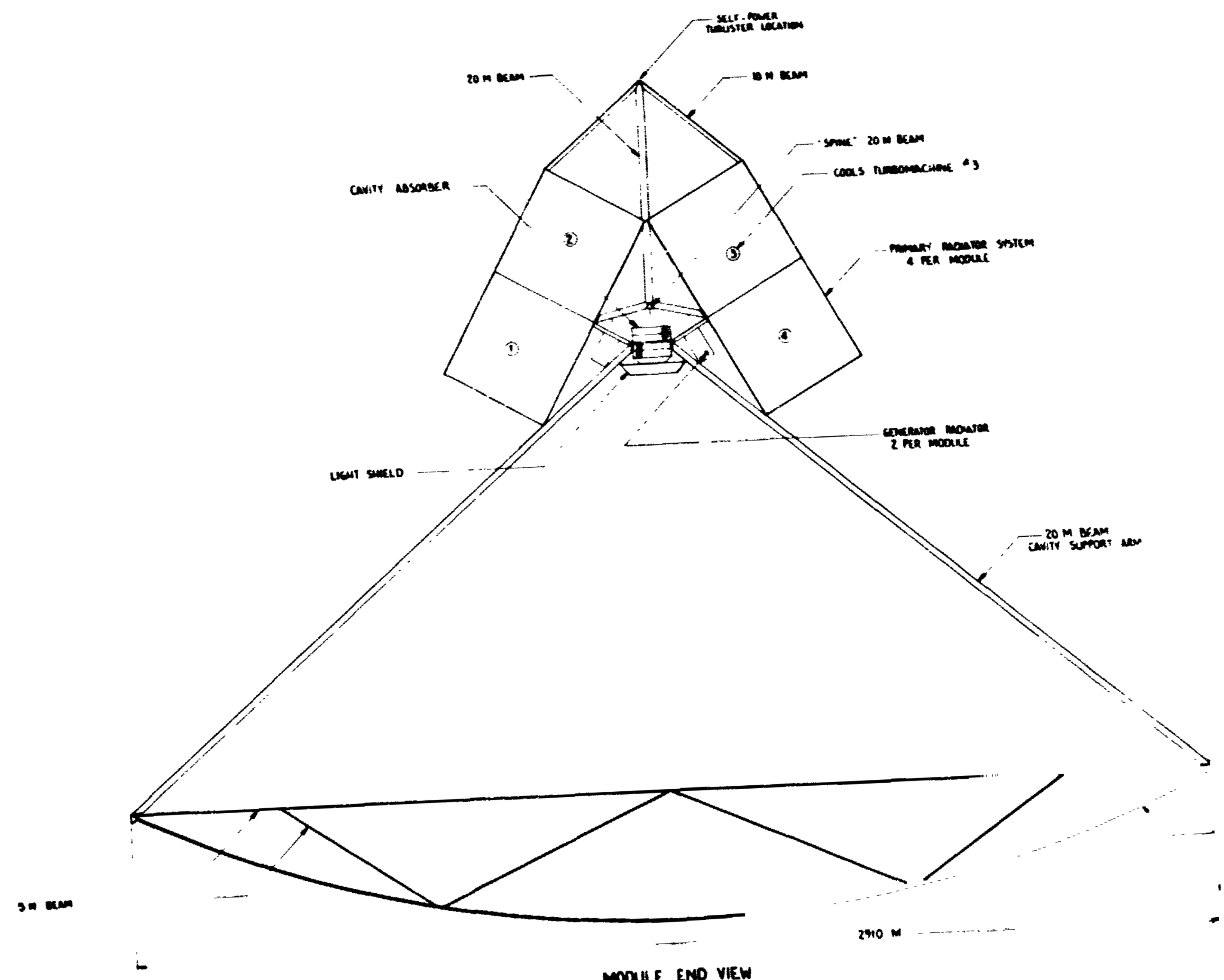

MODULE END VIEW
SCALE: 1/5 10³

ORIGINAL PAGE IS
OF POOR QUALITY

FOLDOUT FRAME 2

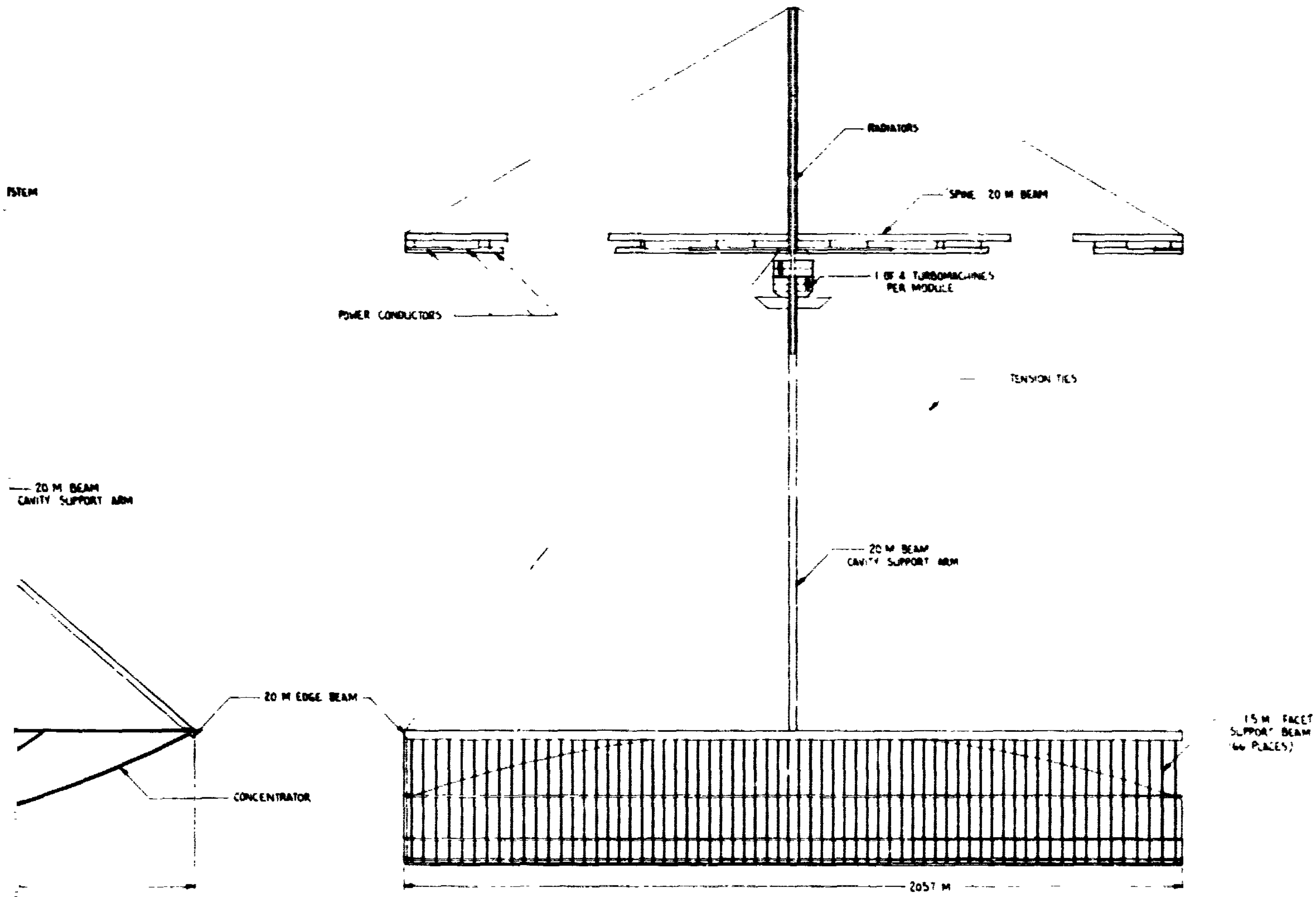

MODULE SIDE VIEW
SCALE 1/5×10'

FOLDOUT FRAME 3

MODULE PLAN VIEW

SCALE 1/5×10⁴

Figure 3.3-9 (Continued)

ORIGINAL PAGE IS
OF POOR QUALITY

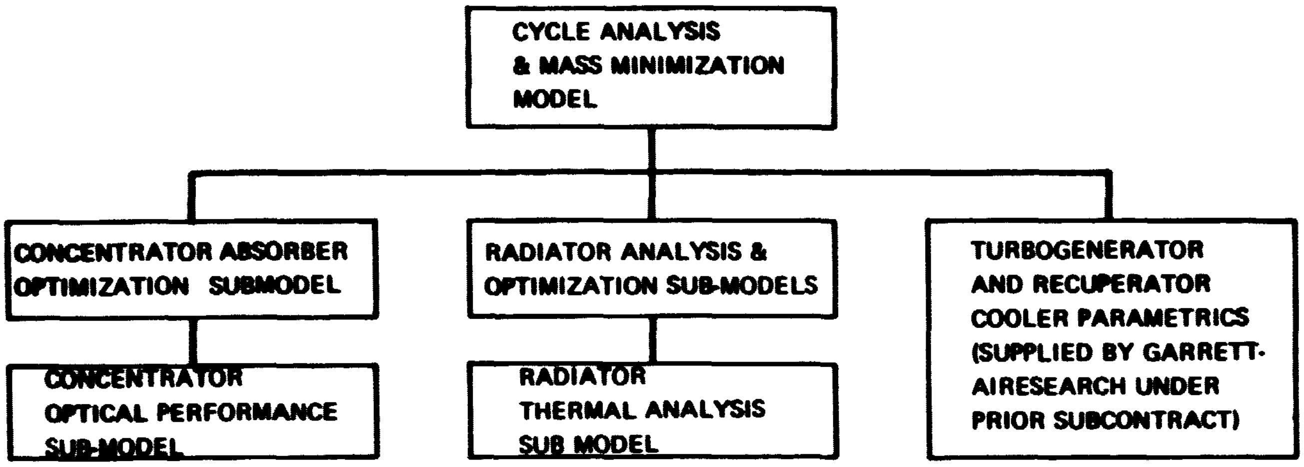

Figure 3.3-10: Cycle Analysis Model Hierarchy

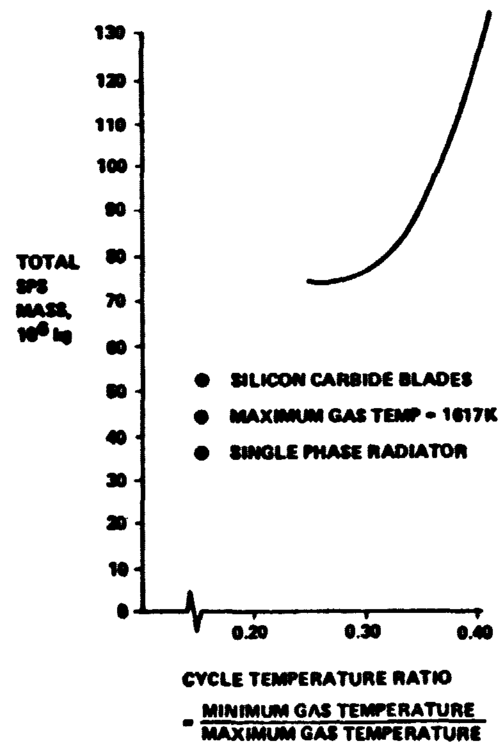

Figure 3.3-11 Effect of Cycle Temperature Ratio

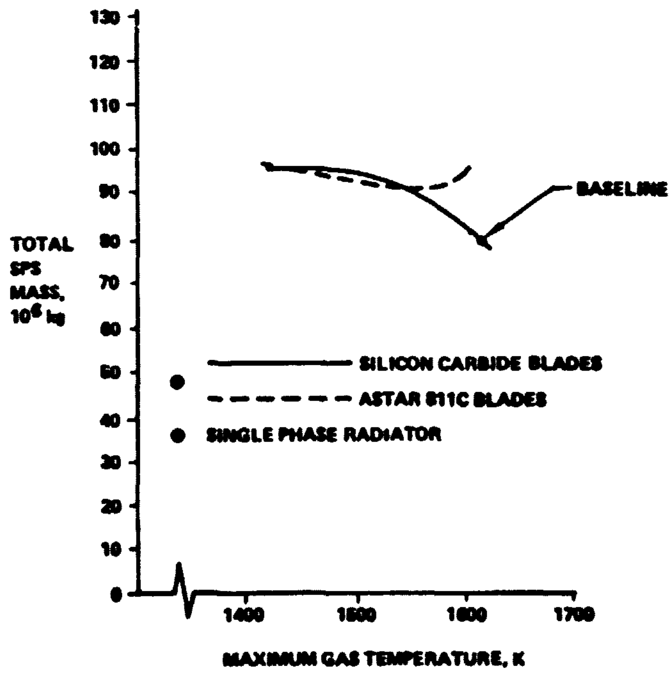

Figure 3.3-12 Effect of Gas Temperature

ORIGINAL PAGE IS
OF POOR QUALITY

Table 3.3-2 Selected Cycle State Points

TW,	(Wall Temp)	1650	1450	K
T0	(Min. Gas Temp)	404	355	K
T1	(Comp. Outlet Temp)	603	527	K
T2	(Absorber Inlet Temp)	1108	977	K
T3	(Turbine Inlet Temp)	1617	1421	K
T4	(Turbine Outlet Temp)	1190	1048	K
T5	(Cooler Inlet Temp)	685	598	K
TL1	(Minimum NaK Temp)	377	339	K
TL2	(Maximum NaK Temp)	644	564	K
T0/T3		0.25	0.25	–
T3/TW		0.98	0.98	–
E_R	(Recuperator Effectiveness)	0.86	0.86	–
ε_C	(Cooler Effectiveness)	0.[illegible]13	0.937	–
P_C	(Compressor Outlet Press)	4.239	4.220	$X10^6$
$\Delta P/P_{REC}$		0.029	0.030	–
$\Delta P/P_{CAV}$		0.014	0.008	–
$\Delta P/P_{COOL}$		0.010	0.009	–
$\Delta P/P_{TOT}$		0.053	0.047	–
CYCLE EFFICIENCY		0.439	0.444	–
CYCLE PRESSURE RATIO		2.453	2.424	–

Reheat is the use of two turbine sections with two heat exchanger assemblies in the cavity. After turbine expansion of gas heated in one heat exchanger the flow reenters the cavity for further heating in the second heat exchanger and is then expanded through the second turbine as shown in Figures 3.3-13. Intercooling is the use of two compressor sections and two coolers (gas-to-liquid heat exchangers interfacing the gas flow to the radiator system).

After passing through one cooler and compressor, the flow is cooled again (heating occurs during compression) and then passes through the second cooler and second compressor. The net effect is to increase the average cycle temperature ratio, which tends to increase cycle efficiency. However, the radiator mean heat rejection temperature reduces, so that there is less heat rejection per unit area. Higher efficiency means less heat to reject, however a preliminary analysis was performed to determine that reheat may offer net mass reduction sufficient to warrant the additional complexity as noted in the Figure.

3.3.2 Rankine Cycles

3.3.2.1 Rankine Cycle Screening

This section describes the results of a preliminary evaluation of Rankine thermal engine concepts. Liquid metal organic and steam Rankine cycles were investigated, and their performance, size and mass characteristics were compared with the Brayton cycle reference system.

The objectives of this study were to identify thermal engine energy conversion options for the Solar Power Satellite (SPS) and perform a series of screening tests to cull out concepts that fail to meet minimum performance, mass, and cost criteria. Evaluation data were develcped for concepts which successfully passed through all screening tests. The results of this study provide a quantitative comparison of the performance, mass, and cost characteristics of thermal engine energy conversion concepts for generation of electrical power in space.

Specific thermal engine concept investigated in this study were the following:

1. Basic Rankine cycle

2. Regenerated Rankine cycle

3. Regenerated Rankine cycle with reheat

4. Rankine cycle with steam extraction feedwater heating

ORIGINAL PAGE IS
OF POOR QUALITY

Schematic diagram of these cycles are shown in Figure 3.3-14. Three working fluids: potassium, organics, and water, were studied.

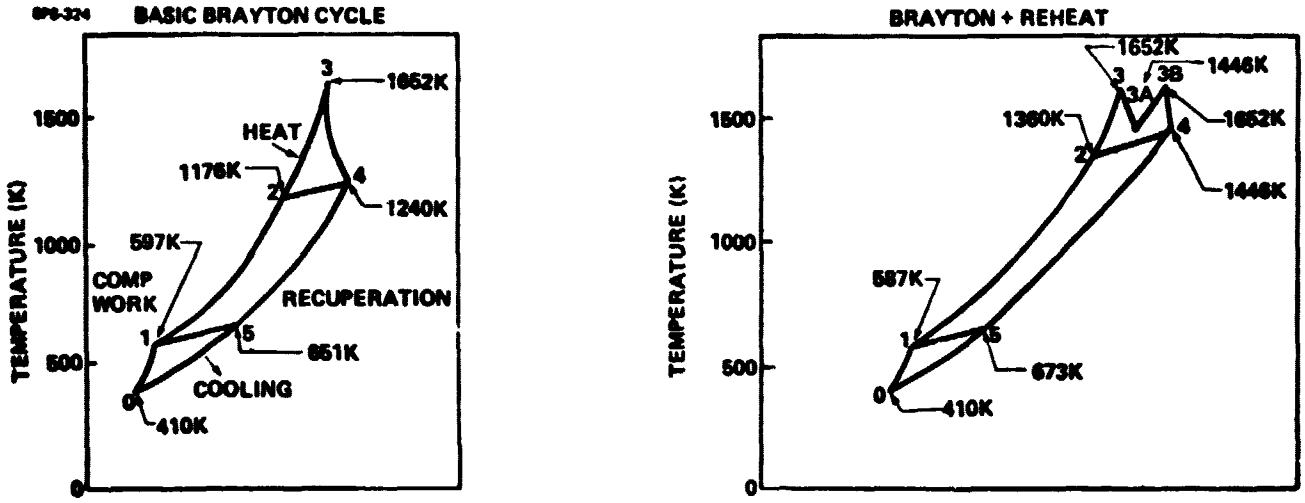

- With reheat, turbine exhaust is applied to another cavity absorber section and then passed through a second turbine.
- As a result, average hot-end temperature increases.
- With same recuperator effectiveness, radiator average temperature increases.
- Net cycle efficiency increases 3.89 %.
- Mass changes: (preliminary)

– Smaller SPS	$-\ 3.74 \times 10^6$ kg
+ Heavier cavity absorber	$+\ 1.29 \times 10^6$ kg
– Lighter radiator	$-\ 4.28 \times 10^6$ kg
	$-\ 6.73 \times 10^6$ kg

Figure 3.3-13 Reheat Could Reduce System Mass Approximately 7%

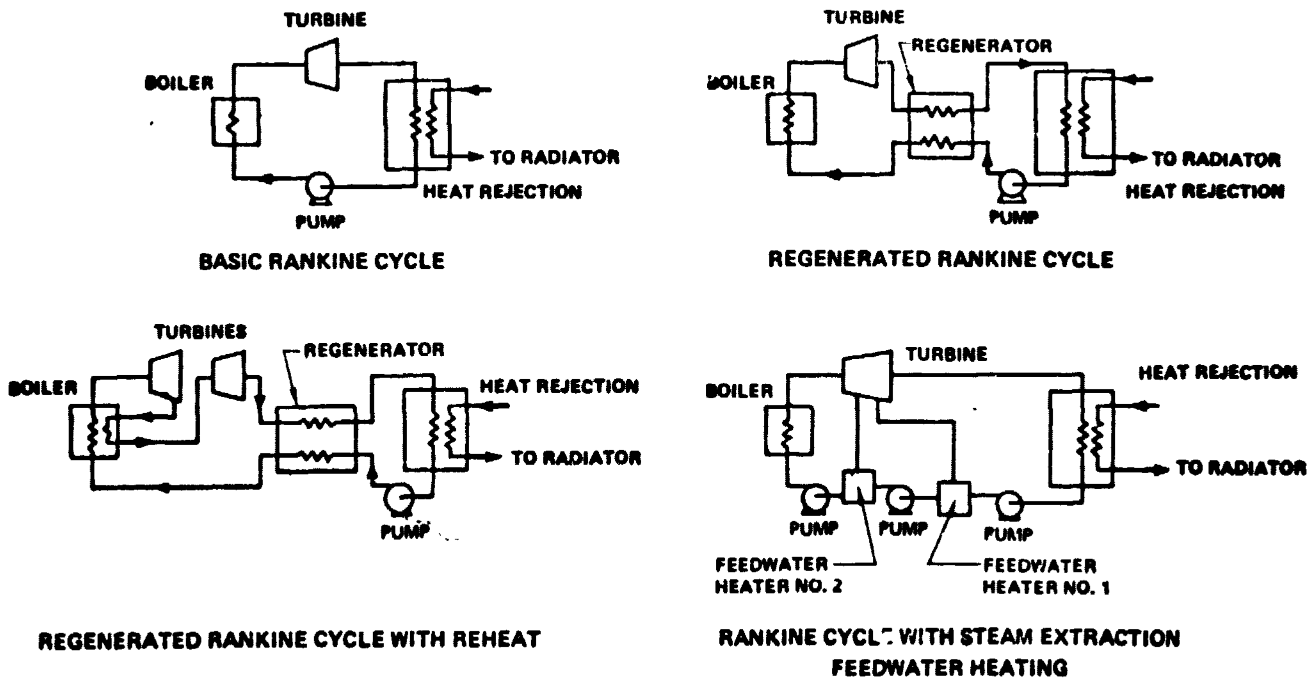

Figure 3.3-14 Rankine Cycle Options

A four-step screening process was adopted to identify viable thermal engine concepts. The screening process steps are shown in Figure 3.3-15. Parametric cycle performance data was developed for all candidate cycles. Figure 3.3-16 shows a typical set of performance data for steam Rankine cycles. The thermal efficiency of each candidate cycle was compared with the efficiency of the Brayton cycle baseline system. Concepts exhibiting efficiencies greater than 45.6% were passed on to the next test. First order mass estimates were made for concepts which failed the performance screen. If the concept was found to be competitive with the Brayton system on the basis of mass, regardless of lower cycle efficiency, then it too was passed on to the next screen. The potassium Rankine cycles, for example. exhibited thermal efficiencies between 27 and 32 percent, well below the Brayton cycle value. However, they were found to have approximately the same mass as the Brayton cycle, in a large part due to smaller radiators, and were therefore advanced to the next screening test. Concepts which failed both the performance and mass-estimate screening tests were the organic Rankine system and basic steam Rankine system.

In the second screening test, candidate concept having peak cycle temperatures in excess of 1644°K were discarded. Low pressure steam Rankine concepts were dropped from further consideration at this point.

Mass models of major energy conversion system components were developed for cycle concepts which successfully advanced through the peak temperature screening test. The energy conversion system was defined as consisting of the solar concentrator reflector facets and structure, cavity heat absorber assembly, regenerator/cooler, turbomachines, and main radiator. Mass models were developed for radiators, heat absorbers, regenerators and turbines. Solar concentrator mass was assumed to vary with cycle efficiency according to the expression

$$M_i = \frac{M_B N_B}{N_i}$$

where
- M_i = solar concentrator mass of candidate system
- N_i = cycle efficiency of candidate system
- M_B = solar concentrator mass of Brayton baseline
- N_B = cycle efficiency of Brayton baseline

ORIGINAL PAGE IS
OF POOR QUALITY

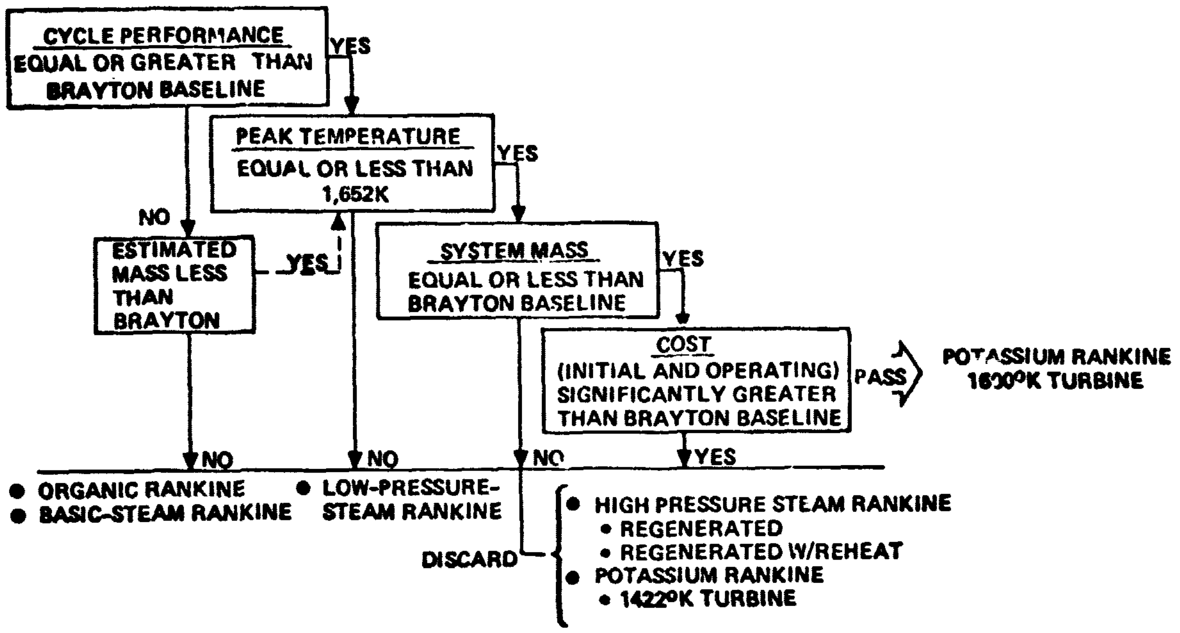

Figure 3.3-15 Thermal Engine Screening Approach

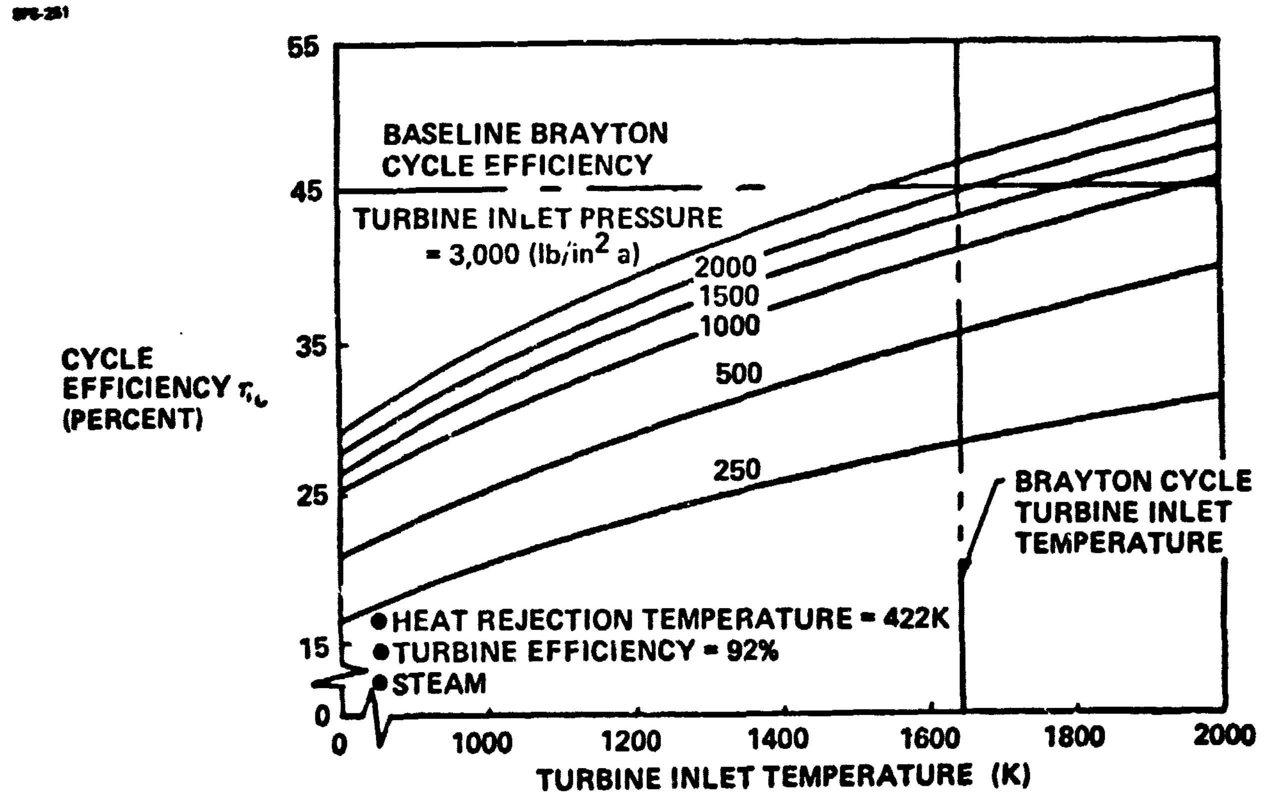

Figure 3.3-16 Steam Rankine Cycle Performance With Regeneration, Reheat, and Heat Rejection at 422K

The conversion system mass of each candidate cycle concept was calculated and compared with the mass of the Brayton cycle conversion system. High pressure steam Rankine cycles, both regenerated and regenerated with reheat, were found to be more massive than the Brayton cycle baseline and were consequently dropped from further consideration. In the case of the steam Rankine cycle options, radiator and turbomachinery masses were significantly greater than the corresponding components of the Brayton cycle system. Radiator mass for the 1422°K potassium Rankine cycle was one-third that of the Brayton cycle radiator, however, turbine and solar concentrator mass were so great that this advantage was lost. High turbine mass was caused by large wheel diameters and large number of stages necessary to expand through an 80:1 ratio.

The large number of stages and great difference in wheel size between high and low pressure ends of the turbine necessitated a design consisting of a high pressure section with its own shaft and housing plus two low pressure sections each having separate shafts and housings. This design was essentially three separate turbo-machines with associated interconnecting ducting and controls. The 1422°K potassium Rankine system was more massive than the reference Brayton system but was retained for comparison with lower temperature Brayton systems.

The potassium Rankine cycle with 1600°K turbine inlet temperature was the only thermal engine option for which initial and operating costs were projected to be approximately equal to Brayton system costs. Hence, the 1600°K potassium Rankine system was passed through the final screening test and therefore was considered as a viable alternative to the Brayton cycle concept.

Table 3.3-3 summarizes performance and significant thermodynamic variables for candidate energy conversion concepts. Cycle efficiencies of the potassium Rankine options were sacrificed in order to keep the low pressure stages of the turbines from growing to untractable dimensions. Steam Rankine cycle efficiencies ranged from 32 to 42%, however efficiencies in the high end of this range could only be achieved at high turbine inlet temperature or pressures.

Effective temperature, heat rejection, projected area, and mass of radiators for candidate thermal engine options are compared in Table 3.3-4. The common denominator for each option in this comparison is equal system power output. Differences in heat rejection levels are due to different cycle efficiencies. Projected area is influenced mainly by effective radiator temperature and heat rejection level according to the relationship.

$$\text{Area} \propto Q/T^4$$

where Q = heat rejection
T = effective radiator temperature

ORIGINAL PAGE IS
OF POOR QUALITY

Table 3.3-3 Cycle Characteristics

CYCLE	TURBINE INLET TEMPERATURE (°K)	TURBINE INLET PRESSURE (PSIA)	TURBINE PRESSURE RATIO	COMPRESSOR INLET TEMPERATURE (°K)	COMPRESSOR INLET PRESSURE (PSIA)	CYCLE EFFICIENCY %
• BRAYTON BASELINE	1617	615	2.45	404	251	43.9
• POTASSIUM RANKINE	1600	410	208	867	2.4	31.6
• POTASSIUM RANKINE	1422	201	84	867	2.4	27.6
• STEAM RANKINE	1644	250	22	367	11.5	42.0
• STEAM RANKINE	811	3000	261	367	11.5	34.8
• STEAM RANKINE	1144	3000	12.1	478	247	32.2

Table 3.3-4 Radiator Comparison For A Single 293 MW_e Output Engine Model

THERMAL ENGINE CYCLE	EFFECTIVE RADIATOR TEMPERATURE (°K)	HEAT REJECTION (KW)	PROJECTED AREA (M^2)	MASS 10^4 KG
BRAYTON CYCLE				
• BASELINE NAK	476	3.75×10^5	9.01×10^4	43.66
• 800°K CONDENSING WATER	441	3.75×10^5	9.85×10^4	43.41
POTASSIUM RANKINE CYCLE				
• CONDENSING POTASSIUM (1600°K TURBINE)	837	6.29×10^5	1.35×10^4	8.50
• NON-CONDENSING NAK (1600°K TURBINE)	707	6.29×10^5	2.61×10^4	21.54
• CONDENSING POTASSIUM (1422°K TURBINE)	837	7.16×10^5	1.83×10^4	12.00
STEAM RANKINE CYCLE				
• CONDENSING STEAM (1644°K TURBINE)	353	3.78×10^5	30.38×10^4	118.38

Several significant results are presented in this comparison. First, an alternative radiator concept utilizing water as a transport fluid was found to be competitive, from a mass standpoint, with the baseline NAK radiator for the Brayton cycle system. The radiator receives an 525°K mixture of saturated liquid and vaporized water from the helium cooler. As the mixture flows through the radiator, it condenses at an almost constant temperature of 525°K. Downstream of the point at which the vapor has completely condensed, the radiator temperature decreases in a normal manner.

Radiators for potassium Rankine cycle options were significantly less massive than Brayton cycle radiators. This was largely due to the higher heat rejection temperatures (837°K vs 476°K) chosen for the potassium Rankine cycles. The least massive radiator designs were those utilizing the potassium working fluid as a heat transport medium. The potassium was assumed to enter these designs as a saturated vapor and exited as a saturated liquid resulting in a uniform temperature radiator which operated at the maximum heat rejection temperature possible for the cycle. Utilization of a noncondensing fluid such as NAK to reject heat from the Rankine cycle options results in lower effective radiator temperatures and consequently larger areas and more massive radiators.

Steam Rankine cycle radiators were two to three times more massive than the Brayton cycle baseline radiator. This was mainly due to the low heat rejection temperature necessary to achieve cycle efficiencies which were approximately equal to those of the Brayton cycle. An additional limit on condensing water radiators was the sharp increase in pressure with increasing temperature for the vapor-liquid state. Thus, as radiator temperature was increased manifolds, headers, and tubing became heavier due to increasing pressure.

The results of cavity heat absorber mass predictions are presented in Table 3.3-5. The factors having major influence on heat absorber mass were fluid temperature and pressure. Absorber tube wall thickness was determined by stress level and the creep rupture strength to the wall material. Massive absorber assemblies resulted from a combination of high fluid pressure and degraded tube wall strength due to elevated temperatures. Convective heat transfer coefficients between the working fluid and absorber tube wall also influenced heat absorber system mass. Absorber tube length varied inversely with heat transfer coefficients and consequently heat absorber mass was less for systems in which high heat transfer coefficients were maintained.

ORIGINAL PAGE IS
OF POOR QUALITY

Table 3.3-5 Heat Absorber Mass Comparison

CYCLE	HEAT ABSORBER TUBE MASS ~ KG X 10^6: SUBCOOLED LIQUID	BOILING	VAPOR	SUPERHEAT & REHEAT	COLD MANIFOLDS & HEADERS KG X 10^6	HOT MANIFOLDS & HEADERS KG X 10^6	WORKING FLUID KG X 10^6	TOTAL* KG X 10^6
• BRAYTON BASELINE 1644°K TURBINE INLET								9.07
• POTASSIUM RANKINE 1600°K TURBINE INLET	.22	2.69	1.80	-	.18	4.11	1.019	10.02
• POTASSIUM RANKINE 1422°K TURBINE INLET	.06	.29	.23	-	.07	.38	1.02	2.05
• STEAM RANKINE 1644° TURBINE INLET 250 PSIA BOILER PRESS	.02	.04	.03	.26	.09	.86	1.75	3.08
• STEAM RANKINE 811°K TURBINE INLET 3000 PSIA BOILER PRESS	.56	.14	.10	.81	3.55	6.80	8.38	19.14

*10 GW_e GROUND POWER OUTPUT SYSTEM

The potassium Rankine system with 1422°K turbine inlet temperature had the lowest absorber mass of all systems considered. This was due to a combination of low (1422°K) peak temperature and low working fluid pressure (1.4 Mpa; 200 psia vs 3.5 Mpa; Soc psia for the Brayton baseline system). The sensitivity of absorber mass to pressure and temperature is demonstrated by a five-fold increase in absorber mass which resulted from an increase in potassium saturation temperature from 1422°K to 1644°K.

A comparison of conversion system mass for five candidate thermal engine options is summarized in Table 3.3-6. The masses are clustered into two discrete groups. The potassium Rankine options and Brayton baseline concept masses are grouped at about 50×10^6 Kg while the steam Rankine systems fall in a region beyond 100×10^6 Kg. The major contributors to conversion system mass of the potassium Rankine options were the turbines, while radiators were by far the most massive element of the steam Rankine systems. No cooler weights are shown for the Rankine cycles because the cycle working fluid was utilized as the radiator fluid thereby eliminating the need for a heat exchanger. Both potassium Rankine cycles and the 811°K turbine inlet temperature steam Rankine cycle were designed with the turbine expansion process terminating in the two phase region. Hence there was no temperature potential for regeneration in these cycles.

3.3.2.2 Potassium Rankine Cycle

The following metal vapor Rankine cycle analysis was provided by General Electric under subcontract.

The alkali metal Rankine cycle provides a thermal energy conversion system operating in the turbine inlet temperature range from 2100°F to 2500°F and a heat rejection radiator temperature of 1100°F. Compared to the Brayton cycle, the system utilizes a low power liquid metal pump rather than a compressor to transport the working fluid and does not utilize a high temperature recuperator. Heat can be directly rejected from the system in a condensing space radiator without the requirement for an intermediate heat exchanger or cooler. Each turbine system consists of a high pressure double flow turbine and two low pressure double flow turbines.

The cycle is diagrammed in Figure 3.3-17.

A broad spectrum of materials evaluation and component design, development and testing exists in alkali metal Rankine cycle technology. Prior efforts for small scale nuclear power applications in space provided the background from which to consider Solar Power Satellite applications. The following items are highlights from these programs:

- 10 years, \$24M prior space power program
- 12,000 hours potassium turbine testing

ORIGINAL PAGE IS
OF POOR QUALITY

SPS-814

Table 3.3-6 Conversion System Mass Comparison

CYCLE	SOLAR CONCENTRATOR MASS KG X 10^6	CAVITY HEAT ABSORBER MASS KG X 10^6	REGENERATOR/ COOLER MASS KG X 10^6	TURBO MACHINERY MASS KG X 10^6	RADIATOR MASS KG X 10^6	TOTAL KG X 10^6
• BRAYTON BASELINE 1644°K TURBINE INLET	4.2	9.07	4.86	1.95	27.94	48.02
• POTASSIUM RANKINE 1600°K TURBINE INLET	5.69	10.02	-	25.5	5.44	46.65
• POTASSIUM RANKINE 1422°K TURBINE INLET	6.51	2.05	-	36.86	7.68	53.10
• STEAM RANKINE 1644°K TURBINE INLET	4.2	3.08	1.81*	23.48	75.75	108.32
• STEAM RANKINE 811°K TURBINE INLET	5.17	19.14	-	28.2	139.15	191.66

*REGENERATOR ONLY REQUIRED

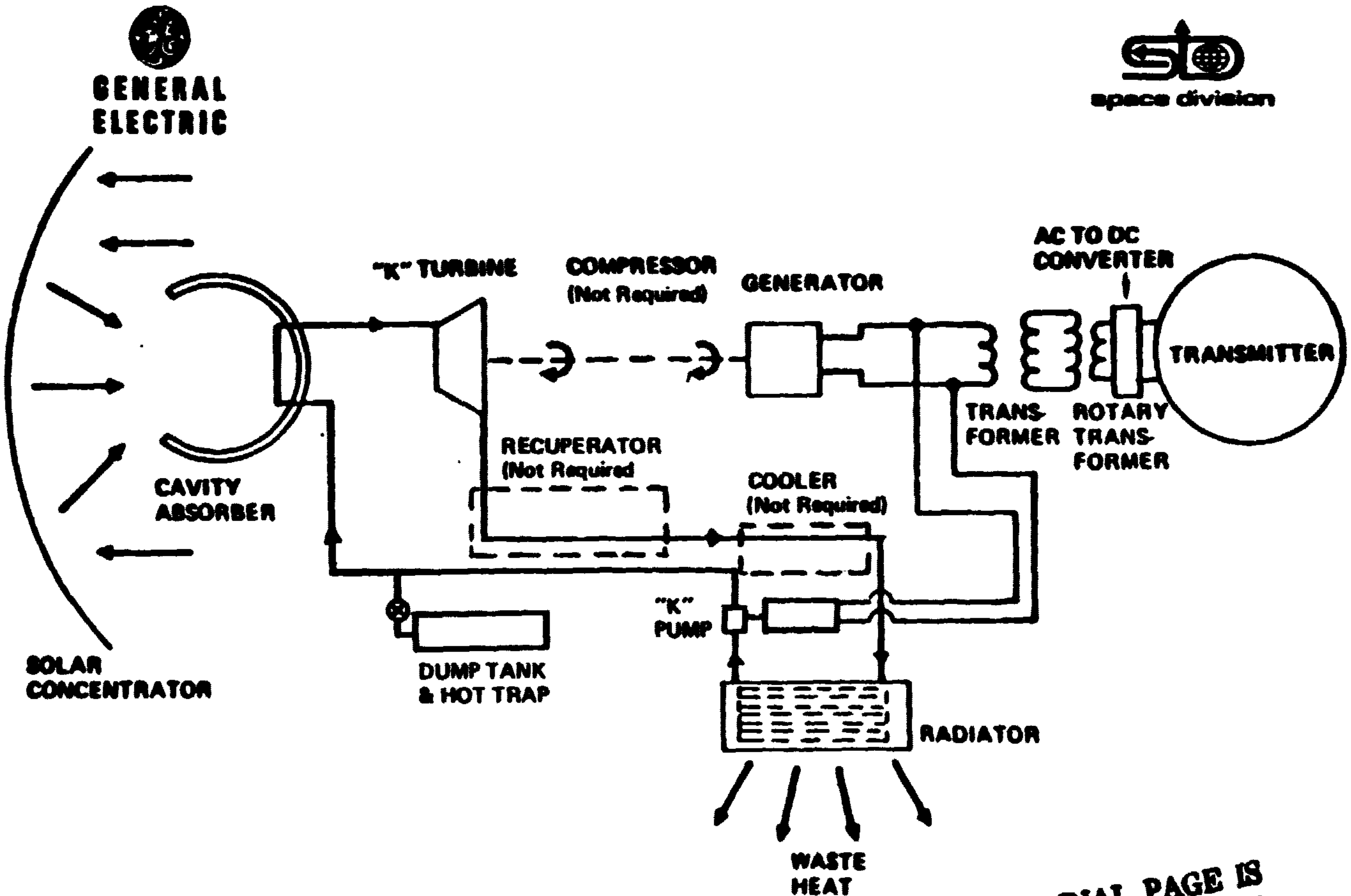

Figure 3.3-17 Alkali Metal Rankine Cycle

ORIGINAL PAGE IS OF POOR QUALITY

- 800,000 hours alkali metal boiling/condensing testing
- Refractory alloy processing forming, machining, & welding established
- Alkali metal purification, analysis, handling and control established
- Materials compatibility in alkali metals determined
- Alkali metal bearings and bearing materials investigated
- EM boiler feed pumps operated 10,000 hours at 1000°F - 1400°F
- Dump tanks, gettering systems, valves, oxygen meters, etc. evaluated
- 450 KWe potassium turboalternator designed for space

A significant amount of boiling-condensing test experience has been developed in several organizations on potassium and, to a much lesser extent on cesium. The effort has included large amounts of work required in establishing materials compatibility, materials processing methods and the necessary controls on alkali metal impurities necessary for satisfactory operation of larger scale facilities. Much development work has been done in subsystem loops to establish heat transfer data or to confirm the design and operating characteristics of various components such as liquid metal bearings, valves, pumps, scales, etc. Testing experience is summarized in Table 3.3-7.

Many hours of test data have been accumulated on "once-through" potassium boilers in the temperature regime from 1400-2200°F. Correlations of heat transfer and pressure drop data have covered:

Liquid phase heat transfer
Nucleate boiling
Film boiling
Critical heat flux
Vapor superheat

Typical correlation data are shown in Figure 3.3-18.

A valid basis of heat transfer data exists for design of alkali metal Rankine cycle components.

Table 3.3-7 Potassium And Cesium Testing

GENERAL ELECTRIC

space division

	Potassium (800,000 hours testing)							Cesium (>23,000 hours testing) (b)
	AiResearch	GE	JPL	NASA-Lewis	ORNL	P&W	Other[a]	
	Testing hours accumulated							
Corrosion test systems:								
Boiling	1300	25 500	----	----	62 800	12 000	----	3500
All-liquid	----	----	----	----	----	----	156 000	----
Component test systems, boiling	5900	19 600	----	1000	2 800	4 900	300	2400
Simulated powerplant systems	----	----	~1000	----	10 200	----	----	----
Boilers	7200	40 100	1000	1000	75 800	16 900	300	6000
Turbines	3050	10 100	----	----	5 000	----	100	----
Boiler feed pumps:								
Electromagnetic	7200	34 600	3600	1000	26 900	4 900	3 300	5600
Turbine driven	----	----	----	----	5 000	----	----	----
Other pumps	5900	18 600	3600	1600	6 100	1 300	57 600	----
Condensers	7200	40 100	~1000	1600	75 800	16 900	300	5600
Seals	3050	10 100	----	----	----	----	----	----
Bearing tests	3000	----	----	----	4 500	----	1 600	----

[a]Includes testing hours of Aerojet Nucleonics, Allison, Rocketdyne, United Nuclear.

[b]Includes testing hours of Brookhaven, Aerojet Nucleonics, Westinghouse Astronuclear.

GENERAL ELECTRIC

space division

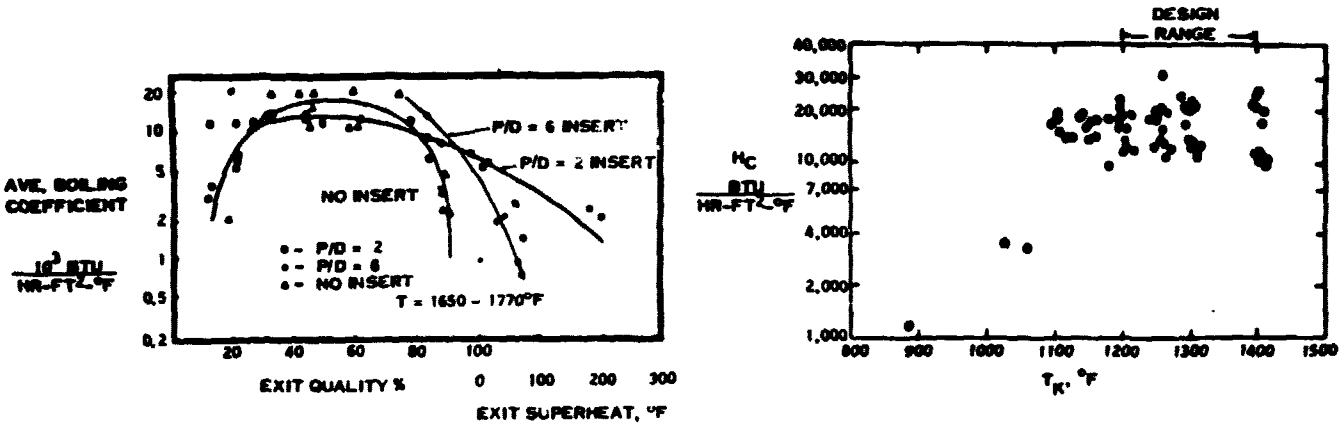

BOILING HEAT TRANSFER

CONDENSING HEAT TRANSFER

Figure 3.3-18 Potassium Boiling/Condensing Heat Transfer

ORIGINAL PAGE IS OF POOR QUALITY

Hydrodynamically lubricated pivot pad bearings were developed and tested under load at temperatures in the 800-1000°F range in liquid potassium for hundreds of hours. The stability of hydrodynamic bearings and shaft assemblies were also evaluated in many fluids as a means of developing bearing stability prediction criteria. The technology of alkali metal bearings also included extensive work on the characterization of potential alkali metal bearing materials such as refractory alloys and metal-bonded carbides, particularly in friction and wear characteristics under vacuum and liquid potassium.

Testing of alkali metal rotating seals were also undertaken in the test facility.

Liquid potassium flow control valves were designed, built and tested under intermittent actuating conditions for 5000 hours at a temperature of 1900°F without siezing or deterioration. Appropriate selection and integration of materials in the design assured reliable operation in both alkali metal and space environments at these high temperatures.

An electromagnetic boiler feed pump, capable of operating at a liquid metal temperature up to 1400°F, was designed, built and tested for 10,000 hours pumping potassium at 1000°F and at flow rates up to 3.25 lb/sec. The pump featured a T-111 alloy helical pump duct and a high temperature stator with a 1000°F maximum operating temperature; the stator materials consisted of Hiperco 27 magnetic laminations, 99% alumina slot insulators, type "S" glass tape interwinding insulation and nickel-clad silver conductors joined by brazing in the end turns. Pump windings were cooled by liquid NaK at 800-900°F.

A 400 KW_{th}, three-loop heat transfer facility was used to confirm the design and performance characteristics of prototypical "once-through" boilers and of condensers suitable for space power applications. This facility featured an electrically heated primary loop of T-111 (Ta-10W-1Hf) containing lithium and operating at temperatures of 2200°F, a secondary T-111 loop containing boiling and condensing potassium and a third, heat rejection loop of AISI Type 316 stainless steel containing NaK and rejecting heat through a NaK/air radiator outside the simulated ultra high vacuum space environment.

The facility operated, trouble free, for over 2500 hours at maximum temperatures up to 2000°F and confirmed the ability to design, fabricate and test space-type boilers and condensers.

The ability to purify and analyze liquid metals for such contaminants as carbon, oxygen, nitrogen, hydrogen and various metallic elements was advanced considerably during the alkali metal Rankine cycle space power program. Contamination levels of less than 10 ppm oxygen were routinely achieved. The technology included the development of analytical methods, specifications, procedures and equipment.

Distillation, hot trapping and cold trapping were used as purification methods, although hot trapping with titanium or zirconium getters were most effective and most commonly used, particularly for controlling impurities immediately prior to and during the course of operation of component development, materials compatibility and heat transfer test loops.

With properly purified liquid metal in a properly alloyed refractory metal, welded in a properly controlled environment and in a component or loop designed to be leak proof, there was no corrosion problem.

The use of direct sampling and analysis of alkali metal from an operating component and the application of continuous reading oxygen meters was most helpful in detecting and correcting system deficiencies. Operating, maintenance and system repair experience was obtained.

The potassium turboalternator shown in Figure 3.3-19 was conceptually designed for the space power program of the 1960's. Its design included fluid dynamic analysis, selection of materials, stress analysis, motor dynamics, vibration analysis, selection and design of radial and thrust bearings, and magnetic and electrical design of the homopolar alternator. The extent of the design analysis, and the supporting technology which it utilized, indicated the feasibility of using Rankine cycle turbine components for nuclear power applications in space at significant power levels.

This background provided the basis for the SPS metal vapor Rankine subsystem analysis.

Cycle studies indicate parametrically, the effects of higher turbine inlet temperatures and reduced condensing temperatures on improvements in cycle efficiency, as shown in Figure 3.3-20.

Turbine inlet temperatures above 2100°F might require considerable technical assessment of the use of materials which are, as yet, unproven.

Improvements in efficiency by use of reduced condensing temperatures are offset by larger turbine flow areas required to accommodate increased vapor volume flows. The volume flow is approximately universely proportional to the vapor pressure of condensing potassium:

Temperature °F	K Vapor Pressure-psia	Volume Flow Ratio
1100°F	2.4	1
1000°F	1.1	2.18
900°F	0.44	5.45

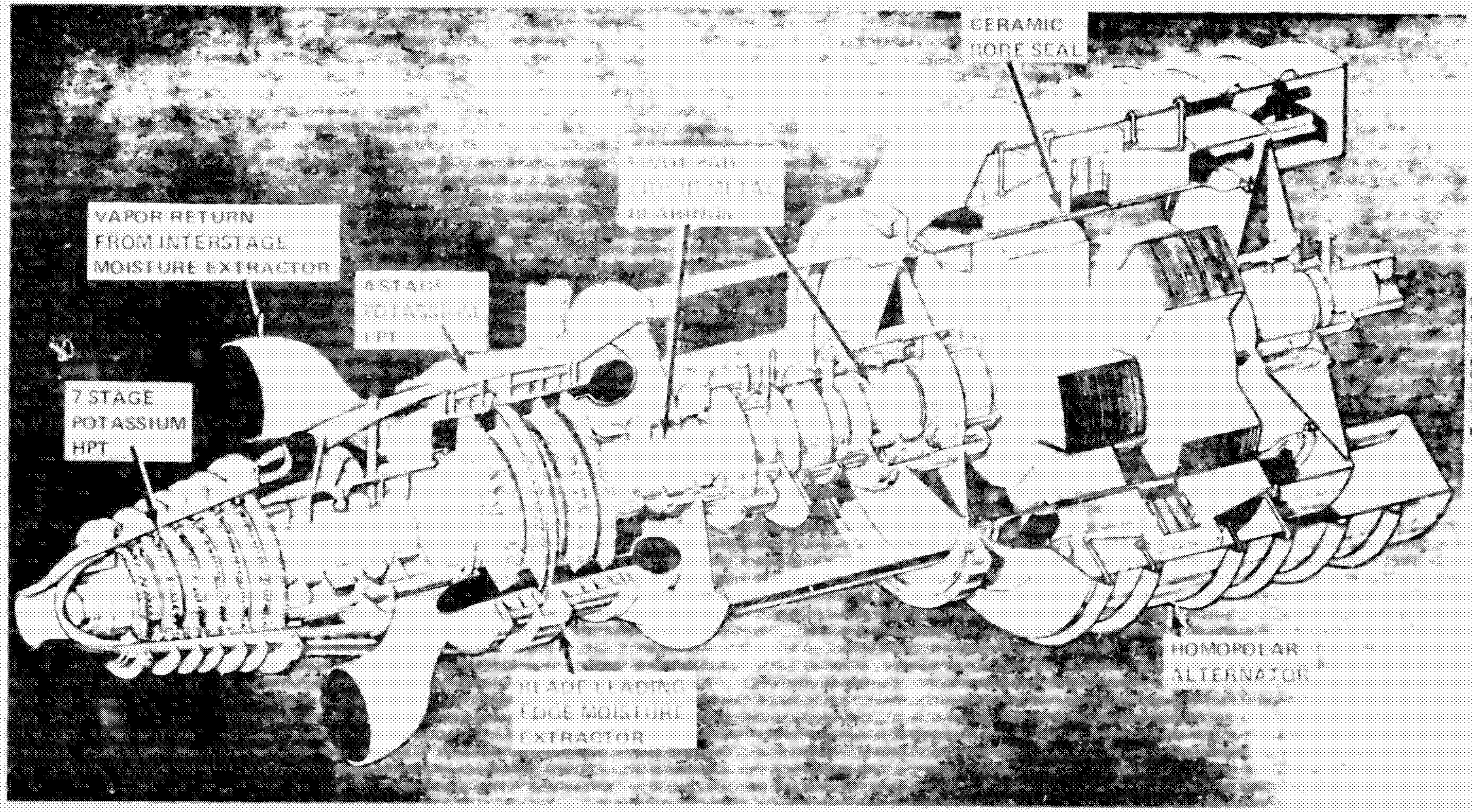

Figure 3.3-19 450 KW_e Potassium Turboalternator

ORIGINAL PAGE IS OF POOR QUALITY

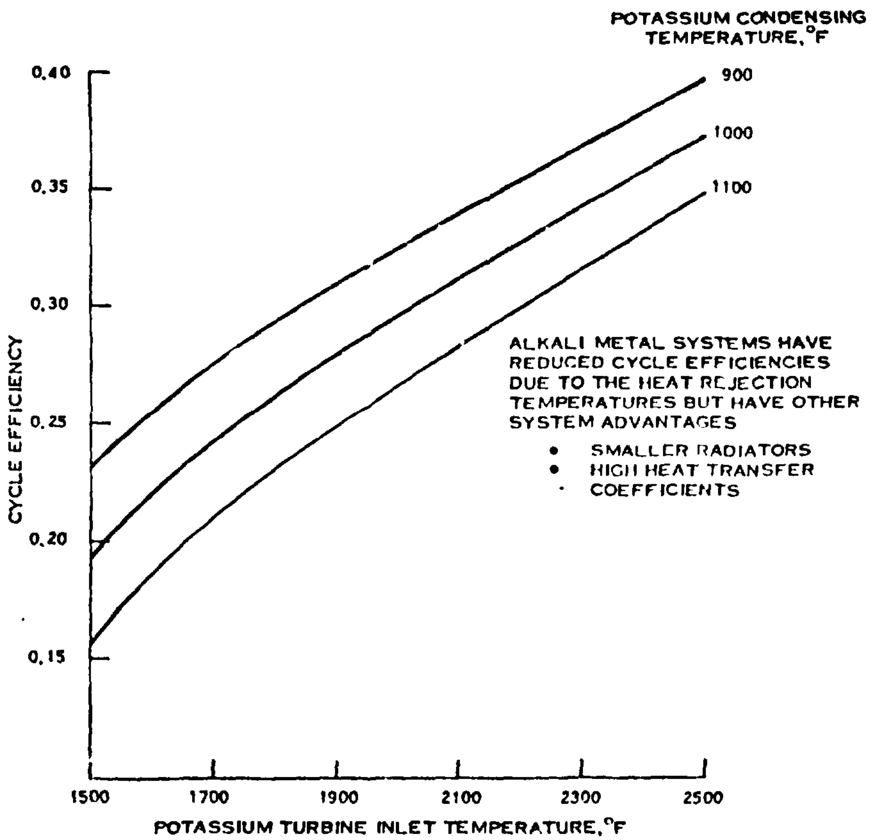

Figure 3.3-20 Variation Of Cycle Efficiency With Potassium Boiling And Condensing Temperatures

While the cycle efficiencies of these Rankine Systems are not as high as the selected 2500°F Brayton cycle, the system has other advantages, principally, improved heat transfer coefficients and higher radiator temperatures. These can impact favorably on other portions of the power conversion system in which substantial weight and size is involved.

The critical cycle parameters are presented in Table 3.3-8 for potassium vapor turbine systems with a condensing temperature of 1100°F and turbine inlet temperatures of either 2100°F to 2500°F. Turbine flow rates and power levels were selected to match appropriately scaled fluid dynamic versions of preliminary potassium turbine designs developed in earlier studies of land based alkali metal topping cycles for steam. The number of turbine systems required for 4800 MW_e is shown. The engineering definition presented here provides the basis for evaluating the effects of these unique cycles on the size (and weight) of the cavity heat absorbers and the space radiators.

TABLE 3.3-8
POTASSIUM RANKINE CYCLES

Turbine Inlet Temperature, °F	2100	2500
Turbine Inlet Pressure, PSIA	200	500
Flow Rate (each turbine) LB/Sec	816	856
Power Generated, MWe	218.2	266.7
Condensing Temperature, °F	1100	1100
Turbine Exit Quality*	0.765	0.735
Condensing Pressure, PSIA	2.4	2.4
Heat Rejection, BTU/Sec	543,610	548,030
Pressure Rise in Pump, PSI	248	623
Pump Work, BTU/Sec	1064	2805
Heat Added in Boiler, BTU/Sec	750,475	800,874
Cycle Efficiency, %	27.6	31.6
Number of Turbines for 3800 MWe	22	18
Total Flow, LB/Sec	17,952	15,408
Total Heat Addition, BTU/Sec	$1.651 \cdot 10^7$	$1.4416 \cdot 10^7$
Total Heat Rejection, BTU/Sec	$1.1757 \cdot 10^7$	$9.28 \cdot 10^6$

*Neglecting Moisture Extraction

ORIGINAL PAGE IS
OF POOR QUALITY

A single stage, split flow refractory alloy high pressure turbine with super alloy and stainless steel inlet and outlet scrolls was developed in preliminary design form for previous public utility power systems studies. It was intended for use at turbine inlet temperatures of 1500 - 1700°F. In its original design form, both weight and cost analysis were made; in subsequent studies the design, weight and cost were rescaled to smaller component sizes appropriate for reasonable component development and manufacture. The high pressure turbine is shown in Figure 3.3-21.

These modified designs and estimates formed the basis for extrapolation of high pressure turbine component designs weights and costs from the 1500-1700°F range to the 2100-2500 range. This was accomplished parametrically by addition of one refractory alloy stage for the 2100 turbine and by addition of two stages for the 2500°F turbine.

While the refractory alloy technology has been demonstrated in earlier component testing and turbine design studies for the Space Power Program, it is not expected that refractory alloy technology would support a 2500°F long life turbine.

Multistage Split Flow Superalloy Turbines were also developed and rescaled in size weight and cost from an original public utility power study in a manner similar to that described for the high pressure turbine.

In the current study, the rescaled turbine designs weight, and costs were used for the required low pressure turbines. For the 1500°F turbine system the low pressure turbine had 3 stages and a 1350°F turbine inlet temperature. For the higher temperature turbine systems the low pressure turbine had 4 stages and a 1450°F turbine inlet temperature.

In all cases the size, flow areas and number of low pressure turbines were scaled or selected to match the required flow from the high pressure turbine. The low pressure turbine concept is shown in Figure 3.3-22.

Preliminary potassium turbine designs have been made for the 2100°F and 2500° cycles. The 2100°F turbine design is based on superalloys in the low pressure stages and molybdenum disks and blades in the high pressure turbine. The high pressure turbine was scaled from a previous design of smaller size (1.5 MW_e) for a space power plant; because of such large scaling factors additional design effort is required to refine the accuracy of the size, weight and cost estimates. The low pressure turbines were scaled from turbines for a topping cycle study for coal fired steam plants; that study also provided the basis for the estimated weights and costs.

GENERAL ELECTRIC

space division

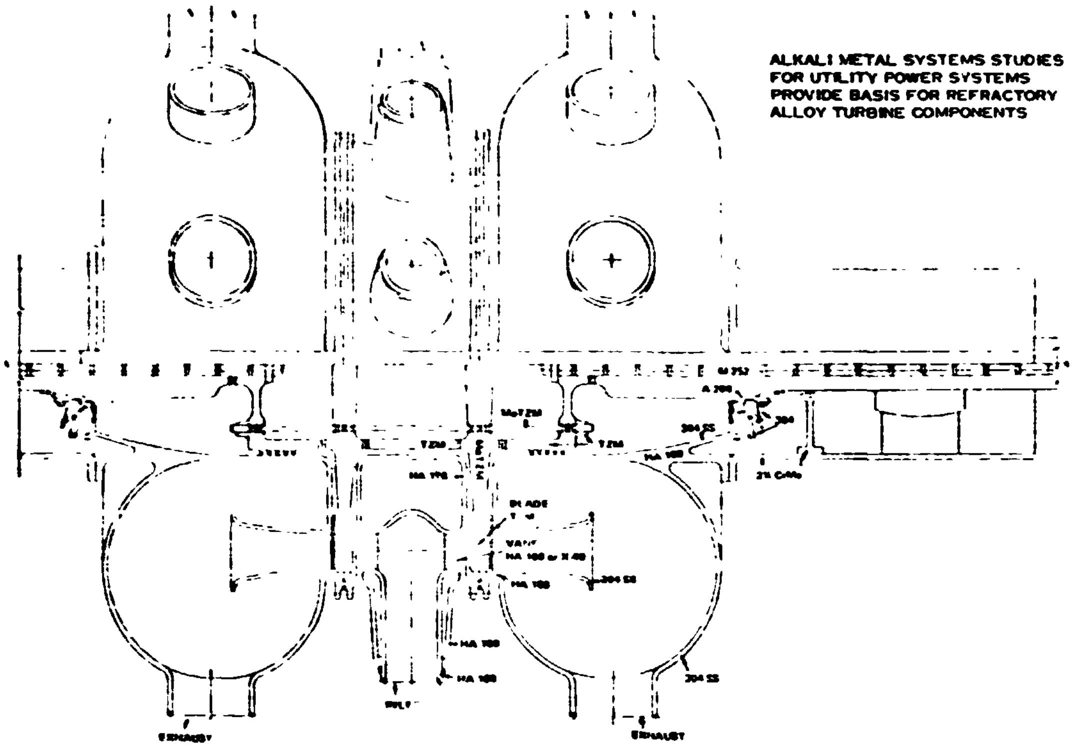

Figure 3.3-21 High Pressure Potassium Turbines

GENERAL ELECTRIC

space division

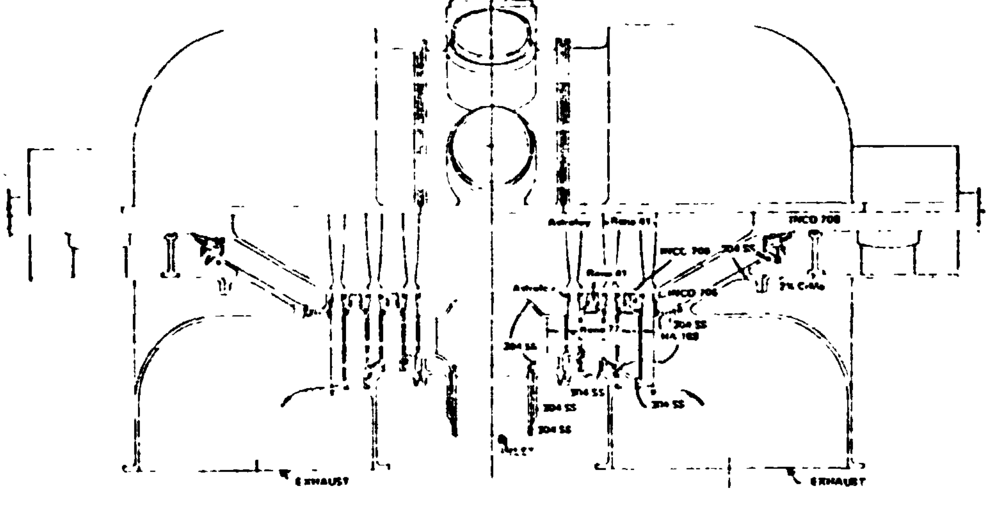

Figure 3.3-22 Low Pressure Potassium Turbines

ORIGINAL PAGE IS
OF POOR QUALITY

For the 2500°F system the low pressure turbines are the same as for the 2100°F system. The high pressure turbine is a preliminary design in which two stages were added in front of a previous design for 1700°F. These two high temperature stages utilize silicon carbide for discs and blades. Preliminary design calculations indicate that these two stages can be designed with stresses of 10,000 psi, but additional design work is needed. The weights and cost for the high pressure turbine are very approximate.

In each cycle the high pressure turbine consists of only a few turbine stages; each high pressure turbine has double flow such that one high pressure turbine feeds two low pressure turbines, each of the latter also being of double flow configuration. This is necessary to handle the increasing turbine flow area in the succeeding turbine stages and adds considerably to the size and weights of high pressure turbine scrolls connecting and feeding the low pressure turbines and the inlet and exhaust scrolls of the low pressure turbine.

Turbine design data are summarized in Figure 3.3-23.

Both Brayton and Rankine cycle systems will require large diameter turbine discs. (Figure 3.3-24).

The largest diameter turbine disc forged from a very high temperature superalloy was the Astroloy forging used in the GE Supersonic Transport Engine (SST); it had a nominal diameter of about 40 inches. A lower temperature alloy, INCO 608, has been forged in diameters to 68 inches. These discs represent the present maximum size for existing state-of-the-art materials technology for superalloys. Refractory alloy turbine discs, such as molybdenum TZM, are restricted to about 40 inches in diameter because of arc casting and extrusion facility size limits.

Studies in the area of powder metallurgy indicate that larger size discs up to, or larger than, 80 inches are possible by preparation of powder metal billets of uniform composition, achieving full density on existing maximum size high temperature, high pressure auto-claves and forging to disc size by a combination of limited upset forging in a 50,000 ton press (maximum size), cross rolling on the largest plate mill in the US and finish localized, or sector, forging in the nation's largest press forge.

The preparation of large size superalloy and refractory alloy discs will be a major undertaking. The preparation of silicon carbide discs of sizes approaching 65 inches will also be a major problem for which the practical difficulties are perhaps more difficult to envision at present.

ORIGINAL PAGE IS
OF POOR QUALITY

	GENERAL ELECTRIC	space division
TURBINE INLET TEMPERATURE, °F	2100	2500
NUMBER OF HP TURBINES	22	18
NUMBER OF STAGES	5	3
ROTATIVE SPEED, RPM	1800	3600
SIZE	20'L X 15'H	18'L X 9'H
ESTIMATED WEIGHT, LBS	6×10^6	2.26×10^6
ESTIMATED COST	$\$142 \times 10^6$	$\$78.7 \times 10^6$
NUMBER OF LP TURBINES	44	36
NUMBER OF STAGES	4	4
ROTATIVE SPEED, RPM	1800	1800
SIZE	27'L X 15'H	27'L X 15'H
ESTIMATED WEIGHT, LBS	16.328×10^6	13.36×10^6
ESTIMATED COST	$\$283.9 \times 10^6$	$\$232.3 \times 10^6$
TOTAL WEIGHT, LBS (4800 MWe)	22.328×10^6	15.62×10^6
TOTAL COST (4800 MWe)	$\$425.9 \times 10^6$	$\$311 \times 10^6$
MATERIALS, HP TURBINE	TZM, TZC, T-111	S C, TZM, T-111
MATERIALS, LP TURBINE	SUPERALLOYS ASTROLOY, RENE '41, INCO 718, RENE '77 HA-188, HASTELLOY X, 316 SS	SUPERALLOYS ASTROLOY, RENE '41, INCO 718, RENE '77 HA-188, HASTELLOY X, 316 SS

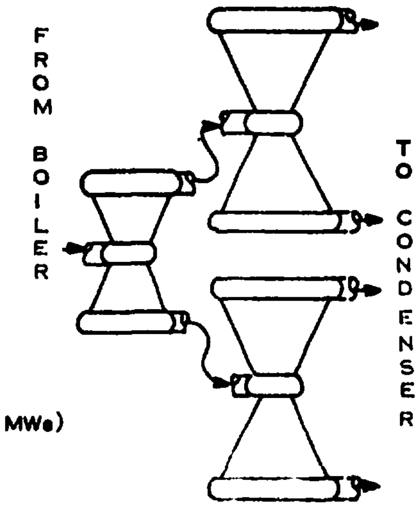

ADDITIONAL TURBINE DESIGN EFFORT REQUIRED

*1100°F CONDENSING TEMPERATURE

Figure 3.3-23 Preliminary Potassium Turbine Configurations*

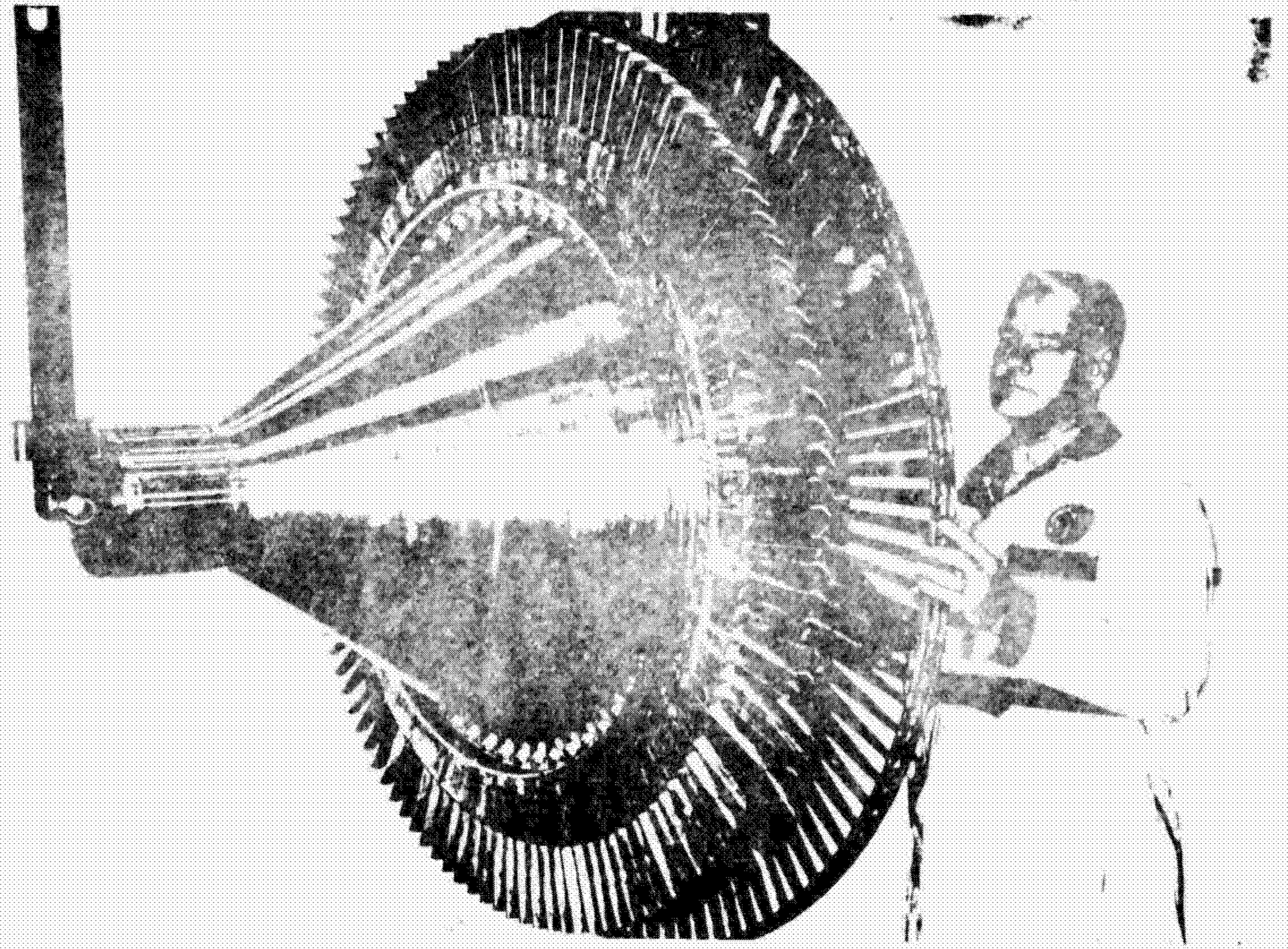

Figure 3.3-24 Large Diameter Turbine Discs

The relatively large turbine sizes and weights of the potassium turbines scaled from prior land-based power conversion system studies suggests the possibility of considering the use of cesium as a working fluid to reduce turbine size. In prior space power studies the relatively low power levels required and small turbine sizes occasioned by the use of cesium as a working fluid would have resulted in small first stage turbines, very short first stage turbine blades and significant first stage tip losses. These effects are of less consequence in the larger power level turbines now being considered

The more significant advantages and disadvantages of cesium turbines are presented qualitatively. The physical and thermodynamic properties of cesium result in smaller diameter turbines with fewer stages. As a result of the reduced number of stages turbine disk temperatures are lower than for equivalent potassium systems; furthermore, the reduced expansion ratio of cesium vapor turbines should limit the growth of scroll weights and sizes in the latter stages.

Prior comparative studies of potassium and cesium turbines over a more limited temperature range indicate cesium turbines could weigh much less than half that of similar potassium turbines. Specific preliminary design effort is necessary to determine the effectiveness of such potential weight reductions.

3.3.3 Thermionic SPS

Figure 3.3-25 shows the thermionic SPS configuration as developed in the "Space Based Power" study (Contract NAS8-31628).

Thermionic diodes surrounded the cavity absorber and rejected their waste heat directly through heat pipe fins. A tradeoff conducted as a part of the subject study showed this design solution to be less massive than the use of separate radiators with a heat transport fluid loop. In addition, it was far simpler.

3.3.3.1 Converter Design

The thermionic converter is inherently a high temperature, high current, low voltage device. Providing a configuration that can reject waste heat and series-connect the converter diodes electrically without heat shorts is a major design problem.

ORIGINAL PAGE IS
OF POOR QUALITY

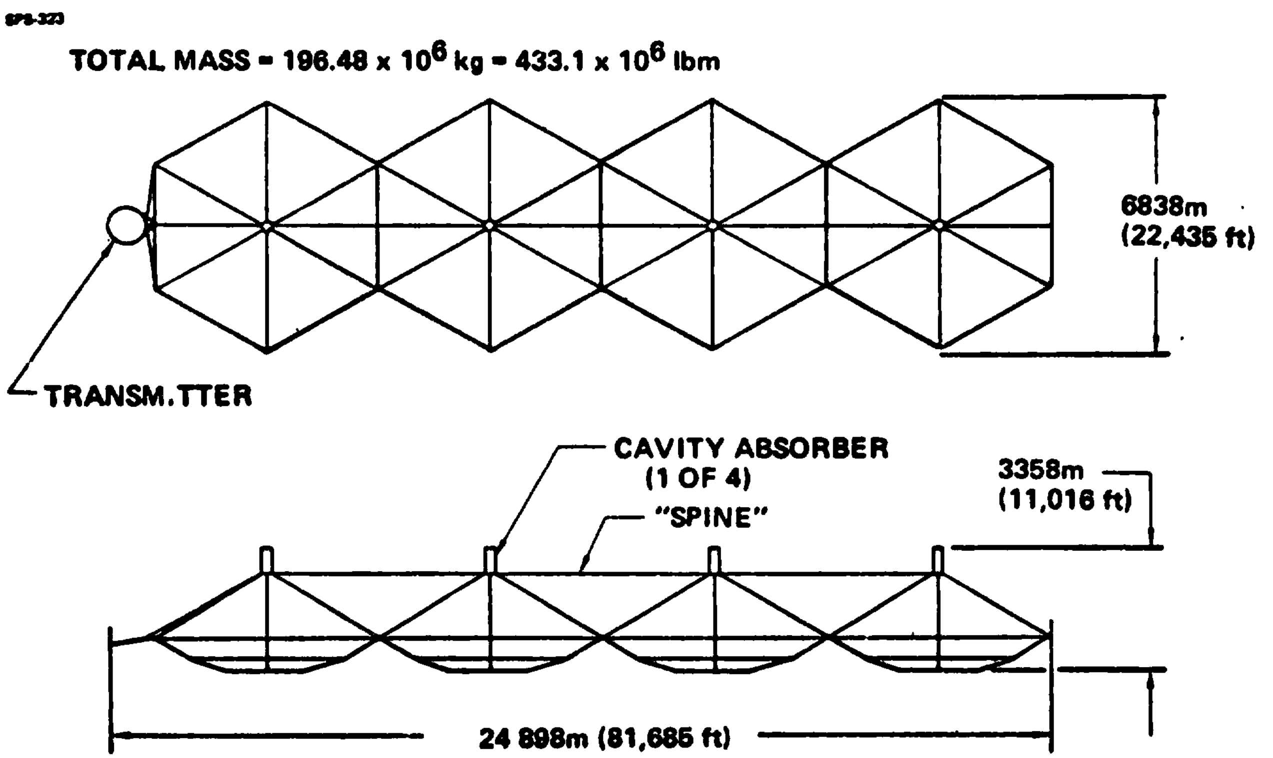

Figure 3.3-25 Solar Thermionic SPS 10-GW Ground Output

Analysis of simple cooling fins indicated that they would be far too massive. The alternative approach is to employ a heat-pipe concept to provide a uniform radiator temperature and, thereby, achieve uniform heat rejection temperature and high fin efficiency. A number of configurations were considered: the one judged best is shown in cross section in Figure 3.3-26. Sizing of the emitter is determined by loss of material from thermal vaporization over its thirty-year lifetime, minimization of resistive power losses, and weight considerations: sizing of the collector depends on resistive and weight considerations.

Note the relatively massive busbars. These must dissipate their I^2R loss to the heat pipe radiator, which is at a temperature of 1000K (1340°K). The higher temperature cavity is blocked from the busbars by the insulation shown. The busbars carry a current of 1290A. Alternative busbar designs, such as sodium filled steel tubes were evaluated: copper is lighter.

Figure 3.3-27 presents an isometric cutaway of the converter. It shows the side of the converter which would face the cavity interior The hexagonal assembly is the heat pipe radiator.

3.3.3.2 Mass Reduction Analysis

Reconfiguration of the heat pipe radiators for the diodes of the thermionic SPS would allow a significant mass reduction. This is because the form of the heat pipes sets the distance between the individual diodes and hence the length of the interelectrode busbars between these diodes The heat pipes are hexagonal with the circular diodes mounted at their centers as shown in Figure 3.3-28.

The heat pipe projected area is 0.1 M^2 each so that the center to center distance is 34 cm. The diodes are 10 cm in diameter. The resultant busbar length (allowing for the curvature) is approximately 26 cm. The busbar cross section is about 13 cm^2: their material is copper. Hence the mass of one busbar is approximately 2.83 kg.

17.47×10^6 diodes were required for a 10 GW ground output SPS. Thus the total busbar mass is 49.6×10^6 kg. which is 25.1% of the total mass of 196.84×10^6 kg for the entire thermionic SPS.

The busbars run quite hot since they can only dissipate their I^2R power to the adjacent heat pipe radiator which has a mean temperature of 900K. The resistivity of the copper is consequently so high that the busbar I^2R loss amounts to 14% of the diode output.

Reconfiguration of the heat pipe radiators to the form shown in Figure 3.3-29 expected to have almost no effect on the mass of the heat pipe.

ORIGINAL PAGE IS
OF POOR QUALITY

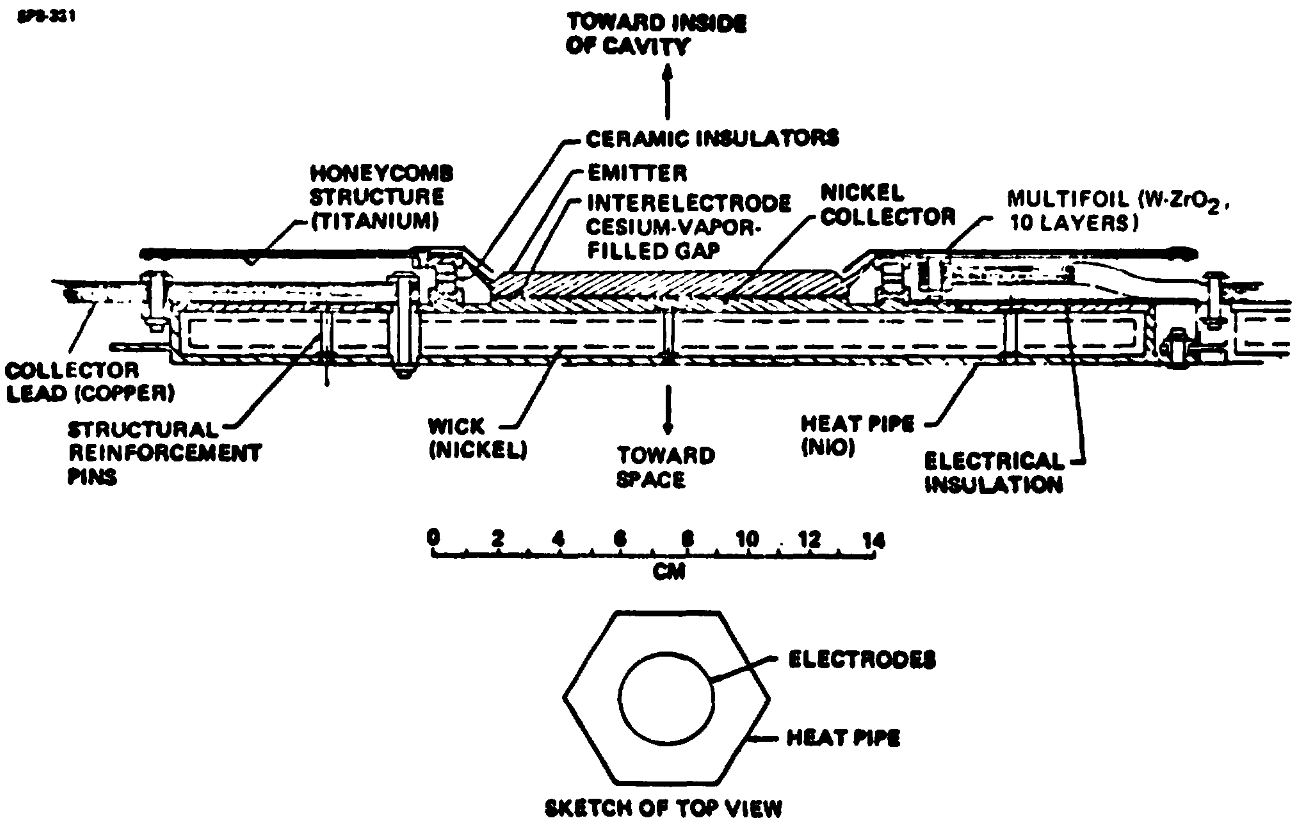

Figure 3.3-26 SPS Thermionic Converter Design

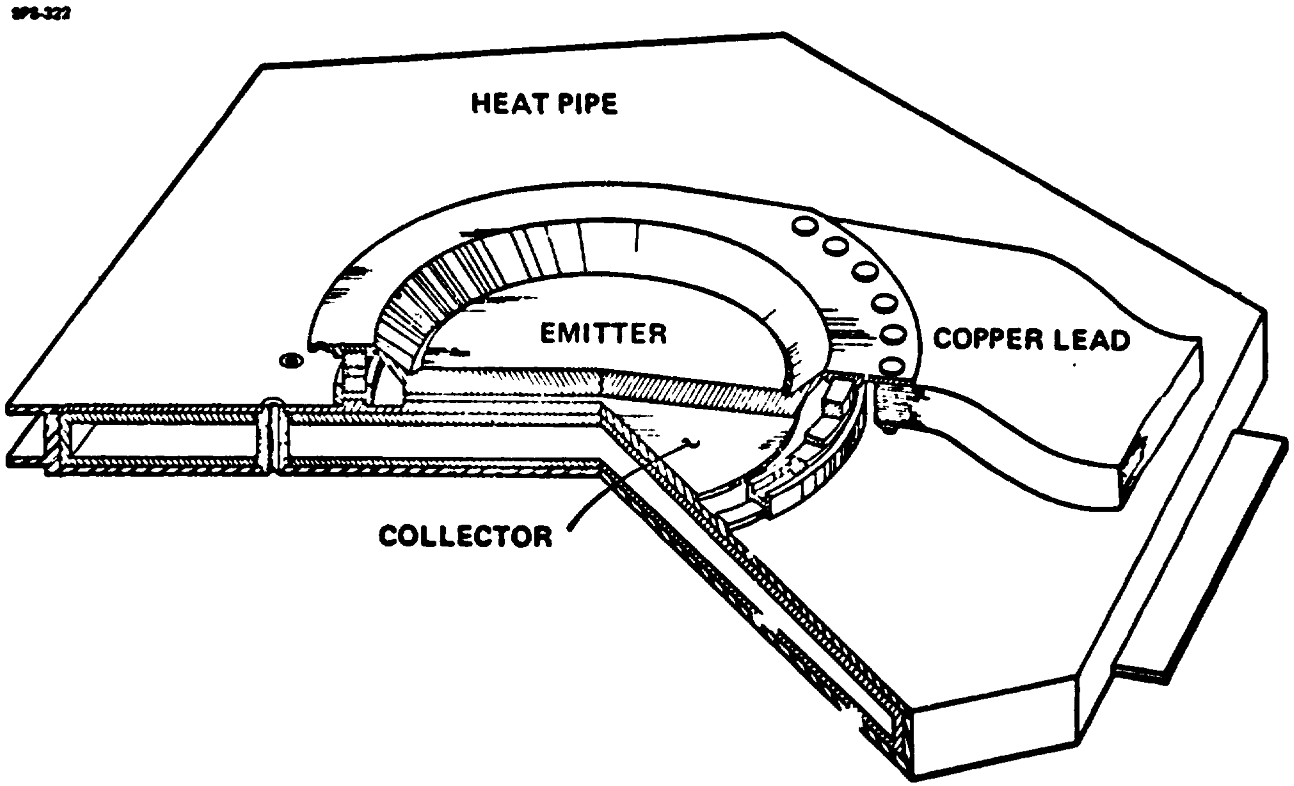

Figure 3.3-27 Isometric Cutaway of SPS Thermionic Converter

ORIGINAL PAGE IS
OF POOR QUALITY

SPS-320

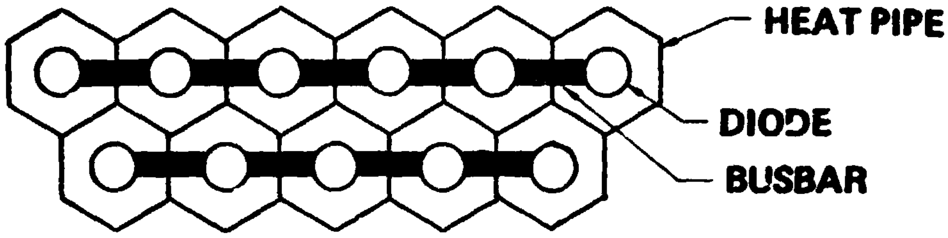

Figure 3.3-28 Diode Configuration From Space-Based Power Study

SPS-320

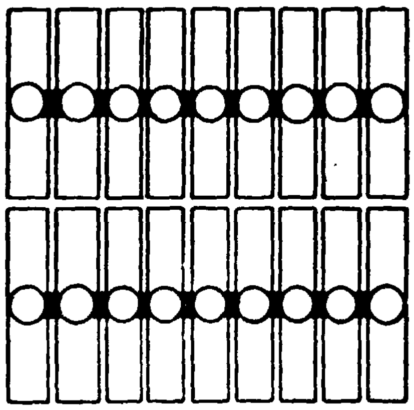

Figure 3.3-29 Improved Diode Configuration

The busbar length in this arrangement would be approximately 7 cm (the busbar must still contain a special section of high thermal resistivity to block emitter to collector thermal losses). The resultant mass is approximately 0.80 kg per busbar. The I^2R loss in the busbars would now only be approximately 4% of the diode output.

Reduction in busbar I^2R loss would impact approximately 185 x 10^6 kg of the original SPS mass (it does not effect the transmitter). The new corresponding mass is:

$$\frac{1-0.14}{1-0.04} \text{ X } 185 \text{ X } 10^6 \text{ kg} = 165.7 \text{ X } 10^6 \text{ kg.}$$

The lower I^2R drop reduces the number of diodes and hence the number of busbars required to 15.65 x 10^6. The busbar mass is thus "only" 12.5 x 10^6 kg instead of the

$$\frac{1-0.14}{1-0.04} \text{ X } 49.47 \text{ X } 10^6 \text{ kg} = 44.3 \text{ X } 10^6 \text{ kg}$$

it would otherwise have been. Thus an additional mass reduction of

$$44.3 \text{ X } 10^6 \text{ kg} - 12.5 \text{ X } 10^6 \text{ kg} = 31.8 \text{ X } 10^6 \text{ kg}$$

may be subtracted from the 165.7 X 10^6 kg. to yield a final mass of 133.9 X 10^6, which plus the transmitter gives a total thermionic SPS mass of 145.8 X 10^6 kg.

This new mass is still about 80% more than that of the Brayton system.

The closer busbar spacing shown above still only allows about 140 diodes to be placed in a 20 m long series string. Thus a series string of this length would not yield more than the 150 volt limit estimated for the high temperature electrical insulation.

3.3.4 Radiator System

3.3.4.1 Radiator Design Requirements

The dominant mass element in the Brayton system is the radiator. It has the job of rejecting 22.5 gigawatts of thermal power in the baseline design (the waste heat to be rejected from the cycle). About 40 gigawatts of energy is input to the gas, about 17 is available to go to the transmitter, and the remainder must be rejected by the radiator. Nominal inlet and outlet temperatures are 644K and 377K, respectively. We must select an appropriate (i.e., optimum) pumping power. If the fluid manifolds are small, they are light but have high pressure drop, so more power must be taken from the output to drive the pumps. Also, we want no net generation of angular momentum. Any loop of fluid flow or turning turbomachine requires another going in the opposite direction, like contra-rotating propellers on an airplane.

We have somewhat arbitrarily selected a meteoroid protection requirement for the manifolds such that a major penetration and repair is expected to occur at five year intervals. Radiators must withstand being shut down when passing through the Earth's shadow and start up again in five minutes.

Figure 3.3-30 shows that as a solar power satellite orbits the Earth and the Earth orbits the Sun, the SPS is always pointing towards the Sun. The smaller figure shows the radiator oriented to be in the plane of the ecliptic and edgewise to the main meteroroid flux.

The previous figure showed the radiator placed in the plane of the ecliptic. Figure 3.3-31 shows the flux concentrated at a low angle to the ecliptic plane. This angular concentration extends round the leading edge of the radiator from helion to anti-helion. Thus, the radiator sees the meteoroid flux impinging in a concentration at an angle of approximately 15° to its plane of motion. Meteoroid armoring analyses used this preferential orientation approach, resulting in a significant reduction in armor requirements.

SPS-332

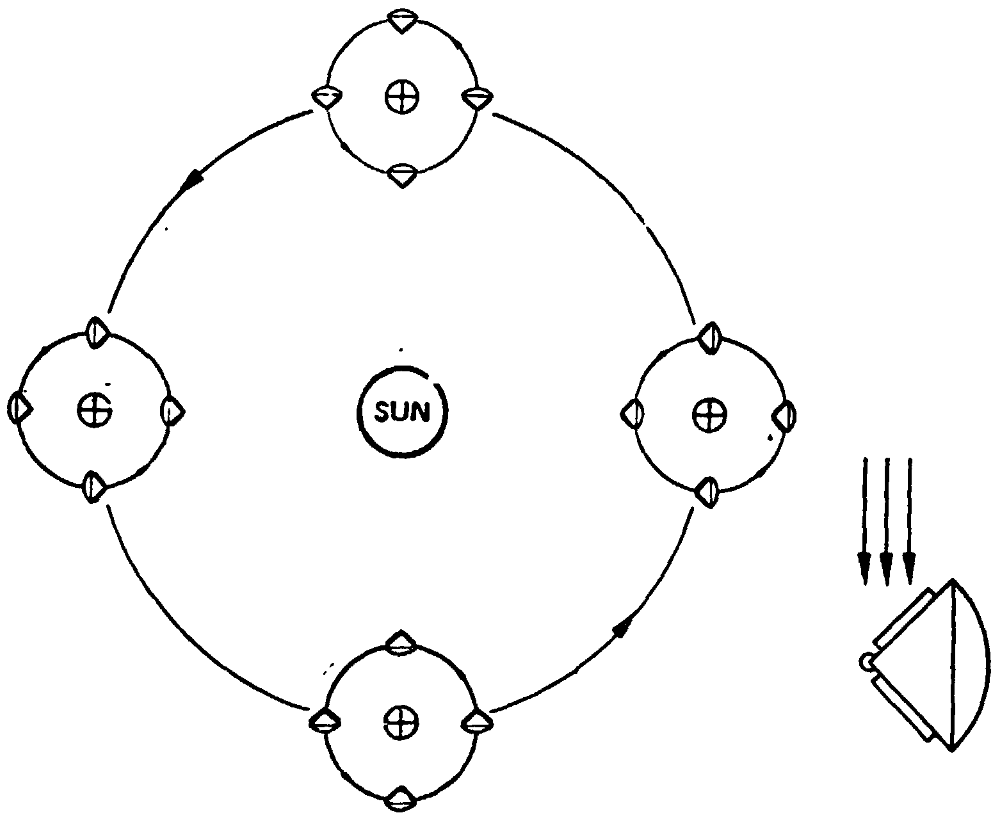

Figure 3.3-30 SPS Radiators Can be Preferentially Oriented

SPS-330

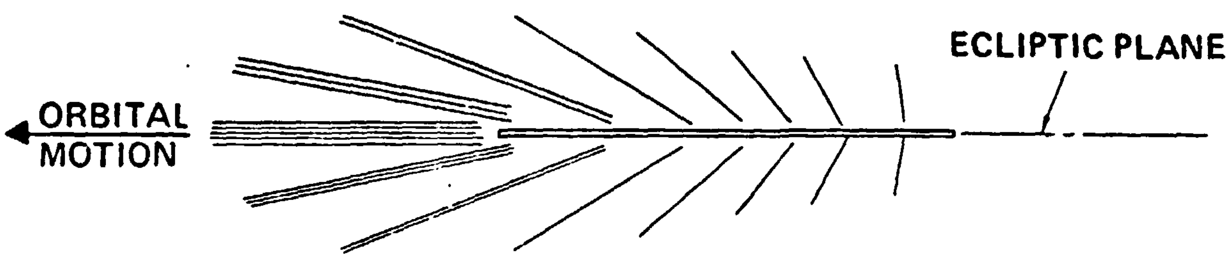

Figure 3.3-31 Meteoroid Flux Seen by Radiator

ORIGINAL PAGE IS
OF POOR QUALITY

3.3.4.2 Reference (4-module SPS) Radiator Design

The radiator for the mid-term configuration (four modules in the satellite) is shown in Figure 3.3-32. With 64 turbomachines, this required 16 engines per module. The cavity absorber with the engines is in the center. The concentrator is below, with its concentrated energy entering the aperture. The radiator panels are divided into groups. Panels with the number 1 cool engine number 1, number 2 cools number 2; 8 cools number 8 and so forth. It is clear that the manifolds for number 8 are much longer than the manifolds for number one. There is a significant mass penalty associated with the liquid metal in manifolds.

The definition of radiator panels was based on this radiator design. The panel design was subsequently applied to the revised radiator design for the 16-module configuration.

Figure 3.3-33 indicates the diameters of the manifolds and headers. The headers are center-fed, so that temperature induced length changes are halved This reduces the angular motion at the ends of the heat dissipation panels.

The basic element of the radiator panels is the heat pipe. Over limited lengths the heat pipe is an extremely efficient heat transport mechanism, being hundreds of time more effective than, for instance, a solid copper rod. Figure 3.3-34 illustrates the heat pipe principle

The working fluid vaporizes as heat input is provided to the evaporator section. The vapor moves through the pipe to the condensor section. Here the fluid gives up its latent heat of vaporization and returns to the liquid state The fluid returns to the evaporator section by capillary action

If compatible materials (fluid, wick and tube) are used, a heat pipe operating within its design range has an almost indefinite operational life.

Heat transport capability is shown in Figure 3.3-35 (non-dimensional) for various heat pipe fluids over a range of temperature. Initial optimizations of the Brayton SPS indicated a radiator temperature range requiring mercury working fluid. Known reserves of mercury were not sufficient for the baselined SPS program. Therefore the temperature range was adjusted to allow the use of water heat pipes.

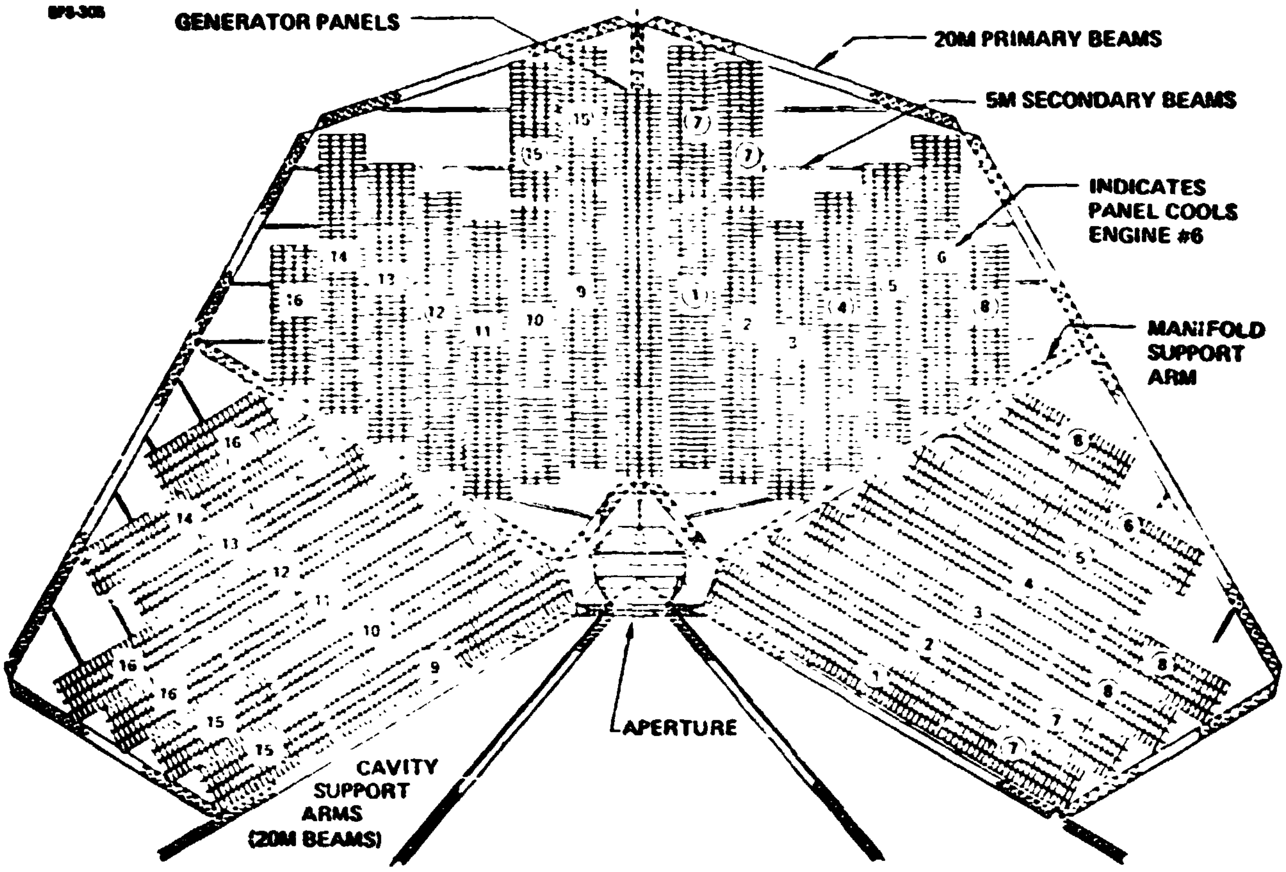

Figure 3.3-32 Radiator Configuration: Brayton SPS Module (Midterm, 16 Engines Per Module)

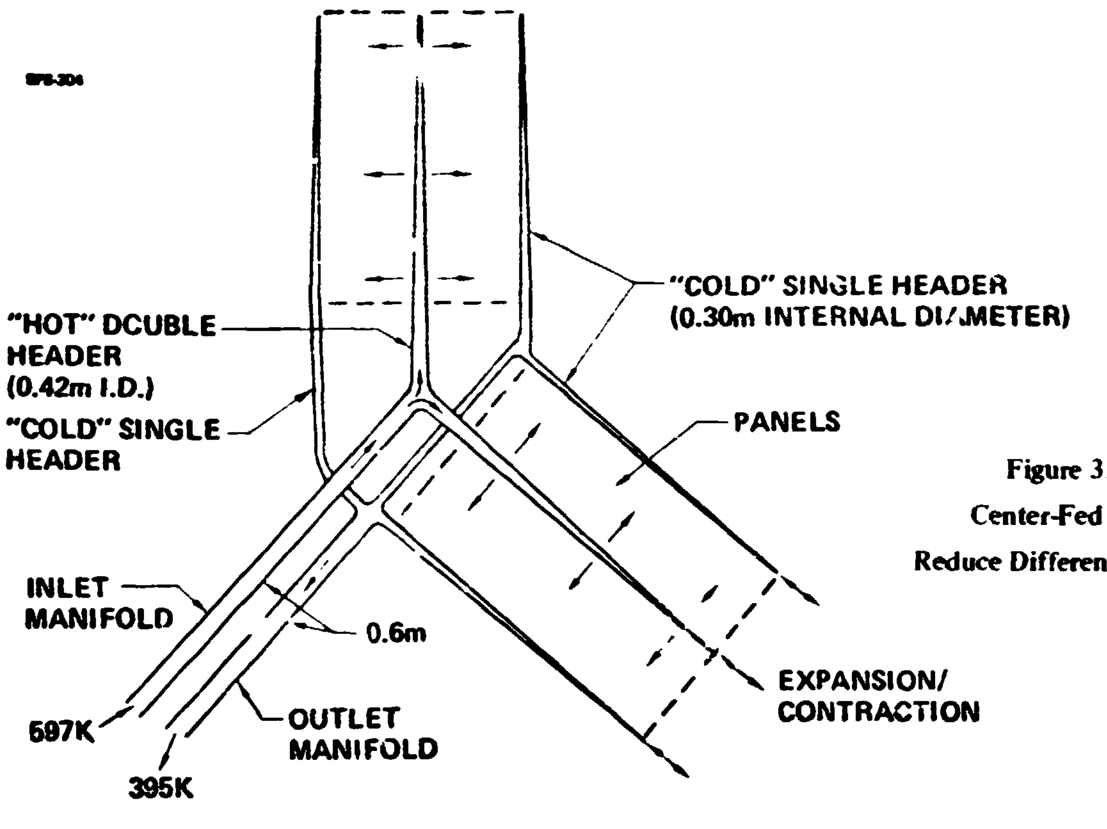

Figure 3.3-33
Center-Fed Headers
Reduce Differential Motion

ORIGINAL PAGE IS
OF POOR QUALITY

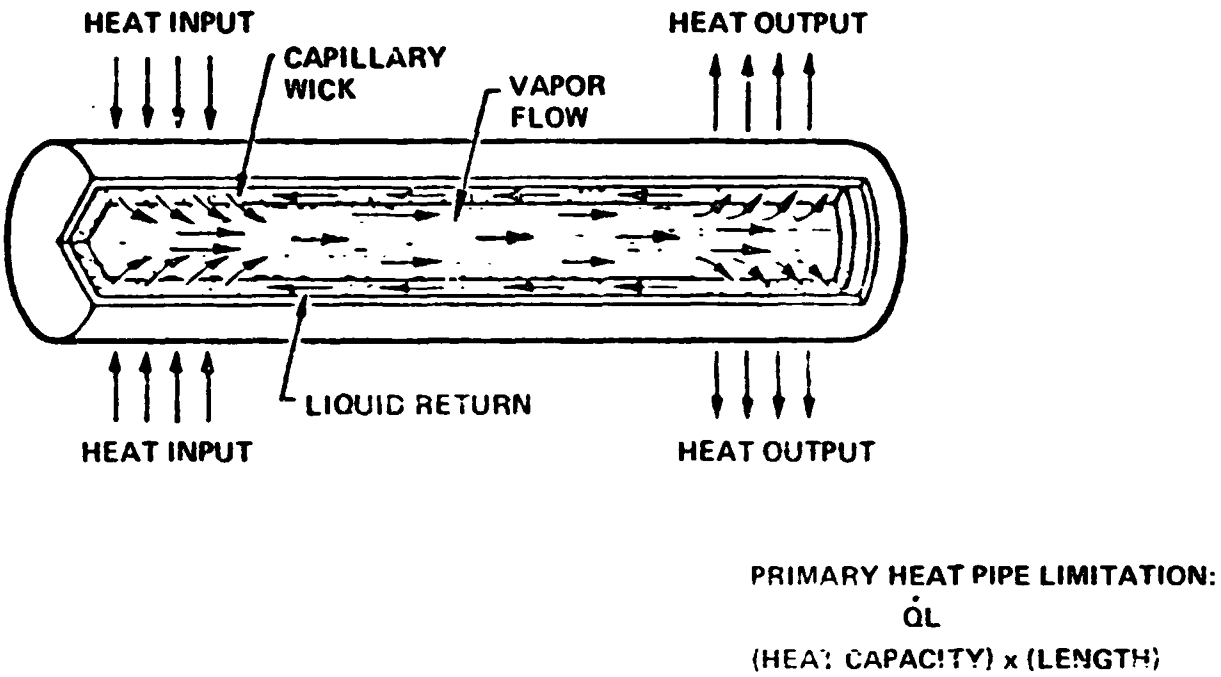

Figure 3.3-34 Heat Pipe Principle

SPS-307

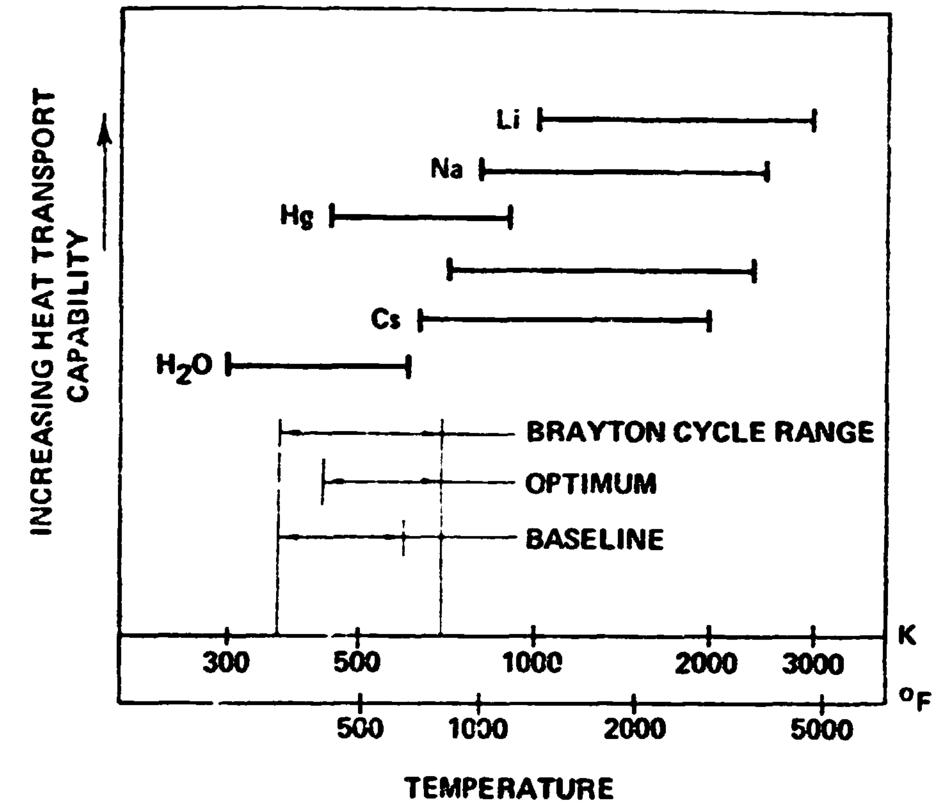

Figure 3.3-35 Heat Pipe Fluids: Heat Transport Capability and Temperature Regime

Shown in Figure 3.3-36 is a cross section of three heatpipes and some pertinent information relative to them. The heatpipes are spaced apart approximately 1.5 diameters. Fins are not used. The heatpipes, themselves, provide the radiating area. The working fluid is water. The heatpipe shell is thin stainless steel, with an internal stainless steel screen wick.

The panels illustrated in Figure 3.3-37 are 5 by 20 meters, and sized to stack in the launch vehicle payload bay. They reject the cycle waste heat from water heat pipes. Hot liquid metal travels through the throughpipe giving up its heat to the heat pipes attached to it; heat pipes alternate in direction as shown. They are the heat rejection elements, there are no fins. The heat pipes are spaced at about one and one half times their diameter.

The 64 turbomachines of the Brayton SPS each have a radiator schematic as shown in Figure 3.3-38. The accumulator (a zero gravity type) keeps the NaK loop full despite volume changes from temperature changes and manifold creep. Hot NaK is admitted to the three pumps. The 57.30 kW indicated is the electrical input to each pump. The manifolds conduct the flow to the header system which directs the flow to the heat-dissiption panels. Valves are provided where appropriate.

Figure 3.3-39 is a layout drawing for the updated reference radiator configuration.

3.3.4.3 Revised (16-Module) Radiator Configuration

This radiator configuration takes advantage of the required large throughpipe diameter, and has shorter manifolds as illustrated in Figure 3.3-40.

One motivation to go to 16 modules was to have a module size closer to the size of a developmental unit. When we changed to that size (four engines per module), the manifolds became short. The basic job of the manifold is to carry the fluid out to the radiator panel. The liquid metal travels through a throughpipe, giving up its heat to the heat pipes it passes through. With four engines per module (sixteen modules) and with square radiator panels as shown here it is clear that we don't have long manifold lengths. The total manifold mass in the SPS has been greatly reduced by going to sixteen modules. Also, we have realized that the throughpipes in the panels can be connected in series to eliminate the numerous intermediate headers, because the throughpipes must have a large diameter and resulting low pressure drop in order to provide enough heat transfer area to transfer the heat to the heat pipes

Note that the pumps include a redundant set for both the hot and the cold (or return) sides. That is, each pump has a redundant or matching pump to reduce the time between servicing periods on the pump set.

ORIGINAL PAGE IS
OF POOR QUALITY

SPS-308

Working fluid:	Water
Material:	Stainless steel (316)
Wick:	Circumferential screen wick
Diameter:	2.5 cm
Length:	2.94m
Evaporator section:	0.44m
Adiabatic section:	0.05m
Condensor section:	2.45m
Q:	332 W
Fins:	None
Interface to NaK manifold:	Single wrap
Spacing:	1.50 diameters
Pipe-to-pipe view factor	0.115

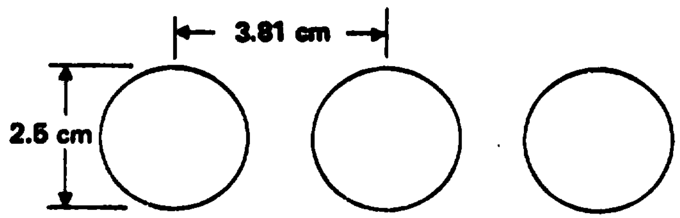

Figure 3.3-36 Baseline Heat Pipe

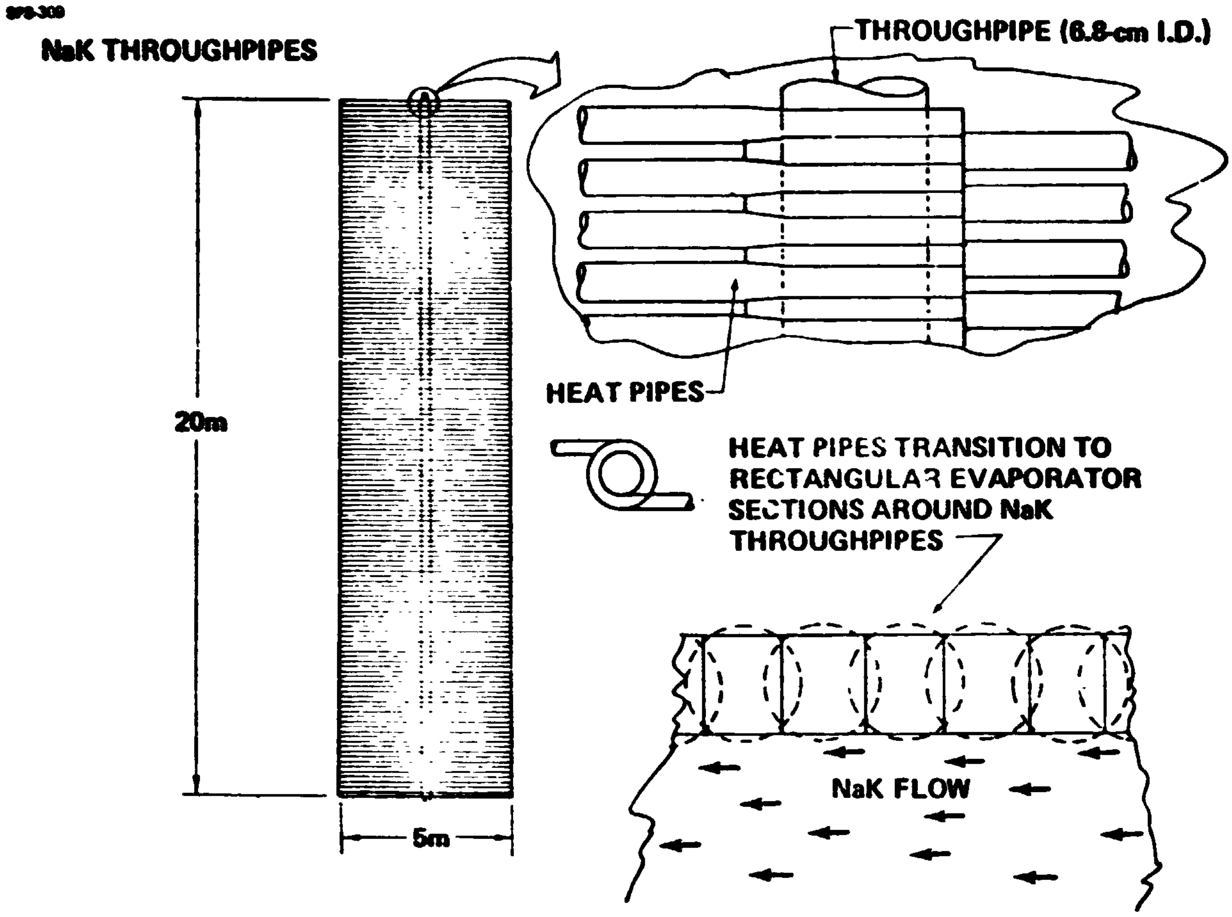

Figure 3.3-37 Heat Pipe Panel Details

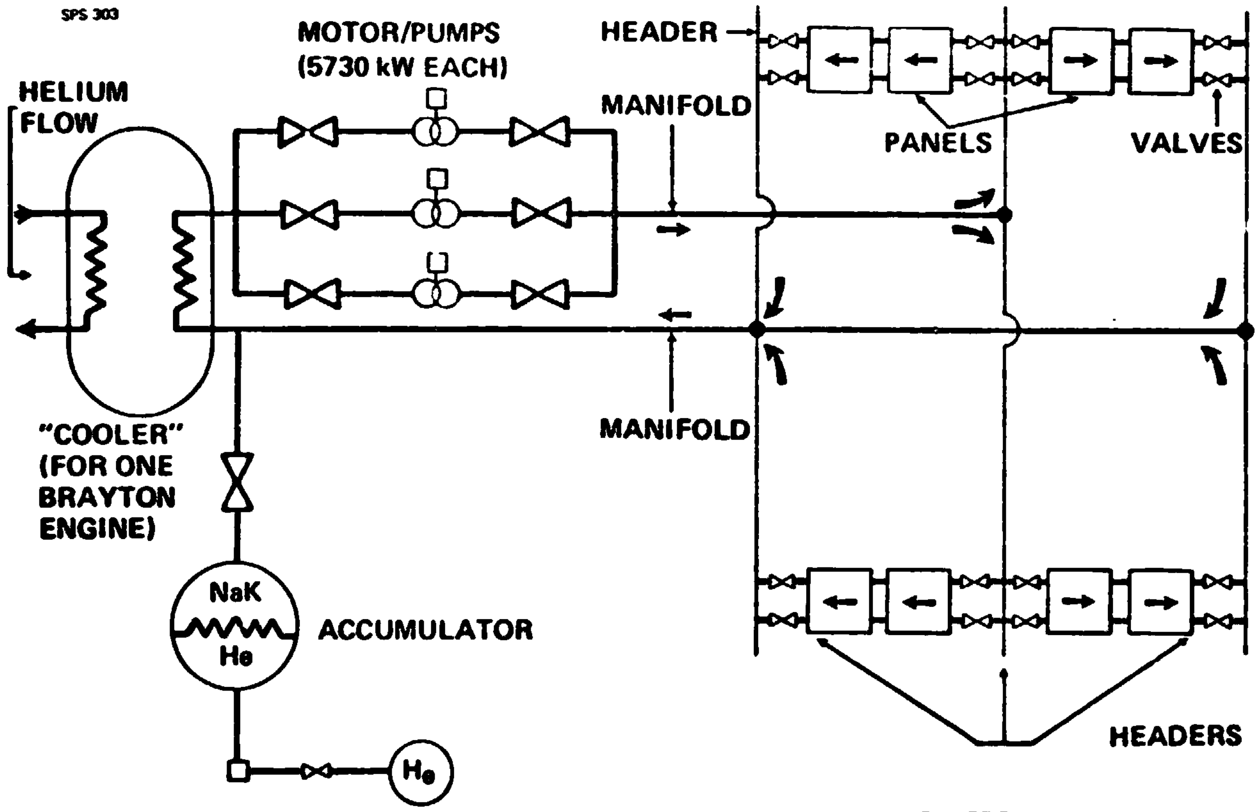

Figure 3.3-38 Radiator Flow Schematic (NaK Loop, 64 Per SPS)

ORIGINAL PAGE IS
OF POOR QUALITY

FOLDOUT FRAME

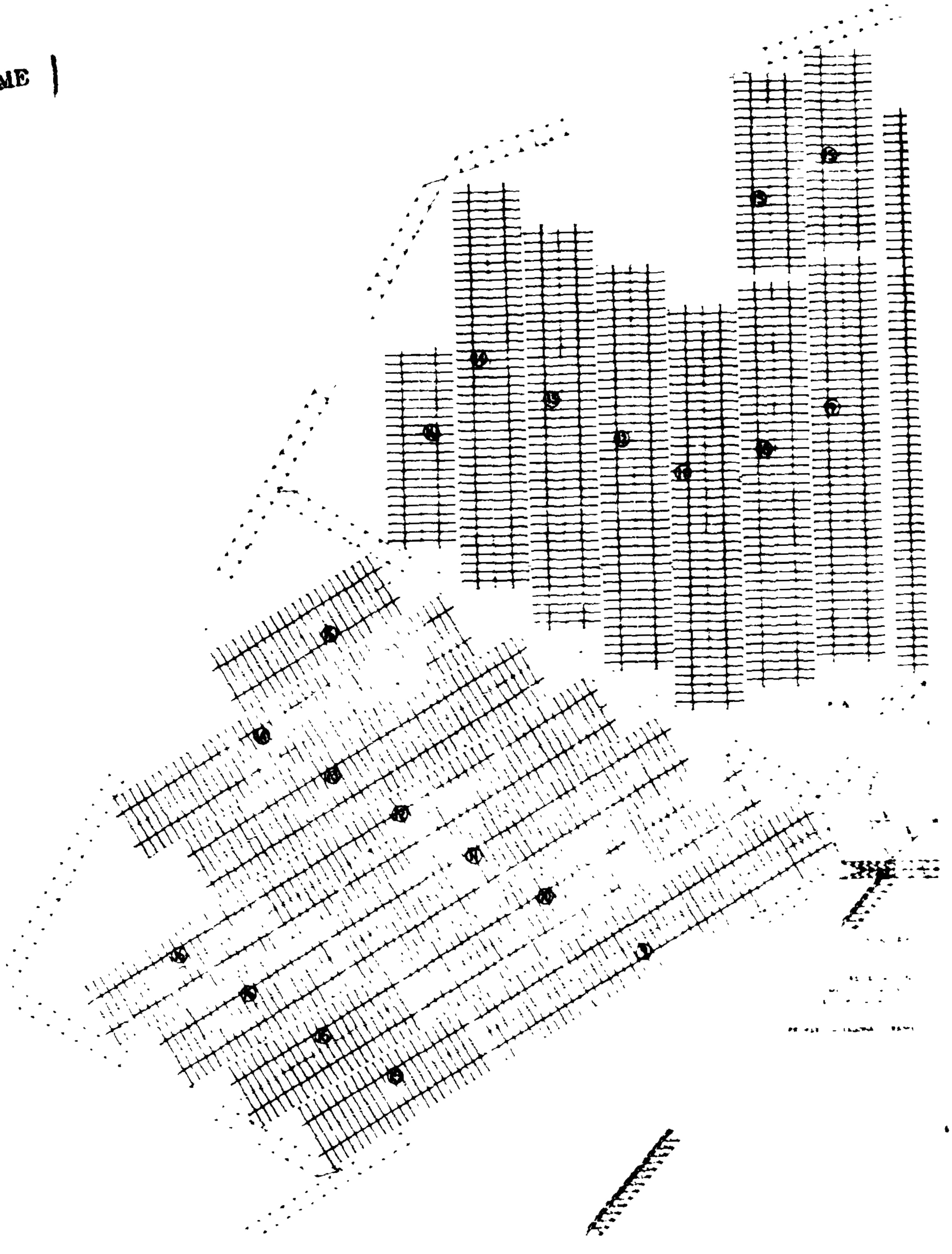

ORIGINAL PAGE IS
OF POOR QUALITY

PRECEDING PAGE BLANK NOT FILMED

FOLDOUT FRAME 2

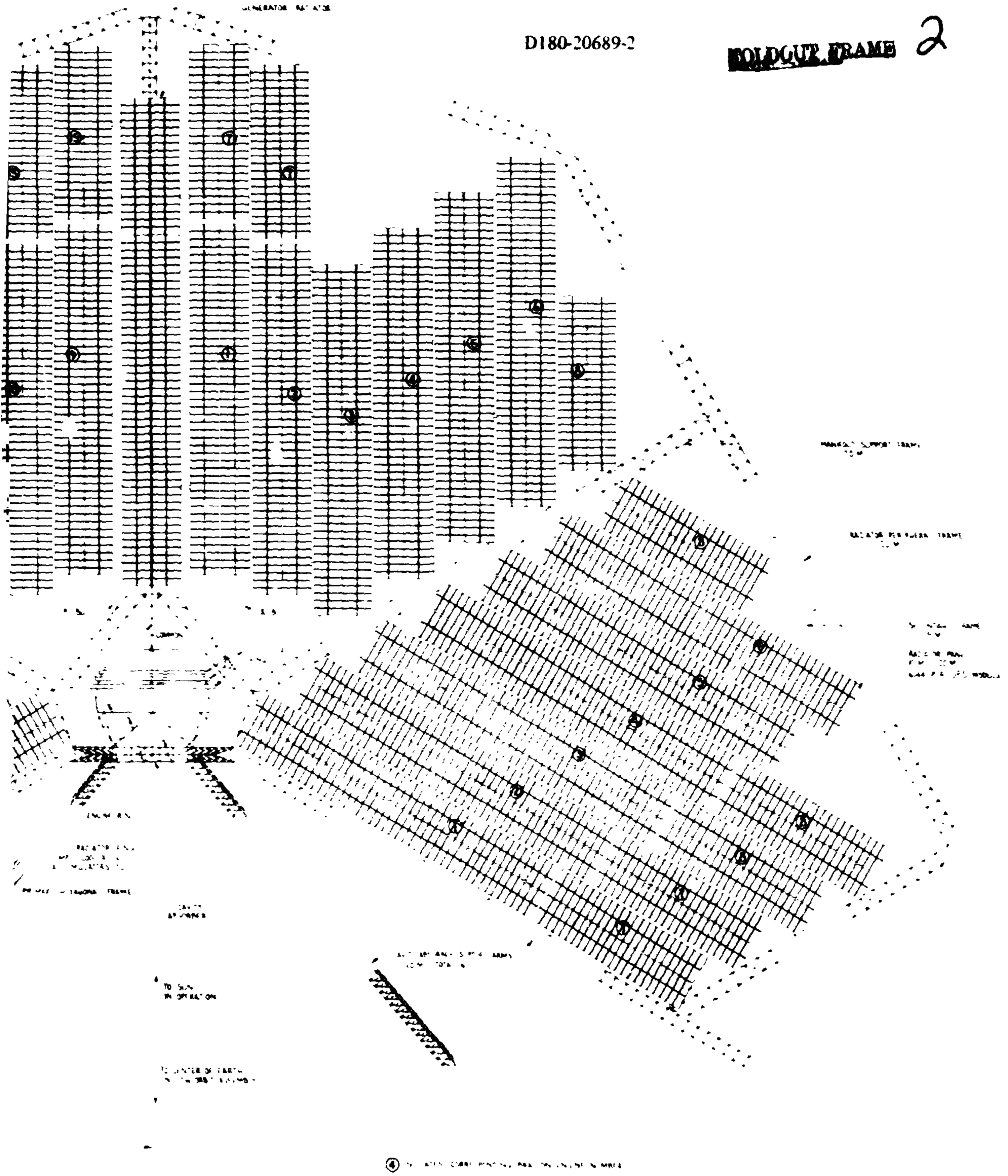

Figure 3.3-39 Radiator Configuration Revised Radiator Configuration

ORIGINAL PAGE IS
OF POOR QUALITY

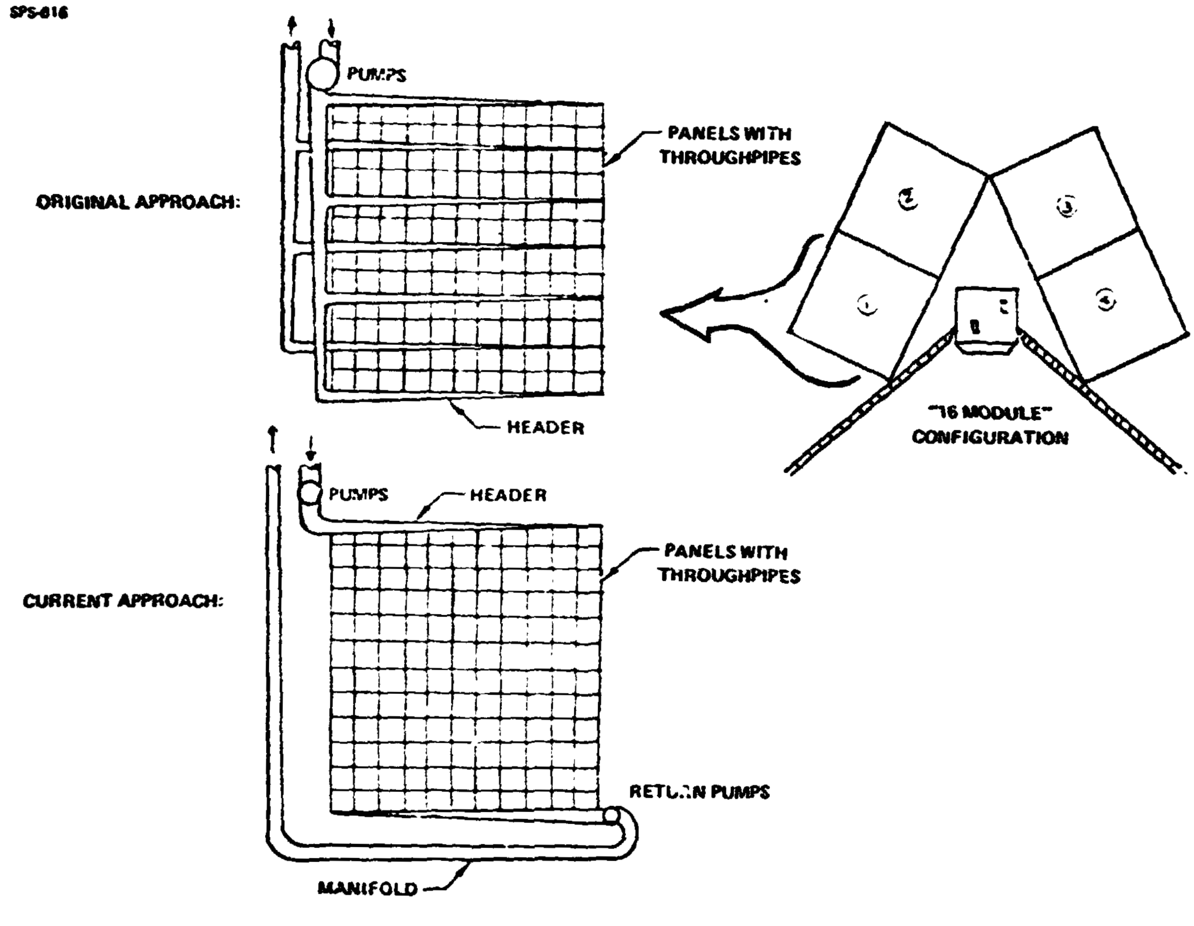

Figure 3.3-40 Radiator Configuration

ORIGINAL PAGE IS
OF POOR QUALITY

3.3.4.4 Radiator Analyses

The result of radiator design analyses are described in this section. The objective of the work was to develop radiator design for the thermal engine energy-conversion options which were advanced to the system mass screening test. The radiator designs were based on first-order considerations and mass estimates made from these designs were used in the system mass screening test to identify low-mass concepts. *Radiator mass comparison data quoted in this section are for one thermal engine of 275 megawatt generating capacity. The figures should be multiplied by 64 to arrive at a total SPS mass comparison.*

Two basic types of radiators were modeled in this analysis. The first type utilized a single-phase fluid, either gas or liquid, to transport energy to the radiating surfaces. The second type of radiator used a condensing vapor as an energy transport fluid.

Computer models were developed for each radiator type. Input variables included heat loss rate, radiator material properties, fluid properties, environmental variables, and fluid boundary conditions (temperature and pressure at inlet and outlet). The models calculated radiator area, ducting size and wall thickness, radiator length and width, fluid mass flow rate and pressure drop, pump size and mass of each major radiator element.

Potassium Rankine Cycle Radiators

Two types of radiators were investigated for the potassium Rankine cycle options. Radiators which utilized the potassium working fluid as a heat transport medium were found to be the least massive of the two radiator options. The potassium entered these radiators in the two-phase state at high vapor quality and was completely condensed at the outlet. These radiators operated at a nearly uniform temperature and, since the cycle working fluid rejected its energy directly to space, there was no requirement for a heat exchanger. The second type of radiator studied was a single phase NaK loop system. Since the Rankine cycle characteristically rejects energy as constant temperature, this concept had a lower effective average temperature than the condensing potassium radiator. This fact, in conjunction with the requirement for a heat exchanger, resulted in NaK radiator system being more than twice as massive as the condensing potassium designs.

Figure 3.3-41 shows the essential element of the condensing potassium radiator. Saturated vapor, or vapor-liquid mixture, enters the tapered inlet header and is distributed to the through-pipes. Energy rejected from the condensing fluid in the throughpipes is conducted into the fins and radiated to space. The condensing region of the radiator, in which the fluid in the throughpipes exists in the two-phase state, is isothermal. An additional element of length is added to the throughpipes to ensure that the fluid is subcooled when it exits from the throughpipes. This eliminates boiling in the

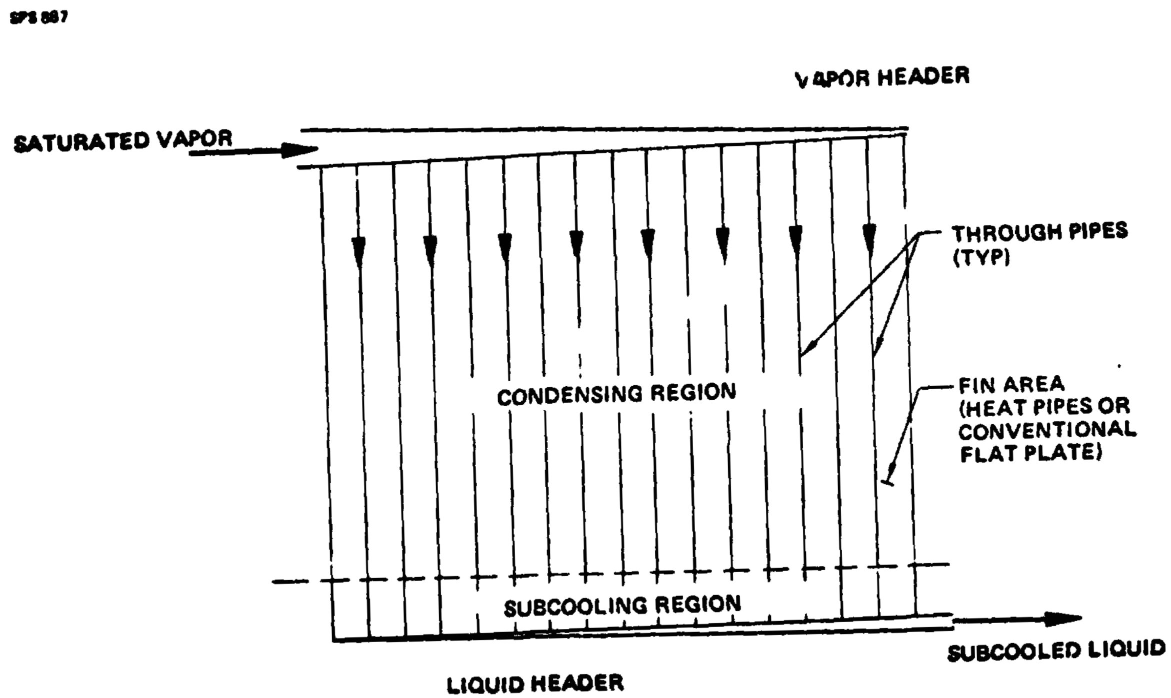

Figure 3.3-41 Condensing Radiator Elements

ORIGINAL PAGE IS
OF POOR QUALITY

collection header by decreasing the saturation pressure below the static pressure at the header outlet.

Figure 3.3-42 shows a plot of thermodynamic states encountered by the potassium as it passes through the radiator ducts. The potassium enters the inlet header in the saturated state and becomes slightly superheated as the static pressure drops due to friction. It enters the throughpipes and reaches saturation temperature. At this point the potassium condenses, and as static pressure drops due to friction, temperature decreases along the saturation temperature - pressure line. The saturation temperature - pressure line is followed until condensation is complete and the fluid becomes subcooled. The amount of subcooling is determined by the frictional pressure drop in the outlet headers. This ensures that the saturation line is not crossed before the fluid exits from the header.

Radiators for 1600°K Potassium Rankine Cycle

Figure 3.3-43 shows the predicted condensing potassium radiator mass as a function of Reynolds number and throughpipe diameter. The maximum Reynolds number was limited by the requirement that frictional pressure drop in the throughpipes and collection header could not exceed the saturation temperature of the potassium at the throughpipe entrance. Minimum mass was found to occur for a throughpipe diameter of 15.24 cm and a Reynolds number of 3.0×10^6.

A summary of the sensitivity of major radiator element mass to throughpipe Reynolds number is presented in Figure 3.3-44. Fluid Reynolds numbers in the throughpipes and headers were related by the condition that the friction pressure drop in each header must equal the pressure drop across the throughpipes. Hence working fluid mass decreased with increasing Reynolds number because header diameter decreased to satisfy the requirement for equal pressure drop in throughpipes and manifolds. The reduction in diameter also caused the mass of header ducts to decrease with increasing Reynolds number. The increase in heat pipe mass with increasing Reynolds number was caused by additional subcooling area required by greater frictional pressure drop in the outlet header.

Noncondensing NaK radiators similar to the design utilized in the Brayton baseline system were investigated for application to the potassium Rankine cycle concept. Sensitivity of radiator element mass to NaK outlet temperature is shown in Figure 3.3-45 for an inlet temperature of 844°K. Inlet temperature was fixed by the condensing temperature of the potassium.

Heat pipe mass dropped with increasing NaK outlet temperature because the average effective radiator temperature increased allowing radiator area to drop. Working fluid and header mass increased with increasing NaK outlet temperature. This was due to a reduction in throughpipe length, causing the radiator to become extremely wide. Since the headers ran along the width of the radiator, an increase in radiator width resulted in long headers with greater wall mass and fluid volume. Total radiator mass was found to be minimized as NaK outlet temperature of about 520°K.

SPS 898

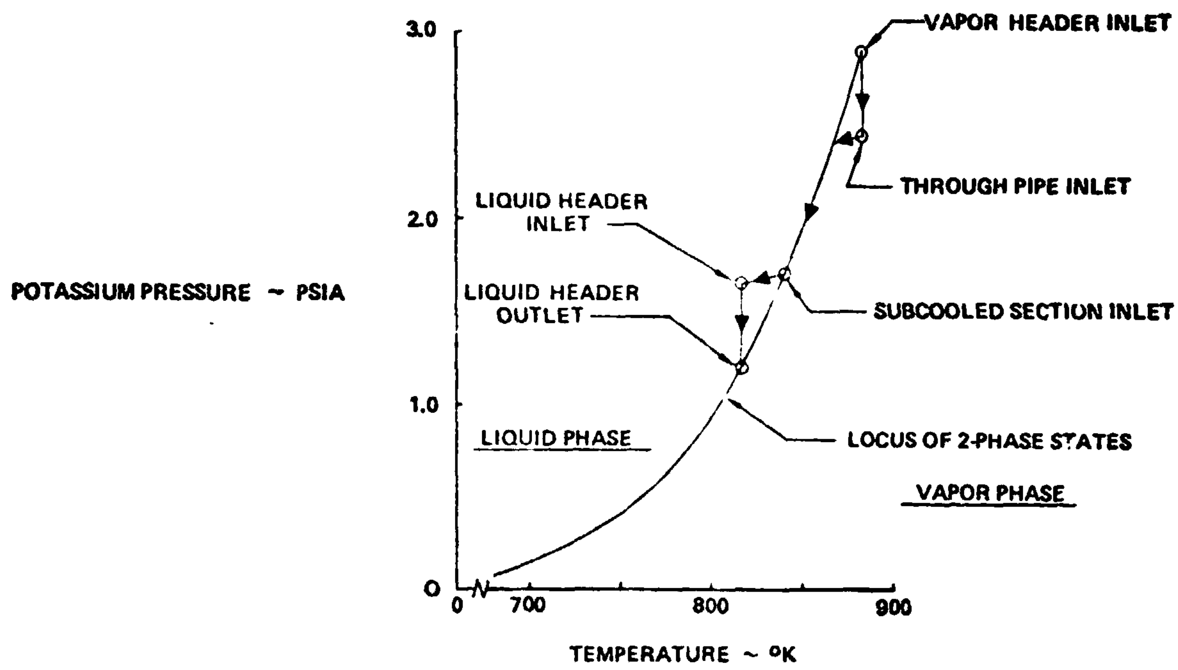

Figure 3.3-42 Thermodynamic States for Radiator Fluid

SPS 893

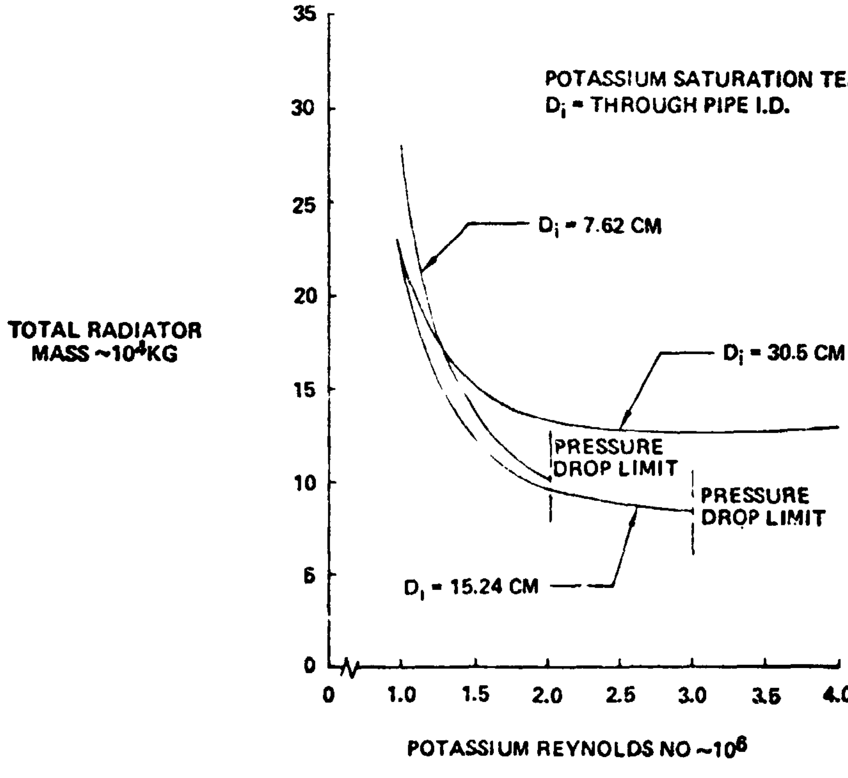

Figure 3.3-43 Influence of Reynolds Number and Throughpipe Diameter on Potassium Radiator Mass 1600°K Rankine Cycle

ORIGINAL PAGE IS OF POOR QUALITY

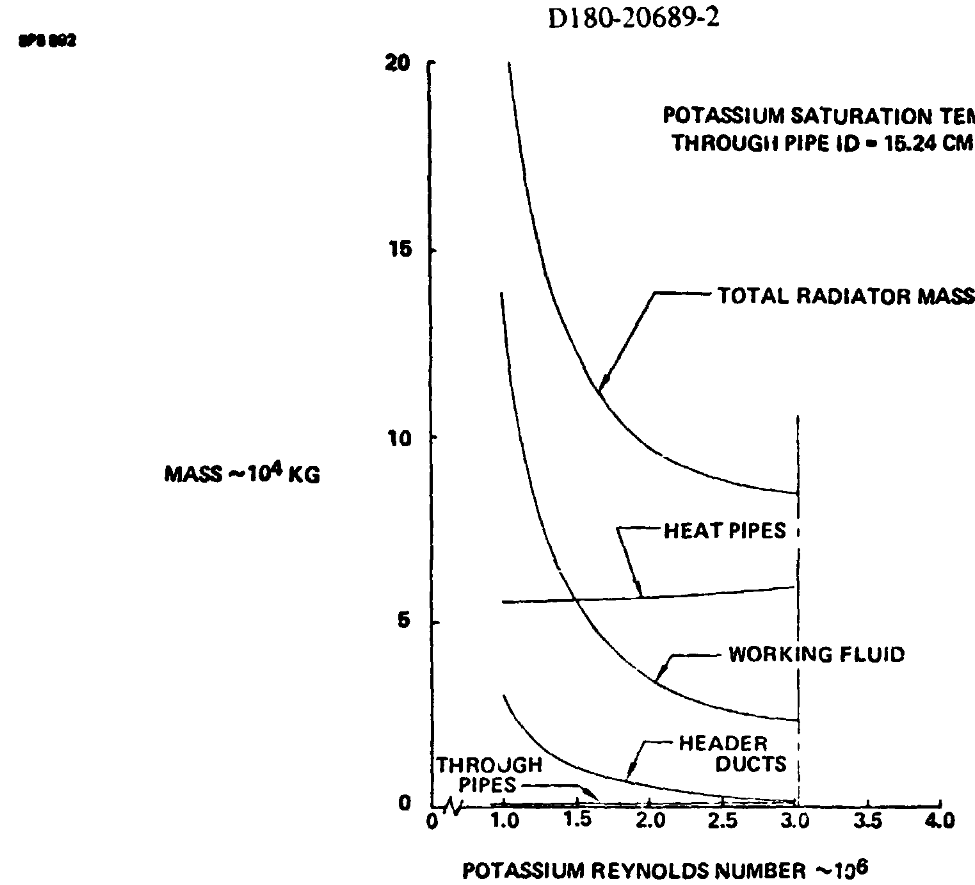

Figure 3.3-44 Influence of Reynolds Number on Radiator Element Mass - 1600°K Rankine Cycle

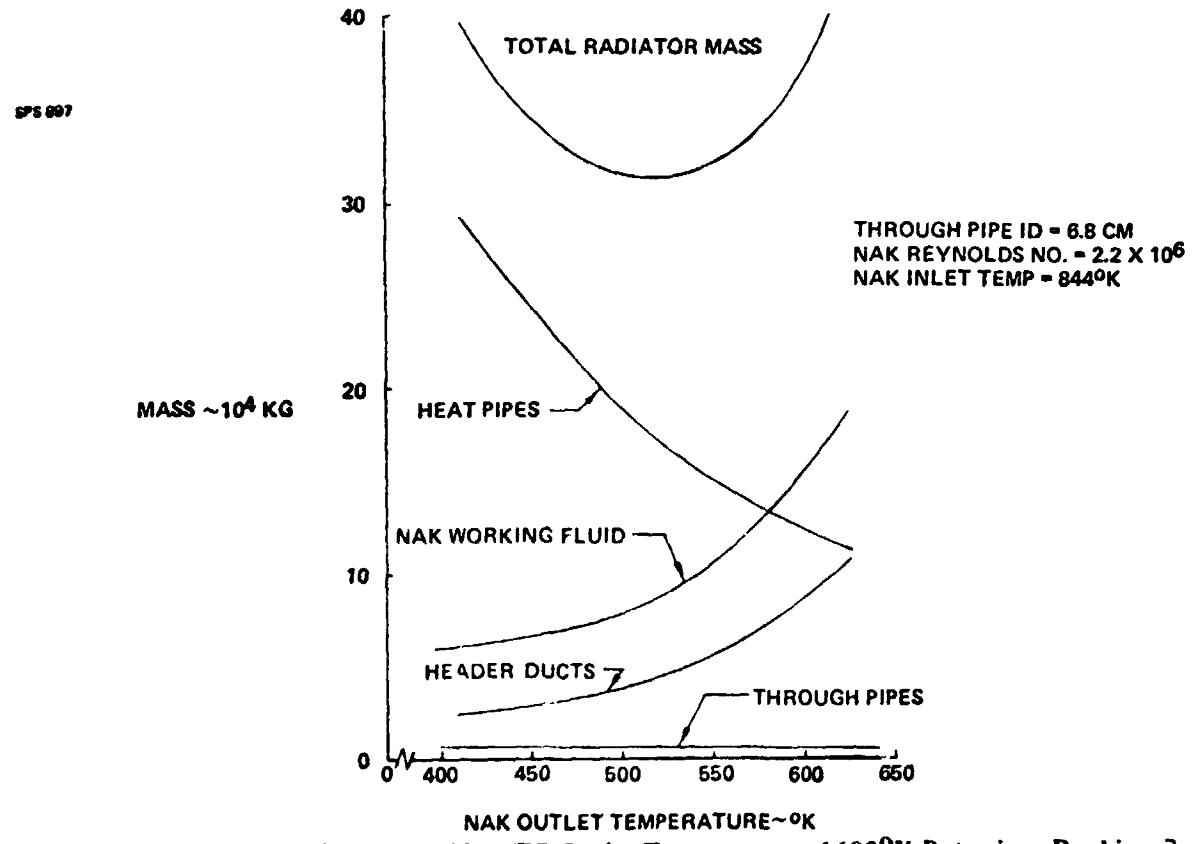

Figure 3.3-45 Sensitivity of NaK Radiator Mass TO Outlet Temperature - 1600°K Potassium Rankine Cycle

The influence of throughpipe diameter on radiator mass is presented in Figure 3.3-46. Throughpipe length increased with increasing diameter. This caused radiator width to decrease and resulted in shorter, less massive headers. Fluid mass in the headers also decreased. However, as diameter increased the throughpipe volume increased and the total NaK inventory was minimum at a throughpipe diameter of 9.5 cm and then increased. Total radiator mass was minimized at a throughpipe diameter of 10 cm.

Figure 3.3-47 shows the influence of throughpipe Reynolds number on the NaK radiator mass. Total radiator mass at the pressure drop limit was 21.5 X 10^4 Kg at a Reynolds number of 4.04 X 10^6. Most of the reduction in mass arose from decreased header diameter which was caused by the requirement that header pressure drop equal the pressure drop in the throughpipes. The total mass of 21.5 X 10^4 Kg for the NaK radiator is almost 3 times greater than the 8.5 X 10^4 Kg mass of the condensing potassium radiator. A large portion of this difference was due to an effective temperature of 707°K for the NaK radiator compared to 837°K for the potassium design.

Radiators for 1422° Potassium Rankine Cycle

Heat rejection for the 1422°K potassium Rankine cycle occurred at 867°K, the same heat rejection temperature selected for the 1600°K potassium Rankine cycle. Figure 3.3-48 shows the variation of total radiator mass with potassium Reynolds number in the throughpipes. Minimum radiator mass at the pressure drop limit was 12 X 10^4 Kg. This value was greater than that of the 1600°K potassium Rankine cycle radiator because a larger area was required to reject the additional energy arising from lower cycle efficiency. The cycle efficiency of the 1422° cycle was 27.6% compared to 31.6% for the 1600°K cycle.

Radiators for Steam Rankine Cycles

Steam Rankine cycle radiators were an order of magnitude more massive than the potassium cycle radiator. This was caused by the low heat rejection temperature which were required to achieve cycle efficiencies in excess of 30%. The influence of throughpipe Reynolds number and pipe diameter on radiator mass are shown in Figure 3.3-49. The temperature of the condensing water at the radiator panel entrance was 367°K at a pressure of 11.5 PSIA. Minimum mass occurred at a throughpipe diameter of 6.8 cm and a Reynolds number of 1.43 X 10^6.

ORIGINAL PAGE IS
OF POOR QUALITY

SPS 806

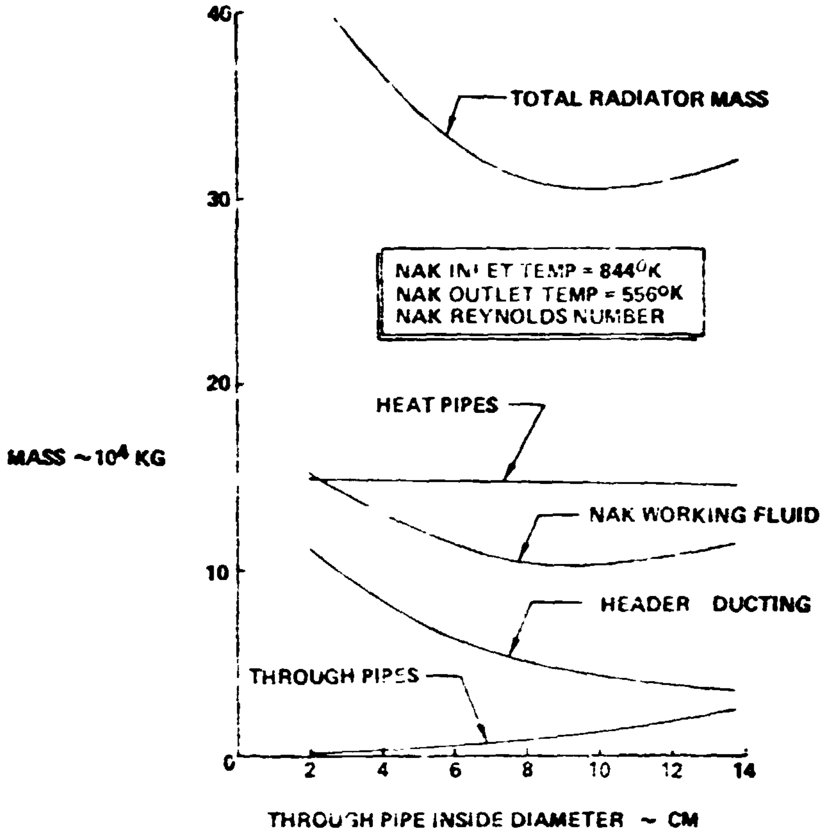

Figure 3.3-46 The Effect of Throughpipe Diameter on NaK Radiator Mass - 1600°K Potassium Rankine Cycle

SPS 804

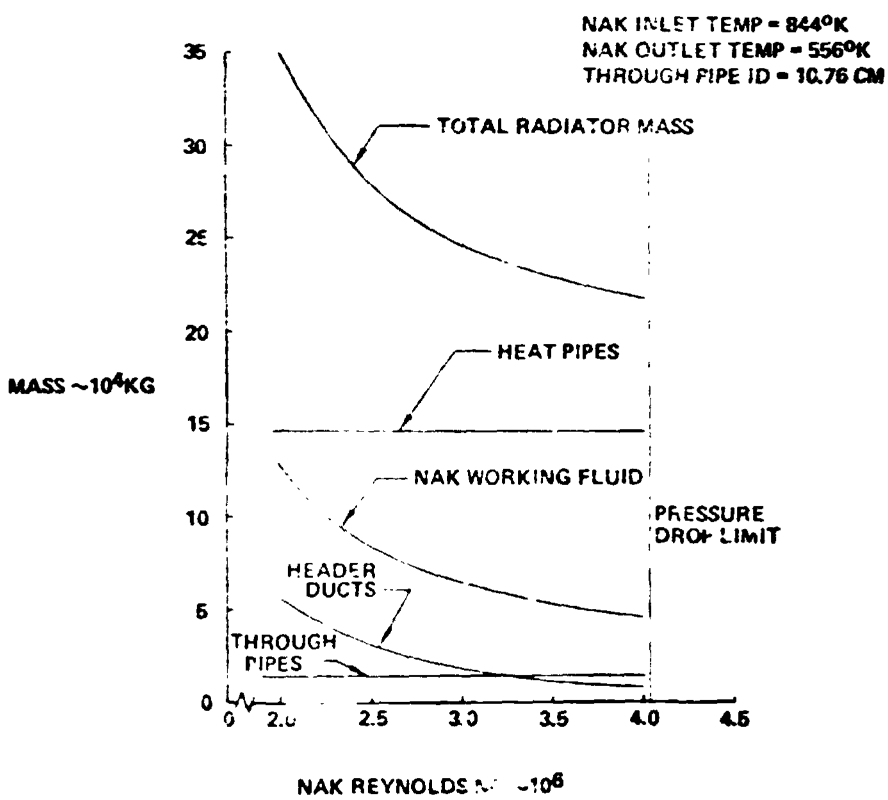

Figure 3.3-47 The Influence of Reynolds Number on NaK Radiator Mass - 1600°K Potassium Rankine Cycle

SPS 891

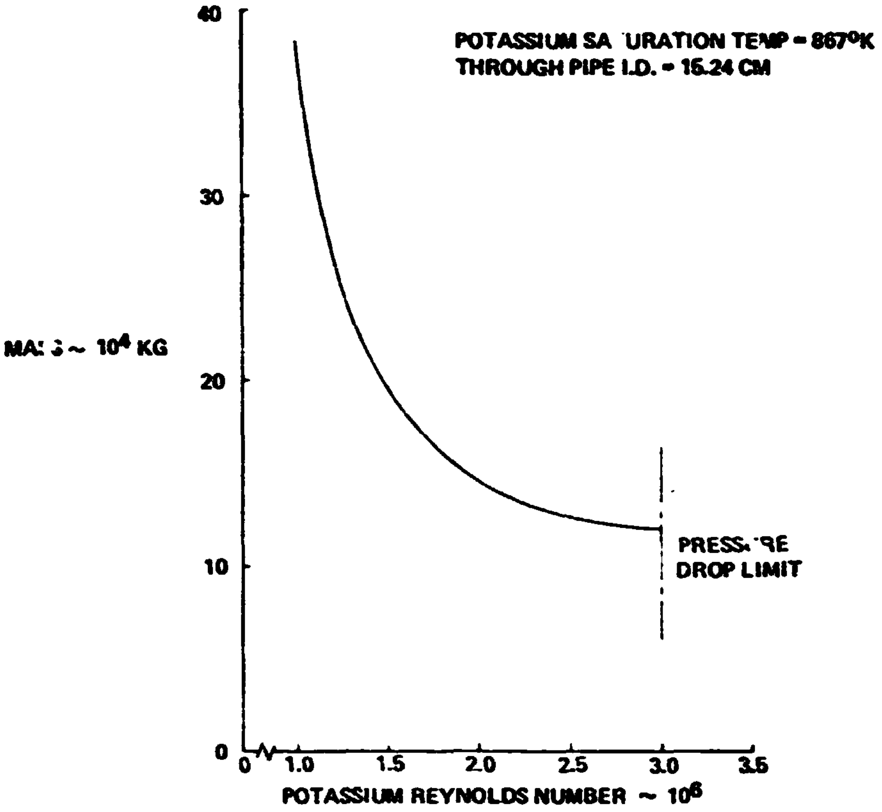

Figure 3.3-48 Variation of Radiator Mass With Potassium Reynolds Number - 1422°K Potassium Rankine Cycle

SPS 890

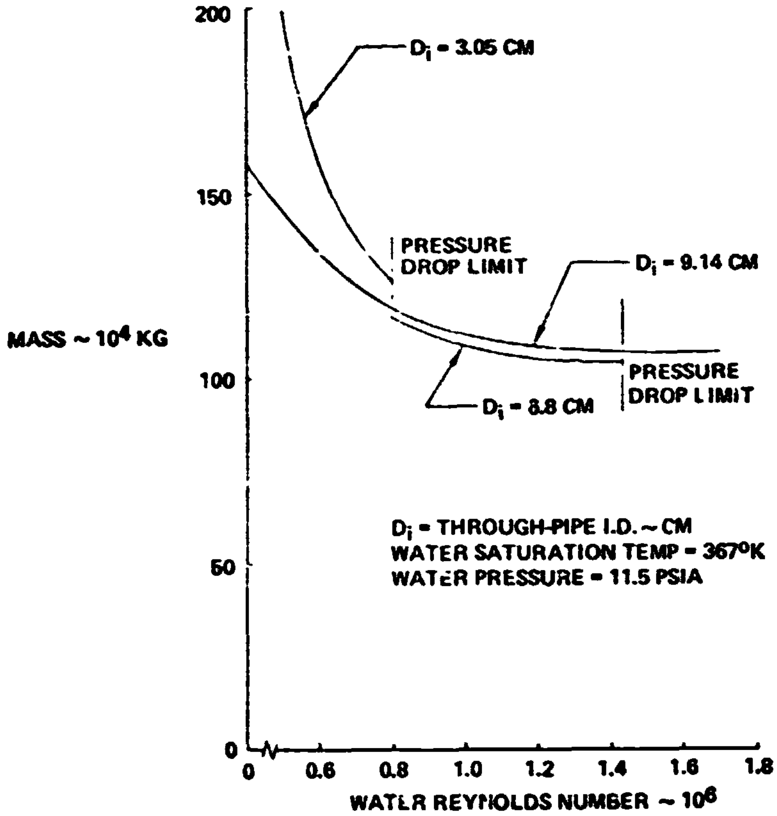

ORIGINAL PAGE IS OF POOR QUALITY

Figure 3.3-49 The Influence of Reynolds Number and Throughpipe Diameter on Radiator Mass - 1644°K Steam Rankine Cycle

Condensing Water Radiator for Brayton Cycle

An alternative radiator concept, utilizing water rather than NaK, was investigated for the Brayton baseline cycle concepts. The advantages of water on its higher density and specific heat, low cost, and compatibility with more structural materials. Major disadvantages are its fairly high freezing temperature and the fact that water expands upon freezing, giving rise to the possibility of tube rupture.

Figure 3.3-50 shows the main elements of the water radiator system. The Brayton cycle working fluid exits from the regenerator and passes through two heat exchangers where it is cooled prior to entering the compressor. The heat exchangers transfer thermal energy from the helium to the water. Subcooled water enters the preheater and exists as saturated liquid. A fraction of the liquid is diverted from the stream and the remainder directed into the boiler. Steam exits from the boiler and is mixed with the saturated liquid. The mixture enters the radiator where it is condensed and subcooled.

The locus of thermodynamic states experienced by the Brayton cycle working fluid and radiator heat transport fluid are shown in Figure 3.3-51. Helium enters the boiler at 672°K and exits at approximately 28°K in excess of the saturation temperature of the boiling water. It then preheats, and the helium temperature is reduced to the compressor inlet temperature, 391°K. The water temperature, on the other hand enters the preheater at 363°K and exits at saturation conditions.

An analysis of water radiator concepts was performed. Independent variables were throughpipe Reynolds number and water saturation temperature. Throughpipe Reynolds number was varied for fixed values of saturation temperature and the minimum mass points were determined. The locus of minimum mass points was then plotted against saturation temperature as shown in Figure 3.3-52. The mass of the subcooled section of the radiator increased with increasing saturation temperature while the mass of the condensing section decreased Total radiator mass was found to be a minimum at a saturation temperature of 525°K.

The relationship between radiator mass and pump power for condensing water radiators have 525°K saturation temperature and 363°K outlet temperature is shown in Figure 3.3-53. Each point on the abscissa represents a specific throughpipe Reynolds number. Increasing values of pump power correspond to decreasing values of Reynolds number. Radiator mass was found to approach an asymptotic value of about 43.3 X 10^4 Kg as pump power increased beyond 450 KW.

ORIGINAL PAGE IS
OF POOR QUALITY

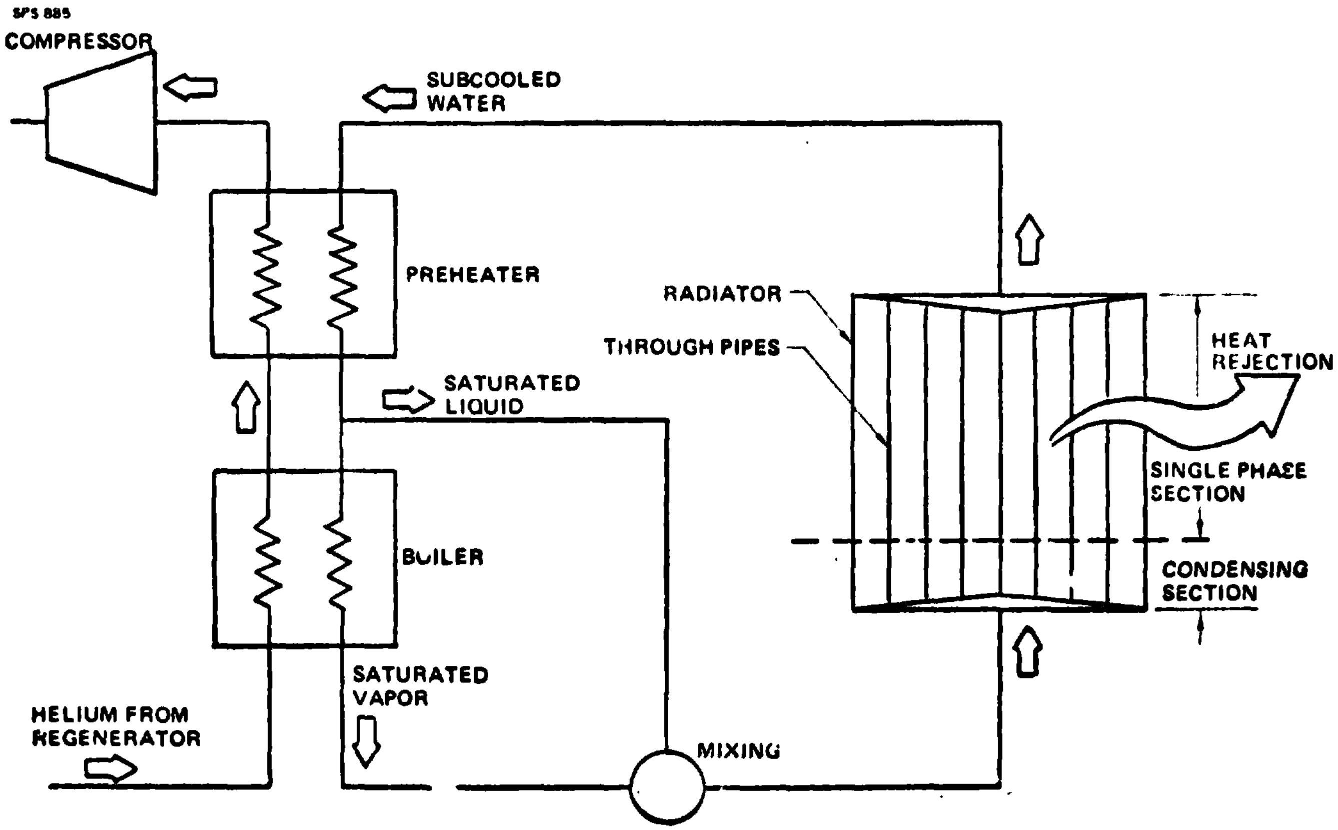

Figure 3.3-50 Water Radiator System For Brayton Cycle Heat Rejection

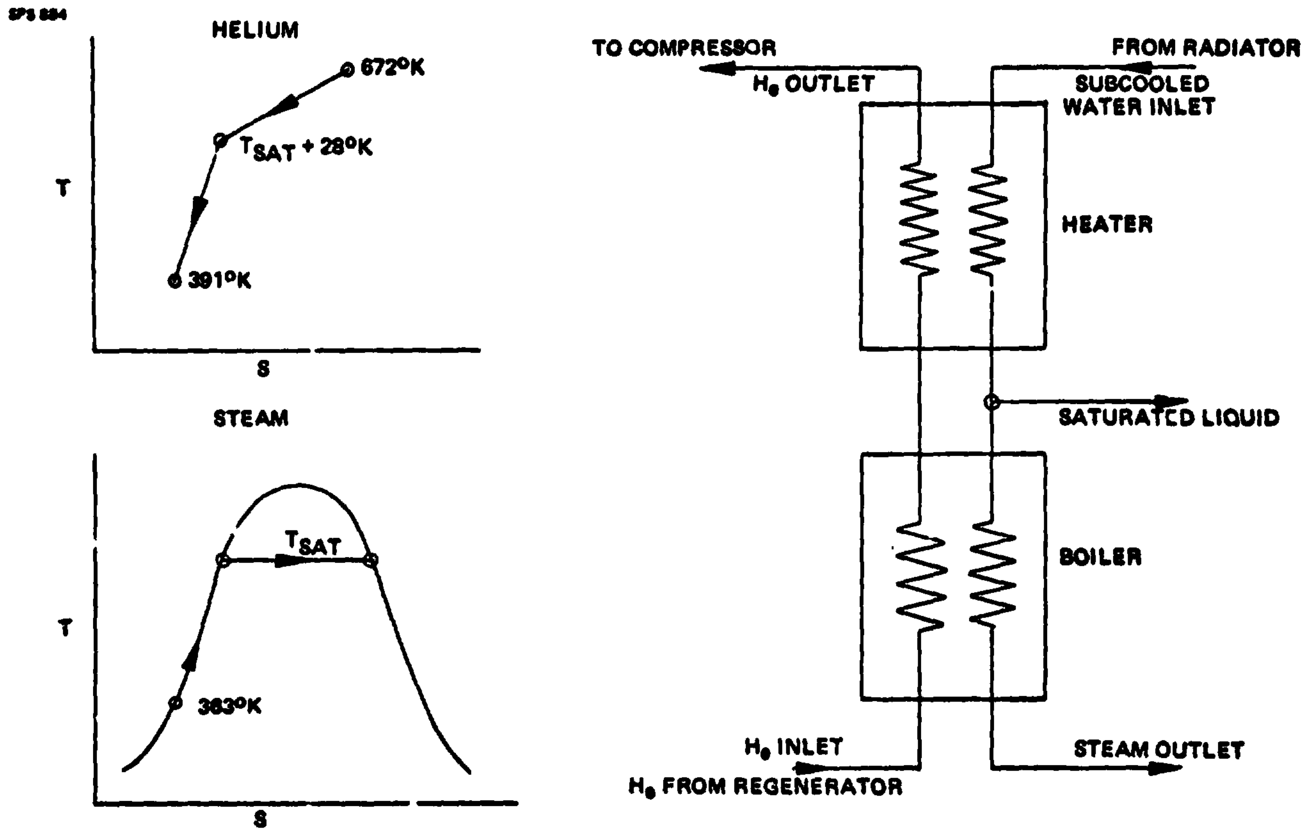

Figure 3.3-51 Thermodynamic State of Brayton Cycle Working Fluid and Radiator Fluid

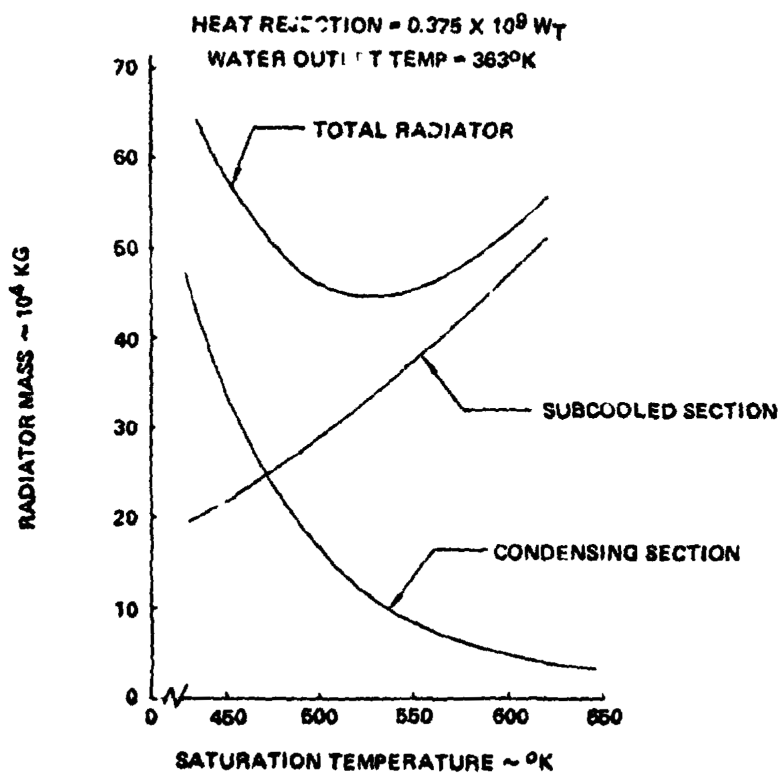

Figure 3.3-52

Variation of Condensing Steam Radiator Mass
With Saturation Pressure -
Baseline Brayton Cycle

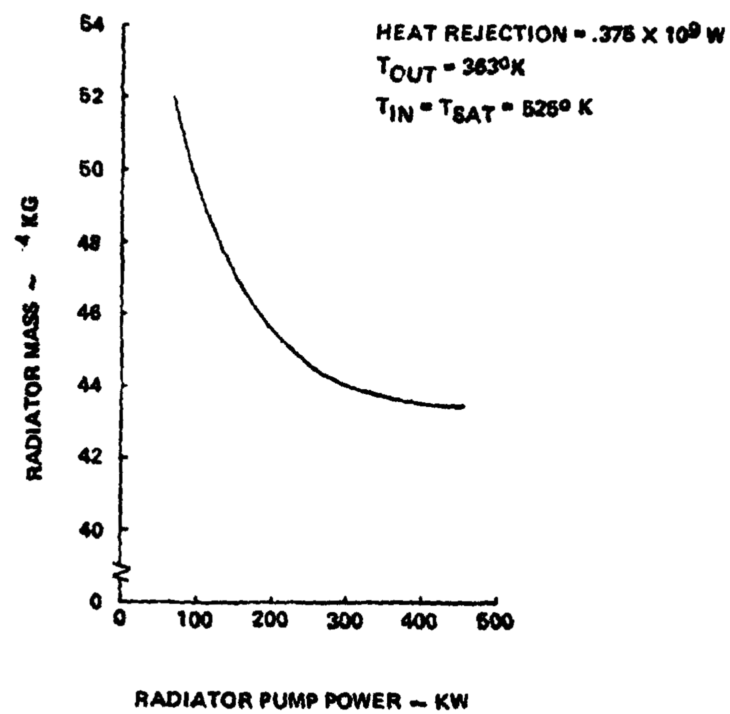

Figure 3.3-53

Relationship Between
Radiator Mass and Pump Power—
Condensing Water Radiator

ORIGINAL PAGE IS
OF POOR QUALITY

A mass breakdown of the minimum mass condensing water radiator is summarized in Figure 3.3-54. The major contributors to total radiator mass were the heat pipes in both the condensing and sub-cooled sections. Heat pipes accounted for 70% of the total mass, while throughpipes accounted for about 13%. Radiator fluid was found to make up 14% of the total radiator mass and header ducting accounted for the remaining 3%.

The condensing water radiator and baseline NaK radiator are compared in Figure 3 3-55. The condensing water radiator was slightly more massive than the baseline NaK radiator, however the condensing water radiator required an order of magnitude less pump power. Additional energy conversion system mass required to supply pump power was calculated for both radiator concepts. When this mass was added to radiator mass, the condensing water concept was to be less massive than the baseline NaK system.

Specific masses of five radiator concepts are compared in Figure 3 3-56 condensing steam radiators for saturation temperatures ranging from 367°K to 476°K were found to have the lowest specific mass. This low specific mass resulted from low fluid pressures and high heats of vaporization associated with the range of saturation temperature considered. Unfortunately advantage could not be taken of the small specific mass characteristic of low temperature condensing steam radiators since low temperatures dictated that large radiating areas were required and the net effect was to produce extremely large and consequently massive radiators.

NaK and condensing steam radiators for the Brayton cycle baseline system were found to have almost identical specific masses. Specific masses of potassium radiator ranged between 6.5 Kg/m^2 and 8.0 Kg/m^2. The high values of specific mass for these radiators was due to heavy heat pipes and a large inventory of potassium. Sodium heat pipes utilized in the potassium radiator were almost 50% heavier than the water-filled heat pipes of the Brayton and steam Rankine radiators. The large potassium inventory resulted from the low specific heat and density of potassium.

3.3 4.5 Investigation of a "Roll-Up" Radiator Concept

The midterm baseline thermal engine SPS radiator system consisted of 23,552 panels, each of which required four welds to connect it into the system. The panel count results from the area requirement for the total radiator and the panel size (10m x 20m) dictated by the capability of the payload bay of the launch vehicle.

A "roll-up" radiator concept was investigated to determine the practicality of a radiator panel, for example 20m x 500m, which would be rolled into a thin cylinder 20m high and 1?m in diameter which would thus fit the payload bay

ORIGINAL PAGE IS
OF POOR QUALITY

SPS 683

RADIATOR MASS BREAKDOWN

	MASS 10^4 KG
CC NDENSING SECTION	
THROUGH PIPES	1.61
HEAT PIPES	5.66
THROUGH PIPE FLUID	0.80
INLETM	
INLET MANIFOLD FLUID	0.03
INLET MANIFOLD DUCT	0.84
SUBCOOLED SECTION	
THROUGH PIPES	4.03
HEAT PIPES	24.80
THROUGH PIPE FLUID	4.9?
OUTLET MANIFOLD FLUID	0.28
OUTLET MANIFOLD DUCT	0.39
TOTAL	43.4

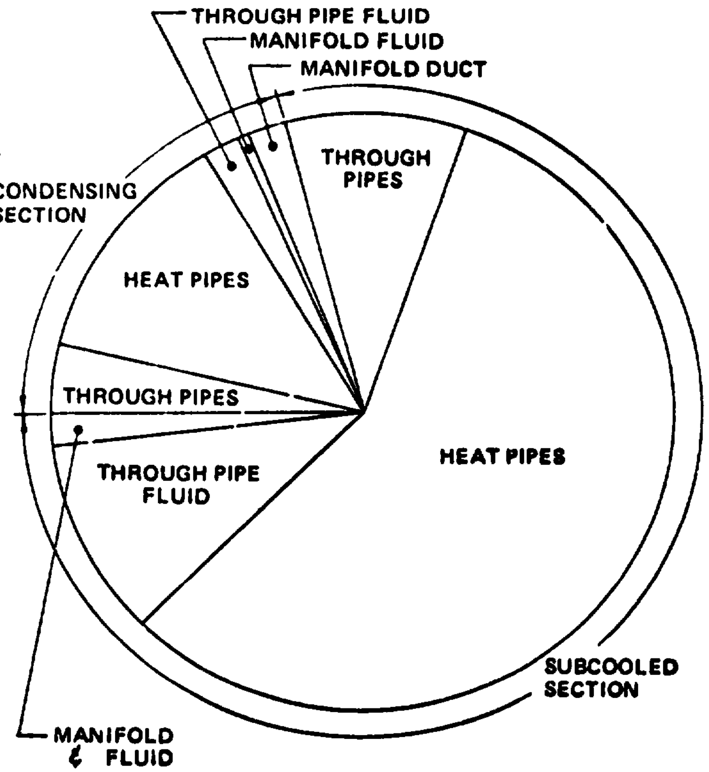

Figure 3.3-54 Radiator Mass Breakdown - Condensing Water Radiator

SPS 882

- **NAK RADIATOR**

RADIATOR WET MASS	42.75×10^4 KG
PUMP POWER	4594 KW
SATELLITE MASS PENALTY FOR PUMP POWER	1.49×10^4 KG

- **CONDENSING WATER RADIATOR**

RADIATOR WET MASS	43.41×10^4 KG
PUMP POWER	536 KW
SATELLITE MASS PENALTY FOR PUMP POWER	0.174×10^4 KG

Figure 3.3-55 Comparison of NaK and Condensing Water Radiators

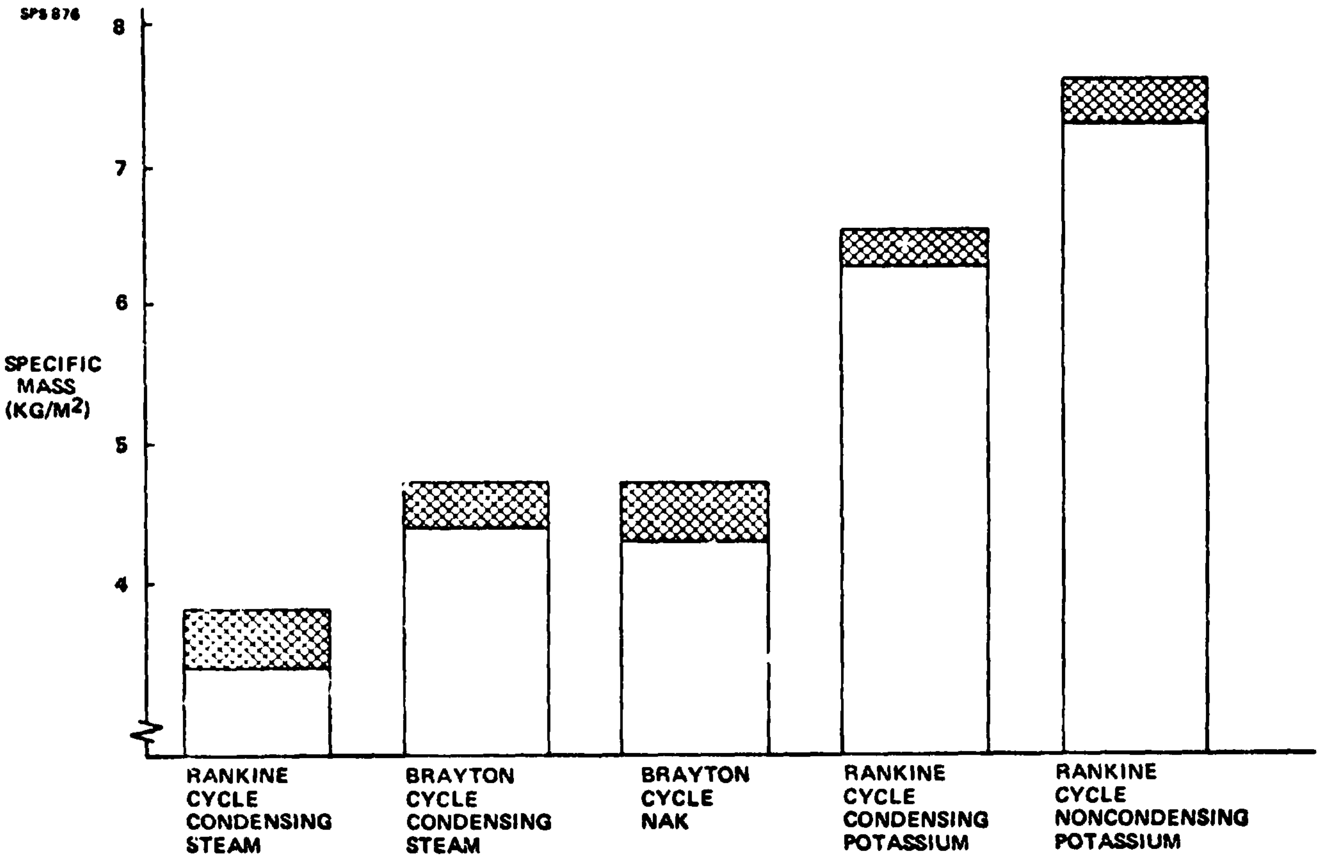

Figure 3.3-56 Specific Mass Comparison For Cycle Option Radiator

ORIGINAL PAGE IS OF POOR QUALITY

In order to roll in this fashion the manifold tubes of the panel must have a relatively small diameter to preclude excessive stress. For a maximum stress of 3.5×10^8 N/M^2 (50,000 psi) and a bend radius of 8.5m, the maximum tube diameter is 3.0 cm.

Pressure drop in the tubes is determined by:

$$\frac{(\text{Constants}) \times (\text{Volume flow})^2 (\text{Length})}{(\text{Diameter})^5}$$

The volume flow is a direct function of the power to be dissipated and temperature drop across the radiator. The flow can be conducted to the heat pipes through various numbers of pipes. A large pipe count means small diameters and high pressure drops; a small pipe count the reverse. High pressure drops require high pumping power, a parasitic drain on the SPS busbar output. Each KW of pumping power requires approximately 4.5 kg of additional power generation system.

No manifold diameter/count combination could be found which did not involve extremely high pumping power penalties. The minimum tube diameter was approximately 7.0 cm, which is too large for rolling.

Thus the roll-up concept does not appear practical. Perhaps in a very advanced SPS with say, 2000K turbine inlet temperatures and a high temperature, high delta temperature radiator the volume flow could be small enough to make 3.0 cm tubes practical.

3.3.5 Power Distribution

The power distribution system for the 4-module (midterm configuration) Brayton thermal engine satellite was analyzed to determine conductor mass and transmission losses. Table 3.3-9 shows the results of the analysis. The transmission losses are 6.1%. The conductor mass does not include any support structure nor any required insulators. This power distribution system is higher in performance and lower in mass than the AC system used in the point-of-departure Brayton system.

Figure 3.3-57 shows a power distribution schematic for the 4-module system.

An analysis was also performed to determine the power distribution system for the 16 module thermal engine SPS. The conductors used in this analysis are 1 millimeter thick conductor grade aluminum sheets

Table 3.3-9
Thermal Engine Satellite Power Distribution
1 mm Sheet Conductor at 100°C

	Section	Distance Meters	End Voltage Volts	Current Amperes	Width Meters	Mass Kg.	I^2R Loss Watts
1.	Rotary Joint to Module A - I_A	3540	42,464	139,560	22.06	210,907	1.15 x 10^8
2.	Rotary Joint to Module A - I_B	3540	40,408	58,900	9.31	89,011	.49 x 10^8
3.	Rotary Joint to Module A - Common	3540	--	198,460	31.37	299,918	1.64 x 10^8
4.	Module A to Module B I_{A2}	4300	44,465	95,553	15.11	175,404	.95 x 10^8
5.	Module A to Module B Common	4300	--	95,553	15.11	175,404	.95 x 10^8
			Total - 1 2 Satellite			950,644	5.18 x 10^8
			Total - Satellite			1,901,288	10.36 x 10^8

ORIGINAL PAGE IS
OF POOR QUALITY

FOLDOUT FRAME

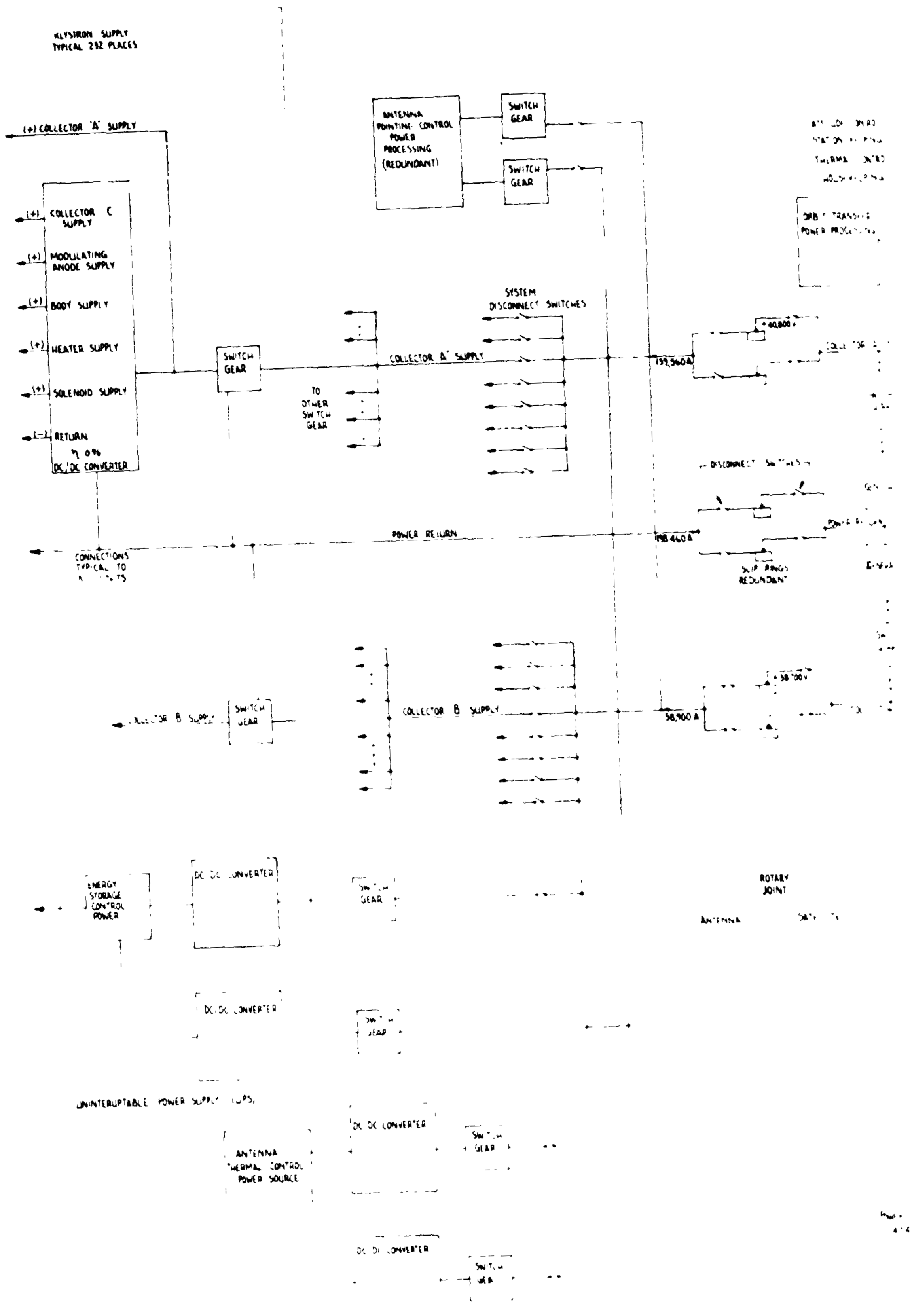

ORIGINAL PAGE IS
OF POOR QUALITY

PRECEDING PAGE BLANK NOT FILMED

FOLDOUT FRAME 2

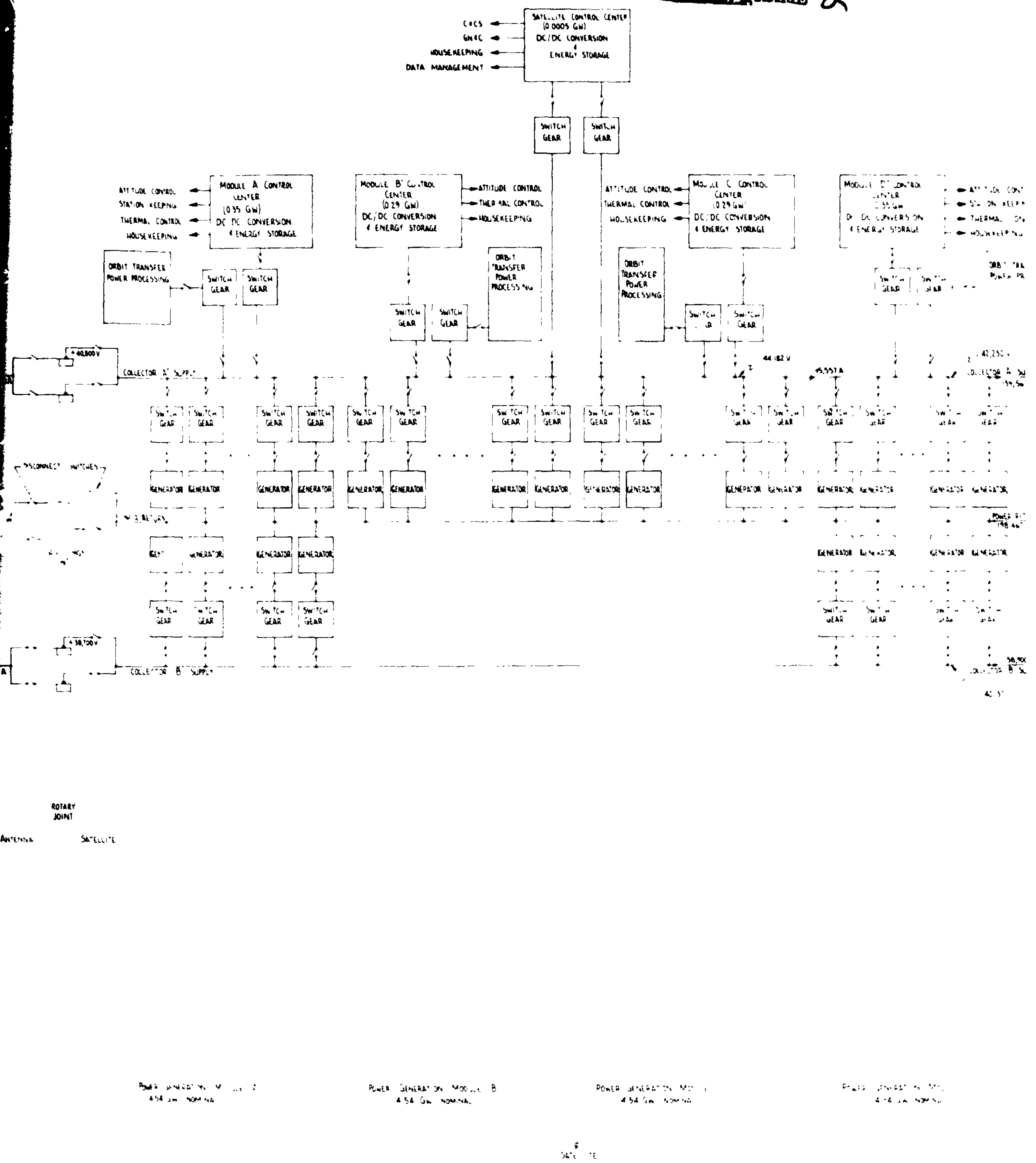

FOLDOUT FRAME 3

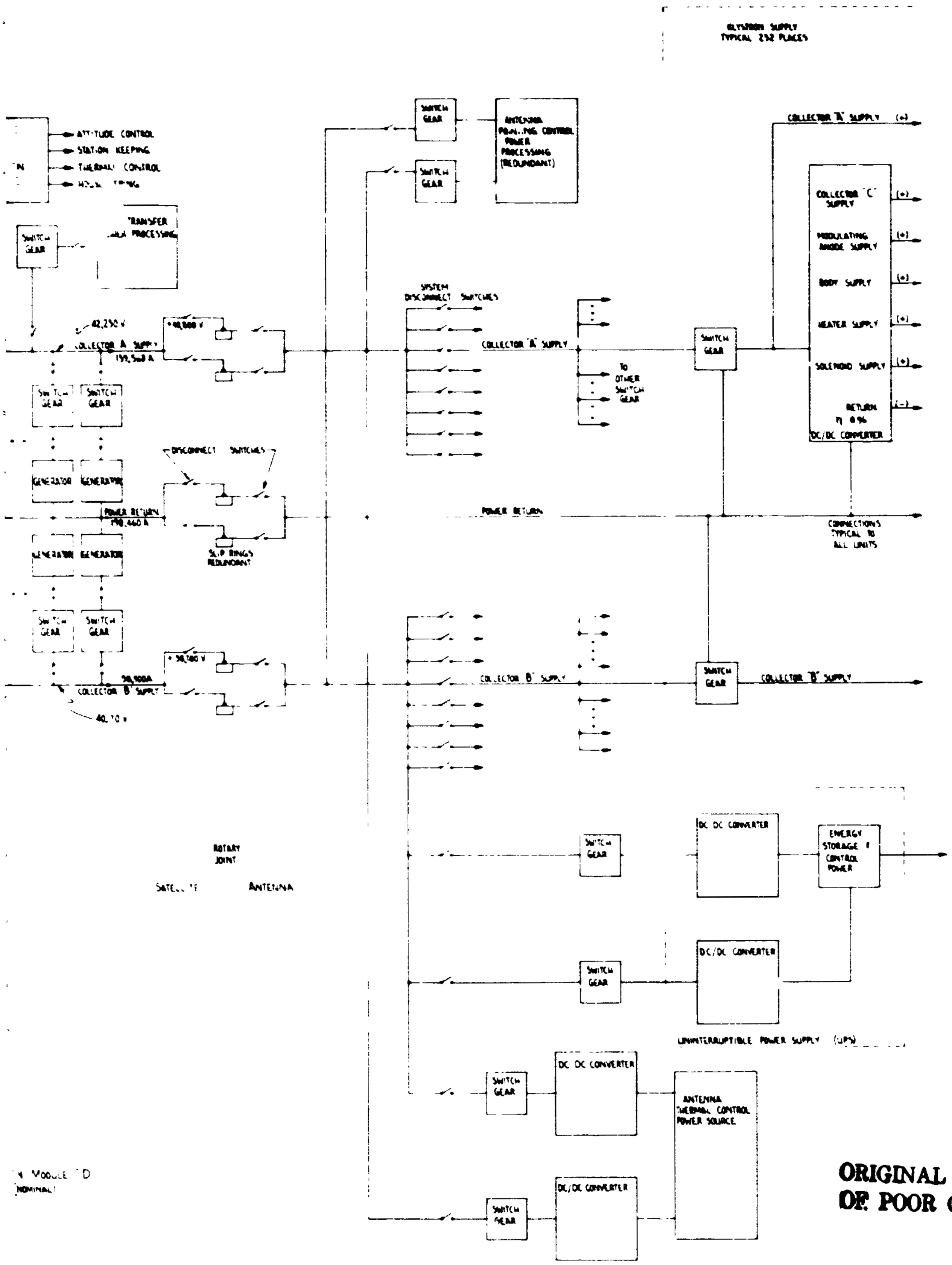

ORIGINAL PAGE IS OF POOR QUALITY

Figure 3.3-57 Thermal Engine SPS Power Distribution System

C-4

The results of a trade to select the optimum conductor design operating temperature are shown in Figure 3.3-58. A value of 3.6 kg/KW was used to compute the power generation mass required to compensate for conductor shown in Table 3.3-10. A conductor design operating temperature of 50°C was selected as optimum.

The 16-module thermal engine SPS with conductors operating at 50°C has I^2R losses of 0.719 gigawatts and conductor mass of 3,193 metric tons. Conductor widths, currents, and module voltages are shown in Figure 3.3-59. An improvement in power distribution mass could be realized if, rather than as shown in the figure, the power from the outer rows of generation modules is routed down conductors attached to a beam from the end modules of the outer rows directly to the rotary joint. For this case the conductor mass is 2,982 metric tons and the I^2R losses are 0.668 gigawatts.

A total of 64 circuit breakers and 70 disconnect switches are required for the power distribution systems. Housekeeping and stationkeeping requirements are as was shown on Figure 3.3-57 except that there will be 16 module control centers instead of 4.

3.3.6 Concentrator/Absorber Systems

3.3.6.1 Solar Concentrator Configuration Evolution

Ideally, the perfect concentrator would be a paraboloid, obtaining a geometric efficiency of about 97% (not including reflectivity of the material). Our baseline at the beginning of the study was an approximate form of this, slightly less efficient but more convenient to build. It evolved as illustrated in Figure 3.3-60 what we call a parabolic trough, which can be more easily constructed. The facets fit in the roughly circular area shown. In other words, there are none in the corners where they would be a long distance away from the cavity. High concentration ratios are achievable with a trough if the facets at the end are tilted up to approximate a 3-dimensional concentrator.

3.3.6.2 Concentrator/Absorber Analyses

The concentrator system that we have used in this study phase and in our previous work obtains high sunlight concentration, ranging from 1,000 to 3,000 times ambient sunlight, into a cavity absorber by a mirror concentrator. This concentrator has a large number of individual reflector facets shaped so that they fit one to another to cover the surface. These facets are pivoted at the center, movable over small angles, so as to steer their reflected solar energy into the cavity. This achieves a high concentration ratio into a small aperture, without requiring an extremely accurate structure that maintains its form over a long period of time. Also, when flying perpendicular to the orbit plane, as the sun "moves" north and south over the seasons (just as it does here on earth) the facets provide the sun-tracking. The concept is illustrated in Figure 3.3-61.

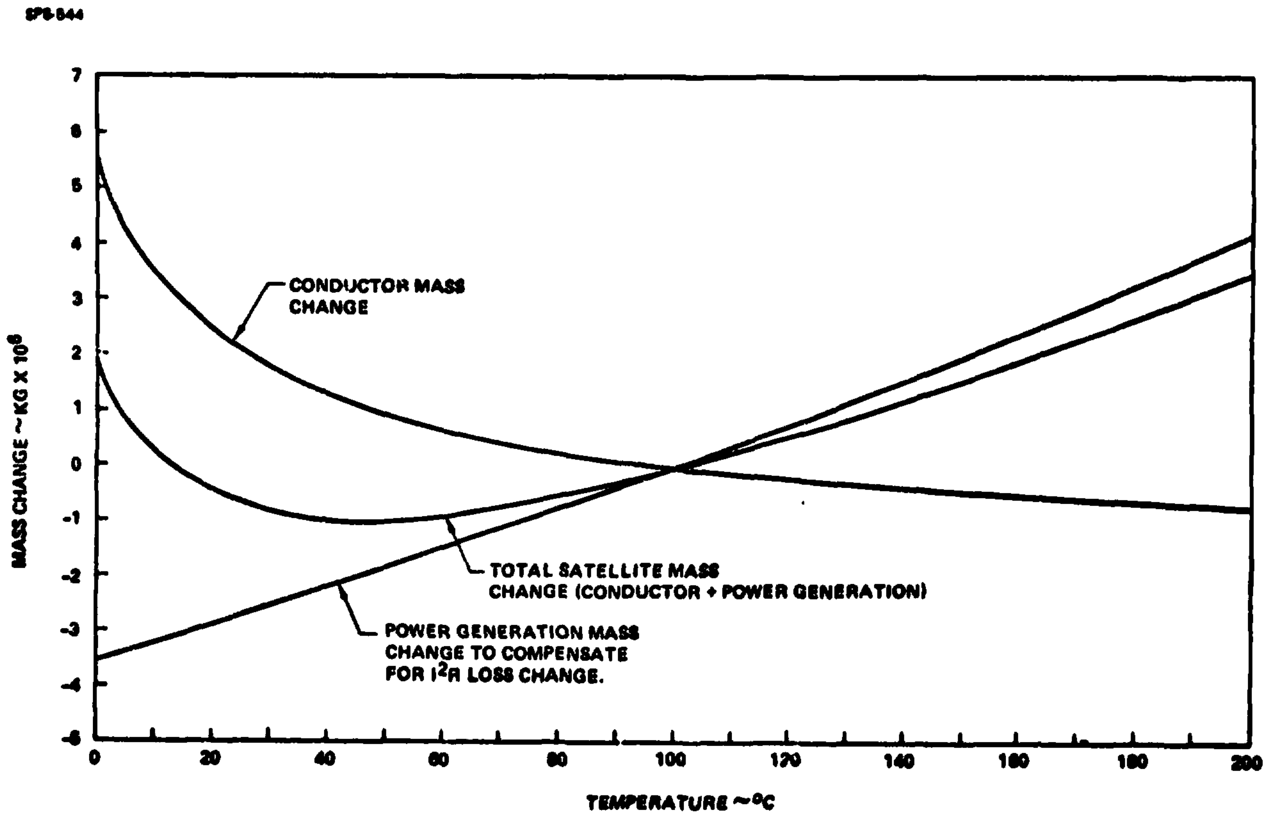

ORIGINAL PAGE IS OF POOR QUALITY

Figure 3.3-58 Thermal Engine SPS Mass Optimization For Power Distribution (16 Modules SPS)

Table 3.3-10 T.E. Generator Output Requirements To Provide Antenna Power (16 Module SPS)

SPS 548

PARAMETER @ TEMP	A1		A2		A3		B1	B2	B3
	COLL A	COLL B	COLL A	COLL B	COLL A	COLL B	COLL A	COLL A	COLL A
VOLTAGE DROP									
0°C	246.6	246.6	444.6	444.6	642.6	642.6	544.2	742.2	940.2
25°C	496.6	496.6	895.4	895.4	1,294.2	1,294.2	1,095.7	1,494.5	1,893.3
50°C	724.7	724.7	1,306.6	1,306.6	1,888.6	1,888.5	1,596.9	2,180.8	2,762.7
75°C	971.1	971.1	1,750.9	1,750.9	2,530.6	2,530.6	2,142.5	2,922.3	3,702.0
100°C	1,251.9	1,251.9	2,257.2	2,257.2	3,264.4	3,264.4	2,762.1	3,767.4	4,772.7
150°C	1,813.6	1,813.6	3,269.9	3,269.9	4,726.1	4,726.1	4,001.4	5,457.7	6,913.9
200°C	2,464.0	2,464.0	4,442.6	4,442.6	6,421.1	6,421.1	5,438.5	7,415.0	9,393.6
CURRENTS									
0°C	5,922.7	19,732.6	5,894.3	18,633.0	5,866.1	19,534.2	24,468.6	24,352.0	24,236.6
25°C	6,113.4	18,832.0	6,054.9	19,631.9	5,997.5	19,436.2	24,580.3	24,228.8	23,776.1
50°C	6,143.9	19,920.3	6,059.0	19,630.6	5,976.4	19,349.1	24,540.2	24,207.9	23,884.6
75°C	6,255.3	20,014.3	6,140.7	19,628.5	6,030.2	19,257.3	24,574.3	24,136.0	23,713.1
100°C	6,380.2	20,119.6	6,231.2	19,625.7	6,088.8	19,154.7	24,611.2	24,056.0	23,525.4
150°C	6,624.0	20,322.7	6,405.1	19,617.6	6,200.2	18,959.7	24,678.2	23,901.3	23,171.8
200°C	6,896.1	20,648.1	6,594.5	19,605.8	6,318.2	18,748.1	24,746.6	23,731.1	22,796.7
VOLTAGES									
0°C	41,046.6	38,946.6	41,244.6	39,144.6	41,442.6	39,342.6	41,344.2	41,542.2	[illegible]
25°C	41,296.6	39,196.6	41,695.4	39,595.4	42,094.2	39,994.2	41,895.7	42,294.5	42,693.3
50°C	41,524.7	39,424.7	42,106.6	40,006.6	42,088.5	40,588.5	42,398.9	42,980.8	43,562.7
75°C	41,771.1	39,671.1	42,550.9	40,450.9	43,330.6	41,230.6	42,942.5	43,722.3	44,502.0
100°C	42,051.9	39,951.9	43,067.2	40,957.2	44,064.4	41,964.4	43,562.1	44,567.4	45,572.7
150°C	42,613.6	40,513.6	44,069.9	41,969.9	46,526.1	43,428.1	44,801.4	46,257.7	47,713.9
200°C	43,264.0	41,164.0	46,242.6	43,142.6	47,221.1	45,121.1	46,236.6	48,215.0	50,193.6

ORIGINAL PAGE IS
OF POOR QUALITY

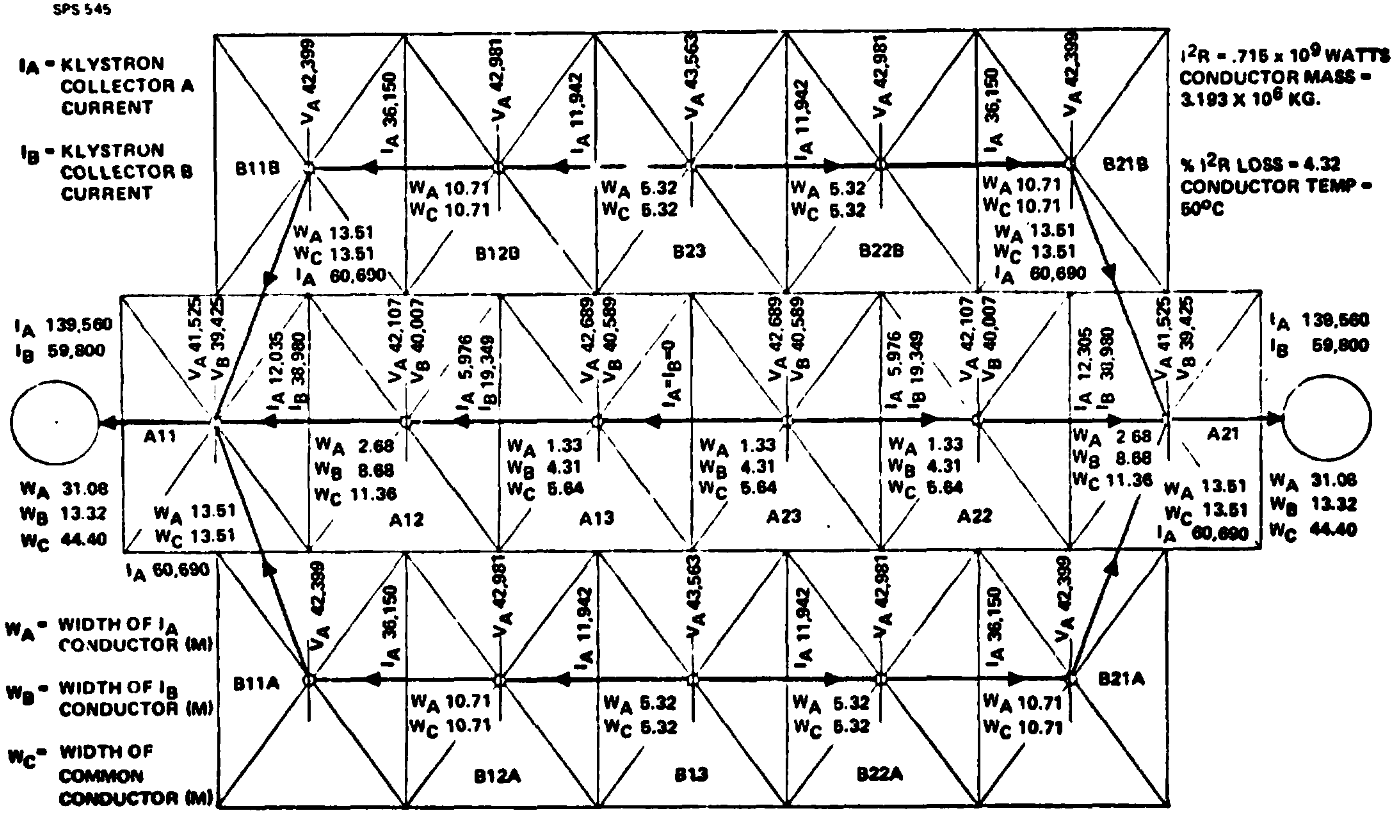

Figure 3.3-59 16 Module Thermal Engine SPS Power Distribution Parameters

ORIGINAL PAGE IS
OF POOR QUALITY

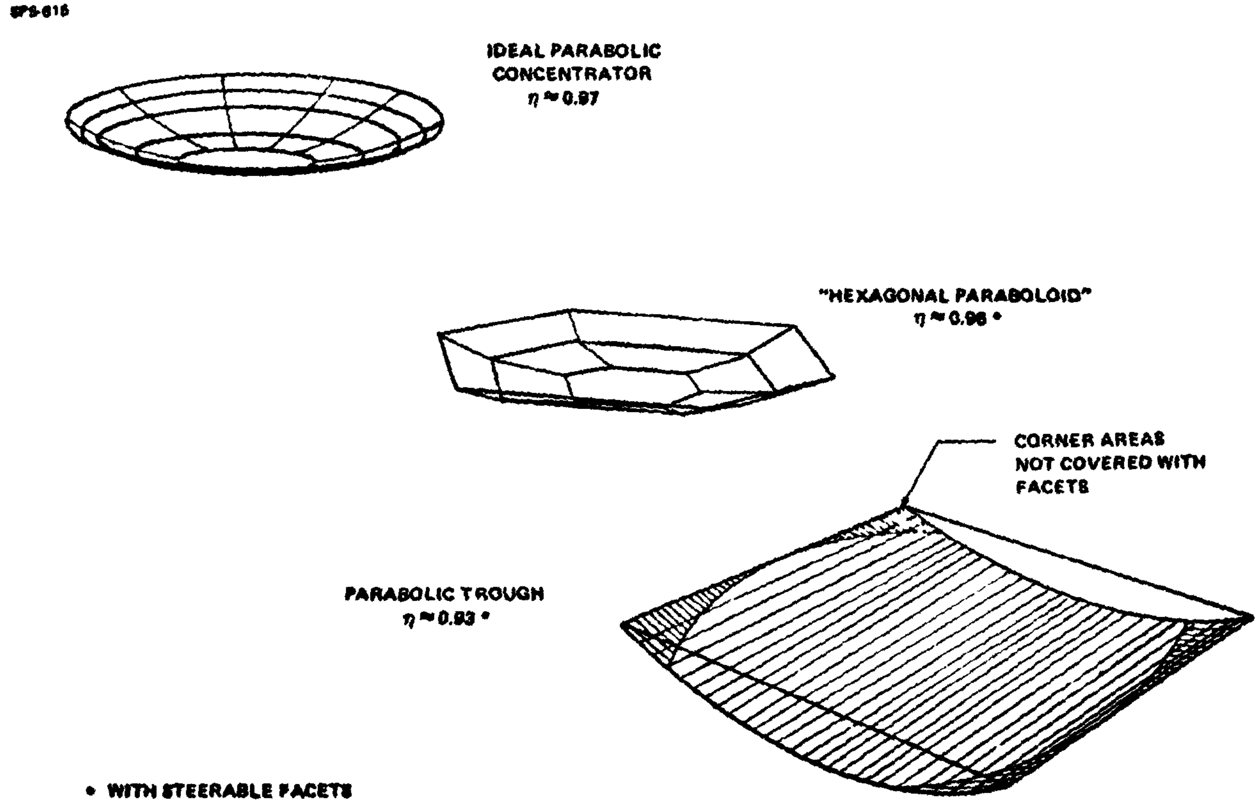

Figure 3.3-60 Solar Concentrator/Configuration Evolution

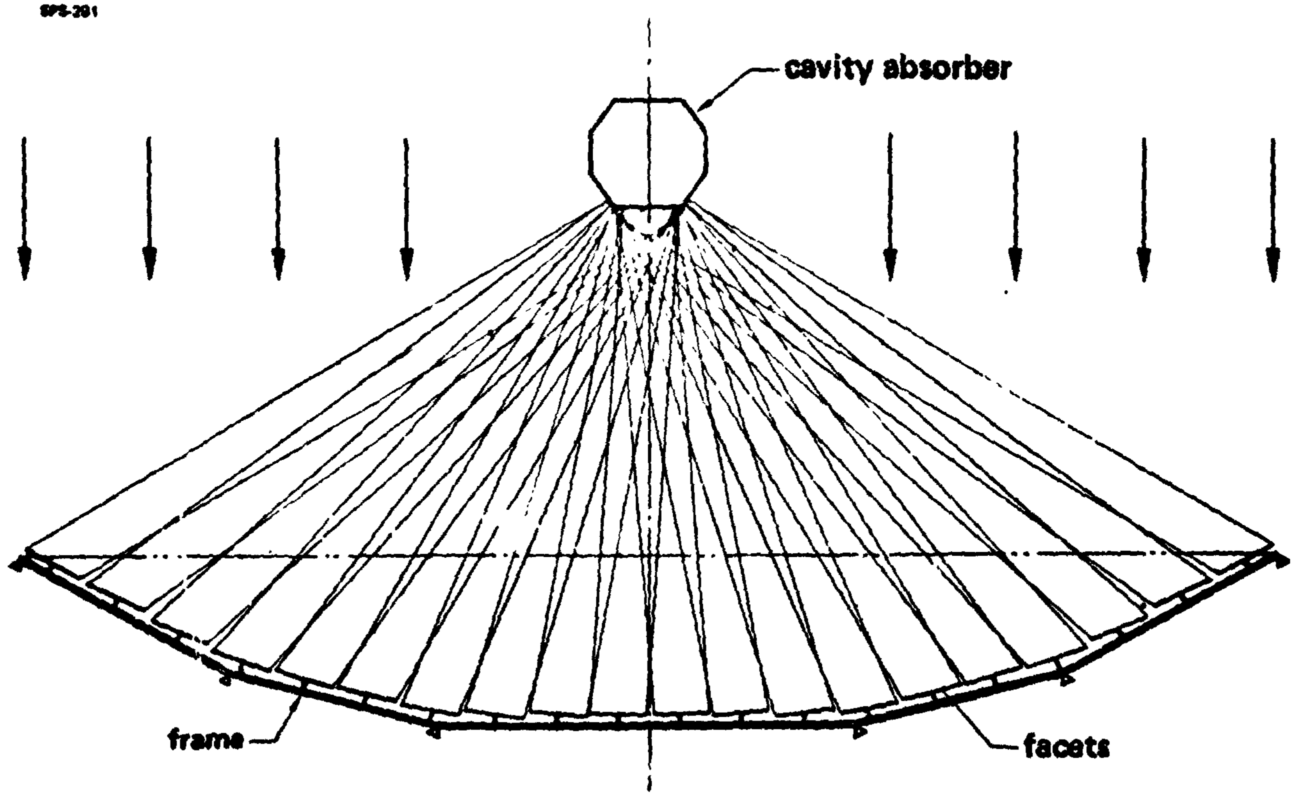

Figure 3.3-61 System Details: Reflector Facets (Heliostats)

The concentrator/absorber design includes four parameters that can be varied to minimize the system mass, at a given cavity interior wall temperature, and for a given thermal power available to operate the engines. (The power withdrawn is the total thermal input to the engines, including cycle waste heat.)

1. Number of facets (heliostats). A higher number increases efficiency (Figure 3.3-62) but also increases mass.

2. Geometric concentration ratio (GCR): concentrator area/cavity aperture area. High GCR improves absorber efficiency but decreases concentrator efficiency.

3. Cavity area ratio, interior wall area/aperture area. Higher values improve absorber efficiency but increases its size and mass.

4. Thickness of cavity wall thermal insulation More insulation reduces heat loss but increases mass.

The mass optimization model diagrammed in Figure 3.3-63 was used to select values of these parameters. Results are shown in Figure 3.3-64. Three of the parameters reviewed essentially constant over the range of wall temperatures investigated. GCR changed slightly. The curve of useful power per unit mass served as an input to the cycle analysis and optimization described in Section [illegible]

3.3.6.3 Reflector Design

The requirements listed below guided the development of the reflector facet system. The sixth and seventh requirements relate to facet pointing relative to the cavity absorber aperture.

REFLECTOR FACET REQUIREMENTS

High reflectivity (0.80 initial)
Low mass per unit area (0.05 gk/m^2)
Flat surface
Accurate point (± 10 minutes, maximum)
No calibration required after installation
Must find "cold" cavity when required
Must look away from "hot" cavity when required
Long mean time between failure
No frame wiring

ORIGINAL PAGE IS
OF POOR QUALITY

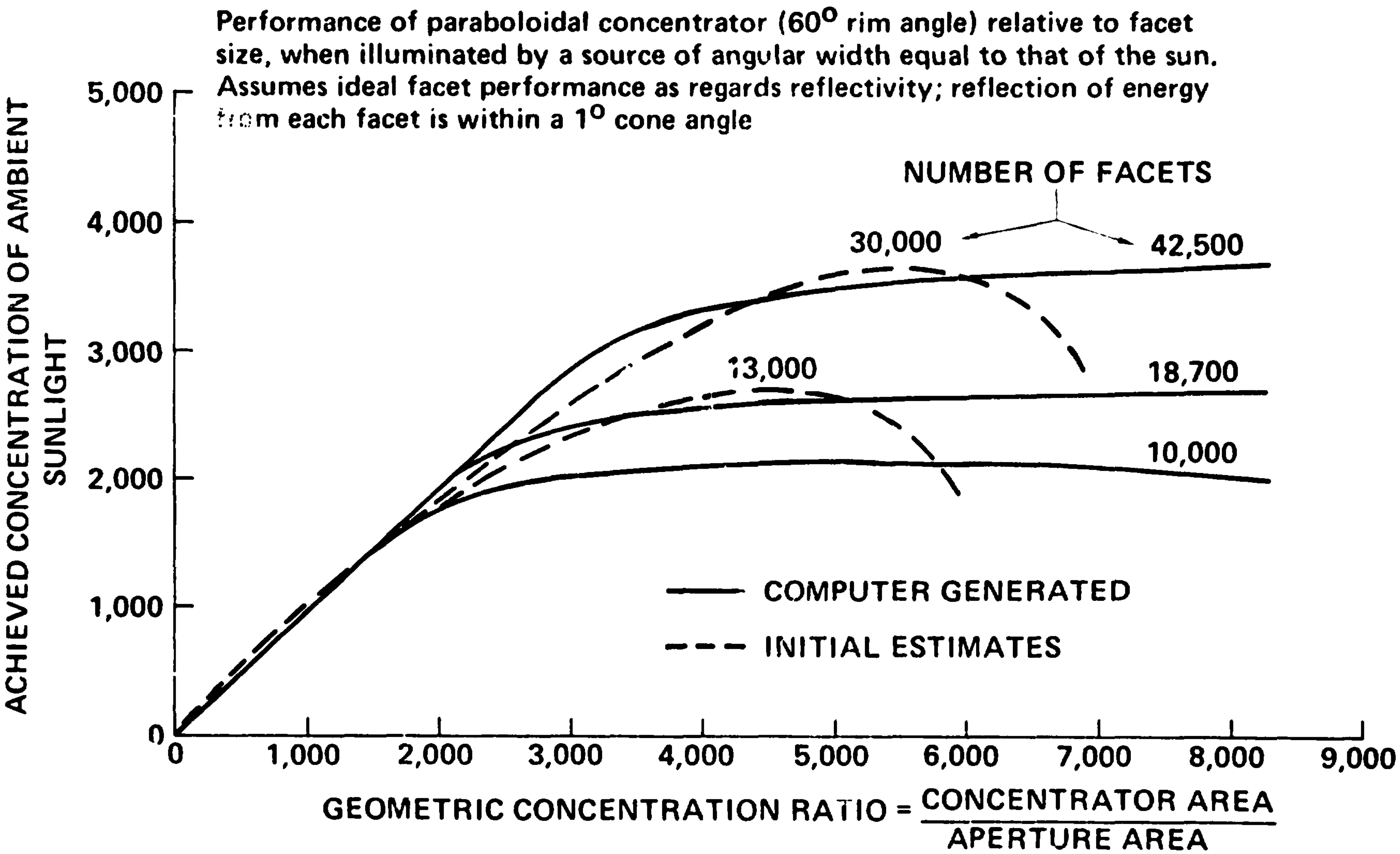

Figure 3.3-62 Comparison of Concentrator Computer Modeling With Initial Estimates

ORIGINAL PAGE IS
OF POOR QUALITY

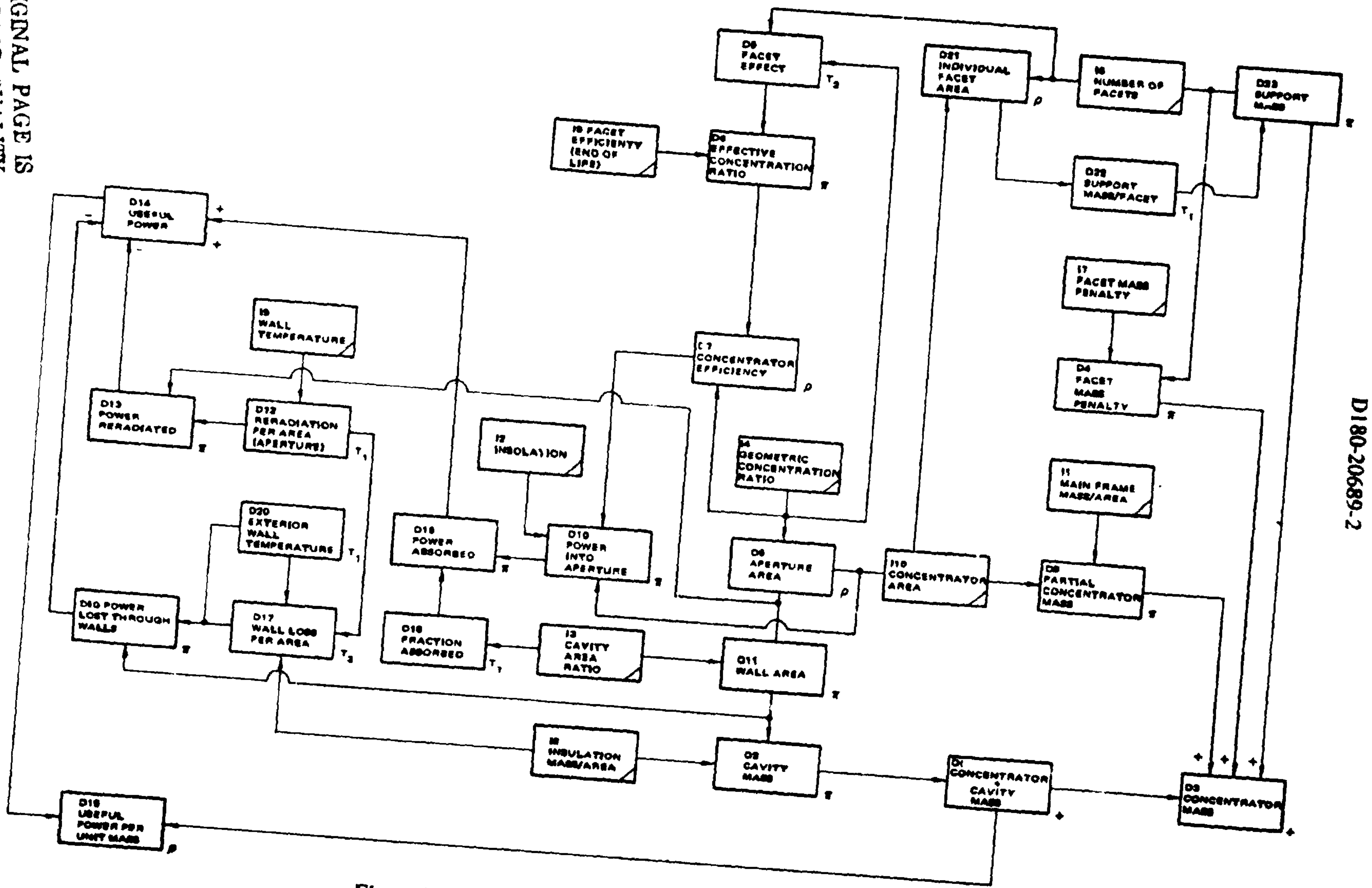

Figure 3.3-63 Concentrator/Cavity Mass Optimization

CONCENTRATOR/CAVITY MASS OPTIMIZATION

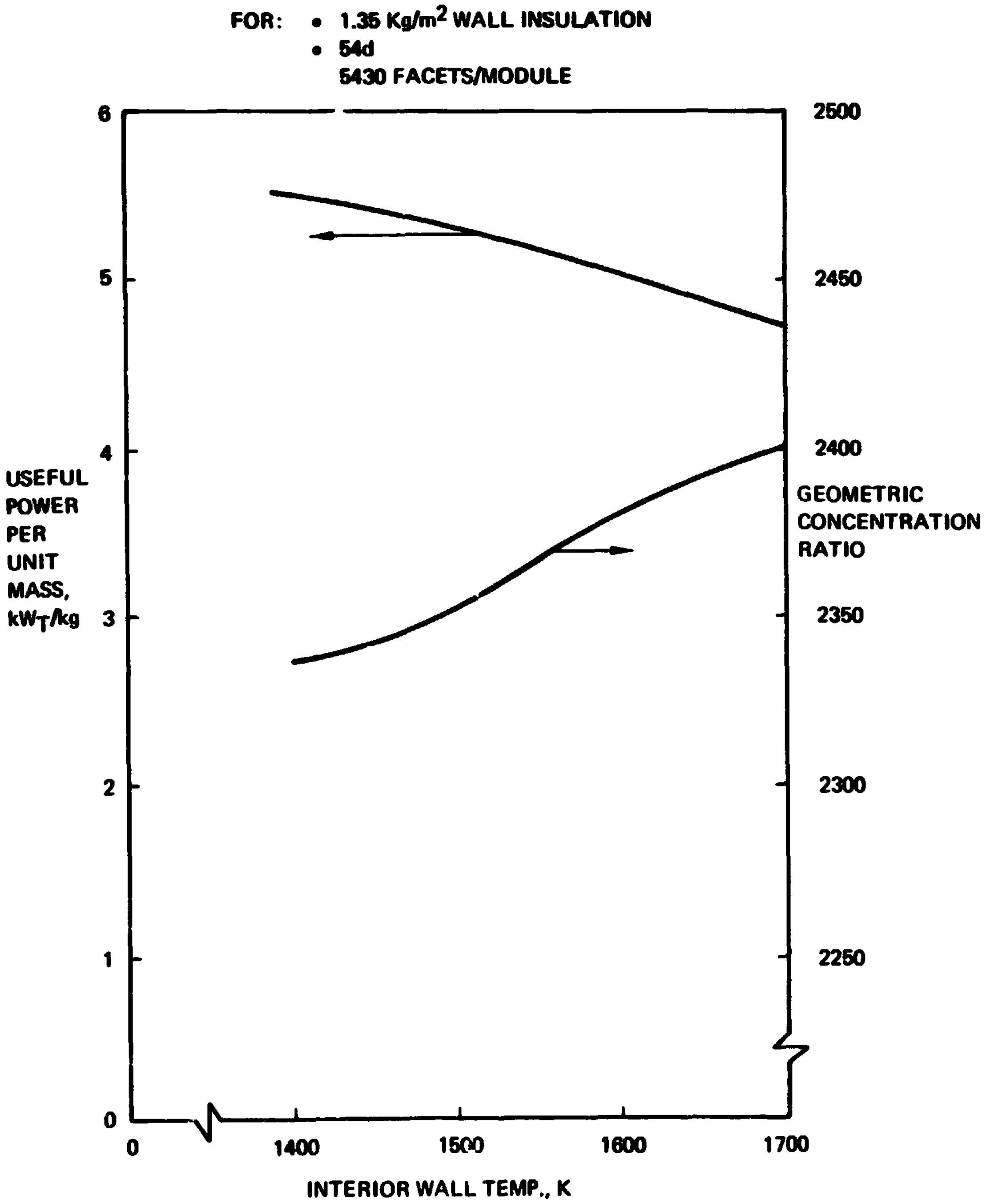
FOR: • 1.35 Kg/m2 WALL INSULATION
• 54d
5430 FACETS/MODULE
USEFUL POWER PER UNIT MASS, kWT/kg
GEOMETRIC CONCENTRATION RATIO
INTERIOR WALL TEMP., K
0
1
2
3
4
5
6
2250
2300
2350
2400
2450
2500
1400
1500
1600
1700

Figure 3.3-64

At the right of Figure 3.3-65 is shown a rear view of the facet, i.e., the reflective surface is on the reverse side. The hexagonal plastic film sheet is formed of 8 micrometer (0.00033 inch) Kapton. Three edges are supported by graphite epoxy edge members. The three edge members are tensioned apart by bridles attached to rocker arms mounted at the end of the three radial members. Springs mounted in the radial arms near the hub are the source of the tension.

The facet is mounted to the 1.5 m support beam by means of a 1.0 m long post. The hub assembly contains the sensor and servo-mechanism systems and the solar cell power supply required for their operation. The actual area of the facet is 933 square meters.

Concentrator performance varies with sun off-axis angle.

The data shown in Figure 3.3-66 resulted from a computerized analysis of a faceted solar concentrator. The aperture of the cavity absorber has 1/1320 of the projected area of the concentrator and 10,000 hexagonal reflector facets were used. The contribution of each facet was calculated, including effects of shadowing and blockage by adjacent facets.

Concentrator efficiency is the ratio of light delivered into the aperture to the light captured by the concentrator allowing for concentrator, tilt, as shown. The concentrator efficiency with the sun on-axis is 0.96 for a light spread angle of 1.0°. (To determine overall concentrator/reflector performance, multiply the concentrator performance at a given spread angle by the facet reflectivity at the same spread angle.)

Plastic film reflectors are believed to degrade with radiation. Very little data are available, but there were some sample tests conducted under Project ABLE.

The Project ABLE tests irradiated plastic film samples with a simulated geosynchronous orbit environment, but at an accelerated rate. The material used was Kapton (which showed lower degradation that Mylar). The primary damage mechanism was apparantly bubbling within the plastic film by stopped low energy protons which found electronis and became hydrogen. An interpretation of the data is shown in Figure 3.3-67.

With the "tilt and roll" design the facets must track the sun through the apparent angular range of + and -11.74°. Consequently the facets must be capable of moving + and -5.88°, a total capability of + and -7° is baselined, + and -1° is assumed to be sufficient for the other axis. For the revised configuration (no tilt and roll) the facets must track through $\pm 24^{\circ}$.

ORIGINAL PAGE IS
OF POOR QUALITY

FOLDOUT FRAME

ORIGINAL PAGE IS OF POOR QUALITY

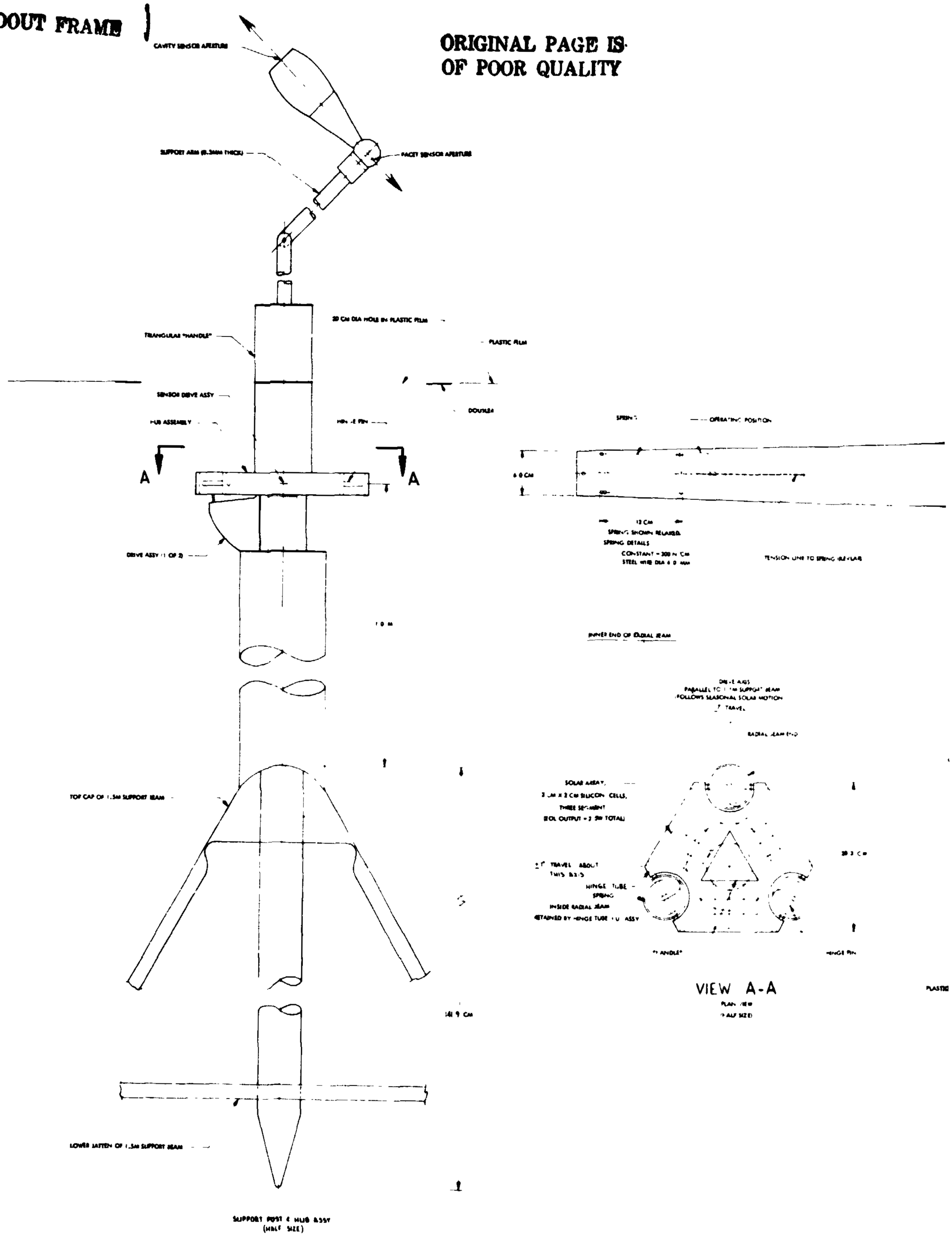

PRECEDING PAGE BLANK NOT FILMED

FOLDOUT FRAME 2

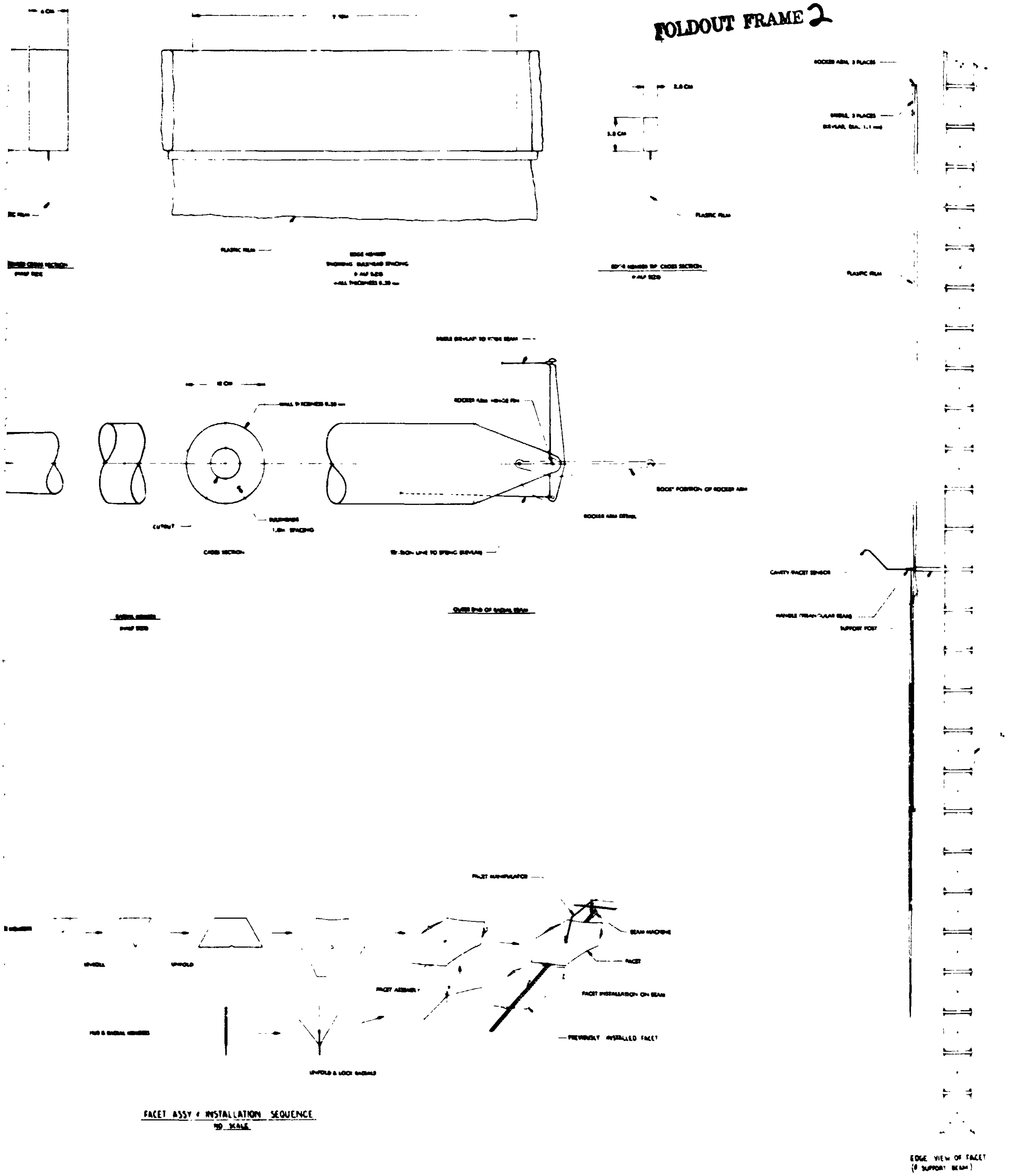

FOLDOUT FRAME 3

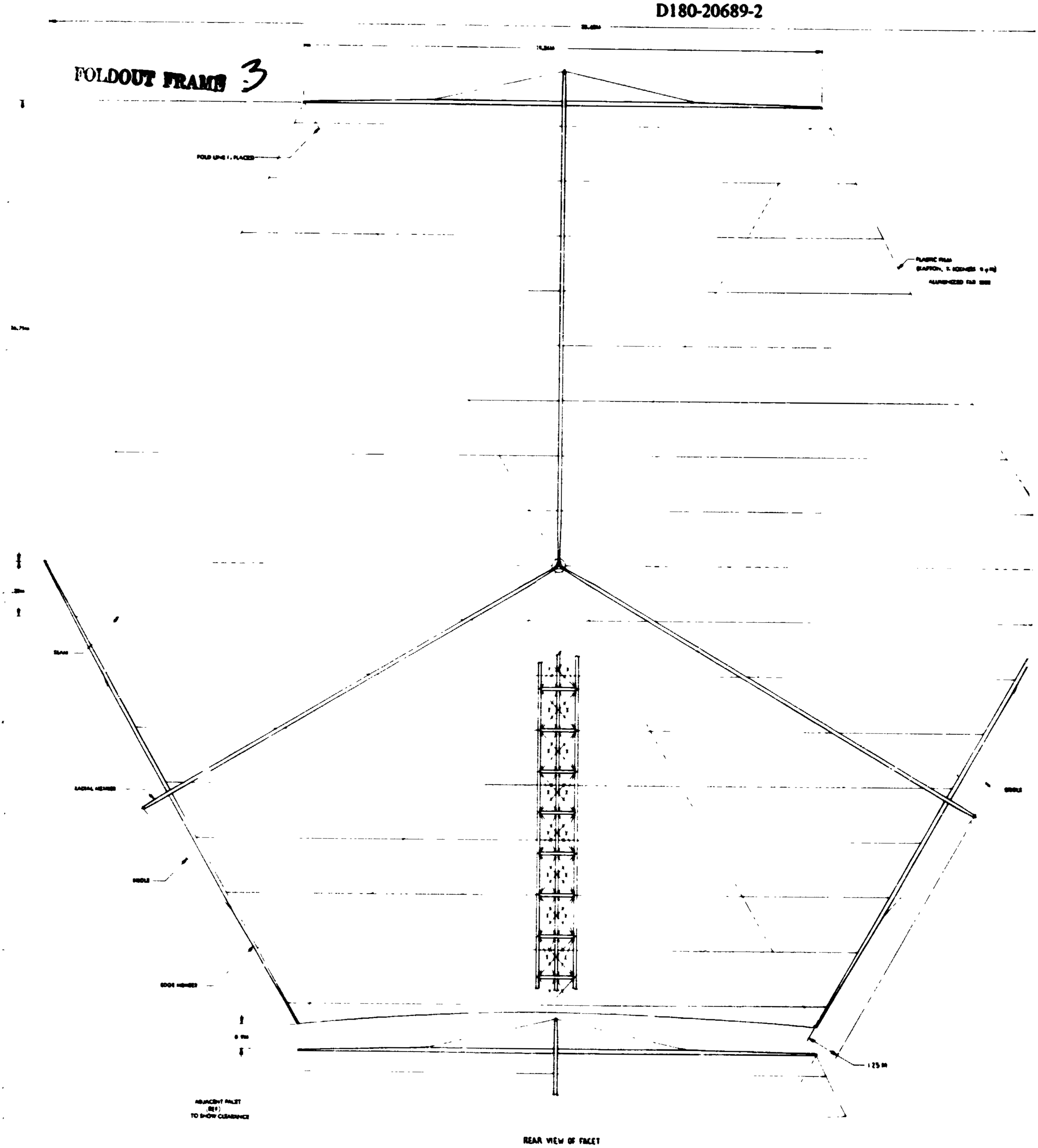

Figure 3.3-65 Reflector Facet–(Heliostat) Thermal Engine S.P.S.

ORIGINAL PAGE IS
OF POOR QUALITY

SPS-295

- For baseline concentrator ratio of 1320, 10,000 facets, 30-degree rim angle
- Light spread angle as defined here does not include the 0.5-degree inherent from the width of the Sun
- Does not include effect of film reflectivity and facet gaps

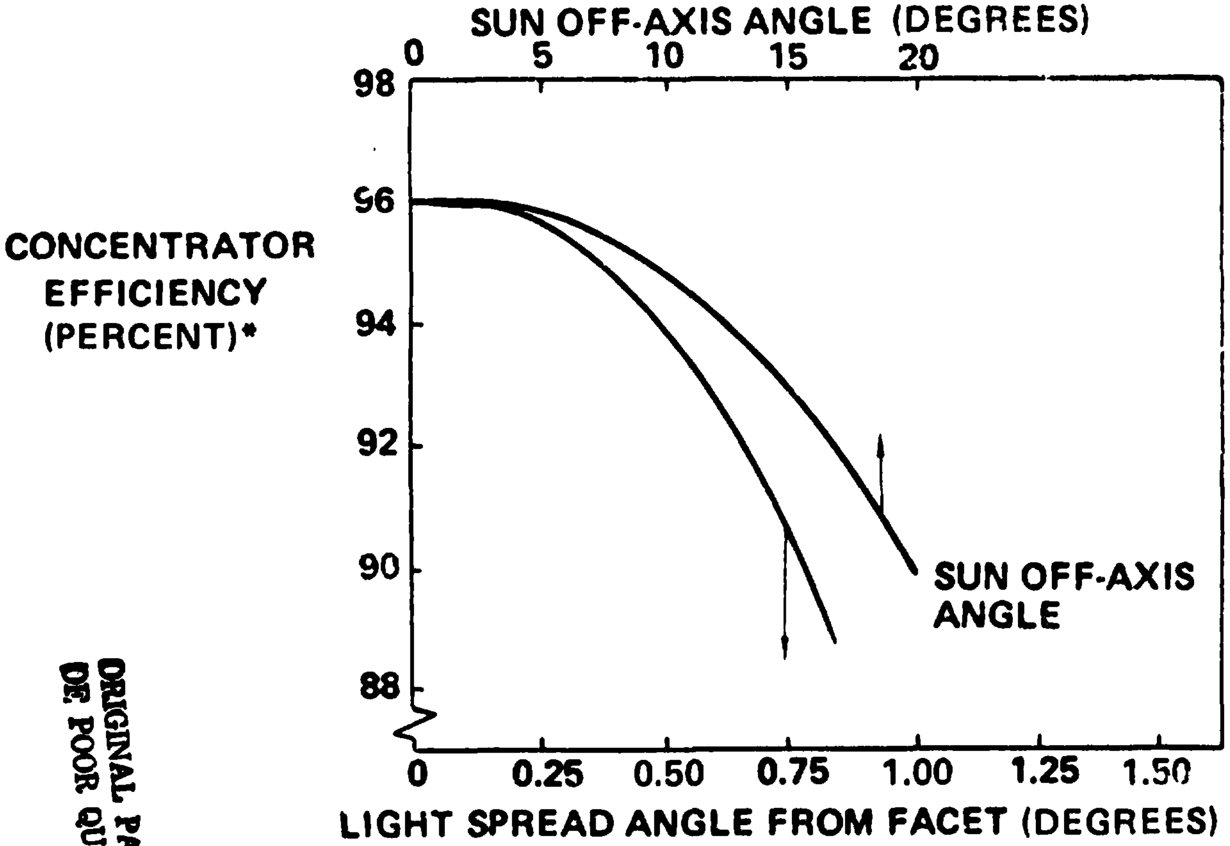

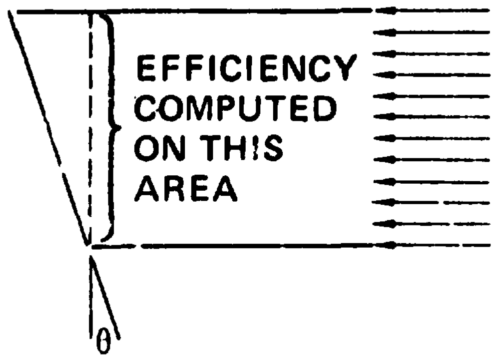

Effect on concentrator flying P.O.P.

- Cosine 23.47° = 0.917
- Concentrator efficiency at 23.47° = 0.87

The product of the above is 0.80 (this represents the solstice performance). Averaged over the year, a loss of approximately 9.5% results.

* For "straight-beam, three-zone concentrator," the curved-dish efficiency is estimated at 97%.

Figure 3.3-66 Response of Faceted Concentrator to Solar Position (Geometric Efficiency, Reflectivity Not Included)

ORIGINAL PAGE IS OF POOR QUALITY

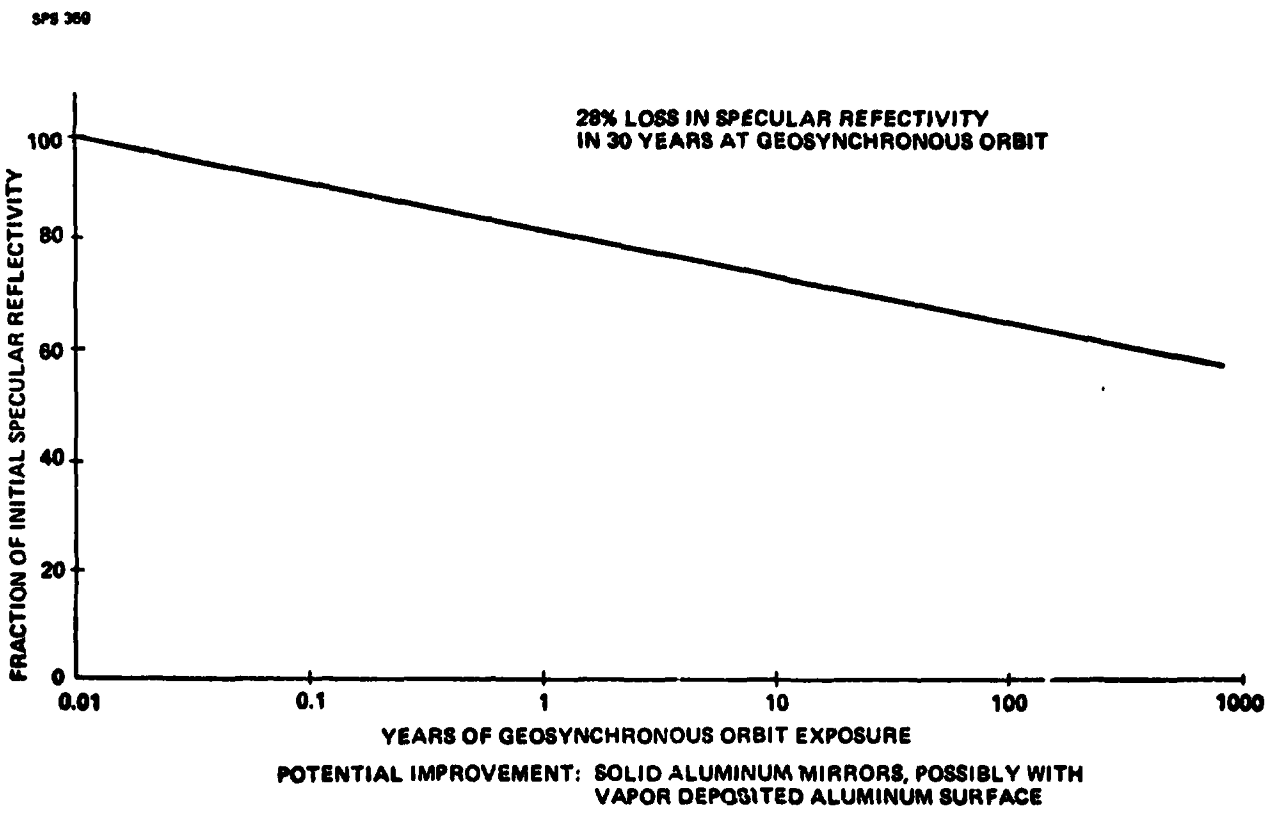

Figure 3.3-67 Plastic Film Performance: Radiation Degradation (From Project 'Able')

The baselined facet pointing system incorporates a swiveling detector tube mounted above the facet surface as illustrated in Figure 3.3-68. On either side of the central partition in the tube are mounted cuads of silicon detector cells. A modulated light source is provided at the cavity aperture; light is admitted to the upper detectors by a small aperture. The detector tube is driven until it is aligned with rays from the modulated light source. The lower silicon detectors respond to light reflected from the metallized surface of the facet. The facet is driven about the two axes as required to position the light spot from the facet on the center of the lower detector quad. Thus the reflected light from the facet is aimed at the cavity aperture.

Two approaches are suggested for provision of a modulated light target at the cavity as illustrated in Figure 3.3-69. Both require some reflectivity from a high temperature surface. Redundant light sources can be used for reliability.

The moments of inertia of the reflector facets are quite low. Thus for the baselined angular acceleration only two milliwatts of mechanical drive power suffices. Consequently a small area of solar cells located at the facet hub will suffice to power the facet.

The drive mechanism should ideally have no bearings, friction, etc. Bimetallics are a potentially desirable solution.

The following design assumptions were used:

1. Facet drive requirement assumptions:

   a. Angular acceleration of 0.01 deg/sec^2
      (attains 0.1 deg/sec in 10 seconds)

   b. Maximum angular rate of 0.1 deg/sec

2. Moments of inertia of facet are such that maximum angular acceleration can be provided in both axes with a mechanical power of less than 2.0 mW.

3. Facet and detector tube drive plus logic circuit operation can probably be accomplished with less than 100 mW. Thus, entire facet operation can be powered by a few solar cells.

4. Logic chip will probably be less complex that that of a pocket calculator.

ORIGINAL PAGE IS
OF POOR QUALITY

SPS-797

- **Silicon detectors can track a modulated light source across the solar disk.**

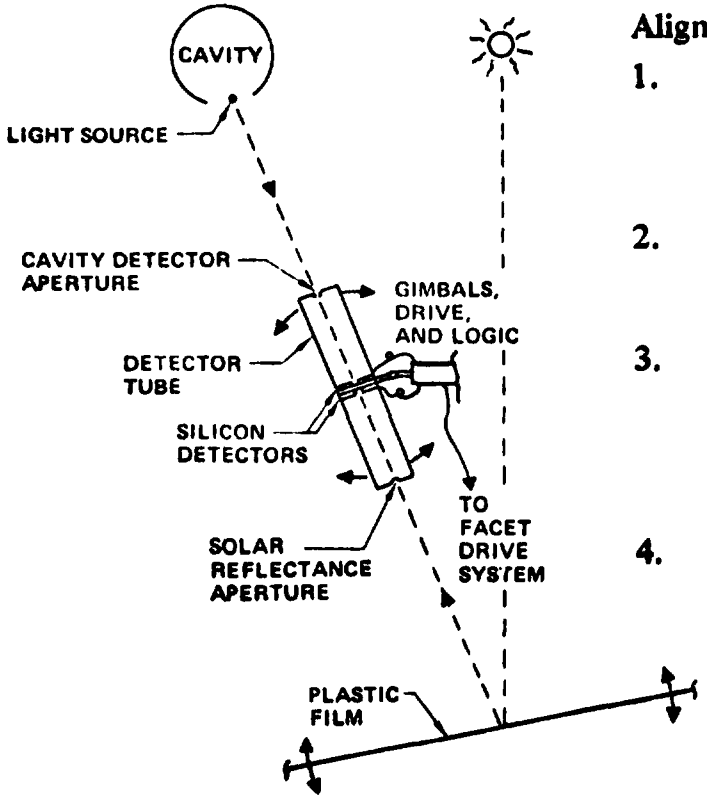

Alignment sequence:

1. **Without cavity light source, facet drive is commanded to end of travel (no power to cavity).**
2. **When modulation of light source is as required, detector tube aligns with light source.**
3. **Facet drive system positions facet such that reflected rays from facet are aligned with detector tube axis and hence are aimed at cavity.**
4. **If modulation is removed, logic causes facet drive to gimbal stop.**

Figure 3.3-68 Pointing the Facets $\pm 7^{\circ}$ and $\pm 1^{\circ}$ Travel

Two approaches to providing a modulated light target:

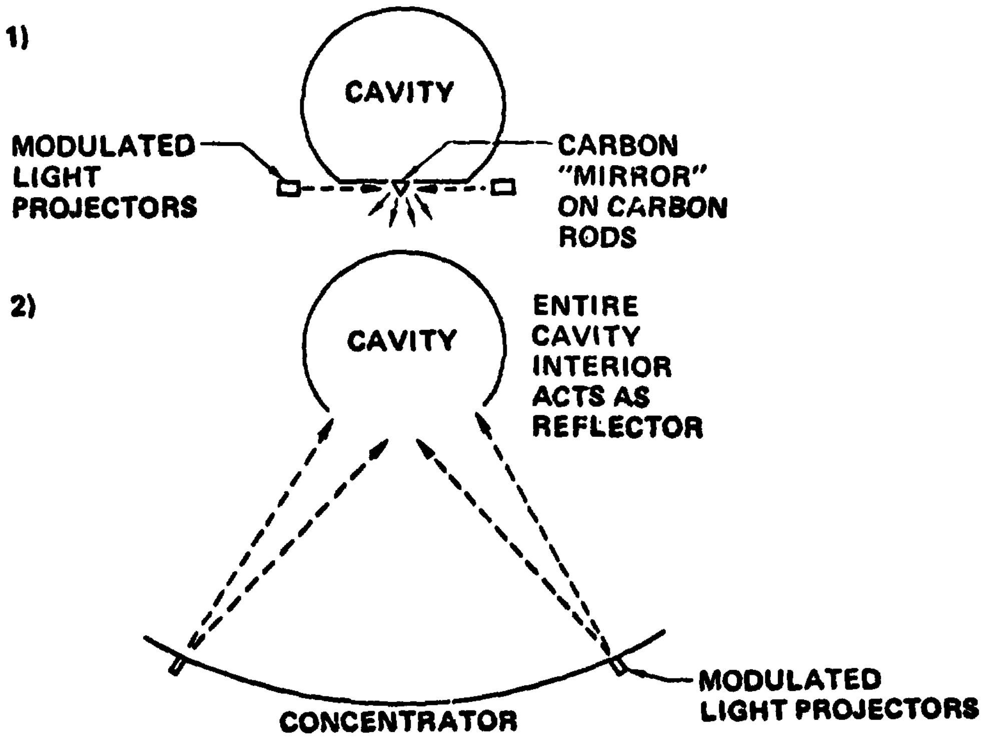

Figure 3.3-69 Pointing the Facets: Additional Details

ORIGINAL PAGE IS OF POOR QUALITY

5. Facet and detector drive options:

   a. Bimetallic elements with controlled electric heaters
   b. Solenoids
   c. Motors with gear trains

The primary circuit elements and their interrelationships are shown in Figure 3.3-70. A critical element is the output from the modulation detector which causes the facet to "look away" when modulation is not present upon the cavity light source.

A possible approach to facet packaging for launch is illustrated in Figure 3.3-71. The facet is folded three times and then rolled around the edge members. The radial arams, when folded, secure the detector tube for launch.

3.3.6.4 Absorber Design

A typical cavity absorber panel is shown in Figure 3.3-72; items such as turbomachines, recuperator/coolers or NaK pumps are not shown. On the cavity interior side are mounted the heat absorber tubing loops which are heated by the concentrated solar radiation. Above the panel are four helium header tubes; these are provided with a meteroroid protection/insulation housing. The "skin" of the panel is multi-layer high temperature, stabilized by a crisscross wire pattern.

Figure 3.3-73 shows one of the 16 cavities which make up the 10 gigawatt ground output SPS. The cavity is supported by two 20-meter beam support arms and has beneath its aperture a light shield which prevents stray high concentration light from falling on the servicing areas associated with the turbo machines. Two turbo machines can be seen along with some of the helium manifolds.

The dashed outline in Figure 3.3-74 represents the cavity absorber, 64 meters in diameter at the aperture, 102 meters in diameter at the major section. Indication is given of the location of a single turbo-machine. Leading to the turbo machine is the hot manifold, that is, the manifold section which directs hot helium to the turbine inlet of the machine. Cooled helium from the radiator section enters the cold manifold and is routed to the header sections both above and below the central hot manifold as shown. On the right is shown a cross section of a panel assembly with a cold and hot header exterior to the cavity and heat absorber tubing inside the cavity.

ORIGINAL PAGE IS
OF POOR QUALITY

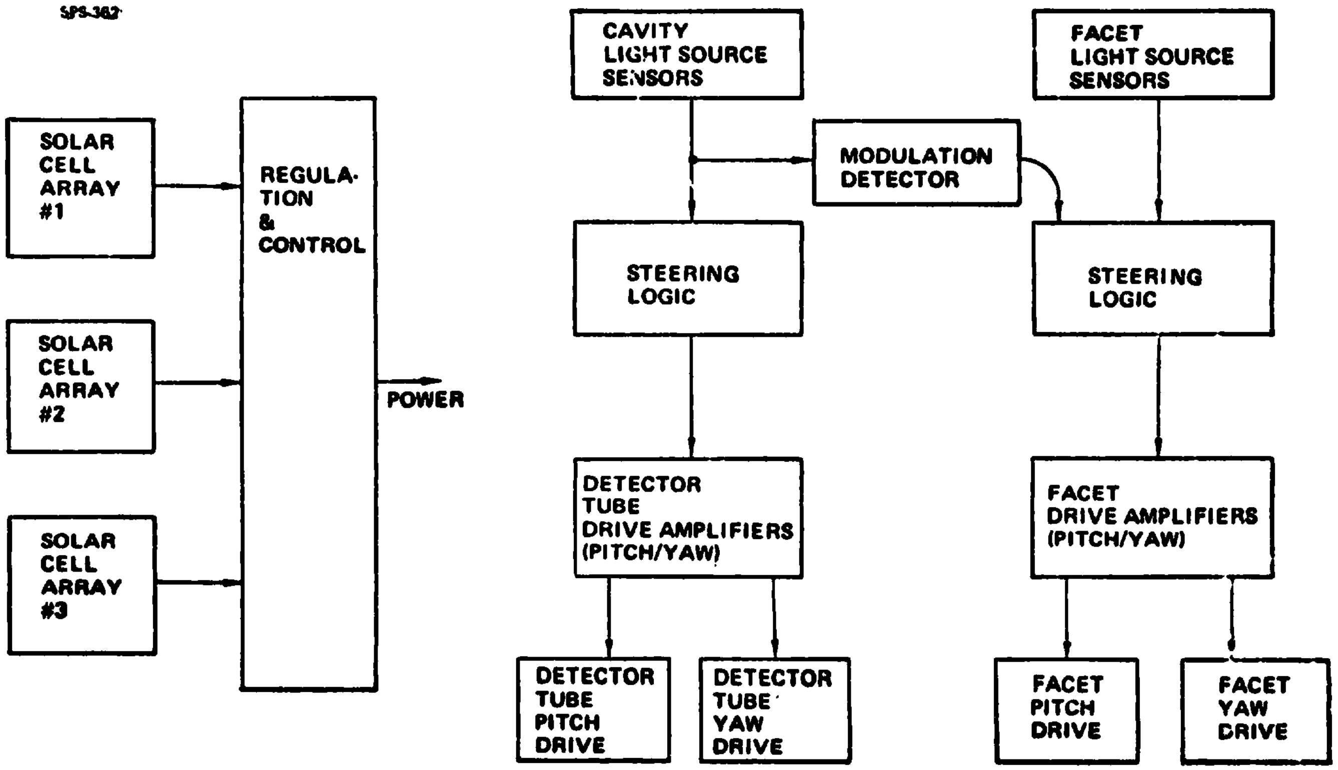

Figure 3.3-70 Facet Electronics Block Diagram

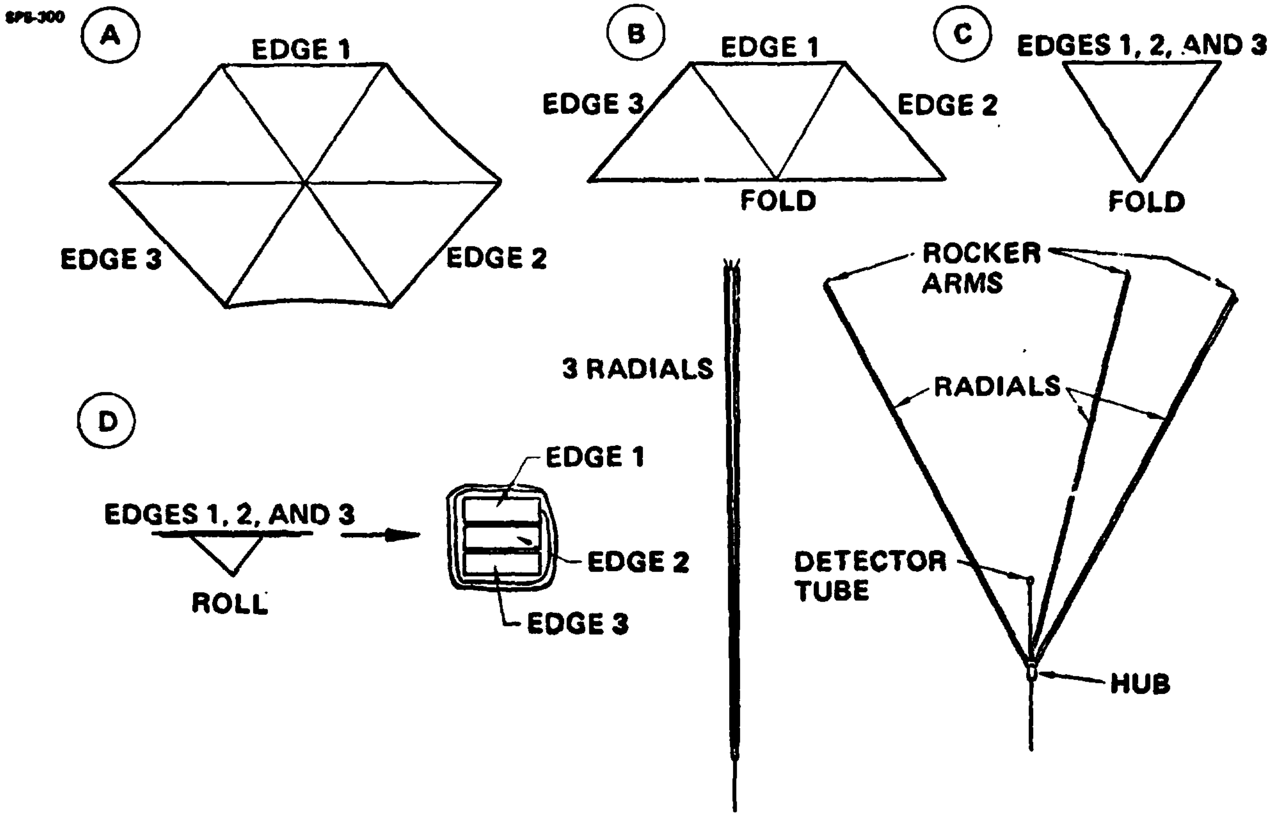

Figure 3.3-71 Facet Folding

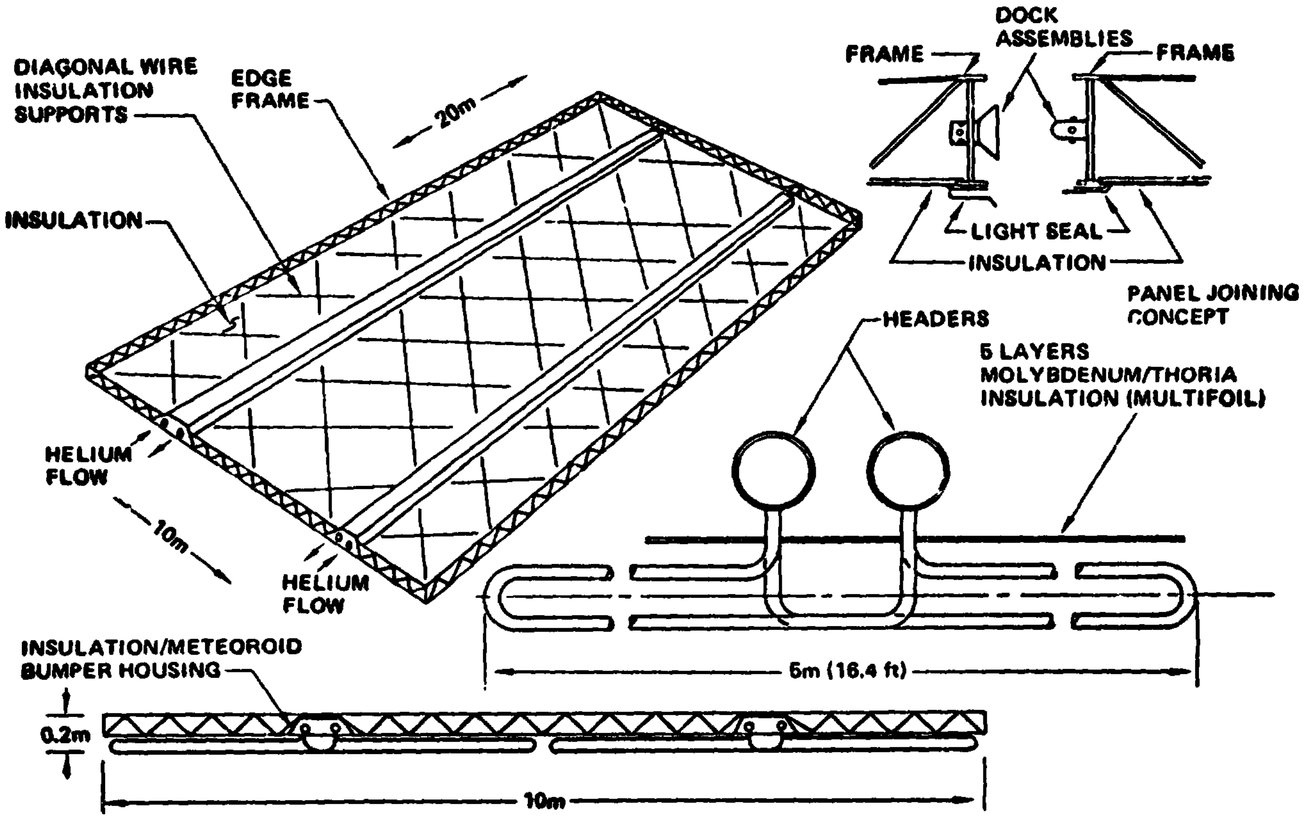

Figure 3.3-72 Cavity Heat Absorber Panels

ORIGINAL PAGE IS
OF POOR QUALITY

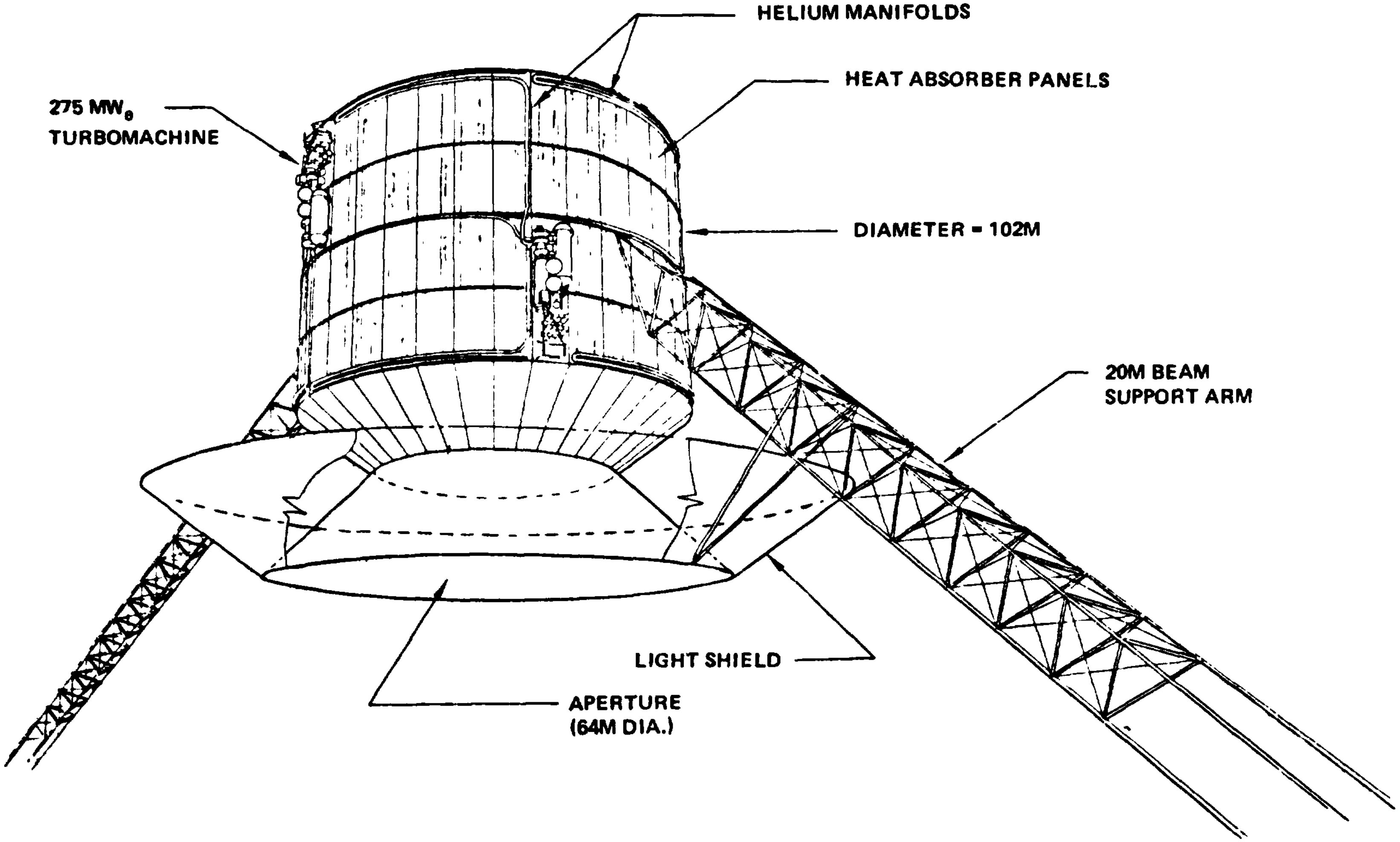

Figure 3.3-73 Focal Point Assembly

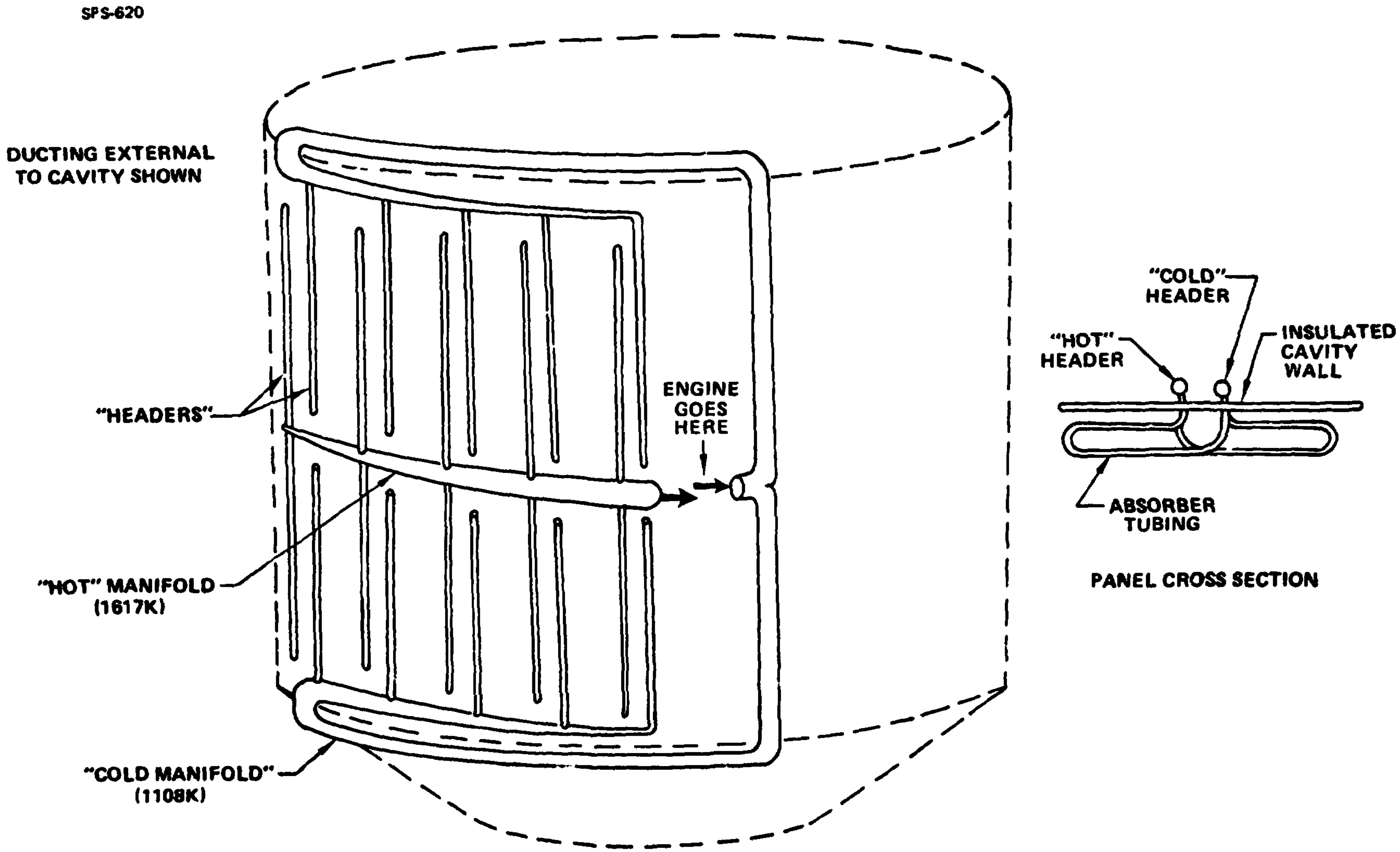

Figure 3.3-74 Primary Heat Exchanger Layout (Simplified)

D180-20689-2

ORIGINAL PAGE IS OF POOR QUALITY

On the right of Figure 3.3-75 is shown an uninsulated helium duct that contains pressurized helium at 1608 Kelvin and 4.14 x 10^6 N/M^2 (600 PSI). The interior diameter of the duct is one meter To withstand these conditions for 30 years requires a pressure shell thickness of 17 centimeters as shown. The resultant mass of a one meter length this ducting is 5,630 kilograms. On the left is shown a insulated section to withstand similar conditions. That is, it is one meter in interior diameter with helium at the same temperatures and pressures. However, this system is insulated That is, there is an interior liner, then insulation (which could be columbium wool), followed by the outside pressure shell. This pressure shell need be only 2.3 centimeters thick to withstand the long term temperatures and pressures, since it operates at only 1,200 Kelvin rather than the full 1608 Kelvin. Critical to this concept are vents in the interior liner. This allows helium to saturate the insulation. Without this, the interior pressure shell or the interior liner would feel the full pressure. With the vents, the helium pressure is transmitted through the insulation to the exterior pressure shell.

The engine configuration shown in Figure 3.3-76 was produced for the "Space-Based Power" study by the Garrett Corp.

The second generation turbocompressor includes a sixteen stage axial compressor and a six stage axial turbine. The rotor is supported by hydrostatic gas journal bearings outboard of the aerodynamic wheels and a hydrostatic gas thrust bearing between the turbine and compressor. An axial thrust balancing piston will be located between the compressor and turbine to limit the thrust loads and thus minimize the thrust bearing size and power loss.

The ASTAR 811C turbine end structure is shown to include internal insulation which is required to reduce the unit mass. No insulation benefit is included in the total turbocompressor mass figure however.

The . erator/cooler package conceptual design shown in Figure 3.3-77 was also developed by the (Corp.

The plate-fin pure counterflow recuperator and finned tube cross counterflow gas to NaK cooler are composed of multiple modules contained within two pressure vessels for each 300 MW engine module. The recuperator/cooler module at right shows the compressor discharge flow entering the package at the top and being distributed to the recuperator modules. The cold exhau. flow of the cooler is directed around the containment pressure vessel to limit the vessel pressure and temperature

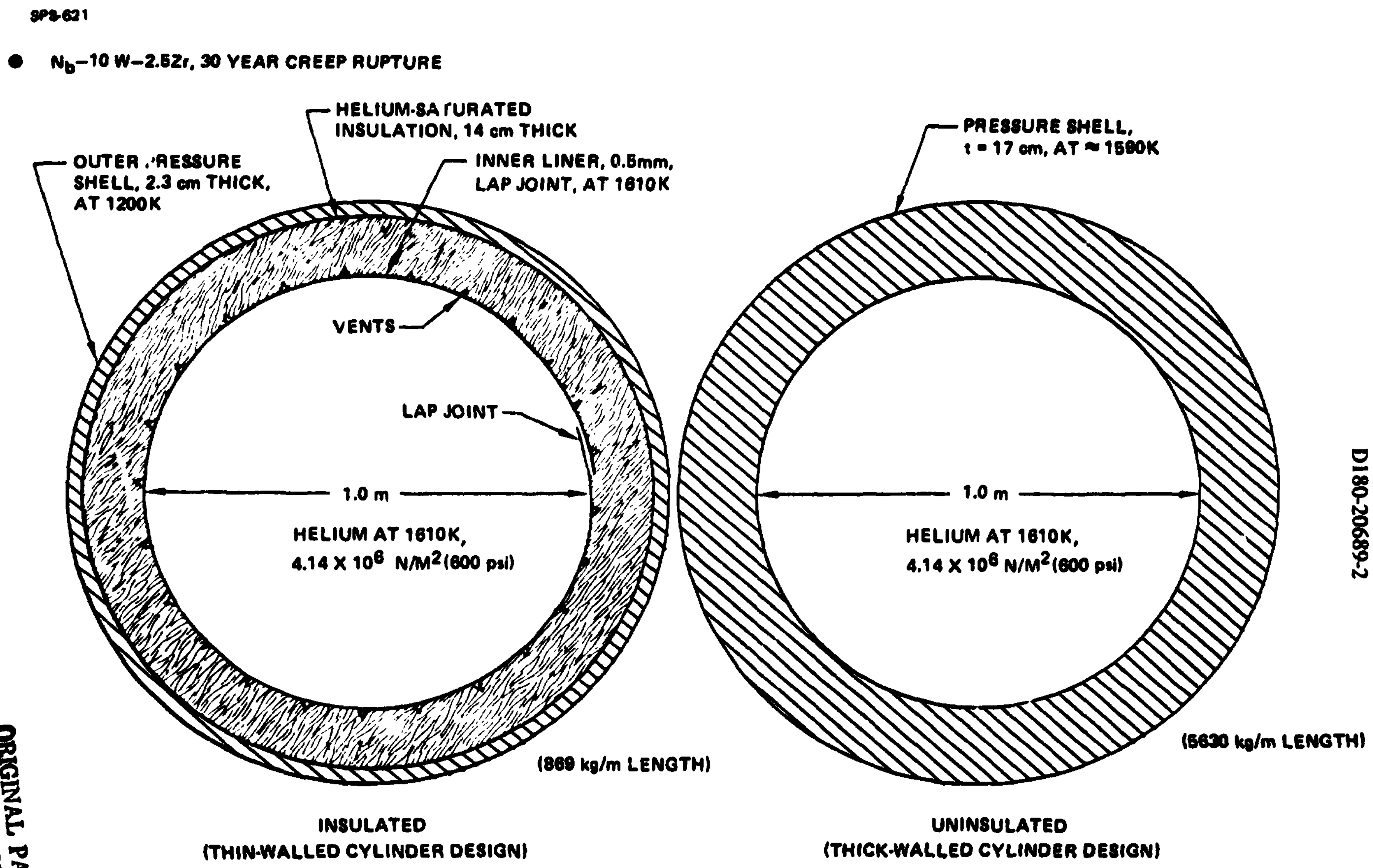

Figure 3.3-75 Helium Duct Comparison

ORIGINAL PAGE IS OF POOR QUALITY

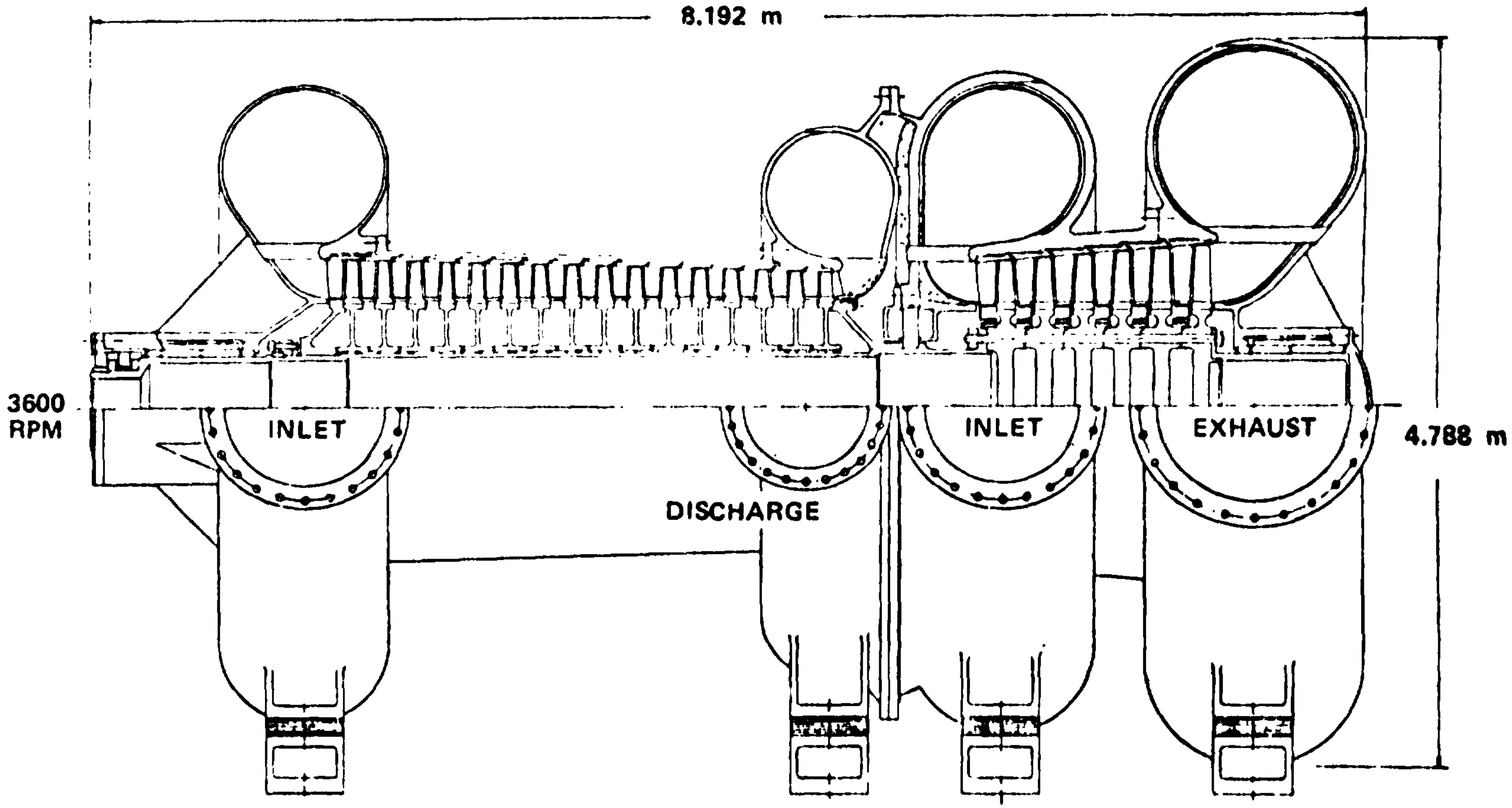

MASS = 156,100 kg SPECIFIC WEIGHT = 0.520 kg/kW$_e$

Figure 3.3-76 Second Generation Turbocompressor Layout

ORIGINAL PAGE IS
OF POOR QUALITY

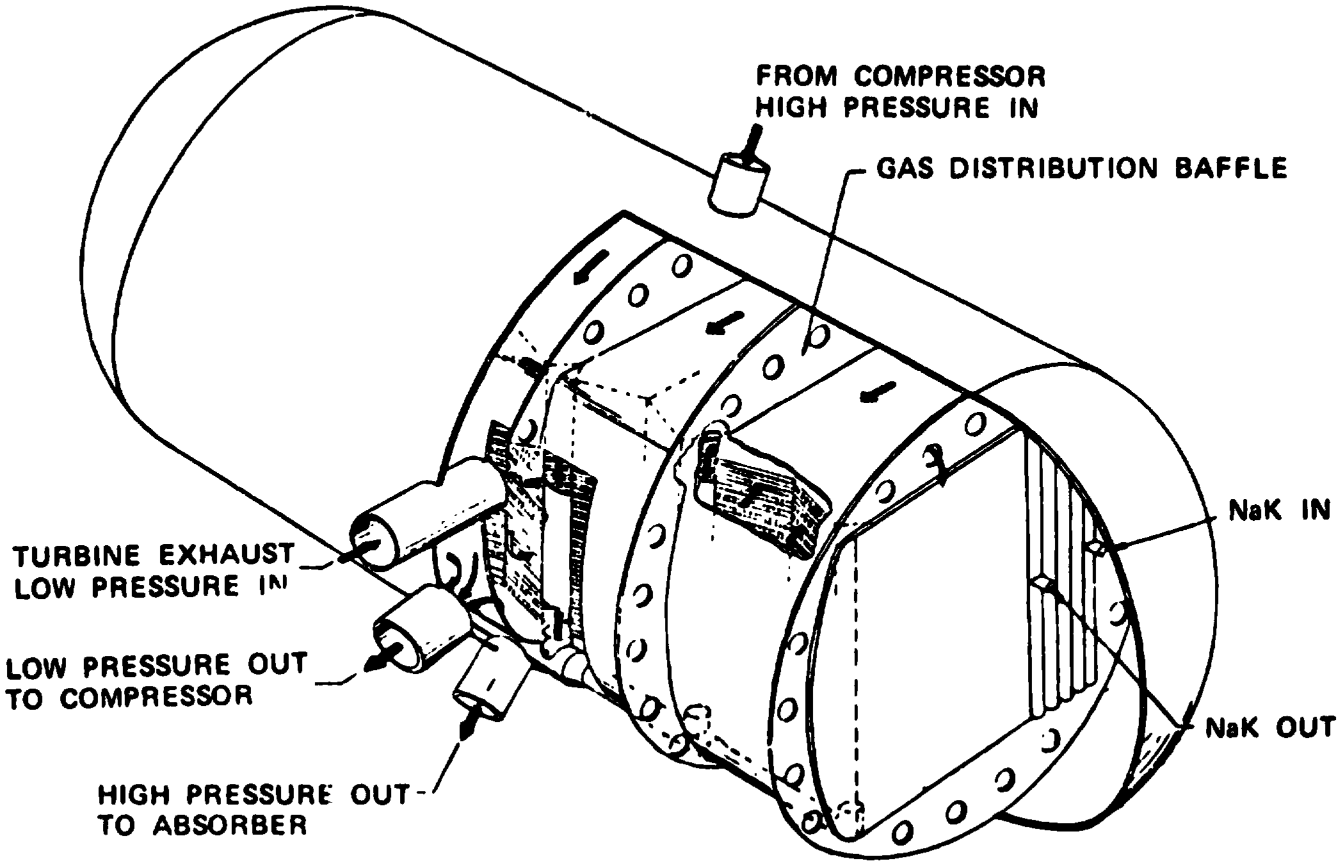

Figure 3.3-77 Recuperator/Cooler Package For Powersat

3.3.6.5 Cavity Heat Absorber Analysis

An analysis of cavity heat absorber mass characteristics was performed to support the thermal engine cycle option mass screening test. Figure 3.3-78 shows the cavity absorber model utilized to predict heat flux incident on absorber tubes. Independent variables affecting tube flux were geometric concentration ratio, tube wall temperature, concentration efficiency, N_e, and the ratio of cavity wall area to aperture area.

Saturation pressure - temperature characteristics of several candidate Rankine working fluids are compared in Figure 3.3-79. This comparison illustrates the high vapor pressures which are characteristic of water and the boiling temperature limit of 650°K. At temperatures below 650°K the vapor pressure of water is about four orders of magnitude greater than that of cesium, rubidium or potassium.

Rankine-cycle cavity heat absorbers have four zones in which distinctly different heat transfer phenomena exist. Fluid entering the heat absorber is in the subcooled state and heat transfer can be described by conventional liquid forced-convection models. When the liquid temperature approaches the saturation value, vapor bubbles form at the tube wall and the nucleate boiling zone is entered. The mass of vapor increases in the flow direction and, when approximately 60 to 80% of the liquid has been vaporized, the tube wall is no longer wetted by a continuous film of liquid. Instead, the remaining liquid exists as droplets borne along by the flowing vapor. This heat transfer regime is referred to at the liquid-deficient regime and heat transfer is described conservatively by gas forced-convection models. The mixture average temperature remains slightly above the saturation value until all the liquid is evaporated. This marks the entrance to the superheat region in which this fluid is completely vaporized.

Development of a model for predicting heat absorber mass required an analysis of heat transfer between the fluid and containment tube walls. Power absorbed by the fluid in each zone of the absorber was determined by the expression.

$\dot{Q} = \dot{m} C p \Delta T$ single phase fluid flow

$\dot{Q} = \dot{m} \Delta x h_{fg}$ boiling or liquid dificient regime

where $\dot{Q}$ = power transferred to fluid
$\dot{m}$ = fluid mass flow rate in all tubers
C_p = specific heat of fluid
ΔT = temperature increase of fluid
ΔX = increase in mass fraction of vaporized liquid
hfg = heat of vaporization

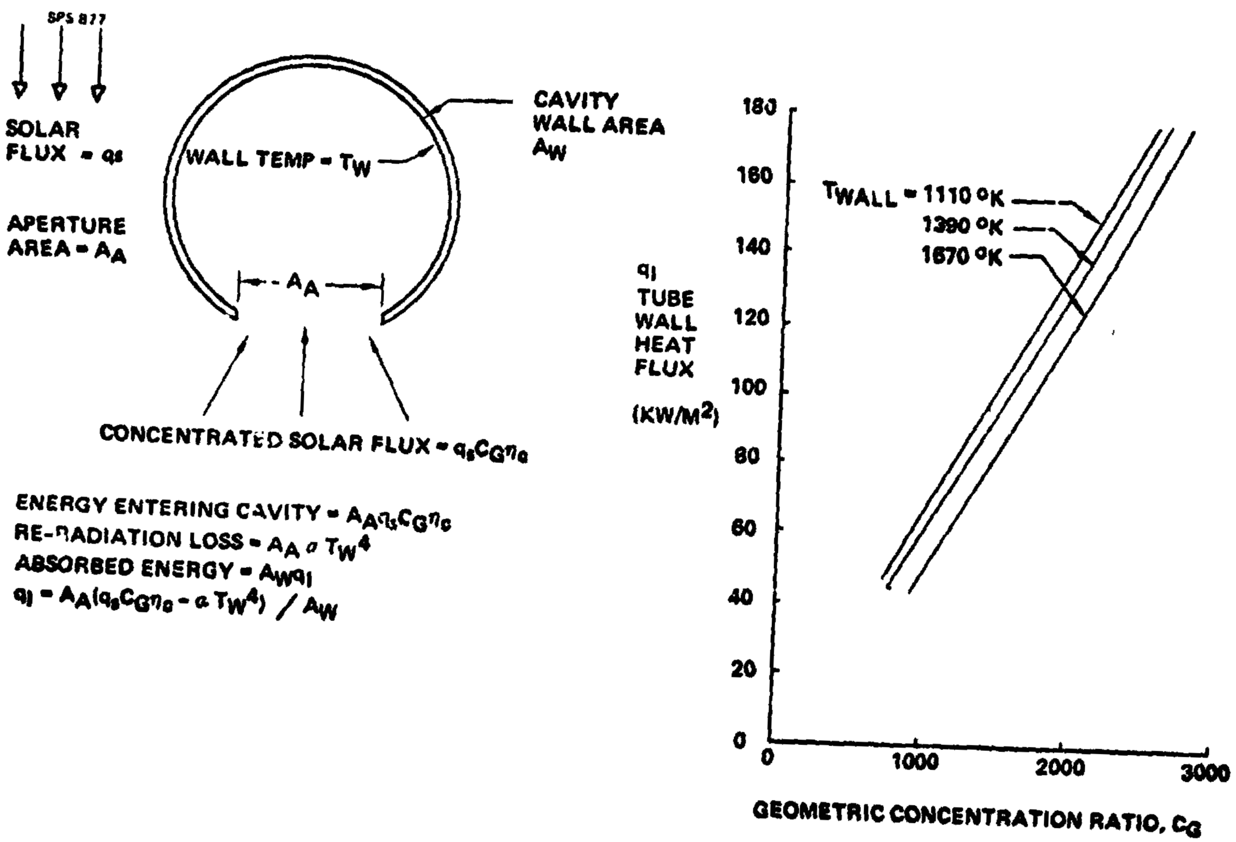

Figure 3.3-78 Cavity Heat Absorber Flux Model

ORIGINAL PAGE IS
OF POOR QUALITY

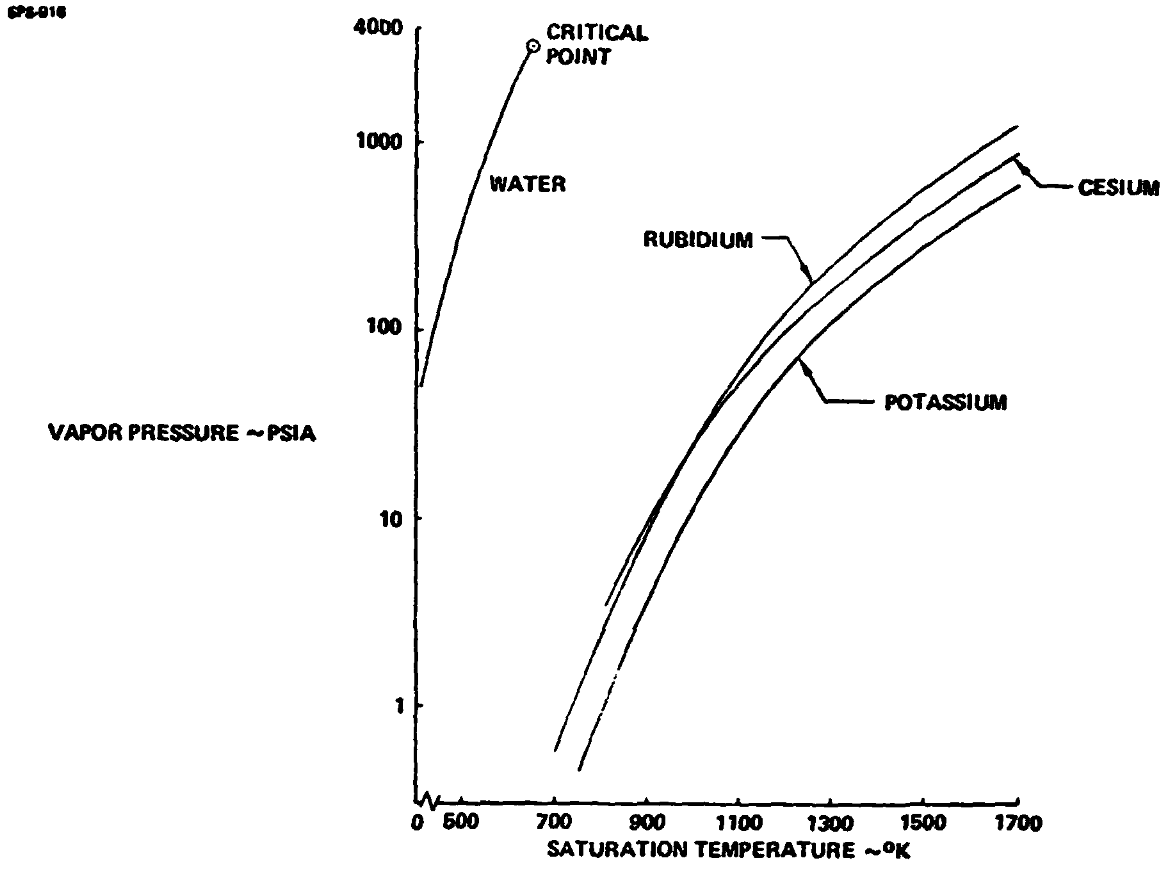

Figure 3.3-79 Saturation Pressures of Candidate Rankine Working Fluids

Tube wall temperature was determined by the expression:

$$T_{wall} = \frac{\dot{q}l}{h} + T_f$$

where $\dot{q}l$ = local net radiative heat flux on tube outer wall (see Figure
h = heat transfer coefficient between tube inner wall and fluid
T_f = local fluid bulk temperature

Values of convective boiling heat transfer coefficient for potassium and water are shown in Figure 3.3-80 and 3.3-81. The range of values for potassium, based on experimental data, is between 15 and 60 kw/m^2-^{o}K while average boiling heat transfer coefficients ranged from 15 to 35 kw/m^2-^{o}K. Tube wall temperature, along with fluid pressure were used in a thick-wall tube stress model to determine wall thickness for 30 year life. Absorber tube lengths required in each heat transfer zone were calculated from the equation:

$$L = \frac{\dot{Q}}{\dot{q}l\pi DN_t}$$

where D = internal diameter of absorber tubes
N_t = total number of parallel flow tubes

Fluid and tube wall temperature profiles in potassium and water heat absorbers are shown in Figures 3.3-82 and 3.3-83. Major differences between the potassium and water temperature profiles were the longer tube length required for boiling and liquid-deficient heat transfer in the potassium heat absorber and the higher average wall temperature. Details of heat absorbers for four thermal engine cycle options are compared with the Brayton baseline heat absorber in Table 3.3-11. The Brayton baseline heat absorber design incorporated 10 to 20 times more tubes than the Rankine cycle absorbers however the tubes were much shorter.

ORIGINAL PAGE IS
OF POOR QUALITY

SPS 878

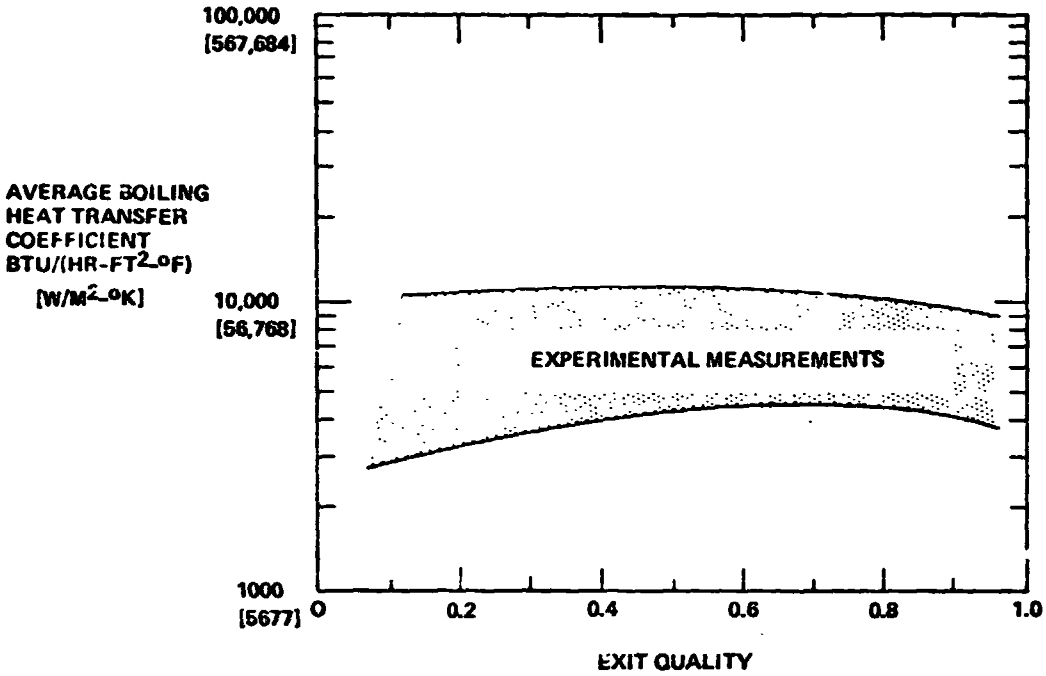

Figure 3.3-80 Average Boiling Heat Transfer Coefficients For Potassium

SPS 899

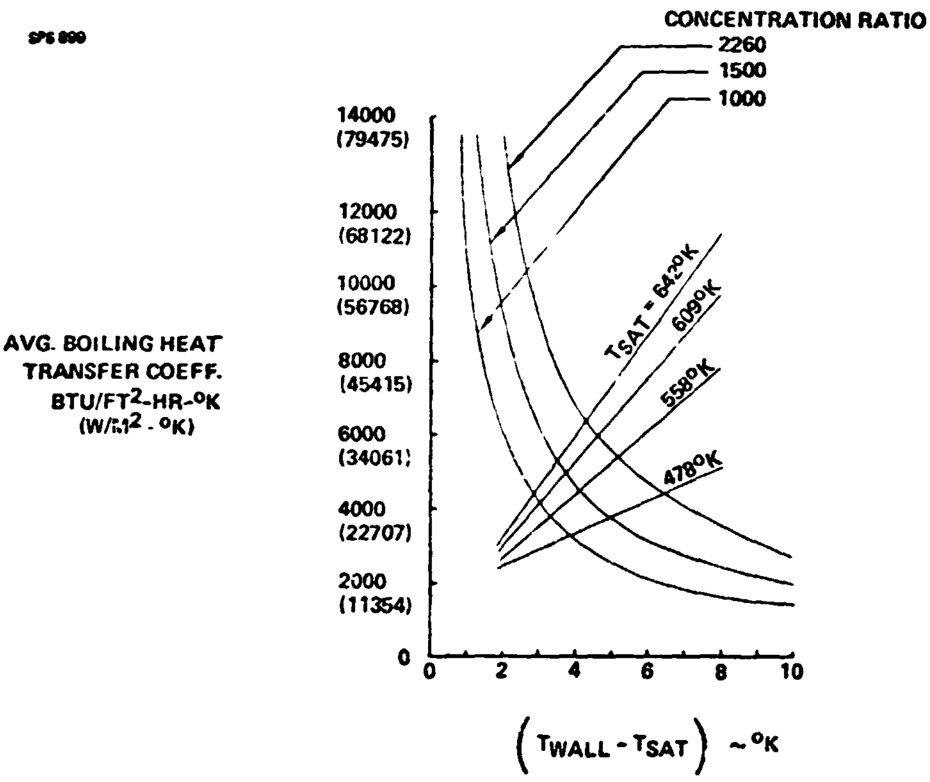

Figure 3.3-81 Average Boiling Heat Transfer Coefficients For Water

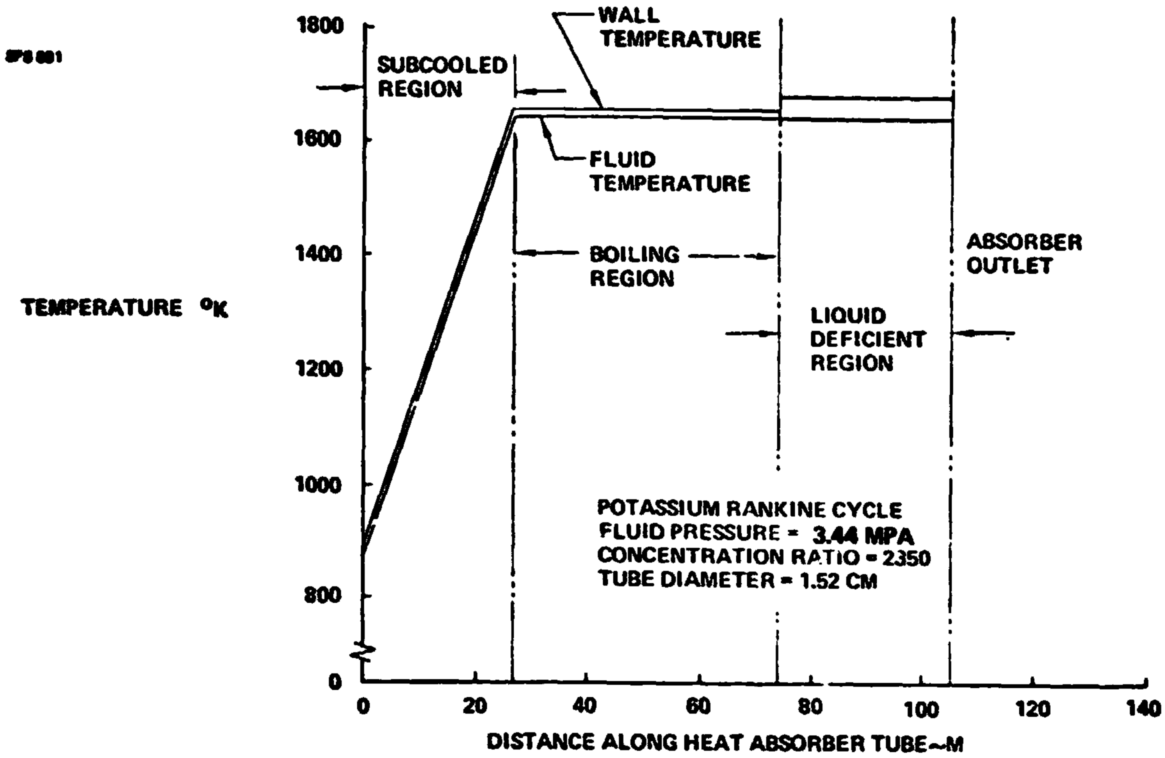

Figure 3.3-82 Fluid and Tube Wall Temperature Profiles Along Potassium Heat Absorbers

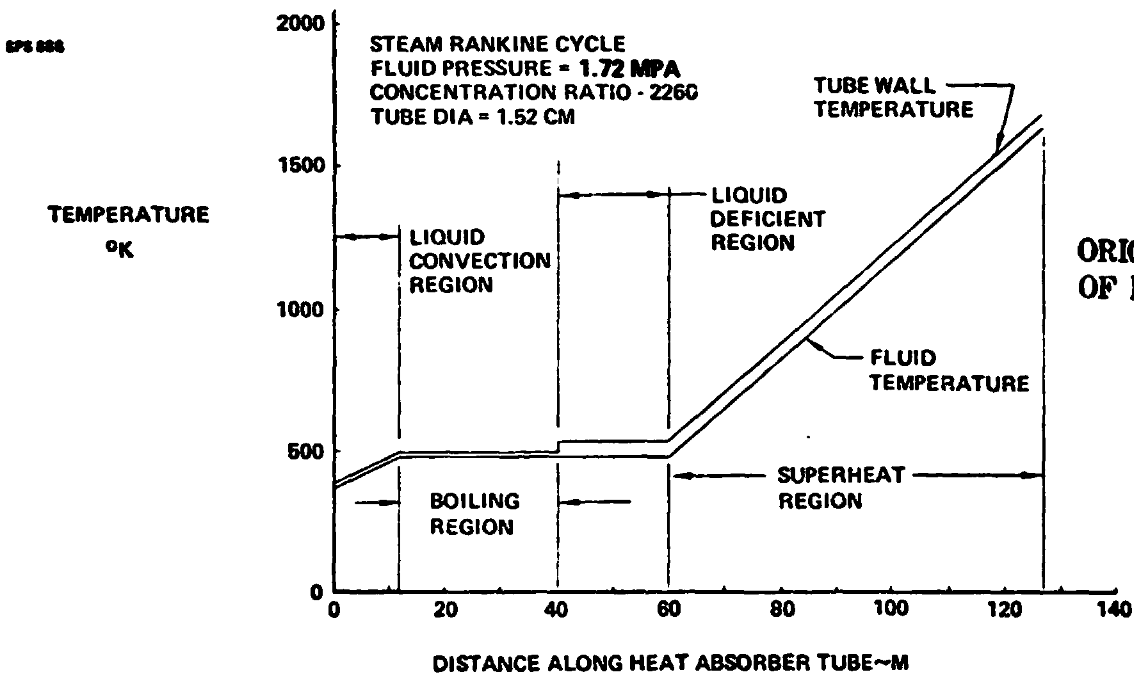

ORIGINAL PAGE IS OF POOR QUALITY

Figure 3.3-83 Fluid and Tube Wall Temperature Profiles Along Water Heat Absorbers

Table 3.3-11 Heat Absorber Comparison

CYCLE	NUMBER OF TUBES	PRESSURE (PSIA)	TUBE DIAMETER (M)	TUBE LENGTH (M)				AVERAGE TUBE TEMPERATURE (°K)			
				SUBCOOLED LIQUID	BOILING	LIQUID DEFICIENT	SUPERHEAT & REHEAT	SUBCOOLED LIQUID	BOILING	LIQUID DEFICIENT	SUPERHEAT & REHEAT
• BRAYTON BASELINE 1644°K TURBINE INLET	24800	3.45	.0125	← 4.516 →				← 1421 (AVE) →			
• POTASSIUM RANKINE 1644°K TURBINE INLET	1000	3.44	.0152	27	47	31	-	1264	1647	1676	-
• POTASSIUM RANKINE 1422°K TURBINE INLET	1000	1.385	.0152	23	65	44	-	1153	1425	1448	-
• STEAM RANKINE 1644°K TURBINE INLET 250 PSIA BOILER PRESS.	2000	1.72	.0152	5.8	14.0	9.4	39.0	447	483	560	1130
• STEAM RANKINE 811°K TURBINE INLET 3000 PSIA BOILER PRESS.	2000	20.7	.0305	11.9	3.0	2.1	11.0	561	646	715	864

ORIGINAL PAGE IS
OF POOR QUALITY

3.3.7 Thermal Engine Structures Analysis

The thermal engine systems utilized the same main structure beams as designed for photovoltaics (section 3.2.6). Since internal material stretching loads were not present, design loading conditions were not identified except for one condition appearing in the self-powered orbit transfer situation. Figure 3.3-84 shows an end view of one module of a 16 module SPS. After construction in low earth orbit, electric thrust is applied to accelerate the module. The thrust is shown here as being applied at each side and directed upward. This is merely one of the orientations which the thrust will take as the module rotates about the earth. However, in this orientation the thrust will tend to buckle the 20 meter beam support arms. Analysis of the resultant loads as shown that the beam support arms have a factor of safety more than 2 for this condition.

3.3.8 Thermal Engine Mass Properties

Thermal engine mass properties analyses concentrated on the radiator as the most massive system element. Mass estimating was performed primarily on a parametric basis.

Figure 3.3-85 shows a breakdown of the mass of all of the radiators in a 10 gigawatt ground output Brayton SPS, i.e., the mass of all 64 radiators for 64 turbomachine sets. The dominant element is the panels, heatpipes plus through-pipes, shown here without the water which fills the heatpipes. Next in order of significance is the NaK (sodium-potassium eutectic) which fills the through-pipes, headers and manifolds. Finally, the water manifolds, pumps, etc., which form a relatively small portion of the overall system mass.

The pumps include a redundant set for both the hot and the cold (or return) sides. That is, each pump has a redundant or matching pump to reduce the time between servicing periods on the pump set.

Figure 3.3-86 mass statement is for a 10 gigawatt ground output Brayton SPS. Note that the radiator system dominates, approximately 31 million kilograms out of the total of approximately 80 million kilograms. Elements such as the structure, turbo machines, cavities, etc., are relatively light. The mass of the facets includes the structure to tension the plastic film supported, etc. Thus, the structural mass of the satellite is truly the sum of the mass given here under structure, plus much of the mass given under facets.

Figure 3.3-87 presents the mass statement for the comparable potassium Rankine SPS.

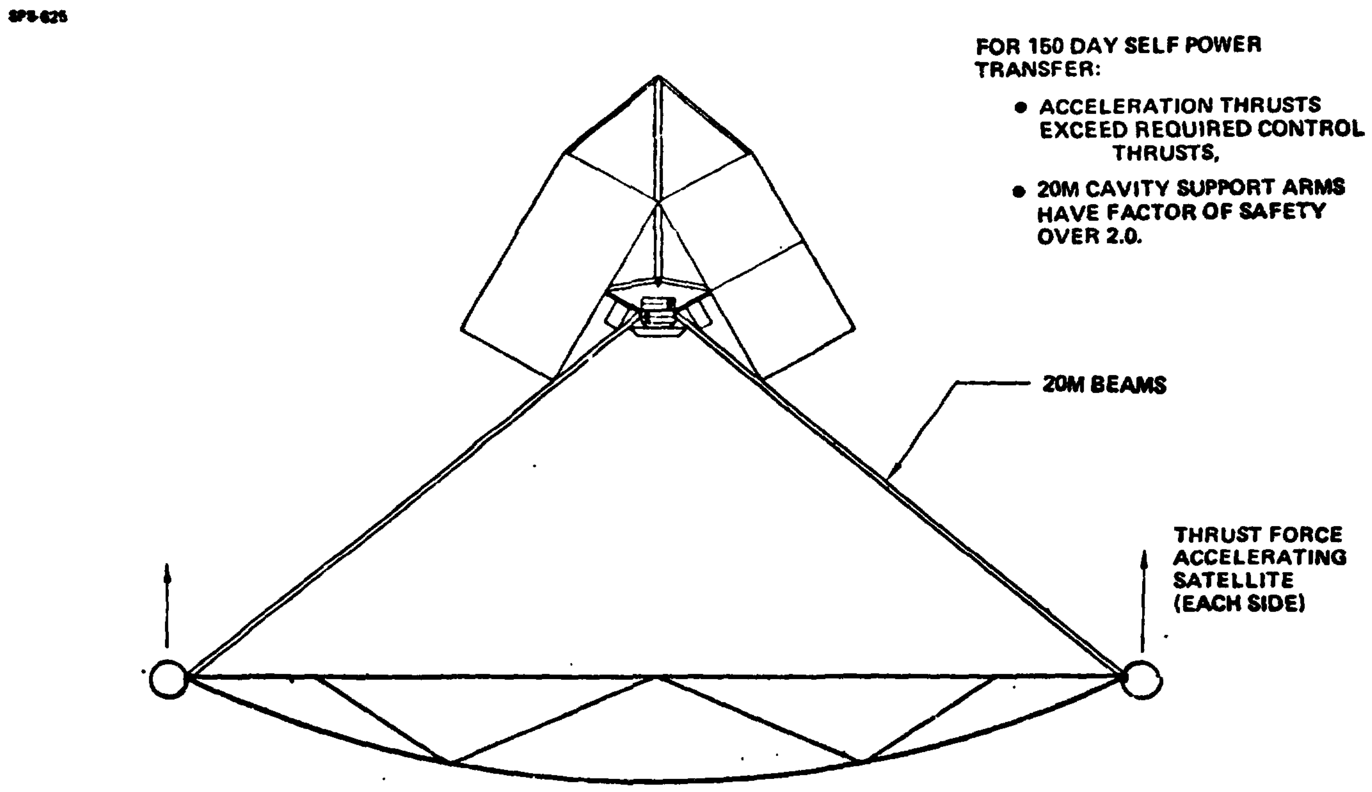

Figure 3.3-84 Impact of LEO Assembly on Thermal Engine SPS Gravity Gradient Forces

ORIGINAL PAGE IS
OF POOR QUALITY

SPS-617

ITEM	10^6 kg	
5 X 20 m PANELS, WITH WATER*	19.296	
MANIFOLDS		
"HOT"*	0.166	
"COLD"*	0.276	
HEADERS		
"HOT"*	0.172	
"COLD"*	0.040	
PUMPS/MOTORS "HOT"	0 211	(INCLUDES REDUNDANT SET)
"COLD"	0.150	(INCLUDES REDUNDANT SET)
ISOLATION VALVES	0.148	
ACCUMULATORS	0.056	
METEOROID BUMPERS	0.096	
NaK INVENTORY	10.134	
DUCT MOUNTS	0.039	
INSULATION FOR ADJACENT STRUCTURE	0.167	
TOTAL/SPS	30.961	

*MINIMUM FACTOR OF SAFETY OF 1.5

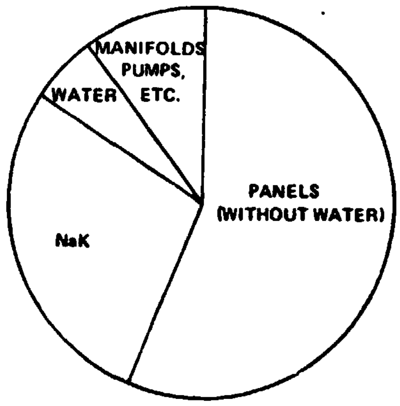

MASS BREAKDOWN

Figure 3.3-85 Radiator Mass Breakdown–Brayton SPS

SPS-628

ITEM	10^6 Kg
RADIATOR SYSTEM	30.951
TRANSMITTERS & SLIP RINGS	15.370
PRIMARY HEAT ABSORBER	9.070
RECUPERATOR/COOLERS	4.860
GENERATORS	4.320
FACETS, INCLUDING STRUCTURE*	4.200
POWER DISTRIBUTION	3.370
STRUCTURE	2.730
TURBOMACHINES	1.950
CAVITY ASSEMBLIES	1.420
GENERATOR COOLING	0.620
SWITCH GEAR	0.400
ATTITUDE CONTROL/STATION KEEPING	0.340
LIGHT SHIELD ASSEMBLIES	0.200
ONE YEAR's CONSUMABLES	0.200
BRAYTON SPS	79.601

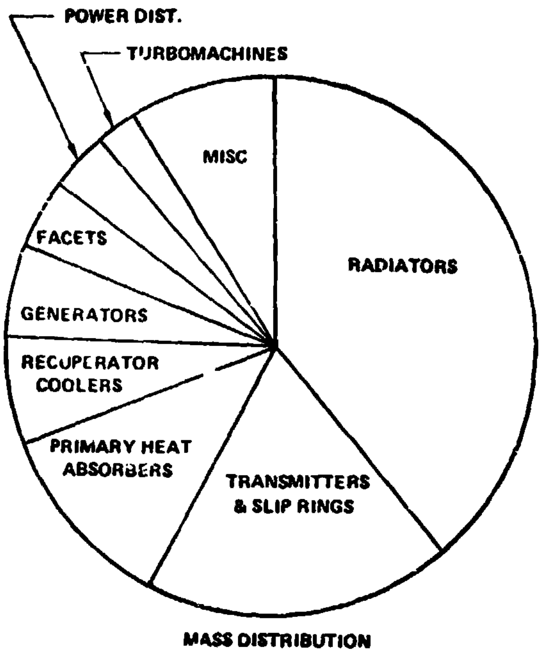

*STRUCTURE SYSTEM ASSOCIATED WITH PLASTIC FILM TENSIONING

Figure 3.3-86 Brayton SPS Mass Statement

SPS-635

RADIATOR SYSTEMS	10 432**
TRANSMITTER & SLIPRINGS	15.370
PRIMARY HEAT ABSORBERS	17.130**
GENERATORS	4.230
FACETS, INCLUDING STRUCTURE*	5.687
POWER DISTRIBUTION	3.919
STRUCTURE	3.696
HIGH PRESSURE TURBINES $\left(^{+15\%}_{-60\%}\right)$	3.690
LOW PRESSURE TURBINES $\left(^{+15\%}_{-60\%}\right)$	21.816
CAVITY ASSEMBLIES	1.923
GENERATOR COOLING	0.607
SWITCH GEAR	0.400
ATTITUDE CONTROL, STATION KEEPING	0.374
LIGHT SHIELD ASSEMBLY	0.270
ONE YEAR'S CONSUMABLES	0.220
RANKINE SPS	89.764

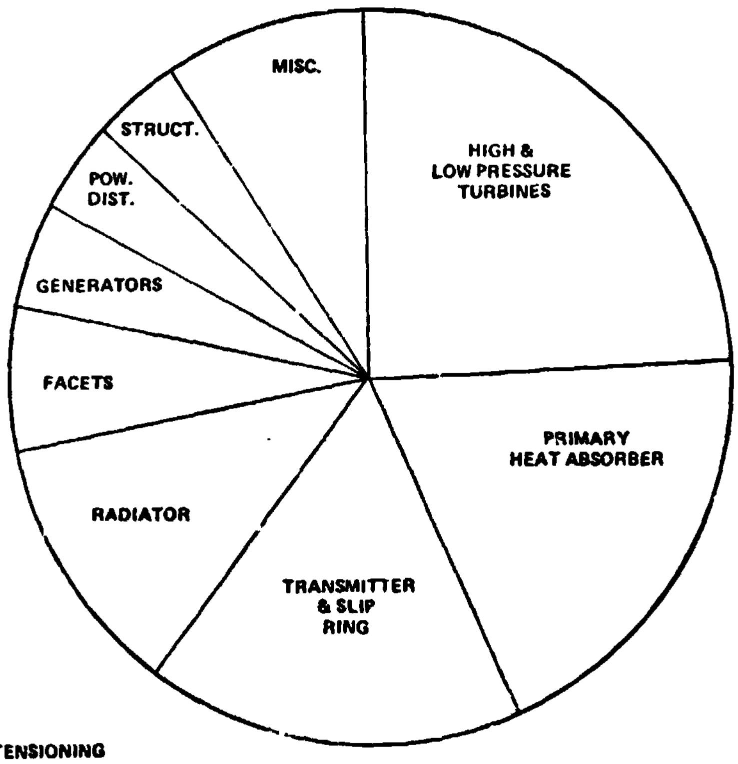

*STRUCTURE SYSTEM ASSOCIATED WITH PLASTIC FILM TENSIONING
**INCLUDING POTASSIUM

MASS DISTRIBUTION

Figure 3.3-87 Preliminary Rankine Mass Statement (165K Turbine Temperature)

3.3.9 Thermal Engine SPS Packaging

Components of thermal engine satellites have been found to be relatively low in density with the exception of a few components. The major components, density and number of flights required with the initial packaging approach (initial design and no component mixing) and the number required for a mass limited condition (82 million kg satellite excluding MPTS) is shown in Table 3.3-12.

The dominating feature of this data is that the number of flights resulting from initial packaging densities exceed a mass limited packaging case by over 400. Further inspection indicates the biggest gain in reducing the actual number of flights can be obtained by further investigation of the radiator panel/header components. Consequently, the following design modifications were incorporated:

a. Removal of the bulky meteoroid bumpers from the NaK throughpipes of the radiator panels; the heat pipes which wrap around the throughpipes provide sufficient protection.

b. Change of the reflector facet edge members to a design which flattens for packaging (Figure 3.3-88).

c. Modification of the radiator panels to not incorporate pre-attached headers.

As a result of these modifications the number of flights was reduced from over 635 to 420.

Since 420 flights is still more than two hundred over the mass limited condition, an additional approach was taken to reducing the number of flights. This was to include more than one type of component in each launch. The result of this approach was to reduce the number of flights to 237. Included in this quantity were 14 expendable shroud flights to accommodate very low density components. Use of recoverable shrouds for these flights would have required 28 flights instead of 14 and resulted in a cost penalty of over $60 million as compared to expending shrouds. A graphical representation of the change in number of flights and the number of flights with multiple component types is shown in Figure 3.3-89.

Payload shroud volume utilization for the thermal engine satellite is generally greater than 90% since the majority of the volume was required to reach a mass limited condition.

As a final note on thermal engine satellite packaging, it should be stated that although the number of flights exceeded the mass limited number of flights by 28 (13%) it is assumed with further design and packaging analysis the number of flights can reach a mass limited condition.

ORIGINAL PAGE IS
OF POOR QUALITY

Table 3.3-12 Thermal Engine Payload Packaging—One Component Type per Launch

[illegible]

1 RECOVERABLE SHROUD ALLOWS 70 KG/M^3

COMPONENT TYPE	PACKAGE 1 DENSITY (KG/M^3)	LAUNCH LIMIT		EST. NO. OF FLIGHTS
		MASS	VOLUME	
BEAMS				
20 METER	850	✓		4
5 METER	TBD			
1.5 METER	TBD			
FACETS				
HUB/RADIALS	5		✓	97
EDGE/PLASTIC	30		✓	21
RADIATORS				
PANELS/HEADERS	40		✓	332
MANIFOLDS	35		✓	7
NAK	900	✓		59
CAVITY				
BASIC PANELS	55		✓	22
RECUPERATOR	65		✓	43
TURBINE	145	✓		21
OTHER	30		✓	26

TOTAL FLIGHTS (ONE COMPONENT TYPE) 632

FLIGHT QUANTITY IF MASS LIMITED 206

ORIGINAL PAGE IS
OF POOR QUALITY

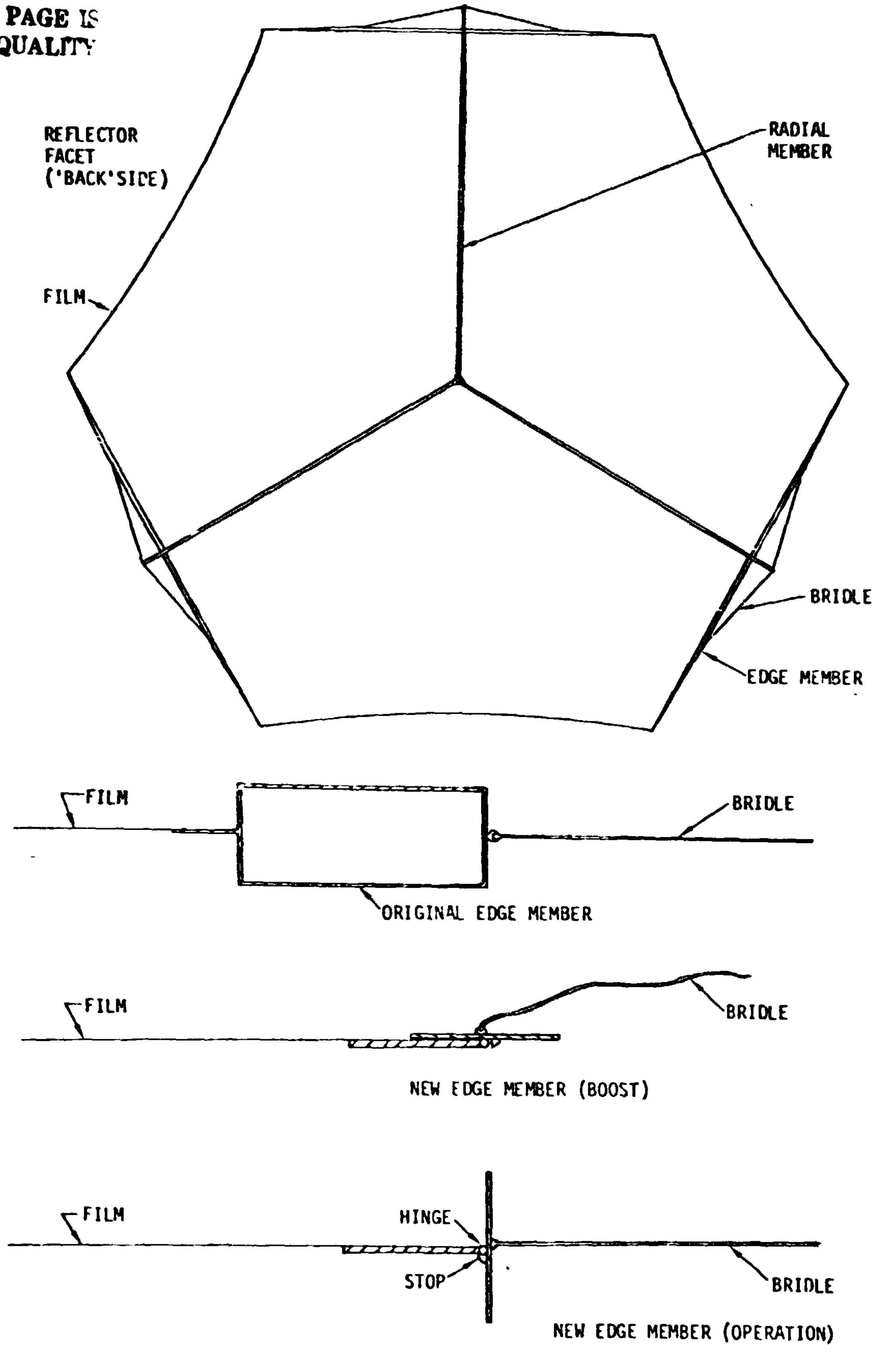

Figure 3 3-88 Facet Changes for Higher Packing Density

ORIGINAL PAGE IS
OF POOR QUALITY

3.3.10 Thermal Engine Reliability and Maintenance

3.3.10.1 Turbomachine Experience

Inspection and maintenance procedures for central power generation station and marine steam turbines in the 300 MW size range are well established. Frequency of inspection is dependent on the type of service experienced by the turbine. For the case of turbines in continuous service the normal inspection period is 5 years. Turbines subjected to intermittent service require more frequent inspections due to greater blade and bearing wear during start and stop transients. Downtime for inspection and preventative maintenance is approximately 5 to 6 weeks with a cost of $300,000 to $400,000.

Steam turbine blade life, based on General Electric field service experience is up to 30 years for condensing turbines and greater than 30 years for noncondensing turbines. Blade replacement costs are greatest for the lower pressure stages where wheel diameter and blade length are greatest.

- Re-blading cost

  Last stage: $200,000 to $300,000 plus labor
  High-pressure stages: $80,000 to $100,000 plus labor

In addition to longer blade life, noncondensing turbines allow higher wheel speeds with resulting improved efficiency and relaxed turbine mounting frame stiffness and alignment requirements.

3.3.10.2 Failure Rate and Maintenance Requirement Estimates

Failure rates and maintenance requirements for thermal engines appear acceptable (MTBF's are much shorter, but the number of components is proportionately smaller), except for leakage of fluid systems.

Fluid leakage in NaK systems may be a problem unless leakage MTBF's much lower than representative industry experience can be obtained. This indicates a need for a technology advancement program to develop the necessary joint reliability. NaK leakage data were primarily from experimental hardware and probably reflect technical immaturity. Results are summarized in Table 3.3-13. A summary of source data is provided in Table 3.3-14.

Table 3.3-13 Failure Rate and Maintenance Requirement Estimates

THERMAL ENGINE SPS

EQUIPMENT NOMENCLATURE		QUANTITY PER SPS (NHA)	FAILURE OR SCHEDULED MAINT.	MAINT. CONCEPT	MAINT. EQUIP.	LOGISTICS CONCEPT	GND. PWR. LOSS (KN)	MTBF OR MTBM	REPAIR RATE	MTTR	PWR. LOSS DUE TO (KWG)/HR MAINT.
2.0	POWER GEN.	4									
2.1	SOLAR CONCENTRATOR	4									
2.1.1	FACET POINTING	87,300					1.15×10^2	(6.1×10^4)	(1.43)	5	822
2.1.1.1	ALIGNMENT SUBSYSTEM	4									
2.1.1.1.1	LIGHT SOURCE	12	• FAILS	• REMOVE & REPLACE	• FREE FLYER	• REDUNDANT ITEM, SPARES IN ORBIT		400	.03	–	
2.1.1.1.2	MIRROR ASSY	4	• FAILS	• REMOVE & REPLACE	• FREE FLYER	• SPARES IN ORBIT		–			
2.1.1.2	ERROR DETECTOR SUBSYSTEM	87,300	• OPEN CIRCUIT, LOGIC ERROR, LOOSE CONNECTION FAILED ELEMENT	• REMOVE & REPLACE DURING SCHEDULED MAINT. CYCLE	BEAM WALKER	• SPARES AVAILABLE DURING MAINT. CYCLE			(.30)		
2.1.1.2.1	DETECTOR TUBE	87,300					1.15×10^2	6.3×10^7	1.4×10^{-3}		
2.1.1.2.2	ERROR ELECT.	87,300					1.15×10^2	2.9×10^6	.31		
2.1.1.3	POWER SOURCE	87,300	• OPEN CIRCUIT, SHORT, FAILED REGULATOR	• REMOVE & REPLACE DURING SCHEDULED MAINT. CYCLE	BEAM WALKER	• SPARES AVAILABLE DURING MAINT. CYCLE			(.32)		
2.1.1.3.1	SOLAR CELLS ASSY	87,300					1.15×10^2	7.1×10^6	.012		
2.1.1.3.2	POWER REG.	174,600					1.15×10^2	9.8×10^6	.31		
2.1.1.4	ACTUATORS ASSY	174,600	• ACTUATOR FAILURE, ELECT. FAILURE	• REMOVE & REPLACE DURING SCHEDULED MAINT. CYCLE	BEAM WALKER	• SPARES AVAILABLE DURING MAINT. CYCLE			(.77)		
2.1.1.4.1	DRIVER AMP'S	349,200					1.15×10^2	1.0×10^6	.36		
2.1.1.4.2	ACTUATORS	349,200					1.15×10^2	8.3×10^5	.42		

ORIGINAL PAGE IS OF POOR QUALITY

Table 3.3-13 (Continued)

THERMAL ENGINE SPS

EQUIPMENT NOMENCLATURE	QUANTITY PER SPS (MHA)	FAILURE OR SCHEDULED MAINT.	MAINT. CONCEPT	MAINT. EQUIP.	LOGISTICS CONCEPT	GND.PWR. LOSS (KW)	MTBF OR MTBM	REPAIR RATE	MTTR	PWR. LOSS DUE TO MAINT. (KM)/HR
2.0 POWER GEN. (CONT.)										
2.2 CAVITY ABSORBER PNL	1624							-		
2.2.1 INSULATION										
2.2.2 DUCTING JOINTS	6762	LEAK	REPAIR OR REPLACE	BEAM WALKER OR FREE FLYER	REPAIR EQUIP. & SPARES IN ORBIT	*3.12×10^5	2×10^9	3.28×10^{-6}	60	63
2.2.3 ABSORBANT	-					-	-	-		
2.3 TURBINE MACH.	64	(FAILURES FROM ALL CAUSES)	REPAIR IN PLACE OR REMOVE & REPLACE	BEAM WALKER OR FREE FLYER	SPARES IN ORBIT	*3.12×10^5	(2.5×10^4)	(2.6×10^{-3})	200	1.8×10^5
2.3.1 & 2.3.2 TURBINE & COMP.	64					*3.12×10^5	8×10^4	6×10^{-4}		
2.3.3 GENERATOR	64					*3.12×10^5	3.33×10^5	1.92×10^{-4}		
2.3.4 & 2.3.5 RECUP./COOLER	64					*3.12×10^5	6.25×10^4	1.02×10^{-3}		
2.3.6 BYPASS REG. VALVE	64					*3.12×10^5	1.04×10^5	6.15×10^{-4}		
						*2 GENS. DOWN				

Table 3.3-13 (Continued)

		QUANTITY PER SPS (MHA)	FAILURE OR SCHEDULED MAINT	MAINT. CONCEPT	MAINT. EQUIP.	LOGISTICS CONCEPT	GND PWR LOSS (KW)	MTBF OR MTBM	REPAIR RATE	MTTR	PWR. LOSS DUE TO MAINT. (KWH)
4.0	POWER DISTRIBUTION										
4.1	CONDUCTOR SYSTEM										
4.1.1	CONDUCTOR										
4.1.1.1	MODULE ACQUISITION BUS	36	• BREAK IN CONDUCTOR	• SPLICE BROKEN SECTION AFTER ISOLATION	BEAM WALKER OR FREE FLIER	SPARE CONDUCTOR & SPLICE MATERIALS	3.13×10^6	1×10^8	3.8×10^{-6}	15	.17
4.1.1.2	MAIN BUS	6	• BREAK IN CONDUCTOR	• SPLICE BROKEN SECTION AFTER ISO.	BEAM WALKER OR FREE FLIER	SPARE CONDUCTOR & SPLICE MATERIALS	2.8×10^6	1×10^8	6×10^{-6}	15	.23
4.1.2	TERMINATIONS	154	• BREAK IN TERMINATION	• ISOLATE & REPLACE	BEAM WALKER OR FREE FLYER	SPARE INTERCONNECTS	1.86×10^5	3.0×10^8	7.7×10^{-8}	6.8	.07
4.1.3	INSTALLATION DEVICES (INSULATORS, SUPPORTS ETC.)	36,000	• BROKEN INSULATOR	• REPLACE (CANNOT DETECT FROM PERF DATA	BEAM WALKER OR FREE FLIER	SPARE INSULATORS & SUPPORT MATERIAL	NEG.	1×10^8	3.8×10^{-6}	6.0	-
			• SHORTED OR LEAKY INSULATOR	• ISOLATE & REPLACE	BEAM WALKER OR FREE FLYER	SPARE INSULATORS	NEG.				
4.2	SWITCHGEAR	74									
4.2.1	DISCONNECTS	80	• INTERMITTENT OR UPON CONTACT	• ISOLATE & ADJUST OR REPLACE	BEAM WALKER OR FREE FLYER	SPARE DISCONNECTS (REPAIR AT DEPOT)	1.86×10^5	2.13×10^6	3.76×10^{-6}	13	76.3
			• FAILURE IN MECHANISM	• ISOLATE & ADJUST OR REPLACE	BEAM WALKER OR FREE FLYER	SPARE DISCONNECTS (REPAIR AT DEPOT)					
4.2.2	ZERO CURRENT SIMULATION DEVICES	74									
4.2.2.1	INDUCTORS	74	• OPEN OR SHORTED WINDINGS	• ISOLATE & REPLACE	BEAM WALKER OR FREE FLYER	SPARE INDUCATORS (REPAIR AT DEPOT OR SCRAP)	1.86×10^5	1.67×10^6	4.4×10^{-7}	13	.89
4.2.2.2	CAPACITORS	74	• SHORTED OR FAILURE TO IGNITE	• ISOLATE & REPLACE	BEAM WALKER OR FREE FLYER	SPARE CAPACITORS (SCRAP)	1.86×10^5	6.6×10^6	1.32×10^{-6}	13	26.0
4.2.2.3	SPARK GAP	74	OPEN OR SHORTED	• ISOLATE & REPLACE	BEAM WALKER OR FREE FLYER	SPARE SPARK GAPS (REPAIR OR SCRAP AT DEPOT)	1.86×10^5				
			• SCHEDULED REPLACE MENT BASED ON NO. OF CYCLES	• ISOLATE & REPLACE	BEAM WALKER OR FREE FLYER	SPARE SPARK GAPS (REPAIR AT DEPOT)					
4.2.3	DC INTERRUPTERS	74	• FAILURE TO OPERATE	• ISOLATE & REPLACE	BEAM WALKER OR FREE FLYER	SPARE D.C. INTERRUPTER (REPAIR AT DEPOT)	1.86×10^5	2.3×10^6	3.2×10^{-6}	12	80.0
			• SCHEDULED INSPECTION	• ISOLATE, INSPECT, REPLACE IF REQ'D.	BEAM WALKER OR FREE FLYER	SPARE D.C. INTERRUPTER (REPAIR AT DEPOT)					

ORIGINAL PAGE IS OF POOR QUALITY

Table 3.3-13 (Continued)

THERMAL ENGINE SPS

EQUIPMENT NOMENCLATURE		QUANTITY PER SPS (MHA)	FAILURE OR SCHEDULED MAINT.	MAINT. CONCEPT	MAINT. EQUIP.	LOGISTICS CONCEPT	GND PWR LOSS (KN)	MTBF OR MTBM	REPAIR RATE	MTTR	PWR LOSS DUE TO MAINT (KM)
4.0	POWER DISTRIBUTION (CONTINUED)										
4.3	POWER CONVERTER (DC/DC, DC/AC)	9	• FAILS TO REGULATE OR PROVIDE OUTPUT	• ISOLATE & REPLACE CONVERTER	• BEAM WALKER OR FREE FLYER	• SPARE CONVERTER (REPAIR AT DEPOT)	0	(1.62×10^{5})	5.6×10^{-6}		
4.3.1	TRANSFORMERS		• OPEN OR SHORTED WINDINGS	• ISOLATE & REPLACE CONVERTER	• BEAM WALKER OR FREE FLYER	• SPARE CONVERTER (REPAIR AT DEPOT)		1.33×10^{5}			
4.3.2	SEMICONDUCTORS										
4.3.2.1	THYRISTORS		• FAILED THYRISTOR	• ISOLATE & REPLACE CONVERTER	• BEAM WALKER OR FREE FLYER	• SPARE CONVERTER (REPAIR AT DEPOT)		2.33×10^{7}			
4.3.2.2	DIODES		• FAILED	• ISOLATE & REPLACE CONVERTER	• BEAM WALKER OR FREE FLYER	• SPARE CONVERTER (REPAIR AT DEPOT)		2.33×10^{7}			
4.3.2.3	TRANSISTORS		• FAILED	• ISOLATE & REPLACE CONDUCTER	• BEAM WALKER OR FREE FLYER	• SPARE CONVERTER (REPAIR AT DEPOT)		2.86×10^{5}			
4.3.2.4	INTEGRATED CIRCUITS		• FAILED	• ISOLATE & REPLACE CONVERTER	• BEAM WALKER OR FREE FLYER	• SPARE CONVERTER (REPAIR AT DEPOT)		1.67×10^{6}			
4.3.3	INDUCTORS		• FAILED-OPEN OR SHORTED	• ISOLATE & REPLACE CONVERTER	• BEAM WALKER OR FREE FLYER	• SPARE CONVERTER (REPAIR AT DEPOT)		6.56×10^{6}			
4.3.4	CAPACITORS		• FAILED	• ISOLATE & REPLACE CONER	• BEAM WALKER OR FREE FLYER	• SPARE CONVERTER (REPAIR AT DEPOT)		$3.33 \times 1.^{7}$			
4.3.5	RESISTORS		• FAILED	• ISOLATE & REPLACE CONVERTER	• BEAM WALKER OR FREE FLYER	• SPARE CONVERTER (REPAIR AT DEPOT)		1.0×10^{4} (SOLDERED)			
4.3.6	CONNECTIONS		• FAILED	• ISOLATE & REPLACE CONVERTER	• BEAM WALKER OR FREE FLYER	• SPARE CONVERTER (REPAIR AT DEPOT)					

Table 3.3-13 (Continued)

THERMAL ENGINE SPS

EQUIPMENT NOMENCLATURE	QUANTITY PER SPS(NHA)	FAILURE OR SCHEDULED MAINT.	MAINT. CONCEPT	MAINT EQUIP	LOGISTICS CONCEPT	GND PWR LOSS (KW)	MTBF OR (MTBM)	REPAIR RATE	MTTR	PWR LOSS DUE TO MAINT (KW-HR)
7.0 THERMAL CONTROL	-									
7.1 POWER GEN.	64									
7.1.1 PUMP SUBSYSTEM	64	-								
7.1.1.1 NaK PUMP	(3)	• FAILS TO PUMP	• REMOVE & REPLACE	• FREE FLYER [1]	• SPARES IN ORBIT	*3.12×10^5	10^4	.019	50	
7.1.1.2 DRIVE MOTOR	(3)	• FAILS TO DRIVE PUMP	• REMOVE & REPLACE	• FREE FLYER [1]	• SPARES IN ORBIT	*3.12×10^5	4.8×10^4	.004	6	
7.1.1.3 CONTROLS	(3)	• FAILS TO OPERATE PUMP	• REMOVE & REPLACE	• FREE FLYER [1]	• SPARES IN ORBIT	*3.12×10^5	1.8×10^4	.01	6	
7.1.2 MANIFOLD SS.	64	-								
7.1.2.1 DUCTING	(66)	• LEAK OR PLUG BREAK	• REPAIR LEAK OR R. & REPLACE	• FREE FLYER [1]	• SPARE MANIFOLDS & DUCT REPAIR CAP.	*3.12×10^5	1.5×10^4	.26	60	
7.1.2.2 SUP. STRUCTURE			• REPAIR	• FREE FLYER [2]	• REPAIR MATERIALS			-		
7.1.3 RADIATOR PNLS	24,576	• LEAK OR PLUG	• ISOLATE FROM SYSTEM REPAIR DURING REGULAR OR ROUTINE MAINTENANCE CYCLES							
7.1.3.1 VALVES	(2)	• FAIL OR LEAK		• FREE FLYER [1]	• SPARE PNLS AVAIL. DURING MAINT. CYCLES		1.7×10^4	2.8	60	
7.1.3.2 NaK DUCTS	(5/2)	• LEAK					1.5×10^4	4.1	60	
7.1.3.3 HEAT PIPES	(1160)	• LEAK					[1]			

*2 GEN'S DOWN

[1] NO FAILURES IN 30,000 HRS OF TEST OPERATION

ORIGINAL PAGE IS OF POOR QUALITY

Table 3.3-14 Source Data—Failure Rate and Maintenance Requirement Estimates

THERMAL CYCLE SOLAR POWER SATELLITE

	MTBF (HRS)	FAIL/10^6 OPER HRS	ENVIRO	ADJ FAC	ADJ VALUE FAIL/10^6 HRS	MTTR	SOURCE
FACET POINTING							
ALIGNMENT							
LASAR	400	2500	SPC	NONE	2500		L460-77-3
PRISM CAVITY,CERAMIC							
ERROR DETECTOR							
TUBES, METAL	476,190	2.1	GND	2	1.05		RADC-TR-75-22 PG 2-101
SENSORS, SILICON SOLAR CELL	-	.002	SPC	NONE	.002		D180-18389-1, PG 69
INTEGRATED CIRCUITS (500G)	285,714	3.5	SPC	NONE	3.5		THERMOELECTRIC OUTER PLANETS SPACECRAFT,*
POWER SOURCE							
SOLAR CELL ARRAYS	R=.99984		SPC				D2-114080-1, PG 19
REGULATORS	555.556	1.80	CMP LAB	NONE	1.80		D2-AGM12101-1
ACTUATORS							
DRIVER AMPLI SOLID STATE (DETECTOR TUBE)	1,000,000	1.0	SPC	NONE	1.0		MDFR-0674, PG 65
DRIVER AMPLI SOLID STATE (FACETS)	1,000,000	1.0	SPC	NONE	1.0		MDFR-0674, PG 65
ACTUATORS-BI METALLIC ELECT (DETECTOR TUBE)	6250	160.0	ACFT-FLT	40	4.0		FRD VOL I, PG 3
ACTUATORS-BI METALLIC (FACETS)	6250	160.0	ACFT-FLT	40	4.0		FRD VOL I, PG 3

*28 SEP 71

Table 3.3-14 (Continued)

THERMAL CYCLE SOLAR POWER SATELLITE

	MTBF (HRS)	FAIL/10^6 OPER HRS	ENVIRO	ADJ FAC	ADJ VALUE FAIL/10^6HR	MTTR	SOURCE
FACETS							
FILM, REFLECTIVE							
FRAME							
PIVOT ASSY							
INSULATION							
DUCTING	16,667	60	ACFT-FLT	30	2.0		RADC-TR-75-22, PG 2-96
ABSORBANT							
TURBO MACHINERY							
AIR TURBINE COMPRESSOR	5,000	200	GND	4	50.0		LMEC 69-7 VOL I, TABLE 1-35, PG 428
GENERATOR (STD ALTENATOR) (40,000v)	83,333	12	GND	4	3.0		RADC-TR-75-22, PG 2-176
ELECT AUX PWR UNITS	51,867	19.28	SHP	20	.96		FRD VOL I, PG 235
ELECT MOTORS	8,000	125	GND	3	41.67		LMEC 69-7 VOL I, PG 1-82
PUMPS (GAS)	40,000	25	GND	2	12.5		RADC-TR-75-22, PG 2-193

ORIGINAL PAGE IS OF POOR QUALITY

Table 3.3-14 (Continued)

THERMAL CYCLE SOLAR POWER SATELLITE

	MTBF (HRS)	FAIL/10^6 OPER HRS	ENVIRO	ADJ FAC	ADJ VALUE FAIL/10^6 HRS	MTTR	SOURCE
HEAT TRANSFER							
CONDENSOR (COOLER)	8,000	125	GND	2	62.5		LMEC 69-7 VOLI, TABLE 1-74 PG 1-85
DUCTING (STAINLESS STEEL) 500-600 PSI	16,667	60	ACFT-FLT	30	2.0		RADC-TR-75-22, PG 2-96
JOINTS, WELDED	-	.0005	CMP LAB	NONE	.0005		D2 AGM 12101-1, PG 38
VALVE, REGULATOR	3,472	288	ACFT-FLT	40	7.2		FRD VOLI, PG 437
THERMAL CONTROL PWR GEN THERMAL CYCLE							
PUMP SUB SYS							
PUMP, LIQUID SODIUM	5,000	200	GND	2	100.0		LMEC 69-7 VOLI, TABLE 1-100 PG 1-263
CONTROLS	4,762	210	GND	4	52.5		LMEC 69-7 VOLI, TABLE 1-434 PG 1-445
TEMP SENSOR	6,711	148	GND	6	24.67		LMEC 69-7 VOL I, TABLE 1-161 PG 1-491
SERVO MOTOR CONTROL	1,250,000	.80	GND	11	.07		RADC-TR-75-22, PG 2-170
MOTOR ELECT DRIVE	8,000	125	GND	6	20.83		LMEC 69-7 VOL I, TABLE 1-34 PG 1-82

Table 3.3-14 (Continued)

THERMAL CYCLE SOLAR POWER SATELLITE

	MTBF (HRS)	FAIL/10^6 OPER HRS	ENVIRO	ADJ FAC	ADJ VALUE FAIL/10^6 HRS	MTTR	SOURCE
MANIFOLD SUB SYS							
DUCTING (15-20 PSI)	166,667	60	ACFT-FLT	30	2.00		RADC-TR-75-22, PG 2-96
RADIATOR PANELS							
VALVES, SODIUM	8,333	120	GND	2	60		LMEC VOL I, TABLE 1-126 PG 1-408
DUCTS, NA-K	7,500	133.33	GND	2	66.67		LMEC VOL I, TABLE 1-90 PG 1-216 TO 1-220
HEAT PIPE	30,000	33.33	GND	2	16.67		N544-77-3

ORIGINAL PAGE IS OF POOR QUALITY